

# Integrating Climate and Water Isotopologue Modelling with Geologic Archives for Reconstructing Paleoclimate Dynamics

## **Dissertation**

der Mathematisch-Naturwissenschaftlichen Fakultät  
der Eberhard Karls Universität Tübingen  
zur Erlangung des Grades eines  
Doktors der Naturwissenschaften  
(Dr. rer. nat.)

vorgelegt von  
**Daniel Boateng, M. Sc.**  
aus Kumasi/Ghana

Tübingen  
2024

Gedruckt mit Genehmigung der Mathematisch-Naturwissenschaftlichen Fakultät der Eberhard Karls Universität Tübingen.

Tag der mündlichen Qualifikation: 10.07.2024

Dekan:	Prof. Dr. Thilo Stehle
1. Berichterstatter:	Prof. Dr. Todd A. Ehlers
2. Berichterstatter:	Dr. Sebastian G. Mutz
3. Berichterstatter:	Prof. Dr. Kira Rehfeld

# Acknowledgments

Wow... it's finally over. Well, I am going to miss all the experiences, especially coding in my dreams... lol. My PhD journey has been a wild adventure, and I can confidently say that this journey has been filled with unexpected twists, sleepless nights, forgetting what weekends look like, and a relentless battle against procrastination. Through it all, I've come to appreciate the importance of *trusting the process* – even when that process seems to involve a lot of coffee, late-night epiphanies, and questionable life choices. Well, you are reading this because of consistency...hard work....and...confidence! First and foremost, I would like to thank my PhD advisors, Dr. Sebastian G. Mutz and Prof. Todd A. Ehlers, for their endless support throughout this journey over the past three years.

*Sebastian: You noticed my strengths and interests despite my convoluted background. Thank you for introducing me to the fascinating world of Climate Science and for always trusting my potential, allowing me to work independently. Your faith in my ability to navigate this complex field has not only guided my research but also shaped my academic career.*

*Todd: You've been an amazing mentor, and I am glad to have learned from your extraordinary experience. You provided all the resources and funds that contributed to my happy journey!*

I would also like to thank the ESD research group in Tübingen and Glasgow for being so friendly and helpful.

*Al Neely: You've been a great friend and an amazing senior scientist from whom I have learned a lot. Thanks for proofreading part of this thesis and for your constructive feedback to improve it. Well, I am going to miss all the Irish pub moments!*

I would also like to thank the **SPACY group in Tübingen** for welcoming me warmly into their group. I have learned a lot from everyone and enjoyed all the scientific discussions.

I would like to thank my collaborators for their contributions to the publications. It's been a pleasure working with you all!

*Armelle: You've been my PhD best friend. You have been very friendly, inclusive, and supportive, and I have learned a lot from you!*

I would also like to thank the administration in GUZ for their endless support. *Artur: You've been very supportive with all my complicated paperwork.* And to all my amazing friends in GUZ, thank you for the great discussions and for being part of this unforgettable journey.

Finally, I would like to express my gratitude to my family for their financial, emotional, and spiritual support.

*Most importantly, I am thankful to my beautiful wife, **Sethembele Patience Boateng**, for patiently supporting me from years 1 to 3. You've encouraged me, prayed for me, taken care of me, sacrificed for me, and been a great study partner.*

*I dedicate this thesis to my mother, **Afua Mansa**, who has effortlessly provided me with everything I need to be successful in life!*

Daniel Boateng  
Tübingen, May 21, 2024  
Trust the process...



# Abstract

Human activities are increasingly leading to the emission of greenhouse gases, altering the Earth's climate into an unprecedentedly warmer state, thus compromising our ability to devise effective adaptation strategies to climate change impacts. Although paleoclimates are not perfect analogues for these warming trends, understanding past climate dynamics provides valuable insights into future climate change. These past climates span a tremendous range of hydroclimates, landscapes, and biodiversity distributions that can contribute to our understanding of the key elements of the climate system and also serve as out-of-sample validations for the strength and stability of climate sensitivity and feedbacks in climate models to ensure accurate future projections. However, understanding the past is contingent upon the availability and accurate interpretation of climate signals from paleoclimate records. Stable isotope ratios of oxygen ( $O^{18}/O^{16}$ ;  $\delta^{18}O_p$ ) and hydrogen ( $D/H$ ;  $\delta D_p$ ) in water imprints in the hydrological cycle reflect many integrated processes of the Earth's system and form the basis of paleoclimate reconstruction. The interpretation of the isotopic composition of precipitation ( $\delta^{18}O_p$ ) signals from paleoclimate records faces significant challenges and uncertainties due to the wide range of large-scale and local climatic and environmental conditions that control its spatio-temporal variability. This implies that the  $\delta^{18}O_p$  signal requires the disentangling of climate signals from non-climate signals and needs paleoclimate-constrained transfer functions to ensure accurate interpretations. This thesis demonstrates how isotope-enabled General Circulation Models (iGCMs) can be combined with paleoclimate records to enhance the interpretability of paleoclimate dynamics. **Part 1** integrates iGCMs with stable isotope paleoaltimetry to reconstruct the Miocene Central Alps paleoelevation. Through topographic sensitivity and Middle Miocene climate experiments, the results show that using contemporary isotopic lapse rates overestimates the paleoelevation by ~1.5 km, suggesting the need for refining the previous estimates with iGCM-simulated paleoclimate-constrained isotopic lapse rates. **Part 2** presents an extensive suite of (paleo)climate experiments with iGCMs from present-day to Mid-Pliocene conditions to understand how large-scale atmospheric modes of variability (i.e., North Atlantic Oscillation and East Atlantic Oscillation patterns) and West African monsoon dynamics influence the regional hydroclimate and  $\delta^{18}O_p$  patterns across Europe and West Africa. Through statistical analysis (e.g., correlations and causality testing), the results indicate that the causal links between the local isotopic proxy and large-scale patterns and regional hydroclimate variables are significantly different under the varied past climates. This proposes the need to understand the time and space-dependent relations between proxy systems and regional paleoclimate dynamics to refine their transfer functions. Due to the computational cost of the proposed paleoclimate reconstruction framework, **Part 3** further explores the potential of using machine learning to emulate the spatio-temporal variability of  $\delta^{18}O_p$  values. The results indicated overall good performance that was at least better than iGCM. Altogether, the findings indicate the importance of combining water isotopologue information from observations, iGCMs, and isotopic paleoclimate records to provide robust statistical and dynamical constraints on paleoclimate reconstructions, which has huge implications for reducing the uncertainties of climate models and thus improving future climate projections.



# Zusammenfassung

Menschliche Aktivitäten führen zunehmend zur Emission von Treibhausgasen, die das Klima der Erde in einen noch nie dagewesenen wärmeren Zustand versetzen und unsere Fähigkeit beeinträchtigt, wirksame Anpassungsstrategien für die Auswirkungen des Klimawandels zu entwickeln. Obwohl Paläoklimata keine perfekten Analogien für diese Erwärmungstendenzen sind, bietet das Verständnis der Klimadynamik der Vergangenheit wertvolle Einblicke in den künftigen Klimawandel. Diese vergangenen Klimata umfassen eine enorme Bandbreite an Hydroklimata, Landschaften und Biodiversität, die zu unserem Verständnis des Klimasystems beitragen können. Zudem können sie und auch als Out-of-Sample-Validierung für die Stärke und Stabilität der Klimasensitivität und der Rückkopplungen in Klimamodellen dienen, um genaue Vorhersagen für die Zukunft zu ermöglichen. Das Verständnis der Vergangenheit hängt jedoch von der Verfügbarkeit und genauen Interpretation von Klimasignalen aus paläoklimatischen Aufzeichnungen ab. Die stabilen Isotopenverhältnisse von Sauerstoff und Wasserstoff im hydrologischen Kreislauf spiegeln viele Prozesse des Erdsystems wider und bilden die Grundlage für die Rekonstruktion des Paläoklimas. Die Interpretation der Isotopenzusammensetzung des Niederschlags ( $\delta^{18}O_p$ ) aus paläoklimatischen Aufzeichnungen ist mit erheblichen Herausforderungen und Unsicherheiten verbunden, da ein breites Spektrum großräumiger und lokaler Klima- und Umweltbedingungen ihre räumlich-zeitliche Variabilität bestimmt. Dies bedeutet, dass das  $\delta^{18}O_p$ -Signal eine Trennung von Klimasignalen von Nicht-Klimasignalen erfordert und Paläoklima-Transferfunktionen benötigt, um genaue Interpretationen zu gewährleisten. Diese Arbeit zeigt, wie isotopen-berücksichtigende allgemeine Zirkulationsmodelle (iGCMs) mit Paläoklimaaufzeichnungen kombiniert werden können, um die Interpretierbarkeit der Paläoklimadynamik zu verbessern. In **Teil 1** werden iGCMs mit Paläoaltimetrie mit stabilen Isotopen kombiniert, um die miozäne Paläohöhe der Zentralalpen zu rekonstruieren. Anhand von topographischen Sensitivitäts- und Klimaexperimenten aus dem mittleren Miozän zeigen die Ergebnisse, dass die Verwendung moderner Isotopengradienten die Paläohöhe um ~1,5 km überschätzt, was auf die Notwendigkeit hinweist, die früheren Schätzungen mit iGCM-simulierten Paläoklima-gebundenen Isotopengradienten zu verfeinern. **Teil 2** präsentiert eine umfangreiche Reihe von (Paläo-)Klimaexperimenten mit iGCMs in Zeiträumen von der Gegenwart bis zum mittleren Pliozän, um zu verstehen, wie großräumige atmosphärische Variabilitätsmodi (d. h. nordatlantische Oszillationsmuster und ostatlantische Oszillationsmuster) und die westafrikanische Monsun-Dynamik das regionale Hydroklima und  $\delta^{18}O_p$ -Muster in Europa und Westafrika beeinflussen. Durch statistische Analysen (z. B. Korrelations- und Kausalitätstests) zeigen die Ergebnisse, dass die kausalen Beziehungen zwischen den lokalen isotopischen Proxies und den großräumigen Mustern sowie den regionalen Hydroklimavariablen in den verschiedenen Paläoklimazonen signifikant unterschiedlich sind. Daher ist es notwendig, die zeit- und raumabhängigen Beziehungen zwischen den Proxies und der regionalen Paläoklimadynamik zu verstehen, um ihre Transferfunktionen zu verfeinern. Aufgrund der hohen Rechenkosten der Paläoklima-Rekonstruktionen wird das Potenzial des maschinellen Lernens zur Nachahmung der räumlich-zeitlichen Variabilität von  $\delta^{18}O_p$  in **Teil 3** weiter erforscht. Insgesamt zeigen die Ergebnisse, wie wichtig die Kombination von Wasserisotopologie-Informationen aus Beobachtungen, iGCMs und isotopischen Paläoklimaaufzeichnungen ist, um robuste statistische und dynamische Einschränkungen für Paläoklima-Rekonstruktionen zu liefern, was enorme Auswirkungen auf die Verringerung der Unsicherheiten von Klimamodellen und somit auf die Verbesserung zukünftiger Klimaprojektionen hat.





# Table of Contents

<b>Acknowledgments</b>	<b>iii</b>
<b>Abstract</b>	<b>v</b>
<b>Zusammenfassung</b>	<b>vii</b>
<b>Table of Contents</b>	<b>ix</b>
<b>Notation</b>	<b>xi</b>
<b>1. Introduction</b>	<b>1</b>
1.1. Paleoclimate as potential analogues for future climate . . . . .	2
1.2. Isotopic composition of water reflects changes in hydrological cycle . . . . .	4
1.3. Proxies for climate variables: Challenges and Uncertainties . . . . .	5
1.4. Water isotopologues in climate models and proxies . . . . .	7
1.5. Thesis structure . . . . .	9
<b>I. SCIENTIFIC MOTIVATION &amp; QUESTIONS</b>	<b>11</b>
<b>2. Background</b>	<b>13</b>
2.1. Reconstructing the paleoelevation of the European Alps . . . . .	13
2.2. West African monsoon dynamics and $\delta^{18}O_p$ changes in the Late Cenozoic . . . . .	16
2.3. Optimal locations for reconstructing the past variability of the North Atlantic Oscillation . . . . .	19
2.4. Machine learning based emulators for spatio-temporal variability of $\delta^{18}O_p$ . . . . .	21
<b>II. RESEARCH OBJECTIVES AND STRATEGIES</b>	<b>25</b>
<b>3. Objectives</b>	<b>27</b>
3.1. Part 1: Reconstructing the Paleoelevation of the Alps . . . . .	27
3.2. Part 2: Reconstructing Paleoclimate Dynamics . . . . .	30
3.3. Part 3: Machine Learning Framework for Predicting the Variability of local $\delta^{18}O_p$ values . . . . .	33
<b>III. RESULTS AND DISCUSSION</b>	<b>35</b>
<b>4. Results and Discussion</b>	<b>37</b>
4.1. Part 1: Reconstructing the Paleoelevation of the Alps . . . . .	37
4.2. Part 2: Reconstructing Paleoclimate Dynamics . . . . .	44
4.3. Part 3: Machine Learning Framework for Predicting the Variability of local $\delta^{18}O_p$ values . . . . .	51
<b>IV. CONCLUSION &amp; OUTLOOKS</b>	<b>57</b>
<b>5. Conclusions &amp; Outlooks</b>	<b>59</b>
5.1. Summary . . . . .	59
5.2. Future outlook . . . . .	63

<b>Bibliography</b>	<b>65</b>
<b>V. APPENDIX</b>	<b>89</b>
<b>Manuscripts for Part 1 (P1-P3)</b>	<b>91</b>
1. P1: Boateng et al. [1] . . . . .	91
2. P2: Botsyun et al. [2] . . . . .	120
3. P3: Boateng et al. [to be submitted] . . . . .	151
<b>VI. APPENDIX</b>	<b>205</b>
<b>Manuscripts for Part 2 (P4, S1)</b>	<b>207</b>
1. P4: Boateng et al. [3] . . . . .	207
2. S1: supporting results for NAO- $\delta^{18}O_p$ non-stationarity . . . . .	243
<b>VII. APPENDIX</b>	<b>249</b>
<b>Manuscripts for Part 3 (P5, S2)</b>	<b>251</b>
1. P5: Boateng and Mutz [4] . . . . .	251
2. S2: supporting results for predicting $\delta^{18}O_p$ variability across Europe . . . . .	288

# Notation

## Acronyms & Abbreviations

<i>E.g.</i> or <i>e.g.</i>	For example ( <i>exempli gratia</i> )
<i>Etc.</i> or <i>etc.</i>	And so on ( <i>et cetera</i> )
<i>I.e.</i> or <i>i.e.</i>	That is ( <i>id est</i> )
$p\text{CO}_2$	Atmospheric CO <sub>2</sub> concentrations
$\delta^{18}\text{O}_p$	isotopic composition of precipitation
$\delta^{18}\text{O}_w$	isotopic composition of paleo-meteoric water
AGCM	Atmospheric General Circulation Model
ARD	Automatic Relevance Determination regression
AEJ	African Easterly Jet
AMIP	Atmospheric Model Intercomparison Project
CV	Cross-Validation
CMIP	Coupled Model Intercomparison Project
EOF	Empirical Orthogonal Function
ENSO	El Niño-Southern Oscillation
EA	East Atlantic Oscillation
EA/WR	East Atlantic-Western Russia circulation pattern
ExtraTree	Extra Trees Regressor
GMST	Global Mean Surface Temperature
GCMs	General Circulation Models
GNIP	Global Network of Isotopic Composition of Precipitation
iGCMs	Isotope-enabled General Circulation Models
ITD	Inter-Tropical Discontinuity
ITCZ	Intertropical Convergence Zone
LIG	Last Interglacial
LGM	Last Glacial Maximum
LassoLarsCV	LassoLars regression with cross-validation
ka	kiloyears
Ma	Million years
MAE	Mean Absolute Error
ML	Machine learning
MLR	Multiple Linear Regression
MCO	Middle Miocene Climate Optimum
MioMIP	Miocene Modelling Intercomparison Project
MPI-ESM	Max Planck Institute for Meteorology Earth System Model
NAO	North Atlantic Oscillation patterns
PCA	Principal Component Analysis
PI	Pre-Industrial
PMIP	Paleoclimate Modelling Intercomparison Project
PP-ESD	Perfect Prognosis Empirical Statistical Downscaling
RandomForest	Random Forest Regressor
SCAND	Scandinavian oscillation patterns
SMB	Swiss Molasse Basin
SMC	Shallow Meridional Cell
Stacking	Stacked Generalization Ensemble
TEJ	Tropical Easterly Jet

## List of Publications

1. **(P1)** Boateng, D., Mutz, S. G., Ballian, A., Meijers, M. J. M., Methner, K., Botsyun, S., Mulch, A., and Ehlers, T. A.: The effects of diachronous surface uplift of the European Alps on regional climate and the oxygen isotopic composition of precipitation, *Earth System Dynamics*, 14, 1183–1210, <https://doi.org/10.5194/esd-14-1183-2023>, 2023.
2. **(P2)** Botsyun, S., Ehlers, T. A., Koptev, A., Böhme, M., Methner, K., Risi, C., Stepanek, C., Mutz, S. G., Werner, M., Boateng, D., and Mulch, A.: Middle Miocene Climate and Stable Oxygen Isotopes in Europe Based on Numerical Modeling, Paleoceanography and Paleoclimatology, 37, e2022PA004442, <https://doi.org/10.1029/2022PA004442>, 2022.
3. **(P3)** Boateng, D., et al. Refinement of Middle Miocene paleoelevation of the Alps through topographic sensitivity experiments and paleo-meteoric water isotopic composition modelling **[to be submitted]**.
4. **(P4)** Boateng, D., Aryee, J. N. A., Baidu, M., Arthur, F., and Mutz, S. G.: West African Monsoon dynamics and its control on stable oxygen isotopic composition of precipitation in the Late Cenozoic, *Journal of Geophysical Research: Atmospheres*, 129, e2024JD040748, <https://doi.org/10.1029/2024JD040748>, 2024.
5. **(P5)** Boateng, D. and Mutz, S. G.: pyESDv1.0.1: an open-source Python framework for empirical-statistical downscaling of climate information, *Geoscientific Model Development*, 16, 6479–6514, <https://doi.org/10.5194/gmd-16-6479-2023>, 2023.

## Declaration of author contributions

Here, I present my personal contributions as well as my co-authors as written in the individual manuscript from **P1-P5**. The authors are abbreviated by the first letter of their first and last names.

### 1. **(P1) Boateng et al. [1]**

**DB:** conceptualization, model simulation, data analysis, visualization, and writing of the original paper. **SGM, TAE:** conceptualization, supervision, funding acquisition, paper review and editing. **AM, MJMM, KM:** funding acquisition and paper review and editing. **AB, SB:** paper review and editing. All authors contributed to the discussion of the results.

### 2. **(P2) Botsyun et al. [2]**

**SB:** conceptualization, data curation, formal analysis, investigation, methodology, and writing - original draft. **TAE:** funding acquisition, supervision, visualization, and writing -review & editing. **AK:** conceptualization, methodology, visualization, and writing -review & editing. **MB:** data curation, investigation, validation, and writing -review & editing. **CR:** methodology and writing -review & editing. **KM:** investigation, validation, and writing -review & editing. **CS:** investigation, validation, and writing -review & editing. **SGM:** funding acquisition and writing -review & editing.

**DB:** visualization and writing -review & editing. **MW:** software, validation, and writing -review & editing. **AM:** validation and writing -review & editing.

### 3. **(P3) Boateng et al. [to be submitted]**

**DB:** conceptualization, model simulation, formal analysis, visualization, software, and writing of the original draft. **SGM, TAE:** supervision, funding acquisition, paper review and editing. **AM, MJMM, KM:** funding acquisition and paper review and editing. **AB:** data compilation and paper review and editing. All authors contributed to the discussion of the results.

### 4. **(P4) Boateng et al. [3]**

**DB:** conceptualization, model simulation, formal analysis, visualization, software, methodology, and

writing of the original paper. JA, MB; methodology, validation, and writing -review & editing. SGM: supervision, funding acquisition and writing -review & editing.

5. **(P5) Boateng and Mutz [4]**

**DB:** pyESD software and documentation website development, conceptualization, modelling, data analysis, visualization, and writing of the original paper. SGM: supervision, paper editing, and funding acquisition.



# List of Figures

1.1. Global mean surface temperature anomalies variability from Cenozoic (past 66 Ma) to future projections . . . . .	3
2.1. Conceptual sketch of stable isotope paleoaltimetry method . . . . .	15
2.2. West African Monsoon system (Precipitation and Temperature from ERA5 and Schematic illustration)	17
2.3. Schematic illustration for finding optimal locations of proxies for reconstructing NAO index . .	21
2.4. The main features and workflow of PP-ESD implemented in the pyESD package . . . . .	23
4.1. Comparison of simulated and reconstructed $\delta^{18}O_p$ values across the Alps in Middle Miocene .	40
4.2. Miocene Central Alps paleoelevation estimates based on Miocene simulated and modern observed isotopic lapse rates . . . . .	43
4.3. ECHAM5-wiso simulated MAP anomalies and its comparison with proxies over Africa for Mid-Pliocene and Mid-Holocene . . . . .	45
4.4. Northward extent of the WAM in the Mid-Holocene based on climate models and proxy reconstruction . . . . .	46
4.5. Correlation coefficients between $\delta^{18}O_p$ and (1) temperature and (2) precipitation in Pre-Industrial and Mid-Holocene across West Africa . . . . .	48
4.6. Correlation between $\delta^{18}O_p$ and climate variables for winter OP and EQ periods . . . . .	50
4.7. Comparison of selected GNIP stations to ECHAM5-wiso simulations across Europe . . . . .	53
4.8. IsoPP modelling framework and inter-model performance . . . . .	54
4.9. Prediction and evaluation examples of the final model (Stacking) outside the training period . .	55
1. S1.1: Empirical Orthogonal Functions of NAO and EA mode of variability . . . . .	243
2. S1.2: Comparison of winter NAO indices based on ECHAM5-wiso, station observations and ERA5 reanalysis datasets . . . . .	244
3. S1.3: Comparison of summer NAO indices based on ECHAM5-wiso, station observations and ERA5 reanalysis datasets . . . . .	244
4. S4: Correlation between NAO, EA indices and $\delta^{18}O_p$ , temperature and precipitation in winter .	245
5. S1.5: Correlation between NAO, EA indices and $\delta^{18}O_p$ , temperature and precipitation in summer	245
6. S1.6: Correlation between $\delta^{18}O_p$ and climate variables for summer OP and EQ periods . . . . .	246
7. S1.7: Correlation between $\delta^{18}O_p$ and climate variables for winter OP and EQ periods for the last millennium . . . . .	246
8. S1.8: Probability of no Granger causality . . . . .	247
1. S2.1: GNIP Stations availability overview . . . . .	288
2. S2.2: Predictor importance and correlation between potential predictors and station $\delta^{18}O_p$ values (predictand) . . . . .	289
3. S2.3: Comparison of MAE between ECHAM5-wiso and Stacking regressor predicted and observed $\delta^{18}O_p$ values . . . . .	290





# Introduction

# 1.

By the end of this century, without significant changes in human activities to reduce greenhouse gas emissions, atmospheric CO<sub>2</sub> concentrations ( $p\text{CO}_2$ ) are projected to reach levels that are unprecedented on Earth for over 30 million years (Ma) [5, 6]. Understanding the responses of Earth's systems to these elevated  $p\text{CO}_2$  conditions is imperative for developing adaptation strategies and mitigation plans to counteract future climate change impacts [7]. Geological materials preserve information about past warmer periods and major climate transitions in Earth's geological history [8, 9]. Investigating these past climate states yields insights into future climate scenarios and addresses crucial questions directly affecting human well-being: How will global warming affect regional hydroclimate variability, which has profound ecological and societal consequences, such as droughts and floods? How sensitive is the Earth's surface temperature to the rapidly increasing  $p\text{CO}_2$ ? How will this rapid rise in  $p\text{CO}_2$  influence atmospheric circulation patterns, such as the North Atlantic Oscillation (NAO) or global monsoons (*e.g.*, African monsoons) [10, 11], and their impacts on ecosystems [12]? How long would it take for natural processes to reverse human-induced climate changes? How will changes in land surface (*e.g.*, topography) influence biodiversity distribution [13, 14]? How reliable are future climate projections, considering the relatively short historical observations for their validations [15]?

Addressing these critical questions necessitates the integration of high-resolution observational records across essential geological timescales of climate transitions with climate models, such as General Circulation Models (GCMs), that allow the exploration of physical processes. The integration of observations and GCMs is of mutual benefit since it provides a robust assessment of model performance and provides constraints on the missing processes in the climate models [16, 17]. GCMs are based on a set of governing primitive equations that represent physical laws (*e.g.*, the first law of thermodynamics, Navier-Stokes equations for fluid motion), and account for the conservation of mass, energy, and momentum. These equations are numerically solved by discretising the Earth's surface and atmosphere, incorporating subgrid parameterisations for specific processes (*e.g.*, cloud microphysics, atmospheric turbulence), based on recent observational records [18]. GCMs are utilised to project future climates based on assumed greenhouse gas emission scenarios [19] and to reconstruct past climates using appropriate paleoenvironmental boundary conditions (*e.g.*, past land-sea configurations, surface elevation, vegetation, and climate forcings) [20, 21]. It is essential to validate climate models to ensure their accurate projection of future climate changes. However, validation based solely on recent historical observations is insufficient due to the different external forcings and internal feedback mechanisms in a much warmer world. This stresses the need for climate modelling efforts to extend to deep-time warm periods to fully encompass the range of variability and climate-forcing feedbacks expected in future climates [22–25]. Additionally, the capability of climate models to

- 1.1 Paleoclimate as potential analogues for future climate 2
- 1.2 Isotopic composition of water reflects changes in hydrological cycle . . . . . 4
- 1.3 Proxies for climate variables: Challenges and Uncertainties . . . . . 5
- 1.4 Water isotopologues in climate models and proxies 7
- 1.5 Thesis structure . . . . . 9

accurately represent regional climate variability in response to different environmental conditions compared to modern times can be assessed through these paleoclimates.

Understanding past climate dynamics is contingent upon the availability of paleoclimate records. These records play a crucial role in evaluating the ability of GCMs to simulate the climate dynamics of past, present, and future climate change. The records also reflect paleoenvironmental conditions such as vegetation and paleotopography, which are used to generate boundary conditions for paleoclimate experiments [25–28]. Often, these records are sparse, complicating the interpretation of past regional and global climate dynamics. Therefore, understanding paleoclimate dynamics and associated paleoenvironmental conditions requires the integration of paleoclimate records and climate models [29]. This thesis underscores the necessity of such integration by highlighting the uncertainties associated with reconstructing past surface elevation (specifically in the European Alps) and past atmospheric circulation and dynamics (specifically Northern Hemisphere teleconnections and West African monsoon variability).

## 1.1 Paleoclimate as potential analogues for future climate

The Earth's climate system has undergone significant changes in the past due to changes in climate forcings and paleoenvironmental conditions. Since the last 60 million years (Ma), the global climate has cooled, marked by a general decline in  $p\text{CO}_2$ , despite significant variability between geological periods (Figure 1.1). Throughout Earth's paleoclimatic history, there have been several periods warmer than the Pre-Industrial era (PI; the reference year 1850). These historical climates offer insights into potential future climate conditions [9, 23]. Notably, the Eocene epoch (50 Ma) was characterised by substantially higher global mean surface temperatures (GMST; ~10–16 °C warmer than PI) [22, 30–32] and reduced meridional temperature gradients (~38% lower than modern) [33] in a world free of permanent ice sheets. The extreme global warming during the Eocene was due to the highly elevated  $p\text{CO}_2$  levels (1200–25000 ppmv) [34–37], which is within the range of values projected for future scenarios under “business-as-usual emissions” [23]. Paleoclimate records from such deep time can be used as a reference period to constrain the long-term equilibrium climate sensitivity of climate models in response to the increasing  $p\text{CO}_2$  for future predictions [9, 16, 31, 32, 38].

The Middle Miocene (15.97–11.63 Ma) was characterized by significant changes in climate dynamics, paleoenvironmental conditions (such as topography, vegetation, and palaeogeography), and tectonic activity [25]. Particularly, the Middle Miocene Climate Optimum (MCO; 16.75–14.5 Ma) has emerged as an important intermediate deep-time analogue for future climate. This is due to the significantly different palaeogeography and vegetation distribution in the Eocene and already higher modern  $p\text{CO}_2$  levels surpassing the Mid-Pliocene reconstructions. Global proxy reconstructions have indicated a warmer and wetter climate during the MCO, with an estimated GMST of ~8 °C warmer than present [21, 25]. This

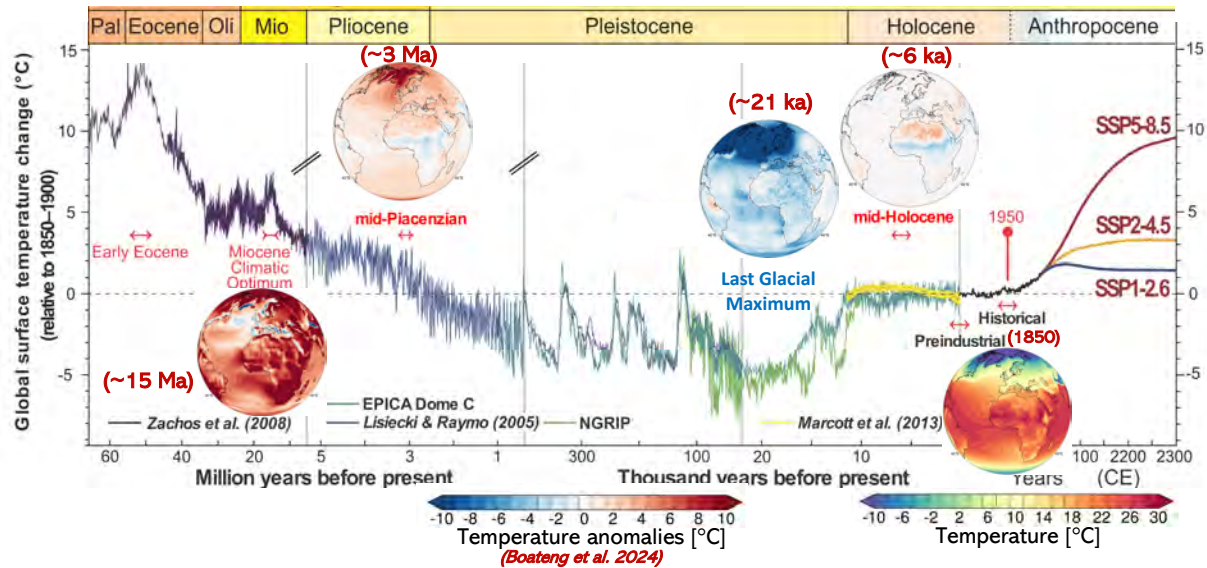


**Figure 1.1:** Global mean surface temperature anomalies (relative to 1850-1900) variations for the past 65 Ma and future projection (up to 2300) from climate models and proxy records. The temperature estimates from the geologic materials are from Andersen et al. [39], Jouzel et al. [40], Lisiecki and Raymo [41], Zachos et al. [42], and Marcott et al. [43]. The future temperature estimates are based on CMIP5 models ensemble for all Shared Socio-economics Pathways (SSP) [19] (Meinshausen et al., 2020). The spatial maps (Pre-Industrial; 1850, Mid-Holocene; ~6 k, Last Glacial Maximum; ~21 k, Mid-Pliocene; ~3 Ma, Middle Miocene Climatic Optimum; ~15 Ma) for the time slices are based on the ECHAM5-wiso simulation presented in this thesis (P3, P4). The figure was adapted from Burke et al. [23]

warming is primarily attributed to elevated  $p\text{CO}_2$  as indicated through climate sensitivity experiments [21, 44–46], ranging from 400 to 700 ppm [25, 47–49], with some estimates reaching as high as 1000 ppm [50, 51]. Climate sensitivity studies, considering various boundary conditions in MCO, have highlighted the importance of non- $p\text{CO}_2$  forcings—such as changes in paleotopography, palaeogeography, and vegetation—in driving regional climatic differences [21, 44, 52–54].

The Mid-Pliocene (~3 Ma) is the most recent warm period with GMST of ~1.8-3.6 °C warmer than PI and higher  $p\text{CO}_2$  levels (~400 ppmv) [27, 55–58]. In fact, the Mid-Pliocene climate can be considered as an analogue for a near-future climate (*e.g.*, “best-case scenario”) as predicted before 2030 if emissions-reducing climate stabilization scenarios are implemented [23]. However, this is contingent on societies successfully meeting the targets set out under the Paris Agreement to limit global temperature rise to 1.5°C-2°C, which currently seems improbable [59]. The unmitigated greenhouse gas emissions scenarios would rapidly push the Earth’s climate to a more vulnerable state beyond the Mid-Pliocene state, with more destabilizing tipping elements such as glaciers, deserts, forests and more [60]. However, the Mid-Pliocene provides useful insights into climate feedbacks of the carbon cycle on geological timescales [61–64].

The Last Interglacial (LIG; 129-116 ka), the warmest period in the recent glacial-interglacial cycle, experienced GSMT of ~0.8 °C higher than PI [65–67]. The slight warming was associated with amplified seasonal variability, particularly due to strong summer solar irradiance in the Northern Hemisphere, which resulted from differing orbital parameters

compared to the present day [68]. The Mid-Holocene (~6 ka), which was mainly driven by the changes in the Earth's orbital cycles, experienced slight global warming, with GMST of ~0.7 °C higher than the PI level [43, 69–71], accompanied by strong seasonal temperature variability and enhanced monsoons in the Northern Hemisphere. Investigating these past warmer climates has been instrumental in attributing the warming due to natural forcings and anthropogenic emissions in modern and future climate changes [9, 23]. This thesis contributes to the understanding of paleoclimate dynamics in response to changes in global climate forcings and paleoenvironmental conditions (e.g., paleotopography) in the past 20 million years (Ma).

While paleoclimates offer valuable insights, they are not perfect analogues for future climate dynamics due to significant changes in their paleoenvironmental conditions (e.g., palaeogeography) through geological timescales. Additionally, most of these paleoclimate states represent equilibrium conditions rather than the transient changes associated with rapidly increasing greenhouse gas emissions in the present day [72]. However, they do not need to be perfect analogues to serve as benchmarks for validating climate models. These past climates, including colder periods such as the Last Glacial Maximum (~21 ka; LGM), offer the opportunity to conduct out-of-sample validations for the strength and stability of key climate system feedbacks, large-scale responses of the hydrological cycle, and, most importantly, climate sensitivity [73]. The LGM was significantly colder and drier than the PI, characterised by extensive continental ice sheets, lower  $p\text{CO}_2$  (~185 ppmv), and reduced sea levels (~115–130 m below present) [74–76]. Since the LGM, the GMST has increased by 4–6 °C, which is of the same order of magnitude increase projected for the future under high emission scenarios [77–79]. This positions the LGM climate as a crucial benchmark for constraining climate models' sensitivity, particularly in areas where thermodynamic and dynamic processes significantly influence the magnitude and seasonality of precipitation patterns [80–82]. Overall, analysing the hydrological responses offers valuable insights to enhance climate models, ensuring accurate regional projections.

## 1.2 Isotopic composition of water reflects changes in hydrological cycle

The Earth's hydrological cycle interconnects solid Earth, land surfaces, oceans, the atmosphere, and biological processes, which are critical for understanding the Earth's system [83]. This suggests that information regarding long-term changes in water cycle variability and dynamics (e.g., moisture transport) and its biogeochemical properties (e.g., stable water isotopologues) can aid in reconstructing past physiogeography and climate [84]. However, gaps remain in our understanding of the hydrological cycle and its response to changes in paleoenvironmental conditions, radiative forcings such as the distribution of incoming solar radiation and volcanic eruptions, and internal variability and feedback mechanisms [85, 86]. Bridging these gaps requires interdisciplinary approaches (e.g., paleoclimate modelling, geodynamics, geochemistry, and statistics) and robust efforts in model-data synthesis on both short- and

long-term timescales. Stable isotope ratios of oxygen ( $O^{18}/O^{16}$ ;  $\delta^{18}O_p$ ) and hydrogen ( $D/H$ ;  $\delta D_p$ ) in water were among the first tools used to understand the hydrological cycle variability [87–89]. Since heavy and light water isotopes transition between phases at different rates due to their atomic masses, diffusivities [88], and vapour pressures, their ratios offer insights into historical atmospheric processes through moisture fluxes. These ratios track moisture exchanges between the land surface, ocean, and atmosphere, thus linking various climate system components. Water isotopes encapsulate integrated processes, providing an additional "degree of freedom" for understanding the hydroclimate system and offering information beyond traditional variables like precipitation amount or specific humidity [90–93]. To an extent, the distribution of water isotopes reflects moisture transport trajectories, mixing of moisture sources, and atmospheric circulation [94–96]. These validate the use of  $\delta^{18}O_p$  as a proxy variable for both local conditions and large-scale variability patterns (*e.g.*, North Atlantic Oscillation; NAO and El Niño–Southern Oscillation; ENSO) [97–100]. Beyond tracking changes in the hydrological cycle, water isotopes reflect the interactions between the climate system and surface processes, enabling their use in reconstructing paleoenvironments such as paleotopography [101–103]. Consequently, isotopic compositions in water are the measured signal for numerous geological archives, including pedogenic carbonates, marine and lake sediments, speleothems, ice cores, and rocks [104]. This makes  $\delta^{18}O_p$  the "common currency" that bridges paleoclimate records with direct modern observations, facilitating the evaluation of hydroclimate processes over longer timescales in climate models [105]. This thesis leverages isotopic signals from geological materials and their tracking in climate models to demonstrate how effective the integration framework contributes to reconstructing paleoclimate and paleoenvironment dynamics.

### 1.3 Proxies for climate variables: Challenges and Uncertainties

The gaps in our understanding of the past hydrological cycle and potential future climate changes are partly due to the short length of instrumental records of proxy variables (*e.g.*,  $\delta^{18}O_p$  measurements). More specifically, validating paleoclimate simulations poses a challenge, as no direct observed records of climate variables (*e.g.*, precipitation amounts, temperatures, wind speeds) existed before 1750. Primarily, indirect records of climate signals (*e.g.*,  $\delta^{18}O_p$  signal), imprinted in various components of the Earth system (climate proxies), are utilised as proxy variables to infer past climate changes. Unlike direct observations, proxies do not record single climate variables. Instead, they often reflect combined information about different environmental conditions, necessitating the disentangling of specific climate signals from others [106, 107]. Most often, the biogeochemical compositions of geological archives (such as paleo-meteoritic  $\delta^{18}O_p$  values) are utilised to infer past climate changes [*e.g.* 105].

The reconstruction of paleoclimate dynamics faces significant challenges and uncertainties, particularly due to the scarcity of proxy records both spatially (*e.g.*, across Africa) and temporally over extended time scales [58,

108–111]. Typically, single-site proxy records are utilised to infer past regional and global climate changes. However, these imprints may reflect local changes rather than regional or global signals. The recent shift towards compiling multi-proxy records from different regions and enhancing their accessibility and usability (*e.g.*, SISAL [108, 109], iso2k [105] databases) has resolved some of these issues. Furthermore, advanced statistical techniques, such as Bayesian inference, have been employed to quantify the uncertainties associated with proxy records, including those related to sample collection, preparation, and analysis [112–114]. Nevertheless, even with well-collected and measured proxy variables, two major issues persist, which are addressed in this thesis:

**1. Disentangling Climate Signals from Non-Climate Signals:** The relationship between proxy data and climate variables is often complex and stochastic [115, 116], making it challenging to separate specific climate signals from other influences. Typically, proxies record climate information during seasonal changes, and shifts in seasonality across different climate states can bias these records. For instance, pollen proxy records reflecting past vegetation variability are influenced by both climatic factors (*e.g.*, seasonal temperature and moisture availability) and non-climatic factors (*e.g.*, plant competition, soil nutrients, light availability for photosynthesis). Furthermore, the impact of climatic factors on vegetation dynamics varies spatially and temporally, complicating the use of pollen as proxies for climate variables such as precipitation or temperature. In regions with complex atmospheric dynamics and teleconnections, such as West Africa, additional uncertainties arise due to the intricate causal mechanisms between the proxy variables (*e.g.*,  $\delta^{18}O_p$ ) and specific climate information [96, 117, 118]. Additionally, the variability  $\delta^{18}O_p$  signals from geologic materials (*e.g.*, pedogenic carbonates) across mountainous areas reflect the land surface-atmosphere interactions, controlled by the changes in geodynamics and climate [101–103]. This necessitates the disentanglement of climate signals from the reconstructed  $\delta^{18}O_p$  signal to attribute the remaining signal to changes in past surface elevation related to the geodynamic evolution [*e.g.* 119, 120]. Therefore, in this thesis, I explore whether the causal mechanism between  $\delta^{18}O_p$  values and climate variables (both regional and large-scale variability patterns) remain stationary through the Late Cenozoic and quantify the implications and uncertainties in reconstructing paleoclimate dynamics.

**2. Assumption of stationarity of transfer functions:** Since proxies do not directly measure climate variables, a conversion—commonly referred to as calibration—is required to translate the reconstructed signal into specific climate variables [121–124]. For example, the width of tree rings, which is indicative of growth rates and climatic conditions at the time (with faster growth in wet and warm conditions), is converted into specific climate variables through this process [116, 125]. This calibration involves the development of a transfer function between the proxy data and historical direct observations of climate variables. This can be achieved in several ways: (1) "calibrated-in-time" for high-resolution proxy records at a specific region and (2) "calibration-in-space" for sparse proxy records in varied environments to establish the transfer function, allowing the location with no direct observation to use in reconstructing the past climate variability. However, a fundamental challenge in proxy climate variable reconstructions is the assumption that the established transfer

function, based on historical direct observation, remains stationary through time and space. This assumption is rarely met, as changes in past climate are often accompanied by shifts in atmospheric circulation and seasonality, affecting the relationship between proxies and climate variables [91, 104, 126, 127]. This thesis delves into the implications of this critical assumption, particularly in the context of reconstructing past surface elevations using water isotopic proxy records.

## 1.4 Water isotopologues in climate models and proxies

Integrating  $\delta^{18}O_p$  signals reconstructed from proxies and simulated by climate models can help address the above challenges [84, 128]. Climate models are instrumental in exploring the large-scale drivers and internal variability of past climate changes, alongside their associated  $\delta^{18}O_p$  variability recorded in proxy materials. Moreover, climate models can be used to fill the spatio-temporal gaps present in proxy records. More importantly, simulating  $\delta^{18}O_p$  values in climate models for past and present climates enables direct model-proxy comparisons, providing opportunities to assess the assumptions behind proxy reconstructions and, simultaneously, to identify the limitations of the climate models [e.g. 129–134]. This implies that isotope-enabled GCMs (iGCMs) can explore regional and global forcings affecting  $\delta^{18}O_p$  signals in proxy records. They also facilitate the refinement of climate models by evaluating complex processes such as cloud microphysics, moisture transport, atmospheric circulation, and precipitation dynamics [92, 93, 129, 135].

Modelling the spatio-temporal variability of  $\delta^{18}O_p$  values provides the means to evaluate the two mentioned major assumptions in proxy reconstruction. Specifically, simulating  $\delta^{18}O_p$  values in response to external forcing and internal feedback across different paleoclimates can ascertain whether the relationship between  $\delta^{18}O_p$  signals and specific climate variables (e.g., precipitation) remains constant over time and space, justifying their reconstruction [e.g. 136–138]. This information can guide the selection of specific proxies or locations optimal for reconstructing certain climate variables. In this thesis, the non-stationarity of the relationship between West African monsoon intensity and  $\delta^{18}O_p$  values is examined throughout the Late Cenozoic, which is critical given the complexity of the region's climate system—a complexity that current climate models still struggle to accurately represent. Furthermore, this thesis investigates how climate change influences the relationship between NAO and  $\delta^{18}O_p$  values across Europe through changes in their teleconnections (other modes of variability such as East Atlantic (EA) oscillation patterns) and seasonality.

Simulated  $\delta^{18}O_p$  values and regional climate variables can also aid in evaluating the stationarity assumption of the proxy transfer function. For example, modelling the  $\delta^{18}O_p$  response to varying paleoenvironmental conditions (e.g., in the Middle Miocene) can determine if the  $\delta^{18}O_p$ -climate gradient changes through time and space. Specifically, water vapour ascending over mountains preferentially precipitates heavy isotopes, resulting in more depleted (more negative)  $\delta^{18}O_p$  values in the

remaining air mass trajectories [95, 103]. The global distribution of  $\delta^{18}O_p$  values has shown a significant relationship with surface elevation. This is due to the predominant topography-related atmospheric processes (*e.g.*, orographic precipitation; “amount effect”) that influence the  $\delta^{18}O$  composition of rainwater [139]. The robust inverse  $\delta^{18}O_p$ -elevation gradient, established either empirically [*e.g.* 139, 140] or theoretically via thermodynamics principles (Rayleigh distillation) [95, 103], underpin stable isotope paleoaltimetry—a method employed to reconstruct past surface elevations of mountain ranges. The rarity of isotopic proxies reflecting long-term climate and topography changes across mountains has directed most studies to depend on modern constant  $\delta^{18}O_p$ -elevation relationship (isotopic lapse rate) over time and space. This presupposes that the isotopic lapse rate at the time of the proxy material’s formation (*e.g.*, pedogenic carbonate) remains unchanged over millions of years compared to the present day. However, wide ranges of climatic processes—including surface recycling, atmospheric circulation, variability in moisture transport and sources, air mass mixing, and shifts in precipitation dynamics—can alter the isotopic lapse rate and complicate the paleoelevation reconstruction [*e.g.* 1, 120, 141–143]. This thesis leverages iGCMs to simulate time-specific paleo-meteoric  $\delta^{18}O_p$  values in response to paleoenvironmental conditions and integrates them with the isotopic signal from geologic archives across the European Alps to determine the uncertainties of paleoelevation estimates associated with the assumption of the stationarity of isotopic lapse rate.

The modelling component of this thesis relies on ECHAM5-wiso, a global three-dimensional atmospheric GCM with isotope tracking ( $H_2^{16}O$ ,  $H_2^{18}O$ , and  $HDO$ ) capability [144]. The model’s ability to simulate the climate and isotopic composition of precipitation has been validated for the present-day [*e.g.* 1, 145] and the geological past [*e.g.* 146–148]. The model includes diagnostics of water isotopes, which are treated as independent tracers in the hydrological cycle and undergo equilibrium and kinetic fractionation during phase transitions in the atmosphere (*e.g.*, snow, vapour, and clouds) [144, 149]. The model tracks vapour fluxes from the sea surface and lakes with non-equilibrium fractionation, which depends on surface temperature, seawater  $^{18}O$ , relative humidity, near-surface wind speed, and  $^{18}O$  vapour content at the atmosphere’s lower level. However, the model does not consider fractionation for vapour fluxes from the land surface, such as evapotranspiration, due to their negligible effect on the isotopic composition [150, 151]. This simplification is common in other state-of-the-art isotope tracking GCMs [*e.g.* 152–154] but must be considered when interpreting the simulated regional isotopic patterns. ECHAM5-wiso was used to simulate Late Cenozoic climates, addressing a broad spectrum of challenges associated with paleoclimate dynamics reconstruction. Given the complexity and computational demands of incorporating water isotopologues tracers in climate models, this thesis also explores the application of machine learning as a surrogate model for predicting the spatio-temporal variability of  $\delta^{18}O_p$  values. The machine learning-based emulators for water isotopes are designed to complement the capabilities of iGCMs, such as downscaling the simulated isotopes to a higher resolution or filling the gaps in historical records.



## 1.5 Thesis structure

The overall goal of this thesis is to demonstrate how water isotopologues modelling with iGCM can be integrated with proxy signals from geologic materials to improve their interpretation in reconstructing paleoclimate dynamics. I used iGCM (ECHAM5-wiso) to simulate the response of paleo-meteoric  $\delta^{18}O_p$  values and global climate variables to Late Cenozoic paleoenvironmental conditions. The simulated variables are used to address challenges associated with proxy records for reconstructing past climate dynamics and environmental conditions. More specifically, the thesis demonstrates how the simulated  $\delta^{18}O_p$  values can be integrated with reconstructed proxy signals to understand paleoclimate dynamics, such as atmospheric circulation (*i.e.*, NAO) and West African monsoon systems, and to reconstruct the evolution of paleotopography in the European Alps. Additionally, since the tracking of water isotopic species in iGCMs is computationally expensive and complex, this thesis explores the potential use of machine learning algorithms to predict the spatio-temporal variability of local  $\delta^{18}O_p$  values. Such statistical modelling can complement the iGCMs by generating high-resolution  $\delta^{18}O_p$  distributions (*i.e.*, downscaling). This can help in understanding the link between isotopic proxies and climate variables and in developing their robust transfer functions. The scientific motivation and questions addressed in this thesis, along with the individual research objectives, are presented in **Part I** and integrated into the main research hypothesis in **Part II**. The main results, along with their discussions and significance, are presented in **Part III** and concluded in **Part IV** with some future outlooks. The reader is referred to the manuscripts (in **Part VII**) associated with the key findings for more detailed results and methods used.



## **Part I.**

# Scientific Motivation & Questions



This section outlines the research questions of this thesis and their respective scientific motivation. I highlight that the presented answers to these questions go beyond the motivation for the thesis and further address the research questions of the individual case studies (*e.g.*, integrating iGCMs with geologic materials to reconstruct the past surface elevation of the European Alps). More specifically, this section highlights the individual studies' research questions and their importance beyond using iGCMs to resolve the mentioned limitations of proxy reconstructions, which is the focus of the thesis.

## 2.1 Reconstructing the paleoelevation of the European Alps

Quantifying the past surface elevation of the Alps is essential for understanding its tectonic-geodynamic processes (*e.g.*, crustal thickening, lower crustal flow, subduction erosion, lithospheric delamination) and post-collisional processes that contribute to the landscape evolution, regional climate dynamics, and biodiversity distribution [14, 155–161]. Although the onset of the Alps' topographic development—resulting from the continent-continent collision between the Adriatic and European plates [162–165]—is well-understood and agreed upon, the timing of its post-collisional processes and associated surface uplift histories remain poorly constrained. Recent modelling studies suggest additional geodynamic processes that may have influenced the surface uplift history of the Alps [166, 167]. These processes include slab break-off (30 Ma) and slab rollback of the subducting lithosphere, alongside lithospheric mantle removal [168–170]. These may have contributed to west-to-east variations in surface uplift, as suggested over the Central Alps. It has been further suggested that slab break-off (20 Ma) occurred under the Eastern Alps [171]. Based on these studies, current tectonic and geodynamic reconstructions indicate that the entire Alps did not experience a uniform rise but rather a diachronous surface uplift across different sections of the Alps.

Stable isotope paleoaltimetry provides a framework for constraining subsurface processes, given that surface elevation primarily reflects mantle and lithospheric dynamics. However, it remains an open question whether such geodynamic processes would yield spatial differences in  $\delta^{18}O_p$  values that would be detectable from geologic archives. Addressing this question validates the use of stable isotope paleoaltimetry reconstructions across the Alps to elucidate their topographic evolution. iGCMs can be used to address these questions by conducting topographic sensitivity experiments under varying Alps topographic scenarios. This leads to this thesis's first question:

2.1 Reconstructing the paleoelevation of the European Alps . . . . .	13
2.2 West African monsoon dynamics and $\delta^{18}O_p$ changes in the Late Cenozoic . . . . .	16
2.3 Optimal locations for reconstructing the past variability of the North Atlantic Oscillation . . . . .	19
2.4 Machine learning based emulators for spatio-temporal variability of $\delta^{18}O_p$ . . . . .	21

**Q1:** How much isotopic ( $\delta^{18}O_p$ ) and regional climate signal (and where) would different west-to-east surface uplift scenarios of the Alps produce?

To address this question, I used ECHAM5-wiso to simulate regional climate changes (precipitation and temperature) and  $\delta^{18}O_p$  values in response to diachronous, along-strike surface uplift variations of the Eastern and Western–Central Alps. The simulated  $\delta^{18}O_p$  signal can help determine if the changes are significant enough to be reflected in paleoaltimetry records, which would ultimately help to understand the geodynamic evolution of the Alps.

Most studies on major mountain ranges, including the Alps, assume the  $\delta^{18}O_p$ -elevation gradient (isotopic lapse rate) necessary for constraining vertical displacement of topography remains constant since the formation of the proxy material [e.g. 140, 172, 173]. However, various climatic processes—such as surface recycling, changes in atmospheric circulation, moisture transport and source variability, air mass mixing, and precipitation dynamics—can affect the isotopic lapse rate Figure 2.1. Given the complex atmospheric dynamics across Europe and the Alps' geometry, understanding the impacts of topography changes on large-scale dynamics is crucial for evaluating the complications associated with the assumption of stationarity in single-site stable isotope paleoaltimetry. This leads to the second question:

**Q2:** To what extent do changes in the topography of the Alps affect the atmospheric circulation, moisture transport, and tropospheric dynamics of the regional climate across Europe?

In addressing this question, I analysed the changes in prominent Northern Hemisphere teleconnection patterns, such as the NAO, EA, Scandinavian (SCAN), and East Atlantic–Western Russia (EA/WR) circulation patterns, in response to different Alps topographic configuration experiments. Additionally, I conducted back-trajectory analysis to determine the influence of topography on moisture transport pathways. The simulated vertical wind velocity, cloud cover, and relative humidity along the strike of the Alps were further examined to determine the influence of topography on tropospheric dynamics.

Despite the European Alps being one of the most intensively studied orogens globally, their surface elevation history remains scarce and poorly constrained. Specifically, Campani et al. [140] combined a modern rainfall-based isotopic lapse rate of  $-2.0 \text{ ‰ km}^{-1}$  with reconstructed isotopic signal less sensitive to climate change to estimate a paleoelevation of 2850 ( $\pm 800$ ) m for the Central Alps during the Miocene. Their estimate relied on near-sea-level pedogenic carbonates' paleo-meteoric water oxygen isotopic composition ( $\delta^{18}O_w$ ; hereafter for reconstructed  $\delta^{18}O$ ) values from the low-elevation Northern Alpine Foreland Basin (Swiss Molasse Basin; SMB) to isolate regional climate changes from the high-elevation isotopic signal. Recently, Krsnik et al. [173] refined the paleoelevation estimates by applying clumped isotope ( $\Delta_{47}$ ) paleothermometry to well-dated Middle Miocene sediments from two Miocene Alpine foreland megafans to calculate the soil carbonates' near-sea-level

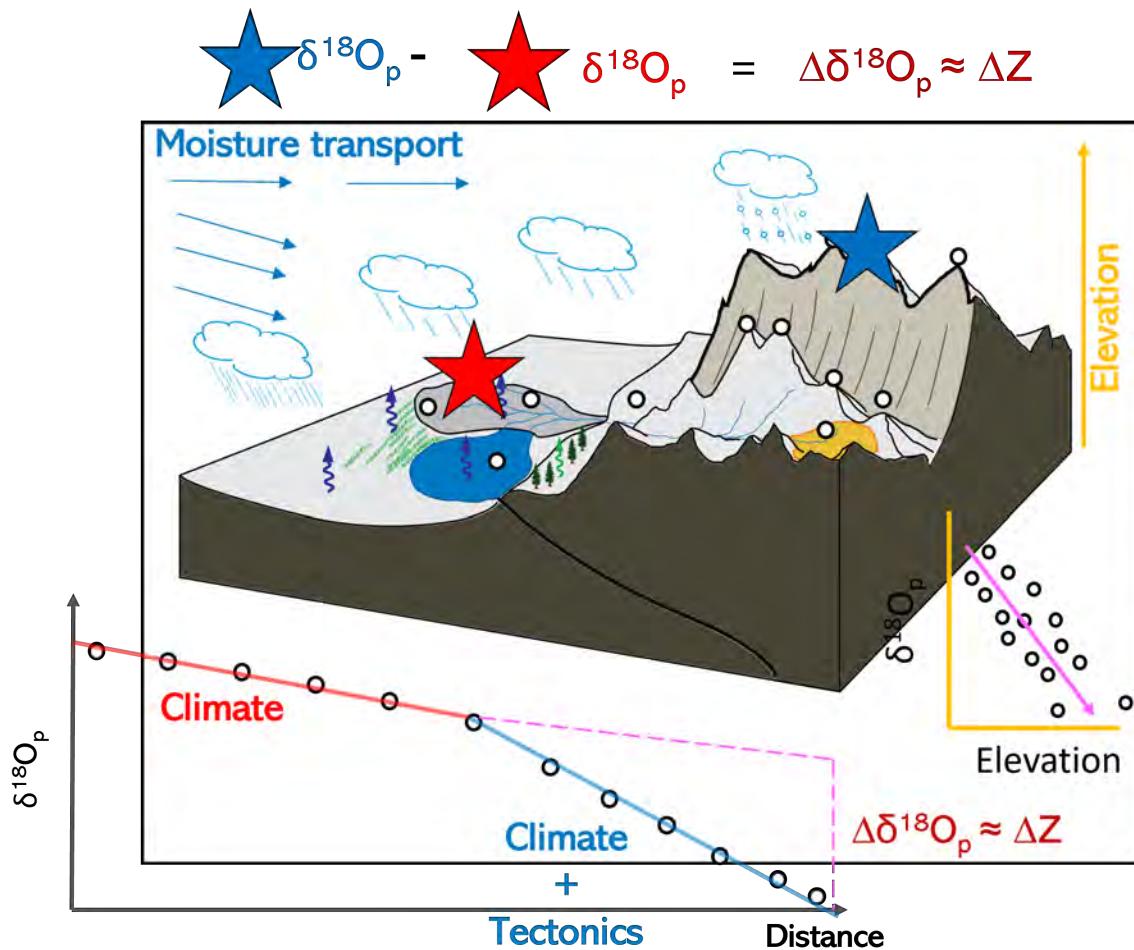


**Figure 2.1:** Simplified sketch of the conceptual framework of stable isotope paleoaltimetry method, which is based on coeval  $\delta^{18}\text{O}$  of paleo-meteoric water between proxies over low- and high-elevation sites along an air mass trajectory. The difference in the  $\delta^{18}\text{O}$  signal is combined with the isotopic lapse rate to estimate the paleoelevation. The figure was adapted from Campani et al. [140]

$\delta^{18}\text{O}_w$  values. Their reconstructed isotopic signal with modern isotopic lapse rates estimated the Miocene Central Alps to be  $> 4400 (\pm 770)$  m. The high elevation estimate was interpreted to reflect the complicated transition from pre- to mid-Miocene Central Alps, characterised by a diverse landscape and complex topography, primarily driven by the rapid exhumation of deep-seated core complexes and a subsequent rearrangement of the drainage system. However, if the answers to **Q1-3** support the application of stable isotope paleoaltimetry across the Alps to decipher the diachronous surface, then the above Middle Miocene paleoelevation estimates, which are based on the assumption that global and regional climate changes would not influence the spatial variability of  $\delta^{18}\text{O}_p$  values and therefore would not affect the isotopic lapse rate through time and space, should be reassessed. Therefore, to evaluate the associated uncertainties, I conducted Middle Miocene simulations reflecting two  $p\text{CO}_2$  conditions (278 and 450 ppm) and topographic configuration from **Q1-2** using ECHAM5-wiso. This leads to the next question:

**Q3:** Does ECHAM5-wiso adequately simulate the Middle Miocene regional climate and  $\delta^{18}O_p$  well across the Alps and Europe?

If the paleoclimate modelling is validated and appears feasible, the subsequent question would be:

**Q4:** How much isotopic ( $\delta^{18}O_p$ ) signal would the changes in the Alps topography and Middle Miocene climate produce?

If the answer to Q4 confirms that the combined influence of climate and surface uplift still produces a significant isotopic signal to be reflected in geologic material, the next logical question would be:

**Q5:** To what extent do Middle Miocene climate and surface uplift affect the isotopic lapse rate across the Alps?

Using the simulated Middle Miocene isotopic lapse rate across the Alps, I recalculated the previously reconstructed paleoelevation across the Central Alps to quantitatively determine the magnitude of uncertainties associated with the assumption of stationarity of the isotopic lapse rate across the Alps. This leads to the crucial question:

**Q6:** Does using the contemporary isotopic lapse rate across the Alps overestimate or underestimate the Middle Miocene paleoelevation across the Alps?

Resolving these questions related to the Alps topography reconstruction demonstrates how integrating  $\delta^{18}O_p$  proxy data with their process-based estimates from iGCM can help resolve the assumption of stationarity of the transfer function and the causal mechanisms between the proxy signal and climate variables.

## 2.2 West African monsoon dynamics and $\delta^{18}O_p$ changes in the Late Cenozoic

Understanding the seasonality, interannual variability, and teleconnections of West Africa's climate represents one of the most challenging issues in climate science. Most state-of-the-art climate models struggle to accurately represent the region's historical variability and demonstrate little consensus regarding future projections [174–176]. Most importantly, climate change in the region has significant environmental and socio-economic consequences for West African countries due to their high vulnerability and over-dependence on the rainfed agriculture economy [177]. Hence, accurate climate change information is essential for their adaptation and mitigation strategies, necessitating improved representation in climate models. Studying past hydroclimate and atmospheric dynamics changes beyond the historical period can help constrain the key features of the West African Monsoon (WAM) system that require enhancement in climate models.



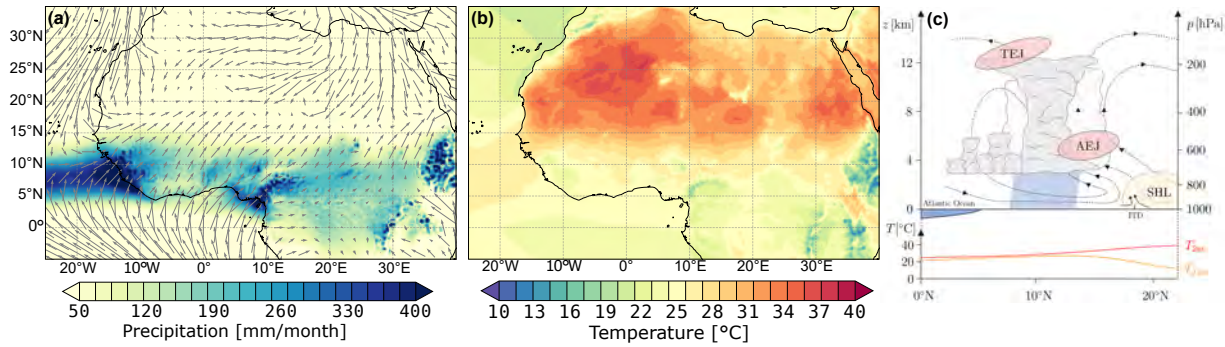


**Figure 2.2:** Long-term seasonal means (June-September) of present-day (1979-2022) (a) precipitation and near-surface winds showing the monsoon rain-belt and low-level south-westerlies from the equatorial Atlantic and (b) near-surface temperature showing the meridional temperature gradient based on ERA5 reanalysis [196, 197]. (c) Schematic sketch of the vertical-latitude profile of the WAM system showing the location of the Africa Easterly Jet (AEJ), Tropical Easterly Jet (TEJ), Inter-tropical Discontinuity (ITD), Sahara Heat Low (SHL), and near-surface temperature ( $T_{2m}$ ) and dew-point temperature ( $T_{d2m}$ ) from Fischer et al. [198] (originally inspired from Fink et al. [199])

The WAM is characterised by the seasonal reversal of moisture (winds) transported from the equatorial Atlantic to the equator margins of the Sahara and regulates the precipitation distribution of West Africa. Its variability is influenced by complex mechanisms, including large-scale teleconnections and local feedback mechanisms (Figure 2.2) [178–187]. The strong solar surface heating over the Sahara generates a heat-low circulation (Sahara Heat Low) that induces a land-sea thermal gradient, driving the low-level southwesterly moisture convergence from the equatorial Atlantic that deflects the dry northeasterlies (harmattan) of the Sahara [188–191]. The latitude where both winds meet is called the inter-tropical discontinuity (ITD). Above the planetary boundary layer, the meridional temperature gradient also drives the African Easterly Jet (AEJ), which spans across West Africa at altitude of ca. 500-700 hPa [184, 186, 187, 192], and beneath the upper tropospheric Tropical Easterly Jet (TEJ). The TEJ is primarily driven by large-scale remote features such as the convective heating of the North Indian Ocean and the outflow of the South Asian Monsoon [193]. Nonetheless, the latent heat flux through convection over the WAM region can amplify upper-level shear, thus strengthening the TEJ. On interannual timescales, the sea surface temperature of the tropical oceans influences the precipitation seasonality [174, 181]. At intraseasonal scales, the dynamics of the WAM are affected by equatorial waves and interactions with the midlatitudes and the Mediterranean, while land surface-atmospheric feedback additionally governs the precipitation distribution [194, 195]. All these indicate the complexity of the WAM system dynamics and its teleconnections.

The sensitivity of the WAM and its atmospheric dynamics to paleoenvironmental forcing and feedbacks (*e.g.*, changes in  $p\text{CO}_2$ , orbital forcing, vegetation, and orography) can shed light on their representation in climate models for future projections. For example, the response of WAM dynamics to orbitally driven seasonal and latitudinal distributions of incoming solar radiation can be examined under Mid-Holocene conditions. The long-term (geological timescales) sensitivity of the WAM to  $p\text{CO}_2$  levels similar to the present, along with surface conditions changes over the Sahel-Sahara and a globally enhanced hydrological cycle, can also be assessed under Mid-Pliocene paleoenvironmental conditions. Numerous modelling studies, including those from the Paleoclimate

Modelling Intercomparison Project (PMIP) [e.g. 76, 200–203], have simulated precipitation changes associated with the WAM in response to various forcings and paleoclimates in the Late Cenozoic. However, differences in experimental design and model setup, such as spatial resolution, paleoenvironmental conditions, and GCM complexity (e.g., some including dynamic vegetation), make it difficult to identify the predominant atmospheric dynamics influencing WAM precipitation changes. GCMs with varied spatial resolutions and parameterisations of clouds, atmospheric dynamics, hydrological cycles, and land-atmosphere interactions simulate distinct responses of the WAM to different forcings, leading to inconsistent patterns of WAM dynamics. For instance, monsoons and associated dynamics, such as the Intertropical Convergence Zone (ITCZ), are better resolved at higher spatial resolutions, thus impacting the intensity and spatial distribution of precipitation across the WAM region due to the effects of vegetation, topography, and coastlines [204–206]. Moreover, only a few studies have comprehensively explored past atmospheric dynamics and teleconnections underlying the changes in precipitation patterns and magnitudes under various paleoenvironmental conditions throughout the Late Cenozoic. This leads to the question:

**Q7:** How did the WAM and associated atmospheric dynamics respond to changes in paleoenvironmental conditions during the Late Cenozoic?

I conducted climate experiments with the same iGCM ECHAM5-wiso in a consistent modelling framework (e.g., spatio-temporal resolution) with appropriate paleoenvironmental conditions from the present-day to the Mid-Pliocene. Subsequently, I analysed the intensity and northward migration of the WAM in response to different paleoenvironmental conditions. Additionally, I investigated the atmospheric dynamics behind the changes in the WAM, such as moisture transport (e.g., low-level southwesterlies), the African Easterly Jet (AEJ), the Tropical Easterly Jet (TEJ), the Sahara Heat Low (SHL), and surface heat fluxes.

The scarcity of paleohydrological records over Africa and the spatial resolution of climate models hinder robust model-data comparisons necessary for enhancing climate models [e.g. 58, 111]. Several issues regarding data-model comparison persist in this region. For instance, pollen-based precipitation reconstruction, past lake levels, leaf wax isotopes, and other proxies suggest significantly wetter conditions across the Sahel and Sahara during the Mid-Holocene compared to today [176, 207, 208]. However, most climate models fail to replicate the extent and magnitude of precipitation changes indicated by these proxy records despite incorporating factors such as increased insolation, changes in land surface conditions (e.g., vegetation, lakes, orography, soil moisture), reduced dust emissions, atmospheric-ocean interactions, and atmospheric dynamics [175, 176, 209–213].

While proxy records suggest varying degrees of precipitation increases over North Africa's higher latitudes, climate models generally predict a more moderate intensification of the WAM and underestimate both the reconstructed northward extent and magnitude of precipitation increase [70, 175, 181, 201, 214, 215]. If the proxy data are well preserved and processed efficiently, two possible reasons for this disagreement can be:

(1) The climate models may not adequately represent the atmospheric processes in the region to accurately simulate their hydroclimate variability. (2) The proxy system models, which facilitate the conversion of the proxy signal into a paleoclimate signal (transfer function), may be biased. Transfer functions are often calibrated on the historical records (*e.g.*, regression gradients between water isotopes and precipitation), which are not long enough to account for the long-term variability. This leads to the assumption that the established gradients from the historical period are constant over time and equally valid for reconstructing past climates. Given that this thesis relies on iGCM, the simulated  $\delta^{18}O_p$  responses under different paleoclimates can be explored. This investigation allows for testing the assumption of transfer function stationarity by examining the relationship between  $\delta^{18}O_p$  and climate variables (*e.g.*, precipitation and temperature). Additionally, simulated  $\delta^{18}O_p$  in these paleoclimates facilitates direct model-isotope proxy comparisons and aids in understanding the general causal mechanisms behind the variability in different proxy materials. Thus, this thesis further addresses the question:

**Q8:** Does the relationship (or transfer function) between  $\delta^{18}O_p$  and climate variables over the WAM region remain constant through the different paleoclimates of the Late Cenozoic?

## 2.3 Optimal locations for reconstructing the past variability of the North Atlantic Oscillation

In the North Atlantic region and continental Europe, the interannual to multidecadal climate variability is predominantly controlled by large-scale circulation patterns, among which the North Atlantic Oscillation (NAO) is the primary mode of variability [136, 145, 216–219]. The NAO is often defined as the meridional dipole pressure gradient over the North Atlantic, consisting of a predominant low-pressure system over Iceland (the Icelandic Low) and a high-pressure system over the Azores (the Azores High). The strength of this dipole gradient, whether weak or strong, provides the basis for constructing its index over time. The positive phase of the NAO is associated with strong westerlies, and northerly storm tracks that transport air masses from the eastern Atlantic toward central Europe. This pressure system drives colder and drier conditions across western Greenland, Canada, and southern Europe, including the Mediterranean region, and warmer and wetter conditions across northern Europe, the eastern United States, and parts of the Scandinavian region [220, 221]. During its negative phase, the pressure gradient weakens, which leads to a decrease in the strength of the westerlies and a southward shift of the storm tracks, resulting in opposite climate patterns. Although the influence of the NAO is strongest in boreal winter, it also affects summer conditions [222]. Given that the NAO is a major driver of European climate variability and has a significant influence on marine and terrestrial ecosystems and regional socio-economic activity, understanding its predictability and response to future climate conditions is crucial. However, the relatively short instrumental record of the NAO means that reconstructing its past long-term variability could provide

valuable insights into its dynamics in past climates and serve as a reference for future climates.

The phases of the NAO have been shown to control the variability and distribution of  $\delta^{18}O_p$  records across wide regions in the Northern Hemisphere [136, 145, 218, 223–226]. As a result, many isotopic proxy records (*e.g.*, ice cores, speleothems, tree rings, and lacustrine carbonates) have been utilised to reconstruct the past variability of the NAO [227, 228]. However, since direct measurements of  $\delta^{18}O_p$  values have only been available for the last few decades (since 1958) and have many spatial and temporal gaps (*e.g.*, Global Network of Isotopic composition of Precipitation (GNIP) stations) [229], the NAO- $\delta^{18}O_p$  transfer function relies on the long-term assumption of stationarity on the influence of the atmospheric teleconnection patterns on local  $\delta^{18}O_p$  records. Nonetheless, the relationship between the NAO and surface climate variables has proven to be non-stationary, with previous studies attributing this to changes in the meridional pressure gradient, North Atlantic air-sea dynamics, and ocean circulation [136, 138, 230, 231]. Moreover, recent studies have indicated shifts in the positions of the centres of action of the NAO dipole structure in winter compared to the classical station-based indices [138, 232]. These migrations are linked to shifts in winter temperature and precipitation anomalies in European mid-latitude regions. In addition, the phases of other modes of variability, including the East Atlantic (EA) pattern and the Scandinavian oscillation pattern (SCAN), have been shown to affect the relationship between the NAO and regional climate variables [136, 232–234]. For example, the Azores High shifts northeast when the NAO and EA indices have the same polarity (*e.g.*, both in positive phases). Consequently, the line of no correlation between the NAO and surface climate migrates to higher latitudes when the southern high-pressure centre of action shifts closer to Europe. These shifts in the NAO-winter climate relationship could also impact the spatial patterns of  $\delta^{18}O_p$  and complicate the  $\delta^{18}O_p$ -NAO transfer function.

Most often, the optimal location for selecting proxy records for reconstructing the  $\delta^{18}O_p$ -based NAO can be identified by the  $\delta^{18}O_p$  sensitivity to the NAO using correlation distributions [218] or principal component analysis [224]. Thus, identifying regions less sensitive to other North Atlantic modes of climate variability can help reduce the uncertainties associated with NAO reconstructions (Figure 2.3). iGCMs can be used to simulate historical climate conditions to assess areas where the observed  $\delta^{18}O_p$ -NAO relationship is not robust and also determine how the phases of the EA affect the spatial distribution of  $\delta^{18}O_p$  and regional climate variables such as precipitation and temperature. Therefore, this thesis explores the question:

**Q9:** How and where would the polarity of the East Atlantic pattern phase affect the NAO- $\delta^{18}O_p$  and climate variables across Europe?

To answer this question, I perform an Empirical Orthogonal Function (EOF) analysis [*e.g.* 236, 237] to construct the NAO and EA indices from the mean sea level pressure anomalies from historical simulation (1979–2014) using the iGCM ECHAM5-wiso. I then validated the model-based indices by comparing them with observed station- and reanalysis-based

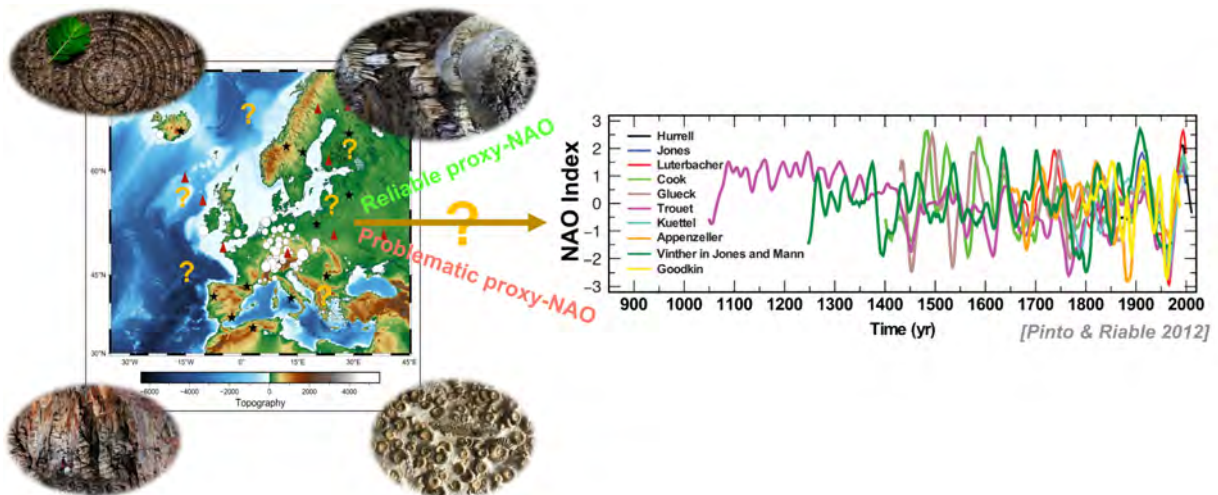


**Figure 2.3:** Schematic illustration of finding the optimal locations of proxies for reconstructing the past variability of the NAO index. The NAO index example shown is from Pinto and Raible [235]

NAO indices. Additionally, I conducted a composite analysis to group periods with the same and opposite phases of the NAO and EA indices and then performed a correlation analysis between the NAO index and (1)  $\delta^{18}O_p$  values, (2) temperature, and (3) precipitation within each of the composites to determine how the concomitant phase changes affect their spatial relationship. Furthermore, to investigate whether the winter NAO indices influence the subsequent summer climate conditions and its transfer function, I performed a Granger causality [238] analysis (*e.g.*, in [239–241]) to statistically determine the influence of the lag component of the winter NAO indices on summer  $\delta^{18}O_p$  values, temperature and precipitation variability. Since recent efforts attempt to extend the NAO reconstruction to the last millennium [*e.g.* 242, 243], I repeated the analysis on the last 1k simulations using different iGCMs from previous studies [132]. Such analysis helps determine if the changes in the correlation structure and their causal mechanism are different in the past 1k years.

## 2.4 Machine learning based emulators for spatio-temporal variability of $\delta^{18}O_p$

Despite the advantages of using iGCMs to combine with natural archives to reconstruct paleoclimate dynamics, the direct measurements of historical variability of water isotopologues are essential for understanding the hydrological cycle in specific regions. The long-term observations of  $\delta^{18}O_p$  distribution across a wide range of regions are needed to identify the atmospheric and land surface processes that control their variability. As explored in this thesis, the influence of the NAO on the spatial distribution of  $\delta^{18}O_p$  requires longer records to identify their long-term co-variability and to develop their transfer function. Although desirable, direct measurements of  $\delta^{18}O_p$  values at high spatio-temporal resolution, globally or regionally (*e.g.*, at all weather stations), are expensive, time-consuming, and logistically infeasible. Direct measurements of  $\delta^{18}O_p$  values are often unavailable when and where needed [*e.g.* 244]. Moreover,

the short-term availability of  $\delta^{18}O_p$  records may bias their long-term variability estimates. Collectively, these concerns have increased the demand for methods that can accurately predict or interpolate  $\delta^{18}O_p$  values from existing datasets or locations without historical records.

iGCMs can be used to predict  $\delta^{18}O_p$  values globally instead of their measurement. However, iGCMs are sensitive to initial boundary conditions and stochasticity; thus, while useful for exploring large-scale mechanisms, they often do not accurately replicate historical variability [245]. Although data assimilation methods can improve their prediction accuracy, they are still insufficient compared to station measurements (e.g., GNIP) [246–248]. Additionally, tracking isotopic tracers in the hydrological cycle in GCMs doubles their computational demands, making it challenging to apply them at the required resolution. In contrast, geostatistical models or isoscapes have been used to statistically predict  $\delta^{18}O_p$  values based on their relationship with climate variables such as latitude, elevation, and surface temperature [249–253]. While precipitation isoscapes have been useful since their introduction, especially due to their availability, they are developed with limited predictors and rely on linear regression as their learning model, which questions their generalisability. Most importantly, isoscapes do not consider the large-scale atmospheric mode of variability indices (e.g. NAO) as predictors and only rely on strong linear relationships with surface climate variables (e.g., temperature). However, the causal mechanism between water isotopologues and surface climate variables is much more complex and would require advanced modelling pipelines to predict their variability. Together, these highlight the need for a robust modelling framework that overcomes all these limitations to accurately predict  $\delta^{18}O_p$  values for a specific location.

The Perfect Prognosis Empirical Statistical Downscaling (PP-ESD) method, which establishes transfer functions between observed large-scale variables (predictors) and local-scale observations (predictands) [e.g. 4, 254–259], can be used to predict the spatio-temporal variability of local  $\delta^{18}O_p$  values (Figure 2.4). More specifically, PP-ESD methods rely on reanalysis datasets to extract informative and relevant predictors that explain the predictand's variability and then use their relationships, normally learned with machine learning models, to predict their historical or future variability. For instance, if the transfer function is well-trained and validated, it can be combined with any GCM outputs to downscale their future or past climate information to a point scale.

PP-ESD models have several advantages, including low computational costs; they are bias-free since they rely on observed historical data and can be combined with any GCM to downscale their outputs to higher spatial resolution. However, the modelling routines of PP-ESD are laborious and complex, with critical steps that determine the accuracy and reliability of the predictions. These steps include data preprocessing, predictor selection and construction, model selection, training, validation, evaluation, and combining with GCMs for downscaling their predicted outputs. For instance, selecting the most informative and relevant predictors generally increases the performance and robustness of PP-ESD models. *The selection should be guided by knowledge of the atmospheric dynamics that govern a specific regional predictand and should not be generalized everywhere* [260, 261]. Additionally, several machine learning algorithms have the ability to capture more complex links between pre-

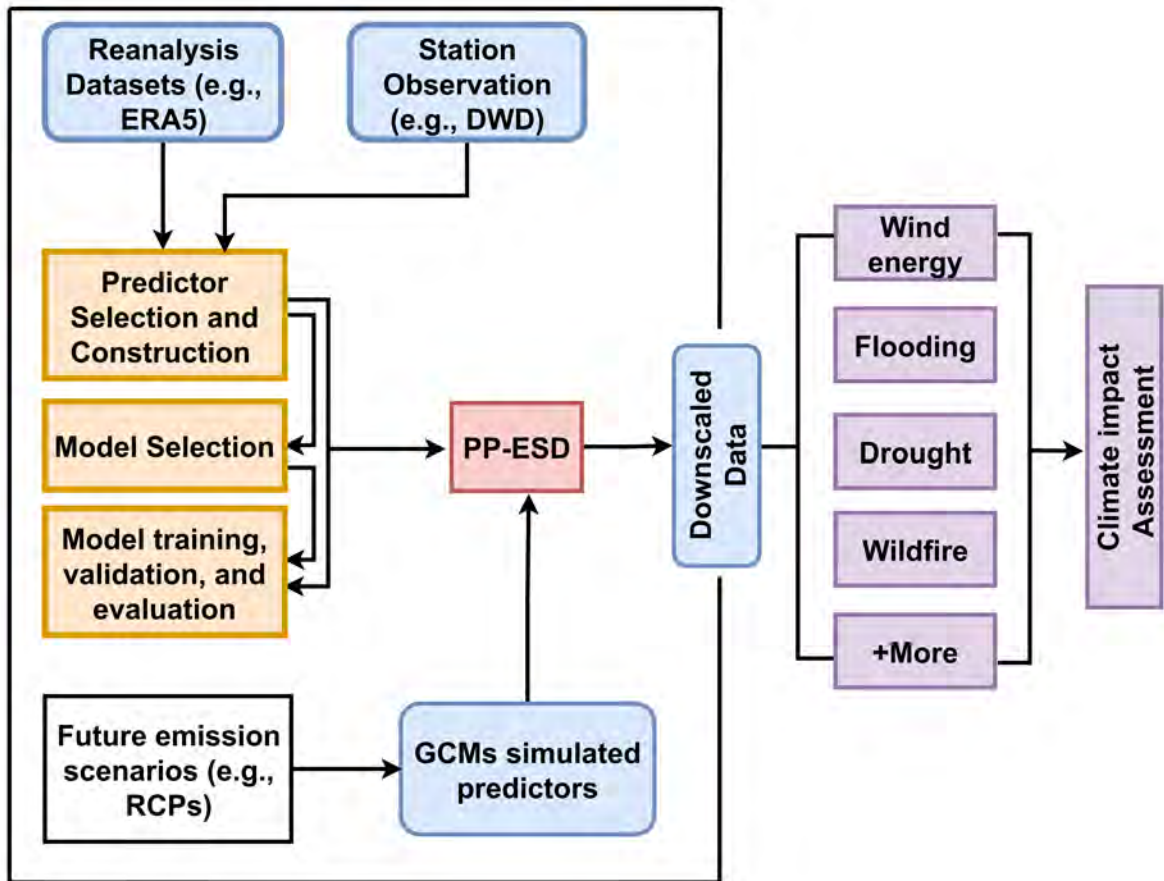


**Figure 2.4:** The main features and workflow of PP-ESD implemented in the pyESD package ([4], P5) (highlighted by the dashed red box). The station observation (e.g., DWD, GNIP) and reanalysis datasets (ERA5) are used to select the robust predictors for model training and validation. The trained PP-ESD model can be combined with GCM to generate the past or future predictions of the predictand. For instance, the combined predicted future climate information can be for climate change impact assessment (not included in the pyESD package)

dictors and predictands and do not require an explicit assumption of the distribution of observational data during the optimisation of the learning model. However, selecting the optimal machine learning algorithm depends on the predictand variable (e.g.,  $\delta^{18}O_p$  values, precipitation, and temperature), length of the observational records, spatiotemporal variability, spatial coherence, regional setting, and temporal stationarity of the learning model. All these factors make it challenging to use PP-ESD easily to predict local variability of  $\delta^{18}O_p$  values, which is very complicated. This thesis explores its applicability by developing a PP-ESD framework comprising these complex modelling routines. Therefore, as a complementary methodological objective of this thesis, I developed an open-source Python PP-ESD software (pyESD) that integrates all the steps (see Figure 2.4 for an overview of the framework of pyESD) into an efficient modelling pipeline to ensure robustness and accuracy of local-scale climate predictions. I validated the model's performance by generating precipitation and temperature predictions for a sub-hydrological catchment in complex mountainous terrain in southwestern Germany. To ensure the efficiency of the developed modelling framework, this thesis first explores the question:

**Q10:** How well do the developed PP-ESD models predict temperature and precipitation variability at stations?

After validating the new PP-ESD model for precipitation and temperature observations, I further explored its potential in predicting the local spatio-temporal variability of  $\delta^{18}O_p$  values using the observed large-scale climate variables, which is more challenging and useful for the focus of this thesis. I applied developed PP-ESD model to the monthly  $\delta^{18}O_p$  values from the GNIP stations across Europe with measurements of more than 30 years. This leads to the question:

**Q11:** Can machine learning in the PP-ESD framework be used to emulate the local spatio-temporal variability of  $\delta^{18}O_p$  values across Europe?

If the modelling framework performs as better as or more than the iGCM, then it would have the potential to replace or complement the explicit diagnostics of water isotopologues in the computationally expensive climate models. Additionally, the PP-ESD can be combined with iGCMs to downscale predicted low-resolution  $\delta^{18}O_p$  values to a point scale where proxy material is located and contribute to their interpretation. Besides, the station-based PP-ESD can be used as an emulator to fill all the missing  $\delta^{18}O_p$  values data in the GNIP stations by specifically including their large-scale drivers and localised conditions instead of using generalized interpolation techniques. Furthermore, the predictor selection method used to select the robust predictors for each station  $\delta^{18}O_p$  values can help determine how large-scale climate variables control their variability.



## **Part II.**

# Research Objectives and Strategies



# Objectives 3.

This thesis demonstrates the importance of integrating isotopic proxy data with iGCMs model output for reconstruction of paleoclimate dynamics and paleoenvironmental conditions. Overall, this thesis shows how iGCMs can resolve some of the uncertainties associated with proxy reconstruction by proposing a new framework for using simulated climate variables to disentangle proxy signals from others and also evaluate the non-stationarity of proxy transfer functions for reconstructing paleoclimate dynamics. These are addressed with two main research objectives (Part 1; [Section 3.1](#) & Part 2; [Section 3.2](#)) on paleoclimate dynamics reconstruction and a complementary objective (Part 3; [Section 3.3](#)) that explores a statistical modelling framework of emulating  $\delta^{18}O_p$  values that can replace or complement iGCMs. The complementary objective is important since it addresses the high computational cost demand of performing paleoclimate experiments with iGCMs and proposes a flexible framework for simulating spatio-temporal variability of  $\delta^{18}O_p$  values with model outputs. Part 1 ([Section 3.1](#)) demonstrates how iGCMs can be used to disentangle climate signals from topography (tectonic) isotopic signals imprinted in proxy materials to accurately reconstruct the past surface elevation of the European Alps. Part 2 ([Section 3.2](#)) demonstrates how iGCMs can be used to understand the causal mechanisms between (1) the large-scale atmospheric mode of variability (*e.g.*, NAO) and (2) the WAM system and its atmospheric dynamics and  $\delta^{18}O_p$  values (as the proxy variable reconstructed from natural archives). Altogether, this thesis addresses the use of iGCMs to resolve the two main challenges of using proxy records to reconstruct paleoclimate dynamics (*i.e.*, disentangling climate signals from non-climate signals and the assumption of stationarity of transfer functions). Here, I outline the research objectives and the strategies employed to address them. However, I highlight that details of the methods can be referred from the respective manuscripts in the Appendix ([Part VII](#)).

3.1 Part 1: Reconstructing the Paleoelevation of the Alps	27
3.2 Part 2: Reconstructing Paleoclimate Dynamics	30
3.3 Part 3: Machine Learning Framework for Predicting the Variability of local $\delta^{18}O_p$ values	33

## 3.1 Part 1: Reconstructing the Paleoelevation of the Alps

This part comprises topographic sensitivity experiments and Middle Miocene climate simulations that address questions 1-6 ([Q1-Q6](#)) in three manuscripts [P1-P3](#) (in [Part V](#)). The buildup research questions and key findings are:

**Q1:** How much isotopic ( $\delta^{18}O_p$ ) and regional climate signal (and where) would different west-to-east surface uplift scenarios of the Alps produce?

*The topographic sensitivity experiments for the diachronous surface uplift scenarios indicate  $\Delta\delta^{18}O_p$  values (*i.e.*, the difference between  $\delta^{18}O_p$  values at low- and high-elevation regions) of up to -8 % across the Alps, primarily due to*

*changes in orographic precipitation and adiabatic lapse rate changes in surface temperature (published in P1).*

Q2: To what extent do changes in the topography of the Alps affect the atmospheric circulation, moisture transport, and tropospheric dynamics of the regional climate across Europe?

*The simulated climate responses to changes in the Alps' topography indicate significant changes in synoptic-scale atmospheric pressure systems in the Northern Hemisphere (e.g., shifts of the pressure dipole axis and location of centres of action of the pressure systems), changes in moisture transport distance and pathways, and large-scale atmospheric dynamics that affected the precipitation of adjacent far-field regions of the Alps (published in P1).*

Q3: Does ECHAM5-wiso adequately simulate the Middle Miocene regional climate and  $\delta^{18}\text{O}_p$  well across the Alps and Europe?

*The Middle Miocene warming patterns simulated agree with the reconstruction from paleobotanical temperature records, precipitation patterns are consistent with herpetological fossil assemblages, and the  $\delta^{18}\text{O}_p$  values agree with the magnitude of paleo-meteoric water  $\delta^{18}\text{O}_p$  from pedogenic carbonates and phyllosilicates across Europe (published in P2).*

Q4: How much isotopic ( $\delta^{18}\text{O}_p$ ) signal would the changes in the Alps topography and Middle Miocene climate produce?

*The diachronous surface uplift scenarios of the Alps with Middle Miocene conditions still produce  $\Delta\delta^{18}\text{O}_p$  values of range -4 to -8 ‰ across the Alps, which is significant enough to be recorded by geological archives for reconstructing its paleoelevation and also agrees with the proxy reconstructions (to be submitted in P3).*

Q5: To what extent does the Middle Miocene climate and surface uplift affect the isotopic lapse rate across the Alps?

*The simulated isotopic lapse rates become shallower or decrease by  $\sim 1.0 \text{ ‰ km}^{-1}$  in response to the Middle Miocene conditions compared to the PI period and vary within the range of  $\pm 1.5 \text{ ‰ km}^{-1}$  for the diachronous surface uplifts of the Alps, with spatial differences around the Alps (to be submitted in P3).*

Q6: Does using the contemporary isotopic lapse rate across the Alps overestimate or underestimate the Middle Miocene paleoelevation across the Alps?

*Integrating the simulated Miocene lapse rates with proxy reconstructions indicates an overestimation of the Central Alps' paleoelevation by  $\sim 1.5 \text{ km}$  when the isotopic lapse rate is assumed stationary through time and space from present-day (to be submitted in P3).*

The above research questions enable the test of the hypothesis:

**Hypothesis (H1):** Diachronous west-to-east surface uplift of the Alps and Miocene global climate changes would impact the regional climate and, therefore, influence the  $\delta^{18}O_p$ -elevation gradient (*i.e.*, the isotopic lapse rate).

If this is true, it will violate their assumption of stationarity in paleoelevation estimates using stable isotope paleoaltimetry. This would have implications for interpreting the Alps' topographic evolution and complicate understanding its geodynamic evolution and surface processes. To resolve hypothesis **H1**, the following research strategies were used.

### 3.1.1 Research strategies for H1

In this part of the thesis, I used ECHAM5-wiso to perform topographic sensitivity and paleoclimate experiments to disentangle the climate and topography effects on isotopic signals reconstructed from geologic archives to estimate the past surface elevations of the Alps. Since the kinematic framework of the geodynamic evolution of the Alps is still debated and its surface uplift histories remain scarce, I generated a series of topographic configurations with two free parameters: **(1)** the elevation of the Western-Central Alps (*Wx*) and **(2)** the elevation of the Eastern Alps (*Ex*), to account for all the possible diachronous surface uplift scenarios through time. The elevations were set as a fraction of their present-day value, incrementally ranging from 0 % to 200 %. The topographic configuration W2E1, for example, therefore consists of the West-Central Alps and Eastern Alps set to 200 % and 100 % of their modern elevation, respectively (see **P1** in **Part V**). The main focus of these experiments was to quantify the effect of the specific topographic configurations on  $\delta^{18}O_p$  values and regional climate variables to determine if the signals are sufficient to be reflected in geologic archives (**Q1**). Hence, in the model setup, all other boundary conditions were kept constant at PI conditions (*e.g.*,  $pCO_2$ , orbital parameters, sea surface temperature). I analyzed the effect of topography on regional climate surface variables, moisture transport, atmospheric circulation patterns (NAO, EA, and SCAN), atmospheric dynamics, and isotopic lapse rate (**Q2**).

Since the first set of experiments only considered topographic changes of the Alps while keeping the global climate constant, I performed further simulations to explore the combined effect of the elevation changes under Middle Miocene conditions. I prescribed the realistic topographic configurations (*e.g.*, 200 % West-Central Alps) under two  $pCO_2$  conditions (*i.e.*, 278 and 450 ppm) of the Middle Miocene paleoenvironments (*i.e.*, vegetation, palaeogeography, sea surface temperatures, *etc.*). The Miocene simulations were compared to paleoclimate and isotopic records across continental Europe (**Q3**) to evaluate the model performance in representing the Miocene climate using the paleoenvironmental conditions. The selected topographic configurations for the Miocene experiments are based on previous paleoelevation estimates and geodynamic evolution reconstructions. Specifically, the mean surface elevation of the Central Alps in the Miocene has been suggested to be higher (200 % of modern; >4400 m) than its present-day value. Therefore, I considered the topographic scenarios with 200 % West-Central Alps and incrementally

increased the elevation of the Eastern Alps from 0 % to 200 % due to the lack of paleoelevation estimates in the region. From these experiments, I investigated the effect of the specific topographic scenarios and Middle Miocene global changes on  $\delta^{18}O_p$  values and regional climate variables (Q4). I calculated the isotopic lapse rates for the different scenarios in the Miocene and compared them to their respective estimates under the PI conditions. With this, I estimated the changes in surface uplift and Miocene paleoenvironment on the isotopic lapse rates around the Alps. I used the simulated isotopic lapses to recalculate the paleoelevation of the Central Alps from coeval proxy records and then quantified the uncertainties associated with the assumption of stationarity for the isotopic lapse rates from modern.

## 3.2 Part 2: Reconstructing Paleoclimate Dynamics

This section presents time-slice (paleo)climate simulations with Present-Day (PD), Pre-Industrial (PI), Mid-Holocene, Last Glacial Maximum (LGM), and Mid-Pliocene environmental conditions. These simulations analyse the hydroclimate and associated  $\delta^{18}O_p$  patterns changes across Europe driven by the large-scale atmospheric circulation patterns in the Northern Hemisphere (NAO and EA) and across West Africa by the West African Monsoon (WAM) dynamics. The analysis allows exploring the causal links between local isotopic variability and large-scale drivers and how these relationships change in past climates. Such information is relevant for the accurate interpretation of proxy reconstruction. The simulations address questions 7-9 (Q7-Q9) in a manuscript P4 (in Part VI) and complementary results S1 (in Part VI). The specific questions and key findings are:

**Q7:** How did the WAM and associated atmospheric dynamics respond to changes in paleoenvironmental conditions during the Late Cenozoic?

*The simulated responses reveal the strongest strengthened and more northward extent of the WAM during the Mid-Holocene, despite the enhanced hydrological cycle in the Mid-Pliocene. This was due to the pronounced meridional temperature gradient that drives the low-level westerlies, an increase in evaporative recycling through the expansion of vegetation in the Sahel-Sahara, and the northward shift of the African Easterly Jet (published in P4).*

**Q8:** Does the relationship (or transfer function) between  $\delta^{18}O_p$  and climate variables over the WAM region remain constant through the different paleoclimates of the Late Cenozoic?

*The analysis suggests that the estimated relationship between  $\delta^{18}O_p$  values and climate variables (temperature and precipitation) is non-stationary. This suggests variations in the causal mechanism linking the proxy signal and climate variable and affects the paleoclimate reconstructions (published in P4).*

**Q9:** How and where does the polarity of the East Atlantic (EA) pattern phase affect the NAO- $\delta^{18}O_p$  and climate variables across Europe?

*The findings indicate that the polarity of the EA indices influences the stationarity of the transfer function (i.e., the spatial relationship between NAO- $\delta^{18}O_p$  and climate variables), which is crucial for reconstructing past NAO variability. The causal analysis estimates also suggest that the winter NAO affects the subsequent summer NAO- $\delta^{18}O_p$  relationship (presented in S1).*

Altogether, the above research questions enable the test of the hypothesis:

**Hypothesis (H2):** The impact of atmospheric dynamics and large-scale variability mechanism on local proxy variables (e.g.,  $\delta^{18}O_p$ ) varies across different paleoclimates.

If this is valid, the contemporary transfer functions established on historical records would be biased, leading to reconstructions that are not entirely accurate. To resolve hypothesis **H2**, the following research strategies were used.

### 3.2.1 Research Strategies for H2

This part of the thesis demonstrates how iGCMs can be used to determine the changes in the relationship between large-scale atmospheric circulation dynamics and local proxy signals ( $\delta^{18}O_p$  values) through time and space. This is important since it helps determine to what extent the proxy transfer function can be used in reconstructing past atmospheric dynamics variability. Specifically, this part focuses on understanding the causal mechanisms and the potential changes in the link between  $\delta^{18}O_p$  values that are imprinted in proxy materials and hydroclimate related to the **(1)** WAM variability through the Late Cenozoic and **(2)** NAO index variability in the historical calibration period. The simulated variability of  $\delta^{18}O_p$  values in response to the different past environmental conditions (from present-day to Mid-Pliocene) was used to investigate the changes in its relationships with the large-scale atmospheric dynamics patterns and regional hydroclimate variability (e.g., precipitation and temperature). The historical simulations (1979-2014) performed following the Atmospheric Model Intercomparison Project (AMIP) protocol were used to validate the model performance against observations:

1. The simulated precipitation and temperature patterns and their seasonality were compared with observed and reanalysis datasets across the WAM region. Additionally, the associated  $\delta^{18}O_p$  values were compared to the available GNIP stations globally. The results indicated that ECHAM5-wiso represents the WAM dynamics and the  $\delta^{18}O_p$  values' spatio-temporal variability reasonably well (see **P4** in **Part VI**).
2. The comparison of the simulated hydroclimate patterns with observations and reanalysis datasets across Europe also indicated similarly good performance. The model outputs were used to construct the seasonal NAO and EA indices for winter and summer.

These indices were computed as the first two leading principal components of EOF analysis using the seasonal mean sea level pressure (SLP) anomalies fields over the North Atlantic-European region (20-80 °N, 80 °W-40 °E) (S1; Figure 1). Before the EOF analysis, a spatial weighting of latitude was applied to geographically equalize the pressure anomalies fields [262]. The simulated-based seasonal NAO index and its associated covariance matrix of the principal components' time series were compared to their equivalent estimates from instrumental records and reanalysis datasets (*i.e.*, ERA5 [196, 197] and NCEP/NCAR [263] reanalysis products) (S1; Figure 1 and Figure 2). The station-based instrumental NAO index was computed as the normalized SLP difference between Gibraltar and Iceland stations [264]. Overall, the simulated and observed NAO index comparison indicates good agreement and consistent centres of action. However, the model-observed consistency was more accurate in winter than in summer. This is partly due to the predominant control of NAO on regional climate inter-annual variability in winter than summer (see S1; Figure 3 and Figure 4 in Part VII).

To determine the WAM and its atmospheric dynamics changes through the Late Cenozoic, I computed the long-term seasonal anomalies of the relevant climate variables of the different past climates compared to PI. Specifically, I analyzed the changes in the low-level southwesterlies flow, meridional temperature gradient across the WAM region, surface heat fluxes, Africa Easterly Jet (AEJ), Tropical Easterly Jet (TEJ), Intertropical Discontinuity (ITD), and Shallow Meridional Cell (SMC) in the past climates. Additionally, I compared the simulations by ECHAM5-wiso to the model outputs of the PMIP4 experiments. Furthermore, model-based mean annual precipitation (MAP) estimates were compared to available proxy-based MAP reconstruction across Africa. Most importantly, the higher magnitude of precipitation increase and northward extent of pollen-based MAP estimates in the Mid-Holocene across West Africa were compared to the model estimates. To evaluate the potential changes in the relationship between proxy signals (here  $\delta^{18}O_p$  values) and local-scale (grid box) surface climate variables (here precipitation and temperature), I computed their correlations in the different past climates. This would help determine the potential non-stationarity of the relationship between the proxy signal and surface climate variables that would not be reflected in the proxy transfer functions. However, I highlight that the statistical estimates are only used as surrogates for the potential changes in their causal mechanism and acknowledge the limitations of such analysis.

Furthermore, to determine how the polarity of the EA index influences the NAO- $\delta^{18}O_p$  relationship, I performed a composite analysis by grouping the monthly datasets into two subsets based on the relative polarity of the NAO and EA indices. More specifically, the first set consists of equal phases (hereafter "EQ"), which comprises seasons with NAO and EA indices of the same sign (*e.g.*, winters with positive NAO and EA indices), and the second set is opposite phases (hereafter "OP"), which comprises seasons with NAO and EA indices of opposite signs (*e.g.*, winters with positive NAO index and negative EA index). Within each set, I computed the inter-annual correlation between the NAO index and  $\delta^{18}O_p$  values to determine if the polarity of the EA index influences the NAO- $\delta^{18}O_p$



relationship. Additionally, I computed the seasonal, long-term difference of  $\delta^{18}O_p$  values, temperature, and precipitation between the EQ and OP groups to understand the causes of the changes. I also evaluated how the polarity and intensity of the winter NAO index affect the subsequent summer NAO- $\delta^{18}O_p$  relationship using Granger causality statistical analysis (see **S2** in **Part VII** for more details). The analysis collectively reveals the sensitivity of the relationship between the NAO index and the local proxy signal (transfer function) to other atmospheric modes of variability and seasonality.

### 3.3 Part 3: Machine Learning Framework for Predicting the Variability of local $\delta^{18}O_p$ values

This section comprises method development that explores whether the explicit diagnostics of water isotopologues in iGCMs can be emulated with machine learning models to statistically predict the local  $\delta^{18}O_p$  values variability using large-scale variables. The proposed statistical framework is first validated and evaluated on precipitation and temperature weather stations in **P5** (in **Part VII**). The modelling pipelines are implemented into well-structured, easy-to-use, robust, and open-access Python software (pyESD; published in **P5**). Subsequently, in a complementary analysis, the developed model is used to explore its potential for predicting  $\delta^{18}O_p$  variability for GNIP stations in Europe (**S2**). The specific questions addressed and key findings are:

**Q10:** How well do the developed PP-ESD models predict temperature and precipitation variability at stations?

*The developed modelling pipelines in the empirical statistical downscaling framework show significant performance with explained variance,  $R^2$  of  $> 0.7$  for precipitation and  $R^2$  of  $> 0.9$  for temperature stations. Combining the established transfer functions of the stations with GCM output for future projections generates robust and high-resolution climate change information at the point scale in the hydrological catchment (published in **P5**).*

**Q11:** Can machine learning in the PP-ESD framework be used to emulate the local spatio-temporal variability of  $\delta^{18}O_p$  across Europe?

*The findings suggest that the machine learning framework can predict the spatio-temporal variability of  $\delta^{18}O_p$  across Europe, outperforming the iGCM ECHAM5-wiso to a significant extent. The chosen predictors highlight the importance of large-scale synoptic circulation patterns as key drivers of local-scale  $\delta^{18}O_p$  variability (presented in **S2**).*

These questions are resolved in a complementary objective of this thesis:

**Objective (O1):** To investigate whether machine learning can complement or substitute the stable water isotopes explicit in iGCMs for predicting the spatio-temporal variability of local  $\delta^{18}O_p$  values using large-scale atmospheric variables.

### 3.3.1 Research Strategies for O1

Here, I developed a new framework for using machine learning to downscale climate information to a point scale. The Python-based PP-ESD was first validated in a complex, mountainous hydrological catchment (Neckar) in southwestern Germany for downscaling future climate model outputs of precipitation and temperature. I used observations from German weather stations (DWD) and ERA5 reanalysis [196, 197] to construct the predictors, which included large-scale circulation pattern indices (*e.g.*, NAO, EA, and SCAN). The predictive skills of these potential predictors were evaluated before selecting the robust predictors for the individual stations. This helps explain the physical dynamics of how the large-scale variables control the station  $\delta^{18}O_p$  values. After testing the developed modelling routines and validating their performance on the weather stations, I then used the same framework to predict the spatio-temporal variability of  $\delta^{18}O_p$  values of 39 GNIP stations in Europe based on their sufficient data availability (S2; Figure 1). To evaluate the added value of using machine learning, I compared the GNIP records with the present-day  $\delta^{18}O_p$  simulations by the ECHAM5-wiso presented in Part 2. Overall, the results show good agreement between the GNIP and simulated  $\delta^{18}O_p$  values, although varies among the stations (see S2 in Part VII). The models were trained for each station and were done in many experiments with different algorithms to determine the best framework for predicting the  $\delta^{18}O_p$  values. In total, more than 390 station-based models were generated to explore the applicability of the PP-ESD to station  $\delta^{18}O_p$  values. *Note that this is the first time localized conditions and separate machine learning based-models are developed for the considered GNIP stations.* The models were trained with a “time series split” cross-validation (CV) setting and employed mean absolute error (MAE) as the optimization metric. This implies that in each CV iteration of the model training, subsequent blocks of data (validation period) that do not go into training are used to validate model performance. Aside from validation in the training period, the models were independently evaluated on data from 2013 to 2018 (which was never part of the training, if available) for each station (S2; Figure 1). I then compared the predictions for the training period (using CV predictions) and testing period to the actual observed GNIP measurements and ECHAM5-wiso simulated  $\delta^{18}O_p$  values using the Pearson correlation coefficient (PCC) and MAE.

## **Part III.**

# Results and Discussion



# Results and Discussion

# 4.

This section comprises the summary and discussion of the specific objectives outlined in **Part II**, highlighting their significance and implications. **Section 4.1.1** summarises the main findings of **Part 1** (on reconstructing the paleoelevation of the Alps) from manuscripts **P1** to **P3**, which are discussed comprehensively in their respective manuscripts (**Part V**). **Section 4.2.1** presents the main conclusions of **Part 2** (on reconstructing paleoclimate dynamics) from manuscript **P4** on West African monsoon (details in **Part VI**), and complementary analyses on the influence of the EA on NAO- $\delta^{18}O_p$  relationship and its seasonality changes (supplementary results in **Part VI**). **Section 4.3.1** summarises the modelling framework of using machine learning algorithms to predict the spatio-temporal variability of  $\delta^{18}O_p$  values across Europe (**Part 3**) from model development manuscript **P5** (**Part VII**) and complementary analyses on GNIP stations (supplementary results **S2** in **Part VII**).

4.1 Part 1: Reconstructing the Paleoelevation of the Alps	37
4.2 Part 2: Reconstructing Paleoclimate Dynamics . . .	44
4.3 Part 3: Machine Learning Framework for Predicting the Variability of local $\delta^{18}O_p$ values . . . . .	51

## 4.1 Part 1: Reconstructing the Paleoelevation of the Alps

### 4.1.1 Summary and Discussion

**Q1:** How much isotopic ( $\delta^{18}O_p$ ) and regional climate signal (and where) would different west-to-east surface uplift scenarios of the Alps produce? (details in **Boateng et al. [1] (P1)**)

The topographic configurations of the Alps result in significant changes in  $\delta^{18}O_p$  values, mainly due to associated changes in orographic precipitation (“amount effect”) and adiabatic lapse rate-driven localised changes in near-surface temperature (“altitude effect”). The impact of the topographic changes on precipitation (up to 125 *mm/month* increase) affected farther regions adjacent to the high-elevation region of the Alps, especially when the Western-Central Alps are uplifted by 200 % of modern topography. These far-field precipitation changes are due to the topographic-induced changes in large-scale atmospheric dynamics across Europe. On the other hand, the temperature changes (up to 10 °C cooling) are only significant in regions of modified topography. Altogether, the topographic-induced regional climate changes resulted in distinct profiles of  $\delta^{18}O_p$  values across the Alps. The isotopic profiles indicate a decrease in  $\delta^{18}O_p$  values from west to east and from south to north. Such patterns highlight the influence of increasing distance away from the oceanic source (“continentality effect”) on  $\delta^{18}O_p$  spatial distribution. The difference in  $\delta^{18}O_p$  values along the profiles is estimated to be less than -2 ‰ in low-elevation regions adjacent to the mountains and up to -8 ‰ between the low- and high-elevation ( $\Delta\delta^{18}O_p$ ) regions of the modified topography experiments. These imply that the  $\delta^{18}O_p$  values are highly sensitive to topographic variations to produce distinct

isotopic profiles that would reflect the diachronous surface uplift (*i.e.*, west-to-east surface uplift propagations). These simulated magnitudes of  $\Delta\delta^{18}O_p$  values suggest that the expected isotopic signal would be significant enough to be preserved and measured in geologic archives. Moreover, the simulated slight  $\delta^{18}O_p$  differences of 1 ‰ -2 ‰ across the low-elevation sites support the use of the  $\delta$ - $\delta$  paleoaltimetry approach and highlight the importance of sampling far-field low-elevation sites to differentiate between the different surface uplift scenarios.

**Q2:** To what extent do changes in the topography of the Alps affect the atmospheric circulation, moisture transport, and tropospheric dynamics of the regional climate across Europe? (**details in Boateng et al. [1] (P1)**)

Despite the Alps being a relatively small orogen, different surface uplift scenarios result in changes to the large-scale atmospheric dynamics, thereby driving changes in far-field precipitation patterns. Back-trajectory analyses indicate a greater influence of topography changes on moisture transport distance and pathways, particularly towards the eastern and southern flanks of the Alps, compared to the western and northern localities. The results suggest a predominant transport of summer air masses from the North Atlantic, along with some continental sources from Western Europe, depending on the topographic configuration and the target location. Topographic configurations with higher elevation over the Western-Central Alps (W2) result in shorter moisture transport distances from the North Atlantic. Such scenarios cause air masses to ascend over the Western Alps at a higher vertical level due to the orographic barrier before descending towards the eastern transects. The air mass trajectories towards the eastern flank of the Alps tend to travel a shorter distance at higher altitudes when the topography of the Eastern Alps is elevated but travel a longer distance towards the southern flank. These changes in vapour transport are expected, as mountain barriers force the air to rise, and depending on the strength of the flow, the cross-barrier flow could be blocked or deflected towards precipitation regions. The atmospheric conditions of the moisture source region also influence the precipitation type and amount in the target regions.

The altitude cross-sections of vertical wind velocities ( $\omega$ ), relative humidity, and cloud cover across the Alps suggest that the different surface uplift scenarios would induce sufficient orographic lifting to create notable updrafts, leading to the formation of thick clouds in the troposphere. The W2 experiments show a more significant influence on the vertical atmospheric structure than the W1 (*i.e.*, experiments with 100 % West-Central Alps) experiments, especially at the upper tropospheric levels. The W2 cross-sections exhibit strong ascent velocity in the Western-Central Alps up to the upper troposphere, with low-level subsidence in the Eastern Alps. Overall, due to the size and orientation of the Alpine orogen relative to the dominant wind fields, the regional precipitation dynamics' response to diachronous surface uplift results in a pattern that is unique and highly sensitive to the altitude of the Western-Central Alps.

The response of atmospheric circulation patterns suggests that changes in topography can induce alterations in the synoptic-scale atmospheric

pressure systems in the Northern Hemisphere. Different topographic configurations lead to changes in the NAO patterns by shifting its centres of action and pressure dipole axis and altering its pressure gradient strength, thereby affecting moisture transport to the continent. Such large-scale changes would modify moisture and heat transport pathways, wind patterns, and the intensity of storms and precipitation patterns across the North Atlantic and surrounding continents. For instance, the eastward shift and intensification of positive anomalies over Central Europe in response to the W2 configurations could likely reduce rainfall across central and southern parts of Europe due to northward moisture flow. However, such decadal modes of variability would not be reflected in low-resolution geologic archives used for stable isotope paleoaltimetry but would rather provide insights into the potential impact on the spatial-temporal variability of  $\delta^{18}O_p$  values. Changes in large-scale patterns can also influence the seasonality of hydroclimate variability, affecting the timing of carbonate formation across the Alps ( [e.g. 265]). Altogether, the results indicate that different topographic configurations yield unique atmospheric dynamics responses, which should be considered when investigating past  $\delta^{18}O_p$  changes.

**Q3:** Does ECHAM5-wiso adequately simulate the Middle Miocene regional climate and  $\delta^{18}O_p$  well across the Alps and Europe? (details in Botsyun et al. [2] (P2))

The simulated near-surface mean annual temperature (MAT) and mean annual precipitation (MAP) patterns across continental Europe are compared to proxy reconstructions. These include plant fossil-derived MAT (using the coexistence approach) and MAP estimates based on the paleobotanical and ecophysiological structures of herpetological assemblages. The simulations estimate an MAT of 12.0 °C for Mio278 conditions and 15 °C for Mio450 conditions. The continental response to Miocene conditions shows greater warming across the high elevations (> 1 km) of the Alps, with temperature increases of 3.4 °C and 7.2 °C warmer than the PI for Mio278 and Mio450, respectively. The MAT estimates from the Mio450 experiment align well with the plant fossil reconstructions, whereas the Mio278 estimates suggest a colder MAT than the proxies indicate. This discrepancy implies that increased  $pCO_2$  conditions contribute to better alignment between MAT estimates from models and proxy data.

The simulated MAP distribution across Europe indicates bidirectional patterns, with increases over Northern Europe (up to 50 mm/month) and decreases towards Western and Southern Europe (down to 60 mm/month). This shift in precipitation anomalies is more pronounced under Mio450 than Mio278 conditions. The strong latitudinal gradient in paleoprecipitation has also been suggested by proxy reconstructions during the warm Miocene, indicating warm and dry conditions with subdesertic vegetation over the northwestern Mediterranean and a humidity-adapted plant environment to the north ( [e.g. 266–268]). Despite the strong latitudinal gradient, most European regions experienced less precipitation than in the PI period, aligning with herpetofauna fossil reconstructions. However, paleobotanical MAP estimates suggest wetter conditions in the Miocene than in the PI. Comparisons of the Miocene simulations with other GCMs that participated in the first phase of Miocene inter-model comparison experiments (MioMIP1) show consistent MAT and MAP

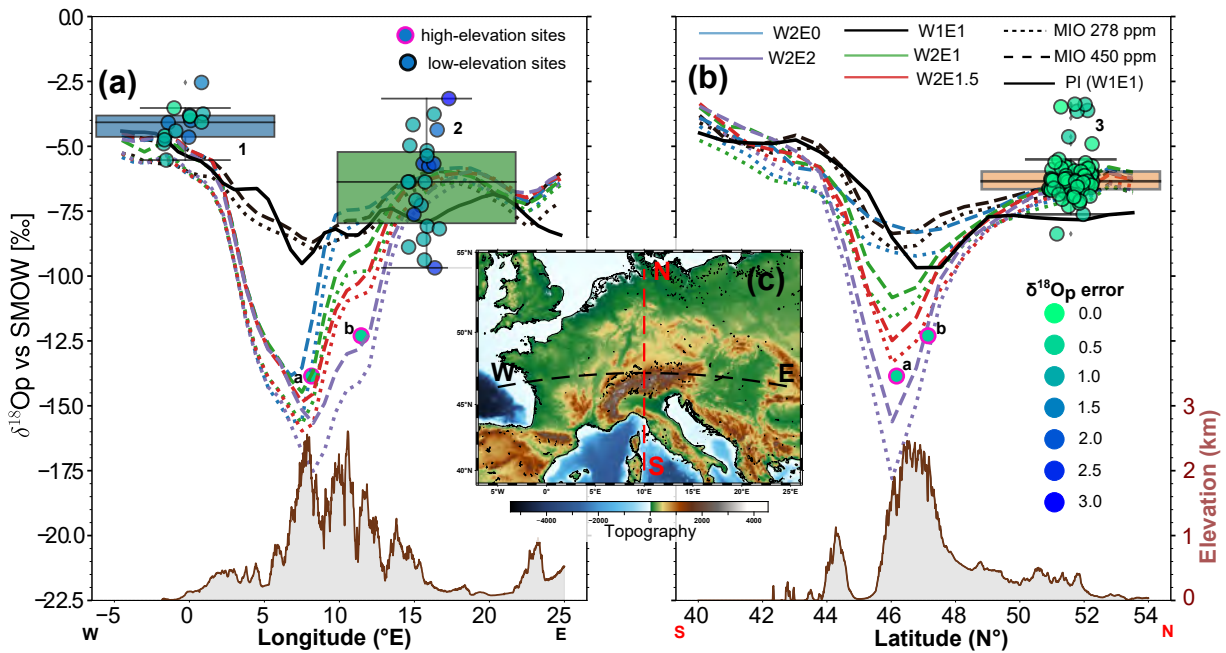


**Figure 4.1:** Annual mean  $\delta^{18}O_p$  values are longitudinal (a) and latitudinal (b) spatial profiles for the different topographic configurations in the Middle Miocene and its comparison to  $\delta^{18}O_w$  from geologic materials (proxies) across low- and high-elevation sites. The black lines represent the control (*i.e.*, W1E1) topographic scenario with Pre-Industrial (PI: solid) and Middle Miocene (Mio278: dotted, Mio450: dashed) boundary conditions. Modern topographic profiles are shown along the swaths (shown in c). The proxy-based  $\delta^{18}O_w$  estimates (shown with boxplot) are from pedogenic carbonates over the Northern Alpine foreland basin (Swiss Molasse Basin; Krsnik et al. [173]) and the Digne-Valensole basin; Cojan et al. [269]) and contained clay minerals from the Swiss and Bavaria freshwater Molasse basin; Bauer et al. [270]). The high-elevation sites are based on hydrogen isotopes from syntectonic high-Alpine fault zone silicates from the Simplon Fault Zone (Campani et al. [140] and Mancktelow et al. [271]). The coloured circles represent the reconstructed  $\delta^{18}O_w$  error. Note that the proxies' locations are extrapolated onto the profiles to compare them with the simulated magnitudes.

estimates.

The simulated  $\delta^{18}O_p$  values are in agreement with the reconstructed  $\delta^{18}O$  of paleo-meteoric water ( $\delta^{18}O_w$ ) from pedogenic carbonates [173, 269] and contained clay minerals (*i.e.*, bentonites and smectite-rich tuffs) [270] over the low-elevation regions around the Alps (Fig 6). Most of the reconstructed  $\delta^{18}O_w$  values fall within the simulated  $\delta^{18}O_p$  range of -3 to -8 ‰ across the low-elevation regions adjacent to the Alps for all Middle Miocene experiments. However, some of the clay mineral-based  $\delta^{18}O_w$  values slightly exceed the simulated range and show the widest spread of  $\delta^{18}O_w$  values and the highest reconstruction  $\delta^{18}O_w$  error of up to  $\pm 3$  ‰. At high-elevation sites,  $\delta^{18}O_w$  values (-12 to -15 ‰) calculated from hydrogen isotope ( $\delta D$ ) reconstructions from syntectonic high-Alpine fault zone silicates [140, 271] align only with model estimates from higher topography scenarios (Figure 4.1). This indicates that the paleoelevation across the Central Alps during the Middle Miocene was significantly higher than present. Overall, the consistency between modelled and reconstructed  $\delta^{18}O_w$  supports the integration of both GCMs and proxy material to ensure accurate reconstruction of past surface elevations.

**Q4:** How much isotopic ( $\delta^{18}O_p$ ) signal would the changes in the Alps topography and Middle Miocene climate produce? (details in Boateng et al. [to be submitted] (P3))



The different topographic configurations under Miocene conditions resulted in greater changes in  $\delta^{18}O_p$  values in areas of modified topography and slight changes in adjacent low-elevation regions ( $< 2 \text{ ‰}$ ) (see P3). Specifically,  $\delta^{18}O_p$  differences of up to  $-10 \text{ ‰}$  and  $-8 \text{ ‰}$  are estimated across the high-elevation modified regions for the Mio278 and Mio450 conditions (Figure 4.1). These estimates are similar to the topography-induced isotopic signal using PI conditions in Q1. The  $\Delta\delta^{18}O_p$  values (difference between the low-elevation regions and high-elevation regions) are  $\sim 2 \text{ ‰}$  less in the Middle Miocene compared to the PI climate. The  $\Delta\delta^{18}O_p$  values range from  $-4$  to  $-6 \text{ ‰}$  for the topographic configurations in Miocene but reach  $-8 \text{ ‰}$  in PI. This implies that changing topography still produces an isotopic signal significant enough to be reflected in geological material under a warmer past climate. The simulated changes in  $\delta^{18}O_p$  values can mainly be attributed to localized adiabatic temperature changes, orographic precipitation, and the associated large-scale precipitation changes. The distinct  $\delta^{18}O_p$  profiles across the Alps highlight the sensitivity of meteoric water isotopes to both direct (altitude) and indirect global forcings (*e.g.*, palaeogeography and  $p\text{CO}_2$ ). The sensitivity of the European climate to the Alps' topography on the local to regional scale, as demonstrated in this thesis, stresses the importance of an accurate representation of past mountain elevations in climate models. Although topographic changes caused by rifting processes often have a second-order forcing factor on global climate responses, their impacts affect the gradients of regional climatic variables, biodiversity, and landscape.

**Q5:** To what extent do Middle Miocene climate and surface uplift affect the isotopic lapse rate across the Alps? (details in Boateng et al. [to be submitted] (P3))

The estimated annual isotopic lapse rate for the topographic configurations under Miocene conditions for the western and northern transects around the Alps indicates notable spatio-temporal changes. The linear regression used to estimate the lapse rate shows a statistically significant relationship between  $\delta^{18}O_p$  values and elevation, with a coefficient of determination ( $r^2$ ) of 0.85-0.99. The lapse rate estimates shallow (or decrease) by  $\sim 1.0 \text{ ‰ km}^{-1}$  and  $0.5 \text{ ‰ km}^{-1}$  in the Mio450 and Mio278 conditions, respectively, compared to the PI. Moreover, different topographic configurations result in lapse rate variations of up to  $\pm 1.5 \text{ ‰ km}^{-1}$  differences compared to the unmodified topographic configuration. The estimated lapse rates in the PI were  $0.19 \text{ ‰ km}^{-1}$  higher over the western transect than over the northern transect of the Alps. These spatial differences increase further (by up to  $0.4 \text{ ‰ km}^{-1}$  more than in PI) in the Middle Miocene, due to the more depleted  $\delta^{18}O_p$  values over the Western Alps in the Middle Miocene compared to the northern foreland basin of the Alps. The spatial changes can be attributed to the seasonal distribution of moisture from the North Atlantic and the increasing distance from the moisture source, leading to more depleted air masses toward the northern and eastern transects. Moreover, moisture redistribution around the Alps due to orographic blocking and rainout across the high topography of the Western-Central Alps also contributes to the spatial variability of the isotopic lapse rates. Overall, the significant changes in isotopic lapse rate in response to different surface uplift scenarios and global climate changes highlight the huge implications of its assumption

of stationarity for stable isotope paleoaltimetry.

Q6: Does using the contemporary isotopic lapse rate across the Alps overestimate or underestimate the Middle Miocene paleoelevation across the Alps? (details in Boateng et al. [to be submitted] (P3))

Even though previous studies have suggested that using a modern isotopic lapse rate might result in inaccurate estimates of paleoelevation [119, 120], no study has quantitatively determined the magnitude of uncertainties related to this issue across the Alps. The simulated  $\delta^{18}O_p$  values in response to Miocene conditions provide an opportunity to use the paleoclimate-constrained simulated and modern observed isotopic lapse rates with reconstructed isotopic signals ( $\Delta\delta^{18}O_w$ ) from proxies, to calculate their respective paleoelevation to determine their differences. Hence, I recalculated the recent Miocene Central Alps paleoelevation based on  $\delta$ - $\delta$  paleoaltimetry by Krsnik et al. [173]. Their  $\Delta\delta^{18}O_w$  values were reconstructed from pedogenic carbonate from three different sections (*i.e.*, Fontanen, Jona, Aabach) of the Northern Alpine Foreland Basin (Swiss Molasse Basin; SMB) and high-Alpine phyllosilicate hydrogen isotope ( $\delta D$ ) values from the Simplon Fault Zone (SFZ). The  $\Delta\delta^{18}O_w$  values between the three reference sites and the high-elevation SFZ site ( $\delta^{18}O_w$  values of  $-14.6 \pm 0.3$ ; Campani et al. [140]) were  $-8.1$  ‰,  $-8.8$  ‰ and  $-11.5$  ‰, respectively. The simulated Miocene  $\Delta\delta^{18}O_p$  values (in the range of  $-4$  to  $-8$  ‰) between the low- ( $< 500$  m) and high-elevation ( $> 1000$  m) regions agree with the estimates from the proxy reconstructions.

The isotopic lapse rates calculated from the Miocene experiments for the 278 and 450 ppm  $pCO_2$  conditions and topographic scenarios ( $-2.02$  to  $-4.65$  ‰  $km^{-1}$ ), from modern precipitation-based measurements at weather stations across the northern slope of the Alps ( $-2.0$  ‰  $km^{-1}$ ; Campani et al. [140], and from surface rivers globally ( $-2.8$  ‰  $km^{-1}$ ; Poage and Chamberlain [139]) were used with the reconstructed  $\Delta\delta^{18}O_w$  values to estimate the Miocene paleoelevation of the Central Alps. The results indicate that using the local observed modern precipitation-based lapse rate ( $-2.0$  ‰  $km^{-1}$ ) overestimates the Miocene Central Alps paleoelevation by  $\sim 1.5$  km (Figure 4.2). The median of the paleoelevation estimates using the varied simulated Miocene lapse rates agrees with the global surface-water-based isotopic lapse rate (Figure 4.2). The agreement might be due to the fact that isotopic distribution in global river catchments integrates long-term climatic processes from different environmental conditions globally [102, 139, 272] and, therefore, might reflect similar long-term changes in the Miocene and surface uplift scenarios. The deviations in the rainfall-based estimates can be due to the sparse distribution of weather stations ( $< 10$ ) across the Alps and based on the fact that their records are event-specific, reflecting only short-term climatic processes. Hence, the results suggest modern global river-based lapse rate is more efficient than the rainfall-based lapse rate in the absence of paleoclimate-constrained lapse rates for reconstructing past surface elevation of orogens.

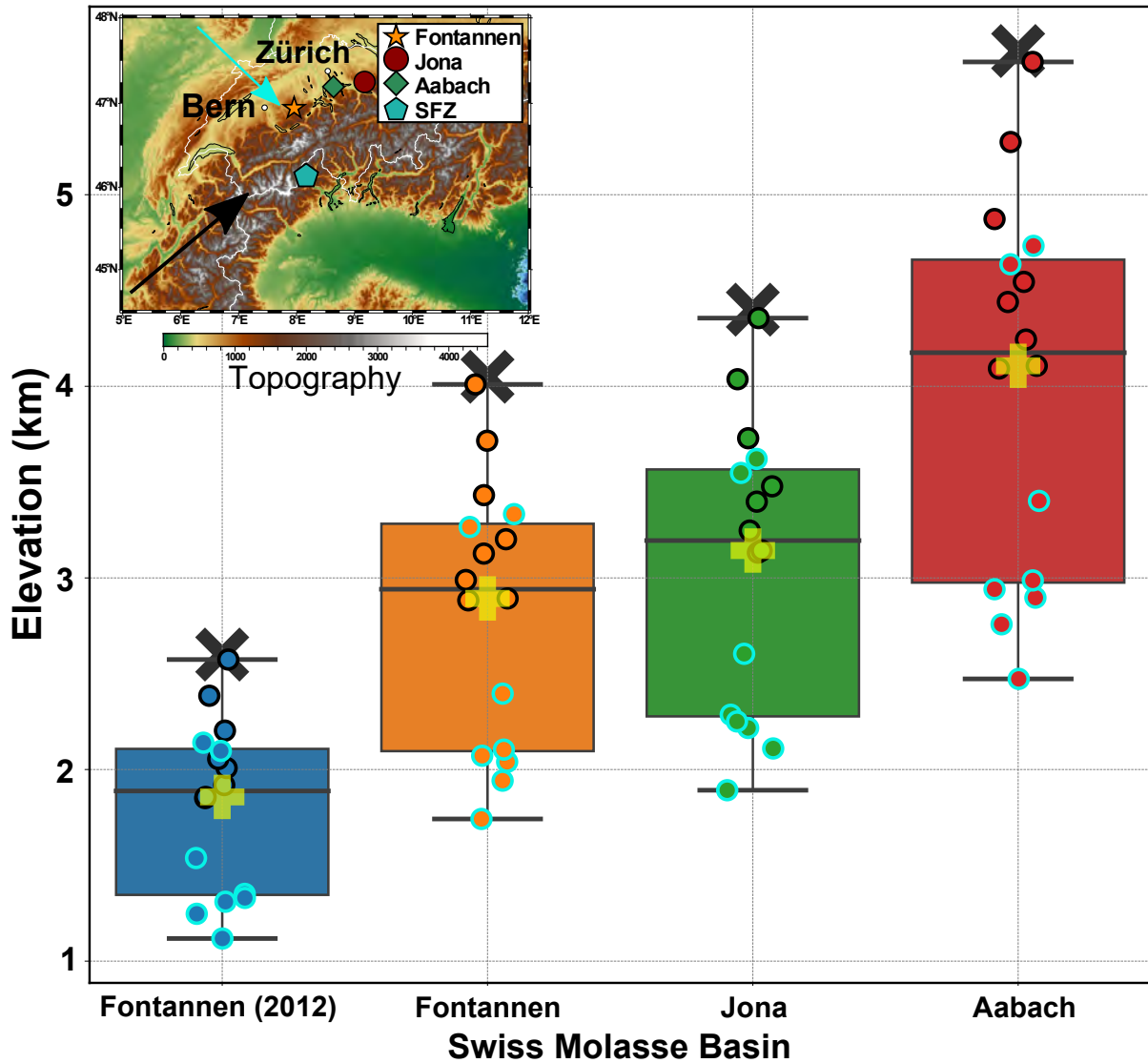


**Figure 4.2:** Paleoelevation estimates of Miocene Central Alps with isotopic lapse rates from (1) Middle Miocene  $p\text{CO}_2$  scenarios (278 ppm (Mio278); 450 ppm (Mio450)), (2) topographic sensitivity experiments, (3) modern station-based observed precipitation across the north slope of the Alps ( $-2.0 \text{ ‰ km}^{-1}$ ; Campani et al. [140]), and (4) global surface waters ( $-2.8 \text{ ‰ km}^{-1}$ ; Poage and Chamberlain [139]). The calculated ranges of paleoelevations for the different topographic configurations with the lapse rate considered along the northern and western flanks of the Alps are shown as distribution (boxplot) for the different foreland basin locations shown in (b). The  $\Delta\delta^{18}\text{O}_w$  values between the low-elevation foreland basins (*i.e.*, Fontannen (both from Campani et al. [140] and Krsnik et al. [173]), Jona, and Aabach) and high-elevation site (Simplon Fault Zone; Campani et al. [140]) are from recent reconstructions by Krsnik et al. [173].

#### 4.1.2 Significance and Implications

This part of the thesis presents the first series of topographic and paleoclimate sensitivity experiments that determine the impact of diachronous surface uplift scenarios of the Alps on regional climate and  $\delta^{18}\text{O}_p$  values. The goal is to determine whether the isotopic signal imprinted in geologic materials would be significant enough to reflect the complex diachronous west-to-east surface uplift scenarios across the Alps. This would enable the use of stable isotope paleoaltimetry to reconstruct the topographic evolution of the Alps through time and space. Overall, the results indicate how iGCMs can be used to isolate the climate signals from non-climate signals imprinted in proxy records through sensitivity experiments to improve their interpretation. These findings significantly contribute to

our understanding of the climate-tectonic interactions within the Earth system, which are pertinent for simulating past climate variability and gaining insights into future climate change. The results indicate that  $\delta^{18}O_p$  values across the Alps are sensitive enough to changes in Alps topography and global past climates to be reflected in proxy records. This would facilitate the reconstruction of the Alps' complex diachronous surface uplift histories. Such estimates can be used as constraints for geodynamic and landscape evolution models, aiding in understanding deep-seated geodynamic and climate-driven surface processes [158, 161, 166, 167, 171].

Additionally, the simulated  $\delta^{18}O_p$  values in response to paleoenvironmental changes reveal spatio-temporal variations in isotopic lapse rates across the Alps compared to modern values. This highlights the necessity for refinements in previously published paleoelevation estimates of the Alps to ensure accurate reconstructions of their geodynamic evolution. The results also indicated that modern global river-based isotopic lapse rates are more appropriate than rainfall-based ones when  $\delta^{18}O_p$  values of paleo-meteoric waters can not be simulated with iGCMs. The reason is that the  $\delta^{18}O_p$  values of the surface rivers reflect long-term climate changes compared to the  $\delta^{18}O_p$  values in rain waters since it is event-specific and does not reflect long-term climate variability. This finding is more important for stable isotope paleoaltimetry since not all paleoelevation estimates across different mountain ranges can be combined with such computationally expensive topographic sensitivity and paleoclimate experiments.

In essence, accurate estimates of paleoelevations are crucial for achieving realistic representations of surface conditions in paleoclimate simulations. This might potentially resolve some of the persistent model-proxy disagreements, such as the controversies regarding wetter or drier Middle Miocene conditions across Europe. Overall, the results of **Part 1** have demonstrated that iGCMs can be used to isolate climate signals from tectonic signals of isotopic signatures in geological material to improve their interpretation in reconstructing paleoenvironmental conditions. Altogether, the presented studies in **Part 1** highlight the importance of employing paleoclimate-constrained transfer functions, such as isotopic lapse rates, in reconstructing paleoclimate dynamics and paleoenvironmental conditions.

## 4.2 Part 2: Reconstructing Paleoclimate Dynamics

### 4.2.1 Summary and Discussion

**Q7:** How did the WAM and associated atmospheric dynamics respond to changes in paleoenvironmental conditions during the Late Cenozoic? (details in **Boateng et al. [3] (P4)**)

The simulated Mean Annual Precipitation (MAP) anomalies in the Late Cenozoic revealed the most strengthened WAM conditions in the Mid-Holocene despite the highest global warming and an enhanced

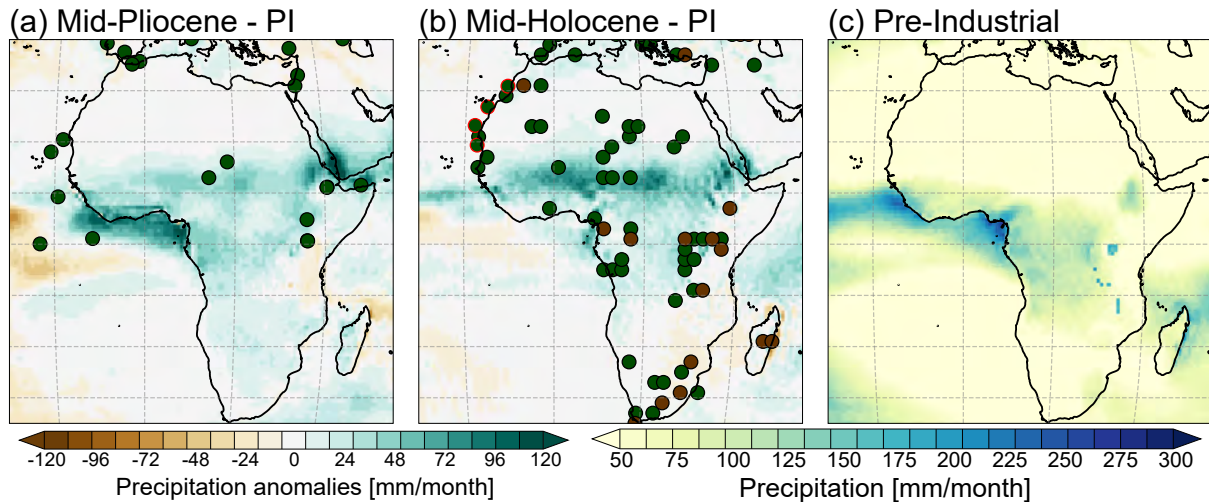


**Figure 4.3:** ECHAM5-wiso simulated mean annual precipitation anomalies relative to (c) Pre-Industrial conditions for (a) Mid-Pliocene, and (b) Mid-Holocene across Africa. Proxy reconstructions are displayed as filled circles (showing green for wetter and brown for drier conditions). The Mid-Holocene proxy data are pollen-inferred (Bartlein et al. [208]; black edge colour) and leaf wax-inferred (Tierney et al. [176]; red edge colour) precipitation estimates and the Mid-Pliocene proxy data are based on hydroclimate multi-proxy compilation by Feng et al. [276].

hydrological cycle in the Mid-Pliocene (Figure 4.3). The WAM seasonal precipitation anomalies in the Mid-Holocene exhibit bidirectional latitudinal patterns, with an increase of  $\sim 150 \text{ mm/month}$  over most parts of the Sahel-Sahara regions ( $7^\circ\text{N} - 30^\circ\text{N}$ ) and a decrease of about  $30 \text{ mm/month}$  over the tropical southern coastal regions ( $2^\circ\text{N} - 6^\circ\text{N}$ ) (Figure 4.3). The atmospheric dynamics and surface heat fluxes associated with MAP anomalies indicate that the orbitally induced pronounced meridional temperature gradient across the WAM region and the high vegetation fraction across the Sahara in the Mid-Holocene strengthened the WAM. More specifically, the strengthened conditions were associated with a northward shift of the core of the AEJ, a higher altitudinal reach of the monsoon (deeper monsoon depth), increased moisture recycling through latent and sensible heat fluxes, and a higher position of the ITD. Additionally, the changes in atmospheric dynamics suggest that the weakening of the AEJ is not solely responsible for the strengthening of the WAM [178, 273–275], especially when the global climate is predominantly controlled by orbital forcings. However, the northward shift of the AEJ plays a crucial role in determining the intensity of the WAM.

The comparison of the simulated MAP anomalies with PMIP4 model outputs for the Mid-Holocene indicated a consistent increase for all models but with the highest intensification of the WAM by ECHAM5-wiso. This might partly be due to the fact that I used higher spatial resolution ( $\sim 80 \text{ km}$  vs  $200 \text{ km}$ ) than the PMIP4 models and also prescribed realistic Mid-Holocene vegetation with BIOME6000 [277–280] compared to the maintained PI vegetation in the PMIP4 Mid-Holocene experiments [20, 68]. Overall, the results underscore the importance of vegetation feedback and land-atmosphere interactions in climate models for representing WAM dynamics and variability. Moreover, the comparison of the simulated MAP anomalies from all the models to pollen-based [208] and leaf wax-based [176] MAP anomalies across Africa indicates good agreement with ECHAM5-wiso in the magnitude of MAP increase across Sahel-Sahara region (Figure 4.3 and Figure 4.4). However, all models underestimate the northward extent of the WAM increase over the Sahara

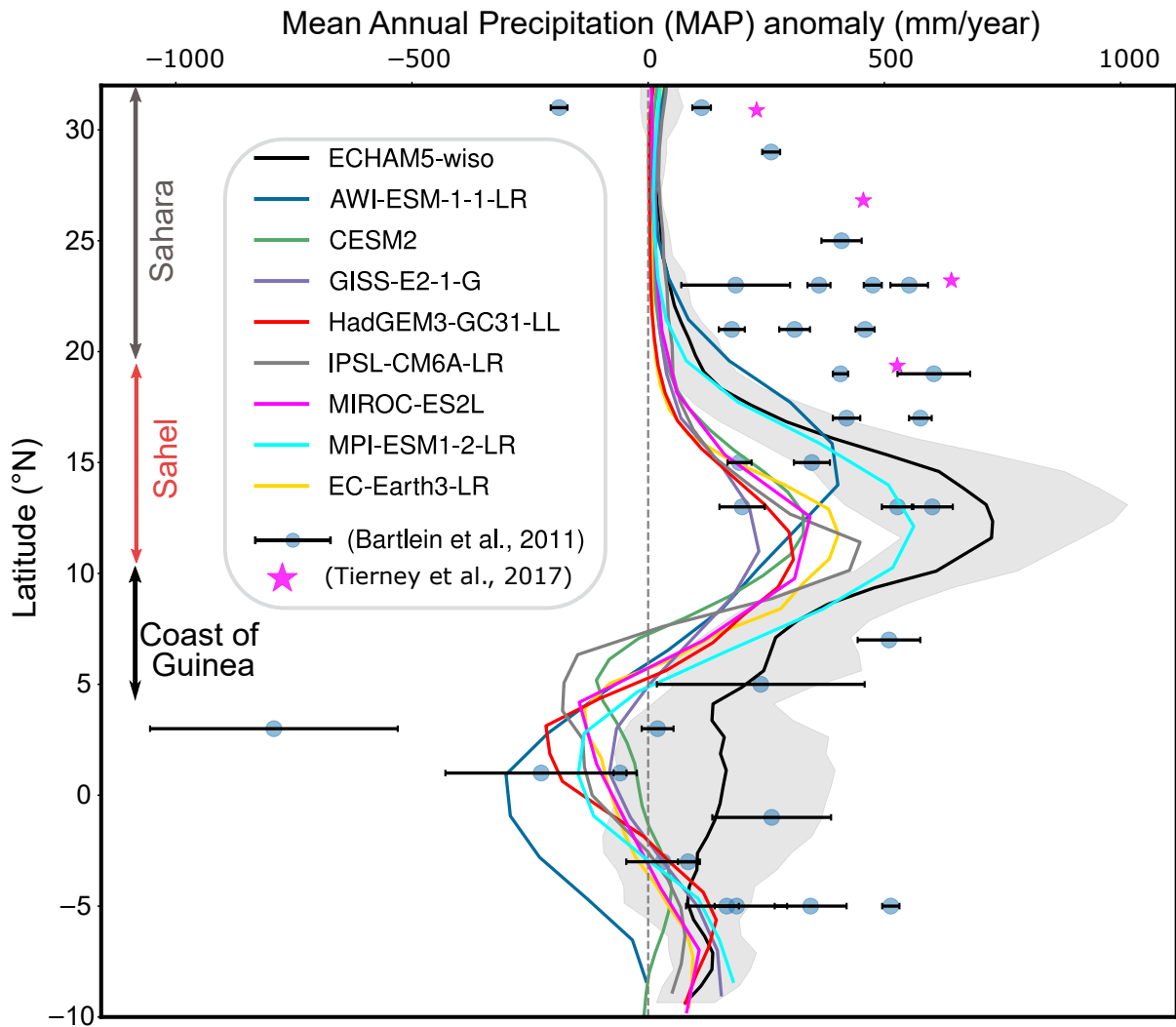


**Figure 4.4:** Comparison of the mean annual precipitation (MAP) anomalies of the latitudinal extent of WAM in the Mid-Holocene for all models (ECHAM5-wiso (black) and PMIP4 models) to pollen-inferred (Bartlein et al. [208]; blue circles) and leaf wax-inferred (Tierney et al. [176]; 1189 magenta stars) precipitation reconstruction. The black shadings denote one standard deviation value from the regional means of the ECHAM5-wiso simulation. The error bars of the proxies represent the standard errors of the precipitation reconstructions.

(Figure 4.4). The discrepancy between the models and proxies over the Sahara can be attributed to some missing processes (*e.g.*, dust loadings, interactive vegetation, and paleolake conditions) and feedback mechanisms not well represented in the climate models [175, 176, 209–212, 281, 282] or biases in the proxy transfer functions that do not account for the regional changes caused by significant orbital conditions compared to the historical calibration period.

**Q8:** Does the relationship (or transfer function) between  $\delta^{18}O_p$  and climate variables over the WAM region remain constant through the different paleoclimates of the Late Cenozoic? (details in Boateng et al. [3] (P4))

The simulated  $\delta^{18}O_p$  value anomalies in the WAM season indicate the most depleted conditions in the Mid-Holocene across the Sahel (decreased by -6 ‰). The decrease in  $\delta^{18}O_p$  values in the Mid-Pliocene

across the Sahel was insignificant ( $< 2 \text{ ‰}$ ) and showed more depleted patterns towards the east. Even though the decrease in  $\delta^{18}\text{O}_p$  values in the Mid-Holocene and Mid-Pliocene followed their respective strengthening of the WAM, the spatial patterns between  $\delta^{18}\text{O}_p$  values and precipitation anomalies differ in the WAM season despite the predominant control of the “amount effect” on  $\delta^{18}\text{O}_p$  spatio-temporal variability in the region [96, 117, 118]. This suggests changes in the regional climate control on the isotopic composition of water in the different past climates. The inter-annual relationships between the simulated monthly means of  $\delta^{18}\text{O}_p$  values and (1) precipitation and (2) near-surface temperature during the WAM season reveal significantly varied patterns in the Mid-Holocene compared to the PI, LGM, and Mid-Pliocene. Overall, the PI simulation shows a north-south bidirectional relationship between precipitation and  $\delta^{18}\text{O}_p$  values, with significant negative correlation coefficients from the Sahel to the Guinea coast and positive values over the Sahara (significant up to  $25^\circ\text{N}$ ). The LGM and Mid-Pliocene show similar patterns but differ in the strength of the relationship compared to PI. The negative relationship between the precipitation and  $\delta^{18}\text{O}_p$  values, which implies that an increase in precipitation amount results in more depletion of heavy oxygen isotopes, is partly due to (1) the increase in rainfall amount moistening the atmosphere, reducing rainfall re-evaporation and diffusive fluxes, and ultimately resulting in more negative  $\delta^{18}\text{O}_p$  values in raindrops; and (2) intense convective activity increasing vertical mixing in the form of unsaturated downdrafts, which results in more negative  $\delta^{18}\text{O}$  values of the low-level vapour feeding into subsequent convective systems with more depleted  $\delta^{18}\text{O}_p$  values [96, 117].

In the Mid-Holocene, the precipitation- $\delta^{18}\text{O}_p$  relationship changes to overall negative correlation coefficients over the entire continent in the WAM season (Figure 4.5). Additionally, the strength of the positive temperature- $\delta^{18}\text{O}_p$  relationship across the Sahel increases compared to PI (Figure 4.5). The changes can be attributed to the northward migration of the WAM caused by the pronounced temperature gradient and evaporative recycling due to the vegetation cover in the Sahara, which differs from the desert condition in the PI. In general, the significant changes in the correlation patterns in the different climates, which are more significant in the Mid-Holocene, suggest the non-stationarity of the controlling mechanism between  $\delta^{18}\text{O}$  values and regional climate dynamics over West Africa. This explains the reason for the model-proxy disagreement in the Mid-Holocene due to the potential bias of the transfer functions calibrated on the historical periods. Although the relationships are only based on empirical evidence and do not reflect the physical causal mechanisms or multivariate covariance, the results clearly indicate non-stationarity of the relationship between  $\delta^{18}\text{O}$  and climate variables through the different paleoclimate periods of the Late Cenozoic.

**Q9:** How and where does the polarity of the East Atlantic (EA) pattern phase affect the NAO- $\delta^{18}\text{O}_p$  and climate variables across Europe? (supplementary results in S1)

The correlation maps between NAO and EA indices and local-scale (grid box) climate variables (including  $\delta^{18}\text{O}_p$  values) indicate stronger relationships in winter than in summer (S1; Figure 4 and Figure 5) and are consistent with previous studies [e.g. 136, 218, 223, 225, 226, 232, 283].

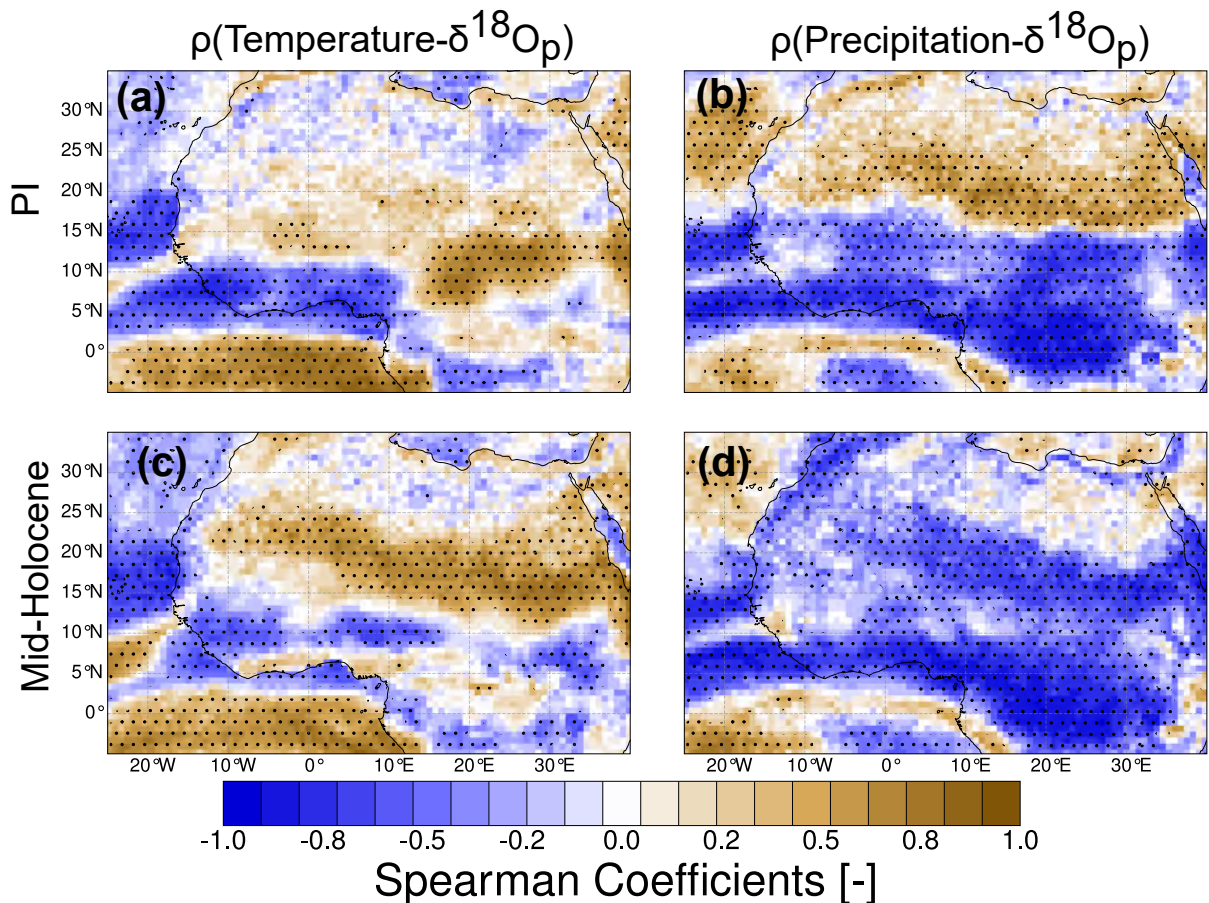


**Figure 4.5:** Spearman correlation coefficients for the inter-annual relationship between the simulated monthly means of  $\delta^{18}O_p$  and precipitation amount (right panel) and temperature (left panel) during the WAM months (JJAS). The dot stippling represents the regions with significant correlation coefficients with a 95 % confidence interval.

This is attributed to the predominant influence of large-scale atmospheric circulation patterns on the inter-annual climate variability and dynamics in the North Atlantic-European region in the winter season [216, 217, 220, 221]. For instance, the winter NAO- $\delta^{18}O_p$  correlation demonstrates a strong positive relationship across most parts of continental Europe, with a shift toward a weaker relationship over the Mediterranean region (S1; Figure 4 and Figure 5). The strong positive correlation can be attributed to contrasting moisture sources and trajectories associated with the phases of the NAO. Conditions during the negative phase reflect an increased frequency of cold easterlies transporting  $^{18}O$ -depleted moisture, while positive NAO winters are dominated by warmer westerly air masses transporting  $^{18}O$ -enriched vapour from the North Atlantic Ocean and the Mediterranean Sea into Central Europe [136, 218, 224, 225, 234]. The correlation over Iceland indicates strong negative values, leading to a northeast line of zero correlation, or an axis of polarity, over which the correlation changes in the North Atlantic (S1; Figure 4).

On the other hand, the winter EA- $\delta^{18}O_p$  correlation shows strong negative values over the Mediterranean and parts of Eastern Europe and positive values over the eastern part of the North Atlantic (S1; Figure 5). Overall, the opposite correlation patterns of NAO- $\delta^{18}O_p$  and EA- $\delta^{18}O_p$  suggest the potential influence of the polarity of the EA (and other teleconnections) on the NAO-climate relationship. However, in summer, both



the NAO and EA indices indicate similarly weak positive correlations over most parts of Europe with  $\delta^{18}O_p$  values (S1). The varied correlation patterns between the EA and  $\delta^{18}O_p$  from summer to winter suggest possible changes in how the EA influences regional hydroclimate across different seasons. Additionally, the winter NAO-temperature relationship indicates similar patterns compared to the winter NAO- $\delta^{18}O_p$ , highlighting their predominant influence on the  $\delta^{18}O_p$  distribution across Europe. The winter NAO-precipitation correlations indicate significantly varied patterns with a north-south bidirectional gradient, showing a positive relationship over northern Europe ( $> 50^\circ\text{N}$ ) and negative values over the southern latitudes (S1; Figure 4). Interestingly, the meridional dipole gradient of winter NAO-precipitation switches to a west-to-east dipole gradient for EA-precipitation correlation, with strong positive values towards southeastern Europe (S1; Figure 4). Altogether, the pronounced differences in the NAO and EA indices' relationships with climate variables and their seasonal changes underscore the complexity of using a generalized transfer function to construct their past variability.

Evaluating how and where the polarity of the EA affects the relationship between the NAO and  $\delta^{18}O_p$  values through composite analysis (*i.e.*, time periods with equal ("EQ") and opposite ("OP") polarity of the NAO and EA indices sign (+ or -)) indicated significant changes in the correlation structure. Overall, EQ conditions shift the winter polarity axis (*i.e.*, where the correlation sign changes for NAO-climate variables relationships) more northward and further south for the OP conditions (Figure 4.6). For instance, in the EQ seasons, the northward shift weakens the winter NAO- $\delta^{18}O_p$  correlation in the Mediterranean region, with some nearby regions even shifting to negative correlation coefficients. On the other hand, the southward shift of the anti-correlation line in OP winter season weakens the positive NAO- $\delta^{18}O_p$  correlation over the British Isles and shifts the strong positive relationship over Central Europe further to southern and eastern Europe (Figure 4.6). The winter seasons characterized by OP (NAO-EA) phases exhibit more depleted  $\delta^{18}O_p$  values (up to -2 ‰) from the North Atlantic towards Central Europe and enriched  $\delta^{18}O_p$  values (1.5 ‰) over the Southern Alps, Iceland, and most of the Scandinavian regions compared to EQ conditions (Figure 4.6). The winter relationship between NAO and temperature, as well as precipitation, also indicates a similar impact from the polarity of the EA index. The spatial changes in regional hydroclimate patterns due to the shifts in the polarity of the NAO and EA imply that periods with different conditions compared to the calibration period of the transfer function will introduce uncertainties in their reconstruction. Analysis of summer months did not reveal any discernible trends but overall showed a relatively stronger correlation of the NAO with climate variables in EQ seasons than OP (S1; Figure 6). In total, the results indicate that the relationship between the NAO and regional climate over Central Europe and the Alps is less sensitive to the polarity of the EA index. The analysis with the last millennium simulation from different models Bühler et al. [132] also reveals similar results, indicating the temporal variability of the changes in the correlation structure between the large-scale patterns and regional climate (S1; Figure 7). Additionally, the local- and regional-scale statistical estimates using Granger causality testing on the influence of the past winter NAO and EA indices on the subsequent summer  $\delta^{18}O_p$  values, temperature and precipitation spatio-temporal variability

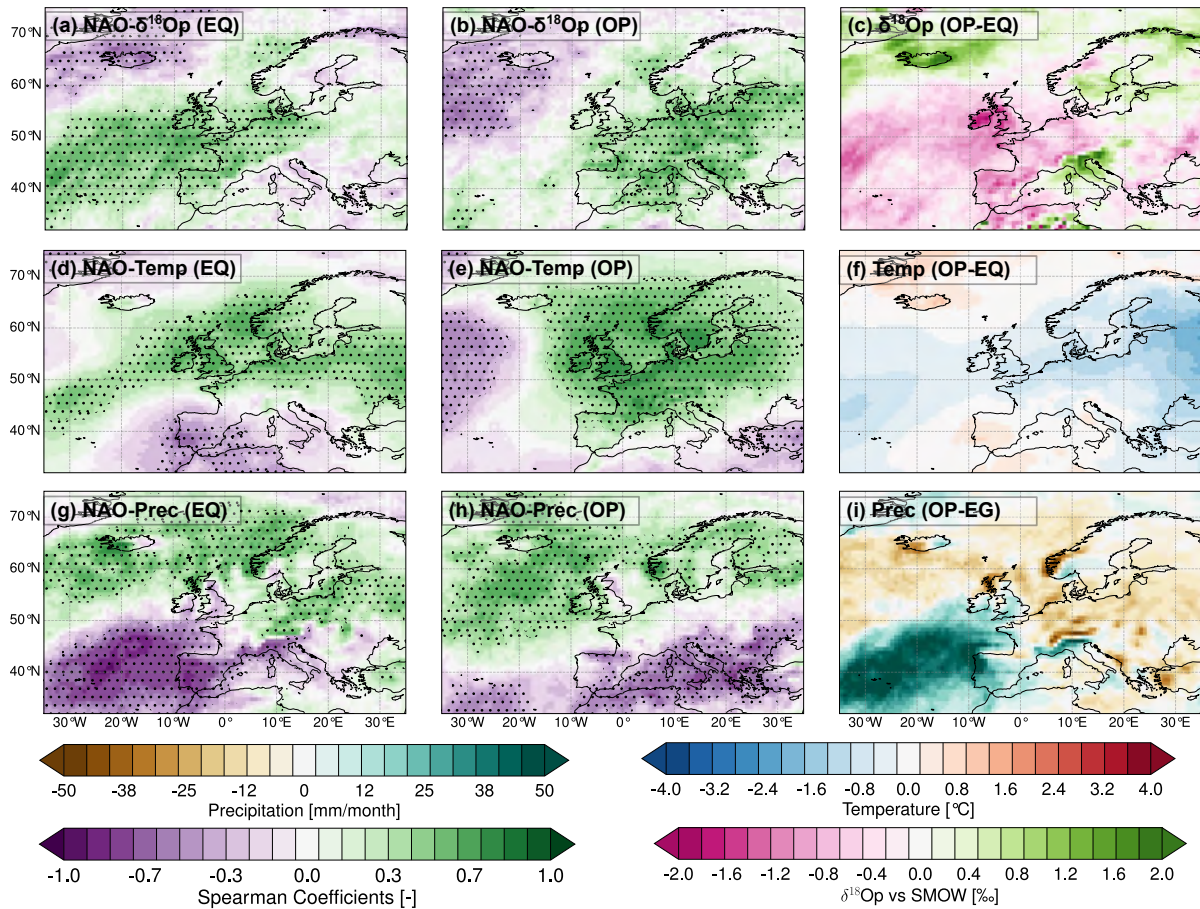


**Figure 4.6:** Spearman correlation between winter  $\delta^{18}O_p$ -NAO index (a-b),  $\delta^{18}O_p$ -temperature (d-e), and  $\delta^{18}O_p$ -precipitation (g-h) for yearly winters (1979-2014) with the same (EQ) and opposite (OP) phases of NAO and EA indices, including OP, EQ, and the difference between OP and EQ. Dot stippling represents regions with significant correlation coefficients within a 95% confidence interval. Composite differences between OP and EQ regional climate variables are depicted for (c)  $\delta^{18}O_p$  values, (f) temperature, and (i) precipitation.

indicate regional scale variations of the probability of causal mechanism between the two seasons. For instance, the results indicate the most likely causal link between winter and summer for NAO- $\delta^{18}O_p$  and more regions (including Central Europe) for precipitation and temperature. Overall, the regional estimates indicate the Alps to have a high probability of inferring past NAO index independent of the proxy signal (S1; Figure 8). The regional scale variability and shift in correlation structure suggest the use of multi-proxy sites in reconstructing the past NAO index variability.

#### 4.2.2 Significance and Implications

This part of the thesis focuses on how iGCMs can be used to explore the non-stationarity of the relationship between large-scale atmospheric circulation patterns (e.g., NAO index and WAM patterns) and regional climate variables (e.g., precipitation) variability. The extensive paleoclimate experiments (from PD to Mid-Pliocene) using iGCM ECHAM5-wiso indicate significant changes in the relationship between  $\delta^{18}O_p$  and regional climate dynamics, highlighting potential changes in their causal mechanisms. More specifically, the pronounced differences in the relationship between  $\delta^{18}O_p$  and precipitation across West Africa in the Mid-Holocene

compared to other paleoclimates (PI, LGM and Mid-Pliocene) suggest the potential biases and associated uncertainties from modern calibrated transfer function used for reconstructing paleoclimate dynamics. This implies that the MAP model-proxy discrepancies in the Mid-Holocene across the Sahara can be due to the biases in the pollen-based transfer function and not entirely due to the limitation of the climate models. The results presented in this study serve as the first step that highlights the need to reevaluate the magnitude of uncertainties of the pollen-based MAP reconstruction (based on the assumption of their transfer function), which has been the basis for the controversies (Green Sahara conundrum) between proxy and climate models [175, 211, 281, 282].

The stationarity of the relationship between the NAO index and  $\delta^{18}O_p$  or any climate variable proxy signal is crucial for reconstructing the past variability of the NAO index. Exploring the stationarity of the correlation structure between the NAO index and  $\delta^{18}O_p$  values across Europe and the North Atlantic region indicates that the second mode of variability (EA index) affects how NAO influences regional hydroclimate variability. The results help identify optimal locations (*e.g.*, Alps) that are less sensitive to the polarity of the EA index and have a strong NAO- $\delta^{18}O_p$  relationship. Such regions with the least non-stationarities can be used as optimal locations of proxy records to ensure accurate reconstruction of paleoclimate dynamics. Additionally, the high regional variability of probability estimates on the impact of the past winter atmospheric state on summer climate dynamics highlights the potential issues of generalising proxy transfer functions. This implies that time-specific regional paleoclimate dynamics must be studied with climate models before seasonal or annual proxy transfer functions to reconstruct past climate variability. The extensive water isotopes modelling and statistical estimates presented in this study reveal that using the traditional two centre-of-action locations [*e.g.* 217, 264] to reconstruct the past NAO variability might not be efficient due to their potential migration and recommend the use of multiple proxies from different regions (identified in this study such as Alps, Central Europe, British Isles). Altogether, the results indicate that combining iGCMs with isotopic proxies for climate variables can help identify the extent of the stationarity of the transfer function used for reconstructing paleoclimate dynamics.

## 4.3 Part 3: Machine Learning Framework for Predicting the Variability of local $\delta^{18}O_p$ values

### 4.3.1 Summary and Discussion

**Q10:** How well do the developed PP-ESD models predict temperature and precipitation variability at stations? (details in **Boateng and Mutz [4](P5)**)

In total, 126 precipitation and 63 temperature models were tested across 22 weather stations using 7 different learning models and 3 predictor selection methods. The results indicated overall good performance, with

a mean CV  $R^2$  of  $\geq 0.5$  for precipitation and  $\geq 0.8$  for temperature stations. Based on the results from the model and predictor selection method experiments, the recursive feature elimination predictor selection method, along with stacking regressor base models of *LassoLars*, *ARD*, *RandomForest*, and *Bagging*, and an *ExtraTree* model as meta-learner (more details about these models in P5) were selected as the final model for generating predictions for the stations. The final model was trained over the period 1958-2010 using *K-Fold* CV with a number of splits set at 10 and was then tested on independently retained data from 2011-2020. The performance of the final model was generally good but varied notably between different stations. The prediction skill estimates were higher for temperature than for precipitation. For temperature, the CV  $R^2$  values ranged from 0.84 to 0.98 ( $\mu=0.93$ ), while for precipitation, the CV  $R^2$  values ranged from 0.54 to 0.72 ( $\mu=0.65$ ). The evaluation of the testing data indicated an  $R^2$  of up to 0.95 for temperature and up to 0.74 for precipitation stations. The discrepancy in performance between temperature and precipitation models is unsurprising, given that the thermodynamics and atmospheric dynamics controlling precipitation variability are more difficult to represent [e.g. 284]. Nevertheless, the overall performance supports the application of this study's approach to downscaling midlatitude climate in complex terrain. Moreover, the models' similar performance during CV and the final evaluation suggests that the models were not overfitted and that the predictand-predictor relationships hold outside the observed period. Finally, it is worth noting that the stacking regressor performed better than the individual base models, even when all potential regressors from the initial experiments were combined into a meta-regressor. Such improvements demonstrate the advantage and ease of experimentation with the developed framework.

**Q11:** Can machine learning in the PP-ESD framework be used to emulate the local spatio-temporal variability of  $\delta^{18}O_p$  across Europe? (supplementary results in S2)

The developed PP-ESD framework demonstrates promising results in predicting station-based  $\delta^{18}O_p$  values for 39 GNIP stations across Europe using machine learning (Figure 4.7). Before generating ML-based predictions, the spatial distribution and seasonality of the GNIP observations were compared to simulated  $\delta^{18}O_p$  values using ECHAM5-wiso. This comparison indicates good agreement between their long-term annual means and seasonal trends (Figure 4.7). The model and GNIP stations reasonably represented the relatively depleted  $\delta^{18}O_p$  values in winter and enriched values in summer. Moreover, the "continentality effect," which indicates more negative  $\delta^{18}O_p$  values towards Central Europe from the North Atlantic, was also reflected in both the modelled and observed  $\delta^{18}O_p$  values.

The correlation between the selected large-scale potential predictors and station  $\delta^{18}O_p$  values shows significant relationships ( $p$ -values  $\leq 0.001$ ), implying high predictive skills for these predictors in emulating the spatio-temporal variability of  $\delta^{18}O_p$  values (S2; Figure 2). For example, most stations exhibit a significant positive correlation ( $PCC > 0.5$ ) between temperature and  $\delta^{18}O_p$  values, suggesting that large-scale temperature increases contribute to the enrichment of  $\delta^{18}O_p$  values at the stations (S2; Figure 2). Additionally, the atmospheric circulation indices demonstrate

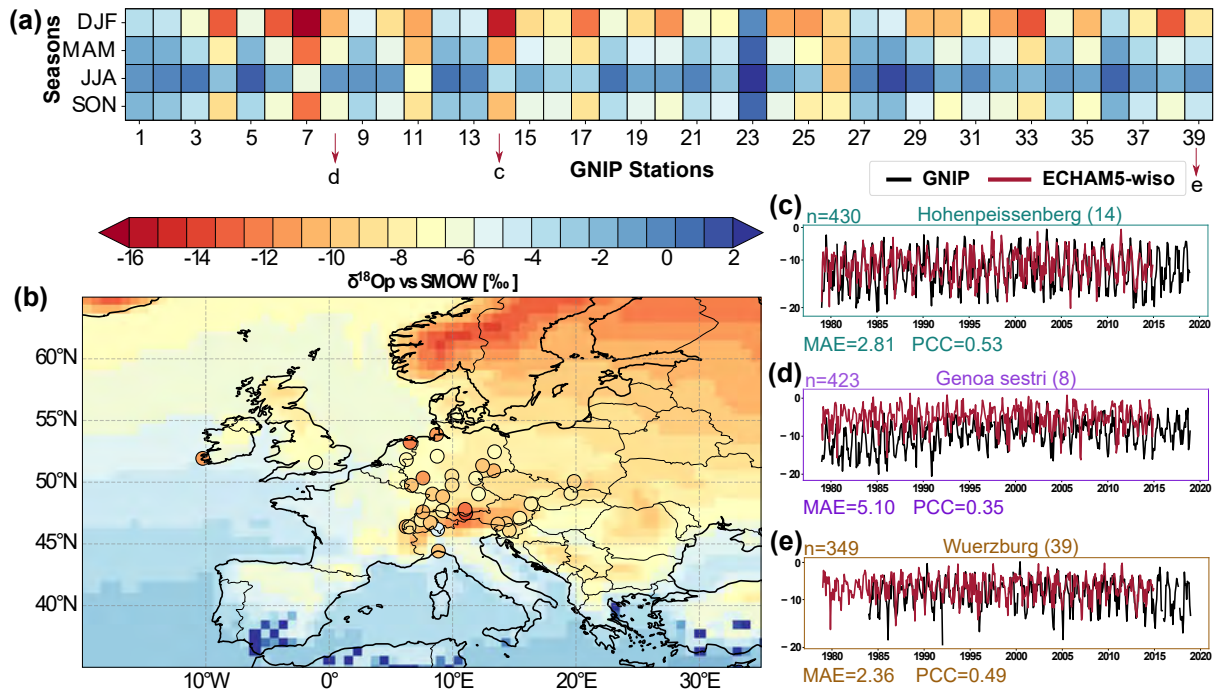


**Figure 4.7:** (a) Long-term (1979–2020) seasonal and annual climatologies of  $\delta^{18}O_p$  values for the selected 39 GNIP stations, and (b) their comparison (filled coloured circles) with the present-day (1979–2014) simulation using ECHAM5-wiso (background map). The comparison of the time series, Mean Absolute Error (MAE), and Pearson correlation coefficient (PCC) between example stations and ECHAM5-wiso are depicted in (c–e).

strong relationships, highlighting their predominant influence on the spatial distribution of  $\delta^{18}O_p$  values.

In the model training routine, a tree-based predictor selection method was employed to select robust predictors for the individual stations. Sorting the predictor importance for all 39 stations, near-surface temperature, mid-tropospheric geopotential height, NAO, and EA emerged as the most predominant predictors (S2; Figure 2). Their inclusion as predictors is physically reasonable due to their influence on hydroclimate variability across Europe and therefore the  $\delta^{18}O_p$  values.

The ten different machine learning estimators tested across the stations exhibited a median validation (1979–2012) performance with a CV MAE of 1.4–2 ‰ for all stations (Figure 4.8). Among these estimators, LassoLarsCV, ARD, RidgeCV, and Random Forest performed the best. Consequently, a stacking regressor was employed to combine predictions from these models as base models, with Random Forest as the meta-learner. The validation of the stacking regressor indicates a median CV MAE of 1.6 ‰, although two stations performed relatively poorly with CV MAE > 2.5 ‰ (Figure 4.8). The evaluation of the final trained model for stations with data available from 2013–2018 (outside the training and validation period) shows similar results compared to the CV MAE. Additionally, a PCC of >0.7 was estimated between the predicted and observed values for some stations (Figure 4.8).

Comparing the predicted monthly  $\delta^{18}O_p$  values time series for the stations to the ECHAM5-wiso simulations and GNIP observations reveals that the machine learning-based estimates are more consistent with the observed values than with the simulated values (S2; Figure 3). Moreover,

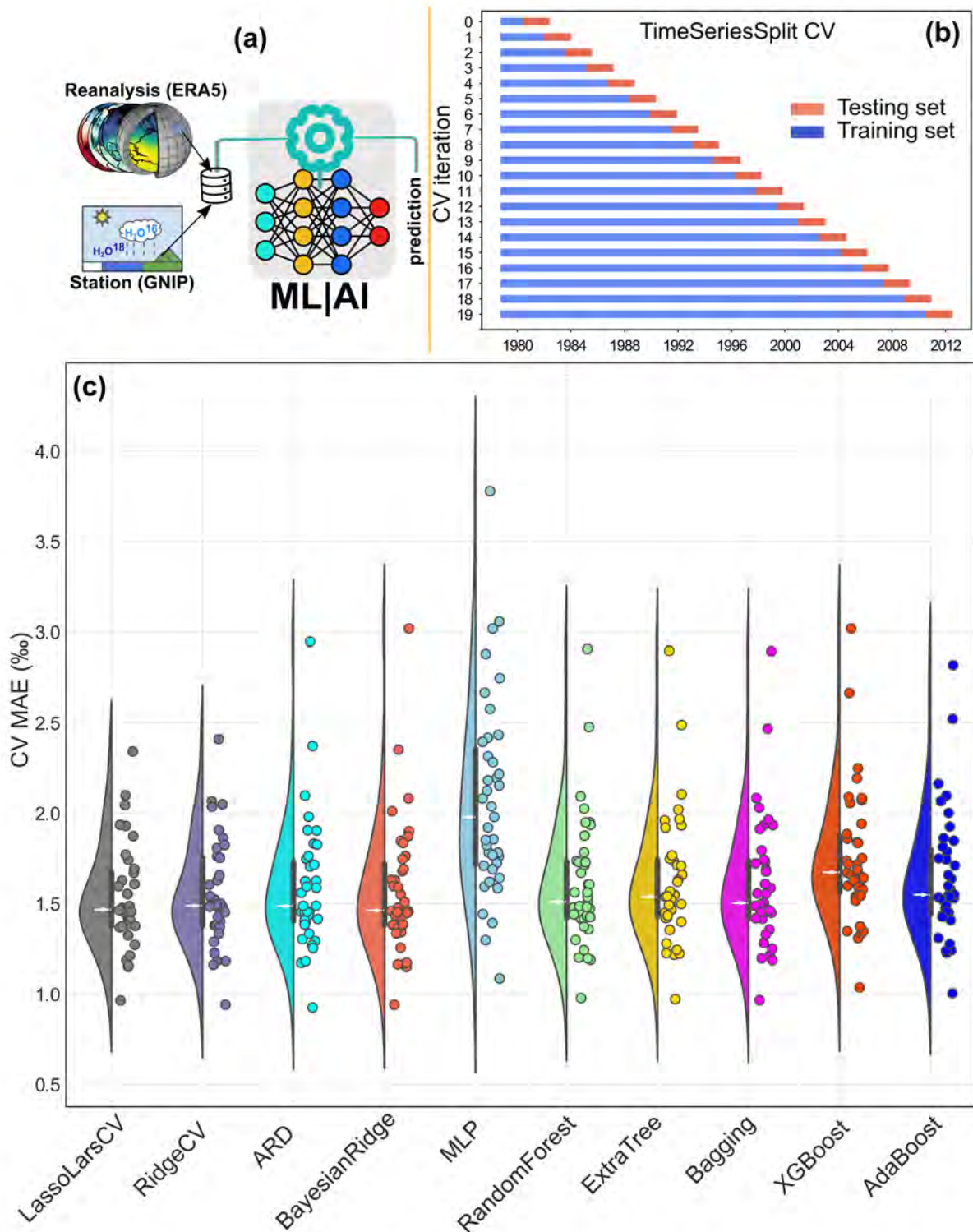


**Figure 4.8:** (a) Overview of the modelling framework of IsoPP (Isotope Modelling with Perfect Prognosis Approach), and (b) time-series split cross-validation (CV) settings used for training and validating the machine learning models. (c) CV Mean Absolute Error (MAE) ranges and distribution (depicted as violin plots) of all stations (represented by circles) for different machine learning models. The white rows within the black boxplot denote the median, with the lower and upper boundaries indicating the 25th and 75th percentiles, respectively. The lower and upper error lines represent the 10th and 90th percentiles, respectively.

estimating the PCC and MAE between the predicted and simulated  $\delta^{18}O_p$  values with the GNIP stations further supports the higher performance of the statistical prediction over the iGCM simulations. Overall,

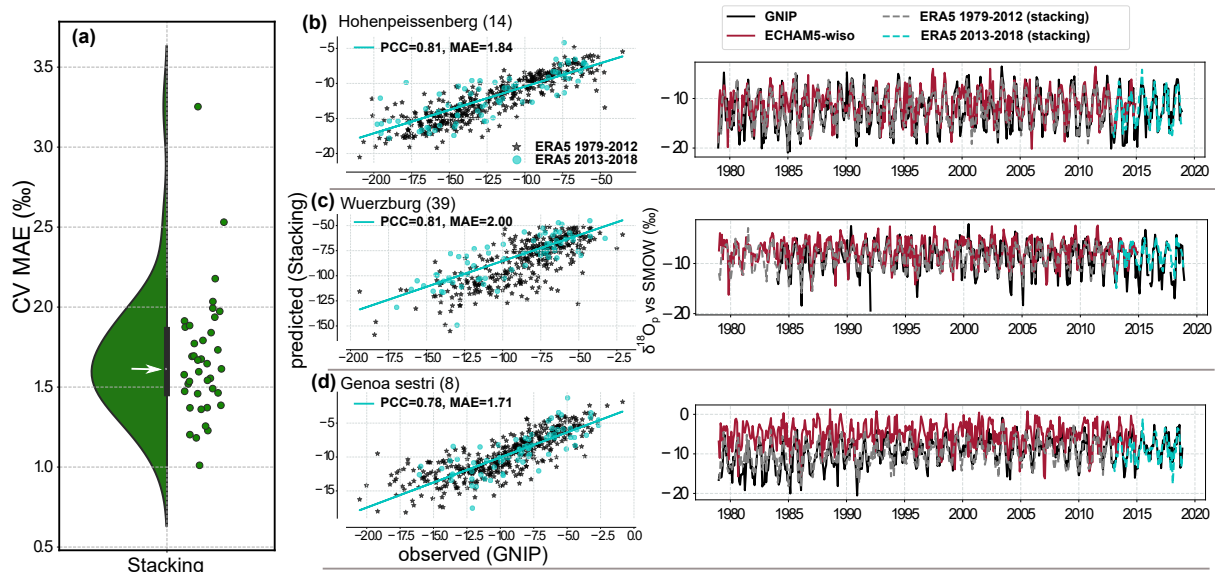


**Figure 4.9:** (a) Cross-validation (CV) Mean Absolute Error (MAE) ranges of the final model (stacking regressor) for all stations, and (b) prediction examples (GNIP stations 8, 14, and 39; refer to Figure 12) along with the evaluation of testing data not included in the model training process. The first column of (b) illustrates the linear relationship between the  $\delta^{18}O_p$  predictions and observed values, along with the Pearson correlation coefficient (PCC) for the testing data (2013–2018). The bottom panels (c, d) display the 1-year moving average of the observed (green, solid) and ERA5-driven predictions for the training period (blue, dash-dotted) and the testing period (red, dashed)

the results highlight the potential of using the developed PP-ESD in a statistical framework to emulate the local-scale  $\delta^{18}O_p$  values. The developed transfer functions for the individual GNIP stations can be combined with iGCMs or GCMs to downscale or emulate  $\delta^{18}O_p$  values based on the simulated large-scale predictors used for training the transfer functions.

### 4.3.2 Significance and Implications

Understanding the spatio-temporal variability of water isotopologues is crucial for numerous hydrological studies and paleoclimate reconstruction [1, 84, 90, 92–94, 96, 102, 132, 285]. However, direct measurements of  $\delta^{18}O_p$  values at high spatio-temporal resolutions, either globally or regionally, are costly, time-consuming, and often logistically impractical and are mostly not available when needed ([e.g. 244]). This issue is particularly problematic for the isotope-based proxy reconstruction of paleoclimate dynamics, where the transfer function requires sufficient information to accurately interpret the climate processes influencing  $\delta^{18}O_p$  variability in a specific region.

The results presented here demonstrate that machine learning can effectively learn the patterns between historical observations of large-scale atmospheric variables and station-specific  $\delta^{18}O_p$  values. This capability enables the development of a transfer function that can predict past and future variations in  $\delta^{18}O_p$  values. Despite adopting a complex approach of generating models for specific stations based on their short historical records—without assuming the generalizability of predictors and by aggregating all observations into a single time series, as in prior studies [249–253]—our findings indicate generally better performance.

Typically, precipitation isoscapes are constructed by aggregating monthly or annual observations across a region to develop a single transfer function based on geostatistical relationships, thereby generating spatially continuous  $\delta^{18}O_p$  maps. Despite the benefits of isoscapes, their transfer functions are calibrated under the assumption that predictors uniformly influence  $\delta^{18}O_p$  values across the region and are thus assigned a consistent weight. This assumption can lead to biases in areas with fewer stations since their information will be less represented in the trained model and will be determined by how the predictors relate to the  $\delta^{18}O_p$  values at the more densely stations regions.

Moreover, the spatial relationships between predictors and regional  $\delta^{18}O_p$  values are not temporally constant, as the atmospheric process and moisture trajectories pathways condition affect the spatial distribution of  $\delta^{18}O_p$  values. The framework proposed in this thesis incorporates localized conditions into the individual trained models and does not propagate it spatially to generate the spatial continuous map. The added value for this approach is that the trained model can be used to fill the missing  $\delta^{18}O_p$  values of the station without necessary interpolating but considers the atmospheric conditions of the unavailable periods. The transferability of the developed models can be further explored in future by assessing how they perform at more distant stations to determine their limitations. Such evaluations will also be useful in assessing the generalizability of proxy transfer functions for reconstructing past climate variability.



## **Part IV.**

# Conclusion & Outlooks



# Conclusions & Outlooks

# 5.

## 5.1 Summary

5.1 Summary . . . . . 59

5.2 Future outlook . . . . . 63

The Earth's climate system has undergone significant changes over past geological timescales due to variations in climate forcings (such as  $p\text{CO}_2$ ) and paleoenvironmental conditions (such as paleotopography, palaeogeography, vegetation, *etc.*). Understanding paleoclimate dynamics provides insights into future climate changes and offers long-term constraints on equilibrium climate sensitivity, transient response, and feedbacks in climate models [9, 16, 21, 31, 32, 38]. These insights help project accurate climate information in response to future climate forcings. The spatio-temporal variability of stable water isotopes (*e.g.*,  $\delta^{18}\text{O}_p$  values) in the hydrological cycle reflects integrated climatic, geologic, and biochemical processes in the Earth system, providing a basis for reconstructing paleoclimate and paleoenvironmental dynamics. Such isotopic signals are imprinted in various geologic materials, such as speleothems, ice cores, carbonates, and leaf waxes [*e.g.* 105], and are widely used in paleoclimate reconstruction.

However, interpreting isotopic signals from geologic archives presents significant challenges and uncertainties due to the wide range of large-scale climate and local conditions influencing their spatio-temporal variability. Specifically, the integrated Earth system processes imprinted in isotopic proxy records require disentangling climate signals from non-climate signals to ensure robust interpretations. Additionally, the conversion of reconstructed isotopic signals from various proxy materials to climate variables (*e.g.*, temperature or precipitation) requires calibration functions, often established under recent historical conditions and assumed to be stable through time and space. The sparsity and short-term records of direct measurements of water isotopologues (*e.g.*, GNIP) also hinder understanding the causal mechanisms between isotopic variability and regional climate dynamics, which is essential for developing their transfer functions. Overall, understanding the processes that influence water isotopes in specific regions under different climatic conditions is crucial. The modelling of water isotopologues in climate models (iGCMs) provides a means to explore large-scale drivers and can help evaluate the extent of the stationarity of transfer functions.

Here, I illustrate how water isotopologue modelling with iGCMs and machine learning can be combined with isotopic proxy data to enhance their interpretability. The findings indicate the need to combine water isotope information from modern monitoring, iGCM outputs, and isotopic proxy data to provide robust statistical and dynamic constraints on paleoclimate variability reconstruction.

This dissertation encompasses extensive climate sensitivity experiments (topographic and paleoclimate) with the iGCM ECHAM5-wiso and machine learning based modelling of  $\delta^{18}\text{O}_p$  spatio-temporal variability, presented in five (5) manuscripts (P1-P5) and two complementary results (S1-S2) (provided in Part VII), contributing to the understanding of

past and present regional climate dynamics' controls on  $\delta^{18}O_p$  patterns. Specifically, the dissertation demonstrates how iGCMs can resolve some of the uncertainties associated with proxy reconstruction by proposing a new framework for using simulated climate variables to disentangle proxy signals and evaluate the non-stationarity of proxy transfer functions for reconstructing paleoclimate dynamics.

These are addressed through a series of research questions (Q1-Q11) discussed in Chapter 4. These questions test two hypotheses (H1 and H2) on paleoelevation (Section 3.1) and paleoclimate dynamics reconstruction (Section 3.2) and a complementary objective (O1) (Section 3.3) that explores a statistical modeling framework of  $\delta^{18}O_p$  values prediction that can replace or complement the iGCMs. I highlight that the details of the results and discussion of the individual studies are summarised in Chapter 4 and presented in detail in Part VII. In the following sections, I only present the key findings that provide an answer to the tested hypotheses and the complementary objective with some future outlooks in Section 5.2.

#### Integrating iGCM with stable isotope paleoaltimetry to reconstruct paleoelevation

Here, I used iGCMs ECHAM5-wiso to explore the atmospheric processes influencing the  $\delta^{18}O_p$  spatial distribution across the Alps and Europe and investigated the impacts of topographic and Middle Miocene regional climate changes on isotopic lapse rates. Through extensive topographic sensitivity experiments that consider diachronous surface uplift scenarios of the Alps (*the first of its kind*) and Miocene climate sensitivity experiments addressing questions (Q1-Q7) in three manuscripts (P1-P3), I determined the uncertainties associated with the assumption of stationarity of the modern isotopic lapse rate across the Alps over time and explored the regional climate dynamics causing lapse rate variability. Specifically, the research questions addressed in P1-P3 test the following hypothesis:

**Hypothesis (H1):** Diachronous west-to-east surface uplift of the Alps and Miocene global climate changes would impact the regional climate and, therefore, influence the  $\delta^{18}O_p$ -elevation gradient (*i.e.*, the isotopic lapse rate).

The topographic sensitivity experiments for the diachronous surface uplift scenarios indicate  $\Delta\delta^{18}O_p$  values of up to -8 ‰ across the Alps under pre-industrial (PI) conditions, primarily due to changes in orographic precipitation and adiabatic lapse rate changes in surface temperature. The simulated climate responses to changes in the Alps' topography indicate significant alterations in synoptic-scale atmospheric pressure systems in the Northern Hemisphere (*e.g.*, shifts in the pressure dipole axis and locations of pressure system centres), changes in moisture transport distances and pathways, and large-scale atmospheric dynamics affecting precipitation in adjacent far-field regions of the Alps. The diachronous surface uplift in the Middle Miocene climate still produces  $\Delta\delta^{18}O_p$  values ranging from -4 to -8 ‰ across the Alps, significant enough to be recorded by geological archives for reconstructing paleoelevation, and consistent

with proxy reconstructions. The simulated isotopic lapse rates become shallower or decrease by approximately  $1.0 \text{ ‰ km}^{-1}$  in response to the Middle Miocene conditions compared to the PI period and vary within the range of  $\pm 1.5 \text{ ‰ km}^{-1}$  for the diachronous surface uplifts of the Alps, with spatial differences around the region.

Integrating the simulated Miocene lapse rates with proxy reconstructions indicates an overestimation of the Central Alps' paleoelevation by  $\sim 1.5$  km when the isotopic lapse rate is assumed to be stationary through time and space from the present day. Therefore, the simulated patterns of  $\delta^{18}\text{O}$  of paleo-meteoric waters in response to topographic and Miocene climate changes confirm the hypothesis that Miocene climate changes and diachronous surface uplift of the Alps result in isotopic lapse rates that significantly deviate from modern estimates ( $-2.0 \text{ ‰ km}^{-1}$ ; Campani et al. [140]) and vary spatially around the Alps. These findings suggest the need to recalculate previous paleoelevation estimates across the Alps (and even globally) using paleoclimate-constrained isotopic lapse rates from iGCMs. Alternatively, the findings also suggest that using modern isotopic lapse rates from surface rivers of diverse hydrological catchments globally [139] is suitable in the absence of paleoclimate-constrained, rather than using modern precipitation-based lapse rates. Therefore, the findings emphasize the variability of isotopic lapse rates in past climates and highlight the advantage of using iGCMs to understand paleoclimate dynamics and regional climate patterns. This approach helps disentangle climate and tectonic signals in paleoaltimetry proxy materials and derive more accurate paleoelevation estimates.

### Evaluating the stationarity of transfer function for reconstructing paleoclimate dynamics

Here, I used iGCM ECHAM5-wiso to evaluate the stationarity of the relationship between isotopic proxy signals and regional atmospheric processes over longer time scales to highlight the potential uncertainties associated with paleoclimate reconstruction from geologic materials. Specifically, I conducted time slice paleoclimate sensitivity experiments from Pre-Industrial (PI) to Mid-Pliocene to understand the West African Monsoon (WAM) system dynamics and how it controls the  $\delta^{18}\text{O}_p$  patterns in the different paleoclimates. This is particularly important due to the complexity of the region's climate dynamics and the persistent struggles of most climate models in representing its past and future hydroclimate variability (see Section 2.2 for more details).

Additionally, I performed historical (1979-2014) simulations to understand how the second mode of atmospheric variability (EA index) influences the stationarity of the relationship between isotopic proxy signals and the NAO index in the winter and summer seasons. The importance of reconstructing past NAO variability is presented in Section 2.3. I also explored the dynamical processes causing the non-stationarity of the NAO- $\delta^{18}\text{O}_p$  relation and examined if the polarity and intensity of the NAO and EA indices in the previous winter season influence the subsequent summer climate dynamics to compromise the NAO- $\delta^{18}\text{O}_p$  relationship. Altogether, I explored the causal links between local isotopic variability and large-scale teleconnections to understand how their relationships can change in past climates. These are addressed in

Q7-Q9 in manuscript (P4) and supplementary results in S1, which overall test the hypothesis:

**Hypothesis (H2):** The impact of atmospheric dynamics and large-scale variability mechanism on local proxy variables (e.g.,  $\delta^{18}O_p$ ) varies across different paleoclimates.

The simulated  $\delta^{18}O_p$  values in response to the different paleoclimates in the Late Cenozoic reveal the most depleted  $\delta^{18}O_p$  conditions in the Mid-Holocene (with up to -6 ‰ across the Sahel) compared to the PI. This is due to the highest intensification and northward extent of the WAM, which contributed to a significant increase in precipitation across the WAM region. The  $\delta^{18}O_p$  values in the Mid-Pliocene also indicate more depleted conditions than the PI, but of less significance compared to the Mid-Holocene, which is consistent with the precipitation anomalies patterns. However, the  $\delta^{18}O_p$  values in the Last Glacial Maximum (LGM) indicate more enriched conditions in most parts of the WAM region than the PI due to colder conditions. The simulation of  $\delta^{18}O_p$  patterns and magnitudes and associated WAM dynamics reveals the non-stationarity of  $\delta^{18}O_p$ -hydroclimate variables relationship throughout the Late Cenozoic, suggesting the need to understand the causal mechanisms for each proxy system and refine their transfer functions to ensure accurate proxy-based reconstructions.

The analysis of the NAO- $\delta^{18}O_p$  relationship reveals that the polarity of the EA index influences their link, which is crucial for reconstructing past NAO variability due to the instability of the NAO- $\delta^{18}O_p$  transfer function. The Granger causal testing also suggests that the winter NAO and EA indices affect the subsequent summer NAO- $\delta^{18}O_p$  relationship. This additional instability in the proxy-NAO relationship implies the need to understand what controls proxy signals in different regions. Altogether, the results suggest optimal locations with a robust NAO- $\delta^{18}O_p$  relationship that are less sensitive to the EA index for reconstructing the past variability of the NAO index.

Collectively, the results confirm the hypothesis that the complex causal mechanisms between atmospheric dynamics and large-scale circulation patterns influence local proxy signals differently through time and require paleoclimate-constrained transfer functions to ensure accurate paleoclimate dynamics reconstruction.

### Exploring the potential of using machine learning to predict the spatial-temporal variability of $\delta^{18}O_p$

Here, I explored the potential of using machine learning to emulate the spatio-temporal variability of  $\delta^{18}O_p$  values across Europe using large-scale predictors such as the NAO, EA, atmospheric winds, etc.. Due to the complexity and difficulty of such a task, given the variety of atmospheric processes and local conditions that control local  $\delta^{18}O_p$  variability, I first developed the Perfect-Prognosis empirical statistical downscaling (PP-ESD) framework in a new open-source Python software called *pyESD* (Boateng and Mutz [4]).

*pyESD* implements the entire downscaling cycle, including routines for data preparation, predictor selection and construction, model selection and training, evaluation, utility tools for relevant statistical tests, visualization, and a collection of well-established machine learning algorithms. It allows users to choose various estimators, cross-validation schemes, objective function measures, and hyperparameter optimization with relatively few lines of code. Believing that science would be more enjoyable if all research outputs were easily reproducible, I implemented extensive documentation ([pyESD website](#)) to help users benefit from the full applicability of the PP-ESD routines. This enables quick and reproducible downscaling of any climate information, such as precipitation, temperature, wind speed, etc.

I demonstrated the use and effectiveness of the new PP-ESD framework by (1) generating weather-station-based downscaling products for precipitation and temperature in complex mountainous terrain in southwestern Germany [4] and (2) for precipitation for all synoptic weather stations in Ghana [286]. The results indicated that the established PP-ESD framework is robust and can be combined with GCM output to generate high-resolution future climate change information.

Specifically, in this thesis, I used the developed framework in a complementary objective:

**Objective (O1):** To investigate whether machine learning can complement or substitute the stable water isotopes explicit in iGCMs for predicting the spatio-temporal variability of local  $\delta^{18}O_p$  values using large-scale atmospheric variables.

The findings suggest that the machine learning framework can predict the spatio-temporal variability of  $\delta^{18}O_p$  across Europe, significantly outperforming the iGCM ECHAM5-wiso. The chosen predictors highlight the importance of large-scale synoptic circulation patterns as key drivers of local-scale  $\delta^{18}O_p$  variability. Evaluating the performance of the trained station-based models on the testing period indicated PCC of  $> 0.7$  (with MAE  $< 1.6$  ‰ for most GNIP stations) between the predicted and observed  $\delta^{18}O_p$  values. Despite the challenging approach of generating models for individual GNIP stations based on their short historical records—without assuming the generalizability of predictors and by aggregating all observations into a single time series—the results indicate impressive performance.

The next logical step is to combine the developed models with iGCMs to downscale the simulated  $\delta^{18}O_p$  values to high resolution or use the simulated predictors from GCM outputs to emulate the spatio-temporal variability of  $\delta^{18}O_p$  values by leveraging the cost-effectiveness of the developed Perfect Prognosis isotope modelling (IsoPP).

## 5.2 Future outlook

The extensive suite of modelling and broad range of research presented in this thesis open numerous avenues for future investigations. Some of these avenues are already highlighted in the respective manuscripts (P1-P5).

These range from extending the modelling framework with fully coupled atmosphere-ocean isotope-enabled models with dynamic vegetation to compiling various hydroclimate proxies from the suggested optimal regions to reconstruct past NAO variability, among other topics. While numerous research directions could stem from this interdisciplinary work, I will focus on one particularly promising and important direction: extending the correlation analysis between large-scale atmospheric teleconnections and regional climate variables and isotopic variability to causal inference methods [287–289].

Despite the usefulness of correlation methods applied to understand the links between large-scale processes and regional climate, they do not entirely reveal the causal interpretation of the established relationships that emerged from their physical interactions. Even though the application of Granger causality [238] contributes to understanding the memory effect of previous winter NAO and EA indices on summer climate dynamics across Europe and the North Atlantic region, the approach is limited to lagged causal dependencies [287, 290]. However, causal discovery methods leverage the assumption of the underlying processes to account for common causes and reconstruct the causal links of the teleconnections [288, 291]. For instance, the conditional independence-based causal discovery method, which relies on the assumptions of causal sufficiency, time order, the causal Markov condition, and faithfulness [287, 288], can be used to identify and quantify the causal interactions between various teleconnections of the West African monsoon system or the Northern Hemisphere teleconnections and the  $\delta^{18}O_p$  patterns in present and past climate conditions. This approach would provide the opportunity to assess model performance [e.g. 292, 293] and evaluate which climatic processes cause the disagreement between the model and proxy data, thereby improving the interpretation of proxy reconstructions.



# Bibliography

- [1] D. Boateng, S. G. Mutz, A. Ballian, M. J. M. Meijers, K. Methner, S. Botsyun, A. Mulch, and T. A. Ehlers. “The effects of diachronous surface uplift of the European Alps on regional climate and the oxygen isotopic composition of precipitation”. English. *Earth System Dynamics* 14.6 (2023). Publisher: Copernicus GmbH, pages 1183–1210. doi: [10.5194/esd-14-1183-2023](https://doi.org/10.5194/esd-14-1183-2023).
- [2] S. Botsyun, T. A. Ehlers, A. Koptev, M. Böhme, K. Methner, C. Risi, C. Stepanek, S. G. Mutz, M. Werner, D. Boateng, and A. Mulch. “Middle Miocene Climate and Stable Oxygen Isotopes in Europe Based on Numerical Modeling”. en. *Paleoceanography and Paleoclimatology* 37.10 (2022). \_eprint: <https://onlinelibrary.wiley.com/doi/pdf/10.1029/2022PA004442>, e2022PA004442. doi: [10.1029/2022PA004442](https://doi.org/10.1029/2022PA004442).
- [3] D. Boateng, J. N. A. Aryee, M. Baidu, F. Arthur, and S. G. Mutz. “West African Monsoon Dynamics and Its Control on the Stable Oxygen Isotopic Composition of Precipitation in the Late Cenozoic”. en. *Journal of Geophysical Research: Atmospheres* 129.10 (2024). \_eprint: <https://onlinelibrary.wiley.com/doi/pdf/10.1029/2024JD040748>. doi: [10.1029/2024JD040748](https://doi.org/10.1029/2024JD040748).
- [4] D. Boateng and S. G. Mutz. “pyESDv1.0.1: an open-source Python framework for empirical-statistical downscaling of climate information”. English. *Geoscientific Model Development* 16.22 (2023). Publisher: Copernicus GmbH, pages 6479–6514. doi: [10.5194/gmd-16-6479-2023](https://doi.org/10.5194/gmd-16-6479-2023).
- [5] G. L. Foster, D. L. Royer, and D. J. Lunt. “Future climate forcing potentially without precedent in the last 420 million years”. en. *Nature Communications* 8.1 (2017). Publisher: Nature Publishing Group, page 14845. doi: [10.1038/ncomms14845](https://doi.org/10.1038/ncomms14845).
- [6] R. E. Zeebe, A. Ridgwell, and J. C. Zachos. “Anthropogenic carbon release rate unprecedented during the past 66 million years”. en. *Nature Geoscience* 9.4 (2016). Publisher: Nature Publishing Group, pages 325–329. doi: [10.1038/ngeo2681](https://doi.org/10.1038/ngeo2681).
- [7] P. Valdes. “Built for stability”. en. *Nature Geoscience* 4.7 (2011). Publisher: Nature Publishing Group, pages 414–416. doi: [10.1038/ngeo1200](https://doi.org/10.1038/ngeo1200).
- [8] C. R. Scotese, H. Song, B. J. W. Mills, and D. G. van der Meer. “Phanerozoic paleotemperatures: The earth’s changing climate during the last 540 million years”. *Earth-Science Reviews* 215 (2021), page 103503. doi: [10.1016/j.earscirev.2021.103503](https://doi.org/10.1016/j.earscirev.2021.103503).
- [9] J. E. Tierney, C. J. Poulsen, I. P. Montañez, T. Bhattacharya, R. Feng, H. L. Ford, B. Hönlisch, G. N. Inglis, S. V. Petersen, N. Sagoo, C. R. Tabor, K. Thirumalai, J. Zhu, N. J. Burls, G. L. Foster, Y. Goddérís, B. T. Huber, L. C. Ivany, S. Kirtland Turner, D. J. Lunt, J. C. McElwain, B. J. W. Mills, B. L. Otto-Bliesner, A. Ridgwell, and Y. G. Zhang. “Past climates inform our future”. *Science* 370.6517 (2020). Publisher: American Association for the Advancement of Science, eaay3701. doi: [10.1126/science.aay3701](https://doi.org/10.1126/science.aay3701).
- [10] A. Seth, A. Giannini, M. Rojas, S. A. Rauscher, S. Bordoni, D. Singh, and S. J. Camargo. “Monsoon Responses to Climate Changes—Connecting Past, Present and Future”. en. *Current Climate Change Reports* 5.2 (2019), pages 63–79. doi: [10.1007/s40641-019-00125-y](https://doi.org/10.1007/s40641-019-00125-y).
- [11] A. Zhisheng, W. Guoxiong, L. Jianping, S. Youbin, L. Yimin, Z. Weijian, C. Yanjun, D. Anmin, L. Li, M. Jiangyu, C. Hai, S. Zhengguo, T. Liangcheng, Y. Hong, A. Hong, C. Hong, and F. Juan. “Global Monsoon Dynamics and Climate Change”. en. *Annual Review of Earth and Planetary Sciences* 43. Volume 43, 2015 (2015). Publisher: Annual Reviews, pages 29–77. doi: [10.1146/annurev-earth-060313-054623](https://doi.org/10.1146/annurev-earth-060313-054623).
- [12] M. C. Urban. “Accelerating extinction risk from climate change”. *Science* 348.6234 (2015). Publisher: American Association for the Advancement of Science, pages 571–573. doi: [10.1126/science.aaa4984](https://doi.org/10.1126/science.aaa4984).
- [13] T. A. Ehlers. “Landscapes through time”. *Science* 379.6635 (2023). Publisher: American Association for the Advancement of Science, pages 879–880. doi: [10.1126/science.adg5546](https://doi.org/10.1126/science.adg5546).

- [14] T. Salles, L. Husson, M. Lorcery, and B. Hadler Boggiani. "Landscape dynamics and the Phanerozoic diversification of the biosphere". en. *Nature* (2023). Publisher: Nature Publishing Group, pages 1–7. doi: [10.1038/s41586-023-06777-z](https://doi.org/10.1038/s41586-023-06777-z).
- [15] Intergovernmental Panel on Climate Change (IPCC). "Climate Change 2021 – The Physical Science Basis: Working Group I Contribution to the Sixth Assessment Report of the Intergovernmental Panel on Climate Change". Cambridge: *Cambridge University Press*, 2023.
- [16] M. Pagani, Z. Liu, J. LaRiviere, and A. C. Ravelo. "High Earth-system climate sensitivity determined from Pliocene carbon dioxide concentrations". en. *Nature Geoscience* 3.1 (2010). Publisher: Nature Publishing Group, pages 27–30. doi: [10.1038/ngeo724](https://doi.org/10.1038/ngeo724).
- [17] A. M. Haywood, H. J. Dowsett, and A. M. Dolan. "Integrating geological archives and climate models for the mid-Pliocene warm period". en. *Nature Communications* 7.1 (2016). Publisher: Nature Publishing Group, page 10646. doi: [10.1038/ncomms10646](https://doi.org/10.1038/ncomms10646).
- [18] G. A. Schmidt, D. Bader, L. J. Donner, G. S. Elsaesser, J.-C. Golaz, C. Hannay, A. Molod, R. B. Neale, and S. Saha. "Practice and philosophy of climate model tuning across six US modeling centers". English. *Geoscientific Model Development* 10.9 (2017). Publisher: Copernicus GmbH, pages 3207–3223. doi: [10.5194/gmd-10-3207-2017](https://doi.org/10.5194/gmd-10-3207-2017).
- [19] V. Eyring, S. Bony, G. A. Meehl, C. A. Senior, B. Stevens, R. J. Stouffer, and K. E. Taylor. "Overview of the Coupled Model Intercomparison Project Phase 6 (CMIP6) experimental design and organization". English. *Geoscientific Model Development* 9.5 (2016). Publisher: Copernicus GmbH, pages 1937–1958. doi: [10.5194/gmd-9-1937-2016](https://doi.org/10.5194/gmd-9-1937-2016).
- [20] M. Kageyama, P. Braconnot, S. P. Harrison, A. M. Haywood, J. H. Jungclauss, B. L. Otto-Bliesner, J.-Y. Peterschmitt, A. Abe-Ouchi, S. Albani, P. J. Bartlein, C. Brierley, M. Crucifix, A. Dolan, L. Fernandez-Donado, H. Fischer, P. O. Hopcroft, R. F. Ivanovic, F. Lambert, D. J. Lunt, N. M. Mahowald, W. R. Peltier, S. J. Phipps, D. M. Roche, G. A. Schmidt, L. Tarasov, P. J. Valdes, Q. Zhang, and T. Zhou. "The PMIP4 contribution to CMIP6 – Part 1: Overview and over-arching analysis plan". en. *Geoscientific Model Development* 11.3 (2018), pages 1033–1057. doi: [10.5194/gmd-11-1033-2018](https://doi.org/10.5194/gmd-11-1033-2018).
- [21] N. J. Burls, C. D. Bradshaw, A. M. De Boer, N. Herold, M. Huber, M. Pound, Y. Donnadieu, A. Farnsworth, A. Frigola, E. Gasson, A. S. von der Heydt, D. K. Hutchinson, G. Knorr, K. T. Lawrence, C. H. Lear, X. Li, G. Lohmann, D. J. Lunt, A. Marzocchi, M. Prange, C. A. Riihimaki, A.-C. Sarr, N. Siler, and Z. Zhang. "Simulating Miocene Warmth: Insights From an Opportunistic Multi-Model Ensemble (MioMIP1)". en. *Paleoceanography and Paleoclimatology* 36.5 (2021). eprint: <https://onlinelibrary.wiley.com/doi/pdf/10.1029/2020PA004054>, e2020PA004054. doi: [10.1029/2020PA004054](https://doi.org/10.1029/2020PA004054).
- [22] R. Caballero and M. Huber. "State-dependent climate sensitivity in past warm climates and its implications for future climate projections". *Proceedings of the National Academy of Sciences* 110.35 (2013). Publisher: Proceedings of the National Academy of Sciences, pages 14162–14167. doi: [10.1073/pnas.1303365110](https://doi.org/10.1073/pnas.1303365110).
- [23] K. D. Burke, J. W. Williams, M. A. Chandler, A. M. Haywood, D. J. Lunt, and B. L. Otto-Bliesner. "Pliocene and Eocene provide best analogs for near-future climates". *Proceedings of the National Academy of Sciences* 115.52 (2018). Publisher: Proceedings of the National Academy of Sciences, pages 13288–13293. doi: [10.1073/pnas.1809600115](https://doi.org/10.1073/pnas.1809600115).
- [24] D. J. Lunt, M. Huber, E. Anagnostou, M. L. J. Baatsen, R. Caballero, R. DeConto, H. A. Dijkstra, Y. Donnadieu, D. Evans, R. Feng, G. L. Foster, E. Gasson, A. S. von der Heydt, C. J. Hollis, G. N. Inglis, S. M. Jones, J. Kiehl, S. Kirtland Turner, R. L. Korty, R. Kozdon, S. Krishnan, J.-B. Ladant, P. Langebroek, C. H. Lear, A. N. LeGrande, K. Littler, P. Markwick, B. Otto-Bliesner, P. Pearson, C. J. Poulsen, U. Salzmann, C. Shields, K. Snell, M. Stärz, J. Super, C. Tabor, J. E. Tierney, G. J. L. Tourte, A. Tripathi, G. R. Upchurch, B. S. Wade, S. L. Wing, A. M. E. Winguth, N. M. Wright, J. C. Zachos, and R. E. Zeebe. "The DeepMIP contribution to PMIP4: experimental design for model simulations of the EECO, PETM, and pre-PETM (version 1.0)". English. *Geoscientific Model Development* 10.2 (2017). Publisher: Copernicus GmbH, pages 889–901. doi: [10.5194/gmd-10-889-2017](https://doi.org/10.5194/gmd-10-889-2017).

- [25] M. Steinthorsdottir, H. K. Coxall, A. M. de Boer, M. Huber, N. Barbolini, C. D. Bradshaw, N. J. Burls, S. J. Feakins, E. Gasson, J. Henderiks, A. E. Holbourn, S. Kiel, M. J. Kohn, G. Knorr, W. M. Kürschner, C. H. Lear, D. Liebrand, D. J. Lunt, T. Mörs, P. N. Pearson, M. J. Pound, H. Stoll, and C. a. E. Strömberg. "The Miocene: The Future of the Past". en. *Paleoceanography and Paleoclimatology* 36.4 (2021). \_eprint: <https://onlinelibrary.wiley.com/doi/pdf/10.1029/2020PA004037>, e2020PA004037. doi: [10.1029/2020PA004037](https://doi.org/10.1029/2020PA004037).
- [26] A. M. Haywood, P. J. Valdes, T. Aze, N. Barlow, A. Burke, A. M. Dolan, A. S. von der Heydt, D. J. Hill, S. S. R. Jamieson, B. L. Otto-Bliesner, U. Salzmann, E. Saupe, and J. Voss. "What can Palaeoclimate Modelling do for you?" en. *Earth Systems and Environment* 3.1 (2019), pages 1–18. doi: [10.1007/s41748-019-00093-1](https://doi.org/10.1007/s41748-019-00093-1).
- [27] H. Dowsett, A. Dolan, D. Rowley, R. Moucha, A. M. Forte, J. X. Mitrovica, M. Pound, U. Salzmann, M. Robinson, M. Chandler, K. Foley, and A. Haywood. "The PRISM4 (mid-Piacenzian) paleoenvironmental reconstruction". English. *Climate of the Past* 12.7 (2016). Publisher: Copernicus GmbH, pages 1519–1538. doi: [10.5194/cp-12-1519-2016](https://doi.org/10.5194/cp-12-1519-2016).
- [28] M. J. Pound, A. M. Haywood, U. Salzmann, J. B. Riding, D. J. Lunt, and S. J. Hunter. "A Tortonian (Late Miocene, 11.61–7.25Ma) global vegetation reconstruction". en. *Palaeogeography, Palaeoclimatology, Palaeoecology* 300.1 (2011), pages 29–45. doi: [10.1016/j.palaeo.2010.11.029](https://doi.org/10.1016/j.palaeo.2010.11.029).
- [29] A. M. Haywood, H. J. Dowsett, A. M. Dolan, D. Rowley, A. Abe-Ouchi, B. Otto-Bliesner, M. A. Chandler, S. J. Hunter, D. J. Lunt, M. Pound, and U. Salzmann. "The Pliocene Model Intercomparison Project (PlioMIP) Phase 2: scientific objectives and experimental design". English. *Climate of the Past* 12.3 (2016). Publisher: Copernicus GmbH, pages 663–675. doi: [10.5194/cp-12-663-2016](https://doi.org/10.5194/cp-12-663-2016).
- [30] D. J. Lunt, P. J. Valdes, T. D. Jones, A. Ridgwell, A. M. Haywood, D. N. Schmidt, R. Marsh, and M. Maslin. "CO<sub>2</sub>-driven ocean circulation changes as an amplifier of Paleocene-Eocene thermal maximum hydrate destabilization". *Geology* 38.10 (2010), pages 875–878. doi: [10.1130/G31184.1](https://doi.org/10.1130/G31184.1).
- [31] C. A. Loptson, D. J. Lunt, and J. E. Francis. "Investigating vegetation&ndash;climate feedbacks during the early Eocene". English. *Climate of the Past* 10.2 (2014). Publisher: Copernicus GmbH, pages 419–436. doi: [10.5194/cp-10-419-2014](https://doi.org/10.5194/cp-10-419-2014).
- [32] G. N. Inglis, F. Bragg, N. J. Burls, M. J. Cramwinckel, D. Evans, G. L. Foster, M. Huber, D. J. Lunt, N. Siler, S. Steinig, J. E. Tierney, R. Wilkinson, E. Anagnostou, A. M. de Boer, T. Dunkley Jones, K. M. Edgar, C. J. Hollis, D. K. Hutchinson, and R. D. Pancost. "Global mean surface temperature and climate sensitivity of the early Eocene Climatic Optimum (EECO), Paleocene–Eocene Thermal Maximum (PETM), and latest Paleocene". English. *Climate of the Past* 16.5 (2020). Publisher: Copernicus GmbH, pages 1953–1968. doi: [10.5194/cp-16-1953-2020](https://doi.org/10.5194/cp-16-1953-2020).
- [33] D. Evans, N. Sagoo, W. Renema, L. J. Cotton, W. Müller, J. A. Todd, P. K. Saraswati, P. Stassen, M. Ziegler, P. N. Pearson, P. J. Valdes, and H. P. Affek. "Eocene greenhouse climate revealed by coupled clumped isotope-Mg/Ca thermometry". *Proceedings of the National Academy of Sciences* 115.6 (2018). Publisher: Proceedings of the National Academy of Sciences, pages 1174–1179. doi: [10.1073/pnas.1714744115](https://doi.org/10.1073/pnas.1714744115).
- [34] E. Anagnostou, E. H. John, K. M. Edgar, G. L. Foster, A. Ridgwell, G. N. Inglis, R. D. Pancost, D. J. Lunt, and P. N. Pearson. "Changing atmospheric CO<sub>2</sub> concentration was the primary driver of early Cenozoic climate". en. *Nature* 533.7603 (2016). Publisher: Nature Publishing Group, pages 380–384. doi: [10.1038/nature17423](https://doi.org/10.1038/nature17423).
- [35] E. A. Jagniecki, T. K. Lowenstein, D. M. Jenkins, and R. V. Demicco. "Eocene atmospheric CO<sub>2</sub> from the nahcolite proxy". *Geology* 43.12 (2015), pages 1075–1078. doi: [10.1130/G36886.1](https://doi.org/10.1130/G36886.1).
- [36] P. N. Pearson and M. R. Palmer. "Atmospheric carbon dioxide concentrations over the past 60 million years". en. *Nature* 406.6797 (2000). Publisher: Nature Publishing Group, pages 695–699. doi: [10.1038/35021000](https://doi.org/10.1038/35021000).
- [37] D. J. Beerling and D. L. Royer. "Convergent Cenozoic CO<sub>2</sub> history". en. *Nature Geoscience* 4.7 (2011). Publisher: Nature Publishing Group, pages 418–420. doi: [10.1038/ngeo1186](https://doi.org/10.1038/ngeo1186).

- [38] J. Zhu and C. J. Poulsen. “Quantifying the Cloud Particle-Size Feedback in an Earth System Model”. en. *Geophysical Research Letters* 46.19 (2019). \_eprint: <https://onlinelibrary.wiley.com/doi/pdf/10.1029/2019GL083829>, pages 10910–10917. doi: [10.1029/2019GL083829](https://doi.org/10.1029/2019GL083829).
- [39] K. K. Andersen, N. Azuma, J.-M. Barnola, M. Bigler, P. Biscaye, N. Caillon, J. Chappellaz, H. B. Clausen, D. Dahl-Jensen, H. Fischer, J. Flückiger, D. Fritzsche, Y. Fujii, K. Goto-Azuma, K. Grønvold, N. S. Gundestrup, M. Hansson, C. Huber, C. S. Hvidberg, S. J. Johnsen, U. Jonsell, J. Jouzel, S. Kipfstuhl, A. Landais, M. Leuenberger, R. Lorrain, V. Masson-Delmotte, H. Miller, H. Motoyama, H. Narita, T. Popp, S. O. Rasmussen, D. Raynaud, R. Rothlisberger, U. Ruth, D. Samyn, J. Schwander, H. Shoji, M.-L. Siggard-Andersen, J. P. Steffensen, T. Stocker, A. E. Sveinbjörnsdóttir, A. Svensson, M. Takata, J.-L. Tison, T. Thorsteinsson, O. Watanabe, F. Wilhelms, J. W. C. White, and North Greenland Ice Core Project members. “High-resolution record of Northern Hemisphere climate extending into the last interglacial period”. en. *Nature* 431.7005 (2004). Publisher: Nature Publishing Group, pages 147–151. doi: [10.1038/nature02805](https://doi.org/10.1038/nature02805).
- [40] J. Jouzel, V. Masson-Delmotte, O. Cattani, G. Dreyfus, S. Falourd, G. Hoffmann, B. Minster, J. Nouet, J. M. Barnola, J. Chappellaz, H. Fischer, J. C. Gallet, S. Johnsen, M. Leuenberger, L. Loulergue, D. Luethi, H. Oerter, F. Parrenin, G. Raisbeck, D. Raynaud, A. Schilt, J. Schwander, E. Selmo, R. Souchez, R. Spahni, B. Stauffer, J. P. Steffensen, B. Stenni, T. F. Stocker, J. L. Tison, M. Werner, and E. W. Wolff. “Orbital and Millennial Antarctic Climate Variability over the Past 800,000 Years”. *Science* 317.5839 (2007). Publisher: American Association for the Advancement of Science, pages 793–796. doi: [10.1126/science.1141038](https://doi.org/10.1126/science.1141038).
- [41] L. E. Lisiecki and M. E. Raymo. “A Pliocene-Pleistocene stack of 57 globally distributed benthic 18O records”. en. *Paleoceanography* 20.1 (2005). \_eprint: <https://onlinelibrary.wiley.com/doi/pdf/10.1029/2004PA001071>. doi: [10.1029/2004PA001071](https://doi.org/10.1029/2004PA001071).
- [42] J. C. Zachos, G. R. Dickens, and R. E. Zeebe. “An early Cenozoic perspective on greenhouse warming and carbon-cycle dynamics”. en. *Nature* 451.7176 (2008). Publisher: Nature Publishing Group, pages 279–283. doi: [10.1038/nature06588](https://doi.org/10.1038/nature06588).
- [43] S. A. Marcott, J. D. Shakun, P. U. Clark, and A. C. Mix. “A Reconstruction of Regional and Global Temperature for the Past 11,300 Years”. *Science* 339.6124 (2013). Publisher: American Association for the Advancement of Science, pages 1198–1201. doi: [10.1126/science.1228026](https://doi.org/10.1126/science.1228026).
- [44] R. P. Acosta, N. J. Burls, M. J. Pound, C. D. Bradshaw, A. M. De Boer, N. Herold, M. Huber, X. Liu, Y. Donnadieu, A. Farnsworth, A. Frigola, D. J. Lunt, A. S. von der Heydt, D. K. Hutchinson, G. Knorr, G. Lohmann, A. Marzocchi, M. Prange, A. C. Sarr, X. Li, and Z. Zhang. “A Model-Data Comparison of the Hydrological Response to Miocene Warmth: Leveraging the MioMIP1 Opportunistic Multi-Model Ensemble”. en. *Paleoceanography and Paleoclimatology* 39.1 (2024). \_eprint: <https://onlinelibrary.wiley.com/doi/pdf/10.1029/2023PA004726>, e2023PA004726. doi: [10.1029/2023PA004726](https://doi.org/10.1029/2023PA004726).
- [45] A. Hossain, G. Knorr, W. Jokat, G. Lohmann, K. Hochmuth, P. Gierz, K. Gohl, and C. Stepanek. “The Impact of Different Atmospheric CO<sub>2</sub> Concentrations on Large Scale Miocene Temperature Signatures”. en. *Paleoceanography and Paleoclimatology* 38.2 (2023). \_eprint: <https://onlinelibrary.wiley.com/doi/pdf/10.1029/2022PA004438>. doi: [10.1029/2022PA004438](https://doi.org/10.1029/2022PA004438).
- [46] G. Knorr, M. Butzin, A. Micheels, and G. Lohmann. “A warm Miocene climate at low atmospheric CO<sub>2</sub> levels”. en. *Geophysical Research Letters* 38.20 (2011). \_eprint: <https://onlinelibrary.wiley.com/doi/pdf/10.1029/2011GL048873>. doi: [10.1029/2011GL048873](https://doi.org/10.1029/2011GL048873).
- [47] G. L. Foster and E. J. Rohling. “Relationship between sea level and climate forcing by CO<sub>2</sub> on geological timescales”. *Proceedings of the National Academy of Sciences* 110.4 (2013). Publisher: Proceedings of the National Academy of Sciences, pages 1209–1214. doi: [10.1073/pnas.1216073110](https://doi.org/10.1073/pnas.1216073110).
- [48] W. M. Kürschner, Z. Kvaček, and D. L. Dilcher. “The impact of Miocene atmospheric carbon dioxide fluctuations on climate and the evolution of terrestrial ecosystems”. *Proceedings of the National Academy of Sciences* 105.2 (2008). Publisher: Proceedings of the National Academy of Sciences, pages 449–453. doi: [10.1073/pnas.0708588105](https://doi.org/10.1073/pnas.0708588105).

- [49] S. M. Sosdian, R. Greenop, M. P. Hain, G. L. Foster, P. N. Pearson, and C. H. Lear. “Constraining the evolution of Neogene ocean carbonate chemistry using the boron isotope pH proxy”. *Earth and Planetary Science Letters* 498 (2018), pages 362–376. doi: [10.1016/j.epsl.2018.06.017](https://doi.org/10.1016/j.epsl.2018.06.017).
- [50] J. W. Rae, Y. G. Zhang, X. Liu, G. L. Foster, H. M. Stoll, and R. D. Whiteford. “Atmospheric CO<sub>2</sub> over the Past 66 Million Years from Marine Archives”. *Annual Review of Earth and Planetary Sciences* 49.1 (2021). \_eprint: <https://doi.org/10.1146/annurev-earth-082420-063026>, pages 609–641. doi: [10.1146/annurev-earth-082420-063026](https://doi.org/10.1146/annurev-earth-082420-063026).
- [51] G. J. Retallack. “Refining a pedogenic-carbonate CO<sub>2</sub> paleobarometer to quantify a middle Miocene greenhouse spike”. *Palaeogeography, Palaeoclimatology, Palaeoecology* 281.1 (2009), pages 57–65. doi: [10.1016/j.palaeo.2009.07.011](https://doi.org/10.1016/j.palaeo.2009.07.011).
- [52] C. M. Brierley and A. V. Fedorov. “Comparing the impacts of Miocene–Pliocene changes in inter-ocean gateways on climate: Central American Seaway, Bering Strait, and Indonesia”. *Earth and Planetary Science Letters* 444 (2016), pages 116–130. doi: [10.1016/j.epsl.2016.03.010](https://doi.org/10.1016/j.epsl.2016.03.010).
- [53] A. Farnsworth, D. J. Lunt, S. A. Robinson, P. J. Valdes, W. H. G. Roberts, P. D. Clift, P. Markwick, T. Su, N. Wrobel, F. Bragg, S.-J. Kelland, and R. D. Pancost. “Past East Asian monsoon evolution controlled by paleogeography, not CO<sub>2</sub>”. *Science Advances* 5.10 (2019). Publisher: American Association for the Advancement of Science, eaax1697. doi: [10.1126/sciadv.aax1697](https://doi.org/10.1126/sciadv.aax1697).
- [54] G. Jung, M. Prange, and M. Schulz. “Influence of topography on tropical African vegetation coverage”. en. *Climate Dynamics* 46.7 (2016), pages 2535–2549. doi: [10.1007/s00382-015-2716-9](https://doi.org/10.1007/s00382-015-2716-9).
- [55] M. P. S. Badger, D. N. Schmidt, A. Mackensen, and R. D. Pancost. “High-resolution alkenone palaeobarometry indicates relatively stable pCO<sub>2</sub> during the Pliocene (3.3–2.8Ma)”. *Philosophical Transactions of the Royal Society A: Mathematical, Physical and Engineering Sciences* 371.2001 (2013). Publisher: Royal Society, page 20130094. doi: [10.1098/rsta.2013.0094](https://doi.org/10.1098/rsta.2013.0094).
- [56] G. Bartoli, B. Hönisch, and R. E. Zeebe. “Atmospheric CO<sub>2</sub> decline during the Pliocene intensification of Northern Hemisphere glaciations”. en. *Paleoceanography* 26.4 (2011). \_eprint: <https://onlinelibrary.wiley.com/doi/pdf/10.1029/2010PA002055>. doi: [10.1029/2010PA002055](https://doi.org/10.1029/2010PA002055).
- [57] A. M. Haywood, J. C. Tindall, H. J. Dowsett, A. M. Dolan, K. M. Foley, S. J. Hunter, D. J. Hill, W.-L. Chan, A. Abe-Ouchi, C. Stepanek, G. Lohmann, D. Chandan, W. R. Peltier, N. Tan, C. Contoux, G. Ramstein, X. Li, Z. Zhang, C. Guo, K. H. Nisancioglu, Q. Zhang, Q. Li, Y. Kamae, M. A. Chandler, L. E. Sohl, B. L. Otto-Bliesner, R. Feng, E. C. Brady, A. S. von der Heydt, M. L. J. Baatsen, and D. J. Lunt. “The Pliocene Model Intercomparison Project Phase 2: large-scale climate features and climate sensitivity”. English. *Climate of the Past* 16.6 (2020). Publisher: Copernicus GmbH, pages 2095–2123. doi: [10.5194/cp-16-2095-2020](https://doi.org/10.5194/cp-16-2095-2020).
- [58] U. Salzmann, A. M. Dolan, A. M. Haywood, W.-L. Chan, J. Voss, D. J. Hill, A. Abe-Ouchi, B. Otto-Bliesner, F. J. Bragg, M. A. Chandler, C. Contoux, H. J. Dowsett, A. Jost, Y. Kamae, G. Lohmann, D. J. Lunt, S. J. Pickering, M. J. Pound, G. Ramstein, N. A. Rosenbloom, L. Sohl, C. Stepanek, H. Ueda, and Z. Zhang. “Challenges in quantifying Pliocene terrestrial warming revealed by data–model discord”. en. *Nature Climate Change* 3.11 (2013). Number: 11 Publisher: Nature Publishing Group, pages 969–974. doi: [10.1038/nclimate2008](https://doi.org/10.1038/nclimate2008).
- [59] H. J. Schellnhuber, S. Rahmstorf, and R. Winkelmann. “Why the right climate target was agreed in Paris”. en. *Nature Climate Change* 6.7 (2016). Publisher: Nature Publishing Group, pages 649–653. doi: [10.1038/nclimate3013](https://doi.org/10.1038/nclimate3013).
- [60] D. I. Armstrong McKay, A. Staal, J. F. Abrams, R. Winkelmann, B. Sakschewski, S. Loriani, I. Fetzer, S. E. Cornell, J. Rockström, and T. M. Lenton. “Exceeding 1.5°C global warming could trigger multiple climate tipping points”. *Science* 377.6611 (2022). Publisher: American Association for the Advancement of Science, eabn7950. doi: [10.1126/science.abn7950](https://doi.org/10.1126/science.abn7950).
- [61] D. Jiang, H. Wang, Z. Ding, X. Lang, and H. Drange. “Modeling the middle Pliocene climate with a global atmospheric general circulation model”. en. *Journal of Geophysical Research: Atmospheres* 110.D14 (2005). \_eprint: <https://onlinelibrary.wiley.com/doi/pdf/10.1029/2004JD005639>. doi: [10.1029/2004JD005639](https://doi.org/10.1029/2004JD005639).

- [62] D. Chandan and W. R. Peltier. “On the mechanisms of warming the mid-Pliocene and the inference of a hierarchy of climate sensitivities with relevance to the understanding of climate futures”. English. *Climate of the Past* 14.6 (2018). Publisher: Copernicus GmbH, pages 825–856. doi: [10.5194/cp-14-825-2018](https://doi.org/10.5194/cp-14-825-2018).
- [63] W. de Nooijer, Q. Zhang, Q. Li, Q. Zhang, X. Li, Z. Zhang, C. Guo, K. H. Nisancioglu, A. M. Haywood, J. C. Tindall, S. J. Hunter, H. J. Dowsett, C. Stepanek, G. Lohmann, B. L. Otto-Bliesner, R. Feng, L. E. Sohl, M. A. Chandler, N. Tan, C. Contoux, G. Ramstein, M. L. J. Baatsen, A. S. von der Heydt, D. Chandan, W. R. Peltier, A. Abe-Ouchi, W.-L. Chan, Y. Kamae, and C. M. Brierley. “Evaluation of Arctic warming in mid-Pliocene climate simulations”. English. *Climate of the Past* 16.6 (2020). Publisher: Copernicus GmbH, pages 2325–2341. doi: [10.5194/cp-16-2325-2020](https://doi.org/10.5194/cp-16-2325-2020).
- [64] G. Zhang and K. H. Cook. “West African monsoon demise: Climatology, interannual variations, and relationship to seasonal rainfall”. en. *Journal of Geophysical Research: Atmospheres* 119.17 (2014). \_eprint: <https://onlinelibrary.wiley.com/doi/pdf/10.1002/2014JD022043>, pages 10,175–10,193. doi: [10.1002/2014JD022043](https://doi.org/10.1002/2014JD022043).
- [65] R. O’ishi, W.-L. Chan, A. Abe-Ouchi, S. Sherriff-Tadano, R. Ohgaito, and M. Yoshimori. “PMIP4/CMIP6 last interglacial simulations using three different versions of MIROC: importance of vegetation”. English. *Climate of the Past* 17.1 (2021). Publisher: Copernicus GmbH, pages 21–36. doi: [10.5194/cp-17-21-2021](https://doi.org/10.5194/cp-17-21-2021).
- [66] X. Shi, M. Werner, Q. Wang, H. Yang, and G. Lohmann. “Simulated Mid-Holocene and Last Interglacial Climate Using Two Generations of AWI-ESM”. EN. *Journal of Climate* 35.23 (2022). Publisher: American Meteorological Society Section: Journal of Climate, pages 7811–7831. doi: [10.1175/JCLI-D-22-0354.1](https://doi.org/10.1175/JCLI-D-22-0354.1).
- [67] B. L. Otto-Bliesner, N. Rosenbloom, E. J. Stone, N. P. McKay, D. J. Lunt, E. C. Brady, and J. T. Overpeck. “How warm was the last interglacial? New model–data comparisons”. *Philosophical Transactions of the Royal Society A: Mathematical, Physical and Engineering Sciences* 371.2001 (2013). Publisher: Royal Society, page 20130097. doi: [10.1098/rsta.2013.0097](https://doi.org/10.1098/rsta.2013.0097).
- [68] B. L. Otto-Bliesner, P. Braconnot, S. P. Harrison, D. J. Lunt, A. Abe-Ouchi, S. Albani, P. J. Bartlein, E. Capron, A. E. Carlson, A. Dutton, H. Fischer, H. Goelzer, A. Govin, A. Haywood, F. Joos, A. N. LeGrande, W. H. Lipscomb, G. Lohmann, N. Mahowald, C. Nehrbass-Ahles, F. S. R. Pausata, J.-Y. Peterschmitt, S. J. Phipps, H. Renssen, and Q. Zhang. “The PMIP4 contribution to CMIP6 – Part 2: Two interglacials, scientific objective and experimental design for Holocene and Last Interglacial simulations”. English. *Geoscientific Model Development* 10.11 (2017). Publisher: Copernicus GmbH, pages 3979–4003. doi: [10.5194/gmd-10-3979-2017](https://doi.org/10.5194/gmd-10-3979-2017).
- [69] P. Braconnot, B. Otto-Bliesner, S. Harrison, S. Joussaume, J.-Y. Peterchmitt, A. Abe-Ouchi, M. Crucifix, E. Driesschaert, T. Fichefet, C. D. Hewitt, M. Kageyama, A. Kitoh, A. Lâiné, M.-F. Loutre, O. Marti, U. Merkel, G. Ramstein, P. Valdes, S. L. Weber, Y. Yu, and Y. Zhao. “Results of PMIP2 coupled simulations of the Mid-Holocene and Last Glacial Maximum &ndash; Part 1: experiments and large-scale features”. English. *Climate of the Past* 3.2 (2007). Publisher: Copernicus GmbH, pages 261–277. doi: [10.5194/cp-3-261-2007](https://doi.org/10.5194/cp-3-261-2007).
- [70] M. Kageyama, P. Braconnot, L. Bopp, V. Mariotti, T. Roy, M.-N. Woillez, A. Caubel, M.-A. Foujols, E. Guilyardi, M. Khodri, J. Lloyd, F. Lombard, and O. Marti. “Mid-Holocene and last glacial maximum climate simulations with the IPSL model: part II: model-data comparisons”. en. *Climate Dynamics* 40.9 (2013), pages 2469–2495. doi: [10.1007/s00382-012-1499-5](https://doi.org/10.1007/s00382-012-1499-5).
- [71] D. Kaufman, N. McKay, C. Routson, M. Erb, C. Dätwyler, P. S. Sommer, O. Heiri, and B. Davis. “Holocene global mean surface temperature, a multi-method reconstruction approach”. en. *Scientific Data* 7.1 (2020). Publisher: Nature Publishing Group, page 201. doi: [10.1038/s41597-020-0530-7](https://doi.org/10.1038/s41597-020-0530-7).
- [72] Y. Godd eris, Y. Donnadieu, G. Le Hir, V. Lefebvre, and E. Nardin. “The role of palaeogeography in the Phanerozoic history of atmospheric CO2 and climate”. *Earth-Science Reviews* 128 (2014), pages 122–138. doi: [10.1016/j.earscirev.2013.11.004](https://doi.org/10.1016/j.earscirev.2013.11.004).

- [73] P. Braconnot, S. P. Harrison, M. Kageyama, P. J. Bartlein, V. Masson-Delmotte, A. Abe-Ouchi, B. Otto-Bliesner, and Y. Zhao. "Evaluation of climate models using palaeoclimatic data". en. *Nature Climate Change* 2.6 (2012). Number: 6 Publisher: Nature Publishing Group, pages 417–424. doi: [10.1038/nclimate1456](https://doi.org/10.1038/nclimate1456).
- [74] B. Bereiter, S. Eggleston, J. Schmitt, C. Nehrbass-Ahles, T. F. Stocker, H. Fischer, S. Kipfstuhl, and J. Chappellaz. "Revision of the EPICA Dome C CO<sub>2</sub> record from 800 to 600 kyr before present". en. *Geophysical Research Letters* 42.2 (2015). \_eprint: <https://onlinelibrary.wiley.com/doi/pdf/10.1002/2014GL061957>, pages 542–549. doi: [10.1002/2014GL061957](https://doi.org/10.1002/2014GL061957).
- [75] P. U. Clark, A. S. Dyke, J. D. Shakun, A. E. Carlson, J. Clark, B. Wohlfarth, J. X. Mitrovica, S. W. Hostetler, and A. M. McCabe. "The Last Glacial Maximum". *Science* 325.5941 (2009). Publisher: American Association for the Advancement of Science, pages 710–714. doi: [10.1126/science.1172873](https://doi.org/10.1126/science.1172873).
- [76] M. Kageyama, S. P. Harrison, M.-L. Kapsch, M. Lofverstrom, J. M. Lora, U. Mikolajewicz, S. Sherriff-Tadano, T. Vadsaria, A. Abe-Ouchi, N. Bouttes, D. Chandan, L. J. Gregoire, R. F. Ivanovic, K. Izumi, A. N. LeGrande, F. Lhardy, G. Lohmann, P. A. Morozova, R. Ohgaito, A. Paul, W. R. Peltier, C. J. Poulsen, A. Quiquet, D. M. Roche, X. Shi, J. E. Tierney, P. J. Valdes, E. Volodin, and J. Zhu. "The PMIP4 Last Glacial Maximum experiments: preliminary results and comparison with the PMIP3 simulations". English. *Climate of the Past* 17.3 (2021). Publisher: Copernicus GmbH, pages 1065–1089. doi: [10.5194/cp-17-1065-2021](https://doi.org/10.5194/cp-17-1065-2021).
- [77] J. D. Annan and J. C. Hargreaves. "A new global reconstruction of temperature changes at the Last Glacial Maximum". English. *Climate of the Past* 9.1 (2013). Publisher: Copernicus GmbH, pages 367–376. doi: [10.5194/cp-9-367-2013](https://doi.org/10.5194/cp-9-367-2013).
- [78] J. D. Annan and J. C. Hargreaves. "A perspective on model-data surface temperature comparison at the Last Glacial Maximum". *Quaternary Science Reviews* 107 (2015), pages 1–10. doi: [10.1016/j.quascirev.2014.09.019](https://doi.org/10.1016/j.quascirev.2014.09.019).
- [79] T. Friedrich, A. Timmermann, M. Tigchelaar, O. Elison Timm, and A. Ganopolski. "Nonlinear climate sensitivity and its implications for future greenhouse warming". *Science Advances* 2.11 (2016). Publisher: American Association for the Advancement of Science, e1501923. doi: [10.1126/sciadv.1501923](https://doi.org/10.1126/sciadv.1501923).
- [80] W. R. Boos. "Thermodynamic Scaling of the Hydrological Cycle of the Last Glacial Maximum". EN. *Journal of Climate* 25.3 (2012). Publisher: American Meteorological Society Section: Journal of Climate, pages 992–1006. doi: [10.1175/JCLI-D-11-00010.1](https://doi.org/10.1175/JCLI-D-11-00010.1).
- [81] J. M. Lora. "Components and Mechanisms of Hydrologic Cycle Changes over North America at the Last Glacial Maximum". EN. *Journal of Climate* 31.17 (2018). Publisher: American Meteorological Society Section: Journal of Climate, pages 7035–7051. doi: [10.1175/JCLI-D-17-0544.1](https://doi.org/10.1175/JCLI-D-17-0544.1).
- [82] J. Scheff and D. M. W. Frierson. "Robust future precipitation declines in CMIP5 largely reflect the poleward expansion of model subtropical dry zones". en. *Geophysical Research Letters* 39.18 (2012). \_eprint: <https://onlinelibrary.wiley.com/doi/pdf/10.1029/2012GL052910>. doi: [10.1029/2012GL052910](https://doi.org/10.1029/2012GL052910).
- [83] G. J. Bowen, Z. Cai, R. P. Fiorella, and A. L. Putman. "Isotopes in the Water Cycle: Regional- to Global-Scale Patterns and Applications". *Annual Review of Earth and Planetary Sciences* 47.1 (2019). \_eprint: <https://doi.org/10.1146/annurev-earth-053018-060220>, pages 453–479. doi: [10.1146/annurev-earth-053018-060220](https://doi.org/10.1146/annurev-earth-053018-060220).
- [84] S. Dee, A. Bailey, J. L. Conroy, A. Atwood, S. Stevenson, J. Nusbaumer, and D. Noone. "Water isotopes, climate variability, and the hydrological cycle: recent advances and new frontiers". en. *Environmental Research: Climate* 2.2 (2023). Publisher: IOP Publishing, page 022002. doi: [10.1088/2752-5295/acce1](https://doi.org/10.1088/2752-5295/acce1).
- [85] N. J. Burls and A. V. Fedorov. "Wetter subtropics in a warmer world: Contrasting past and future hydrological cycles". *Proceedings of the National Academy of Sciences* 114.49 (2017). Publisher: Proceedings of the National Academy of Sciences, pages 12888–12893. doi: [10.1073/pnas.1703421114](https://doi.org/10.1073/pnas.1703421114).
- [86] S. C. Sherwood, R. Roca, T. M. Weckwerth, and N. G. Andronova. "Tropospheric water vapor, convection, and climate". en. *Reviews of Geophysics* 48.2 (2010). \_eprint: <https://onlinelibrary.wiley.com/doi/pdf/10.1029/2009RG000301>. doi: [10.1029/2009RG000301](https://doi.org/10.1029/2009RG000301).

- [87] H. Craig and L. I. Gordon. "Deuterium and oxygen 18 variations in the ocean and the marine atmosphere" (1965). Publisher: Consiglio nazionale delle ricerche, Laboratorio de geologia nucleare Pisa.
- [88] W. Dansgaard. "Stable isotopes in precipitation". *Tellus* 16.4 (1964). Publisher: Taylor & Francis \_eprint: <https://doi.org/10.3402/tellusa.v16i4.8993>, pages 436–468. doi: [10.3402/tellusa.v16i4.8993](https://doi.org/10.3402/tellusa.v16i4.8993).
- [89] H. Craig. "Isotopic Variations in Meteoric Waters". *Science* 133.3465 (1961). Publisher: American Association for the Advancement of Science, pages 1702–1703. doi: [10.1126/science.133.3465.1702](https://doi.org/10.1126/science.133.3465.1702).
- [90] A. Bailey, J. Nusbaumer, and D. Noone. "Precipitation efficiency derived from isotope ratios in water vapor distinguishes dynamical and microphysical influences on subtropical atmospheric constituents". en. *Journal of Geophysical Research: Atmospheres* 120.18 (2015). \_eprint: <https://onlinelibrary.wiley.com/doi/pdf/10.1002/2015JD023403>, pages 9119–9137. doi: [10.1002/2015JD023403](https://doi.org/10.1002/2015JD023403).
- [91] J.-E. Lee and I. Fung. "'Amount effect' of water isotopes and quantitative analysis of post-condensation processes". en. *Hydrological Processes* 22.1 (2008), pages 1–8. doi: [10.1002/hyp.6637](https://doi.org/10.1002/hyp.6637).
- [92] J. Nusbaumer, T. E. Wong, C. Bardeen, and D. Noone. "Evaluating hydrological processes in the Community Atmosphere Model Version 5 (CAM5) using stable isotope ratios of water". en. *Journal of Advances in Modeling Earth Systems* 9.2 (2017). \_eprint: <https://onlinelibrary.wiley.com/doi/pdf/10.1002/2016MS000839>, pages 949–977. doi: [10.1002/2016MS000839](https://doi.org/10.1002/2016MS000839).
- [93] C. Risi, D. Noone, J. Worden, C. Frankenberg, G. Stiller, M. Kiefer, B. Funke, K. Walker, P. Bernath, M. Schneider, D. Wunch, V. Sherlock, N. Deutscher, D. Griffith, P. O. Wennberg, K. Strong, D. Smale, E. Mahieu, S. Barthlott, F. Hase, O. García, J. Notholt, T. Warneke, G. Toon, D. Sayres, S. Bony, J. Lee, D. Brown, R. Uemura, and C. Sturm. "Process-evaluation of tropospheric humidity simulated by general circulation models using water vapor isotopologues: 1. Comparison between models and observations". en. *Journal of Geophysical Research: Atmospheres* 117.D5 (2012). \_eprint: <https://onlinelibrary.wiley.com/doi/pdf/10.1029/2011JD016621>. doi: [10.1029/2011JD016621](https://doi.org/10.1029/2011JD016621).
- [94] J. Galewsky, H. C. Steen-Larsen, R. D. Field, J. Worden, C. Risi, and M. Schneider. "Stable isotopes in atmospheric water vapor and applications to the hydrologic cycle". en. *Reviews of Geophysics* 54.4 (2016). \_eprint: <https://onlinelibrary.wiley.com/doi/pdf/10.1002/2015RG000512>, pages 809–865. doi: [10.1002/2015RG000512](https://doi.org/10.1002/2015RG000512).
- [95] J. R. Gat. "Oxygen and Hydrogen Isotopes in the Hydrologic Cycle". *Annual Review of Earth and Planetary Sciences* 24.1 (1996). \_eprint: <https://doi.org/10.1146/annurev.earth.24.1.225>, pages 225–262. doi: [10.1146/annurev.earth.24.1.225](https://doi.org/10.1146/annurev.earth.24.1.225).
- [96] C. Risi, S. Bony, and F. Vimeux. "Influence of convective processes on the isotopic composition ( $^{18}\text{O}$  and  $\text{D}$ ) of precipitation and water vapor in the tropics: 2. Physical interpretation of the amount effect". en. *Journal of Geophysical Research: Atmospheres* 113.D19 (2008). \_eprint: <https://onlinelibrary.wiley.com/doi/pdf/10.1029/2008JD009943>. doi: [10.1029/2008JD009943](https://doi.org/10.1029/2008JD009943).
- [97] C. E. Jonsson, S. Andersson, G. C. Rosqvist, and M. J. Leng. "Reconstructing past atmospheric circulation changes using oxygen isotopes in lake sediments from Sweden". English. *Climate of the Past* 6.1 (2010). Publisher: Copernicus GmbH, pages 49–62. doi: [10.5194/cp-6-49-2010](https://doi.org/10.5194/cp-6-49-2010).
- [98] G. C. Rosqvist, M. J. Leng, T. Goslar, H. J. Sloane, C. Bigler, L. Cunningham, A. Dadal, J. Bergman, A. Berntsson, C. Jonsson, and S. Wastegård. "Shifts in precipitation during the last millennium in northern Scandinavia from lacustrine isotope records". *Quaternary Science Reviews*. International Association of Limnogeology – Isotopes and Lakes 66 (2013), pages 22–34. doi: [10.1016/j.quascirev.2012.10.030](https://doi.org/10.1016/j.quascirev.2012.10.030).
- [99] C. Xu, B. M. Buckley, S.-Y. S. Wang, W. An, Z. Li, T. Nakatsuka, and Z. Guo. "Oxygen Isotopes in Tree Rings from Greenland: A New Proxy of NAO". en. *Atmosphere* 12.1 (2021). Number: 1 Publisher: Multidisciplinary Digital Publishing Institute, page 39. doi: [10.3390/atmos12010039](https://doi.org/10.3390/atmos12010039).
- [100] Y. Liu, W. Man, T. Zhou, and M. Zuo. "Global Multiproxy ENSO Reconstruction Over the Past Millennium". en. *Journal of Geophysical Research: Atmospheres* 129.10 (2024). \_eprint: <https://onlinelibrary.wiley.com/doi/pdf/10.1029/2023JD040491>. doi: [10.1029/2023JD040491](https://doi.org/10.1029/2023JD040491).



- [101] C. N. Garziona, J. Quade, P. G. DeCelles, and N. B. English. "Predicting paleoelevation of Tibet and the Himalaya from 18O vs. altitude gradients in meteoric water across the Nepal Himalaya". en. *Earth and Planetary Science Letters* 183.1 (2000), pages 215–229. doi: [10.1016/S0012-821X\(00\)00252-1](https://doi.org/10.1016/S0012-821X(00)00252-1).
- [102] A. Mulch, S. A. Graham, and C. P. Chamberlain. "Hydrogen Isotopes in Eocene River Gravels and Paleoelevation of the Sierra Nevada". *Science* 313.5783 (2006). Publisher: American Association for the Advancement of Science, pages 87–89. doi: [10.1126/science.1125986](https://doi.org/10.1126/science.1125986).
- [103] D. B. Rowley and B. S. Currie. "Palaeo-altimetry of the late Eocene to Miocene Lunpola basin, central Tibet". en. *Nature* 439.7077 (2006). Number: 7077 Publisher: Nature Publishing Group, pages 677–681. doi: [10.1038/nature04506](https://doi.org/10.1038/nature04506).
- [104] M. D. Jones, S. Dee, L. Anderson, A. Baker, G. Bowen, and D. C. Noone. "Water isotope systematics: Improving our palaeoclimate interpretations". *Quaternary Science Reviews*. Water Isotope Systematics 131 (2016), pages 243–249. doi: [10.1016/j.quascirev.2015.11.014](https://doi.org/10.1016/j.quascirev.2015.11.014).
- [105] B. L. Konecky, N. P. McKay, O. V. Churakova (Sidorova), L. Comas-Bru, E. P. Dassié, K. L. DeLong, G. M. Falster, M. J. Fischer, M. D. Jones, L. Jonkers, D. S. Kaufman, G. Leduc, S. R. Managave, B. Martrat, T. Opel, A. J. Orsi, J. W. Partin, H. R. Sayani, E. K. Thomas, D. M. Thompson, J. J. Tyler, N. J. Abram, A. R. Atwood, O. Cartapanis, J. L. Conroy, M. A. Curran, S. G. Dee, M. Deininger, D. V. Divine, Z. Kern, T. J. Porter, S. L. Stevenson, L. von Gunten, and I. P. Members. "The Iso2k database: a global compilation of paleo-<sup>18</sup>O and <sup>2</sup>H records to aid understanding of Common Era climate". English. *Earth System Science Data* 12.3 (2020). Publisher: Copernicus GmbH, pages 2261–2288. doi: [10.5194/essd-12-2261-2020](https://doi.org/10.5194/essd-12-2261-2020).
- [106] L. J. Lücke, G. C. Hegerl, A. P. Schurer, and R. Wilson. "Effects of Memory Biases on Variability of Temperature Reconstructions". EN. *Journal of Climate* 32.24 (2019). Publisher: American Meteorological Society Section: Journal of Climate, pages 8713–8731. doi: [10.1175/JCLI-D-19-0184.1](https://doi.org/10.1175/JCLI-D-19-0184.1).
- [107] M. Reschke, K. Rehfeld, and T. Laepple. "Empirical estimate of the signal content of Holocene temperature proxy records". English. *Climate of the Past* 15.2 (2019). Publisher: Copernicus GmbH, pages 521–537. doi: [10.5194/cp-15-521-2019](https://doi.org/10.5194/cp-15-521-2019).
- [108] L. Comas-Bru, K. Rehfeld, C. Roesch, S. Amirnezhad-Mozhdehi, S. P. Harrison, K. Atsawawaranunt, S. M. Ahmad, Y. A. Brahim, A. Baker, M. Bosomworth, S. F. M. Breitenbach, Y. Burstyn, A. Columbu, M. Deininger, A. Demény, B. Dixon, J. Fohlmeister, I. G. Hatvani, J. Hu, N. Kaushal, Z. Kern, I. Labuhn, F. A. Lechleitner, A. Lorrey, B. Martrat, V. F. Novello, J. Oster, C. Pérez-Mejías, D. Scholz, N. Scroton, N. Sinha, B. M. Ward, S. Warken, H. Zhang, and S. W. G. members. "SISALv2: a comprehensive speleothem isotope database with multiple age–depth models". English. *Earth System Science Data* 12.4 (2020). Publisher: Copernicus GmbH, pages 2579–2606. doi: [10.5194/essd-12-2579-2020](https://doi.org/10.5194/essd-12-2579-2020).
- [109] N. Kaushal, F. A. Lechleitner, M. Wilhelm, K. Azennoud, J. C. Bühler, K. Braun, Y. Ait Brahim, A. Baker, Y. Burstyn, L. Comas-Bru, J. Fohlmeister, Y. Goldsmith, S. P. Harrison, I. G. Hatvani, K. Rehfeld, M. Ritzau, V. Skiba, H. M. Stoll, J. G. Szűcs, P. Tanos, P. C. Treble, V. Azevedo, J. L. Baker, A. Borsato, S. Chawchai, A. Columbu, L. Endres, J. Hu, Z. Kern, A. Kimbrough, K. Koç, M. Markowska, B. Martrat, S. Masood Ahmad, C. Nehme, V. F. Novello, C. Pérez-Mejías, J. Ruan, N. Sekhon, N. Sinha, C. V. Tadros, B. H. Tiger, S. Warken, A. Wolf, H. Zhang, and S. W. G. members. "SISALv3: a global speleothem stable isotope and trace element database". English. *Earth System Science Data* 16.4 (2024). Publisher: Copernicus GmbH, pages 1933–1963. doi: [10.5194/essd-16-1933-2024](https://doi.org/10.5194/essd-16-1933-2024).
- [110] T. Kukla, J. K. Rugenstein, E. Driscoll, D. E. Ibarra, and C. P. Chamberlain. "The PATCH Lab V1. 0: A database and workspace for Cenozoic terrestrial paleoclimate and environment reconstruction". *American Journal of Science* 322.10 (2022). Publisher: American Journal of Science, pages 1124–1158.
- [111] U. Salzmann, A. M. Haywood, D. J. Lunt, P. J. Valdes, and D. J. Hill. "A new global biome reconstruction and data-model comparison for the Middle Pliocene". en. *Global Ecology and Biogeography* 17.3 (2008). \_eprint: <https://onlinelibrary.wiley.com/doi/pdf/10.1111/j.1466-8238.2008.00381.x>, pages 432–447. doi: [10.1111/j.1466-8238.2008.00381.x](https://doi.org/10.1111/j.1466-8238.2008.00381.x).

- [112] S. E. Tolwinski-Ward, M. P. Tingley, M. N. Evans, M. K. Hughes, and D. W. Nychka. "Probabilistic reconstructions of local temperature and soil moisture from tree-ring data with potentially time-varying climatic response". en. *Climate Dynamics* 44.3 (2015), pages 791–806. doi: [10.1007/s00382-014-2139-z](https://doi.org/10.1007/s00382-014-2139-z).
- [113] N. Weitzel, A. Hense, and C. Ohlwein. "Combining a pollen and macrofossil synthesis with climate simulations for spatial reconstructions of European climate using Bayesian filtering". English. *Climate of the Past* 15.4 (2019). Publisher: Copernicus GmbH, pages 1275–1301. doi: [10.5194/cp-15-1275-2019](https://doi.org/10.5194/cp-15-1275-2019).
- [114] J. Haslett, M. Whitley, S. Bhattacharya, M. Salter-Townshend, S. P. Wilson, J. R. M. Allen, B. Huntley, and F. J. G. Mitchell. "Bayesian palaeoclimate reconstruction". en. *Journal of the Royal Statistical Society: Series A (Statistics in Society)* 169.3 (2006). \_eprint: <https://onlinelibrary.wiley.com/doi/pdf/10.1111/j.1467-985X.2006.00429.x>. doi: [10.1111/j.1467-985X.2006.00429.x](https://doi.org/10.1111/j.1467-985X.2006.00429.x).
- [115] B. Christiansen, T. Schmith, and P. Thejll. "A Surrogate Ensemble Study of Climate Reconstruction Methods: Stochasticity and Robustness". EN. *Journal of Climate* 22.4 (2009). Publisher: American Meteorological Society Section: Journal of Climate, pages 951–976. doi: [10.1175/2008JCLI2301.1](https://doi.org/10.1175/2008JCLI2301.1).
- [116] B. A. Schubert and A. H. Jahren. "Seasonal temperature and precipitation recorded in the intra-annual oxygen isotope pattern of meteoric water and tree-ring cellulose". *Quaternary Science Reviews* 125 (2015), pages 1–14. doi: [10.1016/j.quascirev.2015.07.024](https://doi.org/10.1016/j.quascirev.2015.07.024).
- [117] J. R. Lawrence, S. D. Gedzelman, D. Dexheimer, H.-K. Cho, G. D. Carrie, R. Gasparini, C. R. Anderson, K. P. Bowman, and M. I. Biggerstaff. "Stable isotopic composition of water vapor in the tropics". en. *Journal of Geophysical Research: Atmospheres* 109.D6 (2004). \_eprint: <https://onlinelibrary.wiley.com/doi/pdf/10.1029/2003JD004046>. doi: [10.1029/2003JD004046](https://doi.org/10.1029/2003JD004046).
- [118] S. Bony, C. Risi, and F. Vimeux. "Influence of convective processes on the isotopic composition (18O and D) of precipitation and water vapor in the tropics: 1. Radiative-convective equilibrium and Tropical Ocean–Global Atmosphere–Coupled Ocean–Atmosphere Response Experiment (TOGA-COARE) simulations". en. *Journal of Geophysical Research: Atmospheres* 113.D19 (2008). \_eprint: <https://onlinelibrary.wiley.com/doi/pdf/10.1029/2008JD009942>. doi: [10.1029/2008JD009942](https://doi.org/10.1029/2008JD009942).
- [119] R. Feng and C. J. Poulsen. "Refinement of Eocene lapse rates, fossil-leaf altimetry, and North American Cordilleran surface elevation estimates". en. *Earth and Planetary Science Letters* 436 (2016), pages 130–141. doi: [10.1016/j.epsl.2015.12.022](https://doi.org/10.1016/j.epsl.2015.12.022).
- [120] T. A. Ehlers and C. J. Poulsen. "Influence of Andean uplift on climate and paleoaltimetry estimates". en. *Earth and Planetary Science Letters* 281.3 (2009), pages 238–248. doi: [10.1016/j.epsl.2009.02.026](https://doi.org/10.1016/j.epsl.2009.02.026).
- [121] B. Christiansen. "Reconstructing the NH Mean Temperature: Can Underestimation of Trends and Variability Be Avoided?" EN. *Journal of Climate* 24.3 (2011). Publisher: American Meteorological Society Section: Journal of Climate, pages 674–692. doi: [10.1175/2010JCLI3646.1](https://doi.org/10.1175/2010JCLI3646.1).
- [122] M. N. Evans, S. E. Tolwinski-Ward, D. M. Thompson, and K. J. Anchukaitis. "Applications of proxy system modeling in high resolution paleoclimatology". *Quaternary Science Reviews* 76 (2013), pages 16–28. doi: [10.1016/j.quascirev.2013.05.024](https://doi.org/10.1016/j.quascirev.2013.05.024).
- [123] M. P. Tingley, P. F. Craigmile, M. Haran, B. Li, E. Mannshardt, and B. Rajaratnam. "Piecing together the past: statistical insights into paleoclimatic reconstructions". *Quaternary Science Reviews* 35 (2012), pages 1–22. doi: [10.1016/j.quascirev.2012.01.012](https://doi.org/10.1016/j.quascirev.2012.01.012).
- [124] M. N. Evans. "Toward forward modeling for paleoclimatic proxy signal calibration: A case study with oxygen isotopic composition of tropical woods". en. *Geochemistry, Geophysics, Geosystems* 8.7 (2007). \_eprint: <https://onlinelibrary.wiley.com/doi/pdf/10.1029/2006GC001406>. doi: [10.1029/2006GC001406](https://doi.org/10.1029/2006GC001406).
- [125] D. McCarroll and N. J. Loader. "Stable isotopes in tree rings". *Quaternary Science Reviews. Isotopes in Quaternary Paleoenvironmental reconstruction* 23.7 (2004), pages 771–801. doi: [10.1016/j.quascirev.2003.06.017](https://doi.org/10.1016/j.quascirev.2003.06.017).

- [126] M. Werner, U. Mikolajewicz, M. Heimann, and G. Hoffmann. "Borehole versus isotope temperatures on Greenland: Seasonality does matter". en. *Geophysical Research Letters* 27.5 (2000). \_eprint: <https://onlinelibrary.wiley.com/doi/pdf/10.1029/1999GL006075>, pages 723–726. doi: [10.1029/1999GL006075](https://doi.org/10.1029/1999GL006075).
- [127] D. P. Schneider and D. C. Noone. "Spatial covariance of water isotope records in a global network of ice cores spanning twentieth-century climate change". en. *Journal of Geophysical Research* 112.D18 (2007), page D18105. doi: [10.1029/2007JD008652](https://doi.org/10.1029/2007JD008652).
- [128] C. Sturm, Q. Zhang, and D. Noone. "An introduction to stable water isotopes in climate models: benefits of forward proxy modelling for paleoclimatology". English. *Climate of the Past* 6.1 (2010). Publisher: Copernicus GmbH, pages 115–129. doi: [10.5194/cp-6-115-2010](https://doi.org/10.5194/cp-6-115-2010).
- [129] J. Hu, S. Dee, and J. Nusbaumer. "The Role of Isotope-Enabled GCM Complexity in Simulating Tropical Circulation Changes in High-CO<sub>2</sub> Scenarios". en. *Journal of Advances in Modeling Earth Systems* 12.8 (2020). \_eprint: <https://onlinelibrary.wiley.com/doi/pdf/10.1029/2020MS002163>, e2020MS002163. doi: [10.1029/2020MS002163](https://doi.org/10.1029/2020MS002163).
- [130] N. J. Steiger, E. J. Steig, S. G. Dee, G. H. Roe, and G. J. Hakim. "Climate reconstruction using data assimilation of water isotope ratios from ice cores". en. *Journal of Geophysical Research: Atmospheres* 122.3 (2017). \_eprint: <https://onlinelibrary.wiley.com/doi/pdf/10.1002/2016JD026011>, pages 1545–1568. doi: [10.1002/2016JD026011](https://doi.org/10.1002/2016JD026011).
- [131] J. Zhu, Z. Liu, E. Brady, B. Otto-Bliesner, J. Zhang, D. Noone, R. Tomas, J. Nusbaumer, T. Wong, A. Jahn, and C. Tabor. "Reduced ENSO variability at the LGM revealed by an isotope-enabled Earth system model". en. *Geophysical Research Letters* 44.13 (2017). \_eprint: <https://onlinelibrary.wiley.com/doi/pdf/10.1002/2017GL073406>, pages 6984–6992. doi: [10.1002/2017GL073406](https://doi.org/10.1002/2017GL073406).
- [132] J. C. Bühler, J. Axelsson, F. A. Lechleitner, J. Fohlmeister, A. N. LeGrande, M. Midhun, J. Sjolte, M. Werner, K. Yoshimura, and K. Rehfeld. "Investigating stable oxygen and carbon isotopic variability in speleothem records over the last millennium using multiple isotope-enabled climate models". English. *Climate of the Past* 18.7 (2022). Publisher: Copernicus GmbH, pages 1625–1654. doi: [10.5194/cp-18-1625-2022](https://doi.org/10.5194/cp-18-1625-2022).
- [133] S. G. Dee, J. Nusbaumer, A. Bailey, J. M. Russell, J.-E. Lee, B. Konecky, N. H. Buenning, and D. C. Noone. "Tracking the Strength of the Walker Circulation With Stable Isotopes in Water Vapor". en. *Journal of Geophysical Research: Atmospheres* 123.14 (2018). \_eprint: <https://onlinelibrary.wiley.com/doi/pdf/10.1029/2017JD027915>, pages 7254–7270. doi: [10.1029/2017JD027915](https://doi.org/10.1029/2017JD027915).
- [134] G. Falster, B. Konecky, M. Madhavan, S. Stevenson, and S. Coats. "Imprint of the Pacific Walker Circulation in Global Precipitation 18O". EN. *Journal of Climate* 34.21 (2021). Publisher: American Meteorological Society Section: Journal of Climate, pages 8579–8597. doi: [10.1175/JCLI-D-21-0190.1](https://doi.org/10.1175/JCLI-D-21-0190.1).
- [135] M. Dütsch, P. N. Blossey, E. J. Steig, and J. M. Nusbaumer. "Nonequilibrium Fractionation During Ice Cloud Formation in iCAM5: Evaluating the Common Parameterization of Supersaturation as a Linear Function of Temperature". en. *Journal of Advances in Modeling Earth Systems* 11.11 (2019). \_eprint: <https://onlinelibrary.wiley.com/doi/pdf/10.1029/2019MS001764>, pages 3777–3793. doi: [10.1029/2019MS001764](https://doi.org/10.1029/2019MS001764).
- [136] L. Comas-Bru, F. McDermott, and M. Werner. "The effect of the East Atlantic pattern on the precipitation 18O-NAO relationship in Europe". en. *Climate Dynamics* 47.7 (2016), pages 2059–2069. doi: [10.1007/s00382-015-2950-1](https://doi.org/10.1007/s00382-015-2950-1).
- [137] S. M. Vicente-Serrano and J. I. López-Moreno. "Nonstationary influence of the North Atlantic Oscillation on European precipitation". en. *Journal of Geophysical Research: Atmospheres* 113.D20 (2008). \_eprint: <https://onlinelibrary.wiley.com/doi/pdf/10.1029/2008JD010382>. doi: [10.1029/2008JD010382](https://doi.org/10.1029/2008JD010382).
- [138] C. C. Raible, F. Lehner, J. F. González-Rouco, and L. Fernández-Donado. "Changing correlation structures of the Northern Hemisphere atmospheric circulation from 1000 to 2100 AD". English. *Climate of the Past* 10.2 (2014). Publisher: Copernicus GmbH, pages 537–550. doi: [10.5194/cp-10-537-2014](https://doi.org/10.5194/cp-10-537-2014).

- [139] M. A. Poage and C. P. Chamberlain. "Empirical Relationships Between Elevation and the Stable Isotope Composition of Precipitation and Surface Waters: Considerations for Studies of Paleoelevation Change". en. *American Journal of Science* 301.1 (2001). Publisher: American Journal of Science Section: ARTICLES, pages 1–15. doi: [10.2475/ajs.301.1.1](https://doi.org/10.2475/ajs.301.1.1).
- [140] M. Campani, A. Mulch, O. Kempf, F. Schlunegger, and N. Mancktelow. "Miocene paleotopography of the Central Alps". en. *Earth and Planetary Science Letters* 337-338 (2012), pages 174–185. doi: [10.1016/j.epsl.2012.05.017](https://doi.org/10.1016/j.epsl.2012.05.017).
- [141] J. Galewsky. "Orographic precipitation isotopic ratios in stratified atmospheric flows: Implications for paleoelevation studies". *Geology* 37.9 (2009), pages 791–794. doi: [10.1130/G30008A.1](https://doi.org/10.1130/G30008A.1).
- [142] N. Insel, C. J. Poulsen, and T. A. Ehlers. "Influence of the Andes Mountains on South American moisture transport, convection, and precipitation". en. *Climate Dynamics* 35.7 (2010), pages 1477–1492. doi: [10.1007/s00382-009-0637-1](https://doi.org/10.1007/s00382-009-0637-1).
- [143] C. J. Poulsen and M. L. Jeffery. "Climate change imprinting on stable isotopic compositions of high-elevation meteoric water cloaks past surface elevations of major orogens". *Geology* 39.6 (2011), pages 595–598. doi: [10.1130/G32052.1](https://doi.org/10.1130/G32052.1).
- [144] M. Werner, P. M. Langebroek, T. Carlsen, M. Herold, and G. Lohmann. "Stable water isotopes in the ECHAM5 general circulation model: Toward high-resolution isotope modeling on a global scale". en. *Journal of Geophysical Research* 116.D15 (2011), page D15109. doi: [10.1029/2011JD015681](https://doi.org/10.1029/2011JD015681).
- [145] P. M. Langebroek, M. Werner, and G. Lohmann. "Climate information imprinted in oxygen-isotopic composition of precipitation in Europe". en. *Earth and Planetary Science Letters* 311.1 (2011), pages 144–154. doi: [10.1016/j.epsl.2011.08.049](https://doi.org/10.1016/j.epsl.2011.08.049).
- [146] S. Botsyun, S. G. Mutz, T. A. Ehlers, A. Koptev, X. Wang, B. Schmidt, E. Appel, and D. E. Scherer. "Influence of Large-Scale Atmospheric Dynamics on Precipitation Seasonality of the Tibetan Plateau and Central Asia in Cold and Warm Climates During the Late Cenozoic". en. *Journal of Geophysical Research: Atmospheres* 127.12 (2022). \_eprint: <https://onlinelibrary.wiley.com/doi/pdf/10.1029/2021JD035810>, e2021JD035810. doi: [10.1029/2021JD035810](https://doi.org/10.1029/2021JD035810).
- [147] R. Feng, C. J. Poulsen, M. Werner, C. P. Chamberlain, H. T. Mix, and A. Mulch. "Early Cenozoic evolution of topography, climate, and stable isotopes in precipitation in the North American Cordillera". en. *American Journal of Science* 313.7 (2013). Publisher: American Journal of Science Section: Articles, pages 613–648. doi: [10.2475/07.2013.01](https://doi.org/10.2475/07.2013.01).
- [148] S. G. Mutz, T. A. Ehlers, M. Werner, G. Lohmann, C. Stepanek, and J. Li. "Estimates of late Cenozoic climate change relevant to Earth surface processes in tectonically active orogens". English. *Earth Surface Dynamics* 6.2 (2018). Publisher: Copernicus GmbH, pages 271–301. doi: [10.5194/esurf-6-271-2018](https://doi.org/10.5194/esurf-6-271-2018).
- [149] G. Hoffmann, M. Werner, and M. Heimann. "Water isotope module of the ECHAM atmospheric general circulation model: A study on timescales from days to several years". en. *Journal of Geophysical Research: Atmospheres* 103.D14 (1998). \_eprint: <https://onlinelibrary.wiley.com/doi/pdf/10.1029/98JD00423>, pages 16871–16896. doi: [10.1029/98JD00423](https://doi.org/10.1029/98JD00423).
- [150] T. Bariac, J. Gonzalez-Dunia, N. Katerji, O. Béthenod, J. M. Bertolini, and A. Mariotti. "Variabilité spatio-temporelle de la composition isotopique de l'eau (18O, 2H) dans le continuum sol-plante-atmosphère 2. Approche en conditions naturelles". *Chemical Geology* 115.3 (1994), pages 317–333. doi: [10.1016/0009-2541\(94\)90195-3](https://doi.org/10.1016/0009-2541(94)90195-3).
- [151] U. Zimmermann, K. O. Münnich, and W. Roether. "Downward Movement of Soil Moisture Traced by Means of Hydrogen Isotopes". en. *Isotope Techniques in the Hydrologic Cycle*. \_eprint: <https://onlinelibrary.wiley.com/doi/pdf/10.1029/GM011p0028>. *American Geophysical Union (AGU)*, 1967, pages 28–36. doi: [10.1029/GM011p0028](https://doi.org/10.1029/GM011p0028).
- [152] J.-E. Lee, I. Fung, D. J. DePaolo, and C. C. Henning. "Analysis of the global distribution of water isotopes using the NCAR atmospheric general circulation model". en. *Journal of Geophysical Research: Atmospheres* 112.D16 (2007). \_eprint: <https://onlinelibrary.wiley.com/doi/pdf/10.1029/2006JD007657>. doi: [10.1029/2006JD007657](https://doi.org/10.1029/2006JD007657).

- [153] C. Risi, S. Bony, F. Vimeux, and J. Jouzel. "Water-stable isotopes in the LMDZ4 general circulation model: Model evaluation for present-day and past climates and applications to climatic interpretations of tropical isotopic records". en. *Journal of Geophysical Research* 115.D12 (2010), page D12118. doi: [10.1029/2009JD013255](https://doi.org/10.1029/2009JD013255).
- [154] J. C. Tindall, P. J. Valdes, and L. C. Sime. "Stable water isotopes in HadCM3: Isotopic signature of El Niño–Southern Oscillation and the tropical amount effect". en. *Journal of Geophysical Research: Atmospheres* 114.D4 (2009). \_eprint: <https://onlinelibrary.wiley.com/doi/pdf/10.1029/2008JD010825>. doi: [10.1029/2008JD010825](https://doi.org/10.1029/2008JD010825).
- [155] S. Cloetingh, P. Sternai, A. Koptev, T. A. Ehlers, T. Gerya, I. Kovács, J. Oerlemans, F. Beekman, Y. Lavallée, D. Dingwell, E. Békési, K. Porkoláb, M. Tesauero, A. Lavecchia, S. Botsyun, V. Muller, F. Roure, E. Serpelloni, L. Matenco, S. Castelltort, D. Giovannelli, A. V. Brovarone, N. Malaspina, G. Coletti, P. Valla, and J. Limberger. "Coupled surface to deep Earth processes: Perspectives from TOPO-EUROPE with an emphasis on climate- and energy-related societal challenges". *Global and Planetary Change* 226 (2023), page 104140. doi: [10.1016/j.gloplacha.2023.104140](https://doi.org/10.1016/j.gloplacha.2023.104140).
- [156] S. Huang, M. J. M. Meijers, A. Eyres, A. Mulch, and S. A. Fritz. "Unravelling the history of biodiversity in mountain ranges through integrating geology and biogeography". en. *Journal of Biogeography* 46.8 (2019). \_eprint: <https://onlinelibrary.wiley.com/doi/pdf/10.1111/jbi.13622>, pages 1777–1791. doi: [10.1111/jbi.13622](https://doi.org/10.1111/jbi.13622).
- [157] A. Mulch. "Stable isotope paleoaltimetry and the evolution of landscapes and life". en. *Earth and Planetary Science Letters* 433 (2016), pages 180–191. doi: [10.1016/j.epsl.2015.10.034](https://doi.org/10.1016/j.epsl.2015.10.034).
- [158] P. G. Valla, P. Sternai, and M. Fox. "How Climate, Uplift and Erosion Shaped the Alpine Topography". *Elements* 17.1 (2021), pages 41–46. doi: [10.2138/gselements.17.1.41](https://doi.org/10.2138/gselements.17.1.41).
- [159] D. B. Rowley. "Stable Isotope-Based Paleoaltimetry: Theory and Validation". *Reviews in Mineralogy and Geochemistry* 66.1 (2007), pages 23–52. doi: [10.2138/rmg.2007.66.2](https://doi.org/10.2138/rmg.2007.66.2).
- [160] T. Salles, L. Husson, P. Rey, C. Mallard, S. Zahirovic, B. H. Boggiani, N. Coltice, and M. Arnould. "Hundred million years of landscape dynamics from catchment to global scale". *Science* 379.6635 (2023). Publisher: American Association for the Advancement of Science, pages 918–923. doi: [10.1126/science.add2541](https://doi.org/10.1126/science.add2541).
- [161] P. R. Eizenhöfer, C. Glotzbach, J. Kley, and T. A. Ehlers. "Thermo-Kinematic Evolution of the Eastern European Alps Along the TRANSALP Transect". en. *Tectonics* 42.4 (2023). \_eprint: <https://onlinelibrary.wiley.com/doi/pdf/10.1029/2022TC007380>, e2022TC007380. doi: [10.1029/2022TC007380](https://doi.org/10.1029/2022TC007380).
- [162] W. Frisch. "Tectonic progradation and plate tectonic evolution of the Alps". en. *Tectonophysics* 60.3 (1979), pages 121–139. doi: [10.1016/0040-1951\(79\)90155-0](https://doi.org/10.1016/0040-1951(79)90155-0).
- [163] T. McCann. "The Geology of Central Europe: Mesozoic and Cenozoic". en. Google-Books-ID: 0KXpt-TYvKv8C. *Geological Society of London*, 2008.
- [164] S. M. Schmid, O. A. Pfiffner, N. Froitzheim, G. Schönborn, and E. Kissling. "Geophysical-geological transect and tectonic evolution of the Swiss-Italian Alps". en. *Tectonics* 15.5 (1996). \_eprint: <https://onlinelibrary.wiley.com/doi/pdf/10.1029/96TC00433>, pages 1036–1064. doi: [10.1029/96TC00433](https://doi.org/10.1029/96TC00433).
- [165] G. M Stampfli, J. Mosar, D. Marquer, R. Marchant, T. Baudin, and G. Borel. "Subduction and obduction processes in the Swiss Alps". en. *Tectonophysics* 296.1 (1998), pages 159–204. doi: [10.1016/S0040-1951\(98\)00142-5](https://doi.org/10.1016/S0040-1951(98)00142-5).
- [166] E. Kissling and F. Schlunegger. "Rollback Orogeny Model for the Evolution of the Swiss Alps". en. *Tectonics* 37.4 (2018). \_eprint: <https://onlinelibrary.wiley.com/doi/pdf/10.1002/2017TC004762>, pages 1097–1115. doi: [10.1002/2017TC004762](https://doi.org/10.1002/2017TC004762).
- [167] F. Schlunegger and E. Kissling. "Slab rollback orogeny in the Alps and evolution of the Swiss Molasse basin". en. *Nature Communications* 6.1 (2015). Number: 1 Publisher: Nature Publishing Group, pages 1–10. doi: [10.1038/ncomms9605](https://doi.org/10.1038/ncomms9605).

- [168] J. Huw Davies and F. von Blanckenburg. "Slab breakoff: A model of lithosphere detachment and its test in the magmatism and deformation of collisional orogens". en. *Earth and Planetary Science Letters* 129.1 (1995), pages 85–102. doi: [10.1016/0012-821X\(94\)00237-5](https://doi.org/10.1016/0012-821X(94)00237-5).
- [169] F. Schlunegger and S. Castelltort. "Immediate and delayed signal of slab breakoff in Oligo/Miocene Molasse deposits from the European Alps". en. *Scientific Reports* 6.1 (2016). Number: 1 Publisher: Nature Publishing Group, page 31010. doi: [10.1038/srep31010](https://doi.org/10.1038/srep31010).
- [170] K. Ustaszewski, S. M. Schmid, B. Fügenschuh, M. Tischler, E. Kissling, and W. Spakman. "A map-view restoration of the Alpine-Carpathian-Dinaridic system for the Early Miocene". en. *Swiss Journal of Geosciences* 101.1 (2008), pages 273–294. doi: [10.1007/s00015-008-1288-7](https://doi.org/10.1007/s00015-008-1288-7).
- [171] M. R. Handy, K. Ustaszewski, and E. Kissling. "Reconstructing the Alps–Carpathians–Dinarides as a key to understanding switches in subduction polarity, slab gaps and surface motion". en. *International Journal of Earth Sciences* 104.1 (2015), pages 1–26. doi: [10.1007/s00531-014-1060-3](https://doi.org/10.1007/s00531-014-1060-3).
- [172] A. Gébelin, A. Mulch, C. Teyssier, M. J. Jessup, R. D. Law, and M. Brunel. "The Miocene elevation of Mount Everest". *Geology* 41.7 (2013), pages 799–802. doi: [10.1130/G34331.1](https://doi.org/10.1130/G34331.1).
- [173] E. Krsnik, K. Methner, M. Campani, S. Botsyun, S. G. Mutz, T. A. Ehlers, O. Kempf, J. Fiebig, F. Schlunegger, and A. Mulch. "Miocene high elevation in the Central Alps". English. *Solid Earth* 12.11 (2021). Publisher: Copernicus GmbH, pages 2615–2631. doi: [10.5194/se-12-2615-2021](https://doi.org/10.5194/se-12-2615-2021).
- [174] M. Biasutti, I. M. Held, A. H. Sobel, and A. Giannini. "SST Forcings and Sahel Rainfall Variability in Simulations of the Twentieth and Twenty-First Centuries". EN. *Journal of Climate* 21.14 (2008). Publisher: American Meteorological Society Section: Journal of Climate, pages 3471–3486. doi: [10.1175/2007JCLI1896.1](https://doi.org/10.1175/2007JCLI1896.1).
- [175] F. S. R. Pausata, G. Messori, and Q. Zhang. "Impacts of dust reduction on the northward expansion of the African monsoon during the Green Sahara period". *Earth and Planetary Science Letters* 434 (2016), pages 298–307. doi: [10.1016/j.epsl.2015.11.049](https://doi.org/10.1016/j.epsl.2015.11.049).
- [176] J. E. Tierney, F. S. R. Pausata, and P. B. deMenocal. "Rainfall regimes of the Green Sahara". *Science Advances* 3.1 (2017). Publisher: American Association for the Advancement of Science, e1601503. doi: [10.1126/sciadv.1601503](https://doi.org/10.1126/sciadv.1601503).
- [177] B. Sultan, C. Baron, M. Dingkuhn, B. Sarr, and S. Janicot. "Agricultural impacts of large-scale variability of the West African monsoon". *Agricultural and Forest Meteorology* 128.1 (2005), pages 93–110. doi: [10.1016/j.agrformet.2004.08.005](https://doi.org/10.1016/j.agrformet.2004.08.005).
- [178] S. E. Nicholson. "The intensity, location and structure of the tropical rainbelt over west Africa as factors in interannual variability". en. *International Journal of Climatology* 28.13 (2008). \_eprint: <https://onlinelibrary.wiley.com/doi/pdf/10.1002/joc.1507>, pages 1775–1785. doi: [10.1002/joc.1507](https://doi.org/10.1002/joc.1507).
- [179] J. P. Grist. "Easterly Waves over Africa. Part I: The Seasonal Cycle and Contrasts between Wet and Dry Years". EN. *Monthly Weather Review* 130.2 (2002). Publisher: American Meteorological Society Section: Monthly Weather Review, pages 197–211. doi: [10.1175/1520-0493\(2002\)130<0197:EW0API>2.0.CO;2](https://doi.org/10.1175/1520-0493(2002)130<0197:EW0API>2.0.CO;2).
- [180] A. Lemburg, J. Bader, and M. Claussen. "Sahel Rainfall–Tropical Easterly Jet Relationship on Synoptic to Intraseasonal Time Scales". EN. *Monthly Weather Review* 147.5 (2019). Publisher: American Meteorological Society Section: Monthly Weather Review, pages 1733–1752. doi: [10.1175/MWR-D-18-0254.1](https://doi.org/10.1175/MWR-D-18-0254.1).
- [181] M. Gaetani, G. Messori, Q. Zhang, C. Flamant, and F. S. R. Pausata. "Understanding the Mechanisms behind the Northward Extension of the West African Monsoon during the Mid-Holocene". EN. *Journal of Climate* 30.19 (2017). Publisher: American Meteorological Society Section: Journal of Climate, pages 7621–7642. doi: [10.1175/JCLI-D-16-0299.1](https://doi.org/10.1175/JCLI-D-16-0299.1).
- [182] D. Chandan and W. R. Peltier. "African Humid Period Precipitation Sustained by Robust Vegetation, Soil, and Lake Feedbacks". en. *Geophysical Research Letters* 47.21 (2020). \_eprint: <https://onlinelibrary.wiley.com/doi/pdf/10.1029/2020GL088728>, e2020GL088728. doi: [10.1029/2020GL088728](https://doi.org/10.1029/2020GL088728).

- [183] J. P. Grist and S. E. Nicholson. "A Study of the Dynamic Factors Influencing the Rainfall Variability in the West African Sahel". EN. *Journal of Climate* 14.7 (2001). Publisher: American Meteorological Society Section: Journal of Climate, pages 1337–1359. doi: [10.1175/1520-0442\(2001\)014<1337:AS0TDF>2.0.CO;2](https://doi.org/10.1175/1520-0442(2001)014<1337:AS0TDF>2.0.CO;2).
- [184] S. E. Nicholson. "On the factors modulating the intensity of the tropical rainbelt over West Africa". en. *International Journal of Climatology* 29.5 (2009). \_eprint: <https://onlinelibrary.wiley.com/doi/pdf/10.1002/joc.1702>, pages 673–689. doi: [10.1002/joc.1702](https://doi.org/10.1002/joc.1702).
- [185] C. Thorncroft and K. Hodges. "African Easterly Wave Variability and Its Relationship to Atlantic Tropical Cyclone Activity". EN. *Journal of Climate* 14.6 (2001). Publisher: American Meteorological Society Section: Journal of Climate, pages 1166–1179. doi: [10.1175/1520-0442\(2001\)014<1166:AEWVAI>2.0.CO;2](https://doi.org/10.1175/1520-0442(2001)014<1166:AEWVAI>2.0.CO;2).
- [186] C. D. Thorncroft and M. Blackburn. "Maintenance of the African easterly jet". en. *Quarterly Journal of the Royal Meteorological Society* 125.555 (1999). \_eprint: <https://onlinelibrary.wiley.com/doi/pdf/10.1002/qj.49712555502>, pages 763–786. doi: [10.1002/qj.49712555502](https://doi.org/10.1002/qj.49712555502).
- [187] S. Janicot, G. Caniaux, F. Chauvin, G. de Coëtlogon, B. Fontaine, N. Hall, G. Kiladis, J.-P. Lafore, C. Lavaysse, S. L. Lavender, S. Leroux, R. Marteau, F. Mounier, N. Philippon, R. Roehrig, B. Sultan, and C. M. Taylor. "Intraseasonal variability of the West African monsoon". en. *Atmospheric Science Letters* 12.1 (2011). \_eprint: <https://onlinelibrary.wiley.com/doi/pdf/10.1002/asl.280>, pages 58–66. doi: [10.1002/asl.280](https://doi.org/10.1002/asl.280).
- [188] C. Lavaysse, C. Flamant, S. Janicot, D. J. Parker, J.-P. Lafore, B. Sultan, and J. Pelon. "Seasonal evolution of the West African heat low: a climatological perspective". en. *Climate Dynamics* 33.2 (2009), pages 313–330. doi: [10.1007/s00382-009-0553-4](https://doi.org/10.1007/s00382-009-0553-4).
- [189] C. Lavaysse, C. Flamant, and S. Janicot. "Regional-scale convection patterns during strong and weak phases of the Saharan heat low". en. *Atmospheric Science Letters* 11.4 (2010). \_eprint: <https://onlinelibrary.wiley.com/doi/pdf/10.1002/asl.284>, pages 255–264. doi: [10.1002/asl.284](https://doi.org/10.1002/asl.284).
- [190] J.-P. Lafore, C. Flamant, F. Guichard, D. J. Parker, D. Bouniol, A. H. Fink, V. Giraud, M. Gosset, N. Hall, H. Höller, S. C. Jones, A. Protat, R. Roca, F. Roux, F. Saïd, and C. Thorncroft. "Progress in understanding of weather systems in West Africa". en. *Atmospheric Science Letters* 12.1 (2011). \_eprint: <https://onlinelibrary.wiley.com/doi/pdf/10.1002/asl.335>, pages 7–12. doi: [10.1002/asl.335](https://doi.org/10.1002/asl.335).
- [191] C. D. Thorncroft, H. Nguyen, C. Zhang, and P. Peyrillé. "Annual cycle of the West African monsoon: regional circulations and associated water vapour transport". en. *Quarterly Journal of the Royal Meteorological Society* 137.654 (2011). \_eprint: <https://onlinelibrary.wiley.com/doi/pdf/10.1002/qj.728>, pages 129–147. doi: [10.1002/qj.728](https://doi.org/10.1002/qj.728).
- [192] M.-L. C. Wu, O. Reale, S. D. Schubert, M. J. Suarez, R. D. Koster, and P. J. Pegion. "African Easterly Jet: Structure and Maintenance". EN. *Journal of Climate* 22.17 (2009). Publisher: American Meteorological Society Section: Journal of Climate, pages 4459–4480. doi: [10.1175/2009JCLI2584.1](https://doi.org/10.1175/2009JCLI2584.1).
- [193] D. Texier, N. d. Noblet, and P. Braconnot. "Sensitivity of the African and Asian Monsoons to Mid-Holocene Insolation and Data-Inferred Surface Changes". EN. *Journal of Climate* 13.1 (2000). Publisher: American Meteorological Society Section: Journal of Climate, pages 164–181. doi: [10.1175/1520-0442\(2000\)013<0164:S0TAAA>2.0.CO;2](https://doi.org/10.1175/1520-0442(2000)013<0164:S0TAAA>2.0.CO;2).
- [194] D. P. Rowell. "The Impact of Mediterranean SSTs on the Sahelian Rainfall Season". EN. *Journal of Climate* 16.5 (2003). Publisher: American Meteorological Society Section: Journal of Climate, pages 849–862. doi: [10.1175/1520-0442\(2003\)016<0849:TIOMS0>2.0.CO;2](https://doi.org/10.1175/1520-0442(2003)016<0849:TIOMS0>2.0.CO;2).
- [195] M. Gaetani, B. Pohl, H. Douville, and B. Fontaine. "West African Monsoon influence on the summer Euro-Atlantic circulation". en. *Geophysical Research Letters* 38.9 (2011). \_eprint: <https://onlinelibrary.wiley.com/doi/pdf/10.1029/2011GL047150>, doi: [10.1029/2011GL047150](https://doi.org/10.1029/2011GL047150).

- [196] H. Hersbach, B. Bell, P. Berrisford, S. Hirahara, A. Horányi, J. Muñoz-Sabater, J. Nicolas, C. Peubey, R. Radu, D. Schepers, A. Simmons, C. Soci, S. Abdalla, X. Abellan, G. Balsamo, P. Bechtold, G. Biavati, J. Bidlot, M. Bonavita, G. De Chiara, P. Dahlgren, D. Dee, M. Diamantakis, R. Dragani, J. Flemming, R. Forbes, M. Fuentes, A. Geer, L. Haimberger, S. Healy, R. J. Hogan, E. Hólm, M. Janisková, S. Keeley, P. Laloyaux, P. Lopez, C. Lupu, G. Radnoti, P. de Rosnay, I. Rozum, F. Vamborg, S. Villaume, and J.-N. Thépaut. “The ERA5 global reanalysis”. en. *Quarterly Journal of the Royal Meteorological Society* 146.730 (2020). \_eprint: <https://onlinelibrary.wiley.com/doi/pdf/10.1002/qj.3803>, pages 1999–2049. doi: [10.1002/qj.3803](https://doi.org/10.1002/qj.3803).
- [197] B. Bell, H. Hersbach, A. Simmons, P. Berrisford, P. Dahlgren, A. Horányi, J. Muñoz-Sabater, J. Nicolas, R. Radu, D. Schepers, C. Soci, S. Villaume, J.-R. Bidlot, L. Haimberger, J. Woollen, C. Buontempo, and J.-N. Thépaut. “The ERA5 global reanalysis: Preliminary extension to 1950”. en. *Quarterly Journal of the Royal Meteorological Society* 147.741 (2021). \_eprint: <https://onlinelibrary.wiley.com/doi/pdf/10.1002/qj.4174>, pages 4186–4227. doi: [10.1002/qj.4174](https://doi.org/10.1002/qj.4174).
- [198] M. Fischer, P. Knippertz, R. van der Linden, A. Lemburg, G. Pante, C. Proppe, and J. H. Marsham. “Quantifying uncertainty in simulations of the West African monsoon with the use of surrogate models”. English. *Weather and Climate Dynamics* 5.2 (2024). Publisher: Copernicus GmbH, pages 511–536. doi: [10.5194/wcd-5-511-2024](https://doi.org/10.5194/wcd-5-511-2024).
- [199] A. H. Fink, T. Engel, V. Ermert, R. van der Linden, M. Schneidewind, R. Redl, E. Afiesimama, W. M. Thiaw, C. Yorke, M. Evans, and S. Janicot. “Mean Climate and Seasonal Cycle”. en. *Meteorology of Tropical West Africa*. Section: 1 \_eprint: <https://onlinelibrary.wiley.com/doi/pdf/10.1002/9781118391297.ch1>. John Wiley & Sons, Ltd, 2017, pages 1–39. doi: [10.1002/9781118391297.ch1](https://doi.org/10.1002/9781118391297.ch1).
- [200] P Braconnot, S Joussaume, N de Noblet, and G Ramstein. “Mid-Holocene and Last Glacial Maximum African monsoon changes as simulated within the Paleoclimate Modelling Intercomparison Project”. en. *Global and Planetary Change*. Paleomonsoon variations and terrestrial environmental change 26.1 (2000), pages 51–66. doi: [10.1016/S0921-8181\(00\)00033-3](https://doi.org/10.1016/S0921-8181(00)00033-3).
- [201] C. M. Brierley, A. Zhao, S. P. Harrison, P. Braconnot, C. J. R. Williams, D. J. R. Thornalley, X. Shi, J.-Y. Peterschmitt, R. Ohgaito, D. S. Kaufman, M. Kageyama, J. C. Hargreaves, M. P. Erb, J. Emile-Geay, R. D’Agostino, D. Chandan, M. Carré, P. J. Bartlein, W. Zheng, Z. Zhang, Q. Zhang, H. Yang, E. M. Volodin, R. A. Tomas, C. Routson, W. R. Peltier, B. Otto-Bliesner, P. A. Morozova, N. P. McKay, G. Lohmann, A. N. Legrande, C. Guo, J. Cao, E. Brady, J. D. Annan, and A. Abe-Ouchi. “Large-scale features and evaluation of the PMIP4-CMIP6 *midHolocene* simulations”. English. *Climate of the Past* 16.5 (2020). Publisher: Copernicus GmbH, pages 1847–1872. doi: [10.5194/cp-16-1847-2020](https://doi.org/10.5194/cp-16-1847-2020).
- [202] M. Kageyama, A. Abe-Ouchi, T. Obase, G. Ramstein, and P. Valdes. “Modeling the climate of the Last Glacial Maximum from PMIP1 to PMIP4”. *Past Global Changes Magazine* 29.2 (2021). Publisher: Past Global Changes (PAGES) project, pages 80–81. doi: [10.22498/pages.29.2.80](https://doi.org/10.22498/pages.29.2.80).
- [203] E. Berntell, Q. Zhang, Q. Li, A. M. Haywood, J. C. Tindall, S. J. Hunter, Z. Zhang, X. Li, C. Guo, K. H. Nisancioglu, C. Stepanek, G. Lohmann, L. E. Sohl, M. A. Chandler, N. Tan, C. Contoux, G. Ramstein, M. L. J. Baatsen, A. S. von der Heydt, D. Chandan, W. R. Peltier, A. Abe-Ouchi, W.-L. Chan, Y. Kamae, C. J. R. Williams, D. J. Lunt, R. Feng, B. L. Otto-Bliesner, and E. C. Brady. “Mid-Pliocene West African Monsoon rainfall as simulated in the PlioMIP2 ensemble”. English. *Climate of the Past* 17.4 (2021). Publisher: Copernicus GmbH, pages 1777–1794. doi: [10.5194/cp-17-1777-2021](https://doi.org/10.5194/cp-17-1777-2021).
- [204] J. H. C. Bosmans, S. S. Drijfhout, E. Tuenter, L. J. Lourens, F. J. Hilgen, and S. L. Weber. “Monsoonal response to mid-holocene orbital forcing in a high resolution GCM”. *Climate of the Past* 8.2 (2012). Publisher: Copernicus Publications Göttingen, Germany, pages 723–740.
- [205] X. Gao, Y. Xu, Z. Zhao, J. S. Pal, and F. Giorgi. “On the role of resolution and topography in the simulation of East Asia precipitation”. en. *Theoretical and Applied Climatology* 86.1 (2006), pages 173–185. doi: [10.1007/s00704-005-0214-4](https://doi.org/10.1007/s00704-005-0214-4).
- [206] L. Jungandreas, C. Hohenegger, and M. Claussen. “Influence of the representation of convection on the mid-Holocene West African Monsoon”. English. *Climate of the Past* 17.4 (2021). Publisher: Copernicus GmbH, pages 1665–1684. doi: [10.5194/cp-17-1665-2021](https://doi.org/10.5194/cp-17-1665-2021).



- [207] Y. Ait Brahim, L. Sha, J. A. Wassenburg, K. Azennoud, H. Cheng, F. W. Cruz, and L. Bouchaou. "The spatiotemporal extent of the Green Sahara during the last glacial period". *iScience* 26.7 (2023), page 107018. doi: [10.1016/j.isci.2023.107018](https://doi.org/10.1016/j.isci.2023.107018).
- [208] P. J. Bartlein, S. P. Harrison, S. Brewer, S. Connor, B. A. S. Davis, K. Gajewski, J. Guiot, T. I. Harrison-Prentice, A. Henderson, O. Peyron, I. C. Prentice, M. Scholze, H. Seppä, B. Shuman, S. Sugita, R. S. Thompson, A. E. Viau, J. Williams, and H. Wu. "Pollen-based continental climate reconstructions at 6 and 21 ka: a global synthesis". en. *Climate Dynamics* 37.3 (2011), pages 775–802. doi: [10.1007/s00382-010-0904-1](https://doi.org/10.1007/s00382-010-0904-1).
- [209] P. deMenocal, J. Ortiz, T. Guilderson, J. Adkins, M. Sarnthein, L. Baker, and M. Yarusinsky. "Abrupt onset and termination of the African Humid Period:: rapid climate responses to gradual insolation forcing". *Quaternary Science Reviews* 19.1 (2000), pages 347–361. doi: [10.1016/S0277-3791\(99\)00081-5](https://doi.org/10.1016/S0277-3791(99)00081-5).
- [210] S. P. Harrison, P. J. Bartlein, S. Brewer, I. C. Prentice, M. Boyd, I. Hessler, K. Holmgren, K. Izumi, and K. Willis. "Climate model benchmarking with glacial and mid-Holocene climates". en. *Climate Dynamics* 43.3 (2014), pages 671–688. doi: [10.1007/s00382-013-1922-6](https://doi.org/10.1007/s00382-013-1922-6).
- [211] P. O. Hopcroft and P. J. Valdes. "On the Role of Dust-Climate Feedbacks During the Mid-Holocene". en. *Geophysical Research Letters* 46.3 (2019). \_eprint: <https://onlinelibrary.wiley.com/doi/pdf/10.1029/2018GL080483>, pages 1612–1621. doi: [10.1029/2018GL080483](https://doi.org/10.1029/2018GL080483).
- [212] P. O. Hopcroft and P. J. Valdes. "Green Sahara tipping points in transient climate model simulations of the Holocene". en. *Environmental Research Letters* 17.8 (2022). Publisher: IOP Publishing, page 085001. doi: [10.1088/1748-9326/ac7c2b](https://doi.org/10.1088/1748-9326/ac7c2b).
- [213] F. S. R. Pausata, D. Alain, R. Ingrassio, K. Winger, M. S. M. Drapeau, and A. Burke. "Changes in climate extremes in Zambia during green and dry Sahara periods and their potential impacts on hominid dispersal". *Quaternary Science Reviews* 321 (2023), page 108367. doi: [10.1016/j.quascirev.2023.108367](https://doi.org/10.1016/j.quascirev.2023.108367).
- [214] A. Perez-Sanz, G. Li, P. González-Sampériz, and S. P. Harrison. "Evaluation of modern and mid-Holocene seasonal precipitation of the Mediterranean and northern Africa in the CMIP5 simulations". English. *Climate of the Past* 10.2 (2014). Publisher: Copernicus GmbH, pages 551–568. doi: [10.5194/cp-10-551-2014](https://doi.org/10.5194/cp-10-551-2014).
- [215] Q. Zhang, E. Berntell, Q. Li, and F. C. Ljungqvist. "Understanding the variability of the rainfall dipole in West Africa using the EC-Earth last millennium simulation". en. *Climate Dynamics* 57.1 (2021), pages 93–107. doi: [10.1007/s00382-021-05696-x](https://doi.org/10.1007/s00382-021-05696-x).
- [216] E. Bartolini, P. Claps, and P. D'Odorico. "Interannual variability of winter precipitation in the European Alps: relations with the North Atlantic Oscillation." English. *Hydrology and Earth System Sciences* 13.1 (2009). Publisher: Copernicus GmbH, pages 17–25. doi: [10.5194/hess-13-17-2009](https://doi.org/10.5194/hess-13-17-2009).
- [217] J. W. Hurrell. "Decadal Trends in the North Atlantic Oscillation: Regional Temperatures and Precipitation". *Science* 269.5224 (1995). Publisher: American Association for the Advancement of Science, pages 676–679. doi: [10.1126/science.269.5224.676](https://doi.org/10.1126/science.269.5224.676).
- [218] L. M. Baldini, F. McDermott, A. M. Foley, and J. U. L. Baldini. "Spatial variability in the European winter precipitation 180-NAO relationship: Implications for reconstructing NAO-mode climate variability in the Holocene". en. *Geophysical Research Letters* 35.4 (2008). \_eprint: <https://onlinelibrary.wiley.com/doi/pdf/10.1029/2007GL032027>. doi: [10.1029/2007GL032027](https://doi.org/10.1029/2007GL032027).
- [219] K. Rozanski, C. Sonntag, and K. O. Münnich. "Factors controlling stable isotope composition of European precipitation". en. *Tellus* 34.2 (1982). \_eprint: <https://onlinelibrary.wiley.com/doi/pdf/10.1111/j.2153-3490.1982.tb01801.x>, pages 142–150. doi: [10.1111/j.2153-3490.1982.tb01801.x](https://doi.org/10.1111/j.2153-3490.1982.tb01801.x).
- [220] A. G. Barnston and R. E. Livezey. "Classification, Seasonality and Persistence of Low-Frequency Atmospheric Circulation Patterns". EN. *Monthly Weather Review* 115.6 (1987). Publisher: American Meteorological Society Section: Monthly Weather Review, pages 1083–1126. doi: [10.1175/1520-0493\(1987\)115<1083:CSAPOL>2.0.CO;2](https://doi.org/10.1175/1520-0493(1987)115<1083:CSAPOL>2.0.CO;2).

- [221] J. W. Hurrell and H. Van Loon. "Decadal Variations in Climate Associated with the North Atlantic Oscillation". en. *Climatic Change at High Elevation Sites*. Edited by H. F. Diaz, M. Beniston, and R. S. Bradley. Dordrecht: Springer Netherlands, 1997, pages 69–94. doi: [10.1007/978-94-015-8905-5\\_4](https://doi.org/10.1007/978-94-015-8905-5_4).
- [222] P. M. Craig and R. P. Allan. "The role of teleconnection patterns in the variability and trends of growing season indices across Europe". en. *International Journal of Climatology* 42.2 (2022), pages 1072–1091. doi: [10.1002/joc.7290](https://doi.org/10.1002/joc.7290).
- [223] L. M. Baldini, F. McDermott, J. U. L. Baldini, M. J. Fischer, and M. Möllhoff. "An investigation of the controls on Irish precipitation 18O values on monthly and event timescales". en. *Climate Dynamics* 35.6 (2010), pages 977–993. doi: [10.1007/s00382-010-0774-6](https://doi.org/10.1007/s00382-010-0774-6).
- [224] M. J. Fischer and D. Matthey. "Climate variability and precipitation isotope relationships in the Mediterranean region". en. *Journal of Geophysical Research: Atmospheres* 117.D20 (2012). \_eprint: <https://onlinelibrary.wiley.com/doi/pdf/10.1029/2012JD018010>. doi: [10.1029/2012JD018010](https://doi.org/10.1029/2012JD018010).
- [225] R. D. Field. "Observed and modeled controls on precipitation 18O over Europe: From local temperature to the Northern Annular Mode". en. *Journal of Geophysical Research: Atmospheres* 115.D12 (2010). \_eprint: <https://onlinelibrary.wiley.com/doi/pdf/10.1029/2009JD013370>. doi: [10.1029/2009JD013370](https://doi.org/10.1029/2009JD013370).
- [226] M. J. Fischer and L. M. Baldini. "A climate-isotope regression model with seasonally-varying and time-integrated relationships". en. *Climate Dynamics* 37.11 (2011), pages 2235–2251. doi: [10.1007/s00382-011-1009-1](https://doi.org/10.1007/s00382-011-1009-1).
- [227] J. Luterbacher, E. Xoplaki, D. Dietrich, R. Rickli, J. Jacobeit, C. Beck, D. Gyalistras, C. Schmutz, and H. Wanner. "Reconstruction of sea level pressure fields over the Eastern North Atlantic and Europe back to 1500". en. *Climate Dynamics* 18.7 (2002), pages 545–561. doi: [10.1007/s00382-001-0196-6](https://doi.org/10.1007/s00382-001-0196-6).
- [228] V. Trouet, J. Esper, N. E. Graham, A. Baker, J. D. Scourse, and D. C. Frank. "Persistent Positive North Atlantic Oscillation Mode Dominated the Medieval Climate Anomaly". *Science* 324.5923 (2009). Publisher: American Association for the Advancement of Science, pages 78–80. doi: [10.1126/science.1166349](https://doi.org/10.1126/science.1166349).
- [229] T. W. D. Edwards, S. J. Birks, and J. J. Gibson. "Isotope tracers in global water and climate studies of the past and present". English (2002).
- [230] E. Zorita and F. González-Rouco. "Are temperature-sensitive proxies adequate for North Atlantic Oscillation reconstructions?" en. *Geophysical Research Letters* 29.14 (2002). \_eprint: <https://onlinelibrary.wiley.com/doi/pdf/10.1029/2002GL015404>. doi: [10.1029/2002GL015404](https://doi.org/10.1029/2002GL015404).
- [231] F. Lehner, C. C. Raible, and T. F. Stocker. "Testing the robustness of a precipitation proxy-based North Atlantic Oscillation reconstruction". en. *Quaternary Science Reviews* 45 (2012), pages 85–94. doi: [10.1016/j.quascirev.2012.04.025](https://doi.org/10.1016/j.quascirev.2012.04.025).
- [232] L. Comas-Bru and F. McDermott. "Impacts of the EA and SCA patterns on the European twentieth century NAO–winter climate relationship". en. *Quarterly Journal of the Royal Meteorological Society* 140.679 (2014). \_eprint: <https://onlinelibrary.wiley.com/doi/pdf/10.1002/qj.2158>. doi: [10.1002/qj.2158](https://doi.org/10.1002/qj.2158).
- [233] G. W. K. Moore, I. A. Renfrew, and R. S. Pickart. "Multidecadal Mobility of the North Atlantic Oscillation". en. *Journal of Climate* 26.8 (2013), pages 2453–2466. doi: [10.1175/JCLI-D-12-00023.1](https://doi.org/10.1175/JCLI-D-12-00023.1).
- [234] M. Deininger, M. Werner, and F. McDermott. "North Atlantic Oscillation controls on oxygen and hydrogen isotope gradients in winter precipitation across Europe; implications for palaeoclimate studies". English. *Climate of the Past* 12.11 (2016). Publisher: Copernicus GmbH, pages 2127–2143. doi: [10.5194/cp-12-2127-2016](https://doi.org/10.5194/cp-12-2127-2016).
- [235] J. G. Pinto and C. C. Raible. "Past and recent changes in the North Atlantic oscillation: Past and recent changes in the NAO". en. *Wiley Interdisciplinary Reviews: Climate Change* 3.1 (2012), pages 79–90. doi: [10.1002/wcc.150](https://doi.org/10.1002/wcc.150).
- [236] H. v. Storch and F. W. Zwiers. "Statistical Analysis in Climate Research". en. Google-Books-ID: bs8hAwAAQBAJ. Cambridge University Press, 2002.

- [237] A. Hannachi, I. T. Jolliffe, and D. B. Stephenson. “Empirical orthogonal functions and related techniques in atmospheric science: A review”. en. *International Journal of Climatology* 27.9 (2007). \_eprint: <https://onlinelibrary.wiley.com/doi/pdf/10.1002/joc.1499>, pages 1119–1152. doi: [10.1002/joc.1499](https://doi.org/10.1002/joc.1499).
- [238] C. W. J. Granger. “Investigating Causal Relations by Econometric Models and Cross-spectral Methods”. *Econometrica* 37.3 (1969). Publisher: [Wiley, Econometric Society], pages 424–438. doi: [10.2307/1912791](https://doi.org/10.2307/1912791).
- [239] T. Le. “Solar forcing of Earth’s surface temperature in PMIP3 simulations of the last millennium”. en. *Atmospheric Science Letters* 16.3 (2015). \_eprint: <https://onlinelibrary.wiley.com/doi/pdf/10.1002/asl2.555>, pages 285–290. doi: [10.1002/asl2.555](https://doi.org/10.1002/asl2.555).
- [240] T. J. Mosedale, D. B. Stephenson, M. Collins, and T. C. Mills. “Granger Causality of Coupled Climate Processes: Ocean Feedback on the North Atlantic Oscillation”. EN. *Journal of Climate* 19.7 (2006). Publisher: American Meteorological Society Section: Journal of Climate, pages 1182–1194. doi: [10.1175/JCLI3653.1](https://doi.org/10.1175/JCLI3653.1).
- [241] D. I. Stern and R. K. Kaufmann. “Anthropogenic and natural causes of climate change”. en. *Climatic Change* 122.1 (2014), pages 257–269. doi: [10.1007/s10584-013-1007-x](https://doi.org/10.1007/s10584-013-1007-x).
- [242] A. Hernández, G. Sánchez-López, S. Pla-Rabes, L. Comas-Bru, A. Parnell, N. Cahill, A. Geyer, R. M. Trigo, and S. Giralt. “A 2,000-year Bayesian NAO reconstruction from the Iberian Peninsula”. en. *Scientific Reports* 10.1 (2020). Number: 1 Publisher: Nature Publishing Group, page 14961. doi: [10.1038/s41598-020-71372-5](https://doi.org/10.1038/s41598-020-71372-5).
- [243] P. Ortega, F. Lehner, D. Swingedouw, V. Masson-Delmotte, C. C. Raible, M. Casado, and P. Yiou. “A model-tested North Atlantic Oscillation reconstruction for the past millennium”. en. *Nature* 523.7558 (2015). Number: 7558 Publisher: Nature Publishing Group, pages 71–74. doi: [10.1038/nature14518](https://doi.org/10.1038/nature14518).
- [244] R. Sánchez-Murillo and C. Birkel. “Groundwater recharge mechanisms inferred from isoscapes in a complex tropical mountainous region”. en. *Geophysical Research Letters* 43.10 (2016). \_eprint: <https://onlinelibrary.wiley.com/doi/pdf/10.1002/2016GL068888>, pages 5060–5069. doi: [10.1002/2016GL068888](https://doi.org/10.1002/2016GL068888).
- [245] A. L. Putman, G. J. Bowen, and C. Strong. “Local and Regional Modes of Hydroclimatic Change Expressed in Modern Multidecadal Precipitation Oxygen Isotope Trends”. en. *Geophysical Research Letters* 48.5 (2021). \_eprint: <https://onlinelibrary.wiley.com/doi/pdf/10.1029/2020GL092006>, e2020GL092006. doi: [10.1029/2020GL092006](https://doi.org/10.1029/2020GL092006).
- [246] A. Cauquoin and M. Werner. “High-Resolution Nudged Isotope Modeling With ECHAM6-Wiso: Impacts of Updated Model Physics and ERA5 Reanalysis Data”. en. *Journal of Advances in Modeling Earth Systems* 13.11 (2021). \_eprint: <https://onlinelibrary.wiley.com/doi/pdf/10.1029/2021MS002532>, e2021MS002532. doi: [10.1029/2021MS002532](https://doi.org/10.1029/2021MS002532).
- [247] H. Bong, A. Cauquoin, A. Okazaki, E.-C. Chang, M. Werner, Z. Wei, N. Yeo, and K. Yoshimura. “Process-Based Intercomparison of Water Isotope-Enabled Models and Reanalysis Nudging Effects”. en. *Journal of Geophysical Research: Atmospheres* 129.1 (2024). \_eprint: <https://onlinelibrary.wiley.com/doi/pdf/10.1029/2023JD038719>, e2023JD038719. doi: [10.1029/2023JD038719](https://doi.org/10.1029/2023JD038719).
- [248] K. Yoshimura, M. Kanamitsu, D. Noone, and T. Oki. “Historical isotope simulation using Reanalysis atmospheric data”. en. *Journal of Geophysical Research: Atmospheres* 113.D19 (2008). \_eprint: <https://onlinelibrary.wiley.com/doi/pdf/10.1029/2008JD010074>. doi: [10.1029/2008JD010074](https://doi.org/10.1029/2008JD010074).
- [249] S. T. Allen, J. W. Kirchner, and G. R. Goldsmith. “Predicting Spatial Patterns in Precipitation Isotope (2H and 18O) Seasonality Using Sinusoidal Isoscapes”. en. *Geophysical Research Letters* 45.10 (2018). \_eprint: <https://onlinelibrary.wiley.com/doi/pdf/10.1029/2018GL077458>, pages 4859–4868. doi: [10.1029/2018GL077458](https://doi.org/10.1029/2018GL077458).
- [250] S. T. Allen, S. Jasechko, W. R. Berghuijs, J. M. Welker, G. R. Goldsmith, and J. W. Kirchner. “Global sinusoidal seasonality in precipitation isotopes”. English. *Hydrology and Earth System Sciences* 23.8 (2019). Publisher: Copernicus GmbH, pages 3423–3436. doi: [10.5194/hess-23-3423-2019](https://doi.org/10.5194/hess-23-3423-2019).

- [251] G. J. Bowen. "Isoscapes: Spatial Pattern in Isotopic Biogeochemistry". en. *Annual Review of Earth and Planetary Sciences* 38. Volume 38, 2010 (2010). Publisher: Annual Reviews, pages 161–187. doi: [10.1146/annurev-earth-040809-152429](https://doi.org/10.1146/annurev-earth-040809-152429).
- [252] D. Erdélyi, I. G. Hatvani, H. Jeon, M. Jones, J. Tyler, and Z. Kern. "Predicting spatial distribution of stable isotopes in precipitation by classical geostatistical- and machine learning methods". en. *Journal of Hydrology* 617 (2023), page 129129. doi: [10.1016/j.jhydro.2023.129129](https://doi.org/10.1016/j.jhydro.2023.129129).
- [253] S. Terzer, L. I. Wassenaar, L. J. Araguás-Araguás, and P. K. Aggarwal. "Global isoscapes for  $^{18}\text{O}$  and  $^2\text{H}$  in precipitation: improved prediction using regionalized climatic regression models". English. *Hydrology and Earth System Sciences* 17.11 (2013). Publisher: Copernicus GmbH, pages 4713–4728. doi: [10.5194/hess-17-4713-2013](https://doi.org/10.5194/hess-17-4713-2013).
- [254] J. Bedia, J. Baño-Medina, M. N. Legasa, M. Iturbide, R. Manzananas, S. Herrera, A. Casanueva, D. San-Martín, A. S. Cofiño, and J. M. Gutiérrez. "Statistical downscaling with the `downscaleR` package (v3.1.0): contribution to the VALUE intercomparison experiment". English. *Geoscientific Model Development* 13.3 (2020). Publisher: Copernicus GmbH, pages 1711–1735. doi: [10.5194/gmd-13-1711-2020](https://doi.org/10.5194/gmd-13-1711-2020).
- [255] J. M. Gutiérrez, D. Maraun, M. Widmann, R. Huth, E. Hertig, R. Benestad, O. Roessler, J. Wibig, R. Wilcke, S. Kotlarski, D. San Martín, S. Herrera, J. Bedia, A. Casanueva, R. Manzananas, M. Iturbide, M. Vrac, M. Dubrovsky, J. Ribalaygua, J. Pórtoles, O. Rätty, J. Räisänen, B. Hingray, D. Raynaud, M. J. Casado, P. Ramos, T. Zerenner, M. Turco, T. Bosshard, P. Štěpánek, J. Bartholy, R. Pongracz, D. E. Keller, A. M. Fischer, R. M. Cardoso, P. M. M. Soares, B. Czernecki, and C. Pagé. "An intercomparison of a large ensemble of statistical downscaling methods over Europe: Results from the VALUE perfect predictor cross-validation experiment". en. *International Journal of Climatology* 39.9 (2019). eprint: <https://onlinelibrary.wiley.com/doi/pdf/10.1002/joc.5462>, pages 3750–3785. doi: [10.1002/joc.5462](https://doi.org/10.1002/joc.5462).
- [256] D. Maraun, F. Wetterhall, A. M. Ireson, R. E. Chandler, E. J. Kendon, M. Widmann, S. Brienen, H. W. Rust, T. Sauter, M. Themeßl, V. K. C. Venema, K. P. Chun, C. M. Goodess, R. G. Jones, C. Onof, M. Vrac, and I. Thiele-Eich. "Precipitation downscaling under climate change: Recent developments to bridge the gap between dynamical models and the end user". en. *Reviews of Geophysics* 48.3 (2010). doi: [10.1029/2009RG000314](https://doi.org/10.1029/2009RG000314).
- [257] S. G. Mutz and J. Aschauer. "Empirical glacier mass-balance models for South America". en. *Journal of Glaciology* (2022), pages 1–15. doi: [10.1017/jog.2022.6](https://doi.org/10.1017/jog.2022.6).
- [258] S. G. Mutz, S. Scherrer, I. Muceniece, and T. A. Ehlers. "Twenty-first century regional temperature response in Chile based on empirical-statistical downscaling". en. *Climate Dynamics* 56.9 (2021), pages 2881–2894. doi: [10.1007/s00382-020-05620-9](https://doi.org/10.1007/s00382-020-05620-9).
- [259] J. Ramon, L. Lledó, P.-A. Bretonnière, M. Samsó, and F. J. Doblas-Reyes. "A perfect prognosis downscaling methodology for seasonal prediction of local-scale wind speeds". en. *Environmental Research Letters* 16.5 (2021). Publisher: IOP Publishing, page 054010. doi: [10.1088/1748-9326/abe491](https://doi.org/10.1088/1748-9326/abe491).
- [260] R. Huth. "Statistical downscaling in central Europe: evaluation of methods and potential predictors". en. *Climate Research* 13 (1999), pages 91–101. doi: [10.3354/cr013091](https://doi.org/10.3354/cr013091).
- [261] "Structure of Statistical Downscaling Methods". *Statistical Downscaling and Bias Correction for Climate Research*. Edited by D. Maraun and M. Widmann. Cambridge: Cambridge University Press, 2018, pages 135–140. doi: [10.1017/9781107588783.011](https://doi.org/10.1017/9781107588783.011).
- [262] G. R. North, T. L. Bell, R. F. Cahalan, and F. J. Moeng. "Sampling Errors in the Estimation of Empirical Orthogonal Functions". EN. *Monthly Weather Review* 110.7 (1982). Publisher: American Meteorological Society Section: Monthly Weather Review, pages 699–706. doi: [10.1175/1520-0493\(1982\)110<0699:SEITE0>2.0.CO;2](https://doi.org/10.1175/1520-0493(1982)110<0699:SEITE0>2.0.CO;2).
- [263] R. Kistler, E. Kalnay, W. Collins, S. Saha, G. White, J. Woollen, M. Chelliah, W. Ebisuzaki, M. Kanamitsu, V. Kousky, H. van den Dool, R. Jenne, and M. Fiorino. "The NCEP–NCAR 50-Year Reanalysis: Monthly Means CD-ROM and Documentation". *Bulletin of the American Meteorological Society* 82.2 (2001). Publisher: American Meteorological Society, pages 247–268.

- [264] P. D. Jones, T. Jonsson, and D. Wheeler. "Extension to the North Atlantic oscillation using early instrumental pressure observations from Gibraltar and south-west Iceland". en. *International Journal of Climatology* 17.13 (1997). \_eprint: <https://onlinelibrary.wiley.com/doi/pdf/10.1002/%28SICI%291097-0088%2819971115%2917%3A13%3C1433%3A%3AAID-JOC203%3E3.0.CO%3B2-P>, pages 1433–1450. doi: [10.1002/\(SICI\)1097-0088\(19971115\)17:13<1433::AID-JOC203>3.0.CO;2-P](https://doi.org/10.1002/(SICI)1097-0088(19971115)17:13<1433::AID-JOC203>3.0.CO;2-P).
- [265] K. Methner, M. Campani, J. Fiebig, N. Löffler, O. Kempf, and A. Mulch. "Middle Miocene long-term continental temperature change in and out of pace with marine climate records". *Scientific Reports* 10.1 (2020). Publisher: Nature Publishing Group UK London, page 7989.
- [266] M. Böhme, A. Ilg, A. Ossig, and H. Küchenhoff. "New method to estimate paleoprecipitation using fossil amphibians and reptiles and the middle and late Miocene precipitation gradients in Europe". *Geology* 34.6 (2006), pages 425–428. doi: [10.1130/G22460.1](https://doi.org/10.1130/G22460.1).
- [267] L. Costeur and S. Legendre. "Mammalian Communities Document a Latitudinal Environmental Gradient during the Miocene Climatic Optimum in Western Europe". *PALAIOS* 23.5 (2008), pages 280–288. doi: [10.2110/palo.2006.p06-092r](https://doi.org/10.2110/palo.2006.p06-092r).
- [268] G. Jiménez-Moreno and J.-P. Suc. "Middle Miocene latitudinal climatic gradient in Western Europe: Evidence from pollen records". *Palaeogeography, Palaeoclimatology, Palaeoecology*. Miocene Climate in Europe - patterns and evolution. First synthesis of NECLIME 253.1 (2007), pages 208–225. doi: [10.1016/j.palaeo.2007.03.040](https://doi.org/10.1016/j.palaeo.2007.03.040).
- [269] I. Cojan, A. Bialkowski, T. Gillot, and M. Renard. "Paleoenvironnement and paleoclimate reconstruction for the early to middle Miocene from stable isotopes in pedogenic carbonates (Digne-Valensole basin, southeastern France)". *Bulletin de la Société Géologique de France* 184.6 (2013), pages 583–599. doi: [10.2113/gssgfbull.184.6.583](https://doi.org/10.2113/gssgfbull.184.6.583).
- [270] K. K. Bauer, T. W. Vennemann, and H. A. Gilg. "Stable isotope composition of bentonites from the Swiss and Bavarian Freshwater Molasse as a proxy for paleoprecipitation". *Palaeogeography, Palaeoclimatology, Palaeoecology* 455 (2016), pages 53–64. doi: [10.1016/j.palaeo.2016.02.002](https://doi.org/10.1016/j.palaeo.2016.02.002).
- [271] N. Mancktelow, H. Zwingmann, M. Campani, B. Fügenschuh, and A. Mulch. "Timing and conditions of brittle faulting on the Silltal-Brenner Fault Zone, Eastern Alps (Austria)". en. *Swiss Journal of Geosciences* 108.2 (2015), pages 305–326. doi: [10.1007/s00015-015-0179-y](https://doi.org/10.1007/s00015-015-0179-y).
- [272] D. B. Rowley, R. T. Pierrehumbert, and B. S. Currie. "A new approach to stable isotope-based paleoaltimetry: implications for paleoaltimetry and paleohypsometry of the High Himalaya since the Late Miocene". en. *Earth and Planetary Science Letters* 188.1 (2001), pages 253–268. doi: [10.1016/S0012-821X\(01\)00324-7](https://doi.org/10.1016/S0012-821X(01)00324-7).
- [273] G. S. Jenkins, A. T. Gaye, and B. Sylla. "Late 20th century attribution of drying trends in the Sahel from the Regional Climate Model (RegCM3)". en. *Geophysical Research Letters* 32.22 (2005). \_eprint: <https://onlinelibrary.wiley.com/doi/pdf/10.1029/2005GL024225>. doi: [10.1029/2005GL024225](https://doi.org/10.1029/2005GL024225).
- [274] S. Nicholson and J. Grist. "A conceptual model for understanding rainfall variability in the West African Sahel on interannual and interdecadal timescales". en. *International Journal of Climatology* 21.14 (2001). \_eprint: <https://onlinelibrary.wiley.com/doi/pdf/10.1002/joc.648>, pages 1733–1757. doi: [10.1002/joc.648](https://doi.org/10.1002/joc.648).
- [275] S. E. Nicholson and P. J. Webster. "A physical basis for the interannual variability of rainfall in the Sahel". en. *Quarterly Journal of the Royal Meteorological Society* 133.629 (2007). \_eprint: <https://onlinelibrary.wiley.com/doi/pdf/10.1002/qj.104>, pages 2065–2084. doi: [10.1002/qj.104](https://doi.org/10.1002/qj.104).
- [276] R. Feng, T. Bhattacharya, B. L. Otto-Bliesner, E. C. Brady, A. M. Haywood, J. C. Tindall, S. J. Hunter, A. Abe-Ouchi, W.-L. Chan, M. Kageyama, C. Contoux, C. Guo, X. Li, G. Lohmann, C. Stepanek, N. Tan, Q. Zhang, Z. Zhang, Z. Han, C. J. R. Williams, D. J. Lunt, H. J. Dowsett, D. Chandan, and W. R. Peltier. "Past terrestrial hydroclimate sensitivity controlled by Earth system feedbacks". en. *Nature Communications* 13.1 (2022). Number: 1 Publisher: Nature Publishing Group, page 1306. doi: [10.1038/s41467-022-28814-7](https://doi.org/10.1038/s41467-022-28814-7).

- [277] N. H. Bigelow, L. B. Brubaker, M. E. Edwards, S. P. Harrison, I. C. Prentice, P. M. Anderson, A. A. Andreev, P. J. Bartlein, T. R. Christensen, W. Cramer, J. O. Kaplan, A. V. Lozhkin, N. V. Matveyeva, D. F. Murray, A. D. McGuire, V. Y. Razzhivin, J. C. Ritchie, B. Smith, D. A. Walker, K. Gajewski, V. Wolf, B. H. Holmqvist, Y. Igarashi, K. Kremenetskii, A. Paus, M. F. J. Pisaric, and V. S. Volkova. "Climate change and Arctic ecosystems: 1. Vegetation changes north of 55°N between the last glacial maximum, mid-Holocene, and present". en. *Journal of Geophysical Research: Atmospheres* 108.D19 (2003). \_eprint: <https://onlinelibrary.wiley.com/doi/pdf/10.1029/2002JD002558>. doi: [10.1029/2002JD002558](https://doi.org/10.1029/2002JD002558).
- [278] S. P. Harrison, G. Yu, H. Takahara, and I. C. Prentice. "Diversity of temperate plants in east Asia". en. *Nature* 413.6852 (2001). Number: 6852 Publisher: Nature Publishing Group, pages 129–130. doi: [10.1038/35093166](https://doi.org/10.1038/35093166).
- [279] E. J. Pickett, S. P. Harrison, G. Hope, K. Harle, J. R. Dodson, A. Peter Kershaw, I. Colin Prentice, J. Backhouse, E. A. Colhoun, D. D'Costa, J. Flenley, J. Grindrod, S. Haberle, C. Hassell, C. Kenyon, M. Macphail, H. Martin, A. H. Martin, M. McKenzie, J. C. Newsome, D. Penny, J. Powell, J. Ian Raine, W. Southern, J. Stevenson, J.-P. Sutra, I. Thomas, S. van der Kaars, and J. Ward. "Pollen-based reconstructions of biome distributions for Australia, Southeast Asia and the Pacific (SEAPAC region) at 0, 6000 and 18,000 14C yr BP". en. *Journal of Biogeography* 31.9 (2004). \_eprint: <https://onlinelibrary.wiley.com/doi/pdf/10.1111/j.1365-2699.2004.01001.x>, pages 1381–1444. doi: [10.1111/j.1365-2699.2004.01001.x](https://doi.org/10.1111/j.1365-2699.2004.01001.x).
- [280] I. C. Prentice, D. Jolly, and B. Participants. "Mid-Holocene and glacial-maximum vegetation geography of the northern continents and Africa". en. *Journal of Biogeography* 27.3 (2000). \_eprint: <https://onlinelibrary.wiley.com/doi/pdf/10.1046/j.1365-2699.2000.00425.x>, pages 507–519. doi: [10.1046/j.1365-2699.2000.00425.x](https://doi.org/10.1046/j.1365-2699.2000.00425.x).
- [281] A. J. Thompson, C. B. Skinner, C. J. Poulsen, and J. Zhu. "Modulation of Mid-Holocene African Rainfall by Dust Aerosol Direct and Indirect Effects". en. *Geophysical Research Letters* 46.7 (2019). \_eprint: <https://onlinelibrary.wiley.com/doi/pdf/10.1029/2018GL081225>, pages 3917–3926. doi: [10.1029/2018GL081225](https://doi.org/10.1029/2018GL081225).
- [282] S. Egerer, M. Claussen, and C. Reick. "Rapid increase in simulated North Atlantic dust deposition due to fast change of northwest African landscape during the Holocene". English. *Climate of the Past* 14.7 (2018). Publisher: Copernicus GmbH, pages 1051–1066. doi: [10.5194/cp-14-1051-2018](https://doi.org/10.5194/cp-14-1051-2018).
- [283] N. Fischer and J. H. Jungclaus. "Effects of orbital forcing on atmosphere and ocean heat transports in Holocene and Eemian climate simulations with a comprehensive Earth system model". English. *Climate of the Past* 6.2 (2010). Publisher: Copernicus GmbH, pages 155–168. doi: [10.5194/cp-6-155-2010](https://doi.org/10.5194/cp-6-155-2010).
- [284] T. G. Shepherd. "Atmospheric circulation as a source of uncertainty in climate change projections". en. *Nature Geoscience* 7.10 (2014). Number: 10 Publisher: Nature Publishing Group, pages 703–708. doi: [10.1038/ngeo2253](https://doi.org/10.1038/ngeo2253).
- [285] X. Xu, M. Werner, M. Butzin, and G. Lohmann. "Water isotope variations in the global ocean model MPI-OM". English. *Geoscientific Model Development* 5.3 (2012). Publisher: Copernicus GmbH, pages 809–818. doi: [10.5194/gmd-5-809-2012](https://doi.org/10.5194/gmd-5-809-2012).
- [286] F. Arthur, D. Boateng, and M. Baidu. "Prediction of Rainfall Response to the 21st-century Climate Change in Ghana using Machine Learning Empirical Statistical Downscaling". 2022 (2022). Conference Name: AGU Fall Meeting Abstracts ADS Bibcode: 2022AGUFM.H25A..04A, H25A-04.
- [287] J. Runge, P. Nowack, M. Kretschmer, S. Flaxman, and D. Sejdinovic. "Detecting and quantifying causal associations in large nonlinear time series datasets". *Science Advances* 5.11 (2019). Publisher: American Association for the Advancement of Science, eaau4996. doi: [10.1126/sciadv.aau4996](https://doi.org/10.1126/sciadv.aau4996).
- [288] J. Runge, S. Bathiany, E. Bollt, G. Camps-Valls, D. Coumou, E. Deyle, C. Glymour, M. Kretschmer, M. D. Mahecha, J. Muñoz-Marí, E. H. van Nes, J. Peters, R. Quax, M. Reichstein, M. Scheffer, B. Schölkopf, P. Spirtes, G. Sugihara, J. Sun, K. Zhang, and J. Zscheischler. "Inferring causation from time series in Earth system sciences". en. *Nature Communications* 10.1 (2019). Number: 1 Publisher: Nature Publishing Group, page 2553. doi: [10.1038/s41467-019-10105-3](https://doi.org/10.1038/s41467-019-10105-3).

- [289] P. Spirtes, C. Glymour, and R. Scheines. "Causation, Prediction, and Search". en. Google-Books-ID: OZ0vEAAAQBAJ. *MIT Press*, 2001.
- [290] P. Spirtes and K. Zhang. "Causal discovery and inference: concepts and recent methodological advances". en. *Applied Informatics* 3.1 (2016), page 3. doi: [10.1186/s40535-016-0018-x](https://doi.org/10.1186/s40535-016-0018-x).
- [291] E. Galytska, K. Weigel, D. Handorf, R. Jaiser, R. Köhler, J. Runge, and V. Eyring. "Evaluating Causal Arctic-Midlatitude Teleconnections in CMIP6". en. *Journal of Geophysical Research: Atmospheres* 128.17 (2023). \_eprint: <https://onlinelibrary.wiley.com/doi/pdf/10.1029/2022JD037978>, e2022JD037978. doi: [10.1029/2022JD037978](https://doi.org/10.1029/2022JD037978).
- [292] P. Nowack, J. Runge, V. Eyring, and J. D. Haigh. "Causal networks for climate model evaluation and constrained projections". en. *Nature Communications* 11.1 (2020). Publisher: Nature Publishing Group, page 1415. doi: [10.1038/s41467-020-15195-y](https://doi.org/10.1038/s41467-020-15195-y).
- [293] V. Eyring, P. M. Cox, G. M. Flato, P. J. Gleckler, G. Abramowitz, P. Caldwell, W. D. Collins, B. K. Gier, A. D. Hall, F. M. Hoffman, G. C. Hurtt, A. Jahn, C. D. Jones, S. A. Klein, J. P. Krasting, L. Kwiatkowski, R. Lorenz, E. Maloney, G. A. Meehl, A. G. Pendergrass, R. Pincus, A. C. Ruane, J. L. Russell, B. M. Sanderson, B. D. Santer, S. C. Sherwood, I. R. Simpson, R. J. Stouffer, and M. S. Williamson. "Taking climate model evaluation to the next level". en. *Nature Climate Change* 9.2 (2019). Publisher: Nature Publishing Group, pages 102–110. doi: [10.1038/s41558-018-0355-y](https://doi.org/10.1038/s41558-018-0355-y).





**Part V.**

Appendix



# Manuscripts for Part 1 (P1-P3)

## 1 P1: Boateng et al. [1]

**(P1)** Boateng, D., Mutz, S. G., Ballian, A., Meijers, M. J. M., Methner, K., Botsyun, S., Mulch, A., and Ehlers, T. A.: The effects of diachronous surface uplift of the European Alps on regional climate and the oxygen isotopic composition of precipitation, *Earth System Dynamics*, 14, 1183–1210, <https://doi.org/10.5194/esd-14-1183-2023>, 2023.

1 P1: Boateng et al. [1] . . . 91  
2 P2: Botsyun et al. [2] . . . 120  
3 P3: Boateng et al. [to be submitted] . . . . . 151



# The effects of diachronous surface uplift of the European Alps on regional climate and the oxygen isotopic composition of precipitation

Daniel Boateng<sup>1</sup>, Sebastian G. Mutz<sup>1,7</sup>, Armelle Ballian<sup>2,3</sup>, Maud J. M. Meijers<sup>4</sup>, Katharina Methner<sup>2,5</sup>, Svetlana Botsyun<sup>1,6</sup>, Andreas Mulch<sup>2,3</sup>, and Todd A. Ehlers<sup>1,7</sup>

<sup>1</sup>Department of Geosciences, University of Tübingen, Tübingen, Germany

<sup>2</sup>Senckenberg Biodiversity and Climate Research Centre, Frankfurt am Main, Germany

<sup>3</sup>Goethe University Frankfurt, Institute of Geosciences, Frankfurt am Main, Germany

<sup>4</sup>Department of Earth Sciences, NAWI Graz Geocenter, University of Graz, Graz, Austria

<sup>5</sup>Department of Geophysics and Geology, University of Leipzig, Leipzig, Germany

<sup>6</sup>Institute of Meteorology, Freie Universität Berlin, Berlin, Germany

<sup>7</sup>School of Geographical and Earth Sciences, University of Glasgow, Scotland, Glasgow, UK

**Correspondence:** Daniel Boateng (daniel.boateng@uni-tuebingen.de)

Received: 26 October 2022 – Discussion started: 19 December 2022

Revised: 27 September 2023 – Accepted: 28 September 2023 – Published: 17 November 2023

**Abstract.** This study presents the simulated response of regional climate and the oxygen isotopic composition of precipitation ( $\delta^{18}\text{O}_p$ ) to different along-strike topographic evolution scenarios. These simulations are conducted to determine if the previously hypothesized diachronous surface uplift in the Western and Eastern Alps would produce  $\delta^{18}\text{O}_p$  signals in the geologic record that are sufficiently large and distinct to be detected using stable isotope paleoaltimetry. We present a series of topographic sensitivity experiments conducted with the water-isotope-tracking atmospheric general circulation model (GCM) ECHAM5-wiso. The topographic scenarios are created from the variation of two free parameters, (1) the elevation of the Western–Central Alps and (2) the elevation of the Eastern Alps. The results indicate  $\Delta\delta^{18}\text{O}_p$  values (i.e., the difference between  $\delta^{18}\text{O}_p$  values at the low- and high-elevation sites) of up to  $-8\text{‰}$  along the strike of the Alps for the diachronous uplift scenarios, primarily due to changes in orographic precipitation and adiabatic lapse rate driven localized changes in near-surface variables. These simulated magnitudes of  $\Delta\delta^{18}\text{O}_p$  values suggest that the expected isotopic signal would be significant enough to be preserved and measured in geologic archives. Moreover, the simulated slight  $\delta^{18}\text{O}_p$  differences of  $1\text{‰}$ – $2\text{‰}$  across the low-elevation sites support the use of the  $\delta$ – $\delta$  paleoaltimetry approach and highlight the importance of sampling far-field low-elevation sites to differentiate between the different surface uplift scenarios. The elevation-dependent rate of change in  $\delta^{18}\text{O}_p$  (“isotopic lapse rate”) varies depending on the topographic configuration and the extent of the surface uplift. Most of the changes are significant (e.g.,  $-1.04\text{‰ km}^{-1}$  change with slope error of  $\pm 0.09\text{‰ km}^{-1}$ ), while others were within the range of the statistical uncertainties (e.g.,  $-0.15\text{‰ km}^{-1}$  change with slope error of  $\pm 0.13\text{‰ km}^{-1}$ ). The results also highlight the plausible changes in atmospheric circulation patterns and associated changes in moisture transport pathways in response to changes in the topography of the Alps. These large-scale atmospheric dynamics changes can complicate the underlying assumption of stable isotope paleoaltimetry and therefore require integration with paleoclimate modeling to ensure accurate reconstruction of the paleoelevation of the Alps.

## 1 Introduction

The topographic evolution of orogens over geological time is controlled by geodynamic processes (e.g., crustal thickening, lower crustal flow, subduction erosion, and lithospheric delamination) and climate-driven surface processes (e.g., erosion, denudation, and other earth surface processes) (e.g., Valla et al., 2021; Whipple, 2009; Ehlers and Poulsen, 2009). Knowledge of past topography contributes to the understanding of climate–tectonic interactions, the tectonic evolution of collisional domains, and the distribution of biodiversity (Allen, 2008; Clark, 2007; Mulch, 2016; Rowley and Garzzone, 2007; Antonelli et al., 2018; Mulch et al., 2018). Paleoelevations have been reconstructed for numerous high mountain ranges such as the Himalayas and the Tibetan Plateau (e.g., Garzzone et al., 2000; Quade et al., 2011; Gébelin et al., 2013; Rowley and Currie, 2006; Ding et al., 2022; Spicer et al., 2021), the North American Cordillera (e.g., Huntington et al., 2010; Chamberlain et al., 2012; Mulch et al., 2006), the Andean Plateau (e.g., Garzzone et al., 2008, 2014; Barnes and Ehlers, 2009; Mulch et al., 2010; Pingel et al., 2016; Sundell et al., 2019), and areally smaller orogens such as the Pyrenees (Huyghe et al., 2012), the Sierra Nevada Mountains of California (e.g., Mulch et al., 2006, 2008), the Southern Alps of New Zealand (Chamberlain et al., 1999), the Taurides of Turkey (Meijers et al., 2018), and the European Alps (Campani et al., 2012; Fauquette et al., 2015; Krsnik et al., 2021). Past surface elevations have been inferred using a variety of methods, such as foliar physiognomy (Forest et al., 1999), stomatal density in fossil leaves (McElwain, 2004), vesicularity of basaltic flows (Sahagian and Maus, 1994), and water isotopologues from lacustrine and pedogenic carbonates and authigenic minerals (e.g., Kohn and Dettman, 2007; Quade et al., 2007; Rowley and Garzzone, 2007; Mulch and Chamberlain, 2007). Among these techniques, stable isotope paleoaltimetry is the most widely used due to the robust systematic inverse relationships between elevation and oxygen ( $\delta^{18}\text{O}$ ) and hydrogen ( $\delta\text{D}$ ) isotopic composition of meteoric waters reflected in geologic archives such as paleosol carbonates. This  $\delta^{18}\text{O}$ –elevation relationship (or isotopic lapse rate) is commonly attributed to the preferential rainout of heavy isotopologues of water from air masses ascending over topography and is described physically as Rayleigh distillation (Gat, 1996). However, numerous climatic processes, such as surface recycling, aridity, vapor mixing, variability in moisture source, and precipitation dynamics, can also influence the isotopic lapse rate and thus complicate stable isotope paleoaltimetry estimates (Ehlers and Poulsen, 2009; Insel et al., 2010; Feng et al., 2013; Lee and Fung, 2008; Risi et al., 2013; Botysun and Ehlers, 2021). Furthermore, studies of surface uplift in orogens, such as the Andes, Himalayas, and Tibet, have demonstrated the impacts of topographic evolution on atmospheric circulation patterns and the spatial distribution of  $\delta^{18}\text{O}$  in precipitation ( $\delta^{18}\text{O}_p$ ) in a more complicated way than single-site stable isotope pa-

leoaltimetry studies commonly assume (e.g., Takahashi and Battisti, 2007; Yao et al., 2013; Mulch, 2016). This highlights the need for a better quantitative understanding of how topography and regional climate influence the variations of the isotopic composition of ancient waters (Ehlers and Poulsen, 2009; Botysun et al., 2020; Insel et al., 2012). This study comprises a series of climate model experiments that address this need for the European Alps.

The European Alps have been extensively studied, but only a few studies have addressed the reconstruction of its surface uplift histories with stable isotope paleoaltimetry (e.g., Sharp et al., 2005; Campani et al., 2012; Krsnik et al., 2021). Recent studies have suggested that the Alps experienced diachronous surface uplift in response to the post-collisional slab break-off and continuing rollback of the lithosphere and its associated mantle delamination (Schlunegger and Kissling, 2018; Handy et al., 2015). Stable-isotope-based reconstructions of past surface topography can help to constrain such subsurface processes, given that surface elevation is primarily an expression of mantle and lithospheric dynamics. However, whether such geodynamic processes would yield (spatial) differences in  $\delta^{18}\text{O}_p$  values by a magnitude that would be detectable in the geologic record remains an open question. Resolving such a question would justify the use of stable isotope paleoaltimetry reconstructions across the Alps to understand their topographic evolution.

In this study, we simulate changes in regional climate and the oxygen isotopic composition of precipitation ( $\delta^{18}\text{O}_p$ ) that would occur in response to diachronous, along-strike surface uplift variations of the Eastern and Western–Central Alps. We address the question of to what extent (and where) different scenarios of differentiated west-to-east surface uplift would be reflected in  $\delta^{18}\text{O}$  of meteoric water. In answering these questions, we test two hypotheses. We hypothesize that different topographic configurations for the Eastern and Western–Central Alps result in regional climate and  $\delta^{18}\text{O}_p$  patterns that are significantly different from (1) those of today and (2) those produced by scenarios of bulk surface uplift of the entire Alps. We test these hypotheses through a series of sensitivity experiments with two free parameters including variations in the elevation of the Western–Central Alps and the elevation of the Eastern Alps. The experiments are conducted with the isotopic-tracking atmospheric general circulation model (GCM) ECHAM5-wiso and provide quantitative estimates of the expected  $\delta^{18}\text{O}_p$  signal that could be recorded in geological archives used in stable isotope paleoaltimetry. The simulated  $\delta^{18}\text{O}_p$  signal can help determine if the changes are significant enough to be reflected in paleoaltimetry records, which would ultimately help to reconstruct the geodynamic evolution of the Alps. The study therefore also represents an important step toward answering the question of whether the eastward propagation of surface uplift (or different east–west topographic configurations) would be detectable in paleo- $\delta^{18}\text{O}_p$  records.

## 2 Background

### 2.1 Geodynamics of the European Alps

The European Alps are a midlatitude orogenic belt extending over a longitudinal area ( $\sim 1000 \text{ km}^2$ ) subdivided into the Western, Central, and Eastern Alps (Schmid et al., 2004). The onset of their topographic development is attributed to the continent–continent collision of the European and Adriatic plates in the late Eocene. This event was followed by protracted convergence and subduction of oceanic lithosphere (Frisch, 1979; McCann, 2008; Schmid et al., 1996; Stampfli et al., 1998). Major rock exhumation started  $\sim 35 \text{ Ma}$  or earlier, predominantly in response to crustal thickening and associated erosion (Kuhlemann et al., 2002; Schmid et al., 2004, 1996) and drainage reorganization (Lu et al., 2018). Recent modeling studies have suggested additional geodynamic processes that may have influenced the surface uplift history (Kissling and Schlunegger, 2018; Schlunegger and Kissling, 2015). These processes include slab break-off ( $\sim 30 \text{ Ma}$ ) and slab rollback of the subducting lithosphere, as well as lithospheric mantle removal that may have contributed to west-to-east variations in surface uplift as proposed for the Central Alps (Davies and von Blanckenburg, 1995; Schlunegger and Castellort, 2016; Ustaszewski et al., 2008). Subsequently, it has been suggested that slab break-off ( $\sim 20 \text{ Ma}$ ) occurred under the Eastern Alps (Handy et al., 2015). Based on previous studies, current tectonic and geodynamic reconstructions suggest that the entire Alps did not rise monotonically but through diachronous surface uplift across different sections of the orogen. This study explores such a scenario and evaluates changes in  $\delta^{18}\text{O}_p$  values that would be expected to be preserved in the geologic record within the region.

### 2.2 Paleoelevation estimates of the European Alps

Few studies have attempted to quantify the surface elevation history of the Alps. Pollen data suggest that the southwestern Alps reached their maximum mean elevation of more than  $\sim 1900 \text{ m}$  at the early stage after the collision in the early Oligocene (ca.  $30 \text{ Ma}$ ) (Fauquette et al., 2015). Stable-isotope-based paleoelevation estimates for the middle Miocene Central Alps range from 2.5 to 6 km (e.g., Campani et al., 2012; Kocsis et al., 2007; Sharp et al., 2005), and the higher end of these estimates for the Central Alps was confirmed recently with surface elevations of  $> 4 \text{ km}$  being attained not later than the middle Miocene (Krsnik et al., 2021). Collectively, these reconstructions suggest that the Western and Central Alps were already at high elevations in the middle Miocene, and surface uplift must have occurred in the Oligocene to Miocene. In contrast, no long-term quantitative past surface elevation estimates are available for the Eastern Alps. However, geodynamic modeling and geomorphic analysis suggest that the orogenic development of

the Eastern Alps initiated only during the middle Miocene ( $\sim 15\text{--}10 \text{ Ma}$ ), with a major phase at  $\sim 5 \text{ Ma}$  (Bartosch et al., 2017; Hergarten et al., 2010). These previous findings suggest that surface uplift in the Central Alps predates surface uplift in the Eastern Alps. If the isotopic signal created by west-to-east surface uplift propagation is preserved in geological materials (e.g., pedogenic carbonates or hydrous shear zone silicates) and deemed detectable according to the climate modeling studies, then stable isotope paleoaltimetry may be used to address this research gap. Therefore, we use different topographic configurations in sensitivity experiments to quantify the expected isotopic signal. With a present-day mean elevation of peaks of ca.  $2500 \text{ m}$  across the Alps, increasing their elevation by 200 % would reflect the paleoelevation reconstructions across the Western–Central Alps in the middle Miocene (Campani et al., 2012; Krsnik et al., 2021). However, due to the lack of quantitative paleoelevation estimates across the Eastern Alps, we conduct a stepwise increase in the elevation across that transect to explore all the potential surface uplift magnitudes back in time (see Sect. 3.2 for more details about topographic configuration).

### 2.3 Climate of the Alps

The interannual and seasonal variability of regional climate in Europe is predominantly controlled by large-scale circulation patterns (Bartolini et al., 2009; Hurrell, 1995). The topography of the Alps greatly impacts mesoscale temperature, precipitation, moisture transport, wind, and other atmospheric elements (e.g., Schmidli et al., 2002). The Alps act as an orographic barrier, which affects convective and orographic precipitation formation and the associated spatial effects like leeward rain shadows (Bartolini et al., 2009; Beniston, 2005). Today, the Alps experience maximum precipitation rates in summer due to (1) the shifting of pressure fronts to the south and (2) high convective heat transport from oceanic sources and continental evapotranspiration (Schmidli et al., 2002). Most atmospheric moisture received across the Alps, especially over the northern flanks, is transported via the westerlies from the North Atlantic. Regional precipitation histories can thus be explained primarily by variations in atmospheric circulation patterns over the North Atlantic and western Europe (Baldini et al., 2008; Comas-Bru et al., 2016; Langebroek et al., 2011; Rozanski et al., 1982). Therefore,  $\delta^{18}\text{O}$  values in ancient meteoric waters can only be quantitatively evaluated with knowledge about the dominant large-scale atmospheric flows and the locations of associated pressure systems (i.e., quasi-stable systems with high and low sea level pressure), which can shift over time (e.g., Deininger et al., 2016) due to global and regional paleoenvironment changes, such as topography.

Advances in climate modeling allow the use of high-resolution isotope-tracking atmospheric general circulation models (AGCMs) to investigate the impacts of topography

and regional climate change on  $\delta^{18}\text{O}_p$  values (e.g., Botsyun et al., 2020, 2019; Botsyun and Ehlers, 2021; Li et al., 2016; Mutz et al., 2016; Sturm et al., 2010). AGCMs are developed based on atmospheric physical processes. They can simulate climates that are in dynamic equilibrium with prescribed orbital, environmental, and topographic boundary conditions. While GCMs have some deficiencies in predicting precipitation in mountain regions due to model-specific parameterization (e.g., cloud microphysics and the hydrostatic approximation), they have been shown to adequately reproduce important patterns of climate and precipitation  $\delta^{18}\text{O}$  values over orogens, including the Alps (e.g., Botsyun et al., 2020; Werner et al., 2011). Previous studies have used GCMs to perform topographic sensitivity experiments to help improve paleoaltimetry estimates (e.g., Botsyun et al., 2019; Shen and Poulsen, 2019; Ehlers and Poulsen, 2009; Poulsen et al., 2010; Feng et al., 2013; Feng and Poulsen, 2016; Huyghe et al., 2018; Insel et al., 2012). More recently, Botsyun et al. (2020) performed GCM experiments designed to estimate the  $\delta^{18}\text{O}_p$  response to bulk surface elevation changes in the whole Alps. This study builds on their findings by considering diachronous surface uplift (stepwise surface uplift from west to east) as different topographic scenarios.

### 3 Data and methods

#### 3.1 General circulation model (ECHAM5-wiso)

The hypotheses tested in this study are addressed with a series of experiments conducted with the isotope-tracking climate model ECHAM5-wiso. ECHAM5 is the fifth version of a well-established atmospheric GCM that is developed and maintained by the Max Planck Institute for Meteorology (MPIM) based on the spectral weather forecast model of the European Centre for Medium-Range Weather Forecasts (ECMWF) (Roeckner et al., 2003). ECHAM5 has been expanded to include an isotope-tracking module that simulates the isotopic composition of water at every step of the simulated hydrological cycle in the model (Werner et al., 2011). The water isotopologues (i.e.,  $\text{H}_2^{16}\text{O}$ ,  $\text{H}_2^{18}\text{O}$ , and HDO) are treated as independent tracers (Hoffmann et al., 1998; Werner et al., 2011) that undergo kinetic and equilibrium fractionation during phase transitions in the atmosphere (e.g., snow, vapor, clouds). The semi-Lagrangian advection scheme is used for the transport of the passive tracers through all the water components (Lin and Rood, 1996). The resulting isotope-tracking GCM (ECHAM5-wiso) has been demonstrated to reproduce global- and regional-scale isotopic observations well, including for present-day  $\delta^{18}\text{O}_p$  values across Europe (Botsyun et al., 2020; Werner et al., 2011; Langebroek et al., 2011). Compared to its predecessor, the version applied in this study has an improved representation of the land surface and considers orographic drag forces. However, the model does not track isotopic fractionations from surface waters (Hagemann et al., 2006). The model sim-

ulates clouds using the stratiform cloud scheme that consists of the prognostic equations of all the water phase dynamics, bulk cloud microphysics by Lorenz and Lohmann (2004), and statistical cloud cover parameterization by Tompkins (2002). Comprehensive details about the model physics and parameterization are described in Werner et al. (2011) and Roeckner et al. (2003).

#### 3.2 Topography experiments

We investigate the effects of specific topographic configurations on  $\delta^{18}\text{O}_p$  values and regional climate by performing sensitivity experiments with two free parameters, (1) the elevation of the Western–Central Alps (43–48° N, 5–10° E) and (2) the elevation of the Eastern Alps (45–48° N, 10–17° E). For brevity, a two-part notation is used in this study for individual topographic configurations: the first part denotes the elevation of the Western–Central Alps and assumes the form  $Wx$ , where  $x$  expresses the elevation as a fraction of its present-day value. The second part analogously expresses the elevation of the Eastern Alps in the form of  $Ex$ . The topographic configuration W2E0, for example, therefore consists of the Western–Central and Eastern Alps set to 200 % and 0 % of their modern elevation, respectively. The configurations with 0 % topography use 250 m as a mean minimum topography to avoid unrealistic artifacts in the simulations, such as extreme wind speeds due to a completely flat low-elevation surface. The topographic boundary conditions for the different experiments are prepared as follows: we modify the GTOPO30 digital elevation model (DEM) provided by the US Geological Survey, which has a resolution of 30 arcsec (ca. 1 km). Afterward, the modified high-resolution DEMs are interpolated to the ECHAM5-wiso model resolution (i.e., T159, horizontal resolution of  $\sim 80$  km). The associated subgrid orographic variables are calculated from the higher-resolution DEM. These variables include orographic standard deviation (i.e., the variability of the heights of the mountain range), anisotropy, peak elevations, valley elevation, mean slope, and orientation within a grid cell. Such related information is used for the subgrid-scale parameterization that estimates the effect of mountain-induced wave drag on the atmosphere and mountain blocking in the model (Stevens et al., 2013; Roeckner et al., 2003).

We elaborate on two topographic scenarios, each consisting of several topographic configurations (see Table 1 for a complete overview).

*Scenario 1.* The first scenario considers the diachronous west-to-east surface uplift hypothesized from tectonic reconstructions of the Alps (e.g., Bartosch et al., 2017; Fauquette et al., 2015; Handy et al., 2015). Consequently, the Western–Central and Eastern Alps are varied separately. First, the elevation of the Western–Central Alps was kept at its present-day value (W1), and the elevation of the Eastern Alps was incrementally increased from 0 % to 200 % of its present-day value. Following this, the Western–Central Alps were set

to 200 % (W2) of their present-day elevation, and the Eastern Alps were raised incrementally again. W2 was chosen to represent a plausible middle Miocene altitude of more than 4000 m, which is close to 200 % of the modern mean elevation of the Central Alps (Krsnik et al., 2021). However, the resolution of the model underrepresents the magnitude of the orographic mean elevation due to dampening of maximum peak elevations across the Alps in the interpolation process.

*Scenario 2.* For the second scenario, the topography of the entire Alps, including the Western–Central and Eastern Alps, was increased to 200 % (W2E2) and reduced to 0 % (W0E0) of its present-day height. These topographic configurations allow for a comparison of the climatic response to diachronous surface uplift (scenario 1) and bulk surface uplift. Since the W1E1 configuration simply represents modern topography, it is used as the control experiment and given the special designation CTL.

### 3.3 Model setup and boundary conditions

All experiments were performed for 18 model years on a high-spatial-resolution grid to represent the Alps' topography adequately. Specifically, the T159 spectral resolution (which corresponds to  $\sim 0.75^\circ$  or  $\sim 80$  km in latitude and longitude) and 31 vertical pressure levels (up to 10 hPa) were used for the simulations. The output frequency was set to 6 model hours to allow the performance of a trajectory analysis (Sect. 3.6). We only consider the last 15 years of the model output and remove the first 3 years of the simulation to account for the spin-up period, i.e., the time needed for the simulated climate to reach dynamic equilibrium. Since this study aims to quantify and isolate the effects of different topographic configurations (Sect. 3.2) on regional climate and  $\delta^{18}\text{O}_p$  values, all other boundary conditions are kept constant at pre-industrial (PI) levels. These include orbital configurations, greenhouse gas concentrations, sea surface variables, and insolation. For model validation purposes, we additionally conduct a present-day (PD) simulation of 43 model years and analyze the last 30 years (1979–2014). We use the annual mean variations of the sea surface temperature (SSTs) and sea ice concentrations (SICs) from the Atmospheric Model Intercomparison Project (AMIP) as boundary conditions. The simulated PD climate and isotopic patterns are compared with observed values across Europe. The reader is referred to Mutz et al. (2016, 2018) for more details about the PD and PI boundary conditions used in this study.

### 3.4 Model–data comparison

Modern station-based  $\delta^{18}\text{O}_p$  data from the Global Network of Isotopes in Precipitation (GNIP) in Europe (accessible at <https://www.iaea.org>, last access: 5 November 2023) are used as our first validation dataset (Edwards et al., 2002). The precipitation-weighted  $\delta^{18}\text{O}_p$  values from GNIP stations were compared to the PD simulation to assess the per-

formance of ECHAM5-wiso. Specifically, we compute and compare long-term annual means of precipitation-weighted  $\delta^{18}\text{O}_p$  for the period covered by the GNIP station measurements across the European continent. The ERA5 climate reanalysis, produced and managed by the ECMWF, is our second validation dataset. The reanalysis is a state-of-the-art, globally gridded dataset produced from both physical models and observations (e.g., ocean buoys, aircraft, and other platforms) that is dynamically interpolated using the four-dimensional variational (4D-Var) data assimilation scheme (Hersbach et al., 2020). Compared to its predecessor ERA-Interim (Dee et al., 2011), the dataset has improved in both temporal (hourly throughout) and spatial resolution (31 km or TL639) and expanded its data coverage from 1950 onwards (Bell et al., 2021). We use this dataset to construct Northern Hemisphere teleconnection patterns and compare them to their equivalents constructed from topographic scenarios simulations.

### 3.5 Postprocessing and analysis of simulation

Long-term seasonal and annual arithmetic means were calculated from the 6 h model output. The deviations of these means from the CTL mean were calculated by subtracting the CTL mean from the topography scenarios. The resulting anomalies are referred to as “ID–CTL mean differences” hereafter, where ID is an experiment ID such as W2E1 (see Sect. 3.2 and Table 1 for an overview). Two-tailed Student's  $t$  tests with a defined confidence interval threshold of 95 % were applied to assess the statistical significance of these differences against simulated interannual climate variability. In this study, we mainly discuss summer (JJA) estimates since numerous studies use pedogenic carbonates, which are preferentially formed during soil drying when evaporation exceeds precipitation (e.g., Gallagher et al., 2019; Breecker et al., 2009; Zamanian et al., 2016) as a proxy for stable isotope paleoaltimetry. However, since there are uncertainties about the extent of the seasonal bias in pedogenic carbonate formation (e.g., Kelson et al., 2020), the annual means are also provided. The elevation– $\delta^{18}\text{O}_p$  relationships, further referred to as the isotopic lapse rates (ILRs), were estimated for different geographic areas around the Alps (Fig. 1a) by performing ordinary least-squares (OLS) linear regressions on the grid point values within each region. We use the notation  $-1\text{‰ km}^{-1}$  (instead of  $1\text{‰ km}^{-1}$ ) to report a decrease of 1 ‰ for an elevation increase of 1 km. We highlight that the aim of the analysis is to determine if the elevation– $\delta^{18}\text{O}_p$  relationship over a specific transect would change in response to the different topographic configurations. The estimated lapse rates are not intended to serve as a predictive model for calculating paleoelevation but as a comparison among the topographic configurations to highlight the need to consider the potential changes in lapse rate through space and time. This is because the estimated lapse rates only reflect the scenarios of changes in surface uplift through time with-



**Table 1.** Summary of ECHAM5-wise sensitivity experiments and their topographic configurations and boundary conditions.

Model setup	Experiment name	Topography configuration	Boundary conditions
Present day (1979–2000)	PD	100 % of the present-day elevation	Present-day (e.g., CO <sub>2</sub> = 348 ppm)
Control	CTL	100 % of the present-day elevation	Pre-industrial (e.g., CO <sub>2</sub> = 280 ppm)
Scenario 2 (bulk topographic change)	W2E2	200 % of the present-day elevation	same as CTL
	W0E0	The Alps reduced to 250 m	same as CTL
Scenario 1 (W1)	W1E0	100 % of the present-day elevation of the Western–Central Alps and reduction of the Eastern Alps to 250 m	same as CTL
	W1E1.5	100 % of present-day elevation of the Western–Central Alps and 150 % of the Eastern Alps	same as CTL
	W1E2	100 % of the present-day elevation of the Western–Central Alps and 200 % of the Eastern Alps	same as CTL
scenario 1 (W2)	W2E0	200 % of the present-day elevation the Western–Central Alps and reduction of the present-day elevation of the Eastern Alps to 250 m	same as CTL
	W2W1	200 % of the present-day elevation of the Western–Central Alps and 100 % of the Eastern Alps	same as CTL

out changes in the associated global climate and are therefore not realistic enough to constrain past vertical changes of the Alps. The statistical uncertainties of the calculated lapse rate are determined using the 95 % confidence interval around the calculated OLS slope using a  $t$  distribution with  $n - 2$  degrees of freedom where the standard deviation of the slope is the point estimate for  $n$  data points. Additionally, the coefficient of determination ( $R^2$ ), a measure of the fraction of the variability of the  $\delta^{18}\text{O}_p$  values that can be explained by the best-fitted OLS estimates, is also reported. We further show the 95 % confidence and prediction interval around the regression-fitted model to highlight the uncertainties around the individual topographic configuration if it was meant to be used to calculate the paleoelevation for reconstructed  $\delta^{18}\text{O}_p$  values under the assumption of no changes in global climate over time. In such a case, however, it would not be appropriate to compare the error limits around the regression line for the different scenarios, since their estimates are based on samples from different distributions. We refer the reader to Montgomery and Runger (2010) for more details about the mathematical derivation of the reported metrics.

The prominent Northern Hemisphere teleconnection patterns (i.e., North Atlantic Oscillation – NAO, as well as

the East Atlantic – EA, Scandinavian – SCAN, and East Atlantic–Western Russia – EA/WR – patterns) were extracted from the model output to investigate the influence of surface uplift on synoptic-scale atmospheric variability, which in turn affects atmospheric moisture transport and  $\delta^{18}\text{O}_p$  values. These were captured by conducting a principal component analysis (PCA) or empirical orthogonal function (EOF) analysis (e.g., von Storch and Zwiers, 2001; Hannachi et al., 2007) on the summer (JJA) mean sea level pressure (slp) fields in the North Atlantic–European domain (20–80° N, 80° W–40° E). Before the EOF analysis, a spatial weighting of the latitude of the pressure anomalies was applied to equalize the atmospheric field geographically, as North et al. (1982) recommended. The patterns extracted from present-day ERA5 mean sea level pressure data were used as a reference to help group the modes of variability from the topography experiments.

For further analysis of the effects of changing topography on regional climate across the orogen, we extracted variations in vertical wind velocity (omega), cloud cover, and relative humidity along-strike (west to east) of the Alps. Since the position of the Alps is approximately parallel to the present-day prevailing wind direction, along-strike vari-

ations in these climate elements can provide insight into the potential evolution of air parcels originating from the west. This analysis is complemented by trajectory analyses (see Sect. 3.6).

### 3.6 Trajectory analysis

Kinetic back-trajectory analyses were performed to investigate the impacts of the topography scenarios on moisture sources and transport across the Alps. Specifically, the Lagrangian analysis tool LAGRANTO (Sprenger and Wernli, 2015) was used with the three-dimensional wind fields (i.e., zonal  $u$ , meridional  $v$ , and vertical  $\omega$  – wind velocities) of the 6 h model outputs for the trajectory analysis. The tool uses a robust numerical scheme with efficient spatial interpolation (bilinear and linear interpolation for the horizontal and vertical directions, respectively). The trajectories were backtracked for 5 d from a receptor point at the 850 hPa vertical level defined at four different locations (i.e., Graz at 47.06° N, 15.44° E; Munich at 48.14° N, 11.53° E; Bologna at 44.49° N, 11.38° E; Lyon at 45.81° N, 4.82° E).

## 4 Results

This section summarizes the simulated changes in regional climate and  $\delta^{18}\text{O}_p$  values in response to the different topographic configurations across the Alps (Sect. 3.2, Fig. S1 in the Supplement). More specifically, the presentation of results focuses on  $\delta^{18}\text{O}_p$  values, isotopic lapse rate, precipitation amount, near-surface temperature, moisture transport, and atmospheric circulation patterns. The section comprises present-day model validation with observed  $\delta^{18}\text{O}_p$  values (Sect. 4.1), a summary of the CTL experiment (Sect. 4.2), and the changes mentioned above relative to the CTL simulation (Sect. 4.3–4.10). Unless stated otherwise, the results are presented for the summer (JJA) season. The annual-scale changes are included in the Supplement to this paper.

### 4.1 Present-day (PD) simulation and model validation

The simulated annual mean  $\delta^{18}\text{O}_p$  values decrease from the North Atlantic Ocean towards eastern Europe and over the Alps by 10‰ to 12‰ and deviate from the observed GNIP data slightly ( $\sim 1$ –2‰; Fig. 1b). The annual means of near-surface temperature and precipitation across the Alps are 0–4°C and  $\sim 150$ –200 mm month<sup>-1</sup>, respectively. Low-level winds originating from the North Atlantic travel toward Europe and show slight deflections across the Alps (Fig. 1d). Overall, comparing the annual long-term means of the model outputs to observed GNIP stations  $\delta^{18}\text{O}_p$  values and observed PD precipitation and temperature patterns indicates that the model reasonably represents  $\delta^{18}\text{O}_p$  values and the regional climate across Europe. The topography used as an input parameter for the model moderately represents the to-

pography of the Alps with a dampened elevation of the highest peaks (Fig. 1a).

### 4.2 Control simulation (CTL) $\delta^{18}\text{O}_p$ values, near-surface temperature, and precipitation

The simulation with pre-industrial (PI) boundary conditions and PD topography did not show a significant difference in predicted  $\delta^{18}\text{O}_p$  values compared to the PD simulation. Overall, the CTL experiment shows decreasing patterns of summer  $\delta^{18}\text{O}_p$  values towards northeastern Europe and predicts <sup>18</sup>O-depleted  $\delta^{18}\text{O}_p$  values in the range of  $-10$ ‰ to  $-12$ ‰ across the Alps (Fig. 2a). However, the  $\delta^{18}\text{O}_p$  values slightly increase towards the east of the Alps ( $\sim 20^\circ$  E), yielding values from  $-10$ ‰ to  $-6$ ‰. Near-surface temperatures are estimated to be more than 10°C across Europe, with minimum values across the Alps (2–6°C) and a cooling gradient towards the north (Fig. 3a). Moreover, the predicted patterns show maximum near-surface temperatures across the Mediterranean region. The simulated precipitation patterns decrease towards the south, with the Mediterranean region having the driest climate (Fig. 4a). However, the topography of the Alps coincides with higher precipitation (an average of summer months of  $\sim 125$  mm month<sup>-1</sup>) compared to estimates across central Europe. On the western flanks of the Alps, low-level westerly winds are deflected in a north–south bifurcation pattern (Fig. 4a).

### 4.3 Changes in $\delta^{18}\text{O}_p$ values for the different topographic scenarios

The simulated regional patterns of  $\delta^{18}\text{O}_p$  values show significant changes in response to the different topography scenarios, especially in regions of modified topography. Overall, the  $\delta^{18}\text{O}_p$  values decrease with increasing elevation. This decrease is accentuated when the topography of the Western–Central Alps is higher (i.e., for the W2 configurations of scenario 1). More specifically, the W2E1 experiment predicts a significant decrease in  $\delta^{18}\text{O}_p$  values across the Alps in the range of 2‰ to 8‰ with minimum  $\delta^{18}\text{O}_p$  values in the Western–Central Alps (Fig. 2b). The W2E0 experiment predicts a more localized significant decrease of 2 to 6‰ in the Western–Central Alps (Fig. 2d). In contrast, the W1E2 configuration results in a decrease of 2 to 6‰ over the extended east flank of the Alps (Fig. 2e), and the W1E0 simulation does not predict any statistically significant changes in  $\delta^{18}\text{O}_p$  values across the orogen (Fig. 2c). The W2E2 configuration (of scenario 2) results in a decrease in  $\delta^{18}\text{O}_p$  values in the range of 2‰ to 6‰ across the Alps and the adjacent low-elevation regions (Fig. 2f). However, the W2E2 experiment also predicts a substantial increase in  $\delta^{18}\text{O}_p$  values across northwestern Europe (i.e., over Ireland and the United Kingdom – UK). The experiment with no Alps (W0E0) predicts an increase in  $\delta^{18}\text{O}_p$  up to 8‰ (not shown) and is similar to the results presented in Botsyun et al. (2020). We do not

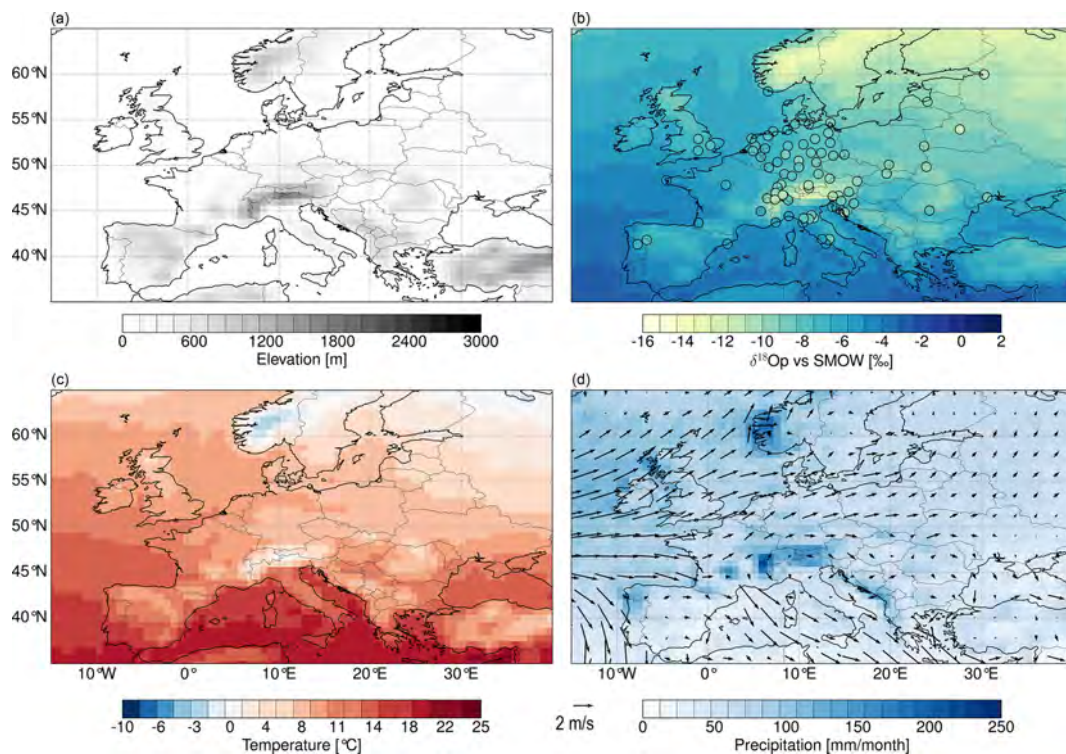


**Figure 1.** Present-day (PD) simulation topography (a) with simulated (shading on map) and observed (circles) annual means of  $\delta^{18}\text{O}_p$  values. Colored circles represent observed  $\delta^{18}\text{O}_p$  values obtained from GNIP stations (b), simulated near-surface temperature (c), and precipitation amount (colored shading) with near-surface wind patterns (arrows: length of arrows indicates wind speed,  $\text{m s}^{-1}$ ) (d).

further discuss this result and refer the reader to Botsyun et al. (2020) for more details. All experiments predict changes in  $\delta^{18}\text{O}_p$  values of 1‰ to 2‰ across Europe independent of direct topographic changes. However, these independent changes are only statistically significant for the W2 experiments. On the annual scale, the predictions show similar patterns, but changes are more localized and reduced in magnitude by  $\sim 2\%$  (Fig. S5).

#### 4.4 Changes in near-surface temperature for the topographic scenarios

The topographic scenarios predict significant localized cooling or warming where the topography is raised or lowered, respectively. The W2E1 experiment predicts a significant decrease of 5 to 12 °C in the Western–Central Alps (Fig. 3b). The W2E0 simulation predicts similar changes in the Western–Central Alps, but with a corresponding increase of  $\sim 5\text{ °C}$  in the Eastern Alps in response to the reduced elevation (Fig. 3d). On the other hand, the W1E2 simulation predicts a significant decrease in near-surface temperature by 2 to 7 °C in the Eastern Alps and shows a slight increase of  $\sim 1\text{ °C}$  over southeastern Europe (Fig. 3e). The W1E0 experiment also estimates an increase of 2 to 5 °C in the Eastern Alps (Fig. 3c). In total, the topographic configurations with a steeper gradient across the Alps (e.g., W2E0

and W1E0) result in a decrease in near-surface temperatures of  $\sim 1\text{ °C}$  in parts of northeastern Europe. The W2E2 configuration (of scenario 2) results in a significant temperature decrease of 5 to 10 °C across the Alps from west to east and shows larger affected low-elevation areas around the Alps (Fig. 3f). Specifically, the changes show a decreasing pattern towards the eastern flank of the Alps. The simulated patterns on the annual scale are very similar to the summer estimates (Fig. S6).

#### 4.5 Changes in precipitation for the topographic scenarios

For all scenarios, an increase in elevation results in an increase in precipitation across the orogen. The W2 experiments of scenario 1 predict more important changes in the orogen and other parts of Europe than the W1 experiments. The W2E1 experiment predicts a significant increase in precipitation of up to  $125\text{ mm month}^{-1}$  across the Alps and a decrease of  $25\text{ mm month}^{-1}$  over eastern and central Europe around the Alps (Fig. 4b). Moreover, the W2E0 experiment predicts an increase of up to  $100\text{ mm month}^{-1}$  in the Western–Central Alps and shows a more widespread decrease in the surrounding regions (Fig. 4d). In contrast, the W1E2 experiment estimates an increase of  $< 80\text{ mm month}^{-1}$  across the Alps from the west, which peaks

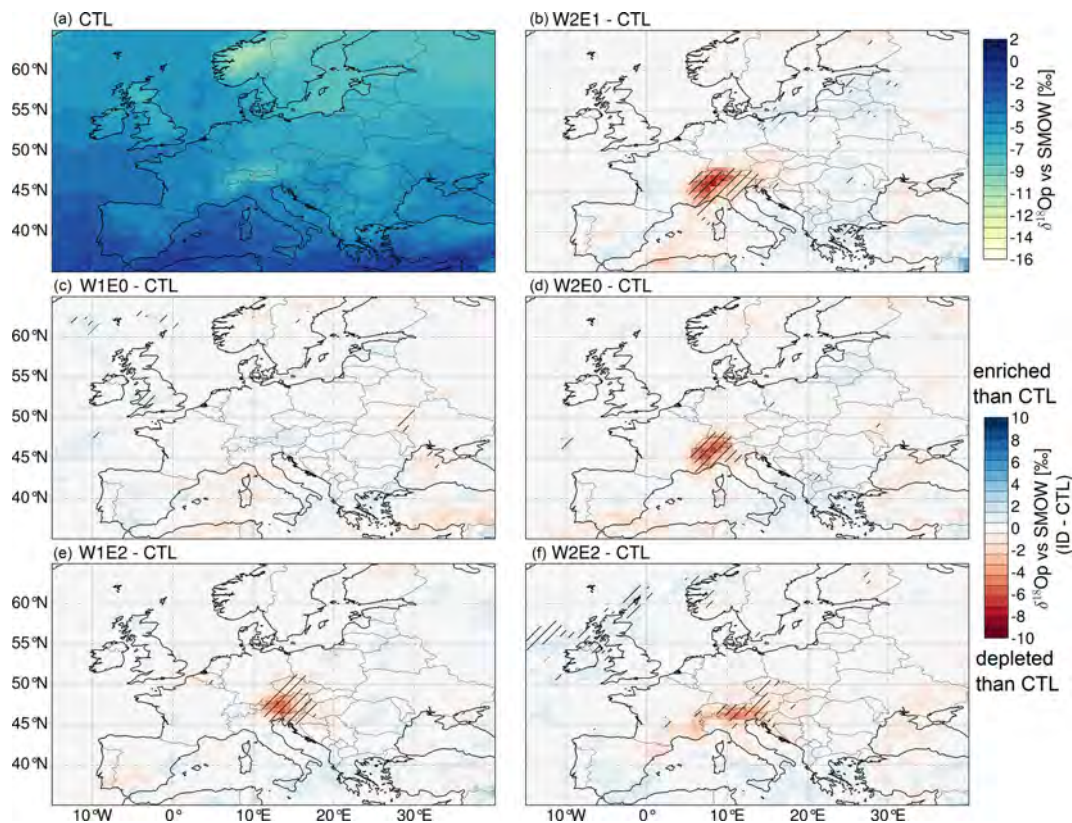


**Figure 2.** Seasonal (JJA) long-term mean of  $\delta^{18}\text{O}_p$  values of the CTL experiment (a) and seasonal (JJA) mean difference of  $\delta^{18}\text{O}_p$  values for the different topography scenarios, i.e., W2E1-CTL (b), W1E0-CTL (c), W2E0-CTL (d), W1E2-CTL (e), and W2E2-CTL (f). Red color ranges represent heavy isotope depletion, and blue color ranges represent an enrichment in heavy isotopes relative to the CTL experiment. Regions that experience changes that are statistically significant, as indicated by a Student's *t*-test analysis with a 95 % confidence level, are marked with black slashed stippling.

in the Eastern Alps (Fig. 4e), and the W1E0 experiment predicts a decrease of  $\sim 25 \text{ mm month}^{-1}$  in the Eastern Alps (Fig. 4c). The W2E2 configuration of scenario 2 results in a significant increase of up to  $125 \text{ mm month}^{-1}$  across the Alps from west to east and a decrease toward northern and eastern Europe (Fig. 4f). However, only precipitation increases in northwestern Russia and northern Europe for experiments W2E1 and W2E0, respectively, are notable and statistically significant changes far from the orogen. Over annual timescales, changes are more localized and restricted to regions with modified topography (Fig. S7).

#### 4.6 Spatial profiles of $\delta^{18}\text{O}_p$ values across the Alps

Spatial mean oxygen isotopic profiles across the Alps in the longitudinal ( $46\text{--}47^\circ \text{ N}$ ) and latitudinal ( $11\text{--}15^\circ \text{ E}$ ) directions reveal varied responses to the different topographic scenarios. Overall, the isotopic profiles show a decrease in  $\delta^{18}\text{O}_p$  values across the Alps from west to east and from south to north. The difference in  $\delta^{18}\text{O}_p$  values along the profiles is estimated to be less than  $-2\text{‰}$  in low-elevation regions adjacent to the mountains and up to  $-8\text{‰}$  between the low-

and high-elevation ( $\Delta\delta^{18}\text{O}_p$ ) regions of the modified topography experiments (Fig. 5). The W1E2, W1E1.5, and W1E0 configurations of scenario 1 result in locally low  $\delta^{18}\text{O}_p$  values down to  $-11\text{‰}$ ,  $-9\text{‰}$ , and  $-6\text{‰}$ , in the Eastern Alps, respectively (Fig. 5a, b). However, the W1 experiments predict no significant changes in the Western–Central Alps and the north–south direction. In contrast, the W2E1 and W2E0 experiments of scenario 1 predict a decrease down to  $-14\text{‰}$  in the Western–Central Alps. The isotopic values gradually increase up to  $-8\text{‰}$  and  $-6\text{‰}$  in the Eastern Alps for W2E1 and W2E0, respectively.

The comparison of the isotopic profiles for scenarios 1 and 2 (i.e., between the diachronous and bulk surface uplift experiments) reveals a significant difference along the strike of the Alps. The differences in response to the topographic forcing of both scenarios are more visible across the Eastern Alps. They are greater by  $-0.5\text{‰}$  to  $-2\text{‰}$  for scenario 2 (Fig. S8a). However, the scenario 2 experiments show less negative  $\delta^{18}\text{O}_p$  values across the Western–Central Alps (Fig. S8b).

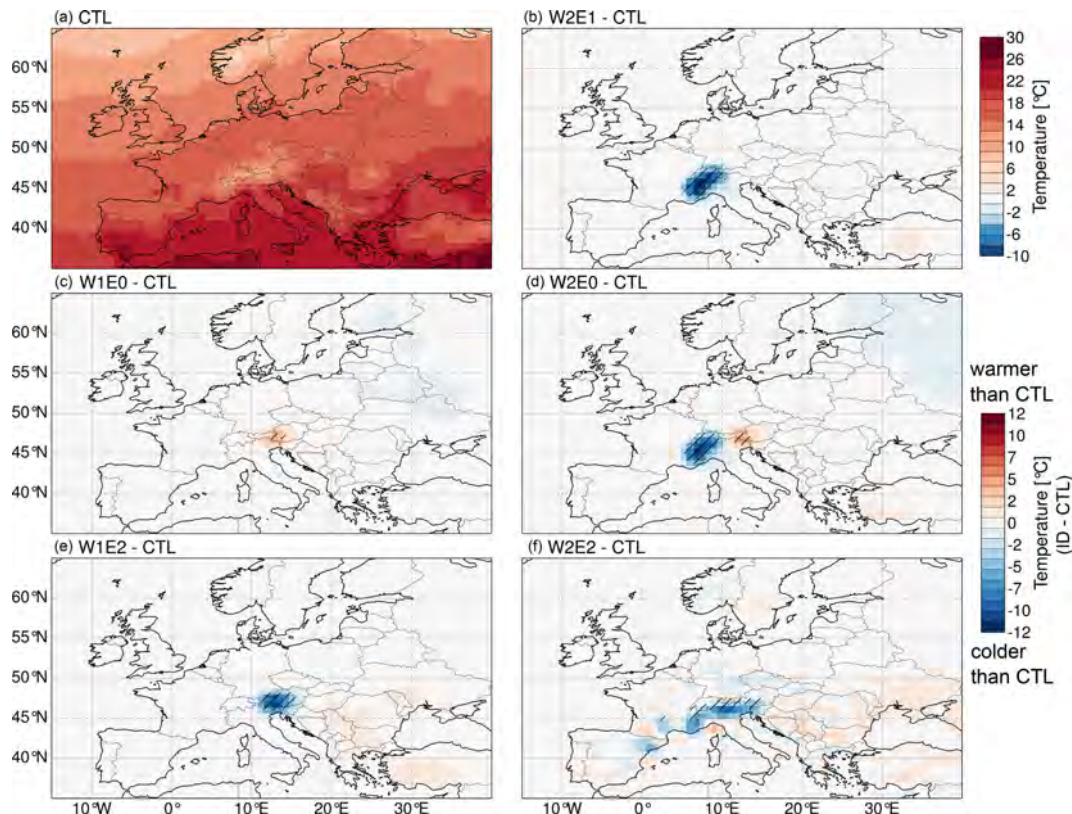


**Figure 3.** Seasonal (JJA) long-term mean of the near-surface temperature of the CTL experiment (a) and seasonal (JJA) mean difference of near-surface temperature for the different topography scenarios, i.e., W2E1-CTL (b), W1E0-CTL (c), W2E0-CTL (d), W1E2-CTL (e), and W2E2-CTL (f). Red color ranges represent warmer temperatures, and blue color ranges represent colder temperatures than in the CTL experiment. Regions that experience changes that are statistically significant, as indicated by a Student's *t*-test analysis with a 95 % confidence level, are marked with black slashed stippling.

#### 4.7 Changes in isotopic lapse rate in response to different scenarios

The isotopic lapse rates (ILRs) estimated for the different geographical windows around the Alps (Fig. 1a) show varied responses to the different topographic configurations. In relation to CTL experiment ILR estimates (i.e.,  $-2.32\text{‰ km}^{-1}$ ,  $-2.18\text{‰ km}^{-1}$ , and  $-3.11\text{‰ km}^{-1}$  with uncertainties ranging from  $0.11\text{‰ km}^{-1}$ – $0.24\text{‰ km}^{-1}$  for the west, north, and south transects, respectively), the W1 experiments predict a decrease in ILRs for the western and southern transects (Fig. 6), and the W2 experiments predict an increase in the west and north transects (Fig. 7). Note that the W1E0 experiment estimates a dampened ILR due to the simultaneous increase in  $\delta^{18}\text{O}_p$  values of the low-elevation areas (i.e.,  $-2.08 (\pm 0.22)\text{‰ km}^{-1}$  for the west,  $-2.01 (\pm 0.14)\text{‰ km}^{-1}$  for the north, and  $-2.17 (\pm 0.13)\text{‰ km}^{-1}$  for the south transect) (Fig. 6). The W1E2 simulation predicts a steeper ILR for the north ( $-2.61 (\pm 0.12)\text{‰ km}^{-1}$ ) and a shallower ILR for the west ( $-1.83 (\pm 0.24)\text{‰ km}^{-1}$ ) and south ( $-2.96 (\pm 0.13)\text{‰ km}^{-1}$ ) transects (Fig. 6). The W2E1 and W2E0 experiments predict

steeper ILRs for both the western ( $-2.78 (\pm 0.15)$  and  $-2.68 (\pm 0.14)\text{‰ km}^{-1}$ ) and northern ( $-3.37 (\pm 0.09)$  and  $-3.22 (\pm 0.09)\text{‰ km}^{-1}$ ) flanks and a dampened ILR for the south ( $-2.91 (\pm 0.13)$  and  $-2.88 (\pm 0.11)\text{‰ km}^{-1}$ ) transect (Fig. 7). On the other hand, the W2E2 experiment estimated a shallower ILR of  $-1.49 (\pm 0.23)\text{‰ km}^{-1}$  for the west and  $-2.39 (\pm 0.16)\text{‰ km}^{-1}$  for the south transect but a steeper ILR of  $-2.59 (\pm 0.14)\text{‰ km}^{-1}$  for the north transect (Fig. 7). The  $r^2$  values associated with the ILRs exceeded 0.85. The estimated ILR changes using annual means are comparable to the patterns of summer means but with generally steeper gradients (see Figs. S9 and S10 in the Supplement).

#### 4.8 Changes in moisture source and transport

The back-trajectory analyses demonstrate that the topographic scenarios have a significant influence on air (and therefore moisture) transport towards target regions on the eastern and southern flanks of the Alps. Therefore, the presentation of results (and the associated discussion in Sect. 5) focuses on regions around the cities of Graz (Fig. 8) and Bologna (Fig. 9), which represent locations in the east and

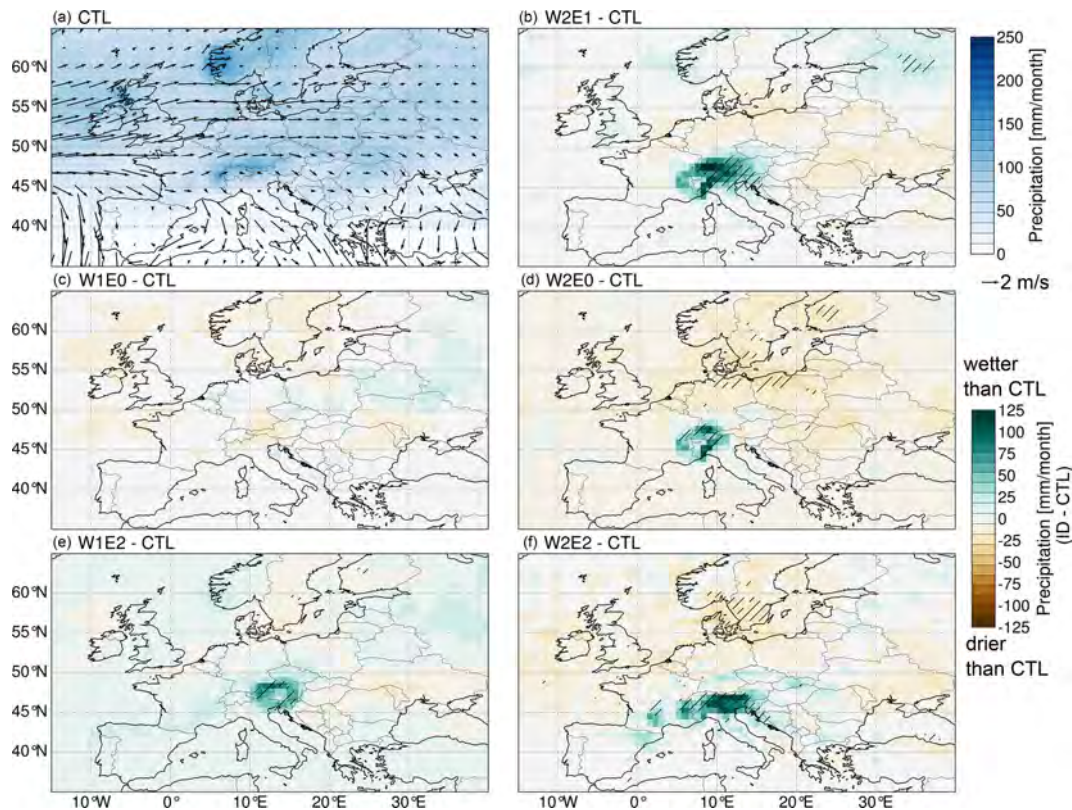


**Figure 4.** Seasonal (JJA) long-term mean of precipitation amount (shading) with near-surface wind patterns (arrows) of the CTL experiment (a) and mean difference of precipitation amount for the different topography scenarios, i.e., W2E1-CTL (b), W1E0-CTL (c), W2E0-CTL (d), W1E2-CTL (e), and W2E2-CTL (f). Green color ranges represent wetter conditions, and brown color ranges represent drier conditions than in the CTL experiment. Regions that experience changes that are statistically significant, as indicated by a Student's *t*-test analysis with a 95 % confidence level, are marked with black slashed stippling.

south, respectively. The reader is referred to the Supplement for the back trajectories for the regions around Lyon (in the west) and Munich (to the north) (Figs. S11 and S12).

Overall, the model tracks most summer air masses back to the North Atlantic and some to a continental moisture source in western Europe, depending on the topography scenario and target location. The W2 experiments of scenario 1 (i.e., W2E1 and W2E0) show moisture ascending over the Western–Central Alps at a higher vertical level before finally descending to the target location in Graz (Fig. 8b, d). Moreover, the W2 experiments also show slight moisture sources from the southern flank of the Alps and predict a shorter moisture transport distance from the North Atlantic relative to the CTL experiment. However, the W1E0 experiment trajectories deviate slightly from the CTL experiment (Fig. 8c). Overall, the W1E2 and W2E2 trajectories toward Graz (Fig. 8e, f) show significant deviations from the CTL trajectories (Fig. 8a). W1E2 and W2E2 backtrack low-level air masses over northwestern Europe, showing a gradual ascent over the Alps towards the east at a shorter distance. However, the W1E2 trajectories show air mass transport at a higher level ( $\sim 700$  hPa) directly from the North Atlantic

to the target region on the east flank of the Alps without any orographic barrier deflection (Fig. 8e).

For the CTL experiment, the air mass transport and distance to the southern location (i.e., Bologna, Fig. 9a) are similar to the results for Graz, but the moisture originates from a higher atmospheric level. The W2 experiments of scenario 1 also predict a significant influence on air mass trajectories to the southern flanks of the Alps. Specifically, the air masses from experiments W2E1 and W2E0 originate from the North Atlantic at a higher atmospheric level ( $\sim 750$  hPa or less) and then divert towards the southeast at the western flank of the Alps before being transported to Bologna (Fig. 9b, d). Moreover, part of the air mass is transported across the Northern Alps and then diverted downwards through the eastern flank to the receptor location in the south. The W2E0 experiment shows a shorter moisture transport distance than the W2E1 trajectories. For the W1 experiments, W1E0 shows no significant difference in moisture transport compared to the CTL trajectories (Fig. 9c). W1E2 predicts a longer moisture transport distance from the North Atlantic at a higher atmospheric level and an ascent over the Alps towards the southern flanks (Fig. 9e). On the other hand, the results from the W2E2 ex-

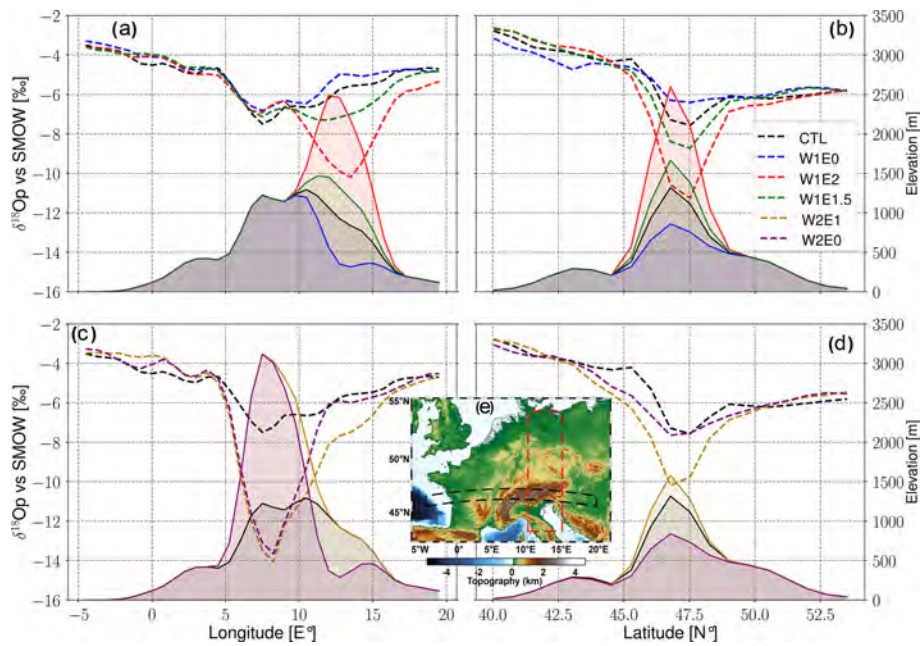


**Figure 5.** Regional seasonal (JJA) means of spatial  $\delta^{18}\text{O}_p$  values across the Alps in the longitudinal (averaged between 46 and 47° N) (a, c) and latitudinal (averaged between 11 and 15° E) (b, d) direction in response to different topographic scenarios (CTL in black, W1E0 in blue, W1E2 in red, W1E1.5 in green, W2E1 in gold, and W2E2 in purple). Colored shading represents topography profiles extracted from the W1 (a, b) and W2 (c, d) scenario 1 experiments. The latitudinal and longitudinal transects are indicated on the original topography used for the topographic modifications (e).

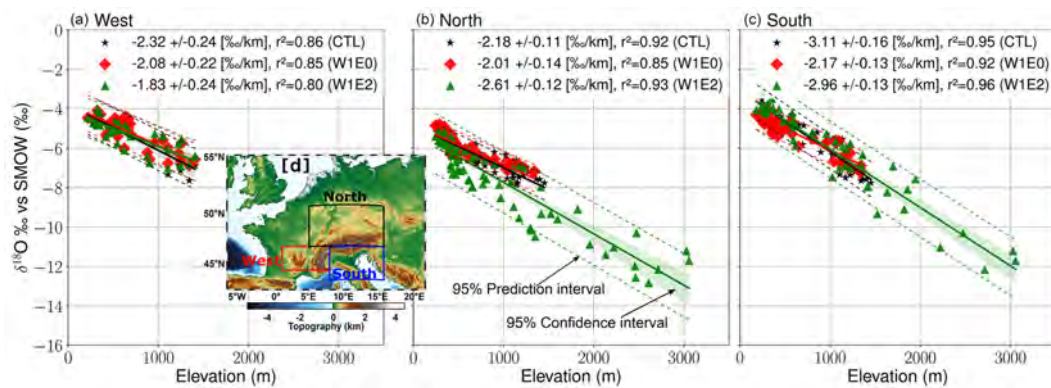


**Figure 6.** Summer isotopic lapse rate (ILR) estimates for the W1 topography scenario (i.e., W1E0 in red, W1E2 in green, and CTL in black) experiments for the different transects around the Alps as shown in panel (d) (west: 44–47° N, 1–8° E; south: 43–47° N, 8–15° E; north: 47–50° N, 5–16° E). The ILRs are estimated as the  $\delta^{18}\text{O}_p$  elevation gradients using linear regression. The lapse rate uncertainties are determined using the 95 % confidence interval around the calculated OLS slope using a  $t$  distribution with  $n - 2$  degrees of freedom where the standard deviation of the slope is the point estimate, the coefficient of determination ( $r^2$ ) is the measure of the fraction of the variability of the  $\delta^{18}\text{O}_p$  values that can be explained by the best-fitted OLS estimates, and the 95 % confidence and prediction intervals around the regression-fitted model highlight the uncertainties around the individual topographic configuration if it was meant to be used to calculate the paleoelevation for reconstructed  $\delta^{18}\text{O}_p$  values.

periment show air masses from western Europe descending towards the south (Fig. 9f). Moreover, the W2E2 experiment also shows some trajectories from the eastern side of the Alps for the calculated 5 d back trajectories. Overall, the target regions at the north and west flanks show fewer significant

changes in air mass transport and source in response to the different topographic forcings (Figs. S11 and S12).

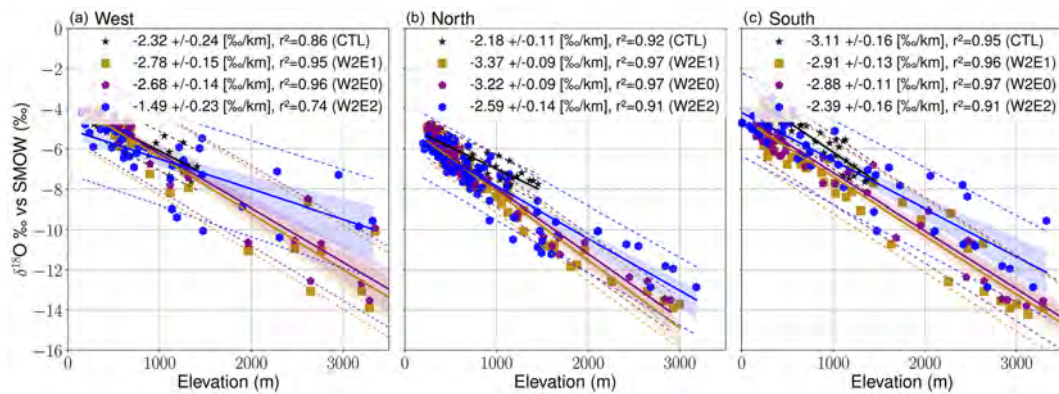


**Figure 7.** Summer isotopic lapse rate (ILR) estimates for the W2 topography scenario (i.e., W2E0 in purple, W2E1 in gold, CTL in black, and W2E2 in blue) experiments for the different transects around the Alps as shown in Fig. 6e (west: 44–47° N, 1–8° E; south: 43–47° N, 8–15° E; north: 47–50° N, 5–16° E). The ILRs are estimated as the  $\delta^{18}\text{O}_p$  elevation gradients using linear regression. The lapse rate uncertainties are determined using the 95 % confidence interval around the calculated OLS slope using a  $t$  distribution with  $n - 2$  degrees of freedom where the standard deviation of the slope is the point estimate, the coefficient of determination ( $r^2$ ) is the measure of the fraction of the variability of the  $\delta^{18}\text{O}_p$  values that can be explained by the best-fitted OLS estimates, and the 95 % confidence and prediction intervals around the regression-fitted model highlight the uncertainties around the individual topographic configuration if it was meant to be used to calculate the paleoelevation for reconstructed  $\delta^{18}\text{O}_p$  values.

#### 4.9 Vertical structure of vertical wind velocity, cloud cover, and relative humidity across the Alps

The vertical cross-sections of the Alps reveal important changes in the tropospheric climate structure in response to the different topographic configurations. The CTL experiment shows negative omega values, indicating wind directions away from the ground, up to the  $\sim 600$  hPa atmospheric level in the Western–Central Alps and positive omega values towards the Eastern Alps (Fig. 10a). These regions of updraft (and subsidence) coincide with regions of high (and low) cloud formation (Fig. 10d). Moreover, the CTL experiment predicts a general decrease in relative humidity from low to high altitude levels (and from west to east) across the Alps but also predicts more humidity near the tropopause (Fig. 10g). Overall, the W1E0 experiment simulates a similar atmospheric structure in the Western–Central Alps (Fig. 10b, e, and h). However, the W1E2 atmospheric structure shows alternating moisture ascent and subsidence across the Alps. More specifically, another area of ascent is introduced over the elevated peak of the Eastern Alps (Fig. 10c). Cloud formation and relative humidity mimic this pattern, with high cloud cover and high relative humidity coinciding with negative omega (Fig. 10e, i). The W2 experiments show a more significant influence on the vertical atmospheric structure than the W1 experiments, especially at the upper-tropospheric levels (Fig. 11). The W2E1 and W2E0 cross-sections show a strong ascent velocity in the Western–Central Alps up to the upper troposphere and low-level subsidence in the Eastern Alps (Fig. 11a, b). A vertically extended region of strong cloud formation and high relative humidity spatially coincides with the area of ascent over the Western–

Central Alps (Fig. 11d, e, g, and h). The high topography in scenario 2 (W2E2) results in an alternating pattern of positive and negative omega values that correspond to topographic troughs and peaks, respectively (Fig. 11c). Ascent (subsidence) spatially coincides with strong (weak) cloud formation and high (low) relative humidity (Fig. 11f, i).

#### 4.10 Changes in atmospheric pressure systems in response to different topographic scenarios

Overall, the different topographic configurations explored in this study impact Northern Hemisphere atmospheric teleconnection patterns. These impacts include geographical shifts and changes in the intensity of quasi-stationary pressure systems (centers of action). The leading mode of atmospheric pressure variability, determined by empirical orthogonal function (EOF) analyses, explains 22 %–35 % of the total pressure variance and is characterized by negative anomalies across Iceland and Greenland, a strong positive anomaly in the midlatitude North Atlantic Ocean near the Azores, and a weak positive anomaly over midlatitude continental Europe. (Fig. 12). These north–south dipole patterns are comparable to the leading mode constructed from ERA5 data (see Fig. S13a in the Supplement). The topographic configurations with high elevation gradients (i.e., W1E0 and W2E0) result in maximum positive anomalies over continental Europe (Fig. 12b, d). The W1E2 experiment shifts the main centers of action of the positive anomaly eastwards by  $\sim 20^\circ$  E and the nodal line of the dipole axis (i.e., the line that separates the positive and negative pressure anomalies) northward by  $\sim 10^\circ$  N (Fig. 12c). W2E1 and W2E2 show two well-defined regions of maximum pressure positive anomalies



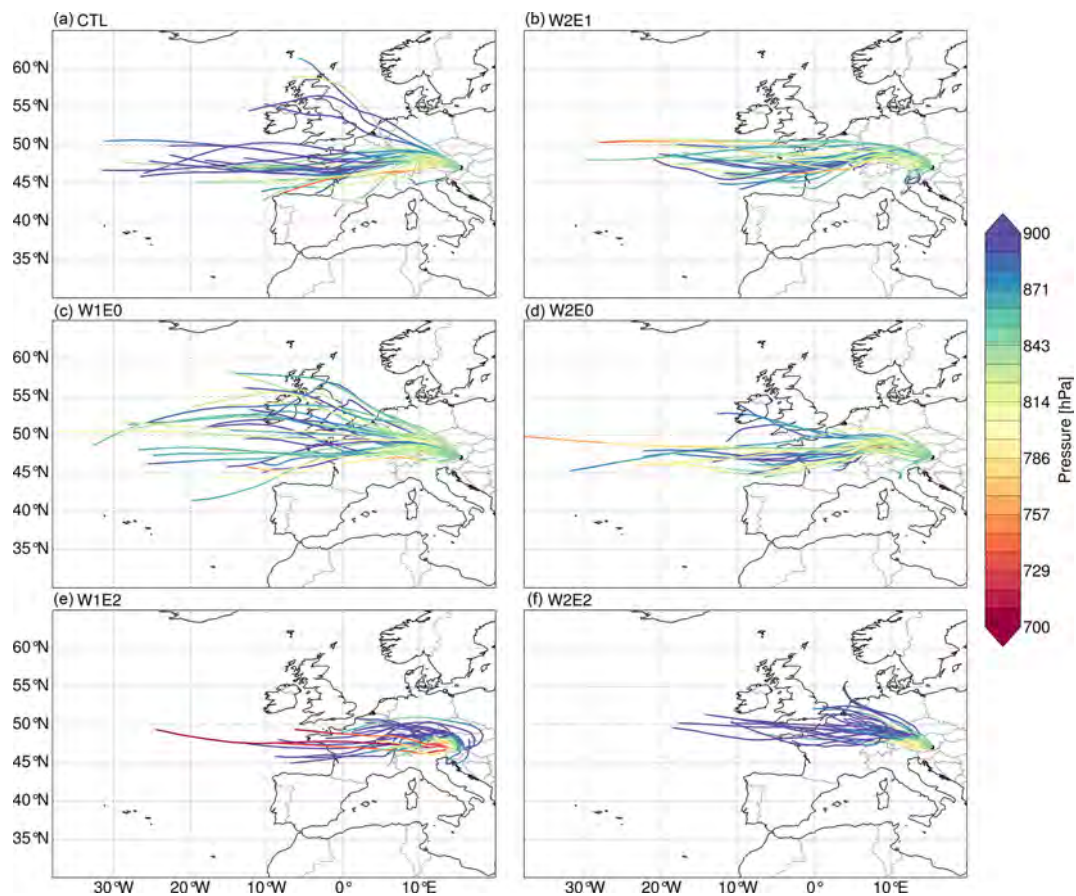


**Figure 8.** 5 d summer back trajectories with the receptor location set to the 850 hPa level above Graz (47.06° N, 15.44° E). The colored lines represent the vertical pressure level of the trajectories. The trajectories were estimated with the 6 h wind fields (i.e.,  $u$ ,  $v$ , and  $\omega$ ) from the topographic experiments using the LAGRANTO tool.

over the North Atlantic and northeastern Europe (Fig. 12e, f). In summary, topographic configurations with high topography in the Western–Central Alps (i.e., W1E0, W2E0, W2E1) result in an intensification of positive anomalies over continental Europe, while experiments forced with higher topography in the Eastern Alps (i.e., W1E2) shift the maximum positive anomalies region to the eastern Atlantic (Fig. 12c).

The pressure systems with the second mode of variability show a monopole pattern of positive anomalies spread across northern ( $> 50^\circ$  N) Europe for most of the topographic configurations. This is comparable to the second EOF pattern extracted from ERA5 data (Fig. S13b). The CTL experiment shows two well-defined regions of maximum positive anomalies over the North Atlantic, western Russia, and the Baltic states (Fig. 13a). The W1E0 simulation predicts a similar spatial pattern as the CTL experiment but intensifies the eastern anomaly (Fig. 13b). The W1E2 and W2E0 configurations significantly intensify the positive anomalies over the eastern Atlantic (Fig. 13c, d). The W2E1 and W2E2 experiments predict a slight ( $\sim 5^\circ$ ) northward shift of the band of positive anomalies over the eastern Atlantic Ocean and west-

ern Europe. Additionally, the W2E2 experiment also results in a northward shift of positive anomalies in eastern Europe. The spatial patterns of the third and fourth EOFs are similar to the ERA5 patterns but are not as clearly defined or sensitive to changes in topographic forcing (Figs. S14 and S15).

## 5 Discussion

In the following sections, the impacts of diachronous surface uplift on regional climate (e.g., near-surface temperature, precipitation dynamics, moisture transport, low-level circulation patterns) and their implications for  $\delta^{18}\text{O}_p$  values and isotopic lapse rates (ILRs) are discussed. While the  $\delta^{18}\text{O}_p$  response is created by the combined effects of all the climate variables previously discussed, we discuss the individual impacts to disentangle the total signal and explain plausible processes for each signal component. Finally, we highlight the study's limitations and implications for stable isotope paleoaltimetry across the Alps (Sect. 5.6 and 5.7).

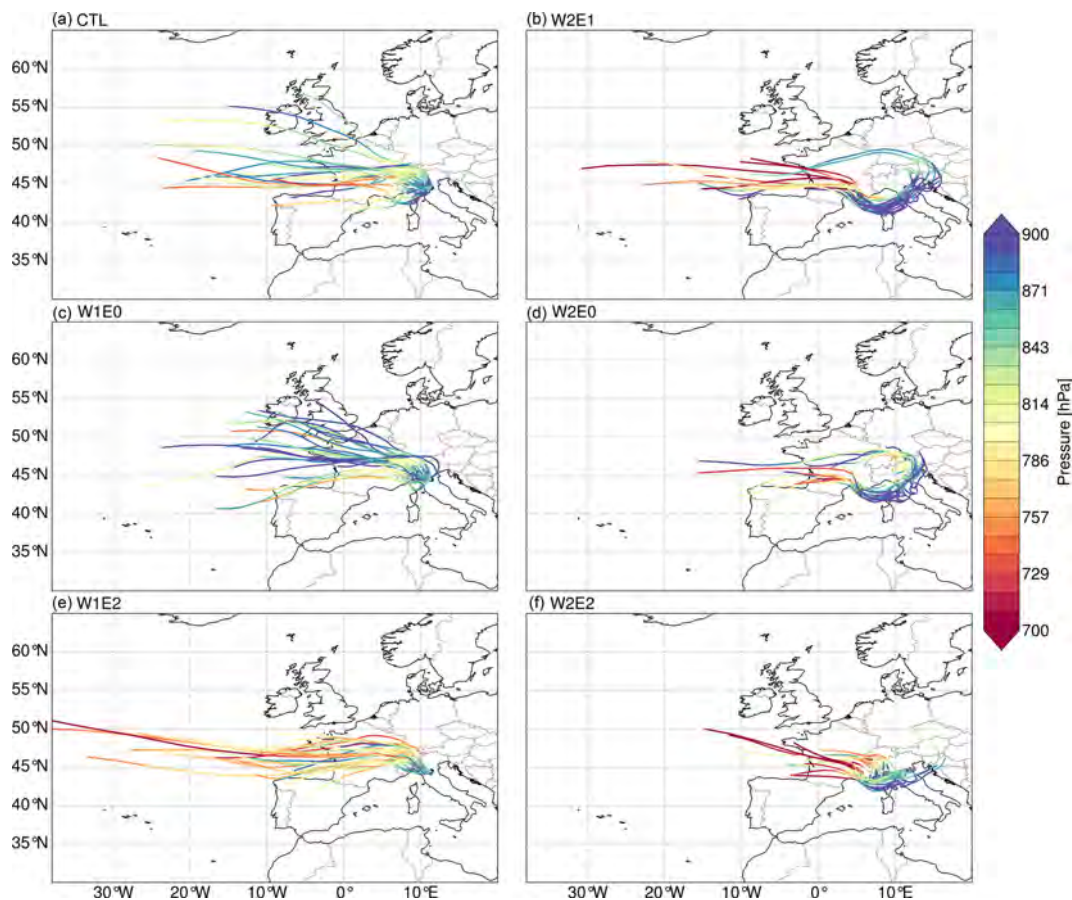


**Figure 9.** 5 d summer back trajectories with the receptor location set to the 850 hPa level above Bologna (44.49° N, 11.38° E). The colored lines represent the vertical pressure level of the trajectories. The trajectories were estimated with the 6 h wind fields (i.e.,  $u$ ,  $v$ , and  $\omega$ ) from the topographic experiments using the LAGRANTO tool.

### 5.1 Impacts of diachronous surface uplift on near-surface temperatures

The topography sensitivity experiments show significant localized changes in the near-surface temperature. For all topographic configurations, maximum changes were estimated for regions of modified topography, while changes in regions farther from the orogen are less pronounced. The less pronounced regional changes farther from the modified topography areas might be due to associated large-scale atmospheric changes and therefore caused by a non-adiabatic mechanism. However, these small and insignificant temperature differences may simply be due to modeling artifacts. On the other hand, the significant changes in regions of modified topography can mainly be attributed to the adiabatic temperature lapse rate, which defines how temperature changes with altitude. Although previous studies have indicated the possibility of non-adiabatic mechanisms (e.g., changes in tropospheric dynamics, local atmospheric humidity, and atmospheric circulation patterns) contributing to changes in addition to the adiabatic lapse rate changes (Ehlers and Poulsen, 2009; Feng and Poulsen, 2016; Kattel et al., 2015), an in-

depth quantification of the relative contributions would be required to confidently attribute the changes to non-adiabatic processes.

### 5.2 Impacts of diachronous surface uplift on precipitation

Topography affects the environment in which precipitation occurs in response to thermodynamic and atmospheric dynamics changes (Beniston, 2005; Houze, 2012; Insel et al., 2010; Poulsen et al., 2010). Our results indicate a systematic increase in precipitation amount in response to surface uplift due to orographic airlifting and associated cloud formation and condensation. For instance, the high-elevation scenarios on the Western–Central Alps focus precipitation on the western flank of the Alps and show a decreasing trend towards the Eastern Alps. Moreover, our results also show a threshold of the magnitude of elevation change (i.e., ca. 200 % of modern topography increase) that triggers significant regional changes across Europe. More specifically, our W2 experiments of scenario 1 show significant changes

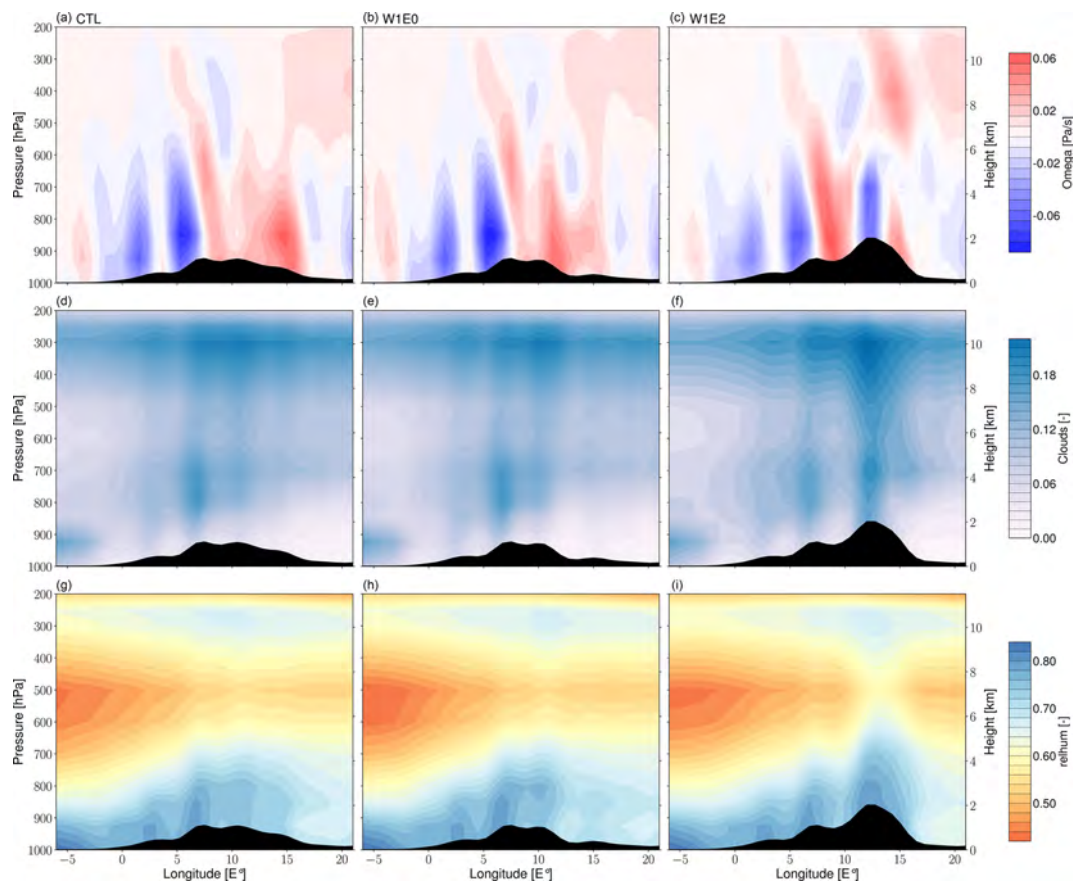


**Figure 10.** Seasonal (JJA) means of vertical wind velocity ( $\omega$ ) (a–c), cloud cover (d–f), and relative humidity (g–i) averaged between 45 and 48° N across the Alps for the W1 (i.e., W1E0, W1E2) and CTL experiments. The black shading represents the cross-section of topography for each scenario. The  $\omega$  values represent the speed of air motion in the upward or downward direction. Since vertical pressure decreases with height, negative values indicate upward or ascent velocity, and positive values indicate downward or subsidence velocity.

(drier conditions) across northern Europe and an extension of a rain shadow region on the eastern flanks of the Alps, whereas changes in the W1 experiments are comparatively mild. These spatial patterns are expected since the rainout on the western flanks of the Alps extracts moisture from the vapor masses on the windward slopes and leads to drier air masses crossing to the northern and eastern flanks of the Alps. The Alps are a relatively small orogen, positioned parallel to moisture transport, which should lead to more moist air mass spill-over and flow around the Alps to the east and less distinct changes in precipitation amount (Sturm et al., 2010). Nevertheless, our calculations of vertical wind velocities ( $\omega$ ), relative humidity, and cloud cover (Figs. 10 and 11) suggest that our uplift scenarios induce enough orographic lifting to create notable updrafts that lead to the formation of thick clouds in the troposphere (Houze, 2012). The higher along-strike terrain created by bulk surface uplift in the W2E2 experiment even results in a clearly defined  $\sim 500$  km wavelength pattern of interchanging moisture uplift and subsidence, which corresponds to high and low cloud

cover and relative humidity (Fig. 11c, f, and i). Note that the local precipitation changes induced by varying the topography of the Eastern Alps are very different from those induced by varying the topography of the Western–Central Alps (e.g., Fig. 4e vs. Fig. 4b). In summary, due to the size and orientation of the Alpine orogen with respect to the dominant wind fields, the regional precipitation response to diachronous surface uplift is unique and highly sensitive to the altitude of the Western–Central Alps in particular.

### 5.3 Impacts of diachronous surface uplift on moisture source and transport

The back-trajectory analyses for the topography experiments reveal notable changes in air mass transport distance and pathways even though the predominant moisture source remains the North Atlantic Ocean (Rozanski et al., 1982). Our simulations demonstrate that diachronous surface uplift impacts the target regions located on the southern and eastern flanks of the Alps in particular compared to western and

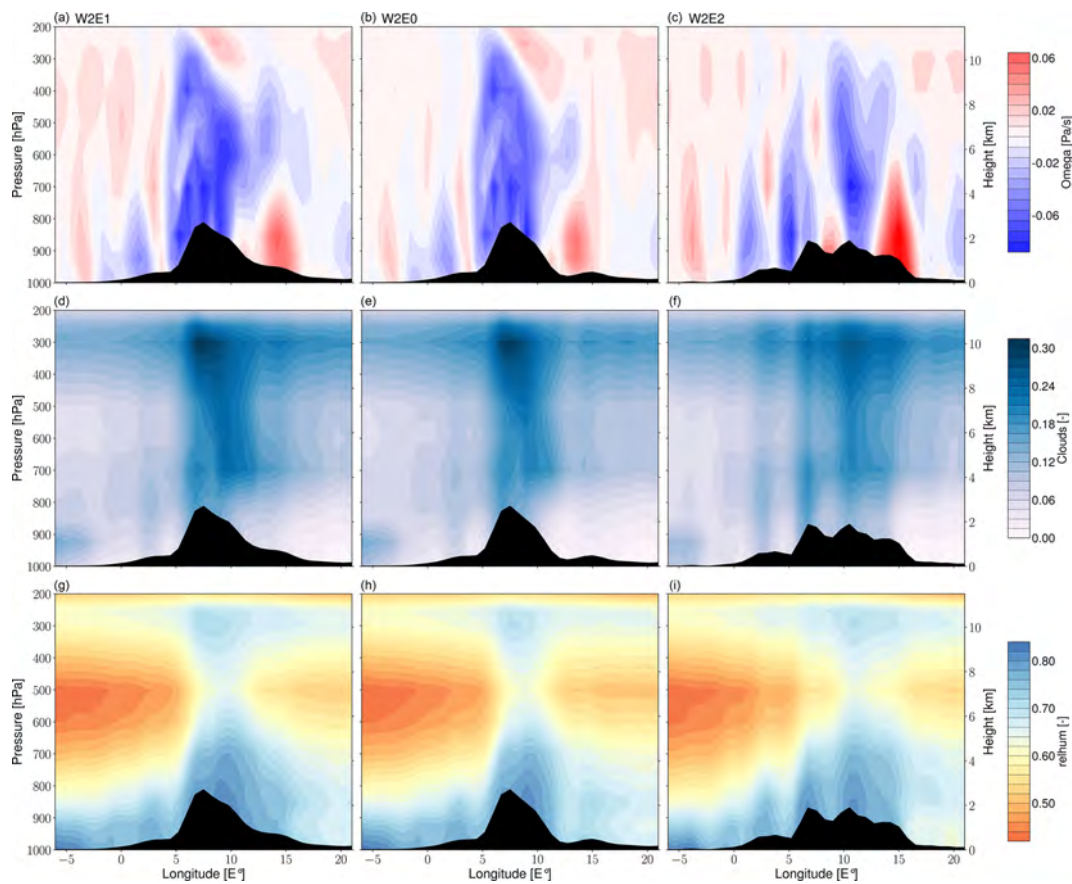


**Figure 11.** Seasonal (JJA) means of vertical wind velocity (omega) (a–c), cloud cover (d–f), and relative humidity (g–i) averaged between 45 and 48° N across the Alps for W2 of scenario 1 (i.e., W2E1, W2E1), scenario 2 (i.e., W2E2), and CTL experiments. The black shading represents the cross-section of topography for each scenario. The omega values represent the speed of air motion in the upward or downward direction. Since vertical pressure decreases with height, negative values indicate upward or ascent velocity, and positive values indicate downward or subsidence velocity.

northern localities. More specifically, the air mass trajectories towards the eastern flank of the Alps tend to travel a shorter distance when the topography of the Eastern Alps is higher (Fig. 8e, f) but travel a longer distance towards the southern flank (Fig. 9e). On the other hand, the trajectories towards the eastern flank originate from higher atmospheric levels when the surface topography of the Western–Central Alps is raised due to the increased orographic barrier but with slight changes in transport distance. For example, our trajectory analysis for the city of Graz in the W2 experiments (i.e., W2E1 and W2E0) indicates that moisture originates at higher atmospheric levels over the east of the North Atlantic and travels a shorter path to its destination (Fig. 8b, d). On the other hand, the W1E2 and W2E2 configurations significantly shorten the moisture transport distance and originate from lower altitudes (Fig. 8e, f). This indicates that the air mass would most likely experience less rainout due to the shorter period to reach condensation, yielding slightly higher  $\delta^{18}\text{O}_p$  values compared to long-distance air mass transport. Furthermore, the W2 experiments deflect moisture from the

Atlantic to the Mediterranean region before redirecting it to the Southern Alps. These changes in vapor transport are not surprising since mountain barriers would force the air to rise, and, depending on the strength of the flow, the cross-barrier flow would be blocked or deflected towards the regions of precipitation (Colle, 2004; Grossman and Durran, 1984). The atmospheric conditions of the moisture source region would also influence the precipitation type and amount in the target regions (Feng et al., 2013). Therefore, our results stress the importance of considering the unique impacts of different topographic configurations on the moisture source and pathways when investigating past changes in precipitation (or  $\delta^{18}\text{O}_p$ ).

#### 5.4 Impacts of the diachronous surface uplift on atmospheric flow and pressure systems

Atmospheric teleconnections control much of the synoptic-scale atmospheric variability that is also important for the climate in mountain ranges (Barnston and Livezey, 1987;

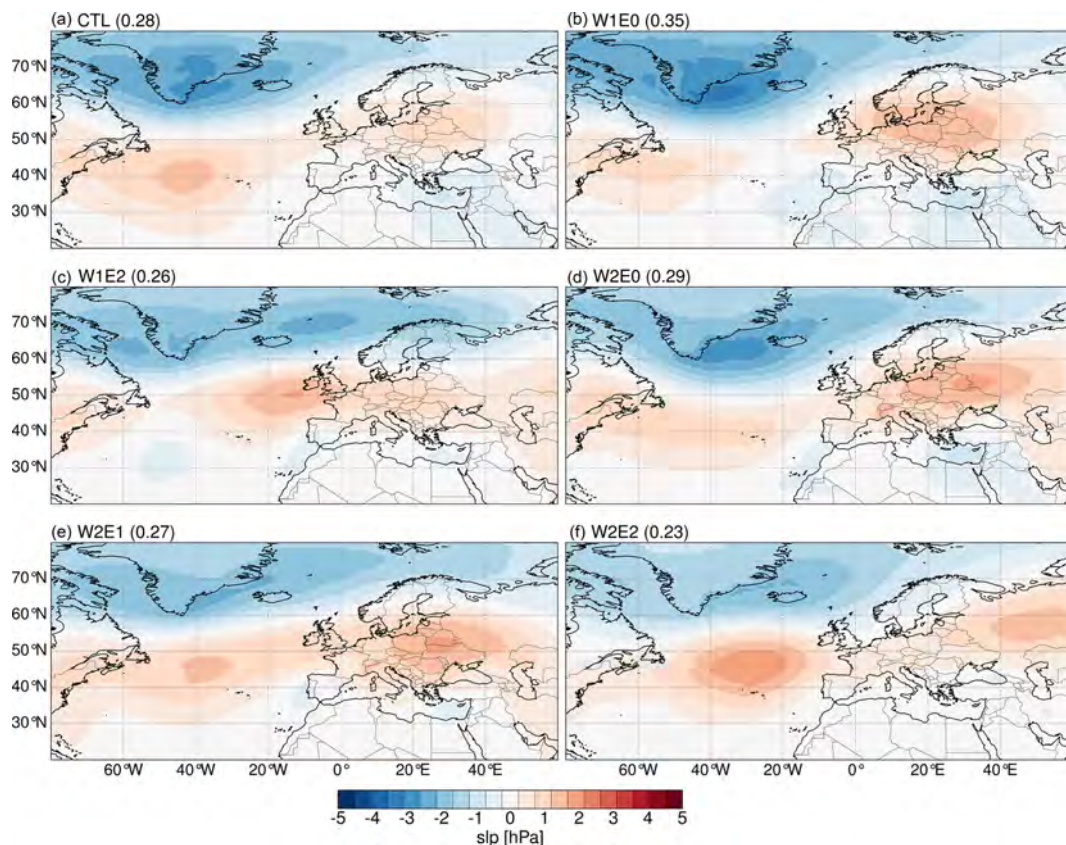


**Figure 12.** The spatial patterns and explained variance of the first empirical orthogonal function (EOF) extracted from the topography experiments. These resemble the leading mode of variability extracted from the ERA5 data (see Fig. S13 in the Supplement) and the patterns associated with the North Atlantic Oscillation. The patterns are calculated from summer mean sea level pressure (slp) anomalies and represent the covariance matrix of the principal component time series and the EOFs.

Rogers, 1990; Wallace and Gutzler, 1981). These patterns influence climate over a large geographic area and affect processes such as precipitation dynamics, storm tracks, jet stream location, atmospheric waves, and temperature (Hurrell, 1995; Woollings et al., 2010). Giorgi et al. (1997) indicate that altitude plays a significant role in determining the regional climate response to large-scale patterns like the North Atlantic Oscillation (NAO). Moreover, Wallace and Gutzler (1981) suggest that the high-pressure anomalies that persisted across the Alps during the 1980s were due to shifting of the upper-level jet stream (i.e., the north–south dipole axis associated with the polar front) to the north. Therefore, the nonstationarity of these recurrent pressure patterns (especially in summer) (Deininger et al., 2016) requires that any attempt to reconstruct past hydrological cycles quantitatively be done with knowledge about the potential changes in atmospheric pressure patterns.

Our simulation results indicate a persistent leading mode of variability that is consistent with the NAO (Fig. 12) (Hurrell, 1995; Hurrell and Van Loon, 1997). The modern (non-simulated) NAO exists in all seasons (Craig and Allan, 2022) but is more prominent and stable in winter. A well-developed

dipole pressure gradient between the Icelandic Low and Azores High in its positive phase induces strong westerlies and northerly storm tracks that transport air masses from the eastern Atlantic towards central Europe. Such a pressure system drives colder and drier conditions across western Greenland and the Mediterranean region and warmer and wetter conditions across northern Europe and some portions of the Scandinavia region. During its negative phase, the pressure gradient is reduced, which causes a decrease in the strength of the westerlies and a southward shift of the storm tracks. This mechanism leads to more precipitation across southern Europe and the Mediterranean and colder and drier climates across northern Europe (Barnston and Livezey, 1987; Hurrell and Van Loon, 1997). Overall, our topography experiments suggest a northeastward shift of the positive anomaly center of the action close to Ireland and the UK when the Eastern Alps (W1E2) are uplifted and more eastward stretch with intensification across eastern Europe when the Western–Central Alps are at a maximum elevation (e.g., W2E1). The shifts of the NAO dipole axis, intensification, and location of the center of action in response to topography changes would alter the moisture and heat transport pathways, wind pat-

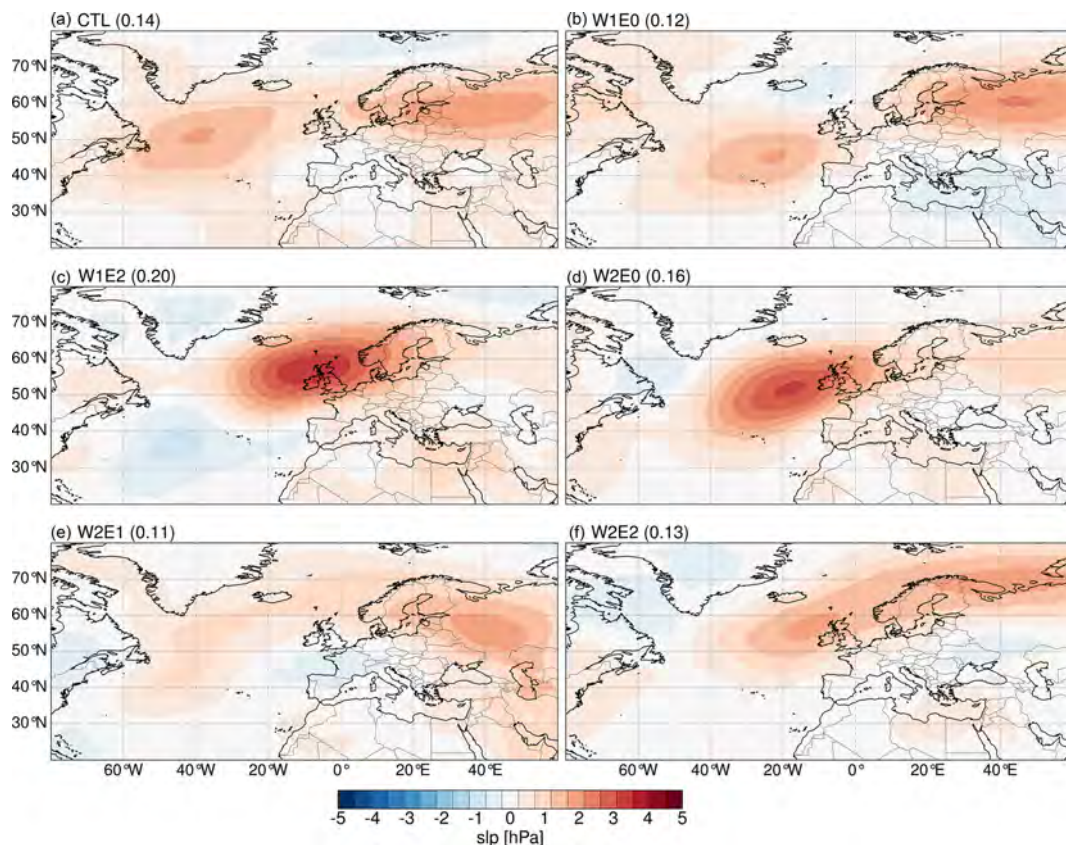


**Figure 13.** The spatial patterns and explained variance of the empirical orthogonal functions (EOFs) that resemble the second mode of variability extracted from the ERA5 data (see Fig. S13 in the Supplement). The patterns are calculated from summer mean sea level pressure (slp) anomalies and represent the covariance matrix of the principal component time series and the EOFs.

terns, and the intensity of storms and precipitation patterns across the North Atlantic and its surrounding continents. For instance, the eastward shift and intensification of the positive anomalies over central Europe in response to higher topography in the Western–Central Alps would likely lead to a reduction of rainfall across the central and southern parts of Europe due to the northward flow of moisture.

The pressure patterns of the second mode of variability in response to the topography changes resemble the East Atlantic (EA) pattern, as originally identified by Wallace and Gutzler (1981). The exact nature of the EA pattern is still debated. While some studies define it as a southward shift of the NAO, showing the north–south dipole pressure gradient with centers of action across the North Atlantic from east to west (Bastos et al., 2016; Chafik et al., 2017), others define it as a well-defined monopole pressure anomaly close to Ireland (Comas-Bru and McDermott, 2014; Josey and Marsh, 2005; Moore et al., 2013; Zubiare et al., 2017). Our simulated pattern matches the latter description best. Such a pattern would lead to wetter conditions across eastern Europe and a drier climate over western Europe (Barnston and Livezey, 1987). The E0 configurations (Fig. 13b, d) result in the most significant changes to the second mode of variability, which high-

lights the potentially significant impact of delayed Eastern Alps uplift on atmospheric pressure patterns and associated changes in precipitation across Europe. An example of such an influence on precipitation is the extensive drying across eastern Europe in response to the W2E0 topography configuration (Fig. 4d)

The second and third modes of variability show some similarity to the Scandinavian (SCAN) pattern and the East Atlantic–Western Russia (EA/WR) pattern as described in other studies (Barnston and Livezey, 1987; Comas-Bru and McDermott, 2014; Ionita, 2014; Lim, 2015). The simulated patterns do not show any clear trends or large and systematic changes in response to the different topographic forcings.

In summary, our results suggest that different topographic configurations, including those describing diachronous surface uplift, can induce significant changes to synoptic-scale atmospheric pressure systems in the Northern Hemisphere. Quantifying the impacts of these changes on regional climate would require an in-depth investigation of atmospheric dynamics and scale interactions in the region and is beyond the scope of this study. Our results highlight plausible changes in atmospheric pressure patterns that would significantly affect the spatial distribution of precipitation across Europe

and change the source region and pathways for moisture carried onto the continent. However, we acknowledge that changes in such a decadal mode of variability would not be reflected in such low-resolution geologic archives used for stable isotope paleoaltimetry. Nevertheless, assessing the role of topography in changing the atmospheric dynamics of such large-scale circulation patterns sheds light on the possibility of its impact on the spatial variability and distribution of  $\delta^{18}\text{O}_p$ . For instance, this has been highlighted by Methner et al. (2020) regarding the possibility of the reorganization of the midlatitude atmospheric circulation in the middle Miocene that led to seasonal changes in the timing of carbonate formation across central Europe.

### 5.5 Impact of regional climate changes on $\delta^{18}\text{O}_p$ and isotopic lapse rates

The sensitivity experiments show that the topographic configurations describing diachronous surface uplift (scenario 1) affect  $\delta^{18}\text{O}_p$  values across the Alps. Specifically, the W2 experiments predict a decrease in  $\delta^{18}\text{O}_p$  values of  $\sim 8\%$  on the western flanks of the Alps and a less significant change of  $\sim 1\%$  to  $2\%$  in the adjacent low-elevation regions around the Alps (Fig. 2). Moreover, the simulations predict an expansion of the area of low  $\delta^{18}\text{O}_p$  values (adjacent to the western side of the orogen) when a high elevation (W2) is assumed for the Western–Central Alps (or the complete orogen). This is not surprising since the predominant moisture transport from west to east would be blocked or deflected by the steeper topography, creating an “isotopic rain shadow.” In contrast, the moderate (present-day) height allows more spill-over of moisture over and around the Western Alps, especially since the Alps are positioned parallel to wind trajectories (Sturm et al., 2010). The decrease in  $\delta^{18}\text{O}_p$  values over the Northern Alps, on the other hand, could be a result of the cross-over flow of moisture transported from the Mediterranean Sea. However, our trajectory analysis did not indicate a plausible moisture source from the Mediterranean in summer, which might be due to the limited model resolution to capture all the relevant air mass sources. Nevertheless, the Late Cretaceous to Paleogene closure of the Tethys Ocean, which led to the surface uplift of the Alps, might have influenced the transport of moisture from the Mediterranean in a past climate. Botsyun et al. (2022) simulate the global climate with middle Miocene paleoenvironment conditions while considering the Paratethys Sea extent in their land–sea mask to determine the impacts of the marine transgression on the regional climate. Their results indicate an increase in precipitation up to  $400\text{ mm yr}^{-1}$  around the regions adjacent to the Paratethys Sea with anticyclonic circulation situated over the Mediterranean in the winter season. Note, however, that a fully coupled ocean–atmosphere GCM would be needed for a realistic assessment of the contribution of ocean circulation to the distribution of  $\delta^{18}\text{O}_p$  patterns across Europe.

In general, the modeled differences in  $\delta^{18}\text{O}_p$  values in response to changes in topography can be attributed to changes in orographic precipitation and adiabatic-lapse-rate-driven near-surface temperature. These can, in turn, be explained by direct altitude-related differences between our topographic scenarios, as well as by indirect effects related to changes in the wind trajectories, changes in the vertical tropospheric structure in an orogen located in a westerlies-dominated wind field, and changes in synoptic-scale atmospheric dynamics (Sect. 5.1–5.4). These changes differ significantly between the topographic configurations and ultimately result in different ILRs. More specifically, the annual ILRs are more negative (steeper) than the summer ILRs (Figs. S9 and S10). These changes in ILRs are likely due to two effects: (1) the increase in isotopic fractionation with decreasing temperature (Dansgaard, 1964; Gat, 1996) affects the winter (and thus the annual) ILR, and (2) evaporative recycling of warmer surface waters in the summer leads to a different isotopic composition of the continental moisture source (Risi et al., 2013).

Overall, this study’s experiments outline the fact that diachronous surface uplift (i.e., the west-to-east surface uplift propagation) across the Alps would have produced distinct spatial profiles of  $\delta^{18}\text{O}_p$  due to both direct (altitudinal) and indirect climatic effects. If the magnitude of change in  $\delta^{18}\text{O}_p$  values presented here for different topographic scenarios is preserved in geologic archives such as paleosol carbonate nodules or hydrous silicates, then the stable isotope record of these changes holds the potential to reconstruct the hypothesized diachronous surface uplift history of the Alps. We highlight that a magnitude of  $\Delta\delta^{18}\text{O}_p$  value of  $-8\%$ , which is significant enough to be preserved in geologic archives, would only be achieved when the mean topography is higher than the modern Alps. Furthermore, our results suggest that the ILR, which for the lack of tracking it through time is often assumed to be constant in stable isotope paleoaltimetry studies, may change across the Alps depending on the specific topographic configuration. For instance, the W2E1 topographic configuration, which best matches the paleoelevation reconstruction in the middle Miocene by Krsnik et al. (2021), would correspond to an increase of  $0.46 (\pm 0.15\text{--}0.24)$  and  $1.19 (\pm 0.09\text{--}0.11)\%$   $\text{km}^{-1}$  across the western and northern flanks (Fig. 7a, b) compared to present-day topography. However, the estimated difference between W2E1 and the CTL across the southern flank is  $0.2 (\pm 0.13\text{--}0.16)\%$   $\text{km}^{-1}$  (Fig. 7c). This indicates that the impact on the isotopic lapse rate changes depends on the topographic rise and configuration, as well as the transect considered. In this scenario, the northern transect lapse rates estimate a higher magnitude of change in lapse rate since the higher topography established across the Western–Central Alps redistributes precipitation due to the orographic barrier to the moisture trajectory paths from the North Atlantic, which cause dryness toward the north (Fig. 4b).

## 5.6 Model limitations and implications

The modeled present-day climate conditions are in good agreement with observational data and the expected climate patterns across Europe, as also indicated by other studies (Langebroek et al., 2011; Werner et al., 2011). The slight deviations across the Alps are likely a result of the model's underrepresentation of the subgrid topographic features (e.g., ridges and slopes in the Alps). Nevertheless, the reader should carefully consider further limitations of the model and this study. ECHAM5-wiso, like other GCMs, has several deficiencies in parameterization schemes and simplifications of the underlying physics (Roeckner et al., 2003; Werner et al., 2011). Most importantly for this study, the model simplifies complex topography by smoothing high-elevation peaks, which leads to an underestimation of  $\delta^{18}\text{O}_p$  values at higher elevations. Furthermore, it uses the hydrostatic approximation, which generally results in a relatively poor representation of precipitation dynamics in mountain regions with steep topographic gradients (e.g., Steppeler et al. 2003). On top of that, ECHAM5-wiso does not simulate the oceanic variables dynamically but uses prescribed sea surface temperatures (SSTs) and sea ice concentrations (SICs) from a coupled ocean–atmosphere GCM, which complicates our EOF analysis to construct the atmospheric teleconnections. The model underestimates summer precipitation across the European Alps due to the parameterization of convective processes that contribute to summer rainfall (Langbroeck et al., 2011). Moreover, ECHAM5-wiso has a simple land surface scheme that does not allow for proper consideration of the isotopic fractionation of surface waters (Werner et al., 2011). Since water vapor from evaporative recycling of surface waters and evapotranspiration influence the  $\delta^{18}\text{O}_p$  values across Europe (Rozanski et al., 1982), the reader is advised to consider this limitation when applying our model results. Furthermore, we note that the trajectory analyses of this study track air masses by disregarding their moisture content. Therefore, changes in air mass trajectories do not inherently lead to significant changes in  $\delta^{18}\text{O}_p$  if, for example, all changes in atmospheric transport only affect air masses that are moisture-depleted. The reader is also made aware that this study uses fixed pre-industrial paleoenvironmental boundary conditions for the GCM topographic sensitivity experiments to isolate the topography-related  $\delta^{18}\text{O}_p$  signal of simplified diachronous surface uplift scenarios for the Alps. The reader is advised that these conditions do not represent the realistic global paleoclimate condition of the time of the Cenozoic major surface uplift, which is why we refer to our results as a sensitivity analysis of potential signals. However, despite these limitations, the results of this sensitivity analysis indicate good potential for detecting and reconstructing a diachronous elevation history in the Alps. Given this, future time-intensive efforts such as stable-isotope-based paleoaltimetry data collection and more paleogeographically realis-

tic GCM studies are considered likely to be worthy endeavors.

## 5.7 Implications for paleoaltimetry reconstructions and hypothesis evaluation

Stable isotope paleoaltimetry exploits the systematic relationship between  $\delta^{18}\text{O}_p$  and elevation to infer past elevation across orogens (e.g., Chamberlain et al., 1999; Kohn and Dettman, 2007; Mulch, 2016; Quade et al., 2007; Rowley and Garzzone, 2007; Sharp et al., 2005). The present-day  $\delta^{18}\text{O}_p$  lapse rate in the Central Alps is  $\sim 0.2\text{‰} 100\text{ m}^{-1}$  (Campani et al., 2012). The present study estimates a similar range of  $\delta^{18}\text{O}_p$  lapse rates across the western and northern flanks of the Alps for present-day topography conditions ( $-0.23\text{‰} 100\text{ m}^{-1}$  and  $-0.22\text{‰} 100\text{ m}^{-1}$ , respectively) and a higher value ( $-0.31\text{‰} 100\text{ m}^{-1}$ ) for the southern flanks (Fig. 6). The W2E1 scenario is the closest to a plausible, albeit very simplified, scenario for the Miocene since the Alps are suggested to have reached their maximum peaks during that period. The simulation for this topography scenario estimates  $\delta^{18}\text{O}_p$  lapse rates of  $-0.28\text{‰} 100\text{ m}^{-1}$ ,  $0.34\text{‰} 100\text{ m}^{-1}$ , and  $-0.29\text{‰} 100\text{ m}^{-1}$  for the west, north, and south transects, respectively (Fig. 7). These results differ from our predictions of lapse rates produced by bulk surface uplift experiments (i.e., W2E2). In other words, the diachronous surface uplift of the Western–Central and Eastern Alps (scenario 1) creates distinct isotopic patterns that differ from those produced by the control simulation (CTL) or the bulk surface uplift (scenario 2) experiments. We can therefore accept our hypotheses that (1) different topographic configurations for the Eastern and Western–Central Alps result in regional climates and spatial distributions of  $\delta^{18}\text{O}_p$  that are significantly different from those of today and that (2) different topographic configurations for the Eastern and Western–Central Alps result in regional climate and spatial distributions of  $\delta^{18}\text{O}_p$  that are significantly different from those produced by scenarios of bulk surface uplift of the whole Alps. Therefore, if the signals produced by diachronous surface uplift are preserved in the geological record, diachronous surface uplift should be reflected in the associated  $\delta^{18}\text{O}_p$  values. This suggests that hypothesized west-to-east surface uplift propagation could be reconstructed with stable isotope paleoaltimetry that takes advantage of these archives.

The topographic changes produce less pronounced  $\delta^{18}\text{O}_p$  values changes at low-elevation sites adjacent to the Alps, which is consistent with findings from experiments presented by Botsyun et al. (2020). The affected area of  $^{18}\text{O}$  depletion expands geographically when high elevation is assumed on the western flanks of the Alps. Since the  $\delta$ - $\delta$  paleoaltimetry approach is based on the premise that low-elevation sites record background climate change unrelated to topographic changes, our results stress the importance of also sampling low-elevation regions at some distance from the orogen, especially for times when the orogen had likely



reached significant elevation. However, sampling at low elevation near the orogenic front may underestimate rather than overestimate the past elevation (because of low-elevation  $\delta^{18}\text{O}_p$  values that are lower than far-field sampling sites unaffected by nearby Alpine topography). Therefore, we recommend that this study's  $\delta^{18}\text{O}_p$  maps be consulted when devising a sampling strategy to ensure that the target low-elevation sampling location lies outside the region in which topographic changes significantly impact  $\delta^{18}\text{O}_p$  values. Paleoclimate modeling with realistic paleoenvironmental conditions may provide important support for future paleoaltimetry studies. Due to the demonstrated link between topographic configurations and the atmospheric teleconnection patterns governing European climate, estimates of past climate and  $\delta^{18}\text{O}_p$  lapse rates should also consider the hypothesized uplift scenarios as part of the paleogeographic and paleoelevation boundary conditions for climate models (e.g., Zhang et al., 2015).

## 6 Conclusions

The European Alps are hypothesized to have experienced diachronous surface uplift in response to post-collisional process such as slab break-off. Understanding the geodynamic and geomorphic evolution of the Alps requires knowledge of its surface uplift history. This study employs a model-based sensitivity analysis to investigate the response of regional climatic and  $\delta^{18}\text{O}_p$  values to diachronous surface uplift across the Alps. Overall, our results let us accept the hypotheses that the diachronous surface uplift of the Western–Central and Eastern Alps would result in distinct regional climates and meteoric  $\delta^{18}\text{O}_p$  patterns that differ from (1) present-day conditions and (2) conditions produced when the whole Alps are uplifted. If this signal is not lost during the formation of geological proxy material like paleosol carbonates, these records can be used in a stable isotope paleoaltimetry approach to test the hypothesis of eastward propagation of surface uplift in the Alps. We summarize the results as follows.

1. The diachronous surface uplift across the Alps significantly decreases  $\delta^{18}\text{O}_p$  values up to  $\sim 8\%$  over the modified areas, mainly due to an increase in orographic precipitation and adiabatic temperature lapse rate. The topographic scenarios with higher elevations in the Western–Central Alps produce a greater decrease in  $\delta^{18}\text{O}_p$  values and an expansion of the affected geographical domain surrounding the Alps when compared to present-day topography. The different topographic scenarios resulted in a less significant change in  $\delta^{18}\text{O}_p$  values of  $1\%$ – $2\%$  over the adjacent low-elevation areas around the Alps.
2. The  $\delta^{18}\text{O}_p$  value changes were predominantly driven by the significant increase in precipitation amount of up to  $\sim 125\text{ mm month}^{-1}$  in response to surface uplift

due to orographic airlifting and changes in precipitation dynamics. The surface uplift scenarios with higher topography in the Western–Central Alps resulted in significantly drier conditions (rain shadow) over northern Europe and towards the eastern flanks.

3. Surface uplift resulted in a localized decrease in near-surface temperature that also contributed to the decrease in  $\delta^{18}\text{O}_p$  values. The temperature changes were only significant over the modified topographic areas, where they can be primarily explained by adiabatic temperature lapse rates. Smaller changes of up to  $-2^\circ\text{C}$  over regions farther from the Alps may be attributed to non-adiabatic processes, such as changes in atmospheric circulation.
4. The changes in elevation– $\delta^{18}\text{O}_p$  relationship (i.e., isotopic lapse rate) among the different topographic scenarios depend on the transect around the Alps and the magnitude of elevation changes. Some changes were small and within the statistical uncertainty range. The differences in isotopic lapse rates are in the ranges of  $-0.24$  to  $-0.83$  (with the highest uncertainty of  $\pm 0.24$ ),  $-0.17$  to  $-1.19$  ( $\pm 0.14$ ), and  $-0.15$  to  $-0.94$  ( $\pm 0.16$ )  $\text{‰ km}^{-1}$  for the western, northern, and southern transect, respectively. The differences in these estimates might be attributed to a different redistribution of precipitation and changes in moisture transport distance and pathways along specific transects.

Note that this study only quantifies the topographic signal while keeping paleoenvironmental conditions constant. Further experiments are needed to investigate the synergistic effects of combined topographic and paleoenvironmental changes and move towards plausible reconstructions of the topography and paleoclimate of Alps at specific times in the past. Furthermore, the next logical step to close the gap between the predicted meteoric  $\delta^{18}\text{O}$  response and isotopic ratios extracted from archives is to employ proxy system models to investigate the signal transformation that takes place between these steps. This would allow for a more accurate back transformation that can ultimately refine paleoelevation estimates for the Alps.

**Code availability.** The ECHAM5 model is available under the MPI-M Software License Agreement ([https://code.mpimet.mpg.de/attachments/download/26986/MPI-ESM\\_SLA\\_v3.4.pdf](https://code.mpimet.mpg.de/attachments/download/26986/MPI-ESM_SLA_v3.4.pdf), last access: 5 November 2023), and the isotope-tracking implementation part (ECHAM5-wiso) is available upon request from the Alfred Wegner Institute (AWI), Germany (<https://gitlab.awi.de/mwerner/mpe-esm-wiso>, last access: 5 November 2023). The LAGRANTO model used for the back-trajectory analysis can be downloaded from <https://iacweb.ethz.ch/staff/sprenger/lagranto/> (last access: 5 November 2023). The scripts used for postprocessing, data analysis, and visualization are based on a Python package (pyClimat) available at <https://doi.org/10.5281/zenodo.7143044> (Boateng, 2022).

**Data availability.** The processed model output variables (i.e., near-surface temperature, precipitation-weighted  $\delta^{18}\text{O}_p$ , precipitation amount, elevation, near-surface meridional, and zonal wind velocity single-level variables, as well as vertical wind velocity, cloud cover, and relative humidity at pressure levels) used in this study for the different topographic scenarios are available in NetCDF format at <https://doi.org/10.5281/zenodo.7143487> (Boateng et al., 2022).

**Supplement.** The supplement related to this article is available online at: <https://doi.org/10.5194/esd-14-1183-2023-supplement>.

**Author contributions.** DB: conceptualization, model simulation, data analysis, visualization, and writing of the original paper. SGM, TAE: conceptualization, supervision, funding acquisition, paper review and editing. AM, MJMM, KM: funding acquisition and paper review and editing. AB, SB: paper review and editing. All authors contributed to the discussion of the results.

**Competing interests.** At least one of the (co-)authors is a member of the editorial board of *Earth System Dynamics*. The peer-review process was guided by an independent editor, and the authors also have no other competing interests to declare.

**Disclaimer.** Publisher's note: Copernicus Publications remains neutral with regard to jurisdictional claims made in the text, published maps, institutional affiliations, or any other geographical representation in this paper. While Copernicus Publications makes every effort to include appropriate place names, the final responsibility lies with the authors.

**Acknowledgements.** This research was supported by the German Science Foundation (DFG) priority research program Mountain Building Processes in Four Dimensions (4D-MB; SPP 2017) through grants EH 329/19-1 and EH329/23-1 (to Todd A. Ehlers), MU4188/1-1 and MU4188/3-1 (to Sebastian G. Mutz), MU2845/6-1 and MU2845/7-1 (to Andreas Mulch), Me4955/1-1 (to Katharina Methner), and ME5579/1-1 (to Maud J. M. Meijers). We thank Joel Saylor and the anonymous reviewer for their constructive reviews.

**Financial support.** This research has been supported by the Deutsche Forschungsgemeinschaft (Mountain Building Processes in Four Dimensions – 4D-MB, SPP 2017; grants EH 329/19-1 and EH329/23-1 to Todd A. Ehlers, MU4188/1-1 and MU4188/3-1 to Sebastian G. Mutz, MU2845/6-1 and MU2845/7-1 to Andreas Mulch, Me4955/1-1 to Katharina Methner, and ME5579/1-1 to Maud J. M. Meijers).

This open-access publication was funded by the University of Tübingen.

**Review statement.** This paper was edited by Gabriele Messori and reviewed by Joel Saylor and one anonymous referee.

## References

- Allen, P. A.: From landscapes into geological history, *Nature*, 451, 274–276, <https://doi.org/10.1038/nature06586>, 2008.
- Antonelli, A., Kissling, W. D., Flantua, S. G. A., Bermúdez, M. A., Mulch, A., Muellner-Riehl, A. N., Kreft, H., Linder, H. P., Badgley, C., Fjeldså, J., Fritz, S. A., Rahbek, C., Herman, F., Hooghiemstra, H., and Hoorn, C.: Geological and climatic influences on mountain biodiversity, *Nat. Geosci.*, 11, 718–725, <https://doi.org/10.1038/s41561-018-0236-z>, 2018.
- Baldini, L. M., McDermott, F., Foley, A. M., and Baldini, J. U. L.: Spatial variability in the European winter precipitation  $\delta^{18}\text{O}$ -NAO relationship: Implications for reconstructing NAO-mode climate variability in the Holocene, *Geophys. Res. Lett.*, 35, L04709, <https://doi.org/10.1029/2007GL032027>, 2008.
- Barnston, A. G. and Livezey, R. E.: Classification, Seasonality and Persistence of Low-Frequency Atmospheric Circulation Patterns, *Mon. Weather Rev.*, 115, 1083–1126, [https://doi.org/10.1175/1520-0493\(1987\)115<1083:CSAPOL>2.0.CO;2](https://doi.org/10.1175/1520-0493(1987)115<1083:CSAPOL>2.0.CO;2), 1987.
- Bartolini, E., Claps, P., and D'Odorico, P.: Interannual variability of winter precipitation in the European Alps: relations with the North Atlantic Oscillation., *Hydrol. Earth Syst. Sci.*, 13, 17–25, <https://doi.org/10.5194/hess-13-17-2009>, 2009.
- Bartosch, Stüwe, K., and Robl, J.: Topographic evolution of the Eastern Alps: The influence of strike-slip faulting activity, *Lithosphere*, 9, 384–398, <https://doi.org/10.1130/L594.1>, 2017.
- Bastos, A., Janssens, I. A., Gouveia, C. M., Trigo, R. M., Ciais, P., Chevallier, F., Peñuelas, J., Rödenbeck, C., Piao, S., Friedlingstein, P., and Running, S. W.: European land CO<sub>2</sub> sink influenced by NAO and East-Atlantic Pattern coupling, *Nat. Commun.*, 7, 10315, <https://doi.org/10.1038/ncomms10315>, 2016.
- Bell, B., Hersbach, H., Simmons, A., Berrisford, P., Dahlgren, P., Horányi, A., Muñoz-Sabater, J., Nicolas, J., Radu, R., Schepers, D., Soci, C., Villaume, S., Bidlot, J.-R., Haimberger, L., Woollen, J., Buontempo, C., and Thépaut, J.-N.: The ERA5 global reanalysis: Preliminary extension to 1950, *Q. J. Roy. Meteor. Soc.*, 147, 4186–4227, <https://doi.org/10.1002/qj.4174>, 2021.
- Beniston, M.: Mountain Climates and Climatic Change: An Overview of Processes Focusing on the European Alps, *Pure Appl. Geophys.*, 162, 1587–1606, <https://doi.org/10.1007/s00024-005-2684-9>, 2005.
- Boateng, D.: A functional based python module for processing, analysis and visualization of climate model output (pyClimat) (0.0.1), Zenodo [code], <https://doi.org/10.5281/zenodo.7143044>, 2022.
- Boateng, D., Mutz, G. S., Ballian, A., Meijers, J. M. M., Methner, K., Botsyun, S., Mulch, A., and Ehlers, A. T.: Processed model output of the climate simulation in the study: The effects of diachronous surface uplift of the European Alps on regional climate and the isotopic composition of precipitation ( $\delta^{18}\text{O}_p$ ) [Boateng et al.] (1.0.0), Zenodo [data set], <https://doi.org/10.5281/zenodo.7143487>, 2022.
- Botsyun, S. and Ehlers, A. T.: How Can Climate Models Be Used in Paleoelevation Reconstructions?, *Front. Earth Sci.*, 9, 624542, <https://doi.org/10.3389/feart.2021.624542>, 2021.

- Botsyun, S., Ehlers, T. A., Koptev, A., Böhme, M., Methner, K., Risi, C., Stepanek, C., Mutz, S. G., Werner, M., Boateng, D., and Mulch, A.: Middle Miocene Climate and Stable Oxygen Isotopes in Europe Based on Numerical Modeling, *Paleoceanogr. Paleoclimatol.*, 37, e2022PA004442, <https://doi.org/10.1029/2022PA004442>, 2022.
- Botsyun, S., Sepulchre, P., Donnadiou, Y., Risi, C., Licht, A., and Caves Rugenstein, J. K.: Revised paleoaltimetry data show low Tibetan Plateau elevation during the Eocene, *Science*, 363, eaaq1436, <https://doi.org/10.1126/science.aaq1436>, 2019.
- Botsyun, S., Ehlers, T. A., Mutz, S. G., Methner, K., Krsnik, E., and Mulch, A.: Opportunities and Challenges for Palealtimetry in “Small” Orogens: Insights From the European Alps, *Geophys. Res. Lett.*, 47, e2019GL086046, <https://doi.org/10.1029/2019GL086046>, 2020.
- Breecker, D. O., Sharp, Z. D., and McFadden, L. D.: Seasonal bias in the formation and stable isotopic composition of pedogenic carbonate in modern soils from central New Mexico, USA, *GSA Bull.*, 121, 630–640, <https://doi.org/10.1130/B26413.1>, 2009.
- Campani, M., Mulch, A., Kempf, O., Schlunegger, F., and Mancktelow, N.: Miocene paleotopography of the Central Alps, *Earth Planet. Sc. Lett.*, 337, 174–185, <https://doi.org/10.1016/j.epsl.2012.05.017>, 2012.
- Chafik, L., Nilsen, J., and Dangendorf, S.: Impact of North Atlantic Teleconnection Patterns on Northern European Sea Level, *J. Mar. Sci. Eng.*, 5, 43, <https://doi.org/10.3390/jmse5030043>, 2017.
- Chamberlain, C. P., Poage, M. A., Craw, D., and Reynolds, R. C.: Topographic development of the Southern Alps recorded by the isotopic composition of authigenic clay minerals, South Island, New Zealand, *Chem. Geol.*, 155, 279–294, [https://doi.org/10.1016/S0009-2541\(98\)00165-X](https://doi.org/10.1016/S0009-2541(98)00165-X), 1999.
- Chamberlain, C. P., Mix, H. T., Mulch, A., Hren, M. T., Kent-Corson, M. L., Davis, S. J., Horton, T. W., and Graham, S. A.: The Cenozoic climatic and topographic evolution of the western North American Cordillera, *Am. J. Sci.*, 312, 213–262, <https://doi.org/10.2475/02.2012.05>, 2012.
- Clark, M. K.: The Significance of Paleotopography, *Rev. Mineral. Geochem.*, 66, 1–21, <https://doi.org/10.2138/rmg.2007.66.1>, 2007.
- Colle, B. A.: Sensitivity of Orographic Precipitation to Changing Ambient Conditions and Terrain Geometries: An Idealized Modeling Perspective, *J. Atmos. Sci.*, 61, 588–606, [https://doi.org/10.1175/1520-0469\(2004\)061<0588:SOOPTC>2.0.CO;2](https://doi.org/10.1175/1520-0469(2004)061<0588:SOOPTC>2.0.CO;2), 2004.
- Comas-Bru, L. and McDermott, F.: Impacts of the EA and SCA patterns on the European twentieth century NAO–winter climate relationship, *Q. J. Roy. Meteor. Soc.*, 140, 354–363, <https://doi.org/10.1002/qj.2158>, 2014.
- Comas-Bru, L., McDermott, F., and Werner, M.: The effect of the East Atlantic pattern on the precipitation  $\delta^{18}\text{O}$ -NAO relationship in Europe, *Clim. Dynam.*, 47, 2059–2069, <https://doi.org/10.1007/s00382-015-2950-1>, 2016.
- Craig, P. M. and Allan, R. P.: The role of teleconnection patterns in the variability and trends of growing season indices across Europe, *Int. J. Climatol.*, 42, 1072–1091, <https://doi.org/10.1002/joc.7290>, 2022.
- Dansgaard, W.: Stable isotopes in precipitation, *Tellus*, 16, 436–468, <https://doi.org/10.3402/tellusa.v16i4.8993>, 1964.
- Dee, D. P., Uppala, S. M., Simmons, A. J., Berrisford, P., Poli, P., Kobayashi, S., Andrae, U., Balmaseda, M. A., Balsamo, G., Bauer, P., Bechtold, P., Beljaars, A. C. M., van de Berg, L., Bidlot, J., Bormann, N., Delsol, C., Dragani, R., Fuentes, M., Geer, A. J., Haimberger, L., Healy, S. B., Hersbach, H., Hólm, E. V., Isaksen, I., Kållberg, P., Köhler, M., Matricardi, M., McNally, A. P., Monge-Sanz, B. M., Morcrette, J.-J., Park, B.-K., Peubey, C., de Rosnay, P., Tavolato, C., Thépaut, J.-N., and Vitart, F.: The ERA-Interim reanalysis: configuration and performance of the data assimilation system, *Q. J. Roy. Meteor. Soc.*, 137, 553–597, <https://doi.org/10.1002/qj.828>, 2011.
- Deininger, M., Werner, M., and McDermott, F.: North Atlantic Oscillation controls on oxygen and hydrogen isotope gradients in winter precipitation across Europe; implications for palaeoclimate studies, *Clim. Past*, 12, 2127–2143, <https://doi.org/10.5194/cp-12-2127-2016>, 2016.
- Ding, L., Kapp, P., Cai, F., Garzzone, C. N., Xiong, Z., Wang, H., and Wang, C.: Timing and mechanisms of Tibetan Plateau uplift, *Nat. Rev. Earth Environ.*, 3, 1–16, <https://doi.org/10.1038/s43017-022-00318-4>, 2022.
- Edwards, T. W. D., Birks, S. J., and Gibson, J. J.: Isotope tracers in global water and climate studies of the past and present, International Atomic Energy Agency (IAEA), ISSN 1563-0153, 2002.
- Ehlers, T. A. and Poulsen, C. J.: Influence of Andean uplift on climate and paleoaltimetry estimates, *Earth Planet. Sc. Lett.*, 281, 238–248, <https://doi.org/10.1016/j.epsl.2009.02.026>, 2009.
- Fauquette, S., Bernet, M., Suc, J.-P., Grosjean, A.-S., Guillot, S., van der Beek, P., Jourdan, S., Popescu, S.-M., Jiménez-Moreno, G., Bertini, A., Pittet, B., Tricart, P., Dumont, T., Schwartz, S., Zheng, Z., Roche, E., Pavia, G., and Gardien, V.: Quantifying the Eocene to Pleistocene topographic evolution of the southwestern Alps, France and Italy, *Earth Planet. Sc. Lett.*, 412, 220–234, <https://doi.org/10.1016/j.epsl.2014.12.036>, 2015.
- Feng, R., Poulsen, C. J., Werner, M., Chamberlain, C. P., Mix, H. T., and Mulch, A.: Early Cenozoic evolution of topography, climate, and stable isotopes in precipitation in the North American Cordillera, *Am. J. Sci.*, 313, 613–648, <https://doi.org/10.2475/07.2013.01>, 2013.
- Feng, R. and Poulsen, C. J.: Refinement of Eocene lapse rates, fossil-leaf altimetry, and North American Cordilleran surface elevation estimates, *Earth Planet. Sc. Lett.*, 436, 130–141, <https://doi.org/10.1016/j.epsl.2015.12.022>, 2016.
- Forest, C. E., Wolfe, J. A., Molnar, P., and Emanuel, K. A.: Palealtimetry incorporating atmospheric physics and botanical estimates of paleoclimate, *Geol. Soc. Am. Bull.*, 111, 497–511, [https://doi.org/10.1130/0016-7606\(1999\)111<0497:PIA-PAB>2.3.CO;2](https://doi.org/10.1130/0016-7606(1999)111<0497:PIA-PAB>2.3.CO;2), 1999.
- Frisch, W.: Tectonic progradation and plate tectonic evolution of the Alps, *Tectonophysics*, 60, 121–139, [https://doi.org/10.1016/0040-1951\(79\)90155-0](https://doi.org/10.1016/0040-1951(79)90155-0), 1979.
- Gallagher, T. M., Hren, M., and Sheldon, N. D.: The effect of soil temperature seasonality on climate reconstructions from paleosols, *Am. J. Sci.*, 319, 549–581, <https://doi.org/10.2475/07.2019.02>, 2019.
- Garzzone, C. N., Quade, J., DeCelles, P. G., and English, N. B.: Predicting paleoelevation of Tibet and the Himalaya from  $\delta^{18}\text{O}$  vs. altitude gradients in meteoric water across the Nepal Himalaya, *Earth Planet. Sc. Lett.*, 183, 215–229, [https://doi.org/10.1016/S0012-821X\(00\)00252-1](https://doi.org/10.1016/S0012-821X(00)00252-1), 2000.

- Garzzone, C. N., Hoke, G. D., Libarkin, J. C., Withers, S., MacFadden, B., Eiler, J., Ghosh, P., and Mulch, A.: Rise of the Andes, *Science*, 320, 1304–1307, <https://doi.org/10.1126/science.1148615>, 2008.
- Garzzone, C. N., Auerbach, D. J., Jin-Sook Smith, J., Rosario, J. J., Passey, B. H., Jordan, T. E., and Eiler, J. M.: Clumped isotope evidence for diachronous surface cooling of the Altiplano and pulsed surface uplift of the Central Andes, *Earth Planet. Sc. Lett.*, 393, 173–181, <https://doi.org/10.1016/j.epsl.2014.02.029>, 2014.
- Gat, J. R.: Oxygen and Hydrogen Isotopes in the Hydrologic Cycle, *Annual Rev. Earth Planet. Sci.*, 24, 225–262, <https://doi.org/10.1146/annurev.earth.24.1.225>, 1996.
- Gébelin, A., Mulch, A., Teyssier, C., Jessup, M. J., Law, R. D., and Brunel, M.: The Miocene elevation of Mount Everest, *Geology*, 41, 799–802, <https://doi.org/10.1130/G34331.1>, 2013.
- Ghosh, P., Garzzone, C. N., and Eiler, J. M.: Rapid Uplift of the Altiplano Revealed Through  $^{13}\text{C}$ – $^{18}\text{O}$  Bonds in Paleosol Carbonates, *Science*, 311, 511–515, <https://doi.org/10.1126/science.1119365>, 2006.
- Giorgi, F., Hurrell, J. W., Marinucci, M. R., and Beniston, M.: Elevation Dependency of the Surface Climate Change Signal: A Model Study, *J. Climate*, 10, 288–296, [https://doi.org/10.1175/1520-0442\(1997\)010<0288:EDOTSC>2.0.CO;2](https://doi.org/10.1175/1520-0442(1997)010<0288:EDOTSC>2.0.CO;2), 1997.
- Grossman, R. L. and Durran, D. R.: Interaction of Low-Level Flow with the Western Ghat Mountains and Offshore Convection in the Summer Monsoon, *Mon. Weather Rev.*, 112, 652–672, [https://doi.org/10.1175/1520-0493\(1984\)112<0652:IOLLFW>2.0.CO;2](https://doi.org/10.1175/1520-0493(1984)112<0652:IOLLFW>2.0.CO;2), 1984.
- Hagemann, S., Arpe, K., and Roeckner, E.: Evaluation of the Hydrological Cycle in the ECHAM5 Model, *J. Climate*, 19, 3810–3827, <https://doi.org/10.1175/JCLI3831.1>, 2006.
- Handy, M. R., Ustaszewski, K., and Kissling, E.: Reconstructing the Alps–Carpathians–Dinarides as a key to understanding switches in subduction polarity, slab gaps and surface motion, *Int. J. Earth. Sci.*, 104, 1–26, <https://doi.org/10.1007/s00531-014-1060-3>, 2015.
- Hannachi, A., Jolliffe, I. T., and Stephenson, D. B.: Empirical orthogonal functions and related techniques in atmospheric science: A review, *Int. J. Climatol.*, 27, 1119–1152, <https://doi.org/10.1002/joc.1499>, 2007.
- Hergarten, S., Wagner, T., and Stüwe, K.: Age and Prematurity of the Alps Derived from Topography, *Earth Planet. Sc. Lett.*, 297, 453–460, <https://doi.org/10.1016/j.epsl.2010.06.048>, 2010.
- Hersbach, H., Bell, B., Berrisford, P., Hirahara, S., Horányi, A., Muñoz-Sabater, J., Nicolas, J., Peubey, C., Radu, R., Schepers, D., Simmons, A., Soci, C., Abdalla, S., Abellan, X., Balsamo, G., Bechtold, P., Biavati, G., Bidlot, J., Bonavita, M., De Chiara, G., Dahlgren, P., Dee, D., Diamantakis, M., Dragani, R., Fleming, J., Forbes, R., Fuentes, M., Geer, A., Haimberger, L., Healy, S., Hogan, R. J., Hólm, E., Janisková, M., Keeley, S., Laloyaux, P., Lopez, P., Lupu, C., Radnoti, G., de Rosnay, P., Rozum, I., Vamborg, F., Villaume, S., and Thépaut, J.-N.: The ERA5 global reanalysis, *Q. J. Roy. Meteor. Soc.*, 146, 1999–2049, <https://doi.org/10.1002/qj.3803>, 2020.
- Hoffmann, G., Werner, M., and Heimann, M.: Water isotope module of the ECHAM atmospheric general circulation model: A study on timescales from days to several years, *J. Geophys. Res.-Atmos.*, 103, 16871–16896, <https://doi.org/10.1029/98JD00423>, 1998.
- Houze, R. A.: Orographic effects on precipitating clouds, *Rev. Geophys.*, 50, RG1001, <https://doi.org/10.1029/2011RG000365>, 2012.
- Huntington, K. W., Wernicke, B. P., and Eiler, J. M.: Influence of climate change and uplift on Colorado Plateau paleotemperatures from carbonate clumped isotope thermometry, *Tectonics*, 29, <https://doi.org/10.1029/2009TC002449>, 2010.
- Hurrell, J. W.: Decadal Trends in the North Atlantic Oscillation: Regional Temperatures and Precipitation, *Science*, 269, 676–679, <https://doi.org/10.1126/science.269.5224.676>, 1995.
- Hurrell, J. W. and Van Loon, H.: Decadal Variations in Climate Associated with the North Atlantic Oscillation, in: *Climatic Change at High Elevation Sites*, edited by: Diaz, H. F., Beniston, M., and Bradley, R. S., Springer Netherlands, Dordrecht, 69–94, [https://doi.org/10.1007/978-94-015-8905-5\\_4](https://doi.org/10.1007/978-94-015-8905-5_4), 1997.
- Huw Davies, J. and von Blanckenburg, F.: Slab breakoff: A model of lithosphere detachment and its test in the magmatism and deformation of collisional orogens, *Earth Planet. Sc. Lett.*, 129, 85–102, [https://doi.org/10.1016/0012-821X\(94\)00237-S](https://doi.org/10.1016/0012-821X(94)00237-S), 1995.
- Huyghe, D., Mouthereau, F., and Emmanuel, L.: Oxygen isotopes of marine mollusc shells record Eocene elevation change in the Pyrenees, *Earth Planet. Sc. Lett.*, 345, 131–141, <https://doi.org/10.1016/j.epsl.2012.06.035>, 2012.
- Huyghe, D., Mouthereau, F., Sébilo, M., Vacherat, A., Ségalen, L., Richard, P., Biron, P., and Bariac, T.: Impact of topography, climate and moisture sources on isotopic composition ( $\delta^{18}\text{O}$  &  $\delta\text{D}$ ) of rivers in the Pyrenees: Implications for topographic reconstructions in small orogens, *Earth Planet. Sc. Lett.*, 484, 370–384, <https://doi.org/10.1016/j.epsl.2017.12.035>, 2018.
- Insel, N., Poulsen, C. J., and Ehlers, T. A.: Influence of the Andes Mountains on South American moisture transport, convection, and precipitation, *Clim. Dynam.*, 35, 1477–1492, <https://doi.org/10.1007/s00382-009-0637-1>, 2010.
- Insel, N., Poulsen, C. J., Ehlers, T. A., and Sturm, C.: Response of meteoric  $\delta^{18}\text{O}$  to surface uplift – Implications for Cenozoic Andean Plateau growth, *Earth Planet. Sc. Lett.*, 317, 262–272, <https://doi.org/10.1016/j.epsl.2011.11.039>, 2012.
- Ionita, M.: The Impact of the East Atlantic/Western Russia Pattern on the Hydroclimatology of Europe from Mid-Winter to Late Spring, *Climate*, 2, 296–309, <https://doi.org/10.3390/cli2040296>, 2014.
- Josey, S. A.: Surface freshwater flux variability and recent freshening of the North Atlantic in the eastern subpolar gyre, *J. Geophys. Res.*, 110, C05008, <https://doi.org/10.1029/2004JC002521>, 2005.
- Kattel, D. B., Yao, T., Yang, W., Gao, Y., and Tian, L.: Comparison of temperature lapse rates from the northern to the southern slopes of the Himalayas, *Int. J. Climatol.*, 35, 4431–4443, <https://doi.org/10.1002/joc.4297>, 2015.
- Kelson, J. R., Huntington, K. W., Breecker, D. O., Burgener, L. K., Gallagher, T. M., Hoke, G. D., and Petersen, S. V.: A proxy for all seasons?, A synthesis of clumped isotope data from Holocene soil carbonates, *Quat. Sci. Rev.*, 234, 106259, <https://doi.org/10.1016/j.quascirev.2020.106259>, 2020.
- Kissling, E. and Schlunegger, F.: Rollback Orogeny Model for the Evolution of the Swiss Alps, *Tectonics*, 37, 1097–1115, <https://doi.org/10.1002/2017TC004762>, 2018.

- Kocsis, L., Vennemann, T. W., and Fontignie, D.: Migration of sharks into freshwater systems during the Miocene and implications for Alpine paleoelevation, *Geology*, 35, 451–454, <https://doi.org/10.1130/G23404A.1>, 2007.
- Kohn, M. J. and Dettman, D. L.: Palealtimetry from Stable Isotope Compositions of Fossils, *Rev. Mineral. Geochem.*, 66, 119–154, <https://doi.org/10.2138/rmg.2007.66.5>, 2007.
- Krsnik, E., Methner, K., Campani, M., Botsyun, S., Mutz, S. G., Ehlers, T. A., Kempf, O., Fiebig, J., Schlunegger, F., and Mulch, A.: Miocene high elevation in the Central Alps, *Solid Earth*, 12, 2615–2631, <https://doi.org/10.5194/se-12-2615-2021>, 2021.
- Kuhlemann, J., Frisch, W., Székely, B., Dunkl, I., and Kázmér, M.: Post-collisional sediment budget history of the Alps: tectonic versus climatic control, *Int. J. Earth Sci.*, 91, 818–837, <https://doi.org/10.1007/s00531-002-0266-y>, 2002.
- Langebroek, P. M., Werner, M., and Lohmann, G.: Climate information imprinted in oxygen-isotopic composition of precipitation in Europe, *Earth Planet. Sc. Lett.*, 311, 144–154, <https://doi.org/10.1016/j.epsl.2011.08.049>, 2011.
- Lee, J.-E. and Fung, I.: “Amount effect” of water isotopes and quantitative analysis of post-condensation processes, *Hydrol. Process.*, 22, 1–8, <https://doi.org/10.1002/hyp.6637>, 2008.
- Li, J., Ehlers, T. A., Mutz, S. G., Steger, C., Paeth, H., Werner, M., Poulsen, C. J., and Feng, R.: Modern precipitation  $\delta^{18}\text{O}$  and trajectory analysis over the Himalaya-Tibet Orogen from ECHAM5-wiso simulations: Tibetan modern precipitation  $\delta^{18}\text{O}$ , *J. Geophys. Res.-Atmos.*, 121, 10432–10452, <https://doi.org/10.1002/2016JD024818>, 2016.
- Lim, Y.-K.: The East Atlantic/West Russia (EA/WR) teleconnection in the North Atlantic: climate impact and relation to Rossby wave propagation, *Clim. Dynam.*, 44, 3211–3222, <https://doi.org/10.1007/s00382-014-2381-4>, 2015.
- Lin, S.-J. and Rood, R. B.: Multidimensional Flux-Form Semi-Lagrangian Transport Schemes, *Mon. Weather Rev.*, 124, 2046–2070, [https://doi.org/10.1175/1520-0493\(1996\)124<2046:MFFSLT>2.0.CO;2](https://doi.org/10.1175/1520-0493(1996)124<2046:MFFSLT>2.0.CO;2), 1996.
- Lorenz, S. J. and Lohmann, G.: Acceleration technique for Milankovitch type forcing in a coupled atmosphere-ocean circulation model: method and application for the Holocene, *Clim. Dynam.*, 23, 727–743, <https://doi.org/10.1007/s00382-004-0469-y>, 2004.
- Lu, G., Winkler, W., Rahn, M., von Quadt, A., and Willett, S. D.: Evaluating igneous sources of the Taveyannaz formation in the Central Alps by detrital zircon U–Pb age dating and geochemistry, *Swiss J. Geosci.*, 111, 399–416, <https://doi.org/10.1007/s00015-018-0302-y>, 2018.
- McCann, T.: *The Geology of Central Europe: Mesozoic and Cenozoic*, Geological Society of London, 760 pp., 2008.
- McElwain, J. C.: Climate-independent palealtimetry using stomatal density in fossil leaves as a proxy for  $\text{CO}_2$  partial pressure, *Geology*, 32, 1017–1020, <https://doi.org/10.1130/G20915.1>, 2004.
- Meijers, M. J. M., Brocard, G. Y., Cosca, M. A., Lüdecke, T., Teyssier, C., Whitney, D. L., and Mulch, A.: Rapid late Miocene surface uplift of the Central Anatolian Plateau margin, *Earth Planet. Sc. Lett.*, 497, 29–41, <https://doi.org/10.1016/j.epsl.2018.05.040>, 2018.
- Merlivat, L. and Jouzel, J.: Global climatic interpretation of the deuterium-oxygen 18 relationship for precipitation, *J. Geophys. Res.-Oceans*, 84, 5029–5033, <https://doi.org/10.1029/JC084iC08p05029>, 1979.
- Methner, K., Fiebig, J., Wacker, U., Umhoefer, P., Chamberlain, C. P., and Mulch, A.: Eocene-Oligocene proto-Cascades topography revealed by clumped ( $\Delta 47$ ) and oxygen isotope ( $\delta^{18}\text{O}$ ) geochemistry (Chumstick Basin, WA, USA), *Tectonics*, 35, 546–564, <https://doi.org/10.1002/2015TC003984>, 2016.
- Methner, K., Campani, M., Fiebig, J., Löffler, N., Kempf, O., and Mulch, A.: Middle Miocene long-term continental temperature change in and out of pace with marine climate records, *Sci. Rep.*, 10, 7989, <https://doi.org/10.1038/s41598-020-64743-5>, 2020.
- Moore, G. W. K., Renfrew, I. A., and Pickart, R. S.: Multidecadal Mobility of the North Atlantic Oscillation, *J. Climate*, 26, 2453–2466, <https://doi.org/10.1175/JCLI-D-12-00023.1>, 2013.
- Mulch, A.: Stable isotope palealtimetry and the evolution of landscapes and life, *Earth Planet. Sc. Lett.*, 433, 180–191, <https://doi.org/10.1016/j.epsl.2015.10.034>, 2016.
- Mulch, A. and Chamberlain, C. P.: Stable Isotope Palealtimetry in Orogenic Belts – The Silicate Record in Surface and Crustal Geological Archives, *Rev. Mineral. Geochem.*, 66, 89–118, <https://doi.org/10.2138/rmg.2007.66.4>, 2007.
- Mulch, A., Graham, S. A., and Chamberlain, C. P.: Hydrogen Isotopes in Eocene River Gravels and Paleoelevation of the Sierra Nevada, *Science*, 313, 87–89, <https://doi.org/10.1126/science.1125986>, 2006.
- Mulch, A., Sarna-Wojcicki, A. M., Perkins, M. E., and Chamberlain, C. P.: A Miocene to Pleistocene climate and elevation record of the Sierra Nevada (California), *P. Natl. Acad. Sci. USA*, 105, 6819–6824, <https://doi.org/10.1073/pnas.0708811105>, 2008.
- Mulch, A., Uba, C. E., Strecker, M. R., Schoenberg, R., and Chamberlain, C. P.: Late Miocene climate variability and surface elevation in the central Andes, *Earth Planet. Sc. Lett.*, 290, 173–182, <https://doi.org/10.1016/j.epsl.2009.12.019>, 2010.
- Mulch, A., Chamberlain, C. P., Cosca, M. A., Teyssier, C., Methner, K., Hren, M. T., and Graham, S. A.: Rapid change in high-elevation precipitation patterns of western North America during the Middle Eocene Climatic Optimum (MECO), *Am. J. Sci.*, 315, 317–336, <https://doi.org/10.2475/04.2015.02>, 2015.
- Mulch, A., Chamberlain, C. P., Hoorn, C., Perrigo, A., and Antonelli, A.: Stable isotope palealtimetry: paleotopography as a key element in the evolution of landscapes and life, *Mountains, Climate and Biodiversity*, Hoboken, NJ, Wiley-Blackwell, 81–93, 2018.
- Mutz, S. G., Ehlers, T. A., Li, J., Steger, C., Paeth, H., Werner, M., and Poulsen, C. J.: Precipitation  $\delta^{18}\text{O}$  over the Himalaya-Tibet orogen from ECHAM5-wiso simulations: Statistical analysis of temperature, topography and precipitation, *J. Geophys. Res.-Atmos.*, 121, 9278–9300, <https://doi.org/10.1002/2016JD024856>, 2016.
- Mutz, S. G., Ehlers, T. A., Werner, M., Lohmann, G., Stepanek, C., and Li, J.: Estimates of late Cenozoic climate change relevant to Earth surface processes in tectonically active orogens, *Earth Surf. Dynam.*, 6, 271–301, <https://doi.org/10.5194/esurf-6-271-2018>, 2018.
- North, G. R., Bell, T. L., Cahalan, R. F., and Moeng, F. J.: Sampling Errors in the Estimation of Empirical Orthogonal Functions, *Mon. Weather Rev.*, 110, 699–706, [https://doi.org/10.1175/1520-0493\(1982\)110<0699:SEITEO>2.0.CO;2](https://doi.org/10.1175/1520-0493(1982)110<0699:SEITEO>2.0.CO;2), 1982.

- Pingel, H., Mulch, A., Alonso, R. N., Cottle, J., Hynek, S. A., Poletti, J., Rohrmann, A., Schmitt, A. K., Stockli, D. F., and Strecker, M. R.: Surface uplift and convective rainfall along the southern Central Andes (Angastaco Basin, NW Argentina), *Earth Planet. Sc. Lett.*, 440, 33–42, <https://doi.org/10.1016/j.epsl.2016.02.009>, 2016.
- Poulsen, C. J., Ehlers, T. A., and Insel, N.: Onset of Convective Rainfall During Gradual Late Miocene Rise of the Central Andes, *Science*, 328, 490–493, <https://doi.org/10.1126/science.1185078>, 2010.
- Quade, J., Garzzone, C., and Eiler, J.: Paleoelevation Reconstruction using Pedogenic Carbonates, *Rev. Mineral. Geochem.*, 66, 53–87, <https://doi.org/10.2138/rmg.2007.66.3>, 2007.
- Quade, J., Breecker, D. O., Daëron, M., and Eiler, J.: The paleoaltimetry of Tibet: An isotopic perspective, *Am. J. Sci.*, 311, 77–115, <https://doi.org/10.2475/02.2011.01>, 2011.
- Risi, C., Noone, D., Frankenberg, C., and Worden, J.: Role of continental recycling in intraseasonal variations of continental moisture as deduced from model simulations and water vapor isotopic measurements: Continental Recycling and Water Isotopes, *Water Resour. Res.*, 49, 4136–4156, <https://doi.org/10.1002/wrcr.20312>, 2013.
- Roeckner, E., Bäuml, G., Bonaventura, L., Brokopf, R., Esch, M., Giorgetta, M., Hagemann, S., Kirchner, I., Kornbluh, L., Manzini, E., Rhodin, A., Schlese, U., Schulzweida, U., and Tompkins, A.: The atmospheric general circulation model ECHAM 5, Part I: Model description, <https://doi.org/10.17617/2.995269>, 2003.
- Rogers, J. C.: Patterns of Low-Frequency Monthly Sea Level Pressure Variability (1899–1986) and Associated Wave Cyclone Frequencies, *J. Climate*, 3, 1364–1379, [https://doi.org/10.1175/1520-0442\(1990\)003<1364:POLFMS>2.0.CO;2](https://doi.org/10.1175/1520-0442(1990)003<1364:POLFMS>2.0.CO;2), 1990.
- Rosenberg, C. L., Berger, A., Bellahsen, N., and Bousquet, R.: Relating orogen width to shortening, erosion, and exhumation during Alpine collision, *Tectonics*, 34, 1306–1328, <https://doi.org/10.1002/2014TC003736>, 2015.
- Rowley, D. B. and Currie, B. S.: Palaeo-altimetry of the late Eocene to Miocene Lunpola basin, central Tibet, *Nature*, 439, 677–681, <https://doi.org/10.1038/nature04506>, 2006.
- Rowley, D. B. and Garzzone, C. N.: Stable Isotope-Based Palaeoaltimetry, *Annu. Rev. Earth Planet. Sci.*, 35, 463–508, <https://doi.org/10.1146/annurev.earth.35.031306.140155>, 2007.
- Rowley, D. B., Pierrehumbert, R. T., and Currie, B. S.: A new approach to stable isotope-based paleoaltimetry: implications for paleoaltimetry and paleohypsometry of the High Himalaya since the Late Miocene, *Earth Planet. Sc. Lett.*, 188, 253–268, [https://doi.org/10.1016/S0012-821X\(01\)00324-7](https://doi.org/10.1016/S0012-821X(01)00324-7), 2001.
- Rozanski, K., Sonntag, C., and Münnich, K. O.: Factors controlling stable isotope composition of European precipitation, *Tellus*, 34, 142–150, <https://doi.org/10.1111/j.2153-3490.1982.tb01801.x>, 1982.
- Sahagian, D. L. and Maus, J. E.: Basalt vesicularity as a measure of atmospheric pressure and palaeoelevation, *Nature*, 372, 449–451, <https://doi.org/10.1038/372449a0>, 1994.
- Schlunegger, F. and Castellort, S.: Immediate and delayed signal of slab breakoff in Oligo/Miocene Molasse deposits from the European Alps, *Sci. Rep.*, 6, 31010, <https://doi.org/10.1038/srep31010>, 2016.
- Schlunegger, F. and Kissling, E.: Slab rollback orogeny in the Alps and evolution of the Swiss Molasse basin, *Nat. Commun.*, 6, 1–10, <https://doi.org/10.1038/ncomms9605>, 2015.
- Schmid, S. M., Pfiffner, O. A., Froitzheim, N., Schönborn, G., and Kissling, E.: Geophysical-geological transect and tectonic evolution of the Swiss-Italian Alps, *Tectonics*, 15, 1036–1064, <https://doi.org/10.1029/96TC00433>, 1996.
- Schmid, S. M., Fügenschuh, B., Kissling, E., and Schuster, R.: Tectonic map and overall architecture of the Alpine orogen, *Eclogae Geol. Helv.*, 97, 93–117, <https://doi.org/10.1007/s00015-004-1113-x>, 2004.
- Schmidli, J., Schmutz, C., Frei, C., Wanner, H., and Schär, C.: Mesoscale precipitation variability in the region of the European Alps during the 20th century: Alpine precipitation variability, *Int. J. Climatol.*, 22, 1049–1074, <https://doi.org/10.1002/joc.769>, 2002.
- Sharp, Z. D., Masson, H., and Lucchini, R.: Stable isotope geochemistry and formation mechanisms of quartz veins; extreme paleoaltitudes of the Central Alps in the Neogene, *Am. J. Sci.*, 305, 187–219, <https://doi.org/10.2475/ajs.305.3.187>, 2005.
- Shen, H. and Poulsen, C. J.: Precipitation  $\delta^{18}\text{O}$  on the Himalaya–Tibet orogeny and its relationship to surface elevation, *Clim. Past*, 15, 169–187, <https://doi.org/10.5194/cp-15-169-2019>, 2019.
- Spicer, R. A., Su, T., Valdes, P. J., Farnsworth, A., Wu, F.-X., Shi, G., Spicer, T. E. V., and Zhou, Z.: Why “the uplift of the Tibetan Plateau” is a myth, *Nat. Sci. Rev.*, 8, nwaa091, <https://doi.org/10.1093/nsr/nwaa091>, 2021.
- Sprenger, M. and Wernli, H.: The LAGRANTO Lagrangian analysis tool – version 2.0, *Geosci. Model Dev.*, 8, 2569–2586, <https://doi.org/10.5194/gmd-8-2569-2015>, 2015.
- Stampfli, G. M., Mosar, J., Marquer, D., Marchant, R., Baudin, T., and Borel, G.: Subduction and obduction processes in the Swiss Alps, *Tectonophysics*, 296, 159–204, [https://doi.org/10.1016/S0040-1951\(98\)00142-5](https://doi.org/10.1016/S0040-1951(98)00142-5), 1998.
- Stappeler, J., Doms, G., Schättler, U., Bitzer, H. W., Gassmann, A., Damrath, U., and Gregoric, G.: Meso-gamma scale forecasts using the nonhydrostatic model LM, *Met. Atmos. Phys.*, 82, 75–96, <https://doi.org/10.1007/s00703-001-0592-9>, 2003.
- Stevens, B., Giorgetta, M., Esch, M., Mauritsen, T., Crueger, T., Rast, S., Salzmann, M., Schmidt, H., Bader, J., Block, K., Brokopf, R., Fast, I., Kinne, S., Kornbluh, L., Lohmann, U., Pincus, R., Reichler, T., and Roeckner, E.: Atmospheric component of the MPI-M Earth System Model: ECHAM6, *J. Adv. Model. Earth Sy.*, 5, 146–172, <https://doi.org/10.1002/jame.20015>, 2013.
- Storch, H. and von Zwiern, F. W.: *Statistical Analysis in Climate Research*, Cambridge University Press, 995 pp., 2002.
- Sturm, C., Zhang, Q., and Noone, D.: An introduction to stable water isotopes in climate models: benefits of forward proxy modelling for paleoclimatology, *Clim. Past*, 6, 115–129, <https://doi.org/10.5194/cp-6-115-2010>, 2010.
- Sundell, K. E., Saylor, J. E., Lapen, T. J., and Horton, B. K.: Implications of variable late Cenozoic surface uplift across the Peruvian central Andes, *Sci. Rep.*, 9, 4877, <https://doi.org/10.1038/s41598-019-41257-3>, 2019.
- Takahashi, K. and Battisti, D. S.: Processes Controlling the Mean Tropical Pacific Precipitation Pattern, Part I: The Andes and the Eastern Pacific ITCZ, *J. Climate*, 20, 3434–3451, <https://doi.org/10.1175/JCLI4198.1>, 2007.

- Tompkins, A. M.: A Prognostic Parameterization for the Subgrid-Scale Variability of Water Vapor and Clouds in Large-Scale Models and Its Use to Diagnose Cloud Cover, *J. Atmos. Sci.*, 59, 1917–1942, [https://doi.org/10.1175/1520-0469\(2002\)059<1917:APPFTS>2.0.CO;2](https://doi.org/10.1175/1520-0469(2002)059<1917:APPFTS>2.0.CO;2), 2002.
- Ustaszewski, K., Schmid, S. M., Fügenschuh, B., Tischler, M., Kissling, E., and Spakman, W.: A map-view restoration of the Alpine-Carpathian-Dinaridic system for the Early Miocene, *Swiss J. Geosci.*, 101, 273–294, <https://doi.org/10.1007/s00015-008-1288-7>, 2008.
- Valla, P. G., Sternai, P., and Fox, M.: How Climate, Uplift and Erosion Shaped the Alpine Topography, *Elements*, 17, 41–46, <https://doi.org/10.2138/gselements.17.1.41>, 2021.
- Wallace, J. M. and Gutzler, D. S.: Teleconnections in the Geopotential Height Field during the Northern Hemisphere Winter, *Mon. Weather Rev.*, 109, 784–812, [https://doi.org/10.1175/1520-0493\(1981\)109<0784:TITGHF>2.0.CO;2](https://doi.org/10.1175/1520-0493(1981)109<0784:TITGHF>2.0.CO;2), 1981.
- Werner, M., Langebroek, P. M., Carlsen, T., Herold, M., and Lohmann, G.: Stable water isotopes in the ECHAM5 general circulation model: Toward high-resolution isotope modeling on a global scale, *J. Geophys. Res.*, 116, D15109, <https://doi.org/10.1029/2011JD015681>, 2011.
- Wernli, H.: A Lagrangian-based analysis of extratropical cyclones, II: A detailed case-study, *Q. J. Roy. Meteor. Soc.*, 123, 1677–1706, <https://doi.org/10.1002/qj.49712354211>, 1997.
- Whipple, K. X.: The influence of climate on the tectonic evolution of mountain belts, *Nat. Geosci.*, 2, 97–104, <https://doi.org/10.1038/ngeo413>, 2009.
- Woollings, T., Hannachi, A., and Hoskins, B.: Variability of the North Atlantic eddy-driven jet stream, *Q. J. Roy. Meteor. Soc.*, 136, 856–868, <https://doi.org/10.1002/qj.625>, 2010.
- Zamanian, K., Pustovoytov, K., and Kuzyakov, Y.: Pedogenic carbonates: Forms and formation processes, *Earth-Sci. Rev.*, 157, 1–17, <https://doi.org/10.1016/j.earscirev.2016.03.003>, 2016.
- Zhang, R., Jiang, D., Zhang, Z., and Yu, E.: The impact of regional uplift of the Tibetan Plateau on the Asian monsoon climate, *Palaeogeography, Palaeoclimatology, Palaeoecology*, 417, 137–150, <https://doi.org/10.1016/j.palaeo.2014.10.030>, 2015.
- Zubiate, L., McDermott, F., Sweeney, C., and O'Malley, M.: Spatial variability in winter NAO–wind speed relationships in western Europe linked to concomitant states of the East Atlantic and Scandinavian patterns, *Q. J. Roy. Meteor. Soc.*, 143, 552–562, <https://doi.org/10.1002/qj.2943>, 2017.

## 2 P2: Botsyun et al. [2]

**(P2)** Botsyun, S., Ehlers, T. A., Koptev, A., Böhme, M., Methner, K., Risi, C., Stepanek, C., Mutz, S. G., Werner, M., Boateng, D., and Mulch, A.: Middle Miocene Climate and Stable Oxygen Isotopes in Europe Based on Numerical Modeling, *Paleoceanography and Paleoclimatology*, 37, e2022PA004442, <https://doi.org/10.1029/2022PA004442>, 2022.



# Paleoceanography and Paleoclimatology

## RESEARCH ARTICLE

10.1029/2022PA004442

### Key Points:

- A high-resolution isotope-enabled general circulation model is used to explore Middle Miocene climate and precipitation  $\delta^{18}\text{O}$  across Europe
- Middle Miocene bi-directional precipitation change consistent with herpetological fossils and account for precipitation  $\delta^{18}\text{O}$  variations
- Global Miocene climate forcing contributed a max  $\delta^{18}\text{O}$  change of  $\sim 2\%$  over the high Alpine elevation and to  $\sim 1\%$  over low elevation

### Supporting Information:

Supporting Information may be found in the online version of this article.

### Correspondence to:

S. Botsyun,  
svetlana.botsyun@fu-berlin.de

### Citation:

Botsyun, S., Ehlers, T. A., Koptev, A., Böhme, M., Methner, K., Risi, C., et al. (2022). Middle Miocene climate and stable oxygen isotopes in Europe based on numerical modeling. *Paleoceanography and Paleoclimatology*, 37, e2022PA004442. <https://doi.org/10.1029/2022PA004442>

Received 1 MAR 2022

Accepted 3 OCT 2022

### Author Contributions:

**Conceptualization:** Svetlana Botsyun, Alexander Koptev

**Data curation:** Svetlana Botsyun, Madelaine Böhme

**Formal analysis:** Svetlana Botsyun

**Funding acquisition:** Todd A. Ehlers, Sebastian G. Mutz

**Investigation:** Svetlana Botsyun, Madelaine Böhme, Katharina Methner, Christian Stepanek

**Methodology:** Svetlana Botsyun, Alexander Koptev, Camille Risi

**Software:** Martin Werner

© 2022 The Authors.

This is an open access article under the terms of the [Creative Commons Attribution-NonCommercial License](https://creativecommons.org/licenses/by/4.0/), which permits use, distribution and reproduction in any medium, provided the original work is properly cited and is not used for commercial purposes.

## Middle Miocene Climate and Stable Oxygen Isotopes in Europe Based on Numerical Modeling

Svetlana Botsyun<sup>1,2</sup>, Todd A. Ehlers<sup>1</sup>, Alexander Koptev<sup>1,3</sup>, Madelaine Böhme<sup>1,4</sup>, Katharina Methner<sup>5,6</sup>, Camille Risi<sup>7</sup>, Christian Stepanek<sup>8</sup>, Sebastian G. Mutz<sup>1</sup>, Martin Werner<sup>8</sup>, Daniel Boateng<sup>1</sup>, and Andreas Mulch<sup>5,9</sup>

<sup>1</sup>Department of Geosciences, University of Tübingen, Tübingen, Germany, <sup>2</sup>Institute of Meteorology, Freie Universität Berlin, Berlin, Germany, <sup>3</sup>Helmholtz Centre Potsdam, GFZ German Research Centre for Geosciences, Potsdam, Germany, <sup>4</sup>Senckenberg Centre for Human Evolution and Palaeoenvironment, Tübingen, Germany, <sup>5</sup>Senckenberg Biodiversity and Climate Research Centre, Frankfurt am Main, Germany, <sup>6</sup>Department of Geological Sciences, Stanford University, Stanford, CA, USA, <sup>7</sup>Laboratoire de Météorologie Dynamique, LMD/IPSL, UPMC, CNRS, Paris, France, <sup>8</sup>Alfred Wegener Institute (AWI), Helmholtz Centre for Polar and Marine Research, Bremerhaven, Germany, <sup>9</sup>Institute of Geosciences, Goethe University Frankfurt, Frankfurt am Main, Germany

**Abstract** The Middle Miocene (15.99–11.65 Ma) of Europe witnessed major climatic, environmental, and vegetational change, yet we are lacking detailed reconstructions of Middle Miocene temperature and precipitation patterns over Europe. Here, we use a high-resolution ( $\sim 0.75^\circ$ ) isotope-enabled general circulation model (ECHAM5-wiso) with time-specific boundary conditions to investigate changes in temperature, precipitation, and  $\delta^{18}\text{O}$  in precipitation ( $\delta^{18}\text{O}_p$ ). Experiments were designed with variable elevation configurations of the European Alps and different atmospheric  $\text{CO}_2$  levels to examine the influence of Alpine elevation and global climate forcing on regional climate and  $\delta^{18}\text{O}_p$  patterns. Modeling results are in agreement with available paleobotanical temperature data and with low-resolution Middle Miocene experiments of the Miocene Model Intercomparison Project (MioMIP1). However, simulated precipitation rates are 300–500 mm/yr lower in the Middle Miocene than for pre-industrial times for central Europe. This result is consistent with precipitation estimates from herpetological fossil assemblages, but contradicts precipitation estimates from paleobotanical data. We attribute the Middle Miocene precipitation change in Europe to shifts in large-scale pressure patterns in the North Atlantic and over Europe and associated changes in wind direction and humidity. We suggest that global climate forcing contributed to a maximum  $\delta^{18}\text{O}_p$  change of  $\sim 2\%$  over high elevation (Alps) and  $\sim 1\%$  over low elevation regions. In contrast, we observe a maximum modeled  $\delta^{18}\text{O}_p$  decrease of  $8\%$  across the Alpine orogen due to Alpine topography. However, the elevation- $\delta^{18}\text{O}_p$  lapse rate shallows in the Middle Miocene, leading to a possible underestimation of paleotopography when using present-day  $\delta^{18}\text{O}_p$ –elevation relationships data for stable isotope paleoaltimetry studies.

## 1. Introduction

The Middle Miocene (15.99–11.65 Ma) was a time of major climatic, tectonic, environmental, and vegetation change (Herold et al., 2008; Steinthorsdottir et al., 2021). Proxy records, including global compilations of benthic  $\delta^{18}\text{O}$  and  $\delta^{13}\text{C}$  values (e.g., Foster & Rohling, 2013; Wright et al., 1992), indicate a shift from a period of relatively warm global conditions during the Miocene Climatic Optimum (MCO) (16.75–14.5 Ma) to the less warm Middle Miocene Climate Transition (MMCT) starting at  $\sim 14.7$  Ma. Paleoclimate proxy records document sub-modern to moderately high atmospheric  $p\text{CO}_2$  values ( $\sim 180$ – $600$  ppm) during the Middle Miocene (Foster & Rohling, 2013; Pagani et al., 1999), with possibly elevated  $p\text{CO}_2$  levels of 350–630 ppm (Cui et al., 2020; Greenop et al., 2014; Sosdian et al., 2018; Steinthorsdottir et al., 2021) or up to  $\sim 600$  ppm with over 1,000 ppm permissible (Rae et al., 2021) during the MCO. In addition, during the MCO, sea surface temperatures (SSTs) were  $8^\circ\text{C}$ – $10^\circ\text{C}$  warmer than today in the high southern latitudes (Shevenell et al., 2008) and  $10^\circ\text{C}$ – $15^\circ\text{C}$  warmer in the high northern latitudes (Super et al., 2018, 2020). In contrast, the MMCT was a period when SSTs were similar to present-day (Steinthorsdottir et al., 2021). Middle Miocene glaciation was unipolar, with a substantial reduction in Antarctic ice volume during the MCO (Feakins et al., 2012; Westerhold et al., 2005) and a large expansion of the Antarctic ice sheet volume, comparable to the present-day, during the MMCT (Langebroek et al., 2009, 2010). The aforementioned climate changes during the Middle Miocene had diverse implications for terrestrial settings globally, including Europe, which is the focus of this study.

**Supervision:** Todd A. Ehlers, Andreas Mulch  
**Validation:** Madelaine Böhme, Katharina Methner, Christian Stepanek, Martin Werner, Andreas Mulch  
**Visualization:** Svetlana Botsyun, Todd A. Ehlers, Alexander Koptev, Daniel Boateng  
**Writing – original draft:** Svetlana Botsyun  
**Writing – review & editing:** Todd A. Ehlers, Alexander Koptev, Madelaine Böhme, Katharina Methner, Camille Risi, Christian Stepanek, Sebastian G. Mutz, Martin Werner, Daniel Boateng, Andreas Mulch

Although global climate change during the Miocene is relatively well documented for the marine realm (Gaskell et al., 2022), limited information is available concerning terrestrial climate change (Steinthorsdottir et al., 2021). Moreover, the Miocene has been proposed as a potential analog for future climate scenarios (Steinthorsdottir et al., 2021), making Miocene climate reconstructions from both proxies and models strategically important. However, the mechanisms behind climate change around the Middle Miocene are poorly understood for Europe and warrant further investigation. Although the Miocene climate of Europe has been extensively investigated (e.g., Bruch et al., 2007 and references herein; Bouchal et al., 2018; Methner et al., 2020; Worobiec et al., 2021), paleoclimate data are in parts still controversial. For example, estimates of Middle Miocene precipitation from herpetological fossil assemblages (Böhme et al., 2011) suggest lower precipitation amounts around 300–500 mm/yr less than today. However, these estimates are at odds with plant proxy data showing wetter conditions than today in Central and Eastern Europe with precipitation rates up to 1,400 mm/yr (Bruch et al., 2011). Despite recent advances in simulating Miocene climate (Burls et al., 2021), models have difficulty reproducing the magnitude of warming (Burls et al., 2021), and high-resolution regional studies that better capture orographic effects (Acosta & Huber, 2017, 2020) are still lacking. Moreover, little is known about the dynamics of the hydrological cycle and atmospheric circulation (Eronen et al., 2012; Methner et al., 2020; Quan et al., 2014). Therefore, new high-resolution modeling studies are essential to reconcile different proxy data with each other and with modeling results.

The Miocene was a period of continued mountain building and surface uplift for the European Alps (e.g., Eizenhöfer et al., 2021; Handy et al., 2010; Schmid et al., 1996; Valla et al., 2021). Surface uplift of the Alps has previously been suggested to influence European climate (Botsyun et al., 2020; Campani et al., 2012; Krsnik et al., 2021; Boateng et al., 2022), but detailed time-specific studies quantifying the magnitude of spatial and temporal variations and dynamics of regional climate change are still lacking. Moreover, the timing and rate of the surface uplift of the Alps is still controversial and ranges from reconstructed elevations of  $1,900 \pm 1,000$  m (Schlunegger & Kissling, 2015) to elevations  $>4,000$  m (Jäger & Hantke, 1984; Krsnik et al., 2021; Sharp, 2005). Thus, in order to reconstruct past climate in Europe, the elevation history of the Alps plays a key role.

Among the methods developed to determine the uplift history of orogens, stable isotope paleoaltimetry is the most commonly used. This method is based on a systematic relationship between the oxygen or hydrogen isotopic ratios of precipitation ( $\delta^{18}\text{O}_p$ ,  $\delta\text{D}_p$ ) and elevation (Poage & Chamberlain, 2001; Rowley et al., 2001). However, both global and regional climate change as a consequence of mountain uplift may contribute to  $\delta^{18}\text{O}_p$  patterns used in paleoelevation reconstructions (Botsyun & Ehlers, 2021; Botsyun et al., 2016, 2019; Ehlers & Poulsen, 2009; Insel et al., 2012; Mulch, 2016; Poulsen et al., 2010). The sensitivity of  $\delta^{18}\text{O}_p$  to regional, global, and topographic variations in paleotemperature, environmental conditions of an air mass prior to orographic ascent, evapotranspiration, vegetation changes, water vapor recycling, and changes in vapor source have been shown to contribute to the uncertainty of elevation reconstructions (Botsyun & Ehlers, 2021; Botsyun et al., 2020; Kukla et al., 2019; Mulch, 2016). Therefore, a rigorous reconstruction of the elevation history of the Alps requires careful consideration of both regional and global climate drivers.

Modeling strategies using high-resolution isotope-enabled general circulation model (GCMs) together with time-specific boundary conditions have become a powerful tool not only for reconstructing global and regional paleoclimates but also for enhancing elevation reconstructions from  $\delta^{18}\text{O}_p$  proxy data (Botsyun & Ehlers, 2021). In this study, we complement previous work by providing high-resolution (T159,  $\sim 0.75^\circ$  per grid cell) isotope-enabled GCM experiments with Middle Miocene boundary conditions and investigate temperature, precipitation, and the  $\delta^{18}\text{O}_p$  pattern over the European continent. We compare model predictions with independent sources of information—first, with the result from models within the Miocene Model Intercomparison Project (MioMIP1), and second, with climate characteristics derived from proxy data. In our experiments, we investigate not only the effects of long-term global cooling during the MMCT, including a drop of atmospheric  $\text{CO}_2$  concentration and the impact of an expanded Antarctic ice sheet on climate in Europe, but also the contribution of local geographic changes, such as the uplift of the Alps and the retreat of the Paratethys Sea. We test the hypothesis that global and regional forcing resulted in temperature, precipitation, and humidity changes that in turn affect  $\delta^{18}\text{O}_p$  changes across Europe. We pursue two goals that are closely related, since there is a close relationship between mountain elevations, climate, and  $\delta^{18}\text{O}_p$ . We aim to: (a) investigate Middle Miocene climate in Europe under global and regional forcing and to explain the inconsistencies between different terrestrial proxy records in Europe, and (b) demonstrate the link between regional  $\delta^{18}\text{O}_p$  patterns and paleoclimatic changes in Europe and show consequences for paleoelevation estimates of the Alps. We discuss (a) the large-scale drivers of

climate change in Europe, (b) the sources of discord between GCM predictions of European climate change and different terrestrial proxy records, (c) the implications of global climate change and Alpine surface uplift on the  $\delta^{18}\text{O}$  records and paleoclimate proxy records in Europe, and (d) the consequences of changes in paleoclimate and  $\delta^{18}\text{O}_p$  for paleoelevation estimates of the Alps.

## 2. Background

Tectonic uplift of mountain belts (Raymo & Ruddiman, 1992; Ruddiman & Kutzbach, 1989), as well as smaller orogens, such as the European Alps (Botsyun et al., 2020; Boateng et al., 2022) have been shown to be important for global and regional climate. The Late Cretaceous to Paleogene closure of the Alpine Tethys, the collision between the Adriatic and the European continental plates (Handy et al., 2010; Schmid et al., 1996; Stampfli et al., 1998) and subsequent post-collisional convergence (e.g., Schmid et al., 1996) ultimately resulted in the surface uplift of the Alps. However, the timing and rate of this uplift is still controversial, with Miocene stable-isotope-based paleoelevation estimates ranging from mean elevations of  $1,900 \pm 1,000$  m (Schlunegger & Kissling, 2015) and  $2,300 \pm 650$  m (Kocsis et al., 2007) to  $2,850 + 800/-600$  m (Campani et al., 2012), and  $>4,000$  m (Krsnik et al., 2021; Sharp, 2005). Based on combined evidence from sediment budget curves, thermochronology, and sediment facies, the maximum elevation of the Western and central Alps has been estimated at  $2,500\text{--}3,000$  m for the middle Miocene (Kuhleemann, 2007). Very high Alps ( $>5,000$  m) already at the Oligocene-Miocene boundary were inferred by Jäger and Hantke (1984) based on large erratic boulders found at great distances from their place of origin. These estimates, however, contradict geomorphologic and sediment budget-based modeling studies suggesting that present-day elevations of the Alps were attained only at  $\sim 5\text{--}6$  Ma while Miocene topography was still much lower (Hergarten et al., 2010). Depending on its topographic structure, the impact of the Alpine orogen on regional climate would be different, thus quantitative estimates of the surface elevation of the Alps are extremely important.

Modern efforts to model Miocene climate have recently been combined into a multi-model ensemble of MioMIP1 and are critically reviewed in Burls et al. (2021) and summarized in Steinthorsdottir et al. (2021). Elements other than  $\text{CO}_2$ , such as Miocene paleogeography and ice sheets, have been shown to contribute to the global mean temperature increase of  $\sim 2^\circ\text{C}$  (Burls et al., 2021) compared to pre-industrial times. In general, previous models with realistic  $\text{CO}_2$  concentrations have had difficulty to reproduce the magnitude of warming indicated by proxy data. The models used in MioMIP1 represent the state-of-the-art in modeling of the Miocene epoch, however, they are inhomogeneous (in terms of both experimental design and model physics/parameterization) and not ideal for formal inter-model comparison, as Burls et al. (2021) acknowledge. Furthermore, these model simulations were performed at low spatial resolution (T31 or T42, corresponding to a grid spacing of  $\sim 3.75^\circ$  or  $\sim 2.79^\circ$ , respectively), since high-resolution paleoclimate simulations are timely and computationally expensive, and do not focus specifically on interpreting climate variations across Europe.

## 3. Methods

### 3.1. Model and Experimental Design

We apply the isotope-enabled version (ECHAM5-wiso; Werner et al., 2011) of the atmospheric GCM ECHAM5 developed at Max Planck Institute for Meteorology (Roeckner et al., 2003). The ECHAM5 model incorporates the Subgrid Scale Orographic Parameterization developed by Lott (1999) and Lott and Miller (1997). This parameterization represents the effects of orographic variations at scales smaller than the horizontal resolution of the grid (Roeckner et al., 2003). As an integral part of the climate simulation, the water isotopes ( $\text{HDO}$ ,  $\text{H}_2^{16}\text{O}$ , and  $\text{H}_2^{18}\text{O}$ ) in ECHAM5-wiso undergo kinetic and equilibrium fractionation during phase transitions (e.g., vapor, cloud, snow, etc.) in the atmosphere (Werner et al., 2011). The climate component of ECHAM5-wiso, employed without isotopes, has been shown to capture the large-scale features of global climate reasonably well (e.g., Knorr et al., 2011; Mutz et al., 2018). For the present-day climate, high-resolution ECHAM5-wiso experiments successfully reproduce observed precipitation, temperature, and  $\delta^{18}\text{O}_p$  patterns on both annual and seasonal scales in Europe (Botsyun et al., 2020; Langebroek et al., 2011). However, the model tends to underestimate the present-day precipitation over the Alpine region, especially in summer. ECHAM5-wiso has also been successfully used for paleoclimate simulations (Pliocene and Last Glacial Maximum) and validated for the European region (Botsyun et al., 2020).

We used three ECHAM5-wiso topography sensitivity experiments with pre-industrial boundary conditions described in detail in Botsyun et al. (2020) and performed nine new ECHAM5-wiso experiments with Middle Miocene boundary conditions. The summary of the experiments is shown in Table 1. The control simulation (pre-industrial, PI) is the same as in Botsyun et al. (2020) and Mutz et al. (2018) (their Alps100 experiment) and used pre-industrial boundary conditions (e.g., insolation, greenhouse gases, SSTs) and present-day Alpine topography. This experiment was forced by monthly mean climatology of SSTs and sea ice concentrations (SICs), derived from a low-resolution transient coupled ocean-atmosphere simulation (Lorenz & Lohmann, 2004) conducted for the same time period with a  $p\text{CO}_2$  level set to 280 ppm. Land surface parameters for the PI simulation, including vegetation are based on Hagemann (2002).

Three steps underlie our analysis. First, we used the sensitivity experiments of topographic changes of the European Alps from Botsyun et al. (2020). All boundary conditions, including albedo, surface roughness length, and vegetation distribution, are identical to those in the PI simulation, but in one simulation elevation is reduced to 250 m in the area covering the Alps and Alpine foreland (PI\_noAlps; equivalent to Alps0 in Botsyun et al., 2020) and in one simulation increased to 150% of the present elevations in the same region (PI\_plusAlps; equivalent to Alps150 in Botsyun et al., 2020). The PI\_plusAlps experiment was conducted to test the sensitivity of the climate in Europe to significantly higher-than-present Alpine elevations, as suggested by Krsnik et al. (2021).

Second, we conducted two experiments with Middle Miocene boundary conditions reflecting two  $p\text{CO}_2$  settings (278 and 450 ppm; Mio\_278 and Mio\_450 experiments) within current estimates of the Middle Miocene  $p\text{CO}_2$  (Foster & Rohling, 2013; Sosdian et al., 2018; Steinhorsdottir et al., 2021). These two  $p\text{CO}_2$  settings approximately reflect MCO and MMCT climatic states, with Mio\_450 ppm representing the MCO and Mio\_278 representing the MMCT. We highlight that we chose the Mio\_450 experiment conservatively to rather underestimate  $p\text{CO}_2$  conditions during the MCO. In addition to greenhouse gas concentrations ( $p\text{CO}_2$ ,  $p\text{CH}_4$ ,  $p\text{N}_2\text{O}$ ), the paleoclimate simulations account for changing terrestrial ice sheets, vegetation cover, albedo, orbital variations, SSTs, and SICs (Table 1). We use the SSTs and SICs, generated by the low-resolution fully coupled atmosphere-ocean COSMOS model experiments with Middle Miocene boundary conditions (Huang et al., 2017; Stärz et al., 2017; their Mio\_278 and Mio\_450 experiments). Corresponding COSMOS experiments were part of the MioMIP1 comparison (Burls et al., 2021). Physical soil properties, such as soil albedo and maximum water holding field capacity are derived by adapting vegetation-related parameters computed by a dynamic vegetation module (Brovkin et al., 2009) of the global land surface and carbon cycle model JSBACH (Raddatz et al., 2007) as part of the fully coupled atmosphere-ocean model COSMOS. Orography-related variables were derived from the paleogeographic reconstruction of Herold et al. (2008). Although geography of the Middle Miocene and present are remarkably similar, the Middle Miocene reconstruction has several notable modifications, including rotation of continents, altered ocean gateways, and height of major orogens (Figure 1a). For ECHAM5-wiso simulations, the  $\delta^{18}\text{O}$  values of ocean surface waters have to be prescribed as a model boundary condition. The lack of seawater  $\delta^{18}\text{O}$  from COSMOS coupled simulations and sparse observational data have prevented us from the construction and use of a comprehensive global gridded data set of  $\delta^{18}\text{O}$  for the Middle Miocene. For the Mio\_450 and Mio\_278 simulations, the seawater  $\delta^{18}\text{O}$  values were set identically to present-day. In order to test the sensitivity of Middle Miocene  $\delta^{18}\text{O}_p$  in Europe to changes of ocean surface waters  $\delta^{18}\text{O}$ , we performed two additional simulations (Mio\_278\_iniwiso, Mio\_450\_iniwiso) in which, the  $\delta^{18}\text{O}$  values of ocean surface waters have been computed from the salinity of the upper ocean level of corresponding COSMOS coupled simulations using the relationships from Paul et al. (1999) (Figure S1 in Supporting Information S1). Close agreement between model-simulated  $\delta^{18}\text{O}$  of ocean surface water and  $\delta^{18}\text{O}$  values derived from water salinity is shown by Gaskell et al. (2022) (their Sup Figure 7).

Third, for both Middle Miocene  $p\text{CO}_2$  settings, we conduct three sensitivity experiments to investigate the effects of Alpine topography and marine transgression/regression in Europe (Table 1, Figure 1). We study the effects of surface uplift of the Alps by increasing and decreasing their elevation, similar to the pre-industrial sensitivity experiments. We reduce the elevation in the area covering the Alps and the Alpine forelands to 250 m elevation (Mio\_278\_noAlps, Mio\_450\_noAlps; Figure 1d) and increase the elevation to twice the reconstructed height (Mio\_278\_plusAlps, Mio\_450\_plusAlps; Figure 1e) compared to the original paleogeographic reconstruction of Herold et al. (2011) (used in Mio\_278 and Mio\_450 experiments), which reflects recent hypotheses of very high Alpine elevations in the Middle Miocene (Krsnik et al., 2021). We also tested the influence of a marine transgression and regression within Europe on regional climate and stable water isotopes. For this purpose, we performed two additional experiments (Mio\_278\_SeaLand and Mio\_450\_SeaLand) with modified land-sea distributions

**Table 1**  
*ECHAM5-wiso Experiments Summary*

Experiment name	Greenhouse gases concentration	Orbital parameters	Surface conditions	Alps elevation
PI	CO <sub>2</sub> 280 ppm, CH <sub>4</sub> 760 ppb, N <sub>2</sub> O 270 ppb.	Eccentricity = 0.016804, obliquity = 23.4725, longitude of perihelion = 278.734	Sea surface temperature and sea ice are taken from a transient low-resolution coupled ocean-atmosphere simulation (Dietrich et al., 2013; Lorenz & Lohmann, 2004). Land surface parameters, including vegetation are based on (Hagemann, 2002).	100% of present
PI_noAlps	Same as PI	Same as PI	Same as PI	Reduced to 250 m
PI_plusAlps	Same as PI	Same as PI	Same as PI	Increased by 50%
Mio_278	CO <sub>2</sub> 278 ppm, CH <sub>4</sub> 650 ppb, N <sub>2</sub> O 270 ppb.	Eccentricity = 0.016724, obliquity = 23.4468, longitude of perihelion = 272.157	Sea surface temperature, sea ice and vegetation from Middle Miocene COSMOS (278 ppm) simulations (Stärz et al., 2017). Paleogeography from Middle Miocene reconstruction (Herold et al., 2011). The height of the Antarctic ice-sheet is reduced compared to present-day (Herold et al., 2008) and the Greenland ice-sheet is absent. Seawater $\delta^{18}\text{O}$ values were set identical to present-day. Physical soil characteristics, such as soil albedo and maximum water holding field capacity, derived by adapting vegetation related parameters based on (Stärz et al., 2017).	100% of present
Mio_278_noAlps	Same as Mio_278	Same as Mio_278	Same as Mio_278	Reduced to 250 m
Mio_278_plusAlps	Same as Mio_278	Same as Mio_278	Same as Mio_278	Increased by 100%
Mio_278_iniwiso	Same as Mio_278	Same as Mio_278	Same as Mio_278, except for seawater $\delta^{18}\text{O}$ values, which were computed from upper-level ocean salinity from COSMOS (278 ppm) simulations (Stärz et al., 2017) using the relationships from (Paul et al., 1999).	100% of present
Mio_278_LanSea	Same as Mio_278	Same as Mio_278	Same as Mio_278, except for the Paratethys Sea area, which extends in accordance to Popov et al. (2004).	100% of present
Mio_450	CO <sub>2</sub> 450 ppm, CH <sub>4</sub> 650 ppb, N <sub>2</sub> O 270 ppb.	Eccentricity = 0.016724, obliquity = 23.4468, longitude of perihelion = 272.157	Sea surface temperature, sea ice and vegetation from Middle Miocene COSMOS (450 ppm) simulations (Stärz et al., 2017). Paleogeography from Middle Miocene reconstruction (Herold et al., 2011). The height of the Antarctic ice-sheet is reduced compared to present-day (Herold et al., 2008) and the Greenland ice-sheet is absent. Seawater $\delta^{18}\text{O}$ values were set identical to present-day. Physical soil characteristics, such as soil albedo and maximum water holding field capacity, derived by adapting vegetation related parameters based on (Stärz et al., 2017).	100% of present
Mio_450_noAlps	Same as Mio_450	Same as Mio_450	Same as Mio_450	Reduced to 250 m
Mio_450_plusAlps	Same as Mio_450	Same as Mio_450	Same as Mio_450	Increased by 100%
Mio_450_iniwiso	Same as Mio_450	Same as Mio_450	Same as Mio_450, except for seawater $\delta^{18}\text{O}$ values, which were computed from upper-level ocean salinity from COSMOS (450 ppm) simulations (Stärz et al., 2017) using the relationships from (Paul et al., 1999).	100% of present
Mio_450_LandSea	Same as Mio_450	Same as Mio_450	Same as Mio_450, except for the Paratethys Sea area, which extends in accordance to Popov et al. (2004).	100% of present

Note. PI, pre-industrial.

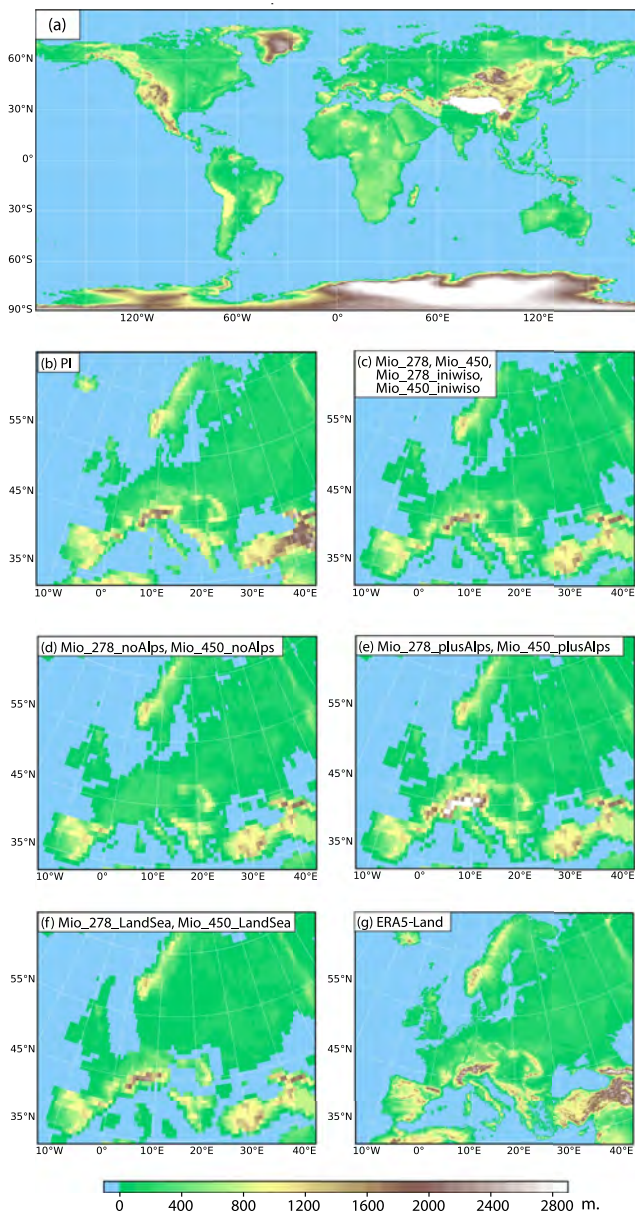


**Figure 1.** (a) Global Middle Miocene paleogeography of Herold et al. (2008) at T159 model resolution, used in the following experiments: Mio\_278, Mio\_450, Mio\_278\_iniwiso, and Mio\_450\_iniwiso experiments; (b) present-day topography of Europe at T159 model resolution, (c) same as subplot (a) but for the European region; (d) modified Middle Miocene paleogeography with Alpine elevation reduced to 250 m compared to the original reconstruction of Herold et al. (2008), applied in Mio\_278\_noAlps and Mio\_450\_noAlps experiments; (e) modified Middle Miocene paleogeography with increased Alpine elevation by 100% compared to the original reconstruction of Herold et al. (2008), applied in the Mio\_278\_plusAlps and Mio\_450\_plusAlps experiments; (f) modified Middle Miocene paleogeography, with the land-sea distribution in the European region according to Popov et al. (2004), applied in Mio\_278\_LandSea and Mio\_450\_LandSea experiments; (g) topography from ERA5-Land data set (Muñoz-Sabater et al., 2021).

over Europe (Figure 1f), corresponding to the mid-Middle Miocene reconstruction (14 Ma) from the Paleogeographic Atlas of the Paratethys region (Popov et al., 2004).

All experiments were performed at high resolution (T159 L31, corresponding to a grid spacing of  $\sim 0.75^\circ$ , or  $\sim 80$  km in latitude and longitude at the equator, with 31 vertical levels up to 10 hPa). A further increase in model resolution, which would be required for a better representation of the topography, was not possible due to limited computing resources. Each model experiment was run for 13 model years. For lower resolutions of the model, simulation in an atmosphere-only setup forced with SST and SIC, has been shown to quickly bring the model into quasi-equilibrium, not instantaneously, but within the first two to three model years (Stepanek & Lohmann, 2012). Therefore, we consider the results of the experiments from the fourth model year onwards. In the Mio\_278 and Mio\_450 experiments, the climate appears to deviate slightly from radiative equilibrium, with an average net energy imbalance of  $\sim -4.2$  W/m<sup>2</sup> and  $\sim -6.7$  W/m<sup>2</sup>. Since the atmosphere cannot generate energy, the SSTs, provided to the model from a quasi-equilibrium simulation of the model that has been coupled at lower resolution to an ocean model, are too warm for the high-resolution atmosphere standalone model in combination with the prescribed radiative forcing. This is a common problem in atmosphere standalone simulations (e.g., Stepanek & Lohmann, 2012). The year-to-year fluctuations of temperatures for both Mio\_278 and Mio\_450 are of the same order of magnitude as in the modern observations (by up to 0.1°C–0.2°C per year), and the trends (decreasing for Mio\_278 and increasing for Mio\_450) are small ( $\sim 0.01^\circ\text{C}/\text{yr}$ ), therefore, we consider our model experiment to be sufficiently equilibrated. We analyzed computed climatological values and inter-annual variations of the last 10 model years for each experiment.

### 3.2. Post-Processing

Our analyses are based on daily and seasonal averages of temperature, precipitation, evaporation, humidity, sea level pressure (SLP), winds, vertical velocity ( $\omega$ ) at 500 hPa level,  $\delta^{18}\text{O}$  in vapor ( $\delta^{18}\text{O}_v$ ), and  $\delta^{18}\text{O}_p$  values. These outputs are presented after calculating arithmetic means of the 6-hourly ECHAM5-wiso output. In the analysis of vertical motion of air, high subsidence areas were detected by positive  $\omega$  as well as low relative humidity. We provide a detailed analysis for three regions in Europe (Figure 2a, black rectangles): (a) central Europe including the Alpine region (from 40°N to 55°N and from 2°W to 25°E), (b) a low-elevation region (from 48°N to 51°N and from 2°E to 16°E; all grid cells lower than 500 m), and (c) a high-elevation region (from 42°N to 48°N and from 2°E to 16°E; all grid cells higher than 1,000 m).

### 3.3. Proxy Data Compilation of Terrestrial Temperature and Precipitation

GCM model predictions are compared to a literature compilation of Middle Miocene terrestrial proxy data for paleotemperature and paleoprecipitation from Europe provided by various previous publications (Tables S1 and S2). We use the compilation of European mean annual temperature (MAT) proxy data from Burls et al. (2021) for the Middle Miocene (Table S1). These values were supplemented with estimates of the mean temperature of the warmest month (WMT) and mean temperature of the coldest month (CMT)

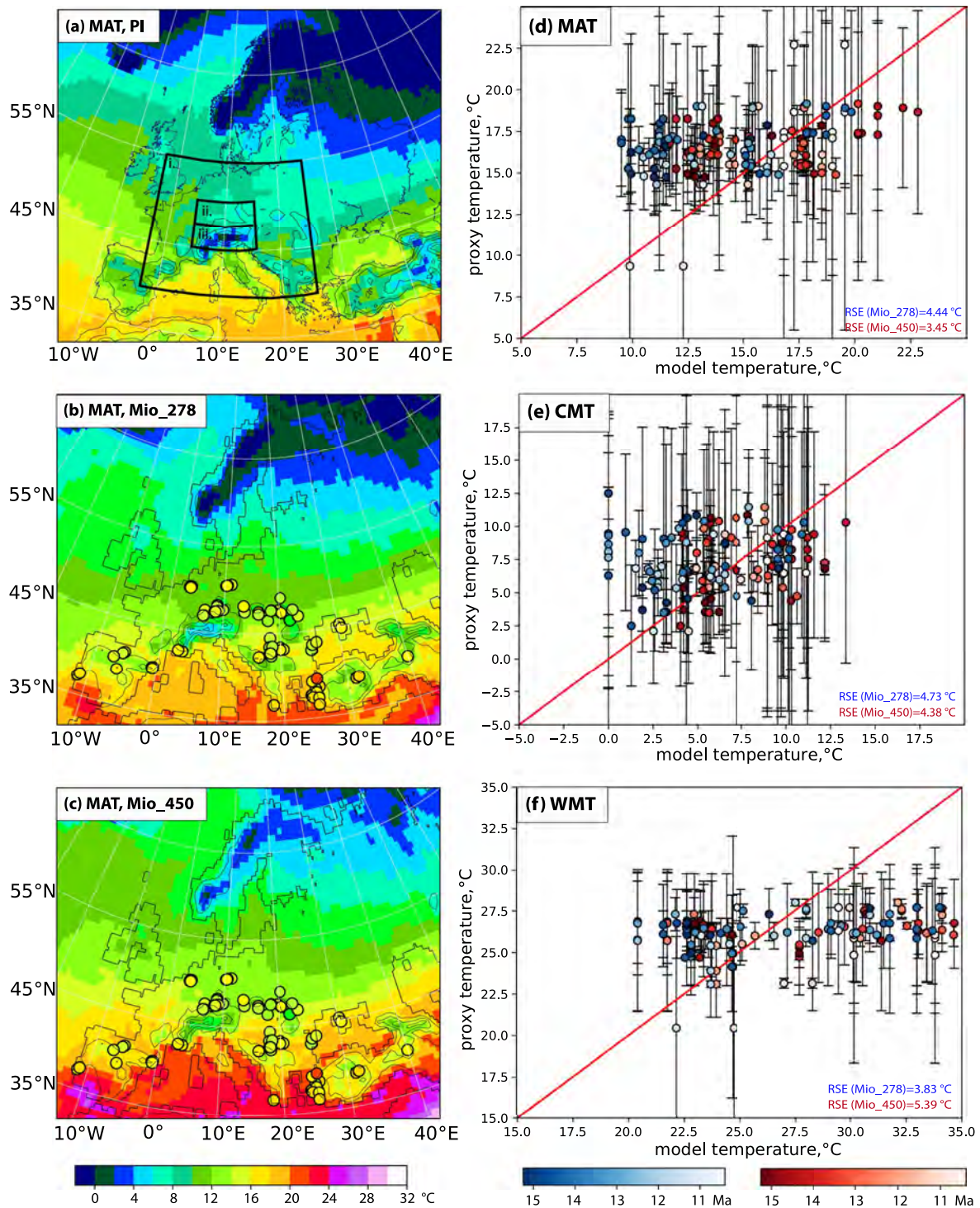


Figure 2.

when available from the original publications. Paleotemperature estimates (Table S1) presented here come from fossil plant data and are based on the coexistence approach. This method uses the modern climatic range of a fossil taxon's nearest living relative to determine the climatic parameters of its habitat and in a second step determines the climatic envelope of coexisting species of an entire fossil assemblage (Mosbrugger & Utescher, 1997; Utescher et al., 2014).

The compilation of mean annual precipitation (MAP) is presented separately in two tables (Tables S1 and S2) depending on the estimation approach. Table S1 contains MAP values reconstructed from fossil plant data using the coexistence approach. This table additionally contains estimates of monthly mean precipitation of the driest month (highest monthly precipitation, LMP) and monthly mean precipitation of the wettest month (lowest monthly precipitation, HMP) when available from the original publications. Table S2 contains the herpetological assemblages presented in Böhme et al. (2007, 2011), with addition of new sites from Böhme and Vasilyan (2014). For both the paleotemperature and the paleoprecipitation databases, all site coordinates were rotated to their position in the middle Miocene using the GPLATES online tool (<http://portal.gplates.org/service/>) based on individually averaged age estimates for each data point.

### 3.4. Comparison to Reanalysis and to Previous Models

To evaluate our ECHAM5-wiso PI experiment, we compare our results with the ERA-Interim reanalysis (Dee et al., 2011) for the European region. With this comparison, we aim to show (a) the similarity of the present-day and PI spatial patterns across Europe at the annual-mean and seasonal scale, and (b) the changes between PI and modern conditions. To evaluate our simulations of the Middle Miocene, we compare our simulated temperature and temperature difference between the Middle Miocene and the PI experiments with the simulated values reported in Burls et al. (2021) for MioMIP1. We caution readers that this is not a formal model intercomparison, because the experiments presented in Burls et al. (2021) and our experiments are inhomogeneous. Apart from the obvious differences in CO<sub>2</sub> forcing, the differences lie in (a) the length of the analysis periods, ranging from 10 years (ECHAM5-wiso) to >100 years in Burls et al. (2021), (b) the model complexity, from atmosphere-only (ECHAM5-wiso) to fully coupled (e.g., CCSM3, HadCM3L, COSMOS, IPSLCM), and (c) the model resolution, from low-resolution (T31 or T42) experiments in Burls et al. (2021) to high-resolution (T159) ECHAM5-wiso experiments.

### 3.5. Comparison of Model Predictions and Proxy Data

We provide a simple statistical analysis in order to compare proxy data and model outputs. With this aim, we adjust the parameters of a model function ( $y = f(x)$ ) to a data set, where  $x$  is MAT, WMT, CMT, MAP, LMP, and or HMP, respectively, from our proxy data compilation, and  $y$  is MAT, WMT, CMT, MAP, LMP, or HMP, respectively, simulated by ECHAM5-wiso. Then, for each pair of  $x$  and  $y$ , the residual standard error (RSE) is calculated, which permits us to identify the optimal model-data fit, which occurs when the RSE is minimized.

## 4. Results

### 4.1. Comparison of Simulated Temperature With Models Participating in MioMIP1

We compare our simulated Middle Miocene temperature (Figure 2) and the temperature difference between Middle Miocene and PI runs with the simulated values reported in Burls et al. (2021). From this publication, we choose the experiments with CO<sub>2</sub> concentrations in the range of 200–280 and 400–450 ppm to compare with our Mio\_278 and Mio\_450 experiments, respectively. For brevity in the main text, we include the comparison of our simulations with the MioMIP1 simulations in the supplementary material (Figures S2 and S3 in Supporting Information S1).

**Figure 2.** Maps of mean annual temperature (MAT) for (a) PI, (b) Mio\_278 and (c) Mio\_450 experiments. Shaded circles on (b and c) show Middle Miocene MAT (as the mean between MAT max and MAT min), compiled from terrestrial paleobotany proxy data (see Table S1). Isolines show topography for experiments PI, Mio\_278 and Mio\_450; isolines are with a 500 m contour interval. Black rectangles on subplot (a) show selected regions: (i) central Europe and Alpine region (from 40°N to 55°N and from 2°W to 25°E; grid cells over the continent only), (ii) low-elevation region (from 48°N to 51°N and from 2°E to 16°E; all grid cells lower than 500 m), (iii) high-elevation region (from 42°N to 48°N and from 2°E to 16°E; all grid cells higher than 1,000 m). Subplot (d) model mean annual temperature (MAT), (e) model coldest month temperature (CMT) and (f) model warmest month temperature (WMT) model vs. corresponding values reconstructed using the coexistence approach on paleofloral data. For the comparison with the two Miocene simulations (Mio\_278 and Mio\_450), the corresponding data (without subdivision by age) are taken from Table S1. Model values in subplots (d–f) are taken at sample locations. The bluish colors show all points data when compared to the Mio\_278 temperatures and the reddish colors when compared to the Mio\_450 temperatures. Color intensity corresponds to the averaged absolute age of the data point (see Table S1): light blue and light red—younger age, dark blue and dark red—older age. The red line shows a 1:1 model-data fit. RSE, residual standard error between proxy data and model temperature. Points restored to their paleo coordinates by means of GPLATES online tool (<http://portal.gplates.org/service/>).



Results indicate that ECHAM5-wiso reproduces global MATs compared to the Middle Miocene model experiments involved in MioMIP1 (Burls et al., 2021; Figures S2 and S3 in Supporting Information S1; Table S3 in Supporting Information S1). For the Mio\_278 simulation, the global mean annual surface temperature is 2.5°C higher than for PI (Table S3 in Supporting Information S1). This is higher than values reported in Burls et al. (2021) for experiments with CO<sub>2</sub> concentration of 200–280 ppm, which provide the multi-model mean of 1.5°C (Table S3 in Supporting Information S1). For the Mio\_450 experiment, the global mean annual surface temperature is 5.9°C higher than for PI (Table S3 in Supporting Information S1). This lies in the high-end of values presented in Burls et al. (2021) for experiments with CO<sub>2</sub> concentration of 400–450 ppm (Table S3 in Supporting Information S1). We note that our modeled temperature anomaly is within the uncertainty range of the MioMIP1 simulations. Particularly pronounced (positive) anomalies are found with respect to simulations based on the HadCM3L model. This model has been shown, however, to produce comparatively cold simulations within the MioMIP1 ensemble (Figure 4a by Burls et al., 2021).

At a regional scale, over central Europe and the Alpine region, (region (i) in Figure 2a), the mean temperature difference between Mio\_278 and the multi-model mean temperature from MioMIP1 experiments at 200–280 ppm is 2.7°C (Table S3 in Supporting Information S1). The regional mean temperature difference between Mio\_450 and the multi-model mean temperature from MioMIP1 experiments at 400–450 ppm is 1.9°C. For both CO<sub>2</sub> setups, ECHAM5-wiso systematically shows higher temperatures (up to max. 4°C) over the low-elevation region (region (ii) in Figure 2a). Lower temperatures (up to max. 10°C) are simulated over the high-elevation region (region (iii) in Figure 2a), and also over Carpathians, Dinarids and other mountainous regions in Europe (Figures S2 and S3 in Supporting Information S1).

#### 4.2. ECHAM5-Wiso Simulated Middle Miocene MAT

We first discuss the simulated near-surface MAT in the Middle Miocene control experiments (Mio\_278 and Mio\_450) and compare those with European plant fossil-derived MAT (based on coexistence approach, see Section 3.3). Finally, we examine changes in simulated near-surface MAT of the Middle Miocene experiments that result from varied elevation of the European Alps.

The simulated MAT over the central Europe and the Alpine region (Figure 2a, region (i)) is 12.0°C and 15.0°C in the Mio\_278 and Mio\_450 experiments, respectively (Figures 2a–2c; Table S4 in Supporting Information S1). The largest difference relative to PI is over the high-elevation region (elevations >1,000 m), which is 3.4°C and 7.2°C warmer in the Mio\_278 and Mio\_450 experiments, respectively. The Mio\_450 simulation shows good agreement with MAT reconstructed by the coexistence approach on fossil plants, while the Mio\_278 simulation shows generally lower temperatures than predicted by the coexistence approach (Figure 2d, Table S4 in Supporting Information S1). The model-proxy data fit estimated using the RSE method is 4.4°C for the Mio\_278 and 3.5°C for Mio\_450 (Table S5 in Supporting Information S1). Thus, the simulation with higher *p*CO<sub>2</sub> concentration shows a better fit to fossil plant data.

Experiments with varied elevation of the Alps show that most temperature changes are restricted to the Alpine region itself (Figures 3a–3d). Experiments with higher Alpine elevations (Mio\_278\_plusAlps, Mio\_450\_plusAlps) show 4.1°C and 3.3°C lower temperatures over high-elevation region of the Alps, compared to Mio\_278 and Mio\_450, respectively (Table S4 in Supporting Information S1). In contrast, over the low-elevation regions, this decrease is minimal with 0.9°C and 0.1°C, respectively. The temperature increase in the experiments with reduced Alpine elevation (Mio\_278\_noAlps, Mio\_450\_noAlps) compared to Mio\_278 and Mio\_450 is less than 1°C for the central Europe region and the low-elevation region, but is up to 4.4°C (Mio\_278) and 4.3°C (Mio\_450) for the high-elevation region. The temperature change over both the low-elevation and the high-elevation region in the Mio\_278\_LandSea and Mio\_450\_LandSea simulations compared to the Miocene control simulation (Mio\_278 and Mio\_450, respectively) is less than 1°C (Figure 3e; Table S4 in Supporting Information S1).

Taken together, these results suggest a warmer-than-PI Miocene climate across Europe, in a good agreement with temperature estimates derived from fossil flora. The experiment with higher *p*CO<sub>2</sub> (Mio\_450) shows better agreement. Different Alpine elevations contribute to temperature changes restricted to the Alpine region and a different land-sea distribution in Europe has only minor effects on the regional temperature pattern.

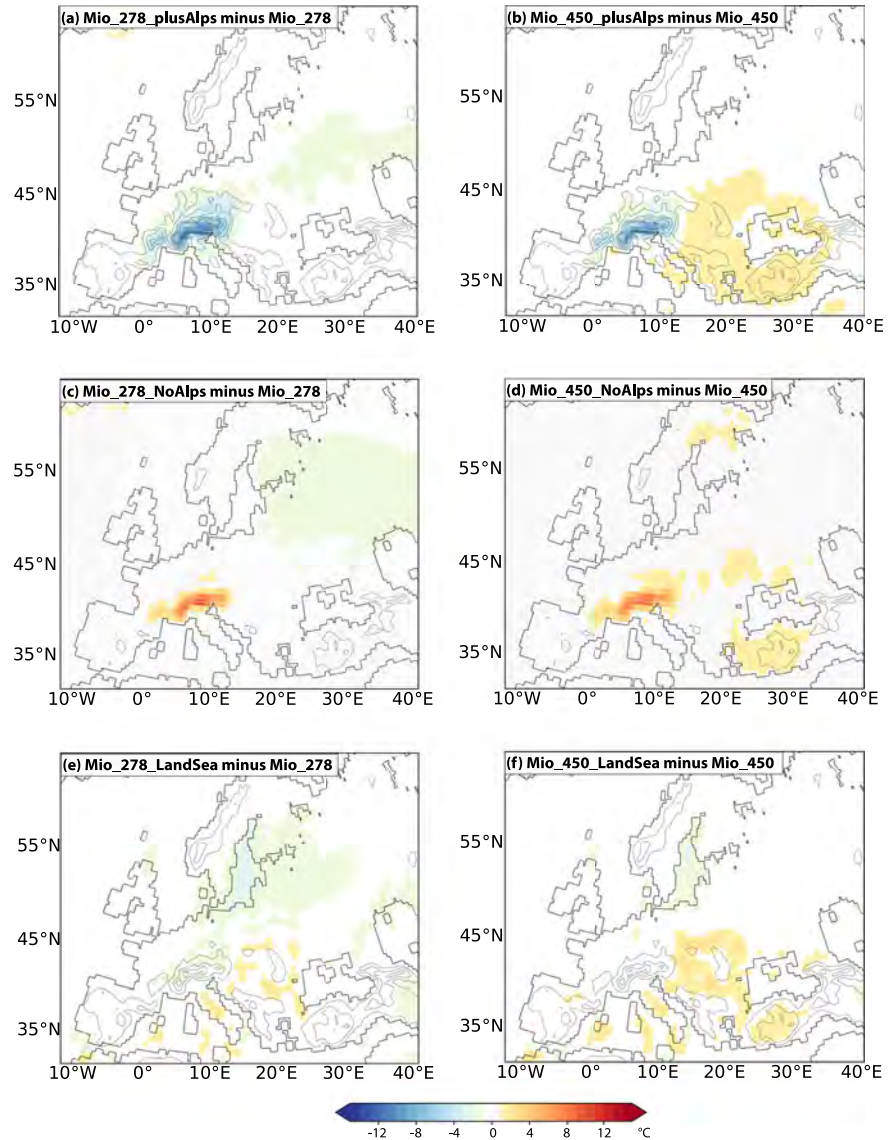


**Figure 3.** Temperature (at 2 m) change for the following simulation comparisons: (a) Mio\_278\_plusAlps relative to Mio\_278, (b) Mio\_450\_plusAlps relative to Mio\_450, (c) and Mio\_278\_noAlps relative to Mio\_278, (d) Mio\_450\_noAlps relative to Mio\_450, (e) Mio\_278\_LandSea relative to Mio\_278, and (f) Mio\_450\_LandSea relative to Mio\_450.

### 4.3. ECHAM5-Wiso Simulated Middle Miocene MAP

Simulations predict lower MAP for both Mio\_278 and Mio\_450 experiments than for PI over most of Western and Southern Europe (compare Figures 4c and 4d–4f). Meanwhile, an increase of 50–400 mm/yr is simulated for the MAP over Scandinavia and northwestern Russia. On average, for central Europe and the Alpine region, MAP for both the Mio\_278 run and the Mio\_450 run is less than for the PI (Table S4 in Supporting Information S1). Over the European Alps, MAP decreases across both the low-elevations and the high-elevation regions in both Miocene experiments compared to PI (Figures 4b–4d).

Investigation of the paleobotanic proxy data indicates larger precipitation amounts than predicted in the Mio\_278 and Mio\_450 experiments (Figure 4g; Table S5 in Supporting Information S1). However, the simulated MAP in the Mio\_278 and Mio\_450 runs is consistent with precipitation estimates from the ecophysiological structure of herpetological assemblages (herpetofaunal fossils; Figure 4h; Table S5 in Supporting Information S1).

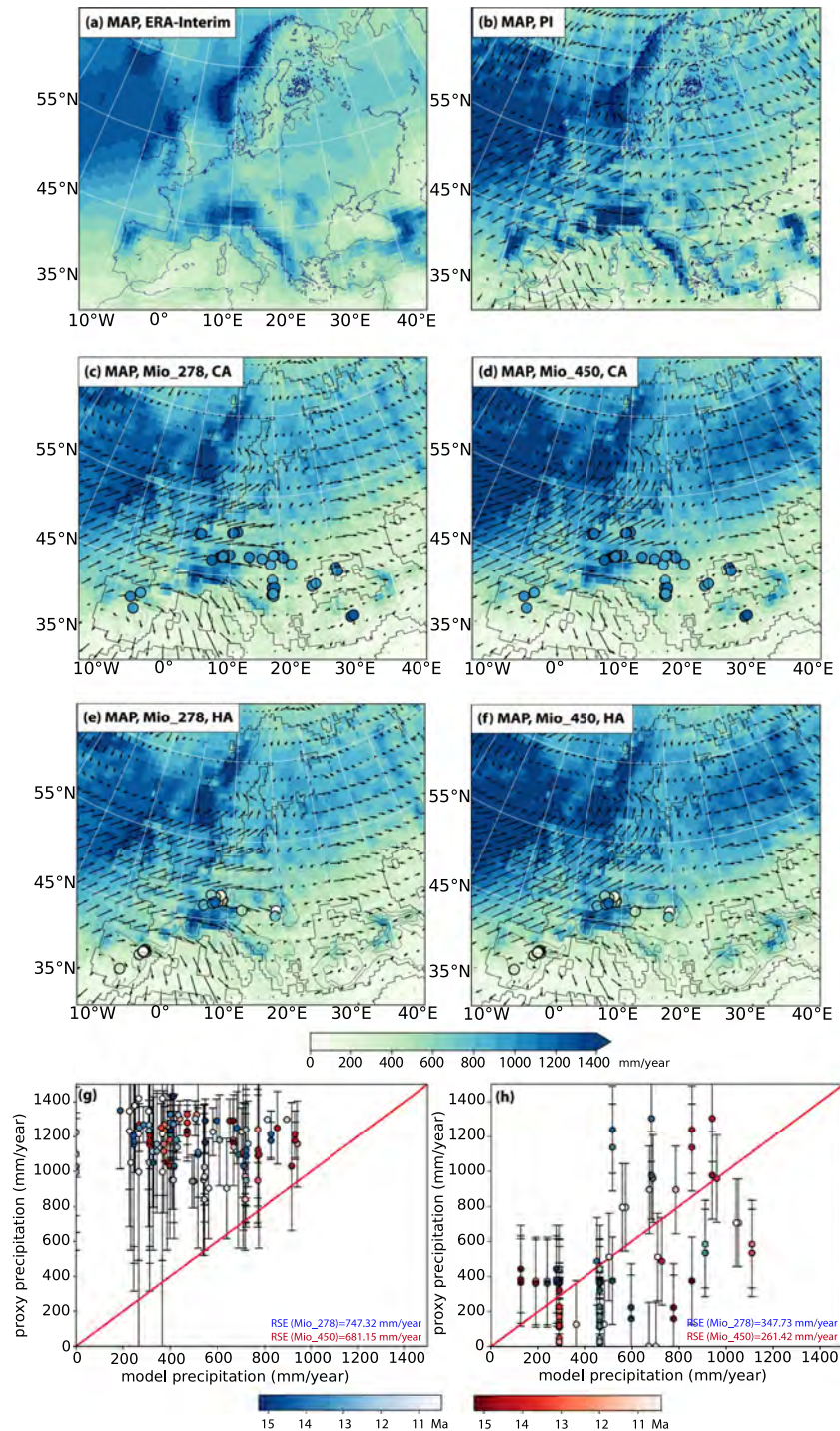


**Figure 4.** Mean annual precipitation (MAP) and mean annual winds at 10 m for ERA-Interim reanalysis (a) and ECHAM5-wiso experiments (b–f). (b) PI, (c, e) Mio\_278, and (d, f) Mio\_450 simulations. Vectors show near-surface winds. In subplots (c and d), the shaded circles show Middle Miocene MAP (as the mean between MAP max and MAP min correspondingly) reconstructed from fossil plant data using the coexistence approach (CA see Table S1). In subplots (e and f), the shaded circles show Middle Miocene MAP, reconstructed from the ecophysiological structure of the herpetological assemblages (HA; see Table S2). Subplot (g) shows the model MAP vs. MAP, reconstructed using the plant coexistence approach, subplot (h) shows the model MAP vs. MAP, reconstructed from the ecophysiological structure of the herpetological assemblages. The bluish colors for the points on subplots (g, h) correspond to the Mio\_278 experiment and the reddish colors to the Mio\_450 experiments. For the comparison with the two simulations, the corresponding data of all available ages are taken from Table S1 (g) and from Table S2 (h). The bluish colors show all points data when compared to the Mio\_278 precipitation and the reddish colors—to the Mio\_450 precipitation. Color intensity corresponds to the averaged absolute age of the data point (see Tables S1 and S2): light blue and light red—younger age, dark blue and dark red—older age. The red line shows a 1:1 model-data fit. Points restored to their paleo coordinates by means of GPLATES online tool (<http://portal.gplates.org/service/>).

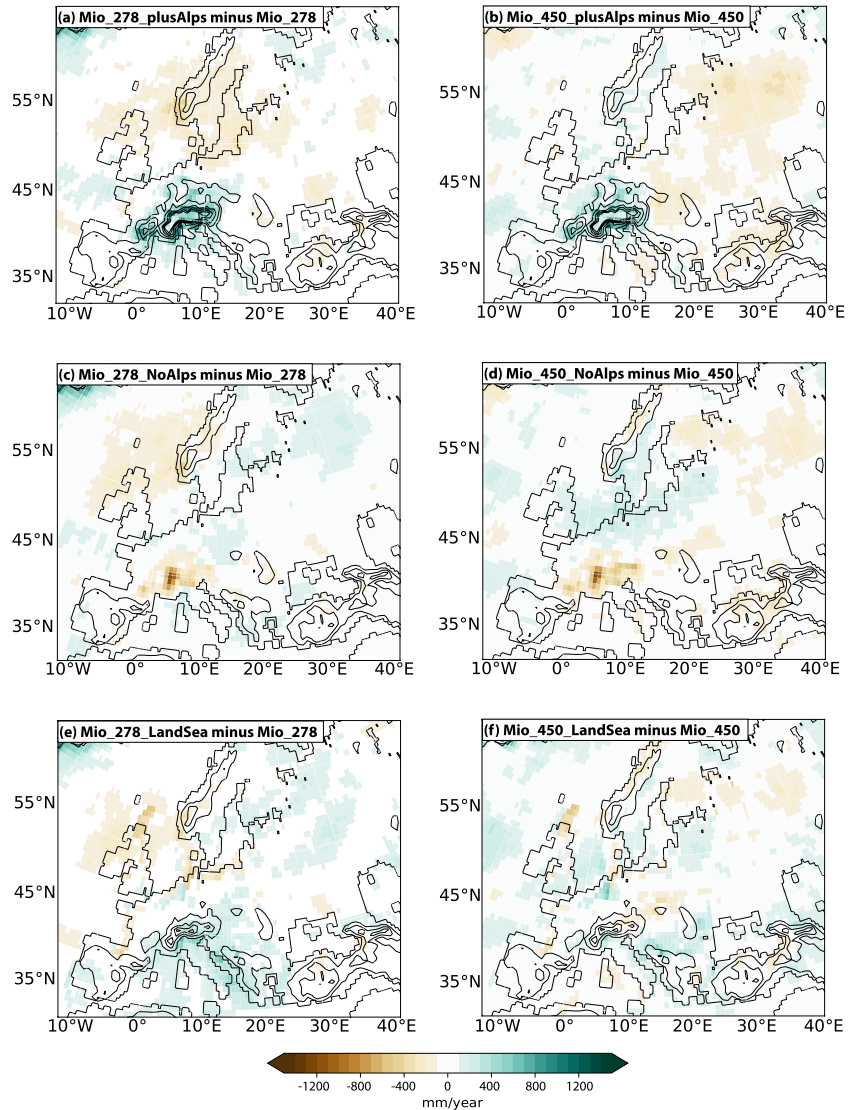


**Figure 5.** Precipitation change for (a) Mio\_278\_plusAlps relative to Mio\_278, (b) Mio\_450\_plusAlps relative to Mio\_450, (c) Mio\_278\_noAlps relative to Mio\_278, (d) Mio\_450\_noAlps relative to Mio\_450, (e) Mio\_278\_LandSea relative to Mio\_278, and (f) Mio\_450\_LandSea relative to Mio\_450.

Surface uplift of the Alps has both a regional and a far-field impact on European precipitation: with mountain growth, precipitation increases over the Alps and precipitation decreases across Eastern Europe (Figures 5a–5d). On average, experiments with higher Alpine elevation (Mio\_278\_plusAlps, Mio\_450\_plusAlps) suggest a precipitation increase by 141 and 57.2 mm/yr, respectively, for central Europe compared to the Mio\_278 and Mio\_450 simulations, respectively (Table S4 in Supporting Information S1). This increase is the most pronounced for the high-elevation region of the Alps. In contrast, experiments with reduced Alpine elevation (Mio\_278\_noAlps, Mio\_450\_noAlps) show a decrease in precipitation, which is most prominent over the high-elevation region. The precipitation change in the Mio\_278\_LandSea and Mio\_450\_LandSea simulations relative to the Mio\_278 and Mio\_450 runs, respectively is below 130 mm/yr over regions adjacent to the Alps (Figures 5e and 5f; Table S4 in Supporting Information S1). Higher changes in precipitation, up to 400 mm/yr, are simulated only for regions adjacent to the Paratethys Sea.

In summary, the key feature identified for the Miocene is a “bi-directional” precipitation change compared to PI conditions: an increase in precipitation over Scandinavia and Northern Europe and a decrease in precipitation over central Europe, Southern Europe, and the Mediterranean. Increased surface elevation of the Alps leads to

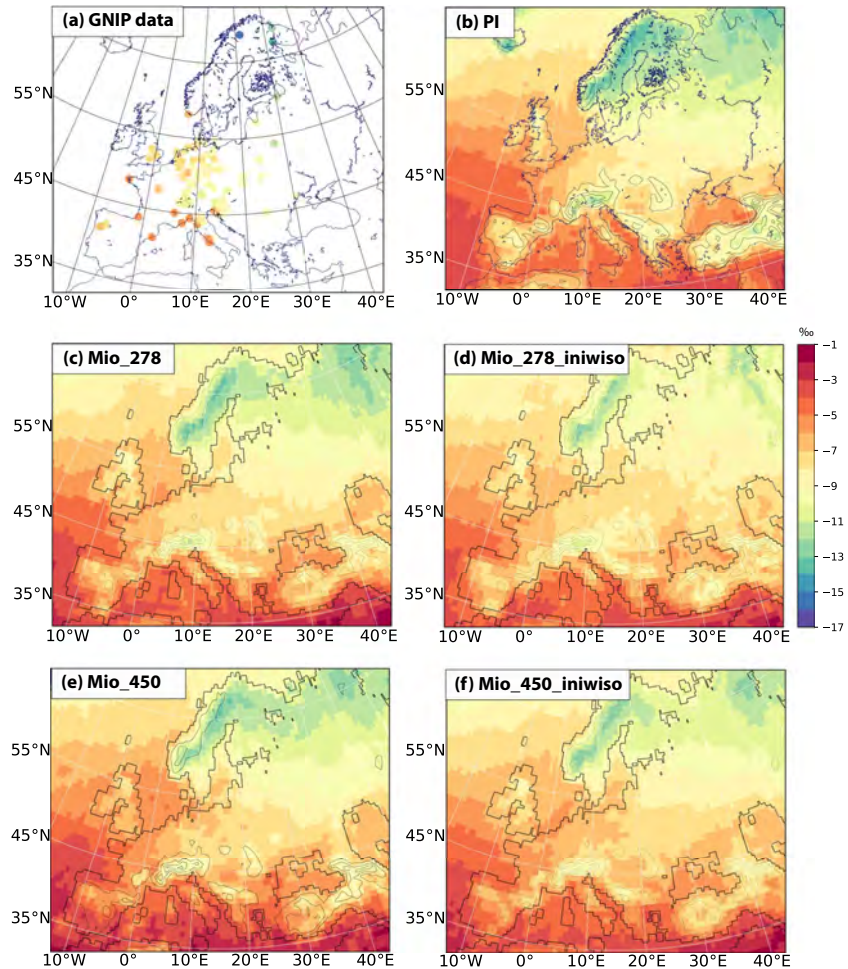


**Figure 6.** Annual mean  $\delta^{18}\text{O}_p$  from the International Atomic Energy Agency (IAEA) Global Network of Isotopes in Precipitation (GNIP) observations (a) and ECHAM5-wiso simulated annual mean  $\delta^{18}\text{O}_p$  values for: (b) the PI, (c) the Mio\_278, (d) Mio\_278\_iniwiso, (e) the Mio\_450, and (f) Mio\_450\_iniwiso experiment.

increased orographic precipitation rates restricted to the Alps region, with most prominent changes over Alpine high elevations. Simulated precipitation rates for both  $p\text{CO}_2$  setups are consistent with precipitation estimates from the ecophysiological structure of herpetological assemblages. However, MAP estimates based on the coexistence approach exceed those from the herpetological assemblages and the Miocene model results.

#### 4.4. ECHAM5-wiso Simulated Middle Miocene Mean Annual $\delta^{18}\text{O}_p$

The simulated mean annual  $\delta^{18}\text{O}_p$  patterns for both the Mio\_278 and the Mio\_450 experiments are qualitatively similar to the predicted PI  $\delta^{18}\text{O}_p$  pattern across Europe. Predicted  $\delta^{18}\text{O}_p$  values generally decrease from south to north, from continental margins to the continental interior and from low-to high-elevation regions (Figure 6; Figure S4 in Supporting Information S1). The most negative values are simulated over Scandinavia, NW Russia, and the Alps. The average annual  $\delta^{18}\text{O}_p$  value for central Europe and the Alpine region in the Mio\_278 and Mio\_450 simulations is 0.5‰ and 1‰ higher than in the PI, respectively (Table S4 in Supporting Information S1). Averaged over the low-elevation region,  $\delta^{18}\text{O}_p$  is 0.6‰ higher for Mio\_450 than for the PI, while Mio\_278 is approximately the same as in the PI. For the high-elevation region, the mean  $\delta^{18}\text{O}_p$  value is 0.7‰ (Mio\_278) and 1.5‰ (Mio\_450) higher than for the PI. Our simulations with modified seawater  $\delta^{18}\text{O}$  (Mio\_278\_iniwiso and Mio\_450\_iniwiso) show low sensitivity of the  $\delta^{18}\text{O}_p$  over central Europe to this parameter (Figure 6; Table S4 in Supporting Information S1).

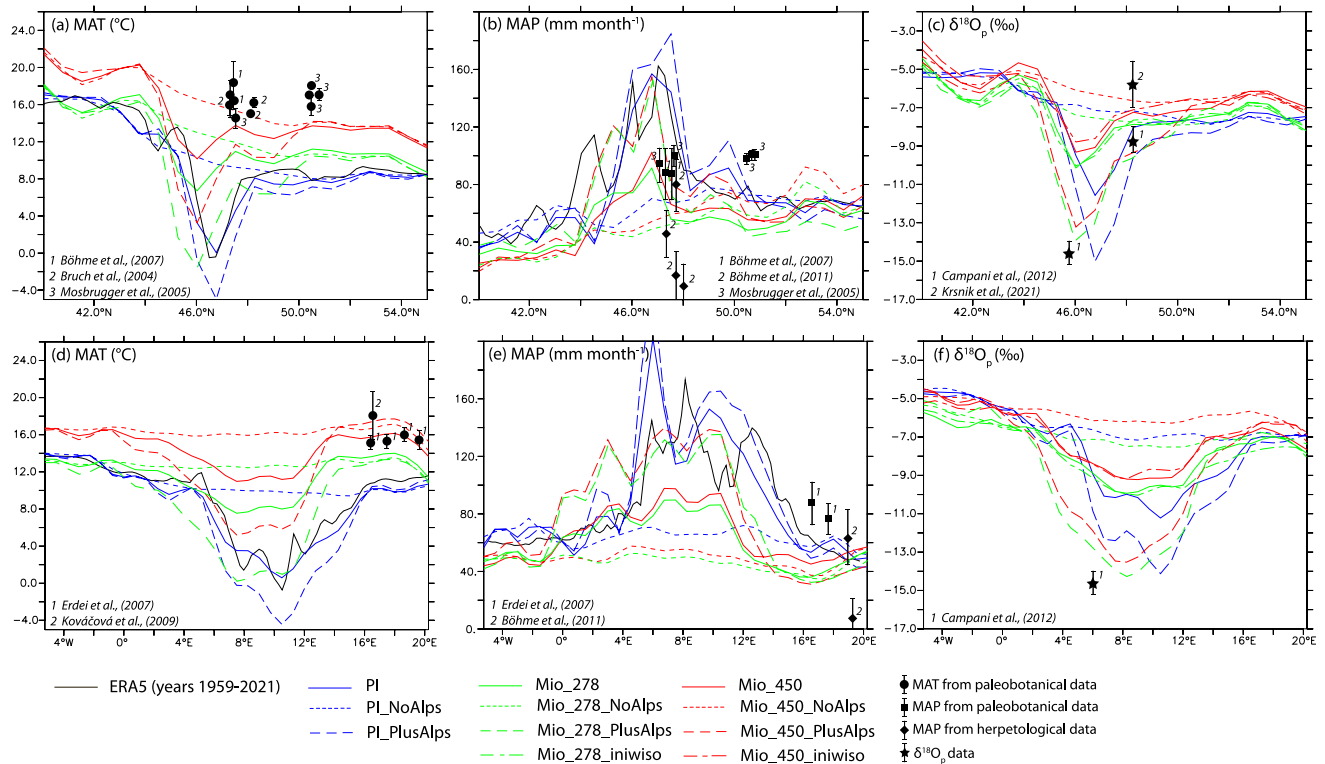


**Figure 7.** Annual mean temperature (a, d), precipitation (b, e), and  $\delta^{18}\text{O}_p$  (c, f) gradients across the Alps: (a–c) averaged between  $9^\circ\text{E}$  and  $10^\circ\text{E}$  and (d–f) between  $46^\circ\text{N}$  and  $47^\circ\text{N}$  for topographic sensitivity experiments with pre-industrial (PI\_NoAlps, PI, PI\_plusAlps) and Middle Miocene (Mio\_278, Mio\_450, Mio\_278\_noAlps, Mio\_450\_noAlps, Mio\_278\_plusAlps, Mio\_450\_plusAlps, Mio\_278\_iniwiso, Mio\_450\_iniwiso) boundary conditions and for ERA5 reanalysis time averaged from 1959 to 2021. Selected data points (for MAT [Table S1], MAP [Table S1 and Table S2], and  $\delta^{18}\text{O}_p$  [Campani et al., 2012; Krsnik et al., 2021]) between  $8^\circ\text{E}$  and  $11^\circ\text{E}$  (a–c) and between  $45^\circ\text{N}$  and  $49^\circ\text{N}$  (d–f) extrapolated to the section line are shown in black.

Over the Alps, the  $\delta^{18}\text{O}_p$  values for the PI show a clear decrease from the foothills to the summit across both South-North (averaged between  $9^\circ\text{E}$  and  $10^\circ\text{E}$ ) and East-West (averaged between  $46^\circ\text{N}$  and  $47^\circ\text{N}$ ) profiles (Figures 7c and 7f). For the PI simulation this change is  $-0.25\text{‰}/100\text{ m}$  in the Northern Alps for annual mean values, which is consistent with the modern precipitation-weighted isotopic lapse rate ( $-0.2\text{‰}/100\text{ m}$  in the Northern Alps; Campani et al., 2012) and close to the empirically determined global river-based average of ( $-0.28\text{‰}/100\text{ m}$ ; Poage & Chamberlain, 2001). For both Mio\_278 and Mio\_450 experiments the annual mean isotopic lapse rate along the North Alpine flank is  $-0.2\text{‰}/100\text{ m}$ .

In the experiments with increased topography (Mio\_278\_plusAlps and Mio\_450\_plusAlps)  $\delta^{18}\text{O}_p$  values are on average  $2.3\text{‰}$  and  $3.0\text{‰}$  lower than in the Mio\_278 and Mio\_450 simulations over the high-elevation region (Figure 8; Figure S4 in Supporting Information S1; Table S4 in Supporting Information S1). The maximum changes are  $-5.3\text{‰}$  and  $-5.8\text{‰}$  for the Mio\_278\_plusAlps minus Mio\_278 and Mio\_450\_plusAlps minus Mio\_450, respectively, for high-elevation region. The differences between these simulations are within  $0.6\text{‰}$  for the central Europe region and for the low-elevation region. In experiments with reduced topography (Mio\_278\_noAlps and Mio\_450\_noAlps)  $\delta^{18}\text{O}_p$  values are on average  $1.5\text{‰}$  and  $1.3\text{‰}$  higher relative to Mio\_278 and Mio\_450, respectively. Note that the maximum change in  $\delta^{18}\text{O}_p$  values occurs over the highest Alpine topography, while over the foothills the magnitude of the difference between experiments with modern and modified topography is within  $1\text{--}2\text{‰}$  (Figure 7).

Taken together, our predicted mean annual  $\delta^{18}\text{O}_p$  values differ by less than  $1.5\text{‰}$  from the PI mean annual  $\delta^{18}\text{O}_p$  values for both  $p\text{CO}_2$  setups in the Miocene. Removal of Alpine topography contribute to an increase in  $\delta^{18}\text{O}_p$  of up to  $5.8\text{‰}$  relative to the Miocene experiment with 100% of the Alps topography and up to  $8\text{‰}$  relative to an experiment with doubling of Alpine topography. Warmer Miocene climate contributes almost imperceptibly ( $0.03\text{‰}/100\text{ m}$ ) to shallowing of the oxygen isotope lapse rate at annual scale. In the following, we investigate seasonal variations of selected variables in order to better understand seasonal bias in annual-mean values.

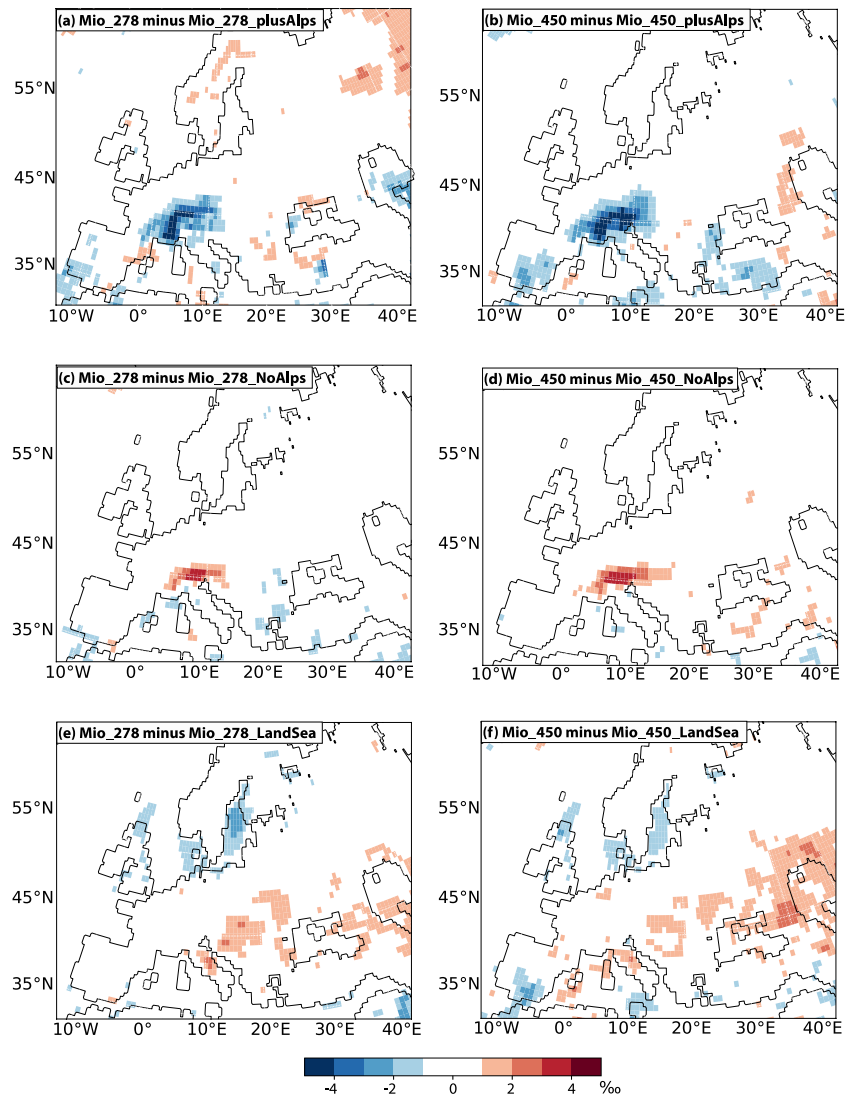


**Figure 8.** Stable oxygen isotopes change for (a) Mio\_278\_plusAlps relative to Mio\_278, (b) Mio\_450\_plusAlps relative to Mio\_450, and (c) Mio\_278\_noAlps relative to Mio\_278, (d) Mio\_450\_noAlps relative to Mio\_450, (e) Mio\_278\_LandSea relative to Mio\_278, and (f) Mio\_450\_LandSea relative to Mio\_450.

#### 4.5. Seasonality of Temperature, Precipitation, Relative Humidity, Evaporation, $\delta^{18}\text{O}$ in Vapor and $\delta^{18}\text{O}$ in Precipitation

In this section, we report intra-annual variations in simulated near-surface temperature, precipitation, evaporation, near-surface relative humidity,  $\delta^{18}\text{O}_v$  and  $\delta^{18}\text{O}_p$  values, averaged over central Europe and the Alpine region (Figure 9). The same variables averaged for the low-elevation region and for the high-elevation region (regions as shown in Figure 2a), are shown in Figures S5 and S6 in Supporting Information S1. We also compare the simulated seasonality of temperature and precipitation with seasonal temperature and precipitation signals derived from proxy data (CMT, WMT, HMP, LMP). We present the intra-annual variations in temperature, precipitation, evaporation and near-surface relative humidity to explain simulated  $\delta^{18}\text{O}_v$  and  $\delta^{18}\text{O}_p$  signals.

##### 4.5.1. Near-Surface Temperature

The seasonal cycles of near-surface temperature in Mio\_278 and Mio\_450 simulations are similar to those in the PI. The minimum monthly mean temperature (CMT) is simulated in January for PI, Mio\_278, and Mio\_450 and a maximum monthly mean temperature (WMT)—in July for PI and Mio\_273 and in August for Mio\_450

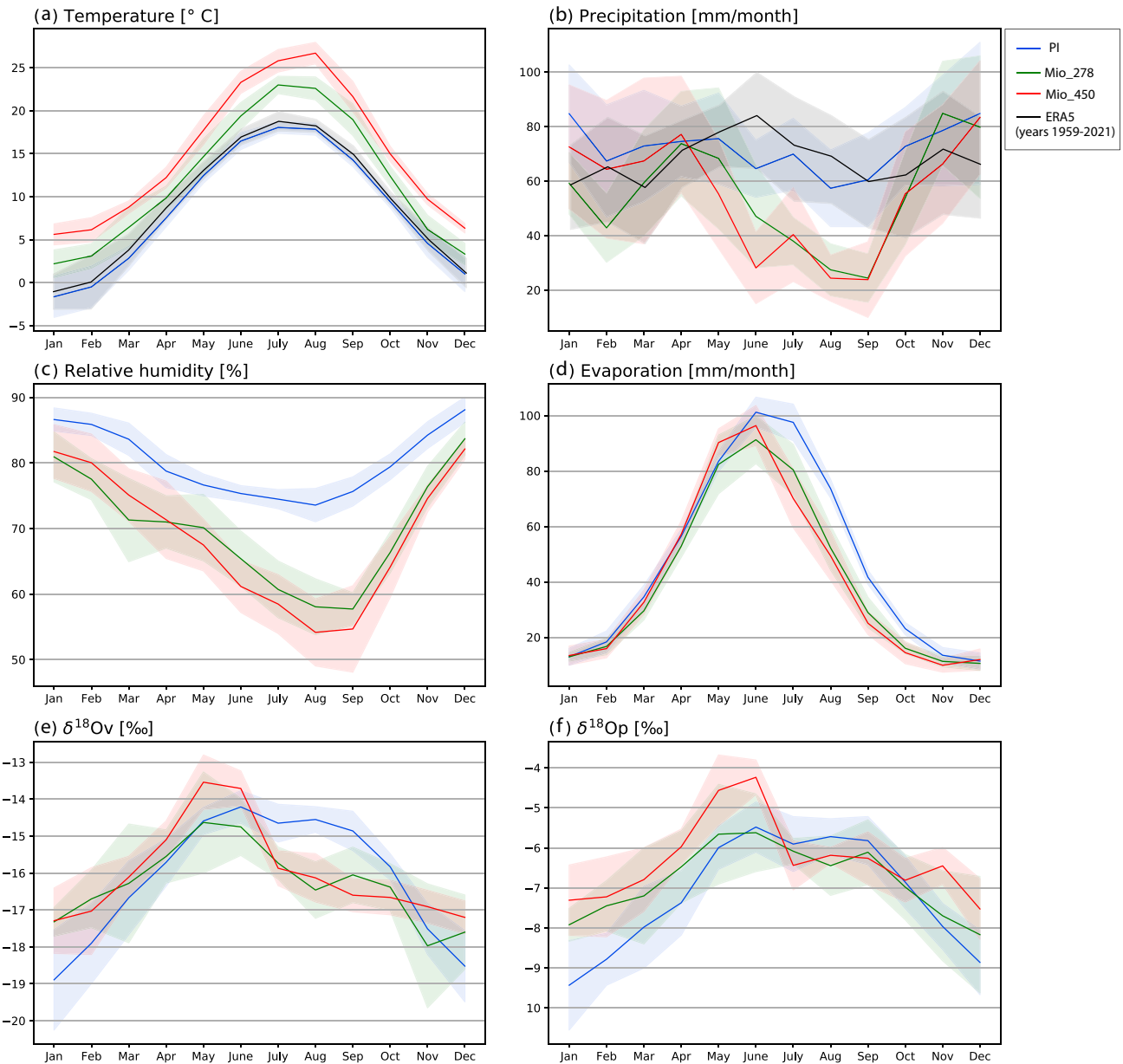


**Figure 9.** Intra-annual variations of (a) near-surface temperature, (b) total precipitation, (c) low-level relative humidity, (d) surface evaporation, (e)  $\delta^{18}\text{O}_v$  values, and (f)  $\delta^{18}\text{O}_p$  values. All variables are averaged for continental central Europe. Blue color corresponds to the PI experiment, green—Mio\_278 experiment, red—Mio\_450 experiment, black—ERA5 reanalysis from 1959 to 2021. Solid lines show multi-annual mean, shade shows interannual variability within one standard deviation for the corresponding variable.

(Figure 9a). However, the mean annual range of temperature increases in Miocene relative to PI (Table S4 in Supporting Information S1). Both Mio\_278 and Mio\_450 experiments show agreement with the data from the coexistence approach in WMT (RSE is 3.8°C and 5.4°C, respectively; Figures 2e and 2f; Table S5 in Supporting Information S1). The Mio\_278 experiment shows a lower fit to CMT derived from proxy data, with RSE values of 4.7°C, while the Mio\_450 experiment shows a better fit of 4.4°C. The best fit in the WMT and the CMT is found for the sites located in Southern Europe (Figure S7 in Supporting Information S1).

#### 4.5.2. Precipitation

Results indicate December as the month with the highest monthly precipitation (HMP) for PI, Mio\_278, and Mio\_450; the driest month (LMP) is August for PI and September for Mio\_278 and Mio\_450 (Figure 9b). The



precipitation seasonality over central Europe increases in the Miocene simulations compared to the PI simulation. For January, February, and March precipitation is similar in the PI and Mio\_450 simulations, whereas there is slightly less precipitation in the Mio\_278 experiment. However, the summer months (from May to October) are drier in the Mio\_278 and Mio\_450 simulations compared to the PI. The November and December precipitation is again similar in the PI, Mio\_278, and Mio\_450 simulations.

When compared to fossil plant data, both the Mio\_278 and Mio\_450 simulations have a low fit for HMP (RSE is 54.7 mm/month and 33.6 mm/month, respectively) and LMP (RSE = 37.0 mm/month for Mio\_278 and RSE = 37.7 mm/month for Mio\_450) (Table S5 in Supporting Information S1; Figure S8 in Supporting Information S1).

#### 4.5.3. Relative Humidity

For the PI simulation, the relative humidity reaches its maximum of 88% in December and its minimum of 73% in August (Figure 9c). The seasonal cycle is different in simulations Mio\_278 and Mio\_450 relative to the PI. While winter values are slightly lower in the Miocene simulations, in summer months a significant drop of humidity is predicted, with the maximum decrease occurring for August–September. The difference in relative humidity between the Mio\_278, Mio\_450, and PI results is 8%–12% for May–June and 18%–20% for August–September.

#### 4.5.4. Evaporation

For PI the maximum evaporation (100 mm/month) occurs in June and July, with a gradual decrease starting in August toward its yearly minimum (14 mm/month) in November and December (Figure 9d). The peak in annual evaporation for both Mio\_278 and Mio\_450 simulations is in June, with a continuous decrease toward the yearly minimum in November (12 and 13 mm/month, respectively) starting in July.

#### 4.5.5. $\delta^{18}\text{O}$ in Vapor, $\delta^{18}\text{O}$ in Precipitation

For the PI simulation both the  $\delta^{18}\text{O}_v$  and  $\delta^{18}\text{O}_p$  have minimum values in January ( $-18.9\text{‰}$  for  $\delta^{18}\text{O}_v$  and  $-9.4\text{‰}$  for  $\delta^{18}\text{O}_p$ ). The values then increase from February to June, toward their maximum in June ( $-14.2\text{‰}$  for  $\delta^{18}\text{O}_v$  and  $-5.5\text{‰}$  for  $\delta^{18}\text{O}_p$ ). From midsummer to September relatively high values occur with a subsequent smooth decrease starting in October (Figures 9e and 9f). Intra-annual variations in  $\delta^{18}\text{O}_v$  and  $\delta^{18}\text{O}_p$  for the Mio\_450 simulation are different from the PI, while  $\delta^{18}\text{O}_v$  and  $\delta^{18}\text{O}_p$  values of the Mio\_278 simulation are different from those of the PI only for November–April, but largely overlap with PI during May–October. For example, minimum  $\delta^{18}\text{O}_v$  and  $\delta^{18}\text{O}_p$  occur in December with values of  $-17.6\text{‰}$  for  $\delta^{18}\text{O}_v$  in the Mio\_278 and  $-17.2\text{‰}$  in the Mio\_450 simulations, and  $-8.1\text{‰}$  and  $-7.5\text{‰}$  for  $\delta^{18}\text{O}_p$  for the Mio\_278 and the Mio\_450. Maximum values are predicted for May and June ( $-14.6\text{‰}$  and  $-13.5\text{‰}$  for  $\delta^{18}\text{O}_v$  for Mio\_278 and Mio\_450, respectively;  $-5.6\text{‰}$  and  $-4.2\text{‰}$  in  $\delta^{18}\text{O}_p$  for Mio\_278 and Mio\_450, respectively) with an abrupt decrease in July.

In summary, the seasonal cycle of  $\delta^{18}\text{O}_v$  and  $\delta^{18}\text{O}_p$  values differs between PI and Miocene simulations, but are similar between the two Miocene simulations. Thus, changes in Miocene  $\text{CO}_2$  concentration have less impact on the seasonality change in  $\delta^{18}\text{O}_v$  and  $\delta^{18}\text{O}_p$ .

#### 4.6. SLP Shifts

We analyzed sea-level pressure shifts for February–March, May–June, August–September, and November–December. We chose these months rather than “classic” seasons (e.g., December–January–February or June–July–August), because we aim to explain the previously described  $\delta^{18}\text{O}_p$  changes, which are most pronounced for these months (Figure 9). In February–March, we find an increase in sea-level pressure over Turkey, Italy and the Balkans, with a maximum increase of 3 and 1 hPa over Italy for the Mio\_278 and Mio\_450 simulations, respectively (Figures 10a and 10b; Figure S9 in Supporting Information S1). This sea-level pressure increase is accompanied by a sea-level pressure decrease over the North Atlantic (from  $20^\circ\text{W}$  to  $0^\circ$  and  $45^\circ\text{N}$  to  $65^\circ\text{N}$ ) up to 6 hPa in both cases. In May–June and August–September, the sea-level pressure for both the Mio\_278 and Mio\_450 simulations is lower than in the PI simulation (Figures 10c and 10f). The most pronounced changes ( $>10$  hPa) for these months occur over Northeast Africa, the Red Sea, and the North Atlantic, while the sea-level pressure change over central Europe is smaller, ranging from 3 to 5 hPa. For November–December, the high Miocene SLP remains over Southern Europe, with a maximum increase of 1 and 3 hPa for the Mio\_278 and Mio\_450 simulations, respectively (Figures 10a and 10b).

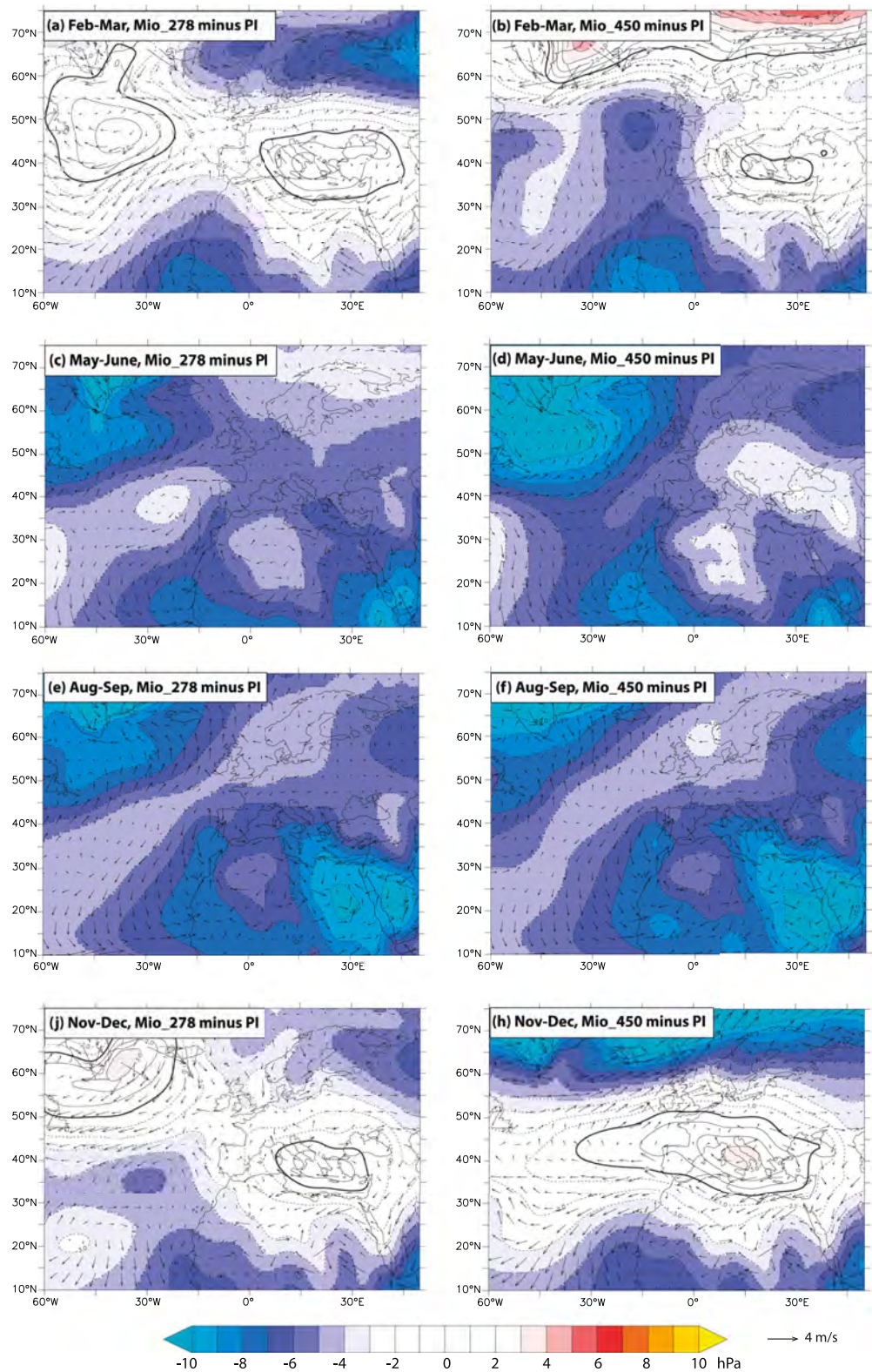


**Figure 10.** Differences in the mean sea level pressure (SLP) and winds between Mio\_278 and PI (a, c, e, j) and between Mio\_450 and PI (b, d, f, h) simulations averaged over selected months: February–March (a, b), May–June (c, d), August–September (e, f), November–December (j, h). The isolines show the SLP difference with an interval of 1 hPa; the black solid line corresponds to zero difference.

## 5. Discussion

In the following sections, we provide explanations for the simulated humidity and precipitation change in the Middle Miocene compared to the PI (Section 5.1). Following this, we assess the potential sources of model-data mismatch in terms of precipitation by comparing the fit of climatic conditions based on different proxy-data reconstruction methodologies to those derived from our model outputs (Section 5.2). In Section 5.3, we explain the simulated  $\delta^{18}\text{O}_p$  on annual and intra-annual scale and examine the impact of global and regional Middle Miocene climate change that is linked to Alpine surface uplift and Paratethys retreat on carbonate  $\delta^{18}\text{O}$  records. In Section 5.4, we conclude by discussing the consequences of these results for stable isotope paleoaltimetry studies.

### 5.1. Large-Scale Drivers of Humidity and Precipitation Change in Europe

For the Middle Miocene we simulate a bi-directional precipitation change pattern in Europe. More specifically, Scandinavia and northern Russia become wetter, while Southern and South-Eastern Europe become drier. This pattern persists for all seasons, but is most pronounced for late summer (Figures 11a–11c). This Middle Miocene bi-directional precipitation change in Europe is similar to the precipitation trends over the past century and the model predictions for future climate from Knutti and Sedláček (2013) and the Fifth Assessment Report of the Intergovernmental Panel on Climate Change (IPCC, 2013). The similarity between precipitation changes during the Middle Miocene (independent of  $\text{CO}_2$  levels) and future climate is consistent with the idea that past warm climates represent analogs for the future climate and can anticipate how European precipitation might respond to global warming. In the following, we discuss possible driving mechanisms for changes in precipitation and humidity in Middle Miocene Europe.

In our Middle Miocene simulations, an anticyclonic circulation is centered over the Mediterranean and Southern Europe in winter (Figures S9k–S9m in Supporting Information S1). In addition, the Icelandic Low gets stronger during summer months (Figures S9d–S9j in Supporting Information S1) and promotes a northward shift of the Atlantic storm track with a deflection of storms north of the Mediterranean to higher latitudes. This mechanism has also been predicted for future climate change in Europe, according to Giorgi and Lionello (2008), who also note that increased high pressure and anticyclonic conditions generally lead to greater atmospheric stability and thus less favorable conditions for storm generation. As a result of these circulation changes, Southern Europe and the Mediterranean region show a general decrease in precipitation in the Middle Miocene, while the northern European regions show an increase.

Anticyclones are generally associated with atmospheric subsidence. During the modern summer, the Mediterranean is directly under the descending branch of the Hadley circulation which is caused by deep convection in the tropics (Lelieveld et al., 2002). Our Middle Miocene simulations show an extended area of positive vertical velocity ( $\omega$ ) over the eastern Mediterranean and the Balkans (Figures 11h and 11j; Figures S11h and S11j in Supporting Information S1), which is a direct indication of subsiding air masses. Compared to the PI (Figure S11g in Supporting Information S1), this area of positive  $\omega$  is larger, especially for late summer, and extends toward central Europe and the Alps (Figures 10g–10j). This large-scale subsidence from upper to lower troposphere during the Middle Miocene, accompanied by advection and limited divergence for the largest part of the tropospheric column, explains the descending relative humidity structures and the dry surface hydroclimate. Sustained subsidence aloft, combined with a cool lower-level marine flow, results in a semi-permanent inversion that suppresses vertical growth of low clouds, and hence inhibits precipitation (Saaroni & Ziv, 2000).

The enhanced subsidence could possibly be related to the remote forcing of tropical circulation. Both the Asian summer monsoon (Rodwell & Hoskins, 2001; Tyrlis et al., 2013; Ziv et al., 2004) and the West African monsoon (Gaetani et al., 2011) have been suggested to influence the subsidence in the Mediterranean region. Rodwell and Hoskins (2001) demonstrated that the diabatic heating in the Asian monsoon region can induce a Rossby wave pattern to the west. They also found that the interaction between the Rossby waves and the mid-latitude westerlies produces an adiabatic descent over the Mediterranean and the subtropical Atlantic Ocean. Gaetani et al. (2011) reported a strong link between the summer Euro-Atlantic circulation and the convective activity of the West African monsoon. They show that the intensification of the Azores High, the northward shift of the West African Intertropical Convergence Zone and a Rossby wave from tropical America have a direct impact on the Euro-Atlantic circulation subsidence pattern. A detailed analysis of the causes of the subsidence change in the Middle Miocene would certainly be worthwhile, but is beyond the scope of this paper.

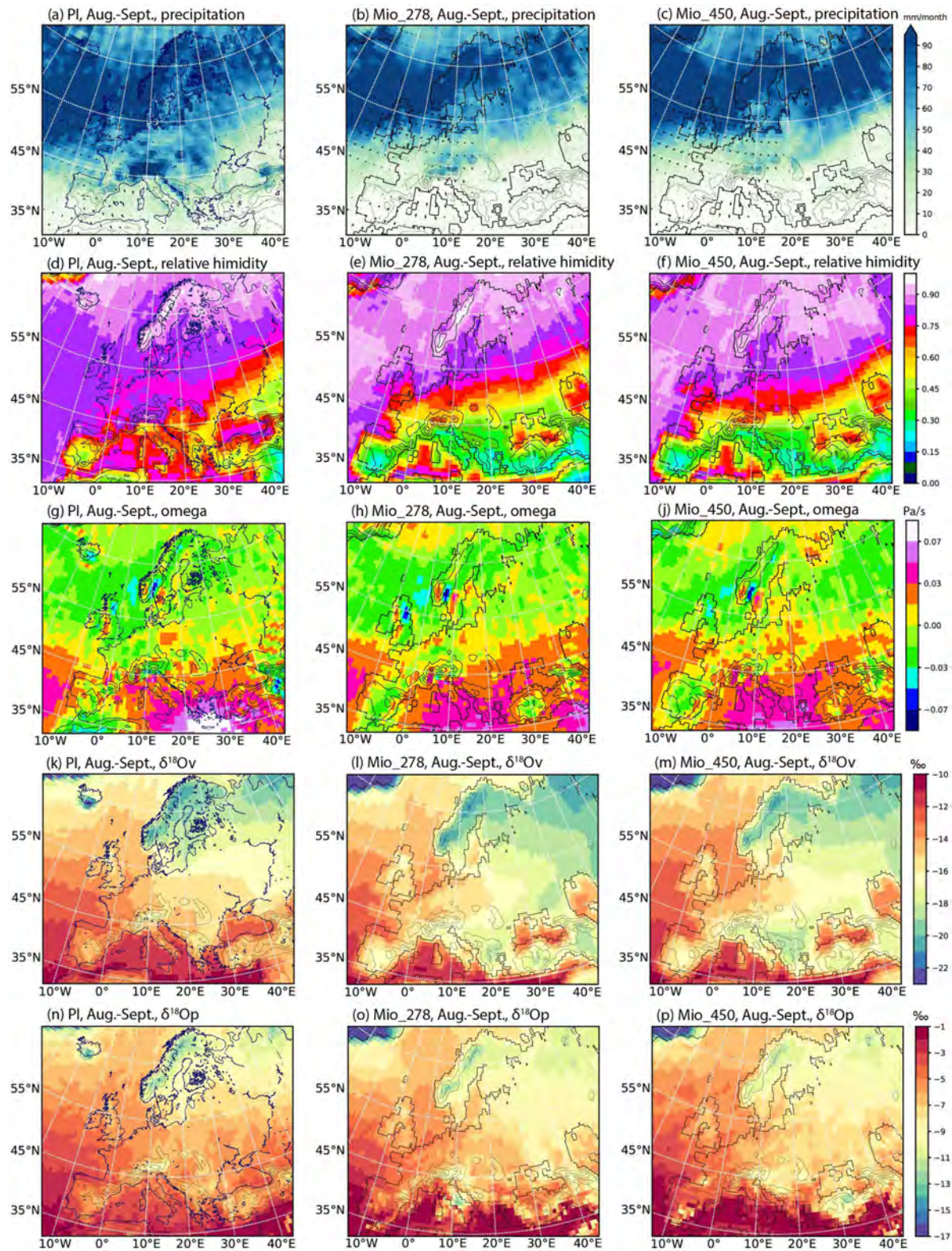


**Figure 11.** Precipitation amount (a–c), relative humidity (d–f), vertical velocity (omega) at 500 hPa (g–j),  $\delta^{18}O_v$  (k–m), and  $\delta^{18}O_p$  (n–p) for PI (a, d, g, k, n), Mio\_278 (b, e, h, l, o), Mio\_450 (c, f, j, m, p) simulations. Variables averaged for August–September.

In addition to the enhanced subsidence, reduced moisture transport from the Northern Atlantic, low precipitation rates and low relative humidity in Southern Europe (Figure S10 in Supporting Information S1) could be further amplified by reduced land evaporation and precipitable water. A reduction in precipitation leads to a depletion of soil moisture, which reduces the contribution of land evaporation to precipitable water, further reducing the precipitation simulated in our Middle Miocene experiments.

## 5.2. Wetter or Drier Europe in the Middle Miocene?

Our Middle Miocene control experiments (Mio\_278 and Mio\_450) show lower MAP for most parts of Central and Southern Europe than in the PI simulation. This is consistent with the results of Böhme et al. (2011), who suggest lower precipitation, up to 300–500 mm/yr less than today, for the Southwest (Calatayud-Teruel basin) and central Europe (Western and Central Paratethys) during the late Langhian (~14.40–13.65 Ma) and Serravallian (13.82–11.63 Ma). These results are also supported by the coeval occurrence of evaporites in the Spanish basins (Abdul Aziz et al., 2003). Moreover, abundant soil carbonate formation in the North Alpine Molasse basin during the Middle Miocene (Campani et al., 2012; Krsnik et al., 2021; Methner et al., 2020; Schlunegger et al., 2007) indicate precipitation rates not higher than 800 mm/yr (Breecker et al., 2009) or even 500 mm/yr (Zamanian et al., 2016) as well as pronounced precipitation seasonality. However, these reconstructions, taken together with our modeling results and herpetological proxy estimates, are at odds with plant proxy data showing wetter than present conditions in Central and Eastern Europe during the Serravallian (~13.8 to ~11.6 Ma; Bruch et al., 2011), with precipitation rates of up to 1,400 mm/yr. The paleobotanical data come from more than a dozen different authors and papers (Table S1), whereas the herpetological data come from only two publications (Table S2). Nevertheless, all paleobotanic papers use the same method (Mosbrugger & Utescher, 1997) and the same reference for the Nearest Living Relative (NLR) of a fossil taxon, that is, they are internally consistent as well as our modeling can be explained by: (a) difficulties in reconstructing dry climates with botanical methods; (b) uncertainties linked to the coexistence approach; and (c) climate model-related uncertainties.

First, problems arising when reconstructing dry conditions from plant fossils are already well known (e.g., in Böhme et al., 2007, 2011; Bruch et al., 2011). Ultimately, the lack of fossil floras preserved under dry conditions leads to a strong bias in the data with gaps toward southern Europe, where plant proxy data are only available from wetter regions of Spain (North-East coast) and northern Italy (Bruch et al., 2011). Moreover, faunal and floral remains from Central and Eastern Europe usually come from different stratigraphic levels and taphonomic settings (Bruch et al., 2011). This could mean that paleobotany proxy data do not have the necessary resolution and taphonomic capability to detect dry climates. On the other hand, the formation of carbonates can occur under overall (annual) rather wet conditions as long as a necessary precipitation seasonality is given. For instance, pedogenic carbonates are known to form under monsoonal climate (Breecker et al., 2009; Quade et al., 2007). As such, pedogenic carbonates can inherit a strong seasonal bias (e.g., Kelson et al., 2020).

Second, most botanical paleoclimate data are derived from the coexistence approach (Mosbrugger & Utescher, 1997). However, concern has been raised about the reliability of climate reconstructions, especially outside the warm-temperate climatic window (see Grimm & Denk, 2012 for detailed discussions). Moreover, the coexistence approach is strongly taxon dependent. In contrast, the herpetological method refers to the relative diversity (taxon count) of eco-physiologic groups of ectothermic animals at a given locality and is therefore largely taxon independent (especially below family levels). As highlighted earlier, the temperature records from palaeobotanical proxies are in a good agreement with the model, unlike the precipitation records. Further model simulations with regional geographic adjustments could help reconcile the herpetological data, botanical data, and modeling results.

Third, in terms of accurate simulation of paleoprecipitation, the application of ECHAM5-wiso has several limitations, related to (a) model resolution, (b) model parameterizations, for example, convective and evapotranspiration schemes, (c) no ocean feedback in an atmosphere-only GCM, (d) uncertainties in the choice of boundary conditions (e.g., vegetation, SSTs, etc.), (e) uncertainties in simulation of higher temporal and spatial scale atmospheric circulations (e.g., Shields et al., 2021), and (f) uncertainties in simulation equator-to-pole SST gradient (Burls et al., 2021). Compared to a coarse model resolution, for example, the experiments participating in MioMIP1 (T31 or T42, corresponding to a grid spacing of ~3.75° or ~2.79°, respectively), we find two dominant patterns

in which the ECHAM5-wiso simulations (T159 resolution, corresponding to a grid spacing of  $\sim 0.75^\circ$ ) differ: generally a cold bias over mountain ranges such as the European Alps, which could be related to differences in orography between low- and high-resolution models (with higher elevation in our high-resolution simulations), and a warm bias over the continents. Models with higher resolution have been shown to have higher climate sensitivity, but this effect is not present in all models (e.g., Ingram & Bushell, 2021 and references therein). Whether the higher climate sensitivity due to resolution contributes to the relative warmth over the continents needs further investigation based on additional simulations.

We refer the reader to Botsyun and Ehlers (2021) for a further discussion of the uncertainties relevant to precipitation and  $\delta^{18}\text{O}_p$  values. In addition, major uncertainties are related to the choice of regional topographic configurations in Europe. Simulations with increased Alpine elevation suggest an increase in precipitation over the Alpine region and a better fit to paleobotany proxy data over these regions. However, for Spanish basins, the Pannonian Basin, the Carpathian region, Crimea, Romania, and Turkey, models with increased Alpine elevation still show lower precipitation amounts comparable to the prediction of the paleobotany data. In our simulations, however, we do not test different uplift scenarios for mountains other than the Alps in Europe or a differentiated uplift history of the Eastern and Western Alps, which could potentially lead to a redistribution of precipitation. Our model resolution is still not high enough to capture microenvironments existing along inland water bodies, which could harbor many flora and fauna species characteristic of wetter climates, even if overall larger scale climate is (sub-)arid. Moreover, such environments have high preservation rates, biasing geologic records toward sheltered locations (Chandler et al., 1992).

In summary, despite some model-related limitations, our modeling results, in accord with herpetological proxy estimates and geological observations (evaporites, soil carbonates) indicate lower than pre-industrial precipitation rates for Central and Southern Europe during the Middle Miocene. High precipitation rates predicted by the coexistence approach are not supported by the model results here.

### 5.3. Implications of Global Climate Change and Alpine Surface Uplift on Water Stable Isotope Records and Paleoclimate Proxy Records in Europe

Changes in terrestrial paleo- $\delta^{18}\text{O}_p$  patterns are typically linked to both mountain uplift and global climate change (Caves et al., 2015; Licht et al., 2014; Methner et al., 2020; Mulch, 2016; Quade et al., 2011). Isotope-enabled GCMs provide a tool for distinguishing the processes impacting  $\delta^{18}\text{O}_p$  values at both regional and local scales (Botsyun & Ehlers, 2021). Comparing pre-industrial and Middle Miocene simulations (Mio\_278 and Mio\_450) allows us to isolate the effect of global climate on the  $\delta^{18}\text{O}_p$  pattern in Europe. Further comparison of Middle Miocene simulations (Mio\_278 and Mio\_450) and simulations with a varied Paratethys Sea extent (Mio\_278\_LandSea and Mio\_450\_LandSea) allows us to isolate the effect of regional climate change associated with the effect of marine transgressions on the  $\delta^{18}\text{O}_p$  pattern. Finally, comparison of simulations with varied elevation (Mio\_278, Mio\_450, Mio\_278\_plusAlps, Mio\_450\_plusAlps, Mio\_278\_noAlps, and Mio\_450\_noAlps) contributes to our understanding of the potential  $\delta^{18}\text{O}_p$  signal associated with topographic uplift. In the following, we organize our discussion around the implications of model-predicted changes in Middle Miocene  $\delta^{18}\text{O}_p$ , the different drivers behind these changes (global change vs. surface uplift) and their effect on interpretations of  $\delta^{18}\text{O}$  records preserved in paleosol carbonates.

#### 5.3.1. Changes in $\delta^{18}\text{O}_p$ Linked to Global Climate Forcing

Variations in temperature, humidity, precipitation, and wind directions are often considered as first-order variables contributing to the distribution pattern of  $\delta^{18}\text{O}_p$  values (Dansgaard, 1953; Gat, 1996). The temperature increase in the Middle Miocene simulations shifts  $\delta^{18}\text{O}_p$  values toward less negative values as a direct consequence of the Rayleigh distillation process (Dansgaard, 1953; Gat, 1996). Both  $\delta^{18}\text{O}_v$  and  $\delta^{18}\text{O}_p$  reach their maximum in May–June, which coincides with the warm season. However, in the case of Middle Miocene Europe, the temperature effect is largely counterbalanced by changes in relative humidity. This is because  $\delta^{18}\text{O}_v$  decreases with decreasing relative humidity during condensation through Rayleigh distillation. Our model results suggest that relative humidity decreases in Southern and central Europe during the Middle Miocene, which drives  $\delta^{18}\text{O}_v$  toward more negative values. This mechanism is most efficient in August–September when relative humidity drops by  $\sim 20\%$  (Figure 9c).

A decrease in relative humidity further contributes to changes in  $\delta^{18}\text{O}_p$  by enhancing post-condensation effects, for example, raindrop evaporation. Since  $^{16}\text{O}$  evaporates more easily, rain re-evaporation leads to an increase in  $\delta^{18}\text{O}_p$  values of raindrops reaching the Earth surface. Therefore, the more re-evaporation occurs, the greater the difference between  $\delta^{18}\text{O}_v$  and  $\delta^{18}\text{O}_p$  values (see e.g., Lee & Fung, 2008). The pronounced difference between  $\delta^{18}\text{O}_v$  and  $\delta^{18}\text{O}_p$  from July to October in the Mio\_278 and Mio\_450 simulations is an indication of enhanced post-condensation effects occurring after initial condensation (Figures 9e and 9f).

Simulated Middle Miocene decrease in  $\delta^{18}\text{O}_v$  in the late summer is most pronounced over the Balkans, which coincides with an area of enhanced atmospheric subsidence (Figure S10 in Supporting Information S1). The effect of subsidence in decreasing  $\delta^{18}\text{O}_v$  has previously been shown by Frankenberg et al. (2009) and by Galewsky and Hurley (2010). Our results suggest (Figure 11) that the subsidence is located broadly over the Mediterranean, but drying and its isotopic effect occurs primarily over land. This is because over the ocean the boundary layer is efficiently separated from the free troposphere by an inversion, allowing it to be replenished by unlimited surface evaporation (Benetti et al., 2015). In contrast, over land, surface evaporation is limited, so that surface evaporation cannot compensate for the drying effect of subsidence.

### 5.3.2. Change in $\delta^{18}\text{O}_p$ Linked to the Regional Climate

In addition to the impact of global climate,  $\delta^{18}\text{O}_p$  is influenced by regional changes of climate, land-sea cover, and topography. However, in our simulations,  $\delta^{18}\text{O}_p$  values over the Alpine region are not sensitive to for example, the retreat of the Paratethys. The simulated changes between the control experiment and the experiment with modified land-sea distribution are below 1‰ (Figures 8e and 8f). These small changes could be explained by the fact that the Paratethys lies outside of major wind directions for Europe (Figure S10 in Supporting Information S1). However, this result is potentially linked to limitations of our modeling methodology, that is, the application of an atmospheric-only, not a fully coupled atmosphere-ocean GCM. Application of a GCM with a comprehensive simulation of marine circulation might result in higher SSTs over the Paratethys region and thus increase evaporation and contribution of this moisture source to the local hydroclimate in Europe.

Differences in  $\delta^{18}\text{O}_p$  values between pairs of simulations with different topography within each  $p\text{CO}_2$  setup are up to 8‰ (e.g., Figures 7c and 7f). The maximum changes are found between experiments with doubling of present Alpine elevation (Mio\_278\_plusAlps, Mio\_450\_plusAlps) and an elevation that is reduced to 250 m (Mio\_278\_noAlps, Mio\_450\_noAlps). However,  $\delta^{18}\text{O}_p$  changes between the experiments with varied topography are strongly limited to the area where the topography has been actually modified by the experimental setup. These findings for the Middle Miocene climate simulations are consistent with results of sensitivity experiments with pre-industrial boundary conditions but varied Alpine elevation (Botsyun et al., 2020). Given this limited-area impact, we hypothesize that  $\delta^{18}\text{O}_p$  increase/decrease for experiments with higher/lower topography is mainly due to changes in local temperature and orographic precipitation.

### 5.4. Consequences for Paleoelevation Estimates

Our results for Middle Miocene seasonality changes in temperature and precipitation in Europe may have impacts for the interpretation of paleosol carbonate  $\delta^{18}\text{O}$  or other isotope proxy data used for paleoelevation reconstructions of the Alps. When pedogenic carbonates are used to assess low-elevation  $\delta^{18}\text{O}_p$  estimates, the MAT has typically been assumed for carbonate-water fractionation temperatures (e.g., Cerling et al., 1993; Garzzone et al., 2000; Quade et al., 2011; Xu et al., 2013). This is based on the assumption that pedogenic carbonates form during conditions reflective of the mean growing season environment, which would typically imply soil temperature conditions between average and the maximum annual soil temperature (Cerling et al., 1993). However, changes in precipitation seasonality and the amplitude of seasonal temperature variation impacts the growth season of soil carbonates (Breecker et al., 2009; Burgener et al., 2016; Gallagher & Sheldon, 2016; Kelson et al., 2020; Peters et al., 2013). With the growing amount of paleosol carbonate formation temperature estimates based on clumped isotope ( $\Delta_{47}$ ) analyses, the timing of carbonate formation during the annual cycle becomes key (e.g., Gallagher et al., 2019; Kelson et al., 2020; Passey et al., 2010; Peters et al., 2013; Quade et al., 2013). Previous work has documented that carbonate in modern soils can precipitate at times of excessive dryness when climate conditions differ strongly from the mean growing season conditions (Breecker et al., 2009). However, carbonate precipitation may occur at different times of the year under different climate regimes and a complicated seasonal bias may strongly affect the formation and isotopic composition of pedogenic carbonate (e.g., Gallagher & Sheldon, 2016).

For the case of the European Alps in the Middle Miocene, prolonged warm seasons might bias carbonate  $\delta^{18}\text{O}$  toward annual mean values, while stronger precipitation seasonality with very dry summers might bias carbonate  $\delta^{18}\text{O}$  toward spring or autumn values. Our model-derived seasonal temperature shifts of  $>16^\circ\text{C}$  (summer/JJA minus winter/DJF) predicted in the Mio\_278 and Mio\_450 simulations are similar to the observed  $\Delta_{47}$ -based carbonate formation temperature change in the North Alpine Foreland Basin (Methner et al., 2020). These authors attributed this large shift in paleosol carbonate  $\Delta_{47}$ -temperatures to at least partly reflect a shift in carbonate formation/preservation seasonality in conjunction with global cooling across the MMCT. They suggest a modification in rainfall seasonality across the MMCT and reorganization of mid-latitude atmospheric circulation across central Europe to account for hypothesized shift in carbonate formation/preservation seasonality.

Recently, Krsnik et al. (2021) used a combined pedogenic carbonate  $\delta^{18}\text{O}$  value and  $\Delta_{47}$  temperature ( $30^\circ\text{C} \pm 4^\circ\text{C}$ ) to reconstruct a near sea level  $\delta^{18}\text{O}_p$  value of  $-5.6 \pm 0.2\text{‰}$  during the Middle Miocene ( $\sim 14.5$  Ma). In combination with a high-Alpine meteoric water  $\delta\text{D}$  record these results suggest that the central Alps attained surface elevations of  $>4,000$  m no later than the mid-Miocene. The results of our new Middle Miocene experiments indicate that  $\delta^{18}\text{O}$  varies on an annual scale between  $-4.9$  and  $-7.6\text{‰}$  (depending on the experimental setup) for the Northern Alps Foreland Basin. We suggest that only  $1\text{--}2\text{‰}$  of this variation is linked to changes in global climate. Thus, high elevation of the central Alps in the Middle Miocene is highly possible and supported by the results presented here. However, caution is needed regarding the timing of the carbonate formation and its potential bias on reconstructed  $\delta^{18}\text{O}_p$  values. Moreover, our Middle Miocene experiments indicate a shallowing of the elevation- $\delta^{18}\text{O}_p$  gradient in the Middle Miocene Alps, permitting a possible underestimation of elevations derived from paleo- $\delta^{18}\text{O}_p$  data using present-day relationships.

## 6. Summary and Conclusions

We present high-resolution isotope-enabled ECHAM5-wiso experiments to study Middle Miocene climate and related  $\delta^{18}\text{O}_p$  signals in Europe. Previous modeling efforts simulating the Middle Miocene climate have been recently joined in MioMIP1 and summarized in Burls et al. (2021). However, low resolution of MioMIP1 simulations (T31 or T42) do not provide a good representation of mountain topography in Europe, leading to: (a) an underestimation of surface temperature in mountain regions, and (b) an underestimation of precipitation. Moreover, it has been previously shown that the low resolution (e.g., T31), typical of past global coupled paleoclimate simulations, are unlikely to properly capture humidity behavior (Sherwood et al., 2010).

We have tackled this problem in generating much higher resolution (grid spacing of  $\sim 0.75^\circ$ ) simulations using the ECHAM5-wiso atmosphere GCM. Our new Middle Miocene simulations show  $3.4^\circ\text{C}\text{--}6.2^\circ\text{C}$  higher temperatures in central Europe when compared to the pre-industrial, depending on the  $\text{CO}_2$  setup. This result is in good agreement with temperatures derived using the proxy data, however, these results have a warm bias for low-elevation areas when compared to the Middle Miocene experiments participating in the MioMIP1 project. The simulated Middle Miocene precipitation is  $300\text{--}500$  mm/yr lower than in the pre-industrial times, which is consistent with estimates from herpetofaunal fossil proxy data. However, it is lower than predicted by paleobotanical (coexistence approach) proxy data. We attribute this precipitation change in Europe to shifts in large-scale pressure patterns in the North Atlantic and over Europe, namely an anticyclonic circulation centered over the Mediterranean and Southern Europe in winter, in addition to a deepened Icelandic Low in the summer. These ultimately result in a northward shift of the Atlantic storm track with a deflection of storms north of the Mediterranean into higher latitudes.

The simulated annual mean  $\delta^{18}\text{O}_p$  pattern for the Middle Miocene is consistent with pre-industrial  $\delta^{18}\text{O}_p$  across Europe in both its pattern and magnitude. The Middle Miocene global climate forcing has contributed to a maximum  $\delta^{18}\text{O}_p$  increase of  $\sim 2\text{‰}$  over the high Alpine elevation and to  $\sim 1\text{‰}$  over low elevation. However, differences between PI and Middle Miocene simulations at seasonal scale are stronger ( $\sim 3\text{‰}$ ), especially when higher  $p\text{CO}_2$  concentration is considered. The most striking difference is the  $\delta^{18}\text{O}_p$  decrease in the late summer, driven by a drop of relative humidity, which coincides with enhanced atmospheric subsidence. Experiments with varied elevations of the Alps show that doubling of Alps elevation causes a maximum  $\delta^{18}\text{O}_p$  decrease, up to  $8\text{‰}$  when compared to the experiment with non-changed topography. However, the isotope lapse rate in the central Alps shallows by  $0.03\text{‰}/100$  m for Middle Miocene setting.



We conclude that higher-resolution paleoclimate modeling is critical to capture regional paleoclimate variability. We suggest that Alpine paleoclimate and paleoaltimetry research would benefit from future studies focusing on (a) using proxies to constrain not only surface temperature and precipitation amount, but also relative humidity (e.g., using triple oxygen isotopic composition of phytoliths [Outrequin et al., 2021]) or the average chain length of n-alkanes (Eley & Hren, 2018), (b) studying the Miocene climate on orbital time scales, given the Miocene climate has been shown to be sensitive to the orbital forcing (Marzocchi et al., 2015) and the insolation changes have a potential impact on temperature in warmer climate (Samakinwa et al., 2020), (c) multi-model isotope enabled studies to avoid warm/cool bias in individual models, and (d) coupling of  $\delta^{18}\text{O}$  proxy records and outputs of isotope-enabled GCM forced by constrained paleogeography (e.g., time appropriate land-sea distribution and different scenarios for orogens) and atmospheric  $p\text{CO}_2$  for specific geological time periods investigated. This combination could help refine calibration of paleo  $\delta^{18}\text{O}_p$ -elevation relationships and refining paleoelevation estimates.

### Conflict of Interest

The authors declare no conflicts of interest relevant to this study.

### Data Availability Statement

The ECHAM model is available under the conditions of the “MPI-M Software Licence Agreement”, which must be signed by each user. The “MPI-M Software Licence Agreement” and the information on the distribution of MPI-M models are given on: [https://mpimet.mpg.de/fileadmin/projekte/ICON-ESM/mpi-m\\_sla\\_201202.pdf](https://mpimet.mpg.de/fileadmin/projekte/ICON-ESM/mpi-m_sla_201202.pdf). The code of the isotopic version ECHAM5-wiso (Werner et al., 2011) is available upon request on the GitLab repository of the Alfred Wegener Institute (Germany): <https://gitlab.awi.de/mwerner/mpi-esm-wiso> (registration and a login is required). The ECHAM5-wiso modeling results are available in netcdf format at Botsyun et al. (2022).

### Acknowledgments

This study was supported by the German Research Foundation (DFG) Grants EH329/19-1, 23-1 (to T.A.E.), MU4188/1-1, 3-1 (to S.G.M.), DFG ME 4955/1-1 (to K.M.), and DFG MU 2845/6-1 (to A.M.) as part of DFG Priority Program MB-4D (SPP-2017). K.M. further acknowledges support through a Feodor-Lynen-Fellowship by the Alexander-von-Humboldt foundation. A.K. is supported through Humboldt Research Fellowship for experienced researchers by the Alexander-von-Humboldt foundation. The authors thank R. Paul Acosta, Lin Li, and an anonymous reviewer for their constructive comments and recommendations, which highly improved this study. This work used computing resources of the Deutsches Klimarechenzentrum (DKRZ) granted by its Scientific Steering Committee (WLA) under project bb1200. Open Access funding enabled and organized by Projekt DEAL.

### References

- Abdul Aziz, H., Sanz-Rubio, E., Calvo, J. P., Hilgen, F. J., & Krijgsman, W. (2003). Paleoenvironmental reconstruction of a Middle Miocene alluvial fan to cyclic shallow lacustrine depositional system in the Calatayud Basin (NE Spain). *Sedimentology*, 50(2), 211–236. <https://doi.org/10.1046/j.1365-3091.2003.00544.x>
- Acosta, R. P., & Huber, M. (2017). The neglected Indo-Gangetic Plains low-level jet and its importance for moisture transport and precipitation during the peak summer monsoon. *Geophysical Research Letters*, 44(16), 8601–8610. <https://doi.org/10.1002/2017GL074440>
- Acosta, R. P., & Huber, M. (2020). Competing topographic mechanisms for the summer Indo-Asian monsoon. *Geophysical Research Letters*, 47(3). <https://doi.org/10.1029/2019GL085112>
- Benetti, M., Aloisi, G., Reverdin, G., Risi, C., & Sèze, G. (2015). Importance of boundary layer mixing for the isotopic composition of surface vapor over the subtropical North Atlantic Ocean. *Journal of Geophysical Research: Atmospheres*, 120(6), 2190–2209. <https://doi.org/10.1002/2014jd021947>
- Böhme, M., Bruch, A. A., & Selmeier, A. (2007). The reconstruction of Early and Middle Miocene climate and vegetation in Southern Germany as determined from the fossil wood flora. *Paleogeography, Paleoclimatology, Paleoecology*, 253(1–2), 91–114.
- Böhme, M., & Vasilyan, D. (2014). Ectothermic vertebrates from the late Middle Miocene of Gratkorn (Austria, Styria). *Paleobiodiversity and Paleoenvironments*, 94(1), 21–40.
- Böhme, M., Winklhofer, M., & Ilg, A. (2011). Miocene precipitation in Europe: Temporal trends and spatial gradients. *Paleogeography, Paleoclimatology, Paleoecology*, 304(3–4), 212–218.
- Boateng, D., Mutz, S. G., Ballian, A., Meijers, J. M. M., Methner, K., Botsyun, S., et al. (2022). The effects of diachronous surface uplift of the European Alps on regional climate and the oxygen isotopic composition of precipitation. *Climate of the Past Discussions*.
- Botsyun, S., & Ehlers, T. A. (2021). How can climate models be used in paleoelevation reconstructions? *Frontiers of Earth Science*, 9, 28. <https://doi.org/10.3389/feart.2021.624542>
- Botsyun, S., Ehlers, T. A., Koptev, A., Böhme, M., Methner, K., Risi, C., et al. (2022). Middle Miocene climate and stable oxygen isotopes in Europe. [Dataset]. Zenodo. <https://zenodo.org/record/6308475#.Y0gmDSFS-2w>
- Botsyun, S., Ehlers, T. A., Mutz, S. G., Methner, K., Krsnik, E., & Mulch, A. (2020). Opportunities and challenges for paleoaltimetry in “small” orogens: Insights from the European Alps. *Geophysical Research Letters*, 47, e2019GL086046. <https://doi.org/10.1029/2019GL086046>
- Botsyun, S., Sepulchre, P., Donnadieu, Y., Risi, C., Licht, A., & Caves Rugenstein, J. K. (2019). Revised paleoaltimetry data show low Tibetan Plateau elevation during the Eocene. *Science*, 363(6430), eaaq1436. <https://doi.org/10.1126/science.aaq1436>
- Botsyun, S., Sepulchre, P., Risi, C., & Donnadieu, Y. (2016). Impacts of Tibetan Plateau uplift on atmospheric dynamics and associated precipitation  $\delta^{18}\text{O}$ . *Climate of the Past*, 12(6), 1401–1420. <https://doi.org/10.5194/cp-12-1401-2016>
- Bouchal, J. M., Güner, T. H., & Denk, T. (2018). Middle Miocene climate of southwestern Anatolia from multiple botanical proxies. *Climate of the Past*, 14(10), 1427–1440. <https://doi.org/10.5194/cp-14-1427-2018>
- Breecker, D. O., Sharp, Z. D., & McFadden, L. D. (2009). Seasonal bias in the formation and stable isotopic composition of pedogenic carbonate in modern soils from central New Mexico, USA. *Bulletin of the Geological Society of America*, 121(3–4), 630–640. <https://doi.org/10.1130/B26413.1>

- Brovkin, V., Raddatz, T., Reick, C. H., Claussen, M., & Gayler, V. (2009). Global biogeophysical interactions between forest and climate. *Geophysical Research Letters*, *36*(7). <https://doi.org/10.1029/2009gl037543>
- Bruch, A. A., Uhl, D., & Mosbrugger, V. (2007). Miocene climate in Europe—patterns and evolution: A first synthesis of NECLIME.
- Bruch, A. A., Utescher, T., & Mosbrugger, V. (2011). Precipitation patterns in the Miocene of central Europe and the development of continentality. *Paleogeography, Paleoclimatology, Paleoecology*, *304*(3), 202–211. <https://doi.org/10.1016/j.palaeo.2010.10.002>
- Burgener, L., Huntington, K. W., Hoke, G. D., Schauer, A., Ringham, M. C., Latorre, C., & Díaz, F. P. (2016). Variations in soil carbonate formation and seasonal bias over > 4 km of relief in the western Andes (30°S) revealed by clumped isotope thermometry. *Earth and Planetary Science Letters*, *441*, 188–199. <https://doi.org/10.1016/j.epsl.2016.02.033>
- Burls, N. J., Bradshaw, C. D., De Boer, A. M., Herold, N., Huber, M., Pound, M., et al. (2021). Simulating Miocene warmth: Insights from an opportunistic Multi-Model ensemble (MioMIP1). *Paleoceanography and Paleoclimatology*, *36*, e2020PA004054. <https://doi.org/10.1029/2020PA004054>
- Campani, M., Mulch, A., Kempf, O., Schlunegger, F., & Mancktelow, N. (2012). Miocene paleotopography of the central Alps. *Earth and Planetary Science Letters*, *337–338*, 174–185. <https://doi.org/10.1016/j.epsl.2012.05.017>
- Caves, J. K., Winnick, M. J., Graham, S. A., Sjöstrom, D. J., Mulch, A., & Chamberlain, C. P. (2015). Role of the westerlies in central Asia climate over the Cenozoic. *Earth and Planetary Science Letters*, *428*, 33–43. <https://doi.org/10.1016/j.epsl.2015.07.023>
- Cerling, T. E., Wang, Y., & Quade, J. (1993). Expansion of C4 ecosystems as an indicator of global ecological change in the late Miocene. *Nature*, *361*(6410), 344–345. <https://doi.org/10.1038/361344a0>
- Chandler, M. A., Rind, D., & Ruedy, R. (1992). Pangean climate during the Early Jurassic: GCM simulations and the sedimentary record of paleoclimate. *The Geological Society of America Bulletin*, *104*(5), 543–559. [https://doi.org/10.1130/0016-7606\(1992\)104<0543:pcdtej>2.3.co;2](https://doi.org/10.1130/0016-7606(1992)104<0543:pcdtej>2.3.co;2)
- Cui, Y., Schubert, B. A., & Jahren, A. H. (2020). A 23 m.y. record of low atmospheric CO<sub>2</sub>. *Geology*, *48*(9), 888–892. <https://doi.org/10.1130/g47681.1>
- Dansgaard, W. (1953). The abundance of O<sup>18</sup> in atmospheric water and water vapor. *Tellus*, *5*(4), 461–469. <https://doi.org/10.3402/tellusa.v5i4.8697>
- Dee, D. P., Uppala, S. M., Simmons, A. J., Berrisford, P., Poli, P., Kobayashi, S., et al. (2011). The ERA-Interim reanalysis: Configuration and performance of the data assimilation system. *Quarterly Journal of the Royal Meteorological Society*, *137*(656), 553–597. <https://doi.org/10.1002/qj.828>
- Dietrich, S., Werner, M., Spanghel, T., & Lohmann, G. (2013). Influence of orbital forcing and solar activity on water isotopes in precipitation during the mid- and late Holocene. *Climate of the Past*, *9*(1), 13–26. <https://doi.org/10.5194/cp-9-13-2013>
- Ehlers, T. A., & Poulsen, C. J. (2009). Influence of Andean uplift on climate and paleoaltimetry estimates. *Earth and Planetary Science Letters*, *281*(3–4), 238–248. <https://doi.org/10.1016/j.epsl.2009.02.026>
- Eizenhöfer, P. R., Glotzbach, C., Büttner, L., Kley, J., & Ehlers, T. A. (2021). Turning the orogenic switch: Slab-reversal in the Eastern Alps recorded by low-temperature thermochronology. *Geophysical Research Letters*, *48*(6), e2020GL092121. <https://doi.org/10.1029/2020GL092121>
- Eley, Y. L., & Hren, M. T. (2018). Reconstructing vapor pressure deficit from leaf wax lipid molecular distributions. *Scientific Reports*, *8*(1), 1–8. <https://doi.org/10.1038/s41598-018-21959-w>
- Eronen, J. T., Fortelius, M., Micheels, A., Portmann, F. T., Puolamäki, K., & Janis, C. M. (2012). Neogene aridification of the Northern Hemisphere. *Geology*, *40*(9), 823–826. <https://doi.org/10.1130/g33147.1>
- Feakins, S. J., Warny, S., & Lee, J. E. (2012). Hydrologic cycling over Antarctica during the Middle Miocene warming. *Nature Geoscience*, *5*(8), 557–560. <https://doi.org/10.1038/ngeo1498>
- Foster, G. L., & Rohling, E. J. (2013). Relationship between sea level and climate forcing by CO<sub>2</sub> on geological timescales. *Proceedings of the National Academy of Sciences of the United States of America*, *110*(4), 1209–1214. <https://doi.org/10.1073/pnas.1216073110>
- Frankenberg, C., Yoshimura, K., Warneke, T., Aben, I., Butz, A., Deutscher, N., et al. (2009). Dynamic processes governing lower-tropospheric HDO/H<sub>2</sub>O ratios as observed from space and ground. *Science*, *325*(5946), 1374–1377. <https://doi.org/10.1126/science.1173791>
- Gaetani, M., Pohl, B., Douville, H., & Fontaine, B. (2011). West African monsoon influence on the summer Euro-Atlantic circulation. *Geophysical Research Letters*, *38*(9). <https://doi.org/10.1029/2011gl047150>
- Galewsky, J., & Hurley, J. V. (2010). An advection-condensation model for subtropical water vapor isotopic ratios. *Journal of Geophysical Research*, *115*(D16). <https://doi.org/10.1029/2009jd013651>
- Gallagher, T. M., Hren, M., & Sheldon, N. D. (2019). The effect of soil temperature seasonality on climate reconstructions from paleosols. *American Journal of Science*, *319*(7), 549–581. <https://doi.org/10.2475/07.2019.02>
- Gallagher, T. M., & Sheldon, N. D. (2016). Combining soil water balance and clumped isotopes to understand the nature and timing of pedogenic carbonate formation. *Chemical Geology*, *435*, 79–91. <https://doi.org/10.1016/j.chemgeo.2016.04.023>
- Garzzone, C. N., Dettman, D. L., Quade, J., De Celles, P. G., & Butler, R. F. (2000). High times on the Tibetan Plateau: Paleoelevation of the Thakkhola graben, Nepal. *Geology*, *28*(4), 339–342. [https://doi.org/10.1130/0091-7613\(2000\)028<0339:htottp>2.3.co;2](https://doi.org/10.1130/0091-7613(2000)028<0339:htottp>2.3.co;2)
- Gaskell, D. E., Huber, M., O'Brien, C. L., Inglis, G. N., Acosta, R. P., Poulsen, C. J., & Hull, P. M. (2022). The latitudinal temperature gradient and its climate dependence as inferred from foraminiferal δ<sup>18</sup>O over the past 95 Myr. *Proceedings of the National Academy of Sciences of the United States of America*, *119*(11), 1–8. <https://doi.org/10.1073/pnas.2111332119>
- Gat, J. R. (1996). Oxygen and hydrogen isotopes in the hydrologic cycle. *Annual Review of Earth and Planetary Sciences*, *24*(1), 225–262. <https://doi.org/10.1146/annurev.earth.24.1.225>
- Giorgi, F., & Lionello, P. (2008). Climate change projections for the Mediterranean region. *Global and Planetary Change*, *63*(2–3), 90–104. <https://doi.org/10.1016/j.gloplacha.2007.09.005>
- Greenop, R., Foster, G. L., Wilson, P. A., & Lear, C. H. (2014). Middle Miocene climate instability associated with high-amplitude CO<sub>2</sub> variability. *Paleoceanography*, *29*(9), 845–853. <https://doi.org/10.1002/2014pa002653>
- Grimm, G. W., & Denk, T. (2012). Reliability and resolution of the coexistence approach—a revalidation using modern-day data. *Review of Palaeobotany and Palynology*, *172*, 33–47.
- Hagemann, S. (2002). An improved land surface parameter data set for global and regional climate models. In *Max Planck Institute for Meteorology Report* (Vol. 162). MPI for Meteorology.
- Handy, M. R., Schmid, S. M., Bousquet, R., Kissling, E., & Bernoulli, D. (2010). Reconciling plate-tectonic reconstructions of Alpine Tethys with the geological-geophysical record of spreading and subduction in the Alps. *Earth-Science Reviews*, *102*(3–4), 121–158. <https://doi.org/10.1016/j.earscirev.2010.06.002>
- Hergarten, S., Wagner, T., & Stüwe, K. (2010). Age and prematurity of the Alps derived from topography. *Earth and Planetary Science Letters*, *297*(3–4), 453–460. <https://doi.org/10.1016/j.epsl.2010.06.048>
- Herold, N., Huber, M., & Müller, R. D. (2011). Modeling the Miocene climatic optimum. Part I: Land and atmosphere. *Journal of Climate*, *24*(24), 6353–6372. <https://doi.org/10.1175/2011jcli4035.1>

- Herold, N., Seton, M., Müller, R. D., You, Y., & Huber, M. (2008). Middle Miocene tectonic boundary conditions for use in climate models. *Geochemistry, Geophysics, Geosystems*, 9(10). <https://doi.org/10.1029/2008GC002046>
- Huang, X., Stürz, M., Gohl, K., Knorr, G., & Lohmann, G. (2017). Impact of Weddell Sea shelf progradation on Antarctic bottom water formation during the Miocene. *Paleoceanography*, 32(3), 304–317. <https://doi.org/10.1002/2016PA002987>
- Ingram, W., & Bushell, A. C. (2021). Sensitivity of climate feedbacks to vertical resolution in a general circulation model. *Geophysical Research Letters*, 48(12), 1–9. <https://doi.org/10.1029/2020GL092268>
- Insel, N., Poulsen, C. J., Ehlers, T. A., & Sturm, C. (2012). Response of meteoric  $\delta^{18}\text{O}$  to surface uplift—Implications for Cenozoic Andean Plateau growth. *Earth and Planetary Science Letters*, 317–318, 262–272. <https://doi.org/10.1016/j.epsl.2011.11.039>
- IPCC. (2013). Climate change 2013: The physical science basis. In T. F. Stocker, D. Qin, G.-K. Plattner, M. Tignor, S. K. Allen, J. Boschung, et al. (Eds.), *Contribution of Working Group I to the Fifth Assessment Report of the Intergovernmental Panel on Climate Change*. Cambridge University Press.
- Jäger, E., & Hantke, R. (1984). Evidenzen für die Vergletscherung eines Alpen Bergeller Hochgebirges an der Grenze Oligozän/Miozän. *Geologische Rundschau*, 73(2), 567–575.
- Kelson, J. R., Huntington, K. W., Breecker, D. O., Burgener, L. K., Gallagher, T. M., Hoke, G. D., & Petersen, S. V. (2020). A proxy for all seasons? A synthesis of clumped isotope data from Holocene soil carbonates. *Quaternary Science Reviews*, 234, 106259. <https://doi.org/10.1016/j.quascirev.2020.106259>
- Knorr, G., Butzin, M., Micheels, A., & Lohmann, G. (2011). A warm Miocene climate at low atmospheric  $\text{CO}_2$  levels. *Geophysical Research Letters*, 38(20). <https://doi.org/10.1029/2011GL048873>
- Knutti, R., & Sedláček, J. (2013). Robustness and uncertainties in the new CMIP5 climate model projections. *Nature Climate Change*, 3(4), 369–373. <https://doi.org/10.1038/nclimate1716>
- Kocsis, L., Vennemann, T. W., & Fontignie, D. (2007). Migration of sharks into freshwater systems during the Miocene and implications for Alpine paleoelevation. *Geology*, 35(5), 451–454. <https://doi.org/10.1130/g23404a.1>
- Krsnik, E., Methner, K., Campani, M., Botsyun, S., Mutz, S. G., Ehlers, T. A., et al. (2021). Miocene high elevation in the Central Alps. *Solid Earth*, 12(11), 2615–2631. <https://doi.org/10.5194/se-12-2615-2021>
- Kuhlemann, J. (2007). Paleogeographic and paleotopographic evolution of the Swiss and eastern Alps since the Oligocene. *Global and Planetary Change*, 58(1–4), 224–236. <https://doi.org/10.1016/j.gloplacha.2007.03.007>
- Kukla, T., Winnick, M. J., Maher, K., Ibarra, D. E., & Chamberlain, C. P. (2019). The sensitivity of terrestrial  $\delta^{18}\text{O}$  gradients to hydroclimate evolution. *Journal of Geophysical Research: Atmospheres*, 124(2), 563–582. <https://doi.org/10.1029/2018jd029571>
- Langebroek, P. M., Paul, A., & Schulz, M. (2009). Antarctic ice-sheet response to atmospheric  $\text{CO}_2$  and insolation in the Middle Miocene. *Climate of the Past*, 5(4), 633–646. <https://doi.org/10.5194/cp-5-633-2009>
- Langebroek, P. M., Paul, A., & Schulz, M. (2010). Simulating the sea level imprint on marine oxygen isotope records during the Middle Miocene using an ice sheet-climate model. *Paleoceanography*, 25(4). <https://doi.org/10.1029/2008pa001704>
- Langebroek, P. M., Werner, M., & Lohmann, G. (2011). Climate information imprinted in oxygen-isotopic composition of precipitation in Europe. *Earth and Planetary Science Letters*, 311(1–2), 144–154. <https://doi.org/10.1016/j.epsl.2011.08.049>
- Lee, J. E., & Fung, I. (2008). “Amount effect” of water isotopes and quantitative analysis of post-condensation processes. *Hydrological Processes*, 22(1), 1–8. <https://doi.org/10.1002/hyp.6637>
- Lelieveld, J., Berresheim, H., Borrmann, S., Crutzen, P. J., Dentener, F. J., Fischer, H., et al. (2002). Global air pollution crossroads over the Mediterranean. *Science*, 298(5594), 794–799. <https://doi.org/10.1126/science.1075457>
- Licht, A., van Cappelle, M., Abels, H. A., Ladant, J.-B., Trabucho-Alexandre, J., France-Lanord, C., et al. (2014). Asian monsoons in a late Eocene greenhouse world. *Nature*, 513(7519), 501–506. <https://doi.org/10.1038/nature13704>
- Lorenz, S. J., & Lohmann, G. (2004). Acceleration technique for Milankovitch type forcing in a coupled atmosphere-ocean circulation model: Method and application for the Holocene. *Climate Dynamics*, 23(7–8), 727–743. <https://doi.org/10.1007/s00382-004-0469-y>
- Lott, F. (1999). Alleviation of stationary biases in a GCM through a mountain drag parameterization scheme and a simple representation of mountain lift forces. *Monthly Weather Review*, 127(5), 788–801. [https://doi.org/10.1175/1520-0493\(1999\)127<0788:aosbia>2.0.co;2](https://doi.org/10.1175/1520-0493(1999)127<0788:aosbia>2.0.co;2)
- Lott, F., & Miller, M. J. (1997). A new subgrid-scale orographic drag parameterization: Its formulation and testing. *Quarterly Journal of the Royal Meteorological Society*, 123(537), 101–127. <https://doi.org/10.1002/qj.49712353704>
- Marzocchi, A., Lunt, D. J., Flecker, R., Bradshaw, C. D., Farnsworth, A., & Hilgen, F. J. (2015). Orbital control on late Miocene climate and the North African monsoon: Insight from an ensemble of sub-precessional simulations. *Climate of the Past*, 11(10), 1271–1295. <https://doi.org/10.5194/cp-11-1271-2015>
- Methner, K., Campani, M., Fiebig, J., Löffler, N., Kempf, O., & Mulch, A. (2020). Middle Miocene long-term continental temperature change in and out of pace with marine climate records. *Scientific Reports*, 10(1), 1–10. <https://doi.org/10.1038/s41598-020-64743-5>
- Mosbrugger, V., & Utescher, T. (1997). The coexistence approach—A method for quantitative reconstructions of tertiary terrestrial paleoclimate data using plant fossils. *Paleogeography, Paleoclimatology, Paleoecology*, 134(1–4), 61–86. [https://doi.org/10.1016/s0031-0182\(96\)00154-x](https://doi.org/10.1016/s0031-0182(96)00154-x)
- Mulch, A. (2016). Stable isotope paleoaltimetry and the evolution of landscapes and life. *Earth and Planetary Science Letters*, 433, 180–191. <https://doi.org/10.1016/j.epsl.2015.10.034>
- Muñoz-Sabater, J., Dutra, E., Agustí-Panareda, A., Albergel, C., Arduini, G., Balsamo, G., et al. (2021). ERA5-Land: A state-of-the-art global reanalysis data set for land applications. *Earth System Science Data*, 13(9), 4349–4383.
- Mutz, S. G., Ehlers, T. A., Werner, M., Lohmann, G., Stepanek, C., & Li, J. (2018). Estimates of late Cenozoic climate change relevant to Earth surface processes in tectonically active orogens. *Earth Surface Dynamics*, 6(2), 271–301. <https://doi.org/10.5194/esurf-6-271-2018>
- Outrequin, C., Alexandre, A., Vallet-Coulomb, C., Piel, C., Devidal, S., Landais, A., et al. (2021). The triple oxygen isotope composition of phytoliths, a new proxy of atmospheric relative humidity: Controls of soil water isotope composition, temperature,  $\text{CO}_2$  concentration, and relative humidity. *Climate of the Past*, 17(5), 1881–1902. <https://doi.org/10.5194/cp-17-1881-2021>
- Pagani, M., Arthur, M. A., & Freeman, K. H. (1999). Miocene evolution of atmospheric carbon dioxide. *Paleoceanography*, 14(3), 273–292. <https://doi.org/10.1029/1999pa900006>
- Passy, B. H., Levin, N. E., Cerling, T. E., Brown, F. H., & Eiler, J. M. (2010). High-temperature environments of human evolution in East Africa based on bond ordering in paleosol carbonates. *Proceedings of the National Academy of Sciences of the United States of America*, 107(25), 11245–11249. <https://doi.org/10.1073/pnas.1001824107>
- Paul, A., Mülitz, S., Pätzold, J., & Wolff, T. (1999). Simulation of oxygen isotopes in a global ocean model. In *Use of proxies in paleoceanography* (pp. 655–686). Springer. [https://doi.org/10.1007/978-3-642-58646-0\\_27](https://doi.org/10.1007/978-3-642-58646-0_27)
- Peters, N. A., Huntington, K. W., & Hoke, G. D. (2013). Hot or not? Impact of seasonally variable soil carbonate formation on paleotemperature and O-isotope records from clumped isotope thermometry. *Earth and Planetary Science Letters*, 361, 208–218. <https://doi.org/10.1016/j.epsl.2012.10.024>

- Poage, M. A., & Chamberlain, C. P. (2001). Empirical relationships between elevation and the stable isotope composition of precipitation and surface waters: Considerations for studies of paleoelevation change. *American Journal of Science*, 301(1), 1–15. <https://doi.org/10.2475/ajs.301.1.1>
- Popov, S. V., Rögl, F., Rozanov, A. Y., Steininger, F. F., Shcherba, I. G., & Kovac, M. (2004). Lithological-paleogeographic maps of Paratethys-10 maps late Eocene to pliocene.
- Poulsen, C. J., Ehlers, T. A., & Insel, N. (2010). Onset of convective rainfall during gradual late Miocene rise of the central Andes. *Science*, 328(5977), 490–493. <https://doi.org/10.1126/science.1185078>
- Quade, J., Breecker, D. O., Daëron, M., & Eiler, J. (2011). The paleoaltimetry of Tibet: An isotopic perspective. *American Journal of Science*, 311(2), 77–115. <https://doi.org/10.2475/02.2011.01>
- Quade, J., Eiler, J., Daëron, M., & Achyuthan, H. (2013). The clumped isotope geothermometer in soil and paleosol carbonate. *Geochimica et Cosmochimica Acta*, 105, 92–107. <https://doi.org/10.1016/j.gca.2012.11.031>
- Quade, J., Garzzone, C., & Eiler, J. (2007). Paleoelevation reconstruction using pedogenic carbonates. *Reviews in Mineralogy and Geochemistry*, 66(1), 53–87. <https://doi.org/10.2138/rmg.2007.66.3>
- Quan, C., Liu, Y.-S. C., Tang, H., & Utescher, T. (2014). Miocene shift of European atmospheric circulation from trade wind to westerlies. *Scientific Reports*, 4. <https://doi.org/10.1038/srep05660>
- Raddatz, T. J., Reick, C. H., Knorr, W., Kattge, J., Roeckner, E., Schnur, R., et al. (2007). Will the tropical land biosphere dominate the climate-carbon cycle feedback during the twenty-first century? *Climate Dynamics*, 29(6), 565–574. <https://doi.org/10.1007/s00382-007-0247-8>
- Rae, J. W. B., Zhang, Y. G., Liu, X., Foster, G. L., Stoll, H. M., & Whiteford, R. D. M. (2021). Atmospheric CO<sub>2</sub> over the past 66 Myr from marine archives. *Annual Review of Earth and Planetary Sciences*, 49. <https://doi.org/10.1146/annurev-earth-082420-063026>
- Raymo, M. E., & Ruddiman, W. F. (1992). Tectonic forcing of late Cenozoic climate. *Nature*, 359(6391), 117–122. <https://doi.org/10.1038/359117a0>
- Rodwell, M. J., & Hoskins, B. J. (2001). Subtropical anticyclones and summer monsoons. *Journal of Climate*, 14(15), 3192–3211. [https://doi.org/10.1175/1520-0442\(2001\)014<3192:saasm>2.0.co;2](https://doi.org/10.1175/1520-0442(2001)014<3192:saasm>2.0.co;2)
- Roeckner, E., Bäuml, G., Bonaventura, L., Brokopf, R., Esch, M., Giorgetta, M., et al. (2003). *The atmospheric general circulation model ECHAM 5. PART I: Model description, Report No. 349*. Max-Planck-Institut für Meteorologie. Retrieved from <http://hdl.handle.net/11858/00-001M-0000-0012-0144-5>
- Rowley, D. B., Pierrehumbert, R. T., & Currie, B. S. (2001). A new approach to stable isotope-based paleoaltimetry: Implications for paleoaltimetry and paleohypsometry of the High Himalaya since the late Miocene. *Earth and Planetary Science Letters*, 188(1–2), 253–268. [https://doi.org/10.1016/S0012-821X\(01\)00324-7](https://doi.org/10.1016/S0012-821X(01)00324-7)
- Ruddiman, W. F., & Kutzbach, J. E. (1989). Forcing of late Cenozoic Northern Hemisphere climate by plateau uplift in southern Asia and the American West. *Journal of Geophysical Research*, 94(D15), 18409–18427. <https://doi.org/10.1029/jd094id15p18409>
- Saaroni, H., & Ziv, B. (2000). Summer rain episodes in a Mediterranean climate, the case of Israel: Climatological-dynamical analysis. *International Journal of Climatology*, 20(2), 191–209. [https://doi.org/10.1002/\(sici\)1097-0088\(200002\)20:2<191::aid-joc464>3.0.co;2-e](https://doi.org/10.1002/(sici)1097-0088(200002)20:2<191::aid-joc464>3.0.co;2-e)
- Samakinwa, E., Stepanek, C., & Lohmann, G. (2020). Sensitivity of mid-Pliocene climate to changes in orbital forcing and PlioMIP's boundary conditions. *Climate of the Past*, 16(4), 1643–1665. <https://doi.org/10.5194/cp-16-1643-2020>
- Schlunegger, F., & Kissling, E. (2015). Slab rollback orogeny in the Alps and evolution of the Swiss Molasse basin. *Nature Communications*, 6. <https://doi.org/10.1038/ncomms9605>
- Schlunegger, F., Rieke-Zapp, D., & Ramseyer, K. (2007). Possible environmental effects on the evolution of the Alps-Molasse Basin system. *Swiss Journal of Geosciences*, 100(3), 383–405. <https://doi.org/10.1007/s00015-007-1238-9>
- Schmid, S. M., Pfiffner, O.-A., Froitzheim, N., Schönborn, G., & Kissling, E. (1996). Geophysical-geological transect and tectonic evolution of the Swiss-Italian Alps. *Tectonics*, 15(5), 1036–1064. <https://doi.org/10.1029/96tc00433>
- Sharp, Z. D. (2005). Stable isotope geochemistry and formation mechanisms of quartz veins; extreme paleoaltitudes of the central Alps in the Neogene. *American Journal of Science*, 305(3), 187–219. <https://doi.org/10.2475/ajs.305.3.187>
- Sherwood, S. C., Ingram, W., Tsuchiya, Y., Satoh, M., Roberts, M., Vidale, P. L., & O’Gorman, P. A. (2010). Relative humidity changes in a warmer climate. *Journal of Geophysical Research*, 115(D9). <https://doi.org/10.1029/2009jd012585>
- Shevenell, A. E., Kennett, J. P., & Lea, D. W. (2008). Middle Miocene ice sheet dynamics, deep-sea temperatures, and carbon cycling: A southern ocean perspective. *Geochemistry, Geophysics, Geosystems*, 9(2). <https://doi.org/10.1029/2007gc001736>
- Shields, C. A., Kiehl, J. T., Rush, W., Rothstein, M., & Snyder, M. A. (2021). Atmospheric rivers in high-resolution simulations of the Paleocene Eocene Thermal Maximum (PETM). *Paleogeography, Paleoclimatology, Paleoecology*, 567, 110293. <https://doi.org/10.1016/j.palaeo.2021.110293>
- Sosdian, S. M., Greenop, R., Hain, M. P., Foster, G. L., Pearson, P. N., & Lear, C. H. (2018). Constraining the evolution of Neogene ocean carbonate chemistry using the boron isotope pH proxy. *Earth and Planetary Science Letters*, 498, 362–376. <https://doi.org/10.1016/j.epsl.2018.06.017>
- Stampfli, G. M., Mosar, J., Marquer, D., Marchant, R., Baudin, T., & Borel, G. (1998). Subduction and obduction processes in the Swiss Alps. *Tectonophysics*, 296(1–2), 159–204. [https://doi.org/10.1016/s0040-1951\(98\)00142-5](https://doi.org/10.1016/s0040-1951(98)00142-5)
- Stärz, M., Jokat, W., Knorr, G., & Lohmann, G. (2017). Threshold in North Atlantic-Arctic Ocean circulation controlled by the subsidence of the Greenland-Scotland Ridge. *Nature Communications*, 8, 15681.
- Steinthorsdottir, M., Coxall, H. K., De Boer, A. M., Huber, M., Barbolini, N., Bradshaw, C. D., et al. (2021). The Miocene: The future of the past. *Paleoceanography and Paleoclimatology*, 36(4), e2020PA004037. <https://doi.org/10.1029/2020pa004037>
- Stepanek, C., & Lohmann, G. (2012). Modeling mid-Pliocene climate with COSMOS. *Geoscientific Model Development*, 5, 1221–1243. <https://doi.org/10.5194/gmd-5-1221-2012>
- Super, J. R., Thomas, E., Pagani, M., Huber, M., O’Brien, C., & Hull, P. M. (2018). North Atlantic temperature and pCO<sub>2</sub> coupling in the early-Middle Miocene. *Geology*, 46(6), 519–522. <https://doi.org/10.1130/g40228.1>
- Super, J. R., Thomas, E., Pagani, M., Huber, M., O’Brien, C. L., & Hull, P. M. (2020). Miocene evolution of North Atlantic sea surface temperature. *Paleoceanography and Paleoclimatology*, 35(5), e2019PA003748. <https://doi.org/10.1029/2019pa003748>
- Tyrllis, E., Lelieveld, J., & Steil, B. (2013). The summer circulation over the eastern Mediterranean and the Middle East: Influence of the South Asian monsoon. *Climate Dynamics*, 40(5–6), 1103–1123. <https://doi.org/10.1007/s00382-012-1528-4>
- Utescher, T., Bruch, A. A., Erdei, B., François, L., Ivanov, D., Jacques, F. M. B., et al. (2014). The coexistence approach—Theoretical background and practical considerations of using plant fossils for climate quantification. *Paleogeography, Paleoclimatology, Paleoecology*, 410, 58–73. <https://doi.org/10.1016/j.palaeo.2014.05.031>
- Valla, P. G., Sternai, P., & Fox, M. (2021). How climate, uplift and erosion shaped the Alpine topography. *Elements*, 17(1), 41–46. <https://doi.org/10.2138/gselements.17.1.41>

- Werner, M., Langebroek, P. M., Carlsen, T., Herold, M., & Lohmann, G. (2011). Stable water isotopes in the ECHAM5 general circulation model: Toward high-resolution isotope modeling on a global scale. *Journal of Geophysical Research*, *116*(15), 1–14. <https://doi.org/10.1029/2011JD015681>
- Westerhold, T., Bickert, T., & Röhl, U. (2005). Middle to late Miocene oxygen isotope stratigraphy of ODP site 1085 (SE Atlantic): New constraints on Miocene climate variability and sea-level fluctuations. *Paleogeography, Paleoclimatology, Paleoecology*, *217*(3–4), 205–222. <https://doi.org/10.1016/j.palaeo.2004.12.001>
- Worobiec, E., Wiedera, M., Worobiec, G., & Kurdziel, B. (2021). Middle Miocene palynoflora from the Adamów lignite deposit, central Poland. *Palynology*, *45*(1), 59–71. <https://doi.org/10.1080/01916122.2019.1697388>
- Wright, J. D., Miller, K. G., & Fairbanks, R. G. (1992). Early and middle Miocene stable isotopes: Implications for deepwater circulation and climate. *Paleoceanography*, *7*(3), 357–389. <https://doi.org/10.1029/92pa00760>
- Xu, Q., Ding, L., Zhang, L., Cai, F., Lai, Q., Yang, D., & Liu-Zeng, J. (2013). Paleogene high elevations in the Qiangtang Terrane, central Tibetan Plateau. *Earth and Planetary Science Letters*, *362*, 31–42. <https://doi.org/10.1016/j.epsl.2012.11.058>
- Zamanian, K., Pustovoytov, K., & Kuzyakov, Y. (2016). Pedogenic carbonates: Forms and formation processes. *Earth-Science Reviews*, *157*, 1–17. <https://doi.org/10.1016/j.earscirev.2016.03.003>
- Ziv, B., Saaroni, H., & Alpert, P. (2004). The factors governing the summer regime of the eastern Mediterranean. *International Journal of Climatology*, *24*(14), 1859–1871. <https://doi.org/10.1002/joc.1113>

## References From the Supporting Information

- Akgün, F., Kayseri, M. S., & Akkiraz, M. S. (2007). Palaeoclimatic evolution and vegetational changes during the Late Oligocene–Miocene period in Western and Central Anatolia (Turkey). *Palaeoecology, Palaeoclimatology, Palaeoecology*, *253*(1–2), 56–90.
- Barrón, E., Rivas-Carballo, R., Postigo-Mijarra, J. M., Alcalde-Olivares, C., Vieira, M., Castro, L., et al. (2010). The Cenozoic vegetation of the Iberian Peninsula: a synthesis. *Review of palaeobotany and palynology*, *162*(3), 382–402.
- Bruch, A. A., Utescher, T., Olivares, C. A., Doláková, N., Ivanov, D., & Mosbrugger, V. (2004). Middle and Late Miocene spatial temperature patterns and gradients in Europe—preliminary results based on palaeobotanical climate reconstructions. *Courier-Forschungsinstitut Senckenberg*, 15–28.
- Chirilă, G., & Tabără, D. (2008). Palaeofloristic study of the Volhyan from Rasca (Moldavian Platform) - palaeoclimatic and palaeoenvironmental implications. *Acta Palaeontologica Romaniaae*, *6*, 29–42.
- Dahinden, F., Aemisegger, F., Wernli, H., Schneider, M., Diekmann, C. J., Ertl, B., et al. (2021). Disentangling different moisture transport pathways over the eastern subtropical North Atlantic using multi-platform isotope observations and high-resolution numerical modeling. *Atmospheric Chemistry and Physics*, *21*(21), 16319–16347. <https://doi.org/10.5194/acp-21-16319-2021>
- Diekmann, C. J., Schneider, M., Knippertz, P., de Vries, A. J., Pfahl, S., Aemisegger, F., et al. (2021). A Lagrangian perspective on stable water isotopes during the West African monsoon. *Journal of Geophysical Research: Atmospheres*, *126*(19), 1–23. <https://doi.org/10.1029/2021JD034895>
- Dütsch, M., Pfahl, S., Meyer, M., & Wernli, H. (2018). Lagrangian process attribution of isotopic variations in near-surface water vapor in a 30 yr regional climate simulation over Europe. *Atmospheric Chemistry and Physics*, *18*(3), 1653–1669. <https://doi.org/10.5194/acp-18-1653-2018>
- Erdei, B., Hably, L., Kázmér, M., Utescher, T., & Bruch, A. A. (2007). Neogene flora and vegetation development of the Pannonian domain in relation to palaeoclimate and palaeogeography. *Palaeoecology, Palaeoclimatology, Palaeoecology*, *253*(1–2), 115–140.
- Figueiral, I., Mosbrugger, V., Rowe, N. P., Utescher, T., Jones, T. P., & Von Der Hocht, F. (2002). Role of charcoal analysis for interpreting vegetation change and paleoclimate in the Miocene Rhine Embayment (Germany). *Palaios*, *17*(4), 347–365.
- Goldner, A., Herold, N., & Huber, M. (2014). The challenge of simulating the warmth of the mid-Miocene climatic optimum in CESM1. *Climate of the Past*, *10*(2), 523–536. <https://doi.org/10.5194/cp-10-523-2014>
- Ivanov, D. A., Ashraf, A. R., & Mosbrugger, V. (2007). Late Oligocene and Miocene climate and vegetation in the Eastern Paratethys area (north-east Bulgaria), based on pollen data. *Palaeoecology, Palaeoclimatology, Palaeoecology*, *255*(3–4), 342–360.
- Kováčová, M., Hohenegger, J., & Čorić, S. (2009). Palaeovegetation and climate based on pollen analysis of the Baden-Soos section (Middle Miocene, Vienna Basin, Austria). In: Filipescu, S. (Ed.), *3rd International Workshop Neogene of Central and South-Eastern Europe*. Cluj University Press, (pp. 65–65). Cluj-Napoca.
- Merlivat, L., & Jouzel, J. (1979). Global climatic interpretation of the deuterium-oxygen 18 relationship for precipitation. *Journal of Geophysical Research: Oceans*, *84*(C8), 5029–5033. <https://doi.org/10.1029/jc084ic08p05029>
- Mosbrugger, V., Utescher, T., & Dilcher, D. L. (2005). Cenozoic continental climatic evolution of Central Europe. *Proceedings of the National Academy of Sciences*, *102*(42), 14964–14969. <https://doi.org/10.1073/pnas.0505267102>
- Özer, K. M. S., & Akgün, F. (2010). The Late Burdigalian–Langhian interval in Turkey and the palaeoenvironmental and palaeoclimatic implications and correlation of Europe and Turkey: Late Burdigalian–Langhian palynofloras and palaeoclimatic properties of the Muğla–Milas (Kultak). *Geological Bulletin of Turkey*, *53*, 1–44.
- Özer, M. S. K., Sozibilir, H., & Akgün, F. (2014). Miocene palynoflora of the Kocaçay and Cumaovası basins: a contribution to the synthesis of Miocene palynology, palaeoclimate, and palaeovegetation in western Turkey. *Turkish Journal of Earth Sciences*, *23*(3), 233–259.
- Pais, J. (1981). Contribuição para o conhecimento da vegetação Miocénica da parte ocidental da Bacia do Tejo, [Ph.D. thesis], Universidade Nova de Lisboa, Portugal.
- Pantic, N. K. (1956). Biostratigraphie des flores tertiaires de Serbie. *Annales Geologiques de la Peninsule Balkanique*, *24*, 199–317.
- Pfahl, S., & Wernli, H. (2008). Air parcel trajectory analysis of stable isotopes in water vapor in the eastern Mediterranean. *Journal of Geophysical Research*, *113*(20), 1–16. <https://doi.org/10.1029/2008JD009839>
- Rivas-Carballo, M. R. (1991). The development of vegetation and climate during the Miocene in the south-eastern sector of the Duero Basin (Spain). *Review of palaeobotany and palynology*, *67*(3–4), 341–351.
- Rozanski, K., Araguás-Araguás, L., & Gonfiantini, R. (1993). Isotopic patterns in modern global precipitation. *Climate Change in Continental Isotopic Records*, 1–36.
- Singh, N. K., Emanuel, R. E., & McGlynn, B. L. (2016). Variability in isotopic composition of base flow in two headwater streams of the southern Appalachians. *Water Resources Research*, *52*(6), 4264–4279. <https://doi.org/10.1002/2015wr018463>
- Stevanovic, M.P., & Pantic, N. (1954). O sarmatskoj flori i fauni iz zeleznickih useka kod Bozdarevca. *Annales Geologiques de la Peninsule Balkanique*, *22*, 53–68.
- Syabryaj, S., Utescher, T., Molchanoff, S., & Bruch, A. A. (2007). Vegetation and palaeoclimate in the Miocene of Ukraine. *Palaeoecology, Palaeoclimatology, Palaeoecology*, *253*(1–2), 153–168.

- Uhl, D., Bruch, A. A., Traiser, C., & Klotz, S. (2006). Palaeoclimate estimates for the Middle Miocene Schrotzburg flora (S Germany): a multi-method approach. *International Journal of Earth Sciences*, *95*(6), 1071–1085.
- Utescher, T., Djordjevic-Milutinovic, D., Bruch, A., & Mosbrugger, V. (2007). Palaeoclimate and vegetation change in Serbia during the last 30 Ma. *Palaeogeography, Palaeoclimatology, Palaeoecology*, *253*(1-2), 141–152.
- Utescher, T., Mosbrugger, V., & Ashraf, A. R. (2000). Terrestrial climate evolution in northwest Germany over the last 25 million years. *Palaios*, *15*, 430–449.
- Valle-Hernández, M., Alonso-Gavilán, G., & Rivas-Carballo, M. R. (1995). Analyse préliminaire du Miocène dans le NE de la Dépression du Duero (aire de Belorado, Burgos, España). *Geobios*, *28*, 407–412.
- Vimeux, F., Gallaire, R., Bony, S., Hoffmann, G., & Chiang, J. C. H. (2005). What are the climate controls on  $\delta D$  in precipitation in the Zongo Valley (Bolivia)? Implications for the Illimani ice core interpretation. *Earth and Planetary Science Letters*, *240*(2), 205–220. <https://doi.org/10.1016/j.epsl.2005.09.031>

### 3 P3: Boateng et al. [to be submitted]

**(P3)** Boateng, D., et al. Refinement of Middle Miocene paleoelevation of the Alps through topographic sensitivity experiments and paleo-meteoric water isotopic composition modelling (to be submitted to ESurf)

1 **Refinement of Miocene paleoelevation estimates of the**  
2 **Alps through topographic sensitivity experiments and**  
3 **modelling of  $\delta^{18}O_p$  of paleo-meteoric water**

4 **Daniel Boateng<sup>1</sup>, Sebastian G. Mutz<sup>2</sup>, Katharina Methner<sup>3</sup>, Armelle**  
5 **Ballian<sup>4,5</sup>, Maud J. M Meijers<sup>4,6</sup>, Andreas Mulch<sup>4,5</sup>, Todd A. Ehlers<sup>1,2</sup>**

6 <sup>1</sup>Department of Geosciences, University of Tübingen, Tübingen, Germany

7 <sup>2</sup>School of Geographical and Earth Sciences, University of Glasgow, Scotland, UK

8 <sup>3</sup>Institute for Earth System Science and Remote Sensing, University of Leipzig, Leipzig, Germany

9 <sup>4</sup>Senckenberg Biodiversity and Climate Research Centre, Frankfurt am Main, Germany

10 <sup>5</sup>Goethe University Frankfurt, Institute of Geosciences, Frankfurt am Main, Germany

11 <sup>6</sup>Department of Earth Sciences, NAWI Graz Geocenter, University of Graz, Austria

12 **Key Points:**

- 13 • Miocene conditions and topographic changes led to a shallower isotopic lapse rate  
14 across the Alps compared to the present.
- 15 • Simulated isotopic lapse rates show an overestimation of Miocene Central Alps pa-  
16 leoelevation by 1.5 km when using the modern rainfall lapse rate.
- 17 • A global river-based lapse rate is more appropriate than a rainfall-based rate when  
18 paleoclimate-constrained lapse rates are available.

---

Corresponding author: Daniel Boateng, [daniel.boateng@uni-tuebingen.de](mailto:daniel.boateng@uni-tuebingen.de)



## Abstract

Estimates of past surface elevations using isotopic imprints in geologic archives are essential for understanding the evolution of the Earth’s physiography and biodiversity distribution. Stable isotope paleoaltimetry is the most widely used method to infer quantitative paleoelevations due to the robust systematic inverse relationship between elevation and oxygen isotopic composition ( $\delta^{18}O$ ) of meteoric waters (i.e., isotopic lapse rate). The difference in  $\delta^{18}O$  of paleo-meteoric water ( $\Delta\delta^{18}O$ ) reconstructed from coeval proxy materials between adjacent low- and high-elevation sites is transformed into paleoelevation changes using the isotopic lapse rate ( $\delta$ - $\delta$  approach). Most often, the isotopic lapse rate is assumed to be stationary through time and space and, therefore, relies on modern estimates to constrain the paleoelevation changes. This study employs model-based sensitivity analysis to assess the spatio-temporal variability of the isotopic lapse rate of the European Alps and to quantify the magnitude of uncertainties in paleoelevation estimates associated with the use of the modern isotopic lapse rate. We used the high-resolution isotope-tracking ECHAM5-wiso General Circulation Model to simulate the  $\delta^{18}O$  in precipitation ( $\delta^{18}O$ ) response to Middle Miocene global paleoenvironmental changes (e.g., atmospheric  $CO_2$ , palaeogeography), and diachronous west-to-east surface uplift propagating along the alpine orogen. The results indicate a  $\Delta\delta^{18}O$  range of -4 to -8 ‰ between the low- and high-elevation regions and agree well with Miocene proxy reconstructions. The  $\delta^{18}O$  values from the model-data comparison only agree in topographic scenarios where the West-Central Alps were uplifted by 200% of the modern mean elevation, implying that the Miocene Alps were higher than today. The simulated isotopic lapse rates become shallower by  $\sim 1.0$  ‰  $km^{-1}$  in response to the Middle Miocene conditions compared to the Pre-Industrial period and vary within the range of  $\pm 1.5$  ‰  $km^{-1}$  for the diachronous surface uplift scenarios of the Alps. Applying the simulated lapse rate with Miocene proxy reconstructions indicates an overestimation of the Central Alps’ paleoelevation by  $\sim 1.5$  km when the lapse rate is assumed to be constant from the time of the proxy formation to the present day.

## 1 Introduction

Reconstructing past surface elevations of mountain ranges is essential for understanding many interrelated geological, climatic, and biological processes. More specifically, paleoelevation estimates contribute to understanding tectonic-geodynamic drivers of surface uplift such as crustal thickening, lithospheric delamination, and post-collisional processes and ultimately, the interactions between the Earth’s surface, climate, and distribution of biodiversity (Cloetingh et al., 2023; S. Huang et al., 2019; Mulch, 2016; Rowley, 2007; Salles, Husson, Rey, et al., 2023; Salles, Husson, Lorcery, & Hadler Boggiani, 2023). Despite the use of sedimentological, geochemical, and palaeontological approaches to reconstruct paleoelevation, the scarcity and often reduced resolution of the geological record inevitably result in a fragmented spatio-temporal representation of the Earth’s past physiography. This hampers the accurate and realistic reconstruction of sediment transport dynamics, geochemical cycles, nutrient fluxes from continents to oceans, landscape evolution, and climate-tectonics interactions.

Despite the European Alps being one of the most intensively and longest-studied orogens globally, its surface elevation history remains understudied. The onset of Alpine topographic development was driven by isostatic compensation of crustal and lithospheric deformation through plate convergence caused by the continent-continent collision of the European and Adriatic plates (Beaumont et al., 1996; Schmid et al., 1996; Stampfli et al., 1998; Willett et al., 1993). Recent studies have suggested additional post-collisional processes that contributed to diachronous surface uplift, resulting in west-to-east topographic variations (Handy et al., 2010; Kissling & Schlunegger, 2018; Schlunegger & Kissling, 2015). These post-collisional processes include slab break-off (at ca. 30 Ma) of the European slab, continuing slab rollback of the subducting lithosphere under the Alpine arc,

71 and lithospheric mantle removal (Huw Davies & von Blanckenburg, 1995; Handy et al.,  
 72 2015; Schlunegger & Castellort, 2016). Global and regional Cenozoic climate change also  
 73 contributed to the development of transient topography through variations in climate-  
 74 driven surface processes such as denudation and erosion intensity (Mey et al., 2016; Valla  
 75 et al., 2021). Understanding and validating the relative roles of geodynamic processes  
 76 and landscape evolution requires quantitative paleoelevation estimates of the European  
 77 Alps through space and time. Stable isotope paleoaltimetry potentially allows us to in-  
 78 form about the rates and magnitudes of these subsurface processes, provided the sur-  
 79 face elevation history reflects the interplay among the deep-seated mantle and lithospheric  
 80 dynamics and regional climate changes.

81 Stable isotope paleoaltimetry has been used to infer past surface elevations of the  
 82 Alps (e.g., Campani et al., 2012; Krsnik et al., 2021; Sharp et al., 2005). The approach  
 83 relies on the robust systematic inverse relationship between stable oxygen and hydro-  
 84 genic isotopic composition of meteoric water and elevation (referred to as the isotopic lapse  
 85 rate) that is recorded in geologic materials such as pedogenic carbonates, hydrous sil-  
 86 icates, fossil tooth enamel or long-chain n-alkanes. Application of such isotopic lapse rates  
 87 assumes preferential rainout of heavy water isotopologues from air masses ascending over  
 88 topography and is estimated physically by the Rayleigh distillation model (Gat, 1996;  
 89 Rowley & Currie, 2006) or empirically from observations (e.g., rainfall or surface waters) (e.g.,  
 90 Poage & Chamberlain, 2001). As the potential change in isotopic lapse rates in the ge-  
 91 ologic past is difficult to ascertain precisely, most studies assume that the isotopic lapse  
 92 rate remains constant through time and, therefore, relies on present-day calibrations (Campani  
 93 et al., 2012; G3belin et al., 2013; Krsnik et al., 2021; Huyghe et al., 2018; Meyer, 2007;  
 94 Rowley, 2007; Poage & Chamberlain, 2001).

95 In the case of the European Alps, Campani et al. (2012) used a local, present-day  
 96 station-based isotopic lapse rate of  $-2.0 \text{ ‰ km}^{-1}$  to estimate a paleoelevation of  $2850 (\pm 800)$   
 97 m for the Miocene Central Alps. Their approach contrasts near-sea-level pedogenic car-  
 98 bonates paleo-meteoric water oxygen isotopic composition ( $\delta^{18}O$ ) values from the low-  
 99 elevation Northern Alpine Foreland Basin (Swiss Molasse Basin; SMB) with high ele-  
 100 vation paleo-meteoric water records from syntectonic fluid flow to disentangle the com-  
 101 peting contributions of elevation and regional climate change on the rainfall isotopic sig-  
 102 nal (e.g., Garzzone et al., 2000; Mulch et al., 2006; Rowley & Currie, 2006). Recently,  
 103 Krsnik et al. (2021) refined these paleoelevation estimates by applying clumped isotope  
 104 ( $\Delta_{47}$ ) paleothermometry on the foreland basin pedogenic carbonate record from differ-  
 105 ent Miocene Alpine foreland megafan systems to calculate the near-sea-level soil water  
 106  $\delta^{18}O$  values. Their reconstructed isotopic signal with modern isotopic lapse rates places  
 107 the Miocene Central Alps at  $>4400 (\pm 770)$  m. However, despite best efforts to isolate  
 108 the surface elevation signal, numerous climatic processes such as mixing and rerouting  
 109 of air masses, evaporation recycling, moisture transport source and pathway changes, and  
 110 precipitation dynamics that are driven by global climate changes and surface uplift can  
 111 influence the spatio-temporal variability of the isotopic lapse rates and thus compromise  
 112 paleoelevation estimates (e.g., Boateng et al., 2023; Ehlers & Poulsen, 2009; Galewsky,  
 113 2009; Insel et al., 2010; Poulsen & Jeffery, 2011).

114 The use of Isotope-enabled General Circulation Models (iGCMs) to simulate the  
 115 impact of Cenozoic climate forcings (e.g., atmospheric  $\text{CO}_2$  levels;  $p\text{CO}_2$ ) and the im-  
 116 pact of surface uplift on atmospheric circulation and surface heating have demonstrated  
 117 the non-stationarity of isotopic lapse rates through space and time (Poulsen & Jeffery,  
 118 2011). Through topographic sensitivity experiments, Boateng et al. (2023) suggested plau-  
 119 sible changes in isotopic lapse rates across the Alps in response to different diachronous  
 120 surface uplift scenarios and confirmed that the expected isotopic signal difference due  
 121 to elevation changes is large enough to be reflected in geologic archives. This study sim-  
 122 ulates the Middle Miocene  $\delta^{18}O_w$  values and regional climate to refine the previous pa-

123 leoelevation estimates and quantify the magnitude of uncertainties associated with the  
124 use of modern isotopic lapse rate.

125 The Middle Miocene (15.97-11.63 Ma) was characterized by significant climate dy-  
126 namics, changes in paleoenvironmental conditions (such as topography, vegetation, and  
127 palaeogeography), and tectonic activity (Steinhorsdottir et al., 2021). Global proxy re-  
128 constructions have indicated a warmer and wetter climate during the Middle Miocene  
129 Climatic Optimum (MCO; 16.9-14.7 Ma), with an estimated global mean surface tem-  
130 perature 8 °C warmer than present-day (Burls et al., 2021; Steinhorsdottir et al., 2021).  
131 This warming is primarily attributed to elevated  $p\text{CO}_2$  as indicated through climate sen-  
132 sitivity experiments (e.g., Acosta et al., 2024; Burls et al., 2021; Hossain et al., 2023; Knorr  
133 et al., 2011), ranging from 400 to 700 ppm (Foster & Rohling, 2013; Kürschner et al.,  
134 2008; Sosdian et al., 2018; Steinhorsdottir et al., 2021), with some estimates reaching  
135 as high as 1000 ppm (Rae et al., 2021; Retallack, 2009). Climate sensitivity studies, con-  
136 sidering various boundary conditions, have highlighted the importance of non- $p\text{CO}_2$  forc-  
137 ings—such as changes in paleotopography, palaeogeography, and vegetation—in driving  
138 regional climatic differences (e.g., Acosta et al., 2024; Brierley & Fedorov, 2016; Burls  
139 et al., 2021; Farnsworth et al., 2019; Jung et al., 2016). In particular, proxy data recon-  
140 structions and climate modelling indicate a pronounced latitudinal gradient in paleopre-  
141 cipitation over European mid-latitudes, with drier conditions at lower latitudes, which  
142 is attributable to changes in atmospheric circulation and the paleotopography of the Alps (Böhme  
143 et al., 2006; Botsyun et al., 2022; Costeur & Legendre, 2008; Jiménez-Moreno & Suc, 2007).  
144 These regional hydroclimatic changes, coupled with global warming effects—such as mid-  
145 tropospheric moistening and reduced vertical temperature stratification—would have led  
146 to a shallower isotopic lapse rate than today (Poulsen & Jeffery, 2011). Consequently,  
147 using contemporary isotopic lapse rates could lead to overestimating paleoelevation. Thus,  
148 simulating the  $\delta^{18}\text{O}_w$  values in response to Middle Miocene paleoenvironmental condi-  
149 tions is crucial for generating accurate paleoelevation reconstructions and quantifying  
150 the uncertainties associated with the assumption of a static isotopic lapse rate.

151 In this study, we employ the high-resolution ECHAM5-wiso isotope-tracking GCM  
152 to simulate the regional climate and  $\delta^{18}\text{O}_p$  values responses to Middle Miocene condi-  
153 tions alongside various surface uplift scenarios of the Alps. While Botsyun et al. (2022)  
154 simulated the impact of the Alps' topography changes under Middle Miocene conditions,  
155 their designed experiments were based on bulk surface uplift scenarios that did not in-  
156 clude west-to-east diachronous surface uplift. Boateng et al. (2023) simulated the effects  
157 of diachronous surface uplift on  $\delta^{18}\text{O}_p$  values and regional climate; however, they only  
158 considered topographic changes while keeping other boundary conditions (i.e. climate)  
159 constant. We build on these experiments by prescribing diachronous surface uplift sce-  
160 narios under two  $p\text{CO}_2$  conditions (i.e., 278 and 450 ppm) for the Middle Miocene. Through  
161 these combined topographic and  $p\text{CO}_2$  sensitivity experiments, we aim to elucidate the  
162 combined effects of climatic and tectonic influence on  $\delta^{18}\text{O}_p$  values, which would be re-  
163 flected in proxy records. The model results are consistent with isotopic lapse rates that  
164 (1) significantly deviate from present-day values, (2) significantly deviate from values that  
165 arise from changing only topography, and (3) exhibit spatial variability across the Alps.  
166 Furthermore, we document how the simulated isotopic lapse rates impact previous paleo-  
167 elevation estimates in the Alps (Krsnik et al., 2021), thereby quantifying the uncer-  
168 tainties associated with applying contemporary lapse rates. We also analyse the global  
169 hydroclimate and change in regional  $\delta^{18}\text{O}_p$  values in response to the different paleoen-  
170 vironmental conditions. Overall, this study introduces a robust framework for reconstruct-  
171 ing past surface elevations by integrating  $\delta$ - $\delta$  paleoaltimetry and paleo-meteoric water-  
172 isotopic composition model using the iGCM ECHAM5-wiso.

## 2 Methods: Middle Miocene climate modelling and topographic sensitivity experiment

### 2.1 ECHAM5-wiso General Circulation Model

The modelling component of this study relies on ECHAM5-wiso, a global three-dimensional atmospheric GCM with water isotopologue tracking ( $H_2^{16}O$ ,  $H_2^{18}O$ , and  $HDO$ ) capability (Werner et al., 2011). The model’s ability to simulate climate and the isotopic composition of precipitation has been validated for the present-day (e.g., Boateng et al., 2023; Langebroek et al., 2011) and the geological past (e.g., Botsyun et al., 2022; Feng et al., 2013; Mutz et al., 2018). The model includes diagnostics of stable oxygen and hydrogen ( $\delta D$ ) isotopes of water, which are treated as independent tracers in the hydrological cycle and undergo equilibrium and kinetic fractionation during phase transitions in the atmosphere. The model tracks vapour fluxes from the sea surface and lakes with non-equilibrium fractionation, which depends on surface temperature,  $\delta^{18}O$  (and  $\delta D$ ) of moisture source and vapour content at the atmosphere’s lower level, relative humidity, and near-surface wind speed. However, the model does not consider the fractionation of vapour fluxes from the land surface, such as evapotranspiration, due to their negligible effect on the isotopic composition (Bariac et al., 1994; Zimmermann et al., 1967). This simplification is common in other state-of-the-art isotope tracking GCMs (e.g., Lee et al., 2007; Risi et al., 2010; Tindall et al., 2009) but must be considered when interpreting the simulated regional isotopic patterns.

We used ECHAM5-wiso to simulate the Middle Miocene global climate and stable water isotopic composition in response to its paleoenvironmental conditions (e.g., changes in  $pCO_2$ , paleogeography, oceanic and land surface conditions) and diachronous surface uplift scenarios across the European Alps. Recently, Botsyun et al. (2022) demonstrated that the global large-scale features simulated for the Middle Miocene are consistent with results from other state-of-the-art Earth system models of the Miocene Model Intercomparison Project (MioMIP1) (Burls et al., 2021). Moreover, their simulated regional hydroclimate patterns across Europe generally agree with proxy-based reconstructions. This study builds on their Middle Miocene climate experiments with updated boundary conditions and simulations of the combined effects of global climate change and diachronous surface uplift across the Alps on the  $\delta^{18}O_p$  values. We focus on how the simulated  $\delta^{18}O_p$  patterns compare to geologic reconstructions and can be used to increase the accuracy of paleoelevation estimates in the Middle Miocene in the Alps.

### 2.2 Boundary conditions and experimental design

We conducted two sets of Middle Miocene climate experiments to reflect the climatic conditions of the MCO (16.9-14.7 Ma) and Middle Miocene Climate Transition (MCT; 14.7-13.8 Ma). The MCO was a time of  $pCO_2$  ( $\sim 400$ -600 ppm) that resulted in a climate warmer than today. In contrast, during the MCT,  $pCO_2$  levels declined towards Pre-Industrial (PI) values, accompanied by global cooling and expansion of East Antarctic ice sheets. We conservatively chose  $pCO_2$  levels of 450 ppm (Mio450) and 278 ppm (Mio278) for the MCO and MCT, respectively, to reflect the average of the range of suggested  $pCO_2$  reconstructions from multiple proxy systems. These values fall within the range of suggested recent  $pCO_2$  reconstructions (e.g., Steinhorsdottir et al., 2021; Sossian et al., 2018; Foster & Rohling, 2013; Kürschner et al., 2008). The defined  $pCO_2$  values are most closely aligned with the 400-500 ppm range at ca. 15.5 Ma and decrease to  $\sim 280$  ppm at 14 Ma (Kürschner et al., 2008). However, we highlight that other studies (e.g., Rae et al., 2021; Retallack, 2009) suggested  $pCO_2$  values of up to 1000 ppm during the MCO. Our simulations may, therefore, underestimate MCO temperatures and result in bias in the precipitation patterns.

To reflect Middle Miocene conditions, we integrate the palaeogeographic and bathymetric boundary conditions from Herold et al. (2008), including continent distribution,

land surface elevation, and shelf seas. Overall, the mean elevation of major mountain ranges such as the Andes, the Tibetan Plateau, ranges in East Africa, and the Rocky Mountains, together with the height of the Antarctic ice sheet, is reduced compared to present-day. Greenland was ice-free with reduced topography. Furthermore, ocean gateways, such as the Canadian archipelago and Bering Strait, were closed during the Middle Miocene, while the Panama gateway, the Indonesian seaway, and the Tethys seaway were open (Herold et al. (2008); Fig. 1 (a)). The timing of the closure of the Tethys gateway is still debated, with most studies suggesting its terminal closure during the Middle Miocene (e.g., Rögl, 1999; Ramsay et al., 1998). In this study, we maintained it open, resulting in a connection between the Parathethys and the global ocean, as defined in previous studies (e.g., Stürz et al., 2017; Botsyun et al., 2022; Herold et al., 2011). Moreover, our decision is based on findings from Botsyun et al. (2022), who conducted sensitivity experiments on the land-sea distribution in open or closed Tethys configurations and found no significant impact on European hydroclimate. However, other studies suggest that the closure of the Tethys gateway contributes significantly to changes in the ocean and atmospheric circulation in the Middle Miocene (Hamon et al., 2013; Ramstein et al., 1997). We emphasize that exploring the Tethys/Parathethys configurations is beyond the scope of this study, and sufficiently accounting for the narrow ocean passages and their dynamics would require high-resolution ocean grids with fully coupled GCMs.

We also explored the potential influence of recent Middle Miocene paleoenvironmental reconstructions by Frigola et al. (2018) on global climate changes in the MCO and MCT. The simulation of Herold et al. (2008) indicates a relatively colder global climate of  $-0.78$  °C (down to  $-10$  °C across Antarctica) during the MCO and slightly warmer of  $0.17$  °C (up to  $8$  °C across Antarctica) during the MCT when compared to the simulations of Frigola et al. (2018) (Fig. S8). Since our analysis primarily focuses on the Alps and European regional climate (Fig. S8), which exhibited fewer changes with both boundary conditions, we decided to maintain the boundary conditions from Herold et al. (2008) to be consistent with previous studies (e.g., Stürz et al., 2017; Botsyun et al., 2022).

Rather than undertaking computationally expensive fully coupled atmosphere-ocean GCM experiments at the spatial resolution required for accurate topographical representation, we prescribed sea surface temperatures (SSTs) and sea ice concentrations (SICs) patterns as the interface between the oceans and the atmosphere. We used SST and SIC patterns from a low-resolution fully coupled atmosphere-ocean-sea ice-vegetation Earth system model COSMOS (Jung et al., 2016) that was conducted with the same boundary conditions as Mio278 and Mio450 scenarios (X. Huang et al., 2017; Stürz et al., 2017). The land-surface conditions, including vegetation changes and physical soil properties such as the total water holding capacity of soils and soil albedo, were also adopted from the COSMOS experiments. The latter were coupled to the dynamic vegetation model JSBACH to take into account Middle Miocene vegetation reconstructions (Micheels et al., 2007).

In all our experiments, we set the initial isotopic conditions of the ocean and atmosphere to PI conditions, as done in previous palaeoclimate simulations with isotope-enabled GCMs (e.g., Werner et al., 2016; Cauquoin et al., 2019). More specifically, we used the  $H_2^{18}O$  and  $HDO$  values of the ocean from the equilibrium 3000-year simulation with the MPI-OM-wiso model by Xu et al. (2012) and initialized the atmosphere with constant values of  $\delta^{18}O$  and  $\delta D$  of  $-10$  and  $-80$  ‰, respectively (c.f., Werner et al., 2016; Cauquoin et al., 2019). The decision to use PI values was made for the following reasons:

1. The sparse availability of oceanic  $\delta^{18}O$  proxy reconstructions in the Middle Miocene hampers the construction of adequate global gridded  $\delta^{18}O$  values of ocean waters.
2. The lack of isotope-enabled fully coupled atmosphere-ocean-vegetation model output, simulated with the same Middle Miocene boundary conditions of this study,

also hindered us from accounting for the spatial variability of the  $\delta^{18}O$  values of the ocean surface in our boundary conditions.

3. Sensitivity experiments with the prescribed Middle Miocene  $\delta^{18}O$  values of the ocean surface, calculated based on their relationship with the salinity of the upper ocean level (Paul et al., 1999) from corresponding COSMOS experiments (Botsyun et al., 2022), indicated no significant changes in the oxygen isotopic composition of precipitation values in Europe when compared to the simulations with prescribed present-day conditions.

We employed ECHAM5-wiso simulated PI climate (reference year 1850) that serves as the reference climate for computing “climate anomalies.” Throughout this study, we report these anomalies as “increases” or “decreases” with reference to the PI estimates.

For all simulations, we used a high-resolution T159 spectral spatial resolution ( $\sim 80 \times 80$  km) and 31 vertical levels up to 10 hPa for all experiments. This resolution is essential to ensure a realistic representation of the spatial and seasonal variations of  $\delta^{18}O$  values across the Alps. On a large scale, Werner et al. (2011) demonstrated that a T159 resolution resulted in a better representation of the deuterium excess over the Antarctic continent. This is particularly important in our Middle Miocene experiments due to the expansion of Antarctic ice sheets during the MCT. All experiments were run for 18 years with a 6-hour model output. Atmosphere-only GCMs require relatively little time ( $< 3$  years) to reach quasi-equilibrium, leaving 15 years for analysis.

### 2.3 Topographic sensitivity experiments

We conducted topographic sensitivity experiments for the two Middle Miocene  $pCO_2$  scenarios (Mio278 and Mio450) to disentangle the impacts of changes in surface elevation and paleoenvironmental conditions on  $\delta^{18}O_p$  values across Europe, including the Alps. These experiments build upon those by Boateng et al. (2023), which revealed significant changes in the spatial patterns of  $\delta^{18}O_p$  values due to variations of topography that reflected the diachronous west-to-east surface uplift across the Alps. In this study, we specifically focus on more realistic topographic configurations of the Alps in the Miocene, based on previous paleoelevation estimates (Campani et al., 2012; Kocsis et al., 2007; Sharp et al., 2005; Krsnik et al., 2021) and geodynamic reconstruction (Kissling & Schlunegger, 2018; Handy et al., 2015; Schlunegger & Kissling, 2015) that suggest a generally higher surface elevation (ca. 2.5 - 6 km) across the West-Central Alps than present. Therefore, we increased the West-Central Alps elevation of the original paleotopography of Herold et al. (2008) by 200% (Fig. 1) to reflect the suggested high elevation in the Middle Miocene. Since no long-term quantitative past surface elevation estimates are available for the Eastern Alps, we incrementally increased its surface elevation from 0% to 200% in steps of 50% of the original Middle Miocene topography to account for all the possible surface uplift scenarios.

A total of four topographic configurations (Fig. 1a-e) were constructed and used with the Mio278 and Mio450 paleoenvironmental conditions, resulting in eight experiments in total. Note that this study’s experiments differ from the topographic sensitivity experiments by Botsyun et al. (2022), which only account for the bulk surface uplift of the entire Alps and do not consider the diachronous uplift of the eastern and western Alps. We highlight that associating the individual topographic configurations with a specific time or tectonic event is impossible due to the ongoing debate on the kinematic framework of the topographic evolution of the Alps and the lack of widespread paleoelevation estimates across the Alps. Despite the reasonable representation of Alpine topography in our experiments, the dampening of maximum peaks through the interpolation process results in an underestimation of mean elevation. To address this, we calculated subgrid-scale orographic variables (e.g., peak elevations, mean slopes, valley elevations, and orographic standard deviation and anisotropy) with interpolated higher

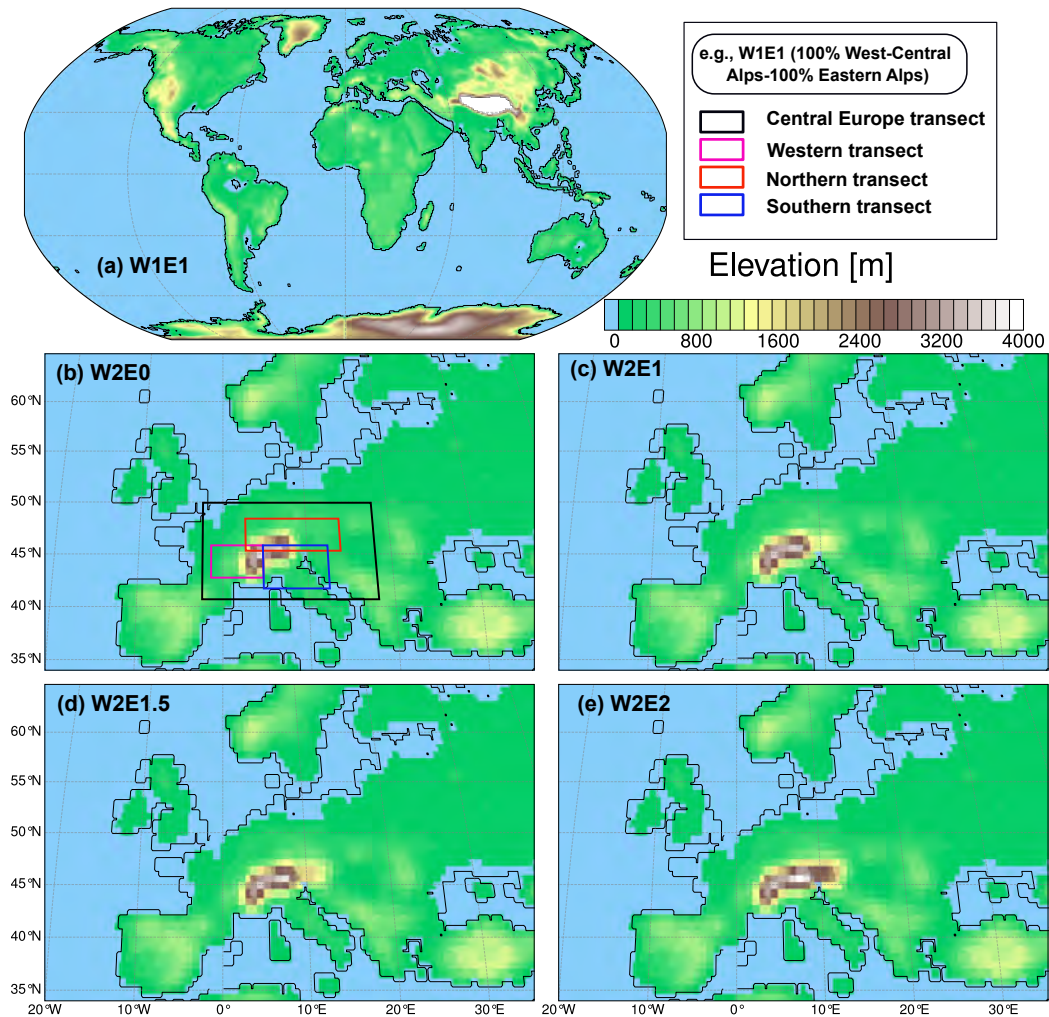


**Figure 1.** Palaeogeographic and topographic boundary conditions of the Middle Miocene experiments for the (a) Middle Miocene from Herold et al. (2018). (b-e) Modified topographic configurations with a 200% increase in elevation across the West-Central Alps (W2) and incremental change in the original Eastern Alps elevation (Ex) by factors of 0%: W2E0 (b), 100%: W2E1 (c), 150%:W2E1.5 (d), and 200%: W2E2 (e). For the configuration with 0% topography of the Eastern Alps, we use 250m as the minimum elevation to avoid unrealistic artefacts in the simulation, such as extreme wind speeds. The different regions shown in (b) are used for regional means estimates of  $\delta^{18}O_p$  values and isotopic lapse rates estimates across the Alps. All paleogeographic and topographic configurations were run for  $pCO_2 = 278$  ppm (Mio278) and  $pCO_2 = 450$  ppm (Mio450) ppm.

327 resolution of the paleotopography. This information is used in the subgrid parameter-  
 328 ization schemes and improves the estimates of orographic precipitation and mountain  
 329 blocking effect in the model (Stevens et al., 2013; Roeckner et al., 2003).

## 330 2.4 Post-processing and statistical analysis

331 We focus on the long-term annual climatologies, which are arithmetic means cal-  
 332 culated from the 6-hour model output. The individual experiments with an unmodified  
 333 topography (W1E1) with Middle Miocene boundary conditions (Mio278 and Mio450)  
 334 are used as references for the individual adjusted topographic configuration experiments  
 335 nested in each of the Miocene experiments (e.g., W2E1 - W1E1 for Mio278). The sta-  
 336 tistical significance of the estimated mean climatic differences is evaluated with two-tailed  
 337 Student’s t-tests, assuming a confidence interval of 95%. We express the simulated iso-  
 338 topic composition of the precipitation in the  $\delta$ -notation relative to Vienna Standard Mean  
 339 Ocean Water (V-SMOW):

$$\delta^{18}O = \left( \frac{([H_2^{18}O] / [H_2^{16}O])_{sample}}{([H_2^{18}O] / [H_2^{16}O])_{V-SMOW}} - 1 \right) \times 1000 \quad (1)$$

340 Throughout our analysis, the  $\delta^{18}O$  values are calculated as precipitation-weighted  
 341 long-term means. The isotopic lapse rates across the different geographic areas of the  
 342 Alps (Fig. 1b) are estimated for the different topographic scenarios using the ordinary  
 343 least-squares (OLS) linear regression. The statistical uncertainties of the calculated iso-  
 344 topic lapse rates are calculated with the Monte Carlo bootstrapping technique to account  
 345 for complex topographic structures, such as valley systems within high elevations. The  
 346 coefficient of determination ( $R^2$ ), which measures the fraction of the variance of the data  
 347 points that the best-fit model can explain, is also reported. This approach assesses the  
 348 changes in isotopic lapse rates in response to changing paleoenvironmental conditions.  
 349 Moreover, the estimated isotopic lapse rates are used to refine the previously estimated  
 350 paleoelevations across the Alps (Campani et al., 2012; Krsnik et al., 2021) to quantify  
 351 the potential uncertainties of assuming stationarity of the Alpine isotopic lapse rate through  
 352 time and space. Furthermore, we perform Spearman correlation analysis to determine  
 353 the relationship between  $\delta^{18}O_p$  values and precipitation as well as temperature across  
 354 Europe and evaluate if paleoenvironmental changes lead to different spatial correlation  
 355 patterns between climate variables and  $\delta^{18}O_p$  values. This would imply the potential changes  
 356 in the causal mechanism between  $\delta^{18}O_p$  values and regional climate dynamics, which would  
 357 explain the changes in the isotopic lapse rates.

## 358 3 Results

### 359 3.1 Simulated global anomalies of near-surface temperature, precipita- 360 tion, and $\delta^{18}O_p$ values for Middle Miocene paleoenvironmental con- 361 ditions

362 We estimate the deviation of Mio278 and Mio450 temperature, precipitation, and  
 363 associated  $\delta^{18}O_p$  values from the PI climate (Fig. 2). Maps of absolute temperature, pre-  
 364 cipitation and  $\delta^{18}O_p$  values are presented in the supplementary material (Fig. S1). Over-  
 365 all, Mio278 and Mio450 simulation results indicate warmer and wetter conditions com-  
 366 pared to PI climate (Fig. 2). More specifically, warmer and wetter regional patterns are  
 367 more enhanced under Mio450 than Mio278, as highlighted in previous studies (e.g., Acosta  
 368 et al., 2024; Burls et al., 2021; Hui et al., 2018; Pound et al., 2011). However, both Mio278  
 369 and Mio450 climate simulations indicate continental warming and detect enhanced pre-  
 370 cipitation over the ocean. The paleoclimate simulations estimate global mean annual tem-  
 371 peratures of 16.3 °C for Mio278 (Fig. S1f) and 19.9 °C for Mio450 (Fig. S1i) conditions,  
 372 indicating climates that are 2.5 °C and 6 °C warmer, respectively. These estimates are



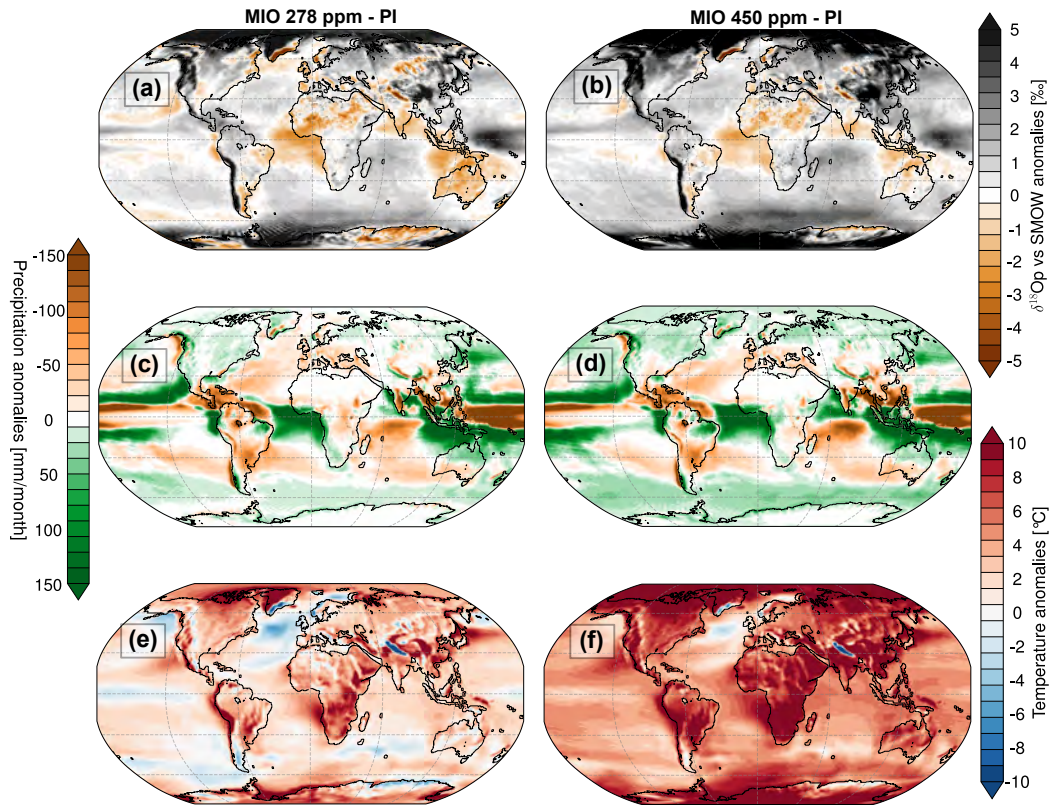


**Figure 2.** Annual mean anomalies relative to Pre-Industrial (PI) for  $\delta^{18}O_p$  values (a, b), precipitation (c, d) and near-surface temperature in response to two Middle Miocene  $pCO_2$  scenarios (278 ppm (Mio278), left panel; 450 ppm (Mio450), right panel). The global climate indicates more pronounced warm and wet patterns under Mio450 conditions than PI and Mio270.

373 within the high-end range of the multi-model mean estimates of MioMIP1 by Burls et  
 374 al. (2021). Continental temperatures are 2.6 °C (Mio278) and 3.7 °C (Mio450), higher  
 375 than the ocean temperatures (Fig. 2 e-f). The highest temperatures (>10 °C higher than  
 376 PI) are simulated across Antarctica, Africa, the Andes, and the Arctic area (i.e., part  
 377 of Greenland, Alaska, and Hudson Bay). These relatively warm regions were more pro-  
 378 nounced in the Mio450 than in the Mio278 simulation. Overall, large-scale Middle Miocene  
 379 temperature patterns show polar amplification, exacerbated in the Mio450 climate simu-  
 380 lation, and a weakened meridional temperature gradient, as indicated in previous stud-  
 381 ies (e.g., Burls et al., 2021).

382 Mio278 and Mio450 climate simulations result in global mean annual precipitation  
 383 (and associated mean  $\delta^{18}O_p$  values) estimates of 92 *mm/month* (-6.2 ‰) (Fig. S1 d-  
 384 e) and 99 *mm/month* (-5.6 ‰) (Fig. S1 g-h), respectively. Overall, the global mean pre-  
 385 cipitation is 1.6% and 9% higher (Mio278 and Mio450, respectively) compared to PI con-  
 386 ditions. Precipitation anomalies show notable regional changes that, in part, were driven  
 387 by non- $pCO_2$  forcing (e.g., palaeogeography). For example, the decrease in precipitation  
 388 over Central America is unlikely caused by the warming but more due to the opening  
 389 of the Panama gateway (Brierley & Fedorov, 2016). The magnitudes of regional precipi-  
 390 tation anomalies further increase under the Mio450 run compared to the Mio278 run  
 391 (Fig. 2 c-d). Across the tropical regions, precipitation anomalies are particularly pro-  
 392 nounced. For instance, the equatorial Atlantic Ocean along West Africa’s southern coast

393 receive  $>150$  *mm/month* more compared to PI, which leads to bidirectional anomalies  
 394 over West Africa with drier conditions across the Sahel.

395 Compared to PI, most oceans received more precipitation in the Middle Miocene  
 396 climate simulations (Fig. 2 c-d), including the subtropical North Pacific, Arabian Sea,  
 397 Bay of Bengal, and the southern gateways around Indonesia towards Australia, as in-  
 398 dicated by the multi-model means of MioMIP1 (Acosta et al., 2024). However, the In-  
 399 dian Ocean received less precipitation of  $\sim 100$  *mm/month* in Mio278 and  $-120$  *mm/month*  
 400 in Mio450 compared to PI, which is contrary to the multi-model means of MioMIP1. The  
 401 North Atlantic was drier due to its overall regional cooling in the Middle Miocene. The  
 402 precipitation anomalies across Europe indicate bi-directional patterns with more rain-  
 403 fall over Northern Europe and less rainfall towards the Mediterranean region compared  
 404 to PI. These latitudinal precipitation gradients are more pronounced in Mio450 than in  
 405 Mio278 climate runs. Overall, regional average precipitation anomalies increase across  
 406 higher latitudes due to amplified warming patterns.

407 To some extent, the simulated  $\delta^{18}O_p$  anomalies are larger across warmer (“tem-  
 408 perature effect”) and drier (“amount effect”) regions (Fig. 2 a-b). The global mean of  
 409  $\delta^{18}O_p$  anomalies increases with higher  $pCO_2$ . Specifically, the simulation results show  
 410 an increase of 0.7 ‰ and 1.31 ‰ in the Mio278 (Fig. 2a) and Mio450 (Fig. 2b) climate  
 411 runs, respectively. Most regions show higher  $\delta^{18}O_p$  values (more  $^{18}O$ -enriched rainfall)  
 412 with some exceptions, such as Tropical Atlantic, Sahel-Sahara, and Indonesia areas to-  
 413 wards Australia. The polar regions experience greater enrichment in the Middle Miocene  
 414 with an increase of  $>5$  ‰ due to the amplified polar warming. Across Europe, the sim-  
 415 ulated  $\delta^{18}O_p$  patterns indicate depleted  $\delta^{18}O_p$  values across Western Europe and a tran-  
 416 sition into enriched  $\delta^{18}O_p$  values across Eastern Europe. The different bi-directional anoma-  
 417 lies between precipitation (north-south gradient) and  $\delta^{18}O_p$  values (west-east gradient)  
 418 suggest a more complex influence of the regional climate on the  $\delta^{18}O_p$  patterns.

### 419 **3.2 Middle Miocene spatial profiles of $\delta^{18}O_p$ values for different topo-** 420 **graphic configurations**

421 The simulated  $\delta^{18}O_p$  values agree with reconstructed  $\delta^{18}O$  values of meteoric water  
 422 (refer to as  $\delta^{18}O_w$  for proxy reconstruction hereafter) from pedogenic carbonates (Cojan  
 423 et al., 2013; Krsnik et al., 2021) and clay minerals (i.e., bentonites and smectite-rich tuffs) (Bauer  
 424 et al., 2016) over the low-elevation regions around the Alps. Most of the reconstructed  
 425  $\delta^{18}O_w$  values were within the simulated range of  $-3$  to  $-8$  ‰ across the adjacent low-elevation  
 426 regions along the profiles for all Middle Miocene experiments (Fig. 3). However, some  
 427 of the clay minerals-based  $\delta^{18}O_w$  values are slightly outside the simulated  $\delta^{18}O_p$  range  
 428 and indicated the widest spread of  $\delta^{18}O_w$  values and the largest uncertainty of up to  $\pm 3$   
 429 ‰. On the high-elevation sites,  $\delta^{18}O_w$  values of  $-12$  to  $-15$  ‰ calculated from  $\delta D$  of syn-  
 430 tectonic high-Alpine fault zone silicates (Campani et al., 2012; Mancktelow et al., 2015)  
 431 only agree with model estimates for higher topography scenarios (Fig. 3). This supports  
 432 the findings that the Middle Miocene elevation of the Central Alps was higher than present-  
 433 day (Sharp et al., 2005; Krsnik et al., 2021).

434 The  $\delta^{18}O_p$  profiles across the Alps indicate a decreasing trend of up to  $-12$  ‰ (W2E2  
 435 scenario) from the foothills towards the peak heights and show varied responses to the  
 436 different topographic and climate scenarios (Fig. 3). The differences between the exper-  
 437 iments over the low-elevation areas adjacent to the Alps are small (less than  $-2$  ‰), while  
 438 the greatest differences are seen across the high-elevation regions (Fig. 3 and 4). For in-  
 439 stance, the reduced topography scenario of the Eastern Alps (W2E0) resulted in a slight  
 440 increase in  $\delta^{18}O_p$  of 0.5 ‰ and the uplift scenario in W2E2 resulted in a decrease down  
 441 to  $-10$  ‰ compared to the topographic control run (W1E1). The unmodified topographic  
 442 scenario (W1E1) in PI results in  $\sim 1.5$  ‰ more depleted  $\delta^{18}O_p$  values over the eastern  
 443 (Fig. 3a) and northern (Fig. 3b) transects than in both Miocene climates. Among the

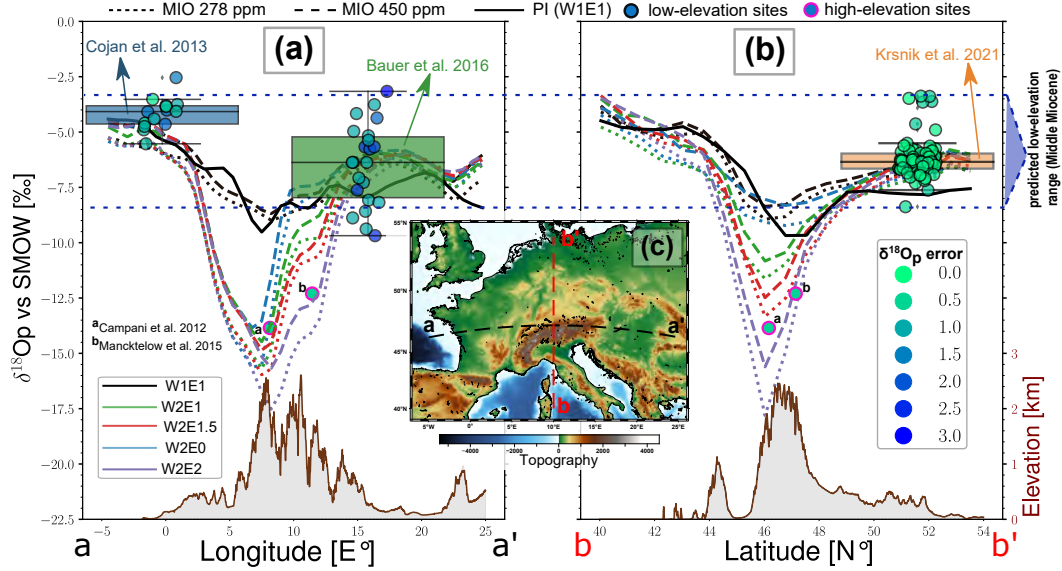


**Figure 3.** Annual mean  $\delta^{18}O_p$  longitudinal (a) and latitudinal (b) spatial profiles for the different topographic configurations in the Middle Miocene and PI and its comparison to  $\delta^{18}O_p$  proxy reconstructions across low- and high-elevation sites. The black lines represent the control (i.e., W1E1) topographic scenario with pre-industrial (PI: solid) and Middle Miocene (Mio278: dotted, Mio450: dashed) boundary conditions. The present-day elevation (in km) of the swaths (c) is plotted to show the topography variations along the profiles (a-a', b-b'). The Middle Miocene low-elevation site proxies are shown as a distribution box plot, including maximum, minimum, median, and quartile values of individual samples. These are based on  $\delta^{18}O$  of meteoric water reconstructed from pedogenic carbonates over the Northern Alpine foreland basin (Swiss Molasse Basin; (Krsnik et al., 2021)) and the Digne-Valensole basin (Cojan et al., 2013). And  $\delta^{18}O$  of meteoric water that is in isotopic equilibrium with contained clay minerals (i.e., bentonites and smectite-rich tuffs) from the northern Alpine foreland basin from Swiss and Bavaria freshwater Molasse basin (Bauer et al., 2016). The high-elevation sites are based on hydrogen isotopes from syntectonic high-Alpine fault zone silicates from the Simplon Fault Zone (Campani et al., 2012; Mancktelow et al., 2015). The coloured circles represent the reconstructed  $\delta^{18}O$  error. Note that the proxies' locations are extrapolated onto the profiles to compare them with the simulated magnitudes. Overall, the simulated  $\delta^{18}O_p$  values over the low-elevation regions are within the magnitudes of reconstructed  $\delta^{18}O_p$  values. The  $\delta^{18}O_w$  reconstruction from the high-elevation sites only matches simulated  $\delta^{18}O_p$  values when Miocene Alpine topography was higher than modern

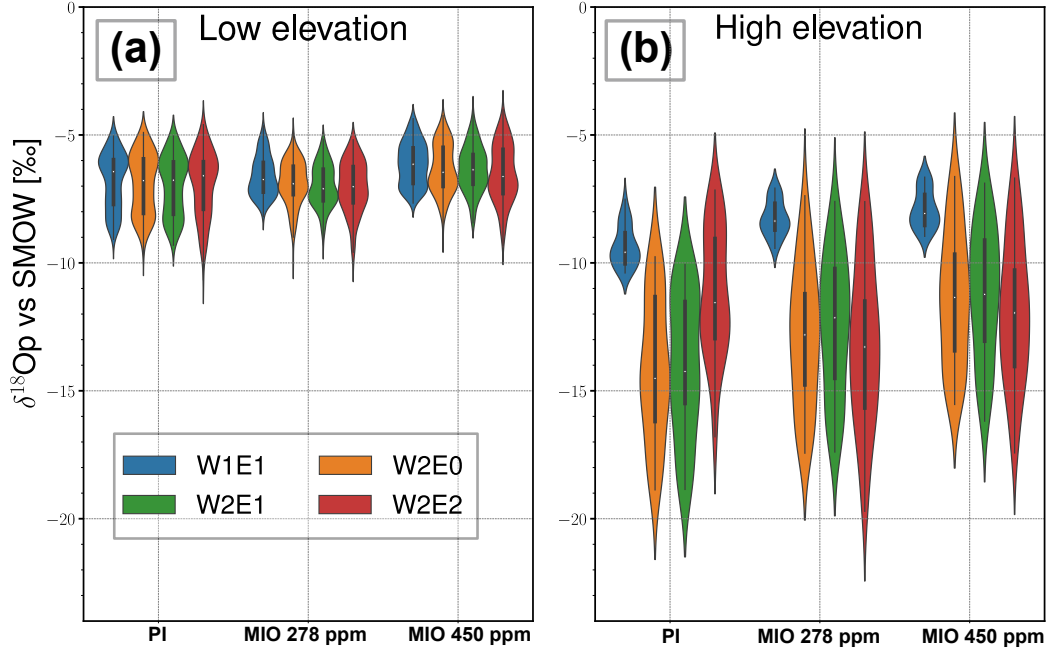


**Figure 4.** Violin plots illustrating the distribution of annual means of  $\delta^{18}O_p$  values over the (a) low (i.e., areas of  $< 500$  m) and (b) high (i.e., areas of  $> 1000$  m) regions (region shown in Fig. 1a; black rectangle) for the different topographic configuration experiments under Pre-Industrial (PI) and the Middle Miocene climatic conditions ( $pCO_2 = 278$  ppm (Mio278) and  $pCO_2 = 450$  ppm (Mio450)). Overall, the distribution of  $\delta^{18}O_p$  values over the low-elevation regions are similar for all topographic and climatic scenarios but show greater differences over the high-elevation regions depending on the topography and climate scenario.

444 Middle Miocene experiments, the Mio278 conditions result in a higher depletion of  $\delta^{18}O_p$   
 445 than Mio450 conditions, especially over the Eastern Alps. Furthermore, the W2E2 ex-  
 446 periments create the largest difference ( $\sim 2$  ‰) between Mio278 and Mio450 runs.

### 447 3.3 Regional annual means of $\delta^{18}O_p$ values over low- and high-elevation 448 regions of the Alps

449 The  $\delta$ - $\delta$  approach relies on  $\delta^{18}O_p$  values from low-elevation sites (e.g., foreland basins)  
 450 adjacent to high-elevation regions to track the isotopic signal contribution from regional  
 451 climate changes through time. Therefore, the sensitivity of the  $\delta^{18}O_p$  values over the low-  
 452 and high-elevation regions in response to the different topographic scenarios and Miocene  
 453 climate change would help validate the  $\delta$ - $\delta$  application across the Alps. We therefore es-  
 454 timate the ranges of the simulated  $\delta^{18}O_p$  values across the low- and high-elevation re-  
 455 gions around the Alps (Fig. 1a).

456 Overall, the Miocene simulations show an increase of  $\delta^{18}O_p$  values compared to PI  
 457 experiments, with the exception of W2E2, which indicates the most depleted  $\delta^{18}O_p$  val-  
 458 ues under the Mio278 conditions over the high-elevation regions (Fig. 4b). The  $\delta^{18}O_p$   
 459 ranges across the low-elevation regions for the topography scenarios in PI, Mio278 and  
 460 Mio450 indicate slight variations of less than 2 ‰ (Fig. 4a). Specifically, the median (of  
 461 all grid-box data points in the defined region) for the individual topographic scenarios  
 462 in the PI and Mio278 are similar, but are less negative in Mio278. Over the high-elevation

463 regions, most of the topographic configurations result in a uniform increase from PI to  
 464 Mio450 (Fig. 4b). For instance, the W1E1 configuration leads to an increase of 2 ‰ be-  
 465 tween the PI and Mio450. Similarly, the modified topographies (W2E0 to W2E2) lead  
 466 to greater differences over the high-elevation regions. Specifically, the W2E1 results in  
 467 an increase of  $\sim 2.5$  ‰ from PI to Mio278 and of  $\sim 4$  ‰ to Mio450 (Fig. 4b). More-  
 468 over, the W2E2 shows a similar distribution of  $\delta^{18}O_p$  values between the PI and Mio450  
 469 but indicates a decrease of 2 ‰ from PI to Mio278. This highlights that global climatic  
 470 changes across the high-elevation regions are much greater than over the low-elevation  
 471 sites. However, such impacts are not uniform due to varied moisture redistribution that  
 472 depends on the topographic configuration.

473 The differences between the low- and high-elevation regions (referred to as  $\Delta\delta^{18}O_p$ )  
 474 are  $\sim 2$  ‰ less in Mio278 and Mio450 compared to the PI climate (Fig. 4). The  $\Delta\delta^{18}O_p$   
 475 values range from -4 to -6 ‰ for the topographic configurations in Mio278 and Mio450,  
 476 but reach -8 ‰ in PI. Note that the Miocene  $\Delta\delta^{18}O_p$  values are still significant enough  
 477 to be reflected in geologic material, and therefore, suitable for the  $\delta$ - $\delta$  approach across  
 478 the Alps.

### 479 3.4 Topography-related changes in $\delta^{18}O_p$ values in the Middle Miocene

480 The difference between the simulated  $\delta^{18}O_p$  response to the varied topographic scen-  
 481 arios and the control experiment (i.e., W1E1) are calculated to quantify the contribu-  
 482 tion of Middle Miocene surface elevation changes to the isotopic signals. All simulated  
 483 annual means of  $\delta^{18}O_p$  values indicate a decreasing gradient towards Northern and East-  
 484 ern Europe (Fig. S2). Such patterns highlight the “continentality effect” from the oceanic  
 485 sources toward the Alps. Overall, the  $\delta^{18}O_p$  values responses indicate larger changes in  
 486 areas of modified topography (up to -10 ‰ and -8 ‰ for the Mio278 and Mio450 con-  
 487 ditions, respectively) and slight changes in adjacent low-elevation regions ( $< -2$  ‰) (Fig.  
 488 S3). These estimates are similar to the topography-induced isotopic signal using pre-industrial  
 489 conditions by Boateng et al. (2023). This implies that changing topography still produces  
 490 an isotopic signal that is significant enough to be reflected in geologic material under a  
 491 warmer past climate.

492 In this study, we determine the magnitude of the isotopic signal that would be mis-  
 493 represented in the Middle Miocene if a present-day lapse rate is assumed by calculating  
 494 the difference between the simulated (shown in Fig. S3) and expected (shown in Fig. S4)  
 495 changes due to topography changes alone (Fig. 5). We first estimate the expected  $\delta^{18}O_p$   
 496 response to a certain topographic rise by using the modern GNIP data-based lapse rate  
 497 of  $-2.0$  ‰  $\text{km}^{-1}$  from Campani et al. (2012) (Fig. S4). This was done by multiplying the  
 498 elevation changes by the lapse rate (e.g., a 2 km elevation change would result in a  $\delta^{18}O_p$   
 499 difference of -4 ‰). We then subtract the expected  $\delta^{18}O_p$  changes from the simulated  
 500  $\delta^{18}O_p$  changes for the different topographic scenarios in the Mio278 and Mio450 simu-  
 501 lations. The residual  $\delta^{18}O_p$  signal (Fig. 5) indicates the fraction of  $\delta^{18}O_p$  changes that  
 502 would account for a paleoelevation signal if based on modern ILR but rather originates  
 503 from the adjustment of the ILR under Middle Miocene climate conditions. For instance,  
 504 a negative difference, as observed over the Alps (brown colours in Fig. 5), indicates that  
 505 in the paleoclimate simulations, the  $\delta^{18}O_p$  values are more depleted than when calcu-  
 506 lated by combining the modern alpine isotopic lapse rate ( $-2.0$  ‰  $\text{km}^{-1}$ ) and forced to-  
 507 pographic changes. This ultimately results in an overestimation of Miocene paleoeleva-  
 508 tion estimates if based on the modern ILR. As a consequence, this indicates that the ILRs  
 509 of the paleoclimate simulations should, in general, be steeper to account for the intro-  
 510 duced paleoelevation (c.f. section 4.5).

511 Overall, the estimates indicate greater affected regions for the Mio278 than the Mio450  
 512 simulation. Specifically, a  $\delta^{18}O_p$  difference of -5 ‰ over the peak elevations and -3 ‰  
 513 to -2 ‰ over the 300 km range adjacent to the Alps would be (falsely) attributed to Mid-

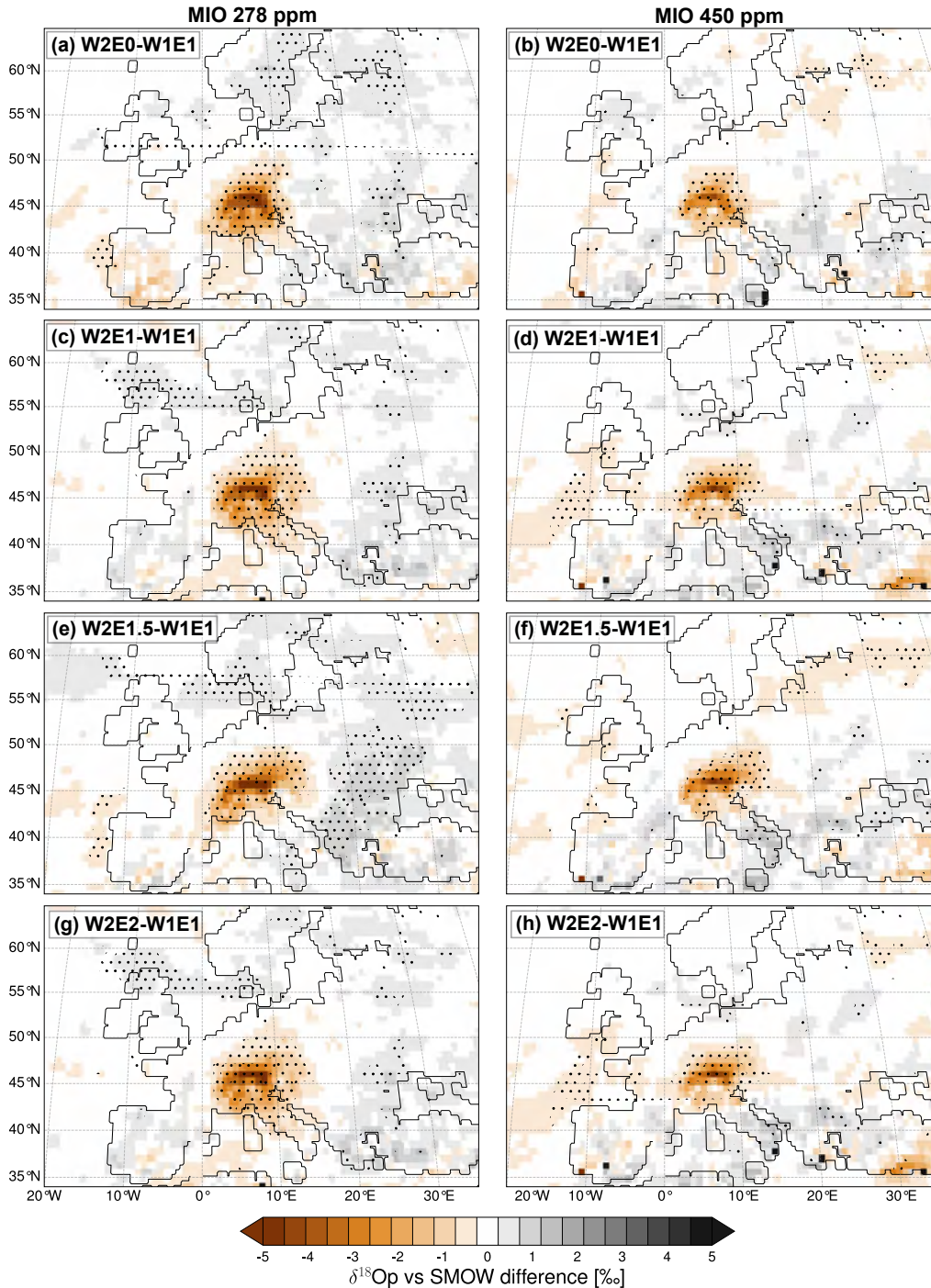


**Figure 5.** Mean annual  $\delta^{18}O_p$  difference between the total simulated changes and expected changes due to the changes of topography (i.e., W2E0 (a, b), W2E1 (c, d), W2E1.5 (e, f), and W2E2 (g, h)) in Middle Miocene conditions with  $pCO_2$  of 278 ppm (Mio278; left) and 450 ppm (Mio450; right). The expected changes are calculated with observed precipitation modern-day isotopic lapse rate of  $2.0 \text{ ‰ km}^{-1}$  (Campani et al., 2012). The ash colour range represents more enriched conditions, and the brown colour ranges indicate more depleted conditions, as expected when using the modern alpine lapse rate to estimate topography-related changes in  $\delta^{18}O_p$  values. Regions of statistically significant difference are marked with black dot stippling. The  $\delta^{18}O_p$  difference highlights the misrepresentation of the isotopic signal when the isotopic lapse rate is assumed stationary. The decrease in  $\delta^{18}O_p$  values across the Alps suggests the potential overestimation of its paleoelevation in the Middle Miocene.

514 dle Miocene paleoelevation changes, if the modern ILR were applied. On the regional  
 515 scale, the  $\delta^{18}O_p$  differences in Mio278 indicate more enriched patterns of 2 ‰ across East-  
 516 ern Europe, with some regions showing significant signals (Fig. 5; left panel). Contrar-  
 517 ily, the regional scale  $\delta^{18}O_p$  differences under Mio450 conditions indicate less enriched  
 518 patterns of 1 ‰ over the Southern Alps and the Mediterranean (Fig. 5; right panel). Such  
 519 remote impacts independent of the surface uplift indicate the large-scale implication of  
 520 assuming stationarity of lapse rate through space and time.

### 521 **3.5 Variations of isotopic lapse rates in response to changing topogra-** 522 **phies and Middle Miocene climates**

523 The estimated mean annual isotopic lapse rate (ILR) for the different experiments  
 524 and regions around the Alps (Fig. 1b) indicate notable spatio-temporal changes (Fig.  
 525 6). The linear regressions used to estimate ILRs indicate a statistically significant rela-  
 526 tionship between  $\delta^{18}O_p$  values and elevation with the coefficients of determination ( $R^2$ )  
 527 of 0.85-0.99 (Fig. 6). Overall, global climate changes with Mio278 and Mio450 condi-  
 528 tions contribute to ILR changes of  $\sim 1.0$  ‰  $\text{km}^{-1}$  and  $0.5$  ‰  $\text{km}^{-1}$ , respectively, compared  
 529 to PI. The estimated ILR differences caused by topographic changes reached values of  
 530 up to  $1.5$  ‰  $\text{km}^{-1}$ . ILR estimates for the PI run with the unmodified Alps topography  
 531 (W1E1) are  $-3.12 (\pm 0.21)$  ‰  $\text{km}^{-1}$  for the western transect and  $-2.93 (\pm 0.21)$  ‰  $\text{km}^{-1}$   
 532 for the northern transect, respectively (Fig 6 a & b). These estimates agree with the global  
 533 modern ILR of  $-2.8$  ‰  $\text{km}^{-1}$  based on  $\delta^{18}O$  values of global surface waters (Poage & Cham-  
 534 berlain, 2001). However, our ILR estimates are higher than the present-day ILR of  $-2.0$   
 535 ‰  $\text{km}^{-1}$  for the northern slope of the Central Alps, estimated from rainfall  $\delta^{18}O_p$  val-  
 536 ues collected from several weather stations across the Alps (GNIP data; Campani et al.  
 537 (2012)). Note that the number of weather stations used for the latter ILR estimate was  
 538 smaller ( $<10$ ), so it may not represent the spatial variation of  $\delta^{18}O_p$  over the Alps. The  
 539 W1E1 scenario with Mio278 conditions results in ILRs of  $2.02 (\pm 0.21)$  ‰  $\text{km}^{-1}$  and  $2.43$   
 540  $(\pm 0.14)$  ‰  $\text{km}^{-1}$  for the western and northern transect, respectively, and the same to-  
 541 pographic configuration produces steeper ILRs of  $2.18 (\pm 0.19)$  ‰  $\text{km}^{-1}$  (northern tran-  
 542 sect) and  $2.48 (\pm 0.16)$  ‰  $\text{km}^{-1}$  (western transect) in the Mio450 run (Fig 6 a & b). Over-  
 543 all, ILRs of the modern-day topography become shallower under warmer Middle Miocene  
 544 conditions, as suggested by previous studies (Poulsen & Jeffery, 2011; Rowley, 2007), but  
 545 with shallowest slopes under Mio278 climate conditions. The shallowing of ILR in the  
 546 warmer climates was  $-0.5$  ‰  $\text{km}^{-1}$  greater across the western transect than for the north-  
 547 ern transect. This is due to the more depleted  $\delta^{18}O_p$  values over the Western Alps in  
 548 the Middle Miocene compared to the northern foreland of the Alps (Fig. 2 a & b).

549 For the topographic sensitivity experiments, most of the ILR estimates across the  
 550 western transect indicate the steepest ILR in the PI climate, except in the case of us-  
 551 ing the W2E2 topography, which results in the steepest ILR with the Mio278 conditions.  
 552 For instance, the W2E1 which indicated the highest ILR estimate of  $-3.71 (\pm 0.15)$  ‰  
 553  $\text{km}^{-1}$ ,  $-2.81 (\pm 0.16)$  ‰  $\text{km}^{-1}$ , and  $-2.36 (\pm 0.14)$  ‰  $\text{km}^{-1}$  for PI, Mio278, and Mio450,  
 554 respectively, along the western transect (Fig. 6e). The ILR changes among these climates  
 555 for W2E1 was up to  $-1.35$  ‰  $\text{km}^{-1}$ . The W2E1 experiment produces the steepest ILR  
 556 of  $-4.17 (\pm 0.12)$  ‰  $\text{km}^{-1}$  with Mio278 and  $-4.10 (\pm 0.11)$  ‰  $\text{km}^{-1}$  and  $-3.85 (\pm 0.11)$  ‰  
 557  $\text{km}^{-1}$  for Mio450 and PI climates (Fig 6f). The ILR changes over the northern transect  
 558 were  $<-0.32$  ‰  $\text{km}^{-1}$  and lower than those ILR changes over the western transects ( $<-$   
 559  $1.35$  ‰  $\text{km}^{-1}$ ). Overall, significant changes of ILR in response to the different surface  
 560 uplift scenarios and global climate changes highlight the huge implications of the assump-  
 561 tion of its stationarity for stable isotope paleoaltimetry.

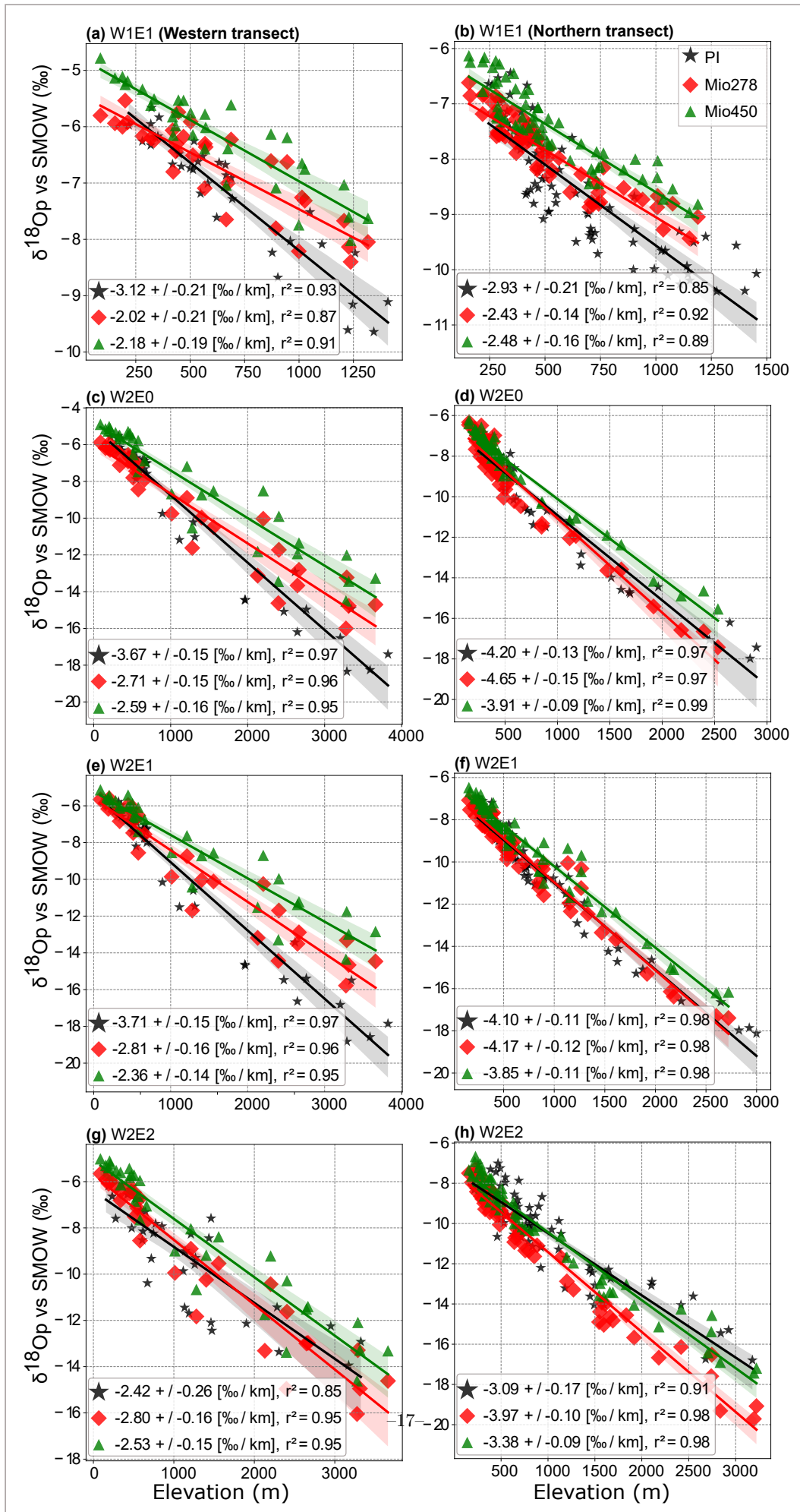


**Figure 6.** Annual isotopic lapse rates (ILRs) estimate for the different topographic scenarios



### 3.6 Changes in precipitation and near-surface temperature in response to the topographic scenarios with Middle Miocene conditions

Here, we present the changes in precipitation (Fig. 7) and near-surface temperature (Fig. S6) in response to the different topographic scenarios under Middle Miocene climatic conditions. The simulated annual climatologies for the individual experiments are presented in the supplementary material (i.e., temperature in Fig. S5 and precipitation in Fig. S7).

The precipitation changes indicate both localised and far-field changes, with the magnitude and spatial patterns of precipitation changes depending on the topographic scenario and climatic boundary conditions (PI, Mio278, Mio450). The localised changes indicate a general increase in precipitation amounts, scaling with elevation. Specifically, increasing the West-Central Alps topography by 200% (W2) induces a precipitation increase of  $>60$  *mm/month* in both Mio278 and Mio450, paleoclimate configurations (Fig. 7). Overall, the simulated magnitudes of changes are greater under Mio278 than under Mio450 conditions. On the regional scale of the Mio278 simulations, the modification of alpine topography results in north-south bi-directional precipitation changes with an increase of  $15$  *mm/month* over the southern transects to the Mediterranean and a decrease of  $20$  *mm/month* over the northern transects ( $> 50$  °N) of the Alps (Fig. 7; left panel). However, the Mio450 simulations show west-east bi-directional changes with wetter conditions (an increase of up to  $30$  *mm/month*) over the North Atlantic towards Central Europe and drier conditions ( $< 30$  *mm/month*) over Eastern Europe (Fig. 7; right panel). Among these changes, the W2E1.5 experiment produces the wettest conditions over the western transects towards the Alps under Mio450 and the driest condition over the northern transects of the Alps under Mio278 conditions (Fig. 7 f).

The near-surface temperature changes show more localised cooling or warming in response to the elevation increase or decrease scenarios. More specifically, the W2 experiments cause a cooling of  $-10$  °C over the West-Central Alps and a uniform decrease down to  $-4$  °C over the Eastern Alps for the incremental increase in elevations (Fig. S6). However, the magnitudes of cooling are greater with Mio278 than with Mio450 conditions. The reduction of Eastern Alps topography (E0) induces warming of up to  $3$  °C with Mio278 and  $5$  °C with Mio450 conditions. The far-field regions experience slight changes of  $-1$  to  $2$  °C with warmer patterns in the Mio450 climate. Overall, the similar localised changes in temperature compared to the localised changes in  $\delta^{18}O_p$  values suggest the predominant influence of temperature at the local scale rather than precipitation. However, the topography-induced far-field regional changes of  $\delta^{18}O_p$  values are mostly likely driven by the atmospheric dynamics processes associated with the precipitation changes.

### 3.7 Inter-annual relationships of $\delta^{18}O_p$ with precipitation and temperature for pre-industrial and Middle Miocene climates

The relationship between water isotopologue distribution at a specific region or globally and climate variables (e.g., precipitation) in the present day is often used as a transfer function (e.g.,  $\delta^{18}O_p$ -precipitation gradient) for reconstructing paleoenvironment changes. Hence, we calculate the inter-annual relationships of monthly  $\delta^{18}O_p$  values with precipitation and temperature using Spearman correlation for the different climates. The focus is to determine if the relationship changes under different climatic conditions. Most regions indicate a significant (i.e.,  $\geq 95\%$  CI) negative correlation between  $\delta^{18}O_p$  values and precipitation and a positive correlation of  $\delta^{18}O_p$  values with temperature across Europe and the North Atlantic (Fig. 8). However, the strength and spatial patterns of these relationships vary among the different climate scenarios (PI, MIO278, MIO450). In the PI climate, the correlation of  $\delta^{18}O_p$  with precipitation over Scandinavia to western Russia shows positive values of up to  $0.4$  (Fig. 8a). However, the correlation patterns over

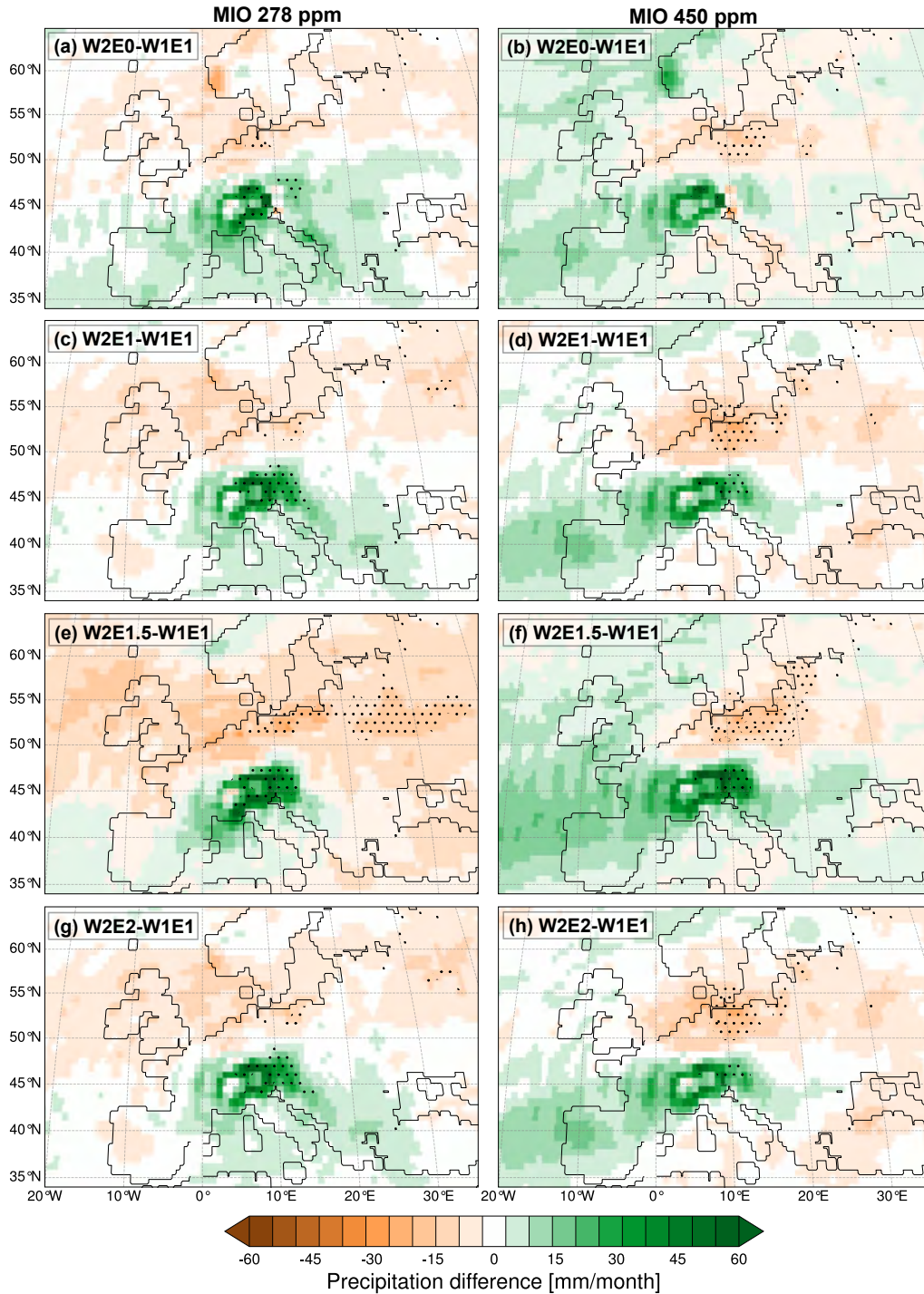


**Figure 7.** Mean annual difference of precipitation in response to the different topographic scenarios (i.e., W2E0 (a, b), W2E1 (c, d), W2E1.5 (e, f), and W2E2 (g, h) relative to control scenario (W1E1) with Middle Miocene boundary conditions (Mio278; left panel and Mio450; right panel)). The green color ranges indicate wetter and the brown color ranges indicate drier conditions than in the W1E1 scenario. Regions that experience significant differences based on students' *t*-tests with a 95% confidence interval (CI) are marked with dot stipplings. The results show that precipitation patterns across Europe depend on the topographic scenario and global climate changes

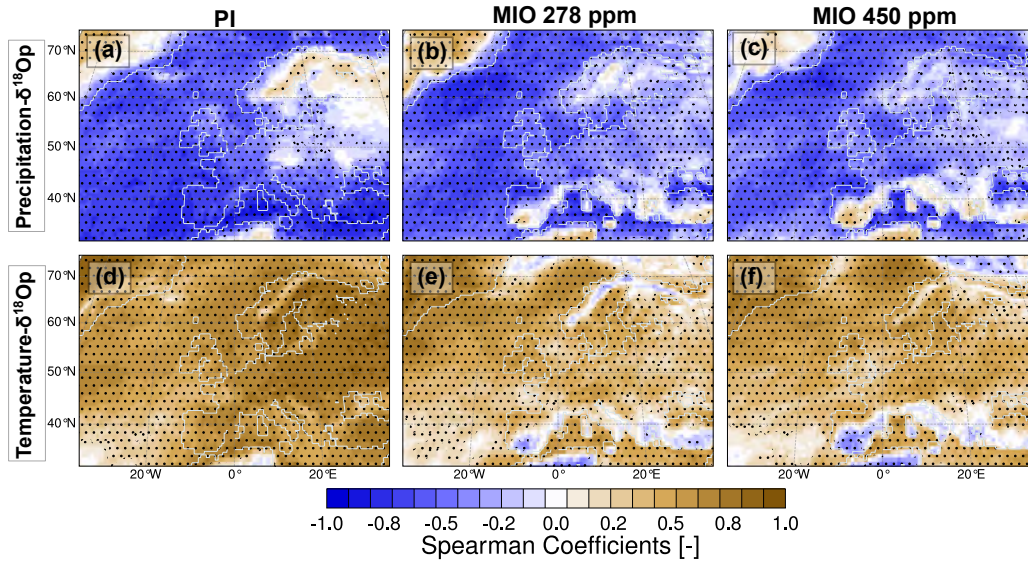


**Figure 8.** Spearman correlation coefficients of the inter-annual relationship between monthly  $\delta^{18}O_p$  values and precipitation (top panel), as well as temperature (bottom panel) for pre-industrial (PI; a, b) and Miocene  $pCO_2$  levels of 278 (Mio278; b,e) and 450 ppm (Mio450; c,f). Regions showing significant correlation with a 95% confidence interval are marked with dot stipplings. The correlation coefficients and spatial patterns suggest that the spatial inter-annual relationship between  $\delta^{18}O_p$  values and regional climate variables (temperature, precipitation) change in response to the different paleoenvironmental conditions.

613 these regions progressively shift to negative values from the Mio278 (Fig. 8b) to the Mio450  
 614 (Fig. 8c) climate. Moreover, the negative values across the southern coastal regions of  
 615 the Mediterranean in the PI (Fig. 8a) shift to positive values under Middle Miocene cli-  
 616 mate conditions (Fig. 8 b-c).

617 For the  $\delta^{18}O_p$ -temperature relationship, the PI simulation estimates a higher posi-  
 618 tive correlation across continental Europe than the North Atlantic (Fig. 8d). However,  
 619 the strength of this relationship reduces in the Middle Miocene simulations, with the south-  
 620 ern coastal regions of the Mediterranean showing negative correlation values (Fig. 8 e-  
 621 f). In the Mio278 simulation, some regions of the Scandinavian mountains indicate neg-  
 622 ative values (Fig. 8e), while PI and Mio450 runs show positive correlation values.

## 623 4 Discussion

### 624 4.1 Global hydroclimate response to the Middle Miocene climatic and 625 paleogeographic conditions

626 Our Middle Miocene simulations point to  $pCO_2$  as the main driver of global cli-  
 627 matic changes (Acosta et al., 2024; Burls et al., 2021; Hossain et al., 2023; Knorr et al.,  
 628 2011), while the  $pCO_2$ -unrelated forcing controls some of the regional-scale changes (Acosta  
 629 et al., 2024; Burls et al., 2021; Brierley & Fedorov, 2016; Farnsworth et al., 2019; Jung  
 630 et al., 2016). More specifically, the Middle Miocene Mio278 simulation with the same  
 631  $pCO_2$  as PI simulation predicts a global warming of  $\sim 2$  °C, which is consistent with pre-  
 632 vious studies (Burls et al., 2021; Knorr et al., 2011; Krapp & Jungclaus, 2011). For in-  
 633 stance, Knorr et al. (2011) estimated global warming shares of  $\sim 0.7$  °C due to changes  
 634 in topography and 2.5 °C due to vegetation changes. Moreover, Herold et al. (2011) also

635 estimated global warming of 1.5 °C due to the combined effect of the changes in Miocene  
 636 paleogeography and vegetation. These studies suggest that the majority of the Middle  
 637 Miocene global climate changes are driven by  $p\text{CO}_2$  and land cover changes that are linked  
 638 to the global energy balance (e.g., planetary albedo, emissivity of longwave radiation) (Burls  
 639 et al., 2021).

#### 640 *4.1.1 Middle Miocene Temperatures*

641 Increasing  $p\text{CO}_2$  to 450 ppm in the Middle Miocene resulted in a global mean annual  
 642 temperature (MAT) increase of 5.9 °C, which is amplified over the continents (8.6  
 643 °C), and is in agreement with previous modelling studies (Burls et al., 2021; Frigola et  
 644 al., 2018; Goldner et al., 2014; Hossain et al., 2023; Krapp & Jungclaus, 2011; Stärz et  
 645 al., 2017). The multi-model mean of the MioMIP1 simulations with a  $p\text{CO}_2$  of 400-450  
 646 ppm predicts a MAT increase of 4.1 °C (Burls et al., 2021), which is  $\sim 1.8$  °C cooler than  
 647 our Mio450 MAT estimate. Aside from the higher model complexity of fully coupled atmosphere-  
 648 ocean GCMs participating in MioMIP1, the key difference compared to our simulation  
 649 is their lower spatial resolution (i.e., T31 or T42, which is up to  $\sim 300$  km at the equa-  
 650 tor compared to our  $\sim 80$  km grid cell width). This suggests that model resolution may  
 651 affect the magnitude of warming estimated by climate models in the Middle Miocene.  
 652 For instance, Hossain et al. (2023) conducted Middle Miocene simulations with  $p\text{CO}_2$   
 653 of 280-720 ppm using AWI-ESM2.1, which has a similar atmospheric component (ECHAM6)  
 654 as our model. Their simulations used a spatial resolution of T63 ( $\sim 180$  km at the equa-  
 655 tor) for the atmosphere, which is coarser than our simulation with T159 ( $\sim 80$  km at the  
 656 equator). Overall, their simulations with  $p\text{CO}_2$  of 280-720 ppm indicate MATs of 17.5-  
 657 20.0 °C, which is within the 16.3-19.9 °C range estimated from our simulation with  $p\text{CO}_2$   
 658 of 278-450 ppm. Specifically, their experiment with 450 ppm estimated a MAT increase  
 659 of  $\sim 3.1$  °C with the increase of  $p\text{CO}_2$  ( $\Delta p\text{CO}_2$ ) contributing to +1.4 °C warming. The  
 660 MAT increase estimated from our Mio450 simulation (i.e., 5.9 °C) is 2.8 °C higher than  
 661 their estimate. Moreover, the  $\Delta p\text{CO}_2$  warming (i.e., +3.6 °C) from Mio450 is also 2.2  
 662 °C higher than their estimates. The comparison of our simulation with the equivalent  
 663 Middle Miocene experiments with low-resolution MPI-ESM by Krapp and Jungclaus (2011)  
 664 indicated similar magnitudes of additional warming from our high spatial resolution es-  
 665 timates. These suggest that the low resolution used by the fully coupled models may un-  
 666 derestimate the warming through the  $p\text{CO}_2$  feedback. A comparison to proxy-based tem-  
 667 perature reconstructions supports this.

668 Overall, the simulated MAT anomalies (i.e., deviation from PI) only agree with the  
 669 lower range of the 7.6  $\sim$  2.3 °C increase estimated from the various temperature prox-  
 670 ies (Burls et al., 2021; Goldner et al., 2014; Hui et al., 2018). However, all models with  
 671 moderate  $p\text{CO}_2$  and Middle Miocene paleoenvironmental boundary conditions still strug-  
 672 gle to simulate the extent of warming suggested by the temperature proxies (Burls et  
 673 al., 2021; Goldner et al., 2014). Mostly, this is because of the far too low high-latitude  
 674 temperatures and strong meridional temperature gradient estimated by the models, which  
 675 is a common problem for modelling studies spanning the Cenozoic era (e.g., Haywood  
 676 et al., 2020; Huber & Caballero, 2003; Steinthorsdottir et al., 2021). Moreover, most mod-  
 677 els underestimate the warming in the extratropics (specifically across the North Atlantic),  
 678 which is required to maintain the reduced meridional temperature gradient suggested  
 679 by proxy data (Herbert et al., 2020, 2022; Super et al., 2020). Recent studies suggest that  
 680 increasing  $p\text{CO}_2$  to up to 1100 ppm provides a better agreement between climate mod-  
 681 els and proxy reconstructions (Herbert et al., 2022). Moreover, the stationarity assump-  
 682 tion of transfer function between proxy signal and climate variables for deep-time pa-  
 683 leoclimate reconstruction (Boateng et al., 2024; Ho & Laepple, 2016) and under-representation  
 684 of certain climatic feedbacks such as cloud-aerosol interactions (Feng et al., 2019; Zhu  
 685 et al., 2019), ocean mixing (Green & Huber, 2013), and orbital forcing (Ladant et al.,  
 686 2014) in the climate models can also be reasons for the discrepancies between the proxy  
 687 data and climate models.

688

#### 4.1.2 Middle Miocene Hydroclimate

689

690

691

692

693

694

695

696

697

698

699

700

701

702

703

704

705

706

707

708

709

710

The simulations indicate an amplified hydroclimate with warmer and wetter conditions for the Middle Miocene (Fig. 2), in agreement with paleobotanical records indicating wetter than modern conditions and an expansion of megathermal forests and habitable regions for leaf-eating mammals (Acosta et al., 2024; Pound et al., 2011; Steinhorsdottir et al., 2021). Our simulations (Fig. 2) indicate an overall increase in mean annual precipitation (MAP) with elevated  $p\text{CO}_2$  (Mio450), resulting in a rainfall increase of 9%. This is generally consistent with other modelling studies with similar  $p\text{CO}_2$  ranges, but most of these studies predict slightly smaller changes in precipitation (e.g., Acosta et al., 2024; Frigola et al., 2018; Krapp & Jungclaus, 2011). The MioMIP1 experiments with  $p\text{CO}_2$  of 400 and 560 ppm estimate a multi-model mean MAP of 1129.5 and 1161.1  $\text{mm}/\text{year}$  (Acosta et al., 2024), which is less than our Mio450 estimates of 1188.2  $\text{mm}/\text{year}$ . The MCO simulation with  $p\text{CO}_2$  of 400 ppm by Frigola et al. (2018) also estimates lower MAP amounts (1095  $\text{mm}/\text{year}$ ). The MCO simulation with a fully coupled atmosphere-ocean model using  $p\text{CO}_2$  of 720 ppm by Krapp and Jungclaus (2011) also indicates a MAP increase of 5% compared to PI. These suggest that the high spatial resolution adopted in our simulations, at least to some extent, enhances the Middle Miocene precipitation response since even the increase of  $p\text{CO}_2$  of up to 720 ppm (MIOMIP) produces a smaller increase of MAP than our Mio450 simulation. Reasons for this may involve a better representation of certain climate features such as large-scale condensation, land-sea interaction, topography and climate feedbacks at high resolution. For instance, previous studies have highlighted that monsoons are better resolved at high resolution (Gao et al., 2006; Sperber et al., 1994).

711

712

713

714

715

716

717

718

719

720

721

722

723

724

725

726

727

728

729

Even though Middle Miocene simulations indicate wetter and warmer global conditions, the regional MAP responses are more variable. This is mostly due to  $p\text{CO}_2$ -unrelated changes (e.g., paleogeography, paleoelevation, vegetation, and land ice) and the indirect response of the hydrological cycle to  $p\text{CO}_2$ -unrelated warming (i.e.,  $2.3\text{ }^\circ\text{C} > \text{PI}$ ) (Acosta et al., 2024; Burls et al., 2021). For instance, the precipitation decrease across South America and Central Asia in the Mio278 simulation (Fig. 2c) can be attributed to the reduced paleoelevation of the Andes and Tibetan Plateau (Acosta et al., 2024; Farnsworth et al., 2019). Similarly, the decrease in precipitation across southern Central Africa can be attributed to the reduced Miocene elevation of the East African Rift system (Jung et al., 2016; Sepulchre et al., 2006). Brierley and Fedorov (2016) suggested that the precipitation changes across the equatorial Atlantic and Central America were caused by the opening of the Panama gateway rather than global warming. These regional changes further intensify under elevated  $p\text{CO}_2$  conditions. The  $\Delta p\text{CO}_2$  contributed to a MAP increase of 80  $\text{mm}/\text{year}$  (7.3%) in the Mio278 experiment. This is close to the  $\Delta p\text{CO}_2$  induced MAP increase of 50  $\text{mm}/\text{year}$  from the MioMIP1 models (Acosta et al., 2024). Overall, our simulations indicate a hydrological cycle sensitivity of 2.05% precipitation increase per  $1\text{ }^\circ\text{C}$  warming. This is similar to what has been estimated for the Eocene Modeling Intercomparison Project (Cramwinckel et al., 2023), Miocene (Acosta et al., 2024) and the Pliocene Modeling Intercomparison Project (Han et al., 2021).

730

731

#### 4.2 Latitudinal gradient of precipitation and $\delta^{18}\text{O}_p$ over Europe in the Middle Miocene

732

733

734

735

736

737

738

739

The simulated precipitation and  $\delta^{18}\text{O}_p$  patterns across Europe (Figs. 2) indicate a more pronounced meridional gradient during the Middle Miocene that intensifies with increased  $p\text{CO}_2$  (278 vs. 450 ppm). The strong Miocene latitudinal gradient of paleoprecipitation has also been suggested from proxy data reconstructions (Böhme et al., 2006; Costeur & Legendre, 2008; Jiménez-Moreno & Suc, 2007). For instance, Jiménez-Moreno and Suc (2007) indicated warm and dry conditions with subdesertic vegetation over the northwestern Mediterranean and humidity-adapted plants environment towards the north. Despite the strong latitudinal precipitation gradient, most European regions experienced

740 less precipitation compared to PI conditions (Fig. 2), which agrees with proxy reconstruc-  
 741 tions (e.g., Abdul Aziz et al., 2003; Böhme et al., 2011). Overall, the simulated precipi-  
 742 tation decreases from Central Europe towards Southern Europe and the Mediterranean.  
 743 The decrease in precipitation and the significant increase in temperature over these lower  
 744 latitude regions results in less negative  $\delta^{18}O_p$  values. Future climate projections in re-  
 745 sponse to increasing  $pCO_2$  forcing indicate similar precipitation latitudinal gradients (Rajczak  
 746 et al., 2013; Rajczak & Schär, 2017). This is partly due to the changes in the atmospheric  
 747 dynamics (e.g., European atmospheric teleconnections) that influence regional climate  
 748 patterns under global warming (Fereday et al., 2018; Giorgi & Lionello, 2008; McKenna  
 749 & Maycock, 2022; Zappa et al., 2015). Botsyun et al. (2022) indicated expanded anti-  
 750 cyclonic circulation over southern Europe and the Mediterranean region in the Middle  
 751 Miocene due to the strengthening of the dipole pressure gradient across the North At-  
 752 lantic. Giorgi and Lionello (2008) suggested that such anticyclonic conditions induce at-  
 753 mospheric stability that inhibits more precipitation over the northern latitudes due to  
 754 the northward migration of the Atlantic storm track. Moreover, the pronounced dipole  
 755 pressure gradient (i.e., Icelandic Low and Azores High) would induce strong westerlies  
 756 that would transport more moisture toward the northern latitudes from the North At-  
 757 lantic, leading to drier conditions in the lower latitudes of Europe (Barnston & Livezey,  
 758 1987; Hurrell, 1995).

### 759 **4.3 Influence of changes of Alps topography on regional climate and $\delta^{18}O_p$** 760 **patterns during the Middle Miocene**

761 The topographic sensitivity experiments indicate significant local (i.e., areas of mod-  
 762 ified topography) cooling (warming) in response to the increase (decrease) of topogra-  
 763 phy across the Alps. This is mainly due to the adiabatic lapse rate (Boateng et al., 2023;  
 764 Botsyun et al., 2020, 2022). The regions adjacent to the modified areas experienced slight  
 765 changes that are too insignificant to explain any potential additional non-adiabatic lapse  
 766 rate influence. The precipitation patterns (Fig. 7) experienced greater spatial impacts  
 767 due to the topographic changes since thermodynamic and dynamic processes that regu-  
 768 late precipitation formation are more altitude-dependent (Insel et al., 2010; Poulsen et  
 769 al., 2010; Sepulchre et al., 2006). Even though topographic rise resulted in a similar in-  
 770 crease in orographic precipitation compared to Boateng et al. (2023), the intensification  
 771 of the drier conditions across the Alps for high  $pCO_2$  suppressed their impact in the Mio450.  
 772 This resulted in more precipitation changes in Mio278 than in Mio450 experiments. The  
 773 topography-induced precipitation changes across the far-field regions adjacent to the Alps  
 774 indicate varied responses depending on the topographic scenario and climate conditions.  
 775 For instance, changes in topography under Mio278 conditions induce a north-south gra-  
 776 dient with wetter conditions over the southern region of the Alps and drier conditions  
 777 over the northern region of the Alps (Fig 7). This is partly due to moisture redistribu-  
 778 tion by deflecting more moisture towards the southern transect due to the orographic  
 779 barrier caused by the surface uplift of the West-Central Alps by 200% (Fig. S9). On the  
 780 other hand, precipitation patterns across the regions outside the Alps in response to to-  
 781 pographic changes under Mio450 show a west-to-east gradient with wetter conditions across  
 782 the western areas of the Alps and slightly drier conditions towards the northern and south-  
 783 ern areas of the Alps. This can be due to the fact that higher  $pCO_2$  levels intensify the  
 784 dipole pressure gradient over the North Atlantic, which then increases the strength of  
 785 the westerlies, leading to more moisture transport towards the northern latitudes of Eu-  
 786 rope. Hence, the reduced moisture transport towards the Alps prevents the spillover of  
 787 more moisture towards the eastern flanks of the Alps and focuses the orographic precipi-  
 788 tation across the western flanks of the Alps. In total, the varied moisture redistributions  
 789 of the Alps in response to the surface uplift scenarios suggest the potential of the non-  
 790 stationarity of the isotopic lapse rate through space and time due to the associated dif-  
 791 ferences of the fractionation process of air mass transport from the oceanic sources. More-  
 over, non-linear effects of surface uplift can also influence the seasonal distribution of pre-

793 precipitation, which may strongly affect the pedogenic carbonate formation and its isotopic  
794 composition (e.g., Burgener et al., 2016; Peters et al., 2013).

795 The simulated changes in  $\delta^{18}O_p$  values (Fig. S3) can mainly be attributed to lo-  
796 calised adiabatic temperature changes, orographic precipitation and the associated large-  
797 scale precipitation changes. The distinct  $\delta^{18}O_p$  profiles across the Alps (Fig. 3) high-  
798 light the sensitivity of the meteoric water isotopes to both the direct (altitude) and in-  
799 direct global forcings (e.g., paleogeography and  $pCO_2$ ). Moreover, estimated  $\delta^{18}O_p$  dif-  
800 ferences of up to -10 ‰ across the Alps in response to changing topography in the Mid-  
801 dle Miocene are substantial enough to be recorded by the geologic archives such as this  
802 and that for paleoelevation reconstructions. However, assuming stationarity of the iso-  
803 topic lapse rate and applying a localised ILR, such as the modern northern slope rainfall-  
804 based IRL of -2.0 ‰ km<sup>-1</sup> (Campani et al., 2012) can result in missing a  $\delta^{18}O_p$  signal  
805 of up to -5 ‰ (Fig. 5), which is significant enough to cause large errors in paleoeleva-  
806 tion estimates.

807 The sensitivity of the European climate to the Alps' topography on the local to re-  
808 gional scale demonstrated from our experiments stresses the importance of an accurate  
809 representation of past elevations of mountains in climate models. Even though topographic  
810 changes caused by tectonic processes often have a second-order forcing factor on global  
811 climate responses, their impacts affect the gradients of regional climatic variables, bio-  
812 diversity and landscape (e.g., Herold et al., 2009; Sepulchre et al., 2006). The simulated  
813 isotopic patterns across the high-elevation region of the Alps agree with the reconstructed  
814 isotopic water of phyllosilicates from the Simplon Fault Zone (Campani et al., 2012; Manck-  
815 telow et al., 2015), only if the topography of the West-Central Alps is increased by 200%  
816 of its modern height. This implies that under-representing the Alps' paleoelevation in  
817 Middle Miocene simulations would lead to regional biases of the topography-dependent  
818 climate variables such as precipitation, moisture patterns, and local temperature. The  
819 transfer functions for proxy reconstruction calibrated with modern climate observations  
820 would also misrepresent the associated regional climate changes due to paleoelevation  
821 changes. For instance, paleobotanical proxies across Europe suggest the overall precip-  
822 itation increase in the Middle Miocene independent of their location (Bruch et al., 2007).  
823 Aside from the difficulties of plant-based proxies in reconstructing dry climates (e.g., Böhme  
824 et al., 2011), the misrepresentation of the precipitation gradients induced by the differ-  
825 ent topographic scenarios in their transfer function (e.g., coexistence method) might be  
826 the reason for these discrepancies.

#### 827 **4.4 Non-stationarity of isotopic lapse rate in response to Middle Miocene** 828 **climate and surface uplift of the Alps**

829 So far, most stable isotope paleoaltimetry studies rely on the assumption of sta-  
830 tionarity of isotopic lapse rate through time and space (e.g., Campani et al., 2012; Gébelin  
831 et al., 2013; Krsnik et al., 2021). This implies that the spatial gradient of paleo-meteoric  
832 water isotopic composition across mountain ranges and their adjacent areas (e.g. fore-  
833 lands) at the time of formation of the proxy material (e.g., pedogenic carbonate and vol-  
834 canic glass) remains unchanged until the present day. However, previous modelling stud-  
835 ies have demonstrated that various climatic processes, such as surface water recycling,  
836 atmospheric circulation changes, variability in moisture transport and sources, air mass  
837 mixing, and changes in precipitation dynamics caused by global and regional climate change  
838 and surface uplift of orogens can complicate the use of modern ILRs for paleoelevation  
839 reconstruction (Boateng et al., 2023; Botsyun et al., 2019; Ehlers & Poulsen, 2009; In-  
840 sel et al., 2010; Poulsen & Jeffery, 2011). Our simulated ILRs decrease by  $\sim 1.0$  ‰ km<sup>-1</sup>  
841 in the Middle Miocene (e.g., -3.12 (PI) to -2.18 (Mio450) ‰ km<sup>-1</sup> over the western flank  
842 of the Alps; Fig. 6a) and deviate by up to 1.5 ‰ km<sup>-1</sup> for the different surface uplift sce-  
843 narios of the Alps. Moreover, the estimated ILRs in the PI runs were 0.19 ‰ km<sup>-1</sup> higher  
844 or steeper over the western transect than the northern transect of the Alps. These spa-

845 tial differences are larger (up to 0.4 ‰ km<sup>-1</sup>) in the Middle Miocene simulations. The  
 846 spatial changes can be attributed to the seasonal variability of moisture transport from  
 847 the North Atlantic and the increased distance from the moisture source, leading to more  
 848 depleted air masses towards the northern and eastern flanks of the Alps (Boateng et al.,  
 849 2023). Moreover, the moisture redistribution around the Alps due to orographic block-  
 850 ing and rainout across the high topography of the Western-Central Alps also contributes  
 851 to the spatial variability of the isotopic lapse rates (e.g., ~1.5 ‰ km<sup>-1</sup> steeper in north-  
 852 ern flanks than western flanks of the Alps for W2E1). Such spatial variability has also  
 853 been identified for other orogens. For instance, the windward side of the Sierra Nevada  
 854 (CA, USA) has a significantly steeper isotopic lapse rate (e.g., -3.1 ‰ km<sup>-1</sup> over the South-  
 855 ern Sierra) than the leeward side (e.g., -0.9 ‰ km<sup>-1</sup> over western slopes of Sierra Nevada (Lechler  
 856 & Niemi, 2011) and the interior of the Great Basin of western North America (e.g., -0.2  
 857 ‰ km<sup>-1</sup> over Ruby Mts.) (Mulch, 2016). The greater decrease in isotopic lapse rate with  
 858 an increase in moisture transport distance from the Pacific Ocean was attributed to the  
 859 closed hydrological system with continental recycling of all moisture through evapotran-  
 860 spiration over the leeward side of the Sierra Nevada (Ingraham & Taylor, 1991). More-  
 861 over, the modern river-based ILR along the central-eastern Andean Cordillera shows a  
 862 progressive decrease towards the southern latitudes (i.e., -1.7 ‰ km<sup>-1</sup> for 22° to 24°S,  
 863 -0.9 ‰ km<sup>-1</sup> for 24° to 26°S and -0.2 ‰ km<sup>-1</sup> for 26° to 28°S) (Rohrman et al., 2014).  
 864 This variability was attributed to convective instabilities rather than orographic lifting-  
 865 induced precipitation gradients. The deep convection events drive more precipitation,  
 866 shifting the predominant control on  $\delta^{18}O_p$  values to precipitation amount instead of tem-  
 867 perature (Mulch, 2016).

868 Furthermore, the  $\delta^{18}O_p$ -elevation gradient has also been shown to be sensitive to  
 869 global climate forcings such as  $pCO_2$  (Poulsen et al., 2007; Poulsen & Jeffery, 2011), SSTs (Sturm  
 870 et al., 2007), sea level fluctuations (Poulsen et al., 2007) and palaeogeography (Botsyun  
 871 et al., 2022; Roe et al., 2016; Sewall & Fricke, 2013). iGCM simulations with elevated  
 872  $pCO_2$  indicate significant warming and moistening in the mid-troposphere, reducing the  
 873 vertical stratification, which causes a shallower isotopic lapse rate (Poulsen & Jeffery,  
 874 2011). The modelling study of Li et al. (2016) revealed notable differences in the precipitation-  
 875 weighted annual mean  $\delta^{18}O_p$  lapse rates across the Tibetan plateau, with an increase  
 876 of ~0.4 ‰ km<sup>-1</sup> during the Middle Holocene and a decrease of 0.2 ‰ km<sup>-1</sup> during the  
 877 Last Glacial Maximum compared to pre-industrial levels. These studies, together with  
 878 our new IRL estimates for the European Alps under different climate scenarios, high-  
 879 light the spatial and temporal variability of ILR of major mountain ranges. Our results  
 880 indicate significant IRL variability to influence the accuracy of paleoelevation estimates  
 881 of the Alps.

#### 882 **4.5 Implications of the non-stationarity of isotopic lapse rates on pa-** 883 **leoelevation estimates across the Alps**

884 To quantitatively assess the potential uncertainties in estimating the Alps' pale-  
 885 o-elevation using modern  $\delta^{18}O_p$  lapse rates, we recalculated the recent reconstruction of  
 886 Miocene Central Alps paleoelevation by (Krsnik et al., 2021) based on the  $\delta$ - $\delta$  approach (Mulch,  
 887 2016). We use the simulated Miocene  $\delta^{18}O_p$  lapse rates with the  $\Delta\delta^{18}O_w$  values of pe-  
 888 dogenic carbonate from the Northern Alpine Foreland Basin (Swiss Molasse Basin; SMB)  
 889 and high-Alpine phyllosilicate hydrogen isotope ( $\delta D$ ) values from the Simplon Fault Zone  
 890 (SFZ) (Krsnik et al., 2021). More specifically, Krsnik et al. (2021) refined paleoaltim-  
 891 etry estimates for the Alps by determining low-elevation  $\delta^{18}O_w$  values through the com-  
 892 bination of  $\delta^{18}O$  values of pedogenic carbonates with clumped isotope-based soil carbon-  
 893 ate formation temperatures ( $\Delta_{47}$ ) for the different sections of the SMB (Fig. 9b). The  
 894  $\delta^{18}O_c$  values combined with  $\Delta_{47}$  temperatures at which carbonates formed estimate  $\delta^{18}O_w$   
 895 values (first quartile mean) of -6.5 (~0.0) ‰ -5.8 (~0.2) ‰ and -3.1 (~0.3) ‰ for Fonta-  
 896 nen, Jona and Aabach (Krsnik et al. (2021); Table S1). Using these  $\delta^{18}O_w$  values of the  
 897 foreland basin sections with the high-Alpine SFZ  $\delta^{18}O_w$  value of -14.6 (~0.3) (Campani



et al., 2012) results in  $\Delta\delta^{18}O_w$  values of -8.1 ‰ -8.8 ‰ and -11.5 ‰ respectively. The simulated  $\Delta\delta^{18}O_p$  range (-4 to -8 ‰) between the low- and high-elevation regions agree with this reconstruction (Fig. 3). More specifically, this agreement suggests that more than 200% of the modern West-Central Alps topography is required to induce significant orographic rainout that would cause the depletion of the paleo-meteoric waters during the formation of the proxy materials.

We then calculate the mean paleoelevation around the SFZ with the modern precipitation-based isotopic lapse of the meteorological stations along the northern slopes of the Alps (-2.0 ‰ km<sup>-1</sup>; Campani et al. (2012)), surface-water-based isotopic lapse rate estimated from global observations (-2.8 ‰ km<sup>-1</sup>; Poage and Chamberlain (2001)), and this study's Miocene isotopic lapse rates for different topographic configurations (Fig. 6). Overall, the paleoelevation estimates using the simulated Miocene lapse rates over the Alps (including estimates over the northern, and western flanks of the Alps) are lower than the estimates using the modern lapse rate of -2.0 ‰ km<sup>-1</sup> (Fig. 9). This suggests an overestimation of Central Alps topography in the Middle Miocene by previous studies (Campani et al., 2012; Krsnik et al., 2021) that relied on the modern ILR of the northern slopes of the Alps. The paleoelevation estimates with the modern -2.0 ‰ km<sup>-1</sup> only agree with the estimates based on the western transect lapse rates for the unmodified topographic configuration (W1E1) experiments with Mio278 (-2.02 ‰ km<sup>-1</sup>) and Mio450 (-2.18 ‰ km<sup>-1</sup>) climates (Table 1). This might be due to their similar topography and predominant moisture path from the North Atlantic towards the Western Alp. The paleoelevation estimates based on the western transect lapse rates were greater than those based on the northern transect rates (Fig. 9 and Table S1). For instance, if we consider the Jona section, i.e. the most conservative near-sea level  $\delta^{18}O_w$  values estimate among the foreland basin sections (Krsnik et al., 2021), the western transect modelled isotopic ILRs (with  $\Delta\delta^{18}O_w$  of -8.8 ‰) produces elevations that are up to 1443 m higher than the elevations estimated from the northern transect modelled ILRs. Therefore, we propose that ignoring spatial variability of lapse rate through time can contribute significantly to the inaccuracy of reconstructing past surface elevations.

On the other hand, the median of Middle Miocene constrained ranges of paleoelevations of the Central Alps (based on our modelled Miocene ILRs) are more consistent with the modern global surface-water ILR (Poage & Chamberlain, 2001) (Fig. 9). Specifically, the modern global ILR of -2.8 ‰ km<sup>-1</sup> with the  $\Delta\delta^{18}O_w$  of -8.8 ‰ for the Jona section yields a paleoelevation of 3143 m. Using the more realistic topographic configuration of W2E1 in the Middle Miocene, the simulated IRLs compared to the global modern ILR indicate paleoelevations differences (i.e., simulation-observed) of -1033 m and -857 m for the northern transect and -11 m and +586 m for the western transect for the Mio278 and Mio450 climates, respectively. Compared to the modern -2.0 ‰ km<sup>-1</sup> ILR of the northern slope of the Alps, the paleoelevation estimates with the W2E1 differ by -2290 m and -2114 m (and -1268 m and -671 m) for the Mio278 and Mio450 climates calculated across the northern (and western) transects (Table S1). These estimates imply that using a global river-based lapse rate would be efficient in the absence of paleoclimate-constrained isotopic lapse rates. As meteorological stations for collecting precipitation for  $\delta^{18}O_w$  measurements are often sparsely distributed and mostly reflect the short-term processes of specific precipitation events conditions, the  $\delta^{18}O_p$ -gradient along river systems are more reliable, predictable and robust (Mulch, 2016; Poage & Chamberlain, 2001; Rowley et al., 2001; Rowley, 2007). In this case, the global river-based ILR is consistent with most of the range of modelled ILR-based paleoelevations estimates because it integrates long-term climatic processes by averaging the precipitation seasonality over the varied hydrological catchments globally. Moreover, it also integrates the spatial variability of the interactions between climatic and topographic changes on the timescales relevant for the isotopic proxy formation (Mulch, 2016). The key point demonstrated here with our paleoelevation refinements is that the Middle Miocene climate change associated with Alps topography changes is significant, and not accounting for its influence

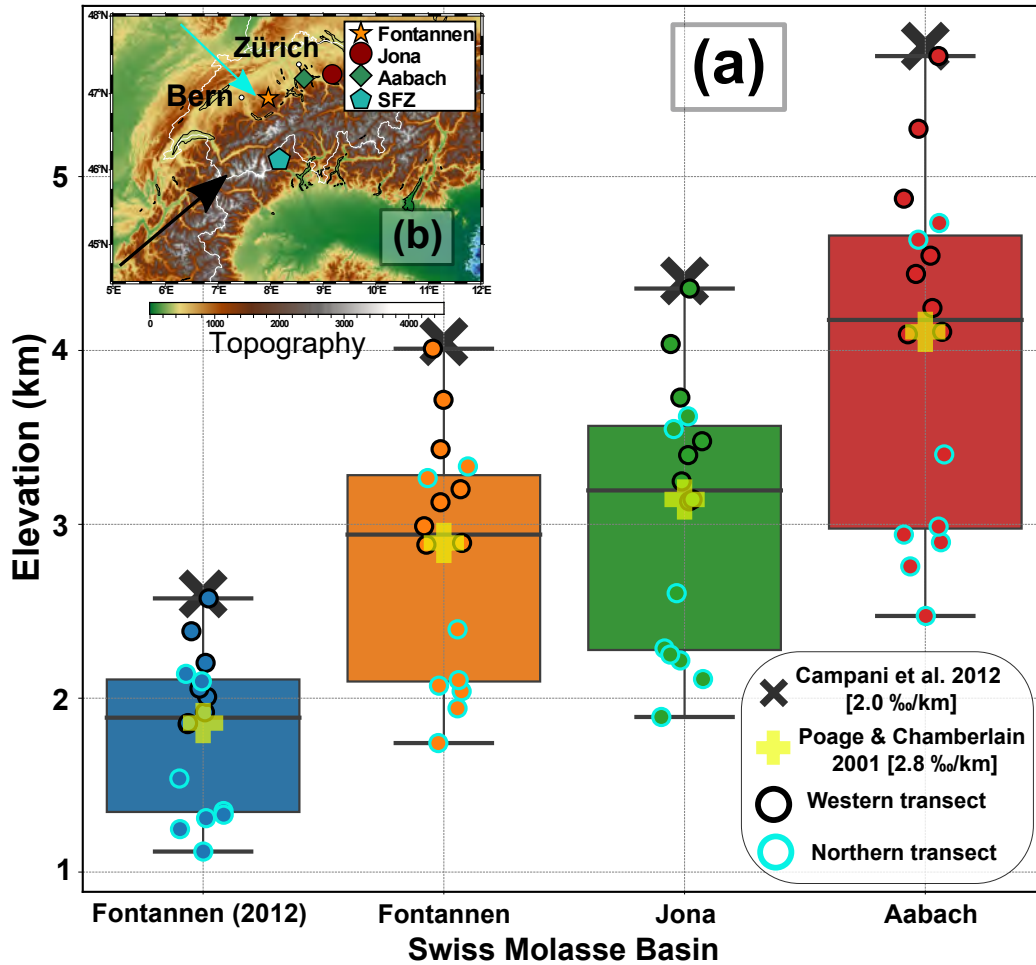


**Figure 9.** Paleoelevation estimates of Miocene Central Alps with isotopic lapse rates from Middle Miocene  $p\text{CO}_2$  scenarios (278 ppm (Mio278); 450 ppm (Mio450)) and topographic sensitivity experiments and modern observed precipitation across the Alps ( $-2.0 \text{ ‰ km}^{-1}$ ; (Campani et al., 2012)) and global surface waters ( $-2.8 \text{ ‰ km}^{-1}$ ; (Poage & Chamberlain, 2001)). The calculated ranges of paleoelevations for the different topographic configurations with the lapse rate considered along the northern and western transects of the Alps are shown as distribution (boxplot) for the different foreland basin locations shown in (b). The  $\Delta\delta^{18}\text{O}_w$  values between the paleo-meteoric water reconstructed from the low-elevation foreland basins (i.e., Fontannen (both from Campani et al. (2012) and Krsnik et al. (2021), Jona, and Aabach) and high-elevation (Simplon Fault Zone; Campani et al. (2012)) are based on the recent reconstruction from Krsnik et al. (2021)

temporally would lead to overestimation of the Alps topography by up to 2 km (local ILR) or less than 1 km (global river ILR). Moreover, assuming a constant spatial isotopic lapse rate across the Alps would also lead to paleoelevation inaccuracy of  $\sim 1.5$  km for the Middle Miocene paleoelevation of the Alps.

## 5 Conclusions

This study demonstrates a robust framework for reconstructing paleoelevations by integrating simulated  $\delta^{18}O$  in precipitation ( $\delta^{18}O_p$ ) in response to Middle Miocene paleoenvironmental conditions with reconstructed  $\delta^{18}O$  of paleo-meteoric water from coeval proxy materials across the Alps. The results indicate that the warmer and wetter conditions across the Alps in the Miocene, together with the diachronous surface uplift across the Alps, affect the  $\delta^{18}O_p$  distribution, which can compromise the  $\delta$ - $\delta$  stable water isotope paleoaltimetry estimates by up to 1.5 km when the paleoclimate changes associated with the topographic evolution are not accounted for. Therefore, the simulated patterns of  $\delta^{18}O$  of paleo-meteoric waters in this study lead us to accept the hypothesis that the changes in the Miocene climate and diachronous surface uplift of the Alps result in isotopic lapse rates that significantly deviate from modern estimates ( $-2.0$  ‰  $\text{km}^{-1}$ ; Campani et al. (2012)) and vary spatially around the Alps. Our approach emphasises the isotopic lapse rate variability in past climates and highlights the advantage of using isotope-enabled GCM to understand paleoclimate dynamics and regional climate patterns, to disentangle the climate and tectonic signals in paleoaltimetry proxy materials, and to derive more accurate paleoelevation estimates. We summarise the key findings as follows:

1. The Middle Miocene simulations suggest warmer and wetter conditions globally, with a mean annual surface temperature increase of  $2.5$  °C and  $6$  °C and a mean annual precipitation increase of  $1.6\%$  and  $9\%$  in response to  $p\text{CO}_2$  of 278 and 450 ppm compared to PI climate. The simulations indicate  $p\text{CO}_2$  as the main driver for the global climate and non- $p\text{CO}_2$  factors for the regional hydroclimate changes. These climate patterns result in more enriched global annual mean  $\delta^{18}O_p$  values of up to  $1.3$  ‰ compared to PI estimates.
2. The European hydroclimate patterns indicate a pronounced meridional gradient with drier conditions over Central Europe towards the Mediterranean region and wetter conditions over northern Europe than the PI climate. The continental warming across Europe (up to  $8$  °C), together with the precipitation gradients, results in more varied  $\delta^{18}O_p$  patterns that show a west-to-east gradient, contributing to the spatial variability of isotopic lapse rate around the Alps.
3. The simulations estimate  $\Delta\delta^{18}O_p$  values (i.e., the difference of  $\delta^{18}O_p$  values between low- and high-elevation regions) range from  $-4$  to  $-8$  ‰ (but are higher in  $p\text{CO}_2$  of 278 ppm) in Miocene and show distinct isotopic profiles across the Alps for the diachronous surface uplift scenarios. These imply that the isotopic imprints in proxy material would be significant enough to decipher the variations in the west-to-east surface uplift propagation across the Alps.
4. The simulated isotopic lapse rates become shallow by  $\sim 1.0$  ‰  $\text{km}^{-1}$  in the Middle Miocene and deviate by up to  $1.5$  ‰  $\text{km}^{-1}$  for diachronous surface uplift scenarios of the Alps. The varied precipitation redistribution in the Miocene resulted in spatial differences in isotopic lapse rates of up to  $0.4$  ‰  $\text{km}^{-1}$ .
5. The refinement of previous paleoelevation estimates (Krsnik et al., 2021) from  $\Delta\delta^{18}O_w$  reconstructed between the near-sea level pedogenic carbonate from the Northern Alpine Foreland Basin (Swiss Molasse Basin; SMB) and high-Alpine phyllosilicate hydrogen isotope ( $\delta D$ ) from the Simplon Fault Zone (SFZ) with the simulated isotopic lapse rates indicates an overestimation of the Central Alps' paleoelevation by  $\sim 1.5$  km when the isotopic lapse rate is assumed stationary through time and

1003 space from present-day (local ILR). However, in the absence of paleoclimate-constraint,  
 1004 modelled ILR, the usage of the global river-based ILR is sufficient and favourable.

## 1005 6 Open Research

1006 The ECHAM5 model is available under the MPI-M Software License Agreement  
 1007 ([https://code.mpimet.mpg.de/attachments/download/26986/MPI-ESM\\_SLA\\_v3.4.pdf](https://code.mpimet.mpg.de/attachments/download/26986/MPI-ESM_SLA_v3.4.pdf),  
 1008 last access: 5 November 2023), and the isotope-tracking implementation part (ECHAM5-  
 1009 wiso) is available upon request from the Alfred Wegner Institute (AWI), Germany (<https://gitlab.awi.de/mwerner>  
 1010 esm-wiso, last access: 5 November 2023). The postprocessing, data analysis, and visu-  
 1011 alization scripts are based on a Python package (pyClimat) available at <https://doi.org/10.5281/zenodo.7143044>.

## 1012 Acknowledgments

1013 This research was supported by the German Science Foundation (DFG) priority research  
 1014 program Mountain Building Processes in Four Dimensions (4D-MB; SPP 2017) through  
 1015 grants EH 329/19-1 and EH329/23-1 (to Todd A. Ehlers), MU4188/1-1 and MU4188/3-  
 1016 1 (to Sebastian G. Mutz), MU2845/6-1 and MU2845/7-1 (to Andreas Mulch), Me4955/1-  
 1017 1 (to Katharina Methner), and ME5579/1-1 (to Maud J. M. Meijers).

## 1018 References

- 1019 Abdul Aziz, H., Sanz-Rubio, E., Calvo, J. P., Hilgen, F. J., & Krijgsman, W.  
 1020 (2003). Palaeoenvironmental reconstruction of a middle Miocene alluvial  
 1021 fan to cyclic shallow lacustrine depositional system in the Calatayud Basin  
 1022 (NE Spain). *Sedimentology*, *50*(2), 211–236. Retrieved 2024-01-31, from  
 1023 [https://onlinelibrary.wiley.com/doi/abs/10.1046/j.1365-3091.2003](https://onlinelibrary.wiley.com/doi/abs/10.1046/j.1365-3091.2003.00544.x)  
 1024 [.00544.x](https://onlinelibrary.wiley.com/doi/pdf/10.1046/j.1365-3091.2003.00544.x) (.eprint: [https://onlinelibrary.wiley.com/doi/pdf/10.1046/j.1365-](https://onlinelibrary.wiley.com/doi/pdf/10.1046/j.1365-3091.2003.00544.x)  
 1025 [3091.2003.00544.x](https://onlinelibrary.wiley.com/doi/pdf/10.1046/j.1365-3091.2003.00544.x)) doi: 10.1046/j.1365-3091.2003.00544.x
- 1026 Acosta, R. P., Burls, N. J., Pound, M. J., Bradshaw, C. D., De Boer, A. M.,  
 1027 Herold, N., ... Zhang, Z. (2024). A Model-Data Comparison of the Hy-  
 1028 drological Response to Miocene Warmth: Leveraging the MioMIP1 Op-  
 1029 portunistic Multi-Model Ensemble. *Paleoceanography and Paleoclima-*  
 1030 *tology*, *39*(1), e2023PA004726. Retrieved 2024-01-08, from [https://](https://onlinelibrary.wiley.com/doi/abs/10.1029/2023PA004726)  
 1031 [onlinelibrary.wiley.com/doi/abs/10.1029/2023PA004726](https://onlinelibrary.wiley.com/doi/abs/10.1029/2023PA004726) (.eprint:  
 1032 <https://onlinelibrary.wiley.com/doi/pdf/10.1029/2023PA004726>) doi:  
 1033 10.1029/2023PA004726
- 1034 Bariac, T., Gonzalez-Dunia, J., Katerji, N., Béthenod, O., Bertolini, J. M., & Mar-  
 1035 iotti, A. (1994, August). Variabilité spatio-temporelle de la composition  
 1036 isotopique de l'eau (18O, 2H) dans le continuum sol-plante-atmosphère 2. Ap-  
 1037 proche en conditions naturelles. *Chemical Geology*, *115*(3), 317–333. Retrieved  
 1038 2023-10-23, from [https://www.sciencedirect.com/science/article/pii/](https://www.sciencedirect.com/science/article/pii/S009254194901953)  
 1039 [009254194901953](https://www.sciencedirect.com/science/article/pii/S009254194901953) doi: 10.1016/0009-2541(94)90195-3
- 1040 Barnston, A. G., & Livezey, R. E. (1987, June). Classification, Seasonal-  
 1041 ity and Persistence of Low-Frequency Atmospheric Circulation Patterns.  
 1042 *Monthly Weather Review*, *115*(6), 1083–1126. Retrieved 2022-04-22,  
 1043 from [https://journals.ametsoc.org/view/journals/mwre/115/6/](https://journals.ametsoc.org/view/journals/mwre/115/6/1520-0493-1987.115.1083_csap01.2.0_co.2.xml)  
 1044 [1520-0493-1987.115.1083\\_csap01.2.0\\_co.2.xml](https://journals.ametsoc.org/view/journals/mwre/115/6/1520-0493-1987.115.1083_csap01.2.0_co.2.xml) (Publisher: Amer-  
 1045 ican Meteorological Society Section: Monthly Weather Review) doi:  
 1046 10.1175/1520-0493(1987)115<1083:CSAPOL>2.0.CO;2
- 1047 Bauer, K. K., Vennemann, T. W., & Gilg, H. A. (2016, August). Stable iso-  
 1048 tope composition of bentonites from the Swiss and Bavarian Freshwater  
 1049 Molasse as a proxy for paleoprecipitation. *Paleogeography, Palaeoclima-*  
 1050 *tology, Palaeoecology*, *455*, 53–64. Retrieved 2023-11-30, from [https://](https://www.sciencedirect.com/science/article/pii/S0031018216000675)  
 1051 [www.sciencedirect.com/science/article/pii/S0031018216000675](https://www.sciencedirect.com/science/article/pii/S0031018216000675) doi:

- 1052 10.1016/j.palaeo.2016.02.002
- 1053 Beaumont, C., Ellis, S., Hamilton, J., & Fullsack, P. (1996, August). Me-  
 1054 chanical model for subduction-collision tectonics of Alpine-type compres-  
 1055 sional orogens. *Geology*, *24*(8), 675–678. Retrieved 2024-03-04, from  
 1056 [https://doi.org/10.1130/0091-7613\(1996\)024<0675:MMFSCT>2.3.CO;2](https://doi.org/10.1130/0091-7613(1996)024<0675:MMFSCT>2.3.CO;2)  
 1057 doi: 10.1130/0091-7613(1996)024(0675:MMFSCT)2.3.CO;2
- 1058 Boateng, D., Aryee, J. N. A., Baidu, M., Arthur, F., & Mutz, S. G. (2024, January).  
 1059 *West African Monsoon dynamics and its control on stable oxygen isotopic*  
 1060 *composition of precipitation in the Late Cenozoic* (preprint). Preprints. Re-  
 1061 trieved 2024-01-19, from [https://essopenarchive.org/users/714333/](https://essopenarchive.org/users/714333/articles/698607-west-african-monsoon-dynamics-and-its-control-on-stable-oxygen-isotopic-composition-of-precipitation-in-the-late-cenozoic?commit=ebaf0fd1f6e632e01f468aff511af3b70ec344d3)  
 1062 [articles/698607-west-african-monsoon-dynamics-and-its-control-on-](https://essopenarchive.org/users/714333/articles/698607-west-african-monsoon-dynamics-and-its-control-on-stable-oxygen-isotopic-composition-of-precipitation-in-the-late-cenozoic?commit=ebaf0fd1f6e632e01f468aff511af3b70ec344d3)  
 1063 [-stable-oxygen-isotopic-composition-of-precipitation-in-the-late](https://essopenarchive.org/users/714333/articles/698607-west-african-monsoon-dynamics-and-its-control-on-stable-oxygen-isotopic-composition-of-precipitation-in-the-late-cenozoic?commit=ebaf0fd1f6e632e01f468aff511af3b70ec344d3)  
 1064 [-cenozoic?commit=ebaf0fd1f6e632e01f468aff511af3b70ec344d3](https://essopenarchive.org/users/714333/articles/698607-west-african-monsoon-dynamics-and-its-control-on-stable-oxygen-isotopic-composition-of-precipitation-in-the-late-cenozoic?commit=ebaf0fd1f6e632e01f468aff511af3b70ec344d3) doi:  
 1065 10.22541/essoar.170560461.19493225/v1
- 1066 Boateng, D., Mutz, S. G., Ballian, A., Meijers, M. J. M., Methner, K., Botsyun, S.,  
 1067 ... Ehlers, T. A. (2023, November). The effects of diachronous surface uplift  
 1068 of the European Alps on regional climate and the oxygen isotopic composi-  
 1069 tion of precipitation. *Earth System Dynamics*, *14*(6), 1183–1210. Retrieved  
 1070 2024-01-03, from <https://esd.copernicus.org/articles/14/1183/2023/>  
 1071 (Publisher: Copernicus GmbH) doi: 10.5194/esd-14-1183-2023
- 1072 Botsyun, S., Ehlers, T. A., Koptev, A., Böhme, M., Methner, K., Risi, C., ...  
 1073 Mulch, A. (2022). Middle Miocene Climate and Stable Oxygen Iso-  
 1074 topes in Europe Based on Numerical Modeling. *Paleoceanography and*  
 1075 *Paleoclimatology*, *37*(10), e2022PA004442. Retrieved 2023-02-10, from  
 1076 <https://onlinelibrary.wiley.com/doi/abs/10.1029/2022PA004442>  
 1077 (\_eprint: <https://onlinelibrary.wiley.com/doi/pdf/10.1029/2022PA004442>)  
 1078 doi: 10.1029/2022PA004442
- 1079 Botsyun, S., Ehlers, T. A., Mutz, S. G., Methner, K., Krsnik, E., & Mulch,  
 1080 A. (2020). Opportunities and Challenges for Paleoaltimetry in “Small”  
 1081 Orogens: Insights From the European Alps. *Geophysical Research Let-*  
 1082 *ters*, *47*(4), e2019GL086046. Retrieved 2022-04-22, from [https://](https://onlinelibrary.wiley.com/doi/abs/10.1029/2019GL086046)  
 1083 [onlinelibrary.wiley.com/doi/abs/10.1029/2019GL086046](https://onlinelibrary.wiley.com/doi/abs/10.1029/2019GL086046) (\_eprint:  
 1084 <https://onlinelibrary.wiley.com/doi/pdf/10.1029/2019GL086046>) doi:  
 1085 10.1029/2019GL086046
- 1086 Botsyun, S., Sepulchre, P., Donnadieu, Y., Risi, C., Licht, A., & Caves Rugenstein,  
 1087 J. K. (2019, March). Revised paleoaltimetry data show low Tibetan Plateau  
 1088 elevation during the Eocene. *Science*, *363*(6430), eaaq1436. Retrieved 2022-  
 1089 08-15, from <https://www.science.org/doi/10.1126/science.aaq1436>  
 1090 (Publisher: American Association for the Advancement of Science) doi:  
 1091 10.1126/science.aaq1436
- 1092 Brierley, C. M., & Fedorov, A. V. (2016, June). Comparing the impacts of  
 1093 Miocene–Pliocene changes in inter-ocean gateways on climate: Central  
 1094 American Seaway, Bering Strait, and Indonesia. *Earth and Planetary*  
 1095 *Science Letters*, *444*, 116–130. Retrieved 2024-01-29, from [https://](https://www.sciencedirect.com/science/article/pii/S0012821X16300978)  
 1096 [www.sciencedirect.com/science/article/pii/S0012821X16300978](https://www.sciencedirect.com/science/article/pii/S0012821X16300978) doi:  
 1097 10.1016/j.epsl.2016.03.010
- 1098 Bruch, A. A., Uhl, D., & Mosbrugger, V. (2007, September). Miocene climate in  
 1099 Europe — Patterns and evolution: A first synthesis of NECLIME. *Palaeo-*  
 1100 *geography, Palaeoclimatology, Palaeoecology*, *253*(1), 1–7. Retrieved 2022-  
 1101 04-28, from [https://www.sciencedirect.com/science/article/pii/](https://www.sciencedirect.com/science/article/pii/S0031018207001915)  
 1102 [S0031018207001915](https://www.sciencedirect.com/science/article/pii/S0031018207001915) doi: 10.1016/j.palaeo.2007.03.030
- 1103 Burgener, L., Huntington, K. W., Hoke, G. D., Schauer, A., Ringham, M. C., La-  
 1104 torre, C., & Diaz, F. P. (2016, May). Variations in soil carbonate formation  
 1105 and seasonal bias over >4 km of relief in the western Andes (30°S) revealed by  
 1106 clumped isotope thermometry. *Earth and Planetary Science Letters*, *441*, 188–

- 1107 199. Retrieved 2024-02-12, from [https://www.sciencedirect.com/science/](https://www.sciencedirect.com/science/article/pii/S0012821X16300504)  
 1108 [article/pii/S0012821X16300504](https://www.sciencedirect.com/science/article/pii/S0012821X16300504) doi: 10.1016/j.epsl.2016.02.033
- 1109 Burls, N. J., Bradshaw, C. D., De Boer, A. M., Herold, N., Huber, M., Pound,  
 1110 M., ... Zhang, Z. (2021). Simulating Miocene Warmth: Insights From  
 1111 an Opportunistic Multi-Model Ensemble (MioMIP1). *Paleoceanography*  
 1112 *and Paleoclimatology*, 36(5), e2020PA004054. Retrieved 2022-04-28, from  
 1113 <https://onlinelibrary.wiley.com/doi/abs/10.1029/2020PA004054>  
 1114 (\_eprint: <https://onlinelibrary.wiley.com/doi/pdf/10.1029/2020PA004054>)  
 1115 doi: 10.1029/2020PA004054
- 1116 Böhme, M., Ilg, A., Ossig, A., & Küchenhoff, H. (2006, June). New method to es-  
 1117 timate paleoprecipitation using fossil amphibians and reptiles and the middle  
 1118 and late Miocene precipitation gradients in Europe. *Geology*, 34(6), 425–  
 1119 428. Retrieved 2024-01-31, from <https://doi.org/10.1130/G22460.1> doi:  
 1120 10.1130/G22460.1
- 1121 Böhme, M., Winklhofer, M., & Ilg, A. (2011, May). Miocene precipitation in  
 1122 Europe: Temporal trends and spatial gradients. *Palaeogeography, Palaeoclima-*  
 1123 *tology, Palaeoecology*, 304(3), 212–218. Retrieved 2023-03-18, from [https://](https://www.sciencedirect.com/science/article/pii/S0031018210005997)  
 1124 [www.sciencedirect.com/science/article/pii/S0031018210005997](https://www.sciencedirect.com/science/article/pii/S0031018210005997) doi:  
 1125 10.1016/j.palaeo.2010.09.028
- 1126 Campani, M., Mulch, A., Kempf, O., Schlunegger, F., & Mancktelow, N. (2012,  
 1127 July). Miocene paleotopography of the Central Alps. *Earth and Planetary*  
 1128 *Science Letters*, 337–338, 174–185. Retrieved 2022-04-22, from [https://](https://www.sciencedirect.com/science/article/pii/S0012821X12002439)  
 1129 [www.sciencedirect.com/science/article/pii/S0012821X12002439](https://www.sciencedirect.com/science/article/pii/S0012821X12002439) doi:  
 1130 10.1016/j.epsl.2012.05.017
- 1131 Cauquoin, A., Werner, M., & Lohmann, G. (2019, November). Water iso-  
 1132 topes – climate relationships for the mid-Holocene and preindustrial pe-  
 1133 riod simulated with an isotope-enabled version of MPI-ESM. *Climate*  
 1134 *of the Past*, 15(6), 1913–1937. Retrieved 2022-10-17, from [https://](https://cp.copernicus.org/articles/15/1913/2019/)  
 1135 [cp.copernicus.org/articles/15/1913/2019/](https://cp.copernicus.org/articles/15/1913/2019/) (Publisher: Copernicus  
 1136 GmbH) doi: 10.5194/cp-15-1913-2019
- 1137 Cloetingh, S., Sternai, P., Koptev, A., Ehlers, T. A., Gerya, T., Kovács, I., ... Lim-  
 1138 berger, J. (2023, July). Coupled surface to deep Earth processes: Perspectives  
 1139 from TOPO-EUROPE with an emphasis on climate- and energy-related so-  
 1140 cietal challenges. *Global and Planetary Change*, 226, 104140. Retrieved  
 1141 2023-10-01, from [https://www.sciencedirect.com/science/article/pii/](https://www.sciencedirect.com/science/article/pii/S0921818123001133)  
 1142 [S0921818123001133](https://www.sciencedirect.com/science/article/pii/S0921818123001133) doi: 10.1016/j.gloplacha.2023.104140
- 1143 Cojan, I., Bialkowski, A., Gillot, T., & Renard, M. (2013, November). Paleoenviron-  
 1144 nement and paleoclimate reconstruction for the early to middle Miocene from  
 1145 stable isotopes in pedogenic carbonates (Digne-Valensole basin, southeastern  
 1146 France). *Bulletin de la Société Géologique de France*, 184(6), 583–599. Re-  
 1147 trieved 2023-11-30, from <https://doi.org/10.2113/gssgfbull.184.6.583>  
 1148 doi: 10.2113/gssgfbull.184.6.583
- 1149 Costeur, L., & Legendre, S. (2008, May). Mammalian Communities Docu-  
 1150 ment a Latitudinal Environmental Gradient during the Miocene Climatic  
 1151 Optimum in Western Europe. *PALAIOS*, 23(5), 280–288. Retrieved  
 1152 2024-01-31, from <https://doi.org/10.2110/palo.2006.p06-092r> doi:  
 1153 10.2110/palo.2006.p06-092r
- 1154 Cramwinckel, M. J., Burls, N. J., Fahad, A. A., Knapp, S., West, C. K., Re-  
 1155 ichgelt, T., ... Inglis, G. N. (2023). Global and Zonal-Mean Hydrolog-  
 1156 ical Response to Early Eocene Warmth. *Paleoceanography and Paleocli-*  
 1157 *matology*, 38(6), e2022PA004542. Retrieved 2024-01-29, from [https://](https://onlinelibrary.wiley.com/doi/abs/10.1029/2022PA004542)  
 1158 [onlinelibrary.wiley.com/doi/abs/10.1029/2022PA004542](https://onlinelibrary.wiley.com/doi/abs/10.1029/2022PA004542) (\_eprint:  
 1159 <https://onlinelibrary.wiley.com/doi/pdf/10.1029/2022PA004542>) doi:  
 1160 10.1029/2022PA004542
- 1161 Ehlers, T. A., & Poulsen, C. J. (2009, May). Influence of Andean uplift on climate

- 1162 and paleoaltimetry estimates. *Earth and Planetary Science Letters*, 281(3),  
 1163 238–248. Retrieved 2022-04-22, from [https://www.sciencedirect.com/](https://www.sciencedirect.com/science/article/pii/S0012821X09001149)  
 1164 [science/article/pii/S0012821X09001149](https://www.sciencedirect.com/science/article/pii/S0012821X09001149) doi: 10.1016/j.epsl.2009.02.026
- 1165 Farnsworth, A., Lunt, D. J., Robinson, S. A., Valdes, P. J., Roberts, W. H. G.,  
 1166 Cliff, P. D., ... Pancost, R. D. (2019, October). Past East Asian mon-  
 1167 soon evolution controlled by paleogeography, not CO<sub>2</sub>. *Science Advances*,  
 1168 5(10), eaax1697. Retrieved 2023-11-30, from [https://www.science.org/](https://www.science.org/doi/10.1126/sciadv.aax1697)  
 1169 [doi/10.1126/sciadv.aax1697](https://www.science.org/doi/10.1126/sciadv.aax1697) (Publisher: American Association for the  
 1170 Advancement of Science) doi: 10.1126/sciadv.aax1697
- 1171 Feng, R., Otto-Bliesner, B. L., Xu, Y., Brady, E., Fletcher, T., & Ballan-  
 1172 tyne, A. (2019). Contributions of aerosol-cloud interactions to mid-  
 1173 Piacenzian seasonally sea ice-free Arctic Ocean. *Geophysical Research*  
 1174 *Letters*, 46(16), 9920–9929. Retrieved 2024-01-27, from [https://](https://onlinelibrary.wiley.com/doi/abs/10.1029/2019GL083960)  
 1175 [onlinelibrary.wiley.com/doi/abs/10.1029/2019GL083960](https://onlinelibrary.wiley.com/doi/abs/10.1029/2019GL083960) (eprint:  
 1176 <https://onlinelibrary.wiley.com/doi/pdf/10.1029/2019GL083960>) doi:  
 1177 10.1029/2019GL083960
- 1178 Feng, R., Poulsen, C. J., Werner, M., Chamberlain, C. P., Mix, H. T., & Mulch,  
 1179 A. (2013, September). Early Cenozoic evolution of topography, climate, and  
 1180 stable isotopes in precipitation in the North American Cordillera. *Ameri-  
 1181 can Journal of Science*, 313(7), 613–648. Retrieved 2022-04-22, from  
 1182 <https://www.ajsonline.org/content/313/7/613> (Publisher: American  
 1183 Journal of Science Section: Articles) doi: 10.2475/07.2013.01
- 1184 Fereday, D., Chadwick, R., Knight, J., & Scaife, A. A. (2018, February). At-  
 1185 mospheric Dynamics is the Largest Source of Uncertainty in Future Winter  
 1186 European Rainfall. *Journal of Climate*, 31(3), 963–977. Retrieved 2024-  
 1187 01-31, from [https://journals.ametsoc.org/view/journals/clim/31/3/](https://journals.ametsoc.org/view/journals/clim/31/3/jcli-d-17-0048.1.xml)  
 1188 [jcli-d-17-0048.1.xml](https://journals.ametsoc.org/view/journals/clim/31/3/jcli-d-17-0048.1.xml) (Publisher: American Meteorological Society Section:  
 1189 Journal of Climate) doi: 10.1175/JCLI-D-17-0048.1
- 1190 Foster, G. L., & Rohling, E. J. (2013, January). Relationship between sea level and  
 1191 climate forcing by CO<sub>2</sub> on geological timescales. *Proceedings of the National*  
 1192 *Academy of Sciences*, 110(4), 1209–1214. Retrieved 2023-10-28, from [https://](https://www.pnas.org/doi/full/10.1073/pnas.1216073110)  
 1193 [www.pnas.org/doi/full/10.1073/pnas.1216073110](https://www.pnas.org/doi/full/10.1073/pnas.1216073110) (Publisher: Proceedings  
 1194 of the National Academy of Sciences) doi: 10.1073/pnas.1216073110
- 1195 Frigola, A., Prange, M., & Schulz, M. (2018, April). Boundary conditions  
 1196 for the Middle Miocene Climate Transition (MMCT v1.0). *Geoscientific*  
 1197 *Model Development*, 11(4), 1607–1626. Retrieved 2022-04-28, from  
 1198 <https://gmd.copernicus.org/articles/11/1607/2018/> (Publisher: Coper-  
 1199 nicus GmbH) doi: 10.5194/gmd-11-1607-2018
- 1200 Galewsky, J. (2009, September). Orographic precipitation isotopic ratios in strati-  
 1201 fied atmospheric flows: Implications for paleoelevation studies. *Geology*, 37(9),  
 1202 791–794. Retrieved 2024-02-17, from <https://doi.org/10.1130/G30008A.1>  
 1203 doi: 10.1130/G30008A.1
- 1204 Gao, X., Xu, Y., Zhao, Z., Pal, J. S., & Giorgi, F. (2006, September). On the  
 1205 role of resolution and topography in the simulation of East Asia precipi-  
 1206 tation. *Theoretical and Applied Climatology*, 86(1), 173–185. Retrieved  
 1207 2023-08-24, from <https://doi.org/10.1007/s00704-005-0214-4> doi:  
 1208 10.1007/s00704-005-0214-4
- 1209 Garzzone, C. N., Quade, J., DeCelles, P. G., & English, N. B. (2000, November).  
 1210 Predicting paleoelevation of Tibet and the Himalaya from 18O vs. altitude  
 1211 gradients in meteoric water across the Nepal Himalaya. *Earth and Plane-  
 1212 tary Science Letters*, 183(1), 215–229. Retrieved 2022-04-22, from [https://](https://www.sciencedirect.com/science/article/pii/S0012821X00002521)  
 1213 [www.sciencedirect.com/science/article/pii/S0012821X00002521](https://www.sciencedirect.com/science/article/pii/S0012821X00002521) doi:  
 1214 10.1016/S0012-821X(00)00252-1
- 1215 Gat, J. R. (1996). Oxygen and Hydrogen Isotopes in the Hydrologic Cycle. *An-  
 1216 nual Review of Earth and Planetary Sciences*, 24(1), 225–262. Retrieved 2022-

- 1217 04-22, from <https://doi.org/10.1146/annurev.earth.24.1.225> (\_eprint:  
1218 <https://doi.org/10.1146/annurev.earth.24.1.225>) doi: 10.1146/annurev.earth.24  
1219 .1.225
- 1220 Giorgi, F., & Lionello, P. (2008, September). Climate change projections for the  
1221 Mediterranean region. *Global and Planetary Change*, *63*(2), 90–104. Retrieved  
1222 2024-01-31, from [https://www.sciencedirect.com/science/article/pii/  
1223 S0921818107001750](https://www.sciencedirect.com/science/article/pii/S0921818107001750) doi: 10.1016/j.gloplacha.2007.09.005
- 1224 Goldner, A., Herold, N., & Huber, M. (2014, March). The challenge of simulat-  
1225 ing the warmth of the mid-Miocene climatic optimum in CESM1. *Climate of  
1226 the Past*, *10*(2), 523–536. Retrieved 2024-01-23, from [https://cp.copernicus  
1227 .org/articles/10/523/2014/](https://cp.copernicus.org/articles/10/523/2014/) (Publisher: Copernicus GmbH) doi: 10.5194/  
1228 cp-10-523-2014
- 1229 Green, J. a. M., & Huber, M. (2013). Tidal dissipation in the early  
1230 Eocene and implications for ocean mixing. *Geophysical Research  
1231 Letters*, *40*(11), 2707–2713. Retrieved 2024-01-27, from [https://  
1232 onlinelibrary.wiley.com/doi/abs/10.1002/grl.50510](https://onlinelibrary.wiley.com/doi/abs/10.1002/grl.50510) (\_eprint:  
1233 <https://onlinelibrary.wiley.com/doi/pdf/10.1002/grl.50510>) doi: 10.1002/  
1234 grl.50510
- 1235 Gébelin, A., Mulch, A., Teyssier, C., Jessup, M. J., Law, R. D., & Brunel, M. (2013,  
1236 July). The Miocene elevation of Mount Everest. *Geology*, *41*(7), 799–802. Re-  
1237 trieved 2022-09-16, from <https://doi.org/10.1130/G34331.1> doi: 10.1130/  
1238 G34331.1
- 1239 Hamon, N., Sepulchre, P., Lefebvre, V., & Ramstein, G. (2013, November). The role  
1240 of eastern Tethys seaway closure in the Middle Miocene Climatic Transition  
1241 (ca. 14 Ma). *Climate of the Past*, *9*(6), 2687–2702. Retrieved 2023-03-18,  
1242 from <https://cp.copernicus.org/articles/9/2687/2013/> (Publisher:  
1243 Copernicus GmbH) doi: 10.5194/cp-9-2687-2013
- 1244 Han, Z., Zhang, Q., Li, Q., Feng, R., Haywood, A. M., Tindall, J. C., ... Burls,  
1245 N. J. (2021, December). Evaluating the large-scale hydrological cycle response  
1246 within the Pliocene Model Intercomparison Project Phase 2 (PlioMIP2) en-  
1247 semble. *Climate of the Past*, *17*(6), 2537–2558. Retrieved 2024-01-29, from  
1248 <https://cp.copernicus.org/articles/17/2537/2021/> (Publisher: Coper-  
1249 nicus GmbH) doi: 10.5194/cp-17-2537-2021
- 1250 Handy, M. R., M. Schmid, S., Bousquet, R., Kissling, E., & Bernoulli, D. (2010,  
1251 October). Reconciling plate-tectonic reconstructions of Alpine Tethys with  
1252 the geological–geophysical record of spreading and subduction in the Alps.  
1253 *Earth-Science Reviews*, *102*(3), 121–158. Retrieved 2023-06-15, from [https://  
1254 www.sciencedirect.com/science/article/pii/S0012825210000668](https://www.sciencedirect.com/science/article/pii/S0012825210000668) doi:  
1255 10.1016/j.earscirev.2010.06.002
- 1256 Handy, M. R., Ustaszewski, K., & Kissling, E. (2015, January). Reconstructing the  
1257 Alps–Carpathians–Dinarides as a key to understanding switches in subduction  
1258 polarity, slab gaps and surface motion. *International Journal of Earth Sci-  
1259 ences*, *104*(1), 1–26. Retrieved 2022-04-22, from [https://doi.org/10.1007/  
1260 s00531-014-1060-3](https://doi.org/10.1007/s00531-014-1060-3) doi: 10.1007/s00531-014-1060-3
- 1261 Haywood, A. M., Tindall, J. C., Dowsett, H. J., Dolan, A. M., Foley, K. M., Hunter,  
1262 S. J., ... Lunt, D. J. (2020, November). The Pliocene Model Intercom-  
1263 parison Project Phase 2: large-scale climate features and climate sensitiv-  
1264 ity. *Climate of the Past*, *16*(6), 2095–2123. Retrieved 2023-08-18, from  
1265 <https://cp.copernicus.org/articles/16/2095/2020/> (Publisher: Coper-  
1266 nicus GmbH) doi: 10.5194/cp-16-2095-2020
- 1267 Herbert, T. D., Dalton, C. A., Liu, Z., Salazar, A., Si, W., & Wilson, D. S. (2022,  
1268 July). Tectonic degassing drove global temperature trends since 20 Ma. *Sci-  
1269 ence*, *377*(6601), 116–119. Retrieved 2023-10-01, from [https://www.science  
1270 .org/doi/full/10.1126/science.abl4353](https://www.science.org/doi/full/10.1126/science.abl4353) (Publisher: American Associa-  
1271 tion for the Advancement of Science) doi: 10.1126/science.abl4353



- 1272 Herbert, T. D., Rose, R., Dybkjær, K., Rasmussen, E. S., & Śliwińska, K. K.  
 1273 (2020). Bihemispheric Warming in the Miocene Climatic Optimum as  
 1274 Seen From the Danish North Sea. *Paleoceanography and Paleoclima-*  
 1275 *tology*, *35*(10), e2020PA003935. Retrieved 2024-05-09, from [https://](https://onlinelibrary.wiley.com/doi/abs/10.1029/2020PA003935)  
 1276 [onlinelibrary.wiley.com/doi/abs/10.1029/2020PA003935](https://onlinelibrary.wiley.com/doi/abs/10.1029/2020PA003935) (\_eprint:  
 1277 <https://onlinelibrary.wiley.com/doi/pdf/10.1029/2020PA003935>) doi:  
 1278 10.1029/2020PA003935
- 1279 Herold, N., Huber, M., Greenwood, D., Müller, R., & Seton, M. (2011, January).  
 1280 Early to Middle Miocene monsoon climate in Australia. *Geology*, *39*(1), 3–  
 1281 6. Retrieved 2022-04-28, from <https://doi.org/10.1130/G31208.1> doi:  
 1282 10.1130/G31208.1
- 1283 Herold, N., Seton, M., Müller, R. D., You, Y., & Huber, M. (2008). Middle  
 1284 Miocene tectonic boundary conditions for use in climate models. *Geo-*  
 1285 *chemistry, Geophysics, Geosystems*, *9*(10). Retrieved 2022-04-28, from  
 1286 <https://onlinelibrary.wiley.com/doi/abs/10.1029/2008GC002046>  
 1287 (\_eprint: <https://onlinelibrary.wiley.com/doi/pdf/10.1029/2008GC002046>)  
 1288 doi: 10.1029/2008GC002046
- 1289 Herold, N., You, Y., Müller, R. D., & Seton, M. (2009, December). Climate  
 1290 model sensitivity to changes in Miocene paleotopography. *Australian*  
 1291 *Journal of Earth Sciences*, *56*(8), 1049–1059. Retrieved 2022-04-28,  
 1292 from <https://doi.org/10.1080/08120090903246170> (Publisher: Tay-  
 1293 lor & Francis \_eprint: <https://doi.org/10.1080/08120090903246170>) doi:  
 1294 10.1080/08120090903246170
- 1295 Ho, S. L., & Laepple, T. (2016, August). Flat meridional temperature gradient  
 1296 in the early Eocene in the subsurface rather than surface ocean. *Nature Geo-*  
 1297 *science*, *9*(8), 606–610. Retrieved 2024-01-27, from [https://www.nature.com/](https://www.nature.com/articles/ngeo2763)  
 1298 [articles/ngeo2763](https://www.nature.com/articles/ngeo2763) (Number: 8 Publisher: Nature Publishing Group) doi:  
 1299 10.1038/ngeo2763
- 1300 Hossain, A., Knorr, G., Jokat, W., Lohmann, G., Hochmuth, K., Gierz, P., ...  
 1301 Stepanek, C. (2023). The Impact of Different Atmospheric CO<sub>2</sub> Concen-  
 1302 trations on Large Scale Miocene Temperature Signatures. *Paleoceanogra-*  
 1303 *phy and Paleoclimatology*, *38*(2), e2022PA004438. Retrieved 2023-05-20,  
 1304 from <https://onlinelibrary.wiley.com/doi/abs/10.1029/2022PA004438>  
 1305 (\_eprint: <https://onlinelibrary.wiley.com/doi/pdf/10.1029/2022PA004438>) doi:  
 1306 10.1029/2022PA004438
- 1307 Huang, S., Meijers, M. J. M., Eyres, A., Mulch, A., & Fritz, S. A. (2019). Unravel-  
 1308 ling the history of biodiversity in mountain ranges through integrating geology  
 1309 and biogeography. *Journal of Biogeography*, *46*(8), 1777–1791. Retrieved  
 1310 2024-05-08, from [https://onlinelibrary.wiley.com/doi/abs/10.1111/jbi](https://onlinelibrary.wiley.com/doi/abs/10.1111/jbi.13622)  
 1311 [.13622](https://onlinelibrary.wiley.com/doi/abs/10.1111/jbi.13622) (\_eprint: <https://onlinelibrary.wiley.com/doi/pdf/10.1111/jbi.13622>)  
 1312 doi: 10.1111/jbi.13622
- 1313 Huang, X., Stäorz, M., Gohl, K., Knorr, G., & Lohmann, G. (2017). Impact of  
 1314 Weddell Sea shelf progradation on Antarctic bottom water formation dur-  
 1315 ing the Miocene. *Paleoceanography*, *32*(3), 304–317. Retrieved 2023-11-02,  
 1316 from <https://onlinelibrary.wiley.com/doi/abs/10.1002/2016PA002987>  
 1317 (\_eprint: <https://onlinelibrary.wiley.com/doi/pdf/10.1002/2016PA002987>) doi:  
 1318 10.1002/2016PA002987
- 1319 Huber, M., & Caballero, R. (2003, February). Eocene El Niño: Evidence for Robust  
 1320 Tropical Dynamics in the "Hothouse". *Science*, *299*(5608), 877–881. Retrieved  
 1321 2024-01-27, from <https://www.science.org/doi/10.1126/science.1078766>  
 1322 (Publisher: American Association for the Advancement of Science) doi:  
 1323 10.1126/science.1078766
- 1324 Hui, Z., Zhang, J., Ma, Z., Li, X., Peng, T., Li, J., & Wang, B. (2018, December).  
 1325 Global warming and rainfall: Lessons from an analysis of Mid-Miocene cli-  
 1326 mate data. *Palaeogeography, Palaeoclimatology, Palaeoecology*, *512*, 106–117.

- 1327 Retrieved 2023-11-21, from [https://www.sciencedirect.com/science/](https://www.sciencedirect.com/science/article/pii/S0031018218300129)  
 1328 [article/pii/S0031018218300129](https://www.sciencedirect.com/science/article/pii/S0031018218300129) doi: 10.1016/j.palaeo.2018.10.025
- 1329 Hurrell, J. W. (1995, August). Decadal Trends in the North Atlantic Oscilla-  
 1330 tion: Regional Temperatures and Precipitation. *Science*, *269*(5224), 676–679.  
 1331 Retrieved 2022-04-24, from [https://www.science.org/doi/abs/10.1126/](https://www.science.org/doi/abs/10.1126/science.269.5224.676)  
 1332 [science.269.5224.676](https://www.science.org/doi/abs/10.1126/science.269.5224.676) (Publisher: American Association for the Advance-  
 1333 ment of Science) doi: 10.1126/science.269.5224.676
- 1334 Huw Davies, J., & von Blanckenburg, F. (1995, January). Slab breakoff: A model  
 1335 of lithosphere detachment and its test in the magmatism and deformation  
 1336 of collisional orogens. *Earth and Planetary Science Letters*, *129*(1), 85–102.  
 1337 Retrieved 2022-04-22, from [https://www.sciencedirect.com/science/](https://www.sciencedirect.com/science/article/pii/0012821X9400237S)  
 1338 [article/pii/0012821X9400237S](https://www.sciencedirect.com/science/article/pii/0012821X9400237S) doi: 10.1016/0012-821X(94)00237-S
- 1339 Huyghe, D., Mouthereau, F., Sébilo, M., Vacherat, A., Ségalen, L., Richard, P.,  
 1340 ... Bariac, T. (2018, February). Impact of topography, climate and mois-  
 1341 ture sources on isotopic composition (18O & D) of rivers in the Pyrenees:  
 1342 Implications for topographic reconstructions in small orogens. *Earth and Plan-*  
 1343 *etary Science Letters*, *484*, 370–384. Retrieved 2022-04-24, from [https://](https://www.sciencedirect.com/science/article/pii/S0012821X17307471)  
 1344 [www.sciencedirect.com/science/article/pii/S0012821X17307471](https://www.sciencedirect.com/science/article/pii/S0012821X17307471) doi:  
 1345 10.1016/j.epsl.2017.12.035
- 1346 Ingraham, N. L., & Taylor, B. E. (1991). Light stable isotope systematics  
 1347 of large-scale hydrologic regimes in California and Nevada. *Water Re-*  
 1348 *sources Research*, *27*(1), 77–90. Retrieved 2024-02-17, from [https://](https://onlinelibrary.wiley.com/doi/abs/10.1029/90WR01708)  
 1349 [onlinelibrary.wiley.com/doi/abs/10.1029/90WR01708](https://onlinelibrary.wiley.com/doi/abs/10.1029/90WR01708) (\_eprint:  
 1350 <https://onlinelibrary.wiley.com/doi/pdf/10.1029/90WR01708>) doi:  
 1351 10.1029/90WR01708
- 1352 Insel, N., Poulsen, C. J., & Ehlers, T. A. (2010, December). Influence of the  
 1353 Andes Mountains on South American moisture transport, convection,  
 1354 and precipitation. *Climate Dynamics*, *35*(7), 1477–1492. Retrieved  
 1355 2022-04-24, from <https://doi.org/10.1007/s00382-009-0637-1> doi:  
 1356 10.1007/s00382-009-0637-1
- 1357 Jiménez-Moreno, G., & Suc, J.-P. (2007, September). Middle Miocene latitudinal  
 1358 climatic gradient in Western Europe: Evidence from pollen records. *Palaeo-*  
 1359 *geography, Palaeoclimatology, Palaeoecology*, *253*(1), 208–225. Retrieved  
 1360 2023-11-10, from [https://www.sciencedirect.com/science/article/pii/](https://www.sciencedirect.com/science/article/pii/S0031018207002015)  
 1361 [S0031018207002015](https://www.sciencedirect.com/science/article/pii/S0031018207002015) doi: 10.1016/j.palaeo.2007.03.040
- 1362 Jung, G., Prange, M., & Schulz, M. (2016, April). Influence of topography on trop-  
 1363 ical African vegetation coverage. *Climate Dynamics*, *46*(7), 2535–2549. Re-  
 1364 trieved 2024-01-08, from <https://doi.org/10.1007/s00382-015-2716-9> doi:  
 1365 10.1007/s00382-015-2716-9
- 1366 Kissling, E., & Schlunegger, F. (2018). Rollback Orogeny Model for the Evolu-  
 1367 tion of the Swiss Alps. *Tectonics*, *37*(4), 1097–1115. Retrieved 2023-11-08,  
 1368 from <https://onlinelibrary.wiley.com/doi/abs/10.1002/2017TC004762>  
 1369 (\_eprint: <https://onlinelibrary.wiley.com/doi/pdf/10.1002/2017TC004762>) doi:  
 1370 10.1002/2017TC004762
- 1371 Knorr, G., Butzin, M., Micheels, A., & Lohmann, G. (2011). A warm  
 1372 Miocene climate at low atmospheric CO<sub>2</sub> levels. *Geophysical Re-*  
 1373 *search Letters*, *38*(20). Retrieved 2022-05-11, from [https://](https://onlinelibrary.wiley.com/doi/abs/10.1029/2011GL048873)  
 1374 [onlinelibrary.wiley.com/doi/abs/10.1029/2011GL048873](https://onlinelibrary.wiley.com/doi/abs/10.1029/2011GL048873) (\_eprint:  
 1375 <https://onlinelibrary.wiley.com/doi/pdf/10.1029/2011GL048873>) doi:  
 1376 10.1029/2011GL048873
- 1377 Kocsis, L., Vennemann, T. W., & Fontignie, D. (2007, May). Migration of  
 1378 sharks into freshwater systems during the Miocene and implications for  
 1379 Alpine paleoelevation. *Geology*, *35*(5), 451–454. Retrieved 2022-04-24, from  
 1380 <https://doi.org/10.1130/G23404A.1> doi: 10.1130/G23404A.1
- 1381 Krapp, M., & Jungclaus, J. H. (2011, November). The Middle Miocene climate

- 1382 as modelled in an atmosphere-ocean-biosphere model. *Climate of the Past*,  
 1383 7(4), 1169–1188. Retrieved 2022-05-11, from [https://cp.copernicus.org/](https://cp.copernicus.org/articles/7/1169/2011/)  
 1384 [articles/7/1169/2011/](https://cp.copernicus.org/articles/7/1169/2011/) doi: 10.5194/cp-7-1169-2011
- 1385 Krsnik, E., Methner, K., Campani, M., Botsyun, S., Mutz, S. G., Ehlers, T. A.,  
 1386 ... Mulch, A. (2021, November). Miocene high elevation in the Cen-  
 1387 tral Alps. *Solid Earth*, 12(11), 2615–2631. Retrieved 2022-09-22, from  
 1388 <https://se.copernicus.org/articles/12/2615/2021/> (Publisher: Coper-  
 1389 nicus GmbH) doi: 10.5194/se-12-2615-2021
- 1390 Kürschner, W. M., Kvaček, Z., & Dilcher, D. L. (2008, January). The impact of  
 1391 Miocene atmospheric carbon dioxide fluctuations on climate and the evolution  
 1392 of terrestrial ecosystems. *Proceedings of the National Academy of Sciences*,  
 1393 105(2), 449–453. Retrieved 2023-10-28, from [https://www.pnas.org/doi/](https://www.pnas.org/doi/full/10.1073/pnas.0708588105)  
 1394 [full/10.1073/pnas.0708588105](https://www.pnas.org/doi/full/10.1073/pnas.0708588105) (Publisher: Proceedings of the National  
 1395 Academy of Sciences) doi: 10.1073/pnas.0708588105
- 1396 Ladant, J.-B., Donnadieu, Y., Lefebvre, V., & Dumas, C. (2014). The re-  
 1397 spective role of atmospheric carbon dioxide and orbital parameters  
 1398 on ice sheet evolution at the Eocene-Oligocene transition. *Paleo-*  
 1399 *ceanography*, 29(8), 810–823. Retrieved 2024-01-29, from [https://](https://onlinelibrary.wiley.com/doi/abs/10.1002/2013PA002593)  
 1400 [onlinelibrary.wiley.com/doi/abs/10.1002/2013PA002593](https://onlinelibrary.wiley.com/doi/abs/10.1002/2013PA002593) (\_eprint:  
 1401 <https://onlinelibrary.wiley.com/doi/pdf/10.1002/2013PA002593>) doi:  
 1402 10.1002/2013PA002593
- 1403 Langebroek, P. M., Werner, M., & Lohmann, G. (2011, November). Climate in-  
 1404 formation imprinted in oxygen-isotopic composition of precipitation in Eu-  
 1405 rope. *Earth and Planetary Science Letters*, 311(1), 144–154. Retrieved  
 1406 2022-04-24, from [https://www.sciencedirect.com/science/article/pii/](https://www.sciencedirect.com/science/article/pii/S0012821X1100522X)  
 1407 [S0012821X1100522X](https://www.sciencedirect.com/science/article/pii/S0012821X1100522X) doi: 10.1016/j.epsl.2011.08.049
- 1408 Lechler, A. R., & Niemi, N. A. (2011, October). Controls on the Spatial Vari-  
 1409 ability of Modern Meteoric  $^{18}\text{O}$ : Empirical Constraints from the Western  
 1410 U.S. and East Asia and Implications for Stable Isotope Studies. *Ameri-*  
 1411 *can Journal of Science*, 311(8), 664–700. Retrieved 2024-02-17, from  
 1412 <https://ajsonline.org/article/61862> (Publisher: American Journal  
 1413 of Science) doi: 10.2475/08.2011.02
- 1414 Lee, J.-E., Fung, I., DePaolo, D. J., & Henning, C. C. (2007). Analy-  
 1415 sis of the global distribution of water isotopes using the NCAR at-  
 1416 mospheric general circulation model. *Journal of Geophysical Re-*  
 1417 *search: Atmospheres*, 112(D16). Retrieved 2023-10-23, from [https://](https://onlinelibrary.wiley.com/doi/abs/10.1029/2006JD007657)  
 1418 [onlinelibrary.wiley.com/doi/abs/10.1029/2006JD007657](https://onlinelibrary.wiley.com/doi/abs/10.1029/2006JD007657) (\_eprint:  
 1419 <https://onlinelibrary.wiley.com/doi/pdf/10.1029/2006JD007657>) doi:  
 1420 10.1029/2006JD007657
- 1421 Li, J., Ehlers, T. A., Mutz, S. G., Steger, C., Paeth, H., Werner, M., ... Feng, R.  
 1422 (2016, September). Modern precipitation  $^{18}\text{O}$  and trajectory analysis over the  
 1423 Himalaya-Tibet Orogen from ECHAM5-wiso simulations: TIBETAN MOD-  
 1424 ERN PRECIPITATION  $^{18}\text{O}$ . *Journal of Geophysical Research: Atmospheres*,  
 1425 121(18), 10,432–10,452. Retrieved 2022-04-25, from [http://doi.wiley.com/](http://doi.wiley.com/10.1002/2016JD024818)  
 1426 [10.1002/2016JD024818](http://doi.wiley.com/10.1002/2016JD024818) doi: 10.1002/2016JD024818
- 1427 Mancktelow, N., Zwingmann, H., Campani, M., Fügenschuh, B., & Mulch, A.  
 1428 (2015, December). Timing and conditions of brittle faulting on the Silltal-  
 1429 Brenner Fault Zone, Eastern Alps (Austria). *Swiss Journal of Geosciences*,  
 1430 108(2), 305–326. Retrieved 2024-01-15, from [https://doi.org/10.1007/](https://doi.org/10.1007/s00015-015-0179-y)  
 1431 [s00015-015-0179-y](https://doi.org/10.1007/s00015-015-0179-y) doi: 10.1007/s00015-015-0179-y
- 1432 McKenna, C. M., & Maycock, A. C. (2022). The Role of the North Atlantic  
 1433 Oscillation for Projections of Winter Mean Precipitation in Europe. *Geo-*  
 1434 *physical Research Letters*, 49(19), e2022GL099083. Retrieved 2024-01-24,  
 1435 from <https://onlinelibrary.wiley.com/doi/abs/10.1029/2022GL099083>  
 1436 (\_eprint: <https://onlinelibrary.wiley.com/doi/pdf/10.1029/2022GL099083>) doi:

- 1437 10.1029/2022GL099083
- 1438 Mey, J., Scherler, D., Wickert, A. D., Egholm, D. L., Tesauro, M., Schildgen, T. F.,  
1439 & Strecker, M. R. (2016, November). Glacial isostatic uplift of the Euro-  
1440 pean Alps. *Nature Communications*, 7(1), 13382. Retrieved 2024-03-04,  
1441 from <https://www.nature.com/articles/ncomms13382> (Publisher: Nature  
1442 Publishing Group) doi: 10.1038/ncomms13382
- 1443 Meyer, H. W. (2007, October). A Review of Paleotemperature–Lapse Rate Methods  
1444 for Estimating Paleoelevation from Fossil Floras. *Reviews in Mineralogy and*  
1445 *Geochemistry*, 66(1), 155–171. Retrieved 2024-05-16, from [https://doi.org/](https://doi.org/10.2138/rmg.2007.66.6)  
1446 [10.2138/rmg.2007.66.6](https://doi.org/10.2138/rmg.2007.66.6) doi: 10.2138/rmg.2007.66.6
- 1447 Micheels, A., Bruch, A. A., Uhl, D., Utescher, T., & Mosbrugger, V. (2007,  
1448 September). A Late Miocene climate model simulation with ECHAM4/ML  
1449 and its quantitative validation with terrestrial proxy data. *Palaeogeogra-*  
1450 *phy, Palaeoclimatology, Palaeoecology*, 253(1), 251–270. Retrieved 2022-  
1451 04-28, from [https://www.sciencedirect.com/science/article/pii/](https://www.sciencedirect.com/science/article/pii/S0031018207002039)  
1452 [S0031018207002039](https://www.sciencedirect.com/science/article/pii/S0031018207002039) doi: 10.1016/j.palaeo.2007.03.042
- 1453 Mulch, A. (2016, January). Stable isotope paleoaltimetry and the evolution of land-  
1454 scapes and life. *Earth and Planetary Science Letters*, 433, 180–191. Retrieved  
1455 2022-04-24, from [https://www.sciencedirect.com/science/article/pii/](https://www.sciencedirect.com/science/article/pii/S0012821X1500669X)  
1456 [S0012821X1500669X](https://www.sciencedirect.com/science/article/pii/S0012821X1500669X) doi: 10.1016/j.epsl.2015.10.034
- 1457 Mulch, A., Graham, S. A., & Chamberlain, C. P. (2006, July). Hydrogen Isotopes  
1458 in Eocene River Gravels and Paleoelevation of the Sierra Nevada. *Science*,  
1459 313(5783), 87–89. Retrieved 2022-04-24, from [https://www.science.org/](https://www.science.org/doi/full/10.1126/science.1125986)  
1460 [doi/full/10.1126/science.1125986](https://www.science.org/doi/full/10.1126/science.1125986) (Publisher: American Association for  
1461 the Advancement of Science) doi: 10.1126/science.1125986
- 1462 Mutz, S. G., Ehlers, T. A., Werner, M., Lohmann, G., Stepanek, C., & Li, J. (2018,  
1463 April). Estimates of late Cenozoic climate change relevant to Earth surface  
1464 processes in tectonically active orogens. *Earth Surface Dynamics*, 6(2), 271–  
1465 301. Retrieved 2022-08-16, from [https://esurf.copernicus.org/articles/](https://esurf.copernicus.org/articles/6/271/2018/)  
1466 [6/271/2018/](https://esurf.copernicus.org/articles/6/271/2018/) (Publisher: Copernicus GmbH) doi: 10.5194/esurf-6-271-2018
- 1467 Paul, A., Mulitza, S., Pätzold, J., & Wolff, T. (1999). Simulation of Oxygen Isotopes  
1468 in a Global Ocean Model. In G. Fischer & G. Wefer (Eds.), *Use of Proxies in*  
1469 *Paleoceanography: Examples from the South Atlantic* (pp. 655–686). Berlin,  
1470 Heidelberg: Springer. Retrieved 2023-11-06, from [https://doi.org/10.1007/](https://doi.org/10.1007/978-3-642-58646-0_27)  
1471 [978-3-642-58646-0\\_27](https://doi.org/10.1007/978-3-642-58646-0_27) doi: 10.1007/978-3-642-58646-0\_27
- 1472 Peters, N. A., Huntington, K. W., & Hoke, G. D. (2013, January). Hot or not?  
1473 Impact of seasonally variable soil carbonate formation on paleotemperature  
1474 and O-isotope records from clumped isotope thermometry. *Earth and Plan-*  
1475 *etary Science Letters*, 361, 208–218. Retrieved 2024-02-12, from [https://](https://www.sciencedirect.com/science/article/pii/S0012821X12005869)  
1476 [www.sciencedirect.com/science/article/pii/S0012821X12005869](https://www.sciencedirect.com/science/article/pii/S0012821X12005869) doi:  
1477 10.1016/j.epsl.2012.10.024
- 1478 Poage, M. A., & Chamberlain, C. P. (2001, January). Empirical Relationships  
1479 Between Elevation and the Stable Isotope Composition of Precipitation  
1480 and Surface Waters: Considerations for Studies of Paleoelevation Change.  
1481 *American Journal of Science*, 301(1), 1–15. Retrieved 2022-04-24, from  
1482 <https://www.ajsonline.org/content/301/1/1> (Publisher: American  
1483 Journal of Science Section: ARTICLES) doi: 10.2475/ajs.301.1.1
- 1484 Poulsen, C. J., Ehlers, T. A., & Insel, N. (2010, April). Onset of Convective  
1485 Rainfall During Gradual Late Miocene Rise of the Central Andes. *Science*,  
1486 328(5977), 490–493. Retrieved 2022-04-25, from [https://www.science.org/](https://www.science.org/doi/10.1126/science.1185078)  
1487 [doi/10.1126/science.1185078](https://www.science.org/doi/10.1126/science.1185078) doi: 10.1126/science.1185078
- 1488 Poulsen, C. J., & Jeffery, M. L. (2011, June). Climate change imprinting on stable  
1489 isotopic compositions of high-elevation meteoric water cloaks past surface ele-  
1490 vations of major orogens. *Geology*, 39(6), 595–598. Retrieved 2023-12-19, from  
1491 <https://doi.org/10.1130/G32052.1> doi: 10.1130/G32052.1

- 1492 Poulsen, C. J., Pollard, D., & White, T. S. (2007, March). General circulation model  
1493 simulation of the 18O content of continental precipitation in the middle Creta-  
1494 ceous: A model-proxy comparison. *Geology*, *35*(3), 199–202. Retrieved 2024-  
1495 02-17, from <https://doi.org/10.1130/G23343A.1> doi: 10.1130/G23343A.1
- 1496 Pound, M. J., Haywood, A. M., Salzmann, U., Riding, J. B., Lunt, D. J., &  
1497 Hunter, S. J. (2011, February). A Tortonian (Late Miocene, 11.61–7.25Ma)  
1498 global vegetation reconstruction. *Palaeogeography, Palaeoclimatology,*  
1499 *Palaeoecology*, *300*(1), 29–45. Retrieved 2022-04-28, from [https://](https://www.sciencedirect.com/science/article/pii/S0031018210007091)  
1500 [www.sciencedirect.com/science/article/pii/S0031018210007091](https://www.sciencedirect.com/science/article/pii/S0031018210007091) doi:  
1501 10.1016/j.palaeo.2010.11.029
- 1502 Rae, J. W., Zhang, Y. G., Liu, X., Foster, G. L., Stoll, H. M., & Whiteford, R. D.  
1503 (2021). Atmospheric CO<sub>2</sub> over the Past 66 Million Years from Marine  
1504 Archives. *Annual Review of Earth and Planetary Sciences*, *49*(1), 609–641. Re-  
1505 trieved 2023-10-28, from [https://doi.org/10.1146/annurev-earth-082420](https://doi.org/10.1146/annurev-earth-082420-063026)  
1506 [-063026](https://doi.org/10.1146/annurev-earth-082420-063026) (eprint: <https://doi.org/10.1146/annurev-earth-082420-063026>) doi:  
1507 10.1146/annurev-earth-082420-063026
- 1508 Rajczak, J., Pall, P., & Schär, C. (2013). Projections of extreme precipitation events  
1509 in regional climate simulations for Europe and the Alpine Region. *Journal of*  
1510 *Geophysical Research: Atmospheres*, *118*(9), 3610–3626. Retrieved 2024-01-31,  
1511 from <https://onlinelibrary.wiley.com/doi/abs/10.1002/jgrd.50297>  
1512 (eprint: <https://onlinelibrary.wiley.com/doi/pdf/10.1002/jgrd.50297>) doi:  
1513 10.1002/jgrd.50297
- 1514 Rajczak, J., & Schär, C. (2017). Projections of Future Precipitation Extremes Over  
1515 Europe: A Multimodel Assessment of Climate Simulations. *Journal of Geo-*  
1516 *physical Research: Atmospheres*, *122*(20), 10,773–10,800. Retrieved 2024-01-24,  
1517 from <https://onlinelibrary.wiley.com/doi/abs/10.1002/2017JD027176>  
1518 (eprint: <https://onlinelibrary.wiley.com/doi/pdf/10.1002/2017JD027176>) doi:  
1519 10.1002/2017JD027176
- 1520 Ramsay, A. T. S., Smart, C. W., & Zachos, J. C. (1998, January). A Model of early  
1521 to middle Miocene Deep Ocean circulation for the Atlantic and Indian Oceans.  
1522 *Geological Society, London, Special Publications*, *131*(1), 55–70. Retrieved  
1523 2023-10-28, from [https://www.lyellcollection.org/doi/abs/10.1144/](https://www.lyellcollection.org/doi/abs/10.1144/gsl.sp.1998.131.01.04)  
1524 [gsl.sp.1998.131.01.04](https://www.lyellcollection.org/doi/abs/10.1144/gsl.sp.1998.131.01.04) (Publisher: The Geological Society of London) doi:  
1525 10.1144/GSL.SP.1998.131.01.04
- 1526 Ramstein, G., Fluteau, F., Besse, J., & Joussaume, S. (1997, April). Effect of  
1527 orogeny, plate motion and land–sea distribution on Eurasian climate change  
1528 over the past 30 million years. *Nature*, *386*(6627), 788–795. Retrieved 2023-  
1529 11-02, from <https://www.nature.com/articles/386788a0> (Number: 6627  
1530 Publisher: Nature Publishing Group) doi: 10.1038/386788a0
- 1531 Retallack, G. J. (2009, October). Refining a pedogenic-carbonate CO<sub>2</sub> paleobarome-  
1532 ter to quantify a middle Miocene greenhouse spike. *Palaeogeography, Palaeocli-*  
1533 *matology, Palaeoecology*, *281*(1), 57–65. Retrieved 2023-10-28, from [https://](https://www.sciencedirect.com/science/article/pii/S0031018209002867)  
1534 [www.sciencedirect.com/science/article/pii/S0031018209002867](https://www.sciencedirect.com/science/article/pii/S0031018209002867) doi: 10  
1535 .1016/j.palaeo.2009.07.011
- 1536 Risi, C., Bony, S., Vimeux, F., & Jouzel, J. (2010, June). Water-stable isotopes  
1537 in the LMDZ4 general circulation model: Model evaluation for present-day  
1538 and past climates and applications to climatic interpretations of tropical iso-  
1539 topic records. *Journal of Geophysical Research*, *115*(D12), D12118. Retrieved  
1540 2022-04-25, from <http://doi.wiley.com/10.1029/2009JD013255> doi:  
1541 10.1029/2009JD013255
- 1542 Roe, G. H., Ding, Q., Battisti, D. S., Molnar, P., Clark, M. K., & Garziona, C. N.  
1543 (2016). A modeling study of the response of Asian summertime climate  
1544 to the largest geologic forcings of the past 50 Ma. *Journal of Geophysical*  
1545 *Research: Atmospheres*, *121*(10), 5453–5470. Retrieved 2024-02-17, from  
1546 <https://onlinelibrary.wiley.com/doi/abs/10.1002/2015JD024370>

- 1547 (\_eprint: <https://onlinelibrary.wiley.com/doi/pdf/10.1002/2015JD024370>)  
 1548 doi: 10.1002/2015JD024370
- 1549 Roeckner, E., Bäuml, G., Bonaventura, L., Brokopf, R., Esch, M., Giorgetta, M.,  
 1550 ... Tompkins, A. (2003, November). The atmospheric general circulation  
 1551 model ECHAM 5. PART I: Model description. Retrieved 2022-04-24,  
 1552 from [https://pure.mpg.de/pubman/faces/ViewItemOverviewPage.jsp](https://pure.mpg.de/pubman/faces/ViewItemOverviewPage.jsp?itemId=item_995269)  
 1553 ?itemId=item\_995269 (Publisher: Max-Planck-Institut für Meteorologie) doi:  
 1554 10.17617/2.995269
- 1555 Rohrmann, A., Strecker, M. R., Bookhagen, B., Mulch, A., Sachse, D., Pingel, H.,  
 1556 ... Montero, C. (2014, December). Can stable isotopes ride out the storms?  
 1557 The role of convection for water isotopes in models, records, and paleoaltimetry  
 1558 studies in the central Andes. *Earth and Planetary Science Letters*, 407,  
 1559 187–195. Retrieved 2023-08-10, from <https://www.sciencedirect.com/science/article/pii/S0012821X14005767> doi: 10.1016/j.epsl.2014.09.021
- 1560 Rowley, D. B. (2007, October). Stable Isotope-Based Paleoaltimetry: Theory and  
 1561 Validation. *Reviews in Mineralogy and Geochemistry*, 66(1), 23–52. Retrieved  
 1562 2023-06-11, from <https://doi.org/10.2138/rmg.2007.66.2> doi: 10.2138/  
 1563 rmg.2007.66.2
- 1564 Rowley, D. B., & Currie, B. S. (2006, February). Palaeo-altimetry of the late  
 1565 Eocene to Miocene Lunpola basin, central Tibet. *Nature*, 439(7077), 677–  
 1566 681. Retrieved 2022-04-24, from <https://www.nature.com/articles/nature04506>  
 1567 (Number: 7077 Publisher: Nature Publishing Group) doi:  
 1568 10.1038/nature04506
- 1569 Rowley, D. B., Pierrehumbert, R. T., & Currie, B. S. (2001, May). A new approach  
 1570 to stable isotope-based paleoaltimetry: implications for paleoaltimetry and pa-  
 1571 leohypsometry of the High Himalaya since the Late Miocene. *Earth and Plan-  
 1572 etary Science Letters*, 188(1), 253–268. Retrieved 2022-04-24, from [https://](https://www.sciencedirect.com/science/article/pii/S0012821X01003247)  
 1573 [www.sciencedirect.com/science/article/pii/S0012821X01003247](https://www.sciencedirect.com/science/article/pii/S0012821X01003247) doi:  
 1574 10.1016/S0012-821X(01)00324-7
- 1575 Rögl, F. (1999). MEDITERRANEAN AND PARATETHYS. FACTS AND HY-  
 1576 POTHESES OF AN OLIGOCENE TO MIOCENE PALEO GEOGRAPHY  
 1577 (SHORT OVERVIEW).  
 1578
- 1579 Salles, T., Husson, L., Lorcery, M., & Hadler Boggiani, B. (2023, November). Land-  
 1580 scape dynamics and the Phanerozoic diversification of the biosphere. *Nature*,  
 1581 1–7. Retrieved 2023-12-04, from [https://www.nature.com/articles/s41586](https://www.nature.com/articles/s41586-023-06777-z)  
 1582 -023-06777-z (Publisher: Nature Publishing Group) doi: 10.1038/s41586-023  
 1583 -06777-z
- 1584 Salles, T., Husson, L., Rey, P., Mallard, C., Zahirovic, S., Boggiani, B. H., ...  
 1585 Arnould, M. (2023, March). Hundred million years of landscape dynamics  
 1586 from catchment to global scale. *Science*, 379(6635), 918–923. Retrieved 2024-  
 1587 02-20, from <https://www.science.org/doi/full/10.1126/science.add2541>  
 1588 (Publisher: American Association for the Advancement of Science) doi:  
 1589 10.1126/science.add2541
- 1590 Schlunegger, F., & Castelltort, S. (2016, August). Immediate and delayed signal of  
 1591 slab breakoff in Oligo/Miocene Molasse deposits from the European Alps. *Sci-  
 1592 entific Reports*, 6(1), 31010. Retrieved 2022-04-24, from [https://www.nature](https://www.nature.com/articles/srep31010)  
 1593 [.com/articles/srep31010](https://www.nature.com/articles/srep31010) (Number: 1 Publisher: Nature Publishing Group)  
 1594 doi: 10.1038/srep31010
- 1595 Schlunegger, F., & Kissling, E. (2015, October). Slab rollback orogeny in the Alps  
 1596 and evolution of the Swiss Molasse basin. *Nature Communications*, 6(1), 1–10.  
 1597 Retrieved 2022-04-24, from <https://www.nature.com/articles/ncomms9605>  
 1598 (Number: 1 Publisher: Nature Publishing Group) doi: 10.1038/ncomms9605
- 1599 Schmid, S. M., Pfiffner, O. A., Froitzheim, N., Schönborn, G., & Kissling, E.  
 1600 (1996). Geophysical-geological transect and tectonic evolution of the  
 1601 Swiss-Italian Alps. *Tectonics*, 15(5), 1036–1064. Retrieved 2022-04-24,

- 1602 from <https://onlinelibrary.wiley.com/doi/abs/10.1029/96TC00433>  
 1603 (\_eprint: <https://onlinelibrary.wiley.com/doi/pdf/10.1029/96TC00433>) doi:  
 1604 10.1029/96TC00433
- 1605 Sepulchre, P., Ramstein, G., Fluteau, F., Schuster, M., Tiercelin, J.-J., & Brunet,  
 1606 M. (2006, September). Tectonic Uplift and Eastern Africa Aridification.  
 1607 *Science*, *313*(5792), 1419–1423. Retrieved 2023-06-19, from [https://](https://www.science.org/doi/10.1126/science.1129158)  
 1608 [www.science.org/doi/10.1126/science.1129158](https://www.science.org/doi/10.1126/science.1129158) (Publisher: American  
 1609 Association for the Advancement of Science) doi: 10.1126/science.1129158
- 1610 Sewall, J. O., & Fricke, H. C. (2013, January). Andean-scale highlands in the Late  
 1611 Cretaceous Cordillera of the North American western margin. *Earth and*  
 1612 *Planetary Science Letters*, *362*, 88–98. Retrieved 2024-02-17, from [https://](https://www.sciencedirect.com/science/article/pii/S0012821X12006875)  
 1613 [www.sciencedirect.com/science/article/pii/S0012821X12006875](https://www.sciencedirect.com/science/article/pii/S0012821X12006875) doi:  
 1614 10.1016/j.epsl.2012.12.002
- 1615 Sharp, Z. D., Masson, H., & Lucchini, R. (2005, March). Stable isotope geochem-  
 1616 istry and formation mechanisms of quartz veins; extreme paleoaltitudes of the  
 1617 Central Alps in the Neogene. *American Journal of Science*, *305*(3), 187–219.  
 1618 Retrieved 2022-04-24, from <https://www.ajsonline.org/content/305/3/187>  
 1619 (Publisher: American Journal of Science Section: ARTICLES) doi:  
 1620 10.2475/ajs.305.3.187
- 1621 Sosdian, S. M., Greenop, R., Hain, M. P., Foster, G. L., Pearson, P. N., & Lear,  
 1622 C. H. (2018, September). Constraining the evolution of Neogene ocean  
 1623 carbonate chemistry using the boron isotope pH proxy. *Earth and Plane-*  
 1624 *tary Science Letters*, *498*, 362–376. Retrieved 2023-10-28, from [https://](https://www.sciencedirect.com/science/article/pii/S0012821X1830356X)  
 1625 [www.sciencedirect.com/science/article/pii/S0012821X1830356X](https://www.sciencedirect.com/science/article/pii/S0012821X1830356X) doi:  
 1626 10.1016/j.epsl.2018.06.017
- 1627 Sperber, K. R., Hameed, S., Potter, G. L., & Boyle, J. S. (1994, November). Sim-  
 1628 ulation of the Northern Summer Monsoon in the ECMWF Model: Sensitivity  
 1629 to Horizontal Resolution. *Monthly Weather Review*, *122*(11), 2461–2481. Re-  
 1630 trieved 2024-01-03, from [https://journals.ametsoc.org/view/journals/](https://journals.ametsoc.org/view/journals/mwre/122/11/1520-0493_1994_122_2461_sotnsm_2_0_co_2.xml)  
 1631 [mwre/122/11/1520-0493\\_1994\\_122\\_2461\\_sotnsm\\_2\\_0\\_co\\_2.xml](https://journals.ametsoc.org/view/journals/mwre/122/11/1520-0493_1994_122_2461_sotnsm_2_0_co_2.xml) (Publisher:  
 1632 American Meteorological Society Section: Monthly Weather Review) doi:  
 1633 10.1175/1520-0493(1994)122<2461:SOTNSM>2.0.CO;2
- 1634 Stampfli, G. M., Mosar, J., Marquer, D., Marchant, R., Baudin, T., & Borel, G.  
 1635 (1998, October). Subduction and obduction processes in the Swiss Alps.  
 1636 *Tectonophysics*, *296*(1), 159–204. Retrieved 2022-04-24, from [https://](https://www.sciencedirect.com/science/article/pii/S0040195198001425)  
 1637 [www.sciencedirect.com/science/article/pii/S0040195198001425](https://www.sciencedirect.com/science/article/pii/S0040195198001425) doi:  
 1638 10.1016/S0040-1951(98)00142-5
- 1639 Steinthorsdottir, M., Coxall, H. K., de Boer, A. M., Huber, M., Bar-  
 1640 bolini, N., Bradshaw, C. D., ... Strömberg, C. a. E. (2021). The  
 1641 Miocene: The Future of the Past. *Paleoceanography and Paleoclima-*  
 1642 *tology*, *36*(4), e2020PA004037. Retrieved 2022-04-28, from [https://](https://onlinelibrary.wiley.com/doi/abs/10.1029/2020PA004037)  
 1643 [onlinelibrary.wiley.com/doi/abs/10.1029/2020PA004037](https://onlinelibrary.wiley.com/doi/abs/10.1029/2020PA004037) (\_eprint:  
 1644 <https://onlinelibrary.wiley.com/doi/pdf/10.1029/2020PA004037>) doi:  
 1645 10.1029/2020PA004037
- 1646 Stevens, B., Giorgetta, M., Esch, M., Mauritsen, T., Crueger, T., Rast, S.,  
 1647 ... Roeckner, E. (2013). Atmospheric component of the MPI-M  
 1648 Earth System Model: ECHAM6. *Journal of Advances in Modeling*  
 1649 *Earth Systems*, *5*(2), 146–172. Retrieved 2023-06-09, from [https://](https://onlinelibrary.wiley.com/doi/abs/10.1002/jame.20015)  
 1650 [onlinelibrary.wiley.com/doi/abs/10.1002/jame.20015](https://onlinelibrary.wiley.com/doi/abs/10.1002/jame.20015) (\_eprint:  
 1651 <https://onlinelibrary.wiley.com/doi/pdf/10.1002/jame.20015>) doi: 10.1002/  
 1652 jame.20015
- 1653 Sturm, C., Hoffmann, G., & Langmann, B. (2007, August). Simulation of the Stable  
 1654 Water Isotopes in Precipitation over South America: Comparing Regional to  
 1655 Global Circulation Models. *Journal of Climate*, *20*(15), 3730–3750. Retrieved  
 1656 2024-02-17, from <https://journals.ametsoc.org/view/journals/clim/20/>

- 15/jcli4194.1.xml (Publisher: American Meteorological Society Section:  
Journal of Climate) doi: 10.1175/JCLI4194.1
- 1657 15/jcli4194.1.xml (Publisher: American Meteorological Society Section:  
1658 Journal of Climate) doi: 10.1175/JCLI4194.1
- 1659 Stärz, M., Jokat, W., Knorr, G., & Lohmann, G. (2017, June). Threshold in  
1660 North Atlantic-Arctic Ocean circulation controlled by the subsidence of the  
1661 Greenland-Scotland Ridge. *Nature Communications*, 8(1), 15681. Retrieved  
1662 2022-12-20, from <https://www.nature.com/articles/ncomms15681> (Num-  
1663 ber: 1 Publisher: Nature Publishing Group) doi: 10.1038/ncomms15681
- 1664 Super, J. R., Thomas, E., Pagani, M., Huber, M., O'Brien, C. L., &  
1665 Hull, P. M. (2020). Miocene Evolution of North Atlantic Sea  
1666 Surface Temperature. *Paleoceanography and Paleoclimatology*,  
1667 35(5), e2019PA003748. Retrieved 2024-01-27, from [https://  
1668 onlinelibrary.wiley.com/doi/abs/10.1029/2019PA003748](https://onlinelibrary.wiley.com/doi/abs/10.1029/2019PA003748) (eprint:  
1669 <https://onlinelibrary.wiley.com/doi/pdf/10.1029/2019PA003748>) doi:  
1670 10.1029/2019PA003748
- 1671 Tindall, J. C., Valdes, P. J., & Sime, L. C. (2009). Stable water iso-  
1672 topes in HadCM3: Isotopic signature of El Niño–Southern Oscilla-  
1673 tion and the tropical amount effect. *Journal of Geophysical Re-  
1674 search: Atmospheres*, 114(D4). Retrieved 2023-10-23, from [https://  
1675 onlinelibrary.wiley.com/doi/abs/10.1029/2008JD010825](https://onlinelibrary.wiley.com/doi/abs/10.1029/2008JD010825) (eprint:  
1676 <https://onlinelibrary.wiley.com/doi/pdf/10.1029/2008JD010825>) doi:  
1677 10.1029/2008JD010825
- 1678 Valla, P. G., Sternai, P., & Fox, M. (2021, February). How Climate, Uplift and Ero-  
1679 sion Shaped the Alpine Topography. *Elements*, 17(1), 41–46. Retrieved 2022-  
1680 04-24, from <https://doi.org/10.2138/gselements.17.1.41> doi: 10.2138/  
1681 gselements.17.1.41
- 1682 Werner, M., Haese, B., Xu, X., Zhang, X., Butzin, M., & Lohmann, G. (2016,  
1683 February). Glacial–interglacial changes in H<sub>2</sub><sup>18</sup>O, HDO and deuterium ex-  
1684 cess – results from the fully coupled ECHAM5/MPI-OM Earth system model.  
1685 *Geoscientific Model Development*, 9(2), 647–670. Retrieved 2023-06-12, from  
1686 <https://gmd.copernicus.org/articles/9/647/2016/gmd-9-647-2016.html>  
1687 (Publisher: Copernicus GmbH) doi: 10.5194/gmd-9-647-2016
- 1688 Werner, M., Langebroek, P. M., Carlsen, T., Herold, M., & Lohmann, G. (2011,  
1689 August). Stable water isotopes in the ECHAM5 general circulation model:  
1690 Toward high-resolution isotope modeling on a global scale. *Journal of Geo-  
1691 physical Research*, 116(D15), D15109. Retrieved 2022-04-25, from [http://  
1692 doi.wiley.com/10.1029/2011JD015681](http://doi.wiley.com/10.1029/2011JD015681) doi: 10.1029/2011JD015681
- 1693 Willett, S., Beaumont, C., & Fullsack, P. (1993, April). Mechanical model for the  
1694 tectonics of doubly vergent compressional orogens. *Geology*, 21(4), 371–374.  
1695 Retrieved 2024-03-04, from [https://doi.org/10.1130/0091-7613\(1993\)  
1696 021<0371:MMFTTO>2.3.CO;2](https://doi.org/10.1130/0091-7613(1993)021<0371:MMFTTO>2.3.CO;2) doi: 10.1130/0091-7613(1993)021<0371:  
1697 MMFTTO>2.3.CO;2
- 1698 Xu, X., Werner, M., Butzin, M., & Lohmann, G. (2012, June). Water isotope vari-  
1699 ations in the global ocean model MPI-OM. *Geoscientific Model Development*,  
1700 5(3), 809–818. Retrieved 2023-06-12, from [https://gmd.copernicus.org/  
1701 articles/5/809/2012/](https://gmd.copernicus.org/articles/5/809/2012/) (Publisher: Copernicus GmbH) doi: 10.5194/  
1702 gmd-5-809-2012
- 1703 Zappa, G., Hoskins, B. J., & Shepherd, T. G. (2015, October). The dependence  
1704 of wintertime Mediterranean precipitation on the atmospheric circulation re-  
1705 sponse to climate change. *Environmental Research Letters*, 10(10), 104012.  
1706 Retrieved 2024-01-31, from [https://dx.doi.org/10.1088/1748-9326/10/10/  
1707 104012](https://dx.doi.org/10.1088/1748-9326/10/10/104012) (Publisher: IOP Publishing) doi: 10.1088/1748-9326/10/10/104012
- 1708 Zhu, J., Poulsen, C. J., & Tierney, J. E. (2019, September). Simulation of Eocene  
1709 extreme warmth and high climate sensitivity through cloud feedbacks. *Sci-  
1710 ence Advances*, 5(9), eaax1874. Retrieved 2024-03-07, from [https://  
1711 www.science.org/doi/10.1126/sciadv.aax1874](https://www.science.org/doi/10.1126/sciadv.aax1874) (Publisher: American



1712 Association for the Advancement of Science) doi: 10.1126/sciadv.aax1874  
1713 Zimmermann, U., MüNnich, K. O., & Roether, W. (1967). Downward  
1714 Movement of Soil Moisture Traced by Means of Hydrogen Isotopes.  
1715 In *Isotope Techniques in the Hydrologic Cycle* (pp. 28–36). Ameri-  
1716 can Geophysical Union (AGU). Retrieved 2023-10-23, from [https://  
1717 onlinelibrary.wiley.com/doi/abs/10.1029/GM011p0028](https://onlinelibrary.wiley.com/doi/abs/10.1029/GM011p0028) (eprint:  
1718 <https://onlinelibrary.wiley.com/doi/pdf/10.1029/GM011p0028>) doi:  
1719 10.1029/GM011p0028

Supporting information for "Refinement of Middle Miocene paleoelevation of the Alps through topographic sensitivity experiments and paleo-meteoric water isotopic composition modelling"

# Supporting Information for ”Refinement of Miocene paleoelevation estimates of the Alps through topographic sensitivity experiments and modelling of $\delta^{18}O_p$ of paleo-meteoric water”

Daniel Boateng<sup>1</sup>, Sebastian G. Mutz<sup>2</sup>, Katharina Methner<sup>3</sup>, Armelle

Ballian<sup>4,5</sup>, Maud J. M Meijers<sup>4,6</sup>, Andreas Mulch<sup>4,5</sup>, Todd A. Ehlers<sup>1,2</sup>

<sup>1</sup>Department of Geosciences, University of Tübingen, Tübingen, Germany

<sup>2</sup>School of Geographical and Earth Sciences, University of Glasgow, Scotland, UK

<sup>3</sup>Institute for Earth System Science and Remote Sensing, University of Leipzig, Leipzig, Germany

<sup>4</sup>Senckenberg Biodiversity and Climate Research Centre, Frankfurt am Main, Germany

<sup>5</sup>Goethe University Frankfurt, Institute of Geosciences, Frankfurt am Main, Germany

<sup>6</sup>Department of Earth Sciences, NAWI Graz Geocenter, University of Graz, Austria

## Contents of this file

1. Figures S1 to S8
2. Tables S1

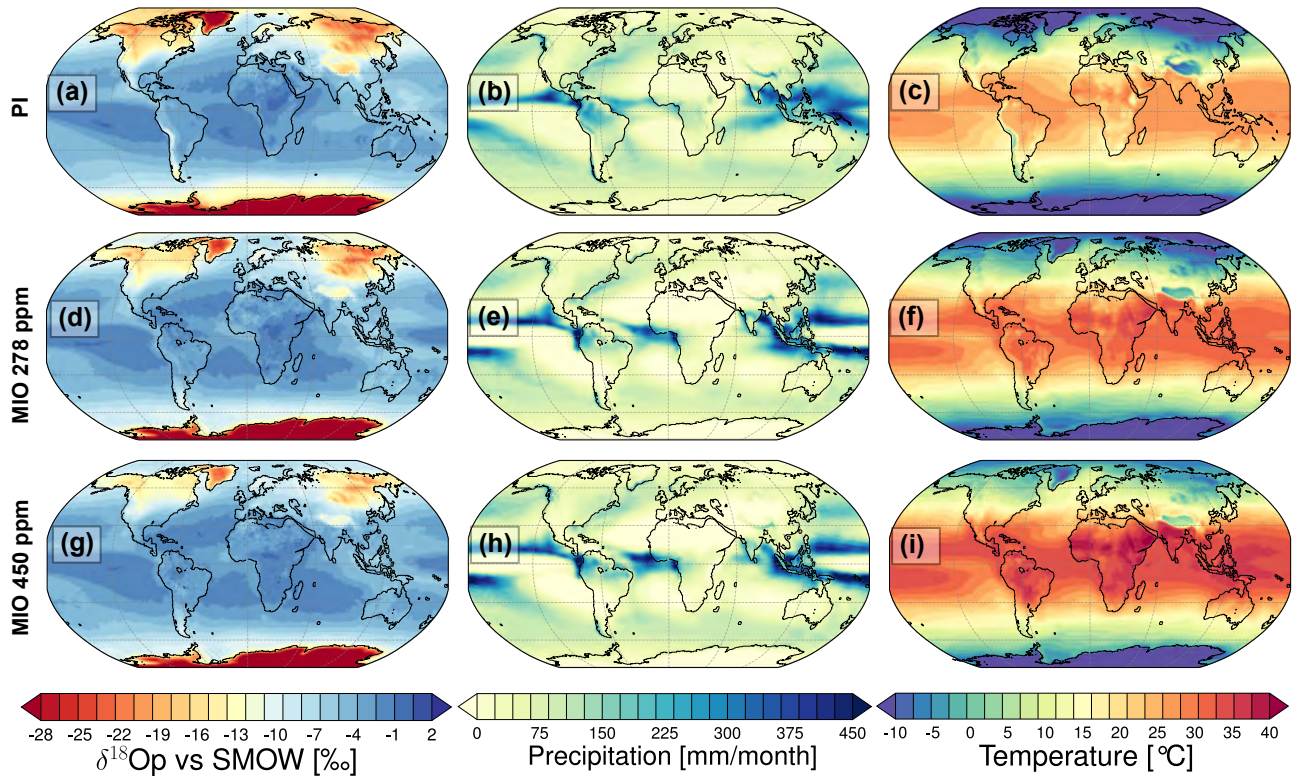


**Figure S1.** Annual means of  $\delta^{18}O_p$  values (first column), precipitation (second column) and near-surface temperature (third column) in response to Pre-Industrial (PI) and two Middle Miocene  $pCO_2$  scenarios (278 ppm (Mio278), 450 ppm (Mio450)).

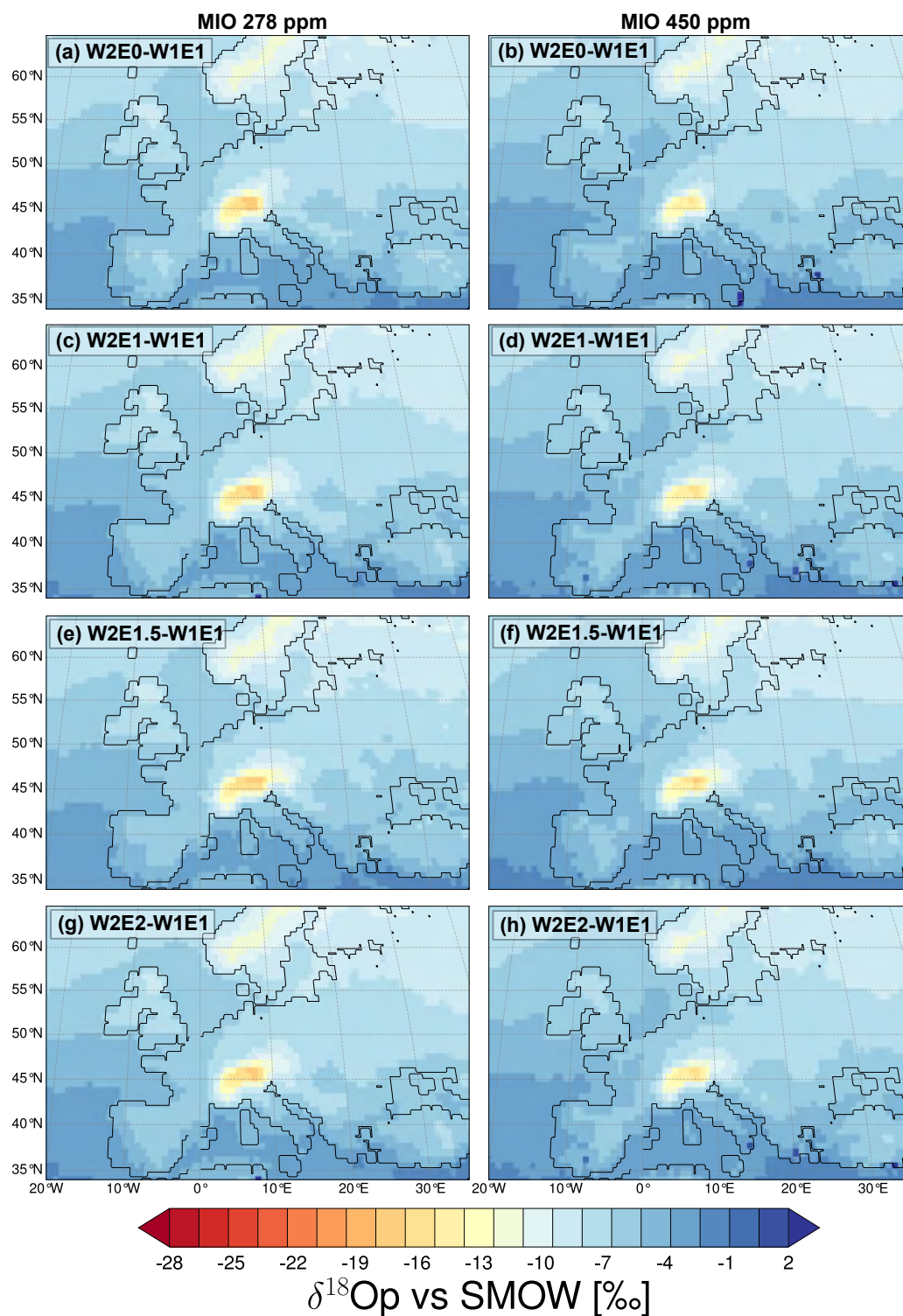


**Figure S2.** Annual means of  $\delta^{18}O_p$  values in response to the topographic configurations (i.e., W2E0 (a, b), W2E1 (c, d), W2E1.5 (e, f), and W2E2 (g, h)) in Middle Miocene conditions with  $pCO_2$  of 278 ppm (Mio278; left) and 450 ppm (Mio450; right)

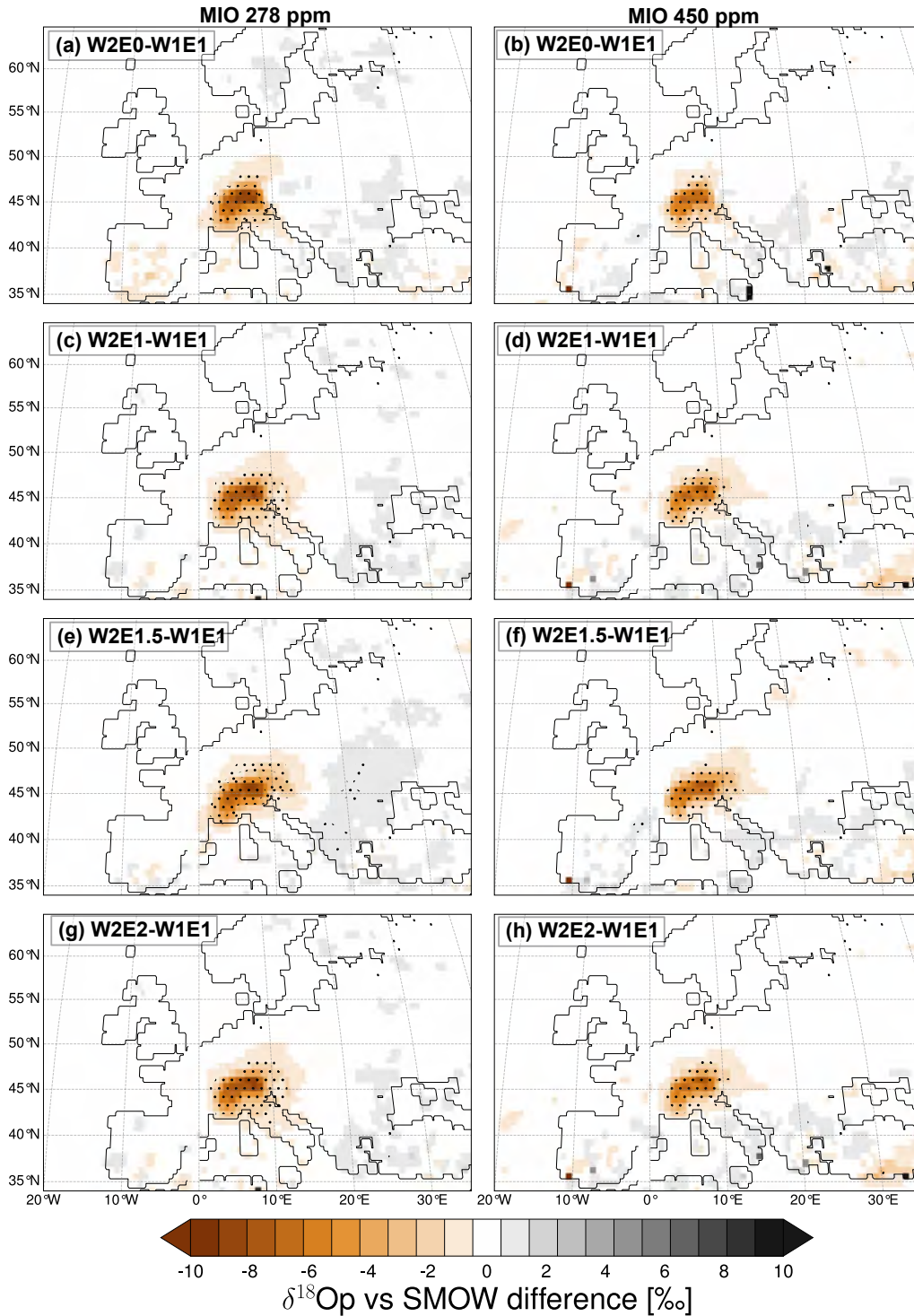


**Figure S3.** Mean annual difference of  $\delta^{18}O_p$  values in response to the different topographic scenarios (i.e., W2E0 (a, b), W2E1 (c, d), W2E1.5 (e, f), and W2E2 (g, h)) relative to control scenario (W1E1) with Middle Miocene boundary conditions (Mio278; left panel and Mio450; right panel)).

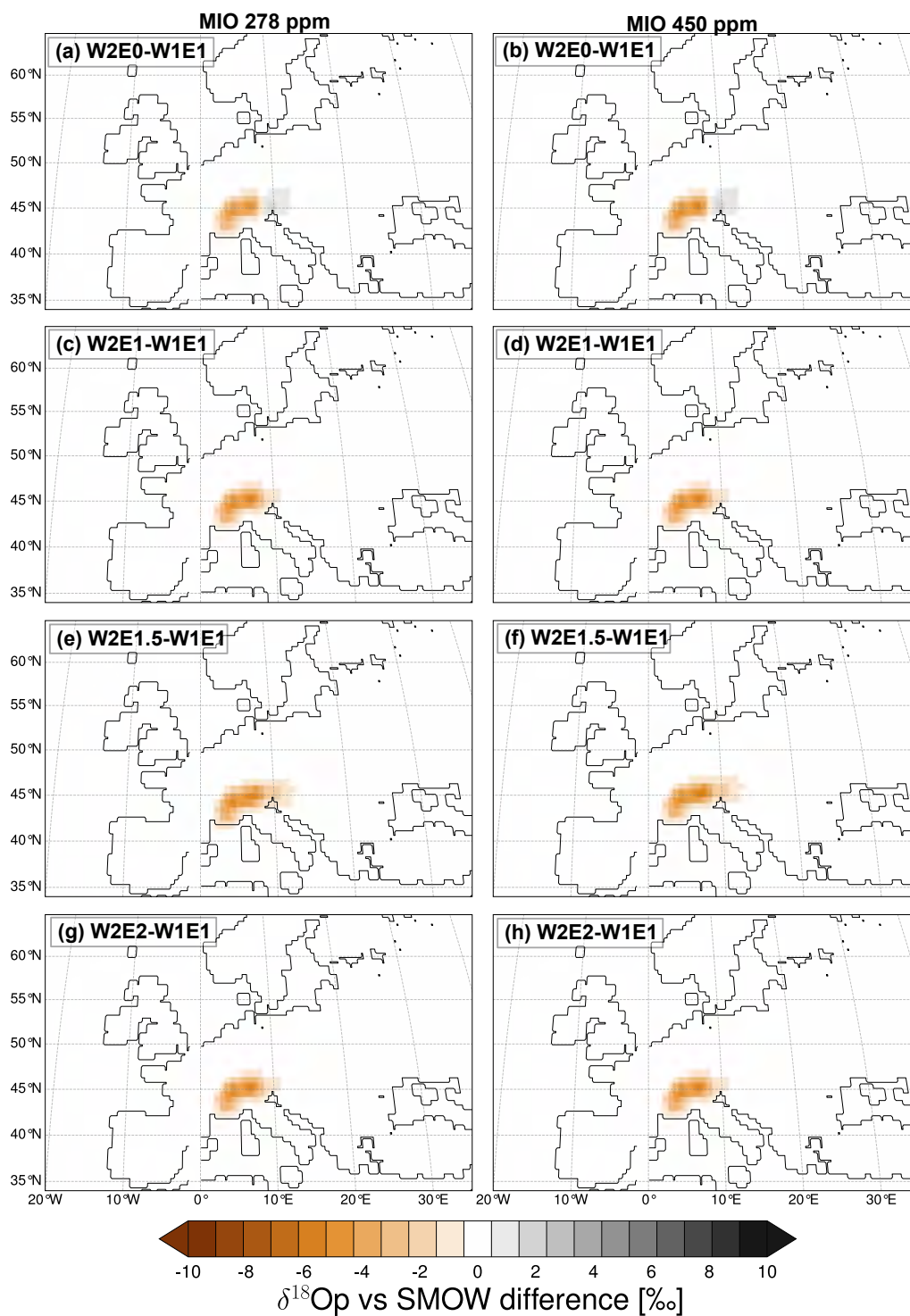


**Figure S4.** Expected  $\delta^{18}O_p$  values due to changes in topography using modern rainfall-based isotopic lapse rate (Campani et al. (2012))

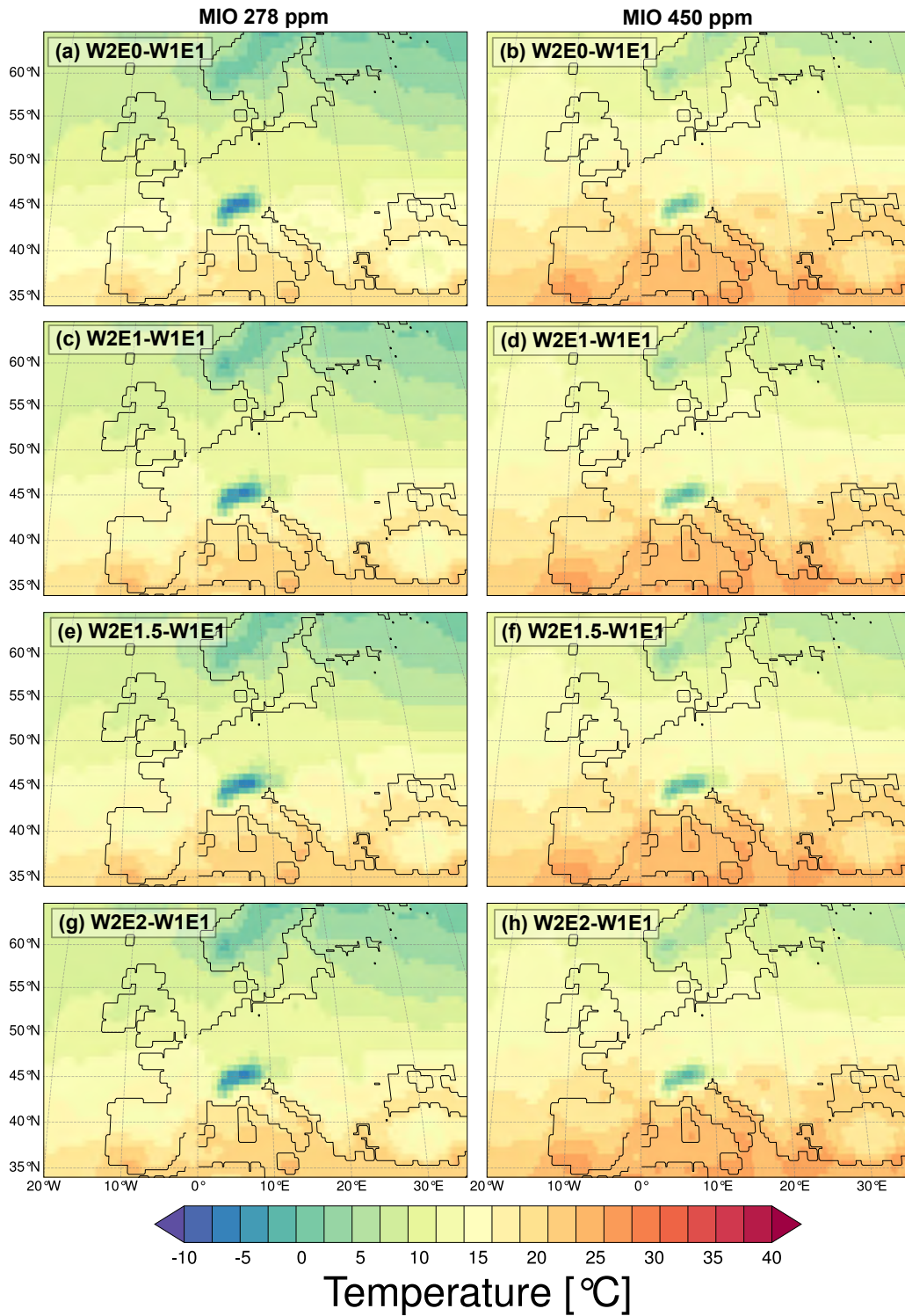


**Figure S5.** Annual means of temperature in response to the topographic configurations (i.e., W2E0 (a, b), W2E1 (c, d), W2E1.5 (e, f), and W2E2 (g, h)) in Middle Miocene conditions with  $p\text{CO}_2$  of 278 ppm (Mio278; left) and 450 ppm (Mio450; right).



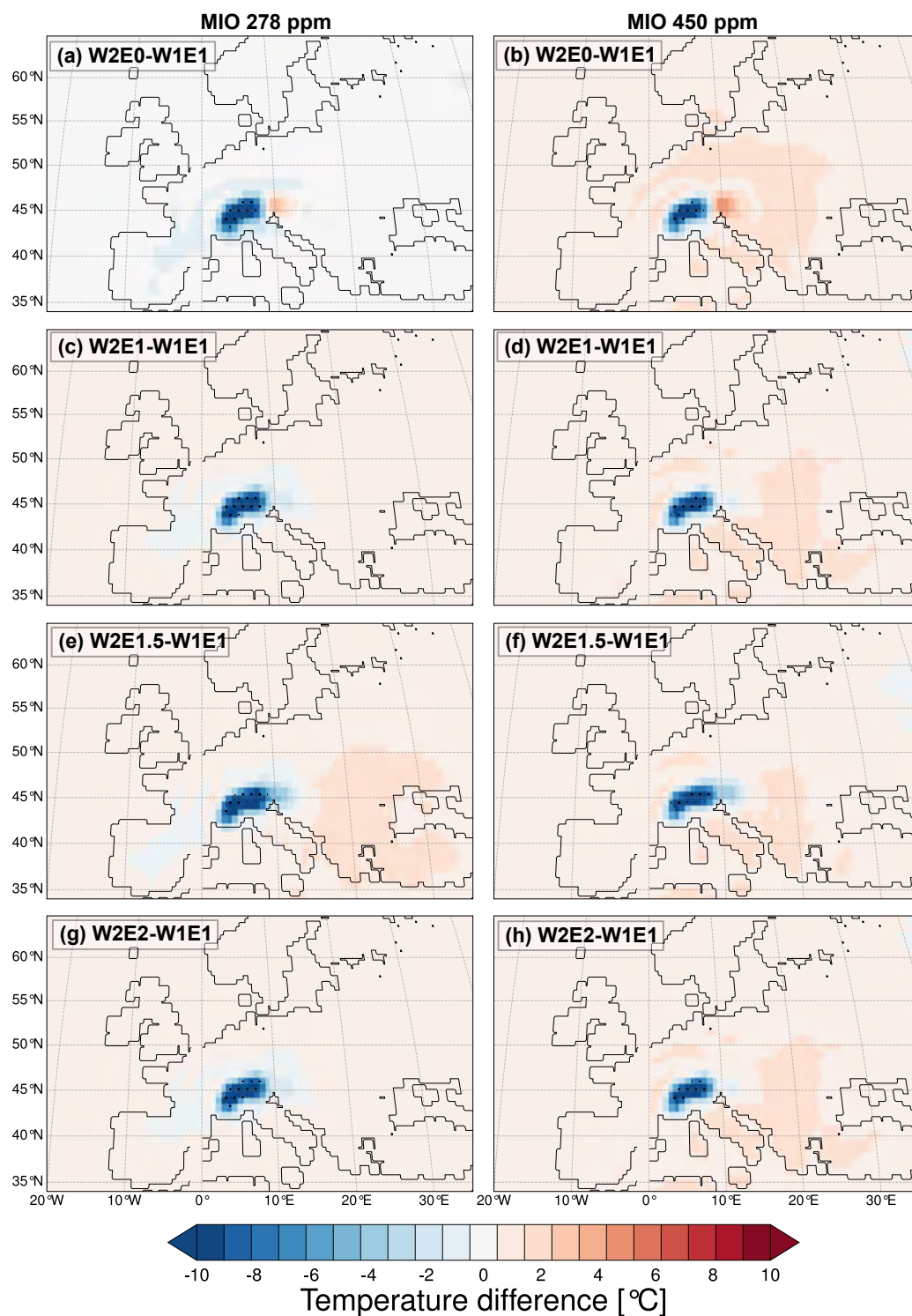


**Figure S6.** Mean annual difference of temperature in response to the different topographic scenarios (i.e., W2E0 (a, b), W2E1 (c, d), W2E1.5 (e, f), and W2E2 (g, h)) relative to control scenario (W1E1) with Middle Miocene boundary conditions (Mio278; left panel and Mio450; right panel))

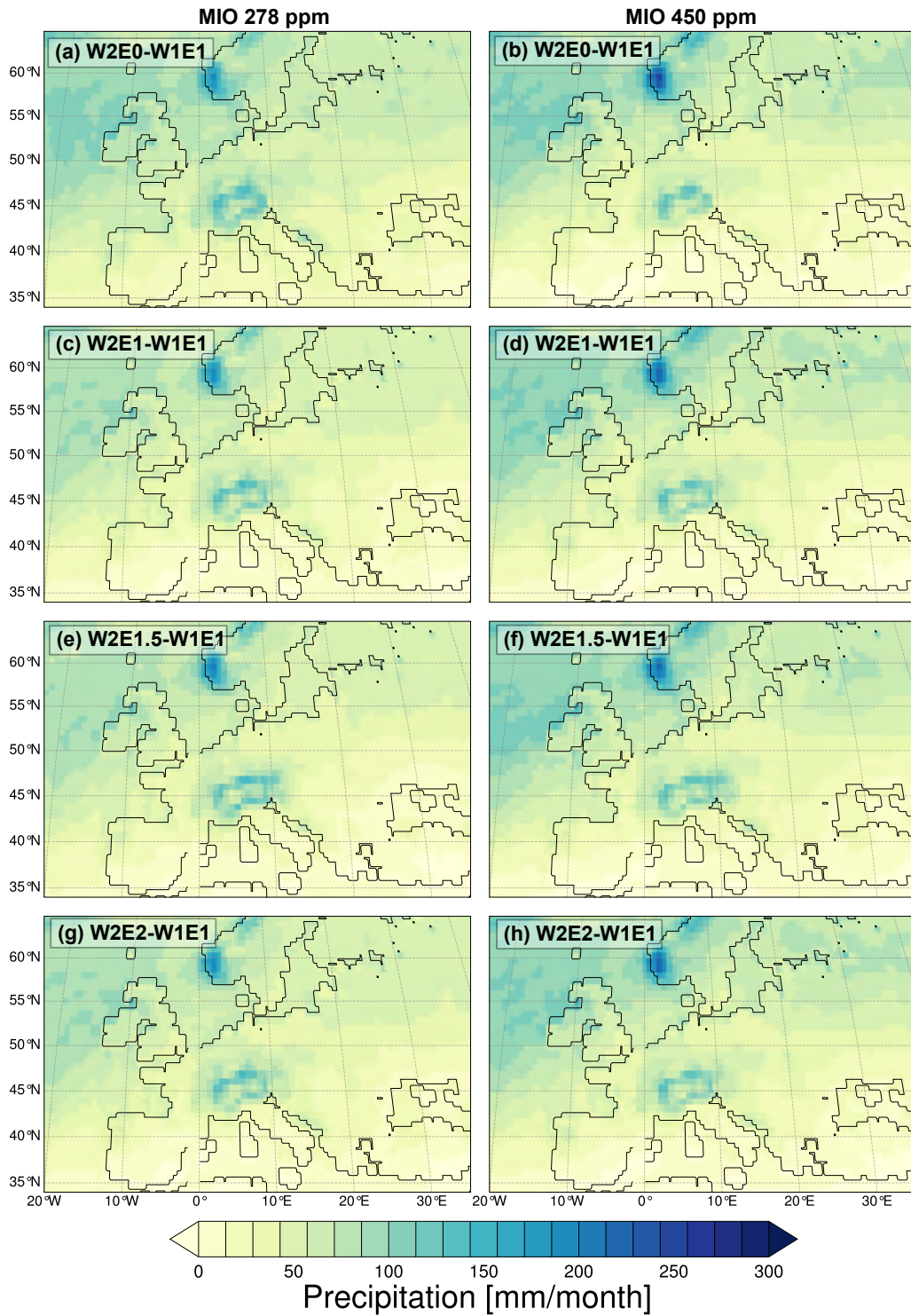


**Figure S7.** Annual means of precipitation in response to the topographic configurations (i.e., W2E0 (a, b), W2E1 (c, d), W2E1.5 (e, f), and W2E2 (g, h)) in Middle Miocene conditions with  $p\text{CO}_2$  of 278 ppm (Mio278; left) and 450 ppm (Mio450; right)

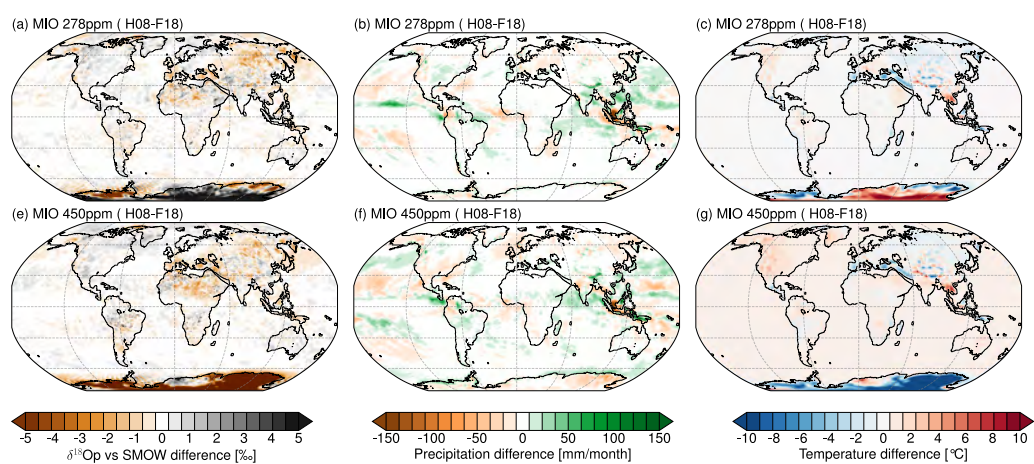


**Figure S8.** Annual mean difference between simulations with boundary conditions from Herold et al 2011 and Frigola et al 2018 for  $\delta^{18}O_p$  values, precipitation and temperature in response to two Middle Miocene  $pCO_2$  scenarios (278 ppm (Mio278), left panel; 450 ppm (Mio450))

High-elevation site (Phyllosilicates)	Low-elevation sites (Paedogenic carbonate)				
	SFZ	SMB (Fontannen 2012)	SMB (Fontan- nen)	SMB (Jona)	SMB (Aabach)
$\delta^{18}\text{Ow}(\text{‰}, \text{vsSMOW})$	-14.6	-9.4	-6.5	-5.8	-3.1
Error $\delta^{18}\text{Ow}(\pm; \text{‰})$	0.3	0.01	0.01	0.20	0.30
$\Delta(\delta^{18}\text{Ow})(\text{‰}, \text{vsSMOW})$	-	-5.2	-8.1	-8.8	-11.5
<b>Isotopic Lapse Rate (<math>\text{‰}/\text{km}</math>)</b>					
<b>Paleoelevation (<math>\Delta z</math>) calculation (m)</b>					
Campani et al. (2012)	-2.0	2600	4050	4400	5750
Poage and Chamberlain (2001)	-2.8	1857	2893	3143	4107
<b>Northern transect</b>					
W1E1 (Mio278)	-2.43	2140	3333	3621	4733
W1E1 (Mio450)	-2.48	2097	3266	3548	4637
W2E1 (Mio278)	-4.17	1247	1942	2110	2758
W2E1 (Mio450)	-3.85	1351	2104	2286	2987
<b>Western transect</b>					
W1E1 (Mio278)	-2.02	2574	4010	4356	5693
W1E1 (Mio450)	-2.18	2385	3716	4037	5275
W2E1 (Mio278)	-2.81	1851	2883	3132	4093
W2E1 (Mio450)	-2.36	2203	3432	3729	4873

**Table S1.** Summary of Miocene Central Alps paleoelevation estimates based on simulated and observed isotopic lapse rates

**Part VI.**

Appendix



# Manuscripts for Part 2 (P4, S1)

## 1 P4: Boateng et al. [3]

(P4) Boateng, D., Aryee, J. N. A., Baidu, M., Arthur, F., and Mutz, S. G.: West African Monsoon dynamics and its control on stable oxygen isotopic composition of precipitation in the Late Cenozoic, Preprints (Accepted in JGR Atmosphere (DOI:10.1029/2024JD040748) and in production), <https://doi.org/10.22541/essoar.170560461.19493225/v1>, 2024.

1 P4: Boateng et al. [3] . . . . . 207





2 S1: supporting results  
for NAO- $\delta^{18}O_p$  non-  
stationarity . . . . . 243



## RESEARCH ARTICLE

10.1029/2024JD040748

# West African Monsoon Dynamics and Its Control on the Stable Oxygen Isotopic Composition of Precipitation in the Late Cenozoic

Daniel Boateng<sup>1</sup> , Jeffrey N. A. Aryee<sup>2</sup> , Michael Baidu<sup>3</sup>, Frank Arthur<sup>4</sup> , and Sebastian G. Mutz<sup>5</sup> 

<sup>1</sup>Department of Geosciences, University of Tübingen, Tübingen, Germany, <sup>2</sup>Department of Meteorology and Climate Science, Kwame Nkrumah University of Science and Technology, Kumasi, Ghana, <sup>3</sup>Institute for Climate and Atmospheric Science, School of Earth and Environment, University of Leeds, Leeds, UK, <sup>4</sup>Department of Natural Sciences and Environmental Health, University of South-Eastern Norway, Bø i Telemark, Norway, <sup>5</sup>School of Geographical and Earth Sciences, University of Glasgow, Glasgow, UK

### Key Points:

- We simulate the Late Cenozoic evolution of the West African Monsoon and the isotopic composition of rainwater
- Using a high-resolution model setup and realistic vegetation cover increases the intensity of the West African Monsoon in the Mid-Holocene due to the pronounced meridional temperature gradient
- The relationship between precipitation and the simulated isotopes is non-stationary in time, which complicates proxy climate reconstructions

### Supporting Information:

Supporting Information may be found in the online version of this article.

### Correspondence to:

D. Boateng,  
[daniel.boateng@uni-tuebingen.de](mailto:daniel.boateng@uni-tuebingen.de)

### Citation:

Boateng, D., Aryee, J. N. A., Baidu, M., Arthur, F., & Mutz, S. G. (2024). West African Monsoon dynamics and its control on the stable oxygen isotopic composition of precipitation in the Late Cenozoic. *Journal of Geophysical Research: Atmospheres*, 129, e2024JD040748. <https://doi.org/10.1029/2024JD040748>

Received 5 JAN 2024  
Accepted 5 MAY 2024

### Author Contributions:

**Conceptualization:** Daniel Boateng  
**Formal analysis:** Daniel Boateng  
**Funding acquisition:** Sebastian G. Mutz  
**Investigation:** Daniel Boateng  
**Methodology:** Daniel Boateng, Jeffrey N. A. Aryee, Michael Baidu, Frank Arthur  
**Software:** Daniel Boateng  
**Supervision:** Sebastian G. Mutz  
**Validation:** Daniel Boateng, Jeffrey N. A. Aryee, Michael Baidu  
**Visualization:** Daniel Boateng  
**Writing – original draft:** Daniel Boateng

**Abstract** This study presents an overview of the Late Cenozoic evolution of the West African Monsoon (WAM), and the associated changes in atmospheric dynamics and oxygen isotopic composition of precipitation ( $\delta^{18}\text{O}_p$ ). This evolution is established by using the high-resolution isotope-enabled GCM ECHAM5-wiso to simulate the climatic responses to paleoenvironmental changes during the Mid-Holocene (MH), Last Glacial Maximum (LGM), and Mid-Pliocene (MP). The simulated responses are compared to a set of GCM outputs from Paleoclimate Model Intercomparison Project Phase 4 (PMIP4) to assess the added value of a high resolution and model consistency across different time periods. Results show WAM magnitudes and pattern changes that are consistent with PMIP4 models and proxy reconstructions. ECHAM5-wiso estimates the highest WAM intensification in the MH, with a precipitation increase of up to 150 mm/month reaching 25°N during the monsoon season. The WAM intensification in the MP estimated by ECHAM5-wiso (up to 80 mm/month) aligns with the mid-range of the PMIP4 estimates, while the LGM dryness magnitude matches most of the models. Despite an enhanced hydrological cycle in MP, MH simulations indicate a ~50% precipitation increase and a greater northward extent of WAM than the MP simulations. Strengthened conditions of the WAM in the MH and MP result from a pronounced meridional temperature gradient driving low-level westerly, Sahel-Sahara vegetation expansion, and a northward shift of the Africa Easterly Jet. The simulated  $\delta^{18}\text{O}_p$  values patterns and their relationship with temperature and precipitation are non-stationarity over time, emphasizing the implications of assuming stationarity in proxy reconstruction transfer functions.

**Plain Language Summary** We use a global climate model to simulate how the West African Monsoon and related climate elements changed over the Late Cenozoic (from ca. 3 million years ago to now). We use a single, high-resolution model to calculate these changes for the Mid-Holocene, Last Glacial Maximum and Mid-Pliocene time periods. We then compare our results to already existing simulations to find out if there are any benefits to using a single, high-resolution model set-up. Overall, our simulations are similar to previous simulations and other climate reconstructions. However, our results also yield two important new findings: (a) our simulations reproduce some aspects of the monsoon better than previous simulations; (b) the chemical composition of rainwater, which is used by geologists to reconstruct climate, is impacted by more factors than previously assumed. This makes it more challenging to create reliable reconstructions of climate from geological records of rainwater composition.

## 1. Introduction

Understanding the complex climate dynamics and variability over West Africa has been a pertinent concern due to its strong environmental and socio-economic impacts. This is especially important since most West African countries rely on a rainfed agriculture economy (Sultan et al., 2005). Most importantly, the long-lasting multi-decadal wet and dry periods during the 20th century emphasize the need to understand the long-term and future variability of the West African Monsoon (WAM) system. This requires knowledge about the response of the WAM dynamics to changes in internal feedbacks and external forcings, such as orbital parameters, atmospheric greenhouse gases, and vegetation distribution. Considering past climate change outside the recent observational period can provide valuable insights into that. More specifically, time periods with atmospheric  $\text{CO}_2$

© 2024 The Authors.

This is an open access article under the terms of the [Creative Commons Attribution-NonCommercial License](https://creativecommons.org/licenses/by/4.0/), which permits use, distribution and reproduction in any medium, provided the original work is properly cited and is not used for commercial purposes.



Writing – review & editing: Jeffrey N. A. Aryee, Michael Baidu, Frank Arthur, Sebastian G. Mutz

concentrations ( $p\text{CO}_2$ ) and paleogeography similar to the present day can serve as analog for a possible future climate in which all forcings have had their full effect. This would require looking back 3 million years in Earth's history (Burke et al., 2018). Therefore, this study focuses on a model-based exploration of the evolution of the WAM from the Mid-Pliocene (MP:  $\sim 3$  Ma) to the present-day, considering the Last Glacial Maximum (LGM:  $\sim 21$  ka), and Mid-Holocene (MH:  $\sim 6$  ka) as important intermediate time steps.

Due to the complicated dynamics and teleconnections of the WAM, state-of-art General Circulation Models (GCMs) still fall short in accurately reproducing its past variability and providing consistent future projections (Biasutti, 2013; Pausata et al., 2016; Tierney et al., 2017). Improving the representation of the WAM system in climate models requires knowledge about its sensitivity to various global and regional paleoenvironment forcings and feedbacks. This knowledge can help identify the elements that need improvement in GCMs to ensure more reliable predictions of the WAM in the future. For instance, the response of the WAM dynamics to orbitally driven seasonal and latitudinal distribution of incoming solar radiation can be evaluated under MH conditions (Joussaume et al., 1999; Kutzbach & Liu, 1997). The LGM provides an opportunity to study the response of the WAM to the most recent global cold extreme, characterized by extensive ice sheet coverage and low  $p\text{CO}_2$  concentrations (e.g., Bereiter et al., 2015). The long-term sensitivity of the WAM to  $p\text{CO}_2$  concentrations similar to the present, along with a less arid Sahara and a globally enhanced hydrological cycle, can also be assessed under MP paleoenvironment conditions (Corvec & Fletcher, 2017; Dowsett et al., 2010; Haywood et al., 2020; Salzmann et al., 2008).

Despite the challenges in replicating the entirety of past climate changes with GCMs under appropriate paleoenvironmental conditions (Braconnot et al., 2012; Harrison et al., 2015), comparing the simulated responses from different climate models would shed more light on the inadequate representation of feedbacks and model biases that can be improved for future climate predictions (e.g., Zheng & Braconnot, 2013). Furthermore, such inter-model comparison across multiple past climates would help determine if the systematic model biases affect the overall strength of the responses and feedbacks in the different climates and help evaluate if such biases are GCM-specific or exist independently of the GCM that is used.

Numerous modeling studies have simulated the precipitation changes associated with the WAM in response to multiple forcings and climate states during the Late Cenozoic (e.g., Berntell et al., 2021; Weldeab et al., 2011; Zheng & Braconnot, 2013). However, the differences between the simulations, such as spatial resolution, boundary conditions, and the complexity of the GCM, make it difficult to identify the predominant atmospheric dynamics behind the WAM precipitation changes. For instance, model-dependent uncertainties of the individual GCMs that simulated these climates in previous studies may not fully capture certain components of the WAM system, which can amplify the systematic biases related to the sensitivity to various forcings or external perturbations across different climates. Moreover, GCMs with varied spatial resolutions and parameterizations of clouds, atmospheric dynamics, hydrological cycles, and atmosphere-land surface interactions would simulate distinct responses of the WAM to different forcings, leading to inconsistent patterns of WAM dynamics. Aside from these, only a few studies have comprehensively delved into atmospheric dynamics and teleconnections behind the changes in precipitation patterns and magnitudes under different paleoenvironmental conditions throughout the Late Cenozoic (e.g., Bosmans et al., 2012; Gaetani et al., 2017; Patricola & Cook, 2007; Su & Neelin, 2005). Furthermore, previous studies have highlighted that monsoons and related circulations, such as the Inter Tropical Convergence Zone (ITCZ), are better resolved at higher resolutions, including improved topographical representation and model parameterization (Bosmans et al., 2012; Gao et al., 2006; Jungandreas et al., 2021). This study addresses the points above by providing details about the WAM atmospheric dynamics across these past climates using a consistent modeling framework with a high-resolution isotope-enabled GCM.

Geological archives can record information about various paleoenvironmental changes in the climate system over time. They can therefore be used for model-data comparisons and as a benchmark for climate models (Braconnot et al., 2012; Harris et al., 2014; Harrison et al., 2015). However, the scarcity of palaeohydrological records over Africa and the spatial resolution of climate models preclude the robust model-data comparison necessary for improving climate models (e.g., Salzmann et al., 2008, 2013). Several problems for data-model persist in this region. For instance, proxy-based reconstructions using pollen, past lake levels, leaf wax isotopes, and other records have suggested significantly wetter conditions across the Sahel and Sahara during the MH (Ait Brahim et al., 2023; Bartlein et al., 2011; Tierney et al., 2017). However, most climate models struggle to replicate the extent and magnitude of precipitation changes indicated by these proxy records despite accounting for factors like

increased insolation, altered land surface condition (e.g., vegetation, lakes, orography, soil moisture), reduced dust emissions, atmospheric-ocean interactions, and atmospheric dynamics (deMenocal et al., 2000; Harrison et al., 2014; Hopcroft & Valdes, 2019, 2022; Pausata et al., 2016; Tierney et al., 2017).

While proxy records point to varying increases in precipitation levels over North Africa's higher latitudes, climate models estimate a more moderate WAM intensification, underestimating both the northward extent and magnitude of precipitation increase suggested by the proxies. If the proxy data is a well-collected, representative sample, there are two possible model-related reasons for this mismatch: (a) The climate models simply do not capture the atmospheric processes in the region well enough to accurately model said hydroclimate changes. (b) Proxy system models, which allow the conversion of the proxy signal to a paleoclimate signal, are flawed. Proxy system models rely on calibrations based on modern-day observations, such as the spatial correlation between water isotopes and precipitation. These are used to establish a transfer function that allows a proxy-to-climate signal conversion. This signal transformation assumes that the transfer functions are stationary in time, that is, that modern correlations are equally valid for past climates. This study uses an isotope-enabled GCM to decipher atmospheric dynamics driving WAM changes and to explore their impacts on water isotopologues under various past global changes. This allows for the testing of this assumption of the stationarity of the transfer function. Furthermore, such an analysis facilitates a direct model-isotope proxy comparison and contributes to understanding the general causal mechanisms behind the variability in different proxy materials (Bühler et al., 2022; Phipps et al., 2013; Risi et al., 2012; Werner et al., 2000).

This study provides the first overview of the changes of the WAM and its associated atmospheric dynamics in response to multiple forcings and feedbacks during the Late Cenozoic, using the high-resolution isotope-enabled GCM ECHAM5-wiso. More specifically, the study addresses the following specific objectives: (a) systematically simulating the responses of the WAM patterns and magnitude to the various paleoenvironment conditions, including changes in vegetation, orbital forcings, ice sheet extent, and atmospheric CO<sub>2</sub> concentrations; (b) investigating the atmospheric dynamics driving the simulated WAM changes, such as moisture transport (e.g., low-level southwesterlies), Africa Easterly Jet (AEJ), Tropical Easterly Jet (TEJ), Sahara Heat Low (SHL) and surface heat fluxes; and (c) exploring the simulated  $\delta^{18}\text{O}_p$  values and how they are influenced by near-surface temperature and precipitation in response to the different boundary conditions. We further compare the simulated changes of the WAM to some of the state-of-the-art models that participated in the Paleoclimate Model Intercomparison Project (PMIP4) Phase 4 to evaluate the added values of using a consistent, high-resolution modeling framework to understand the complex climate system over West Africa and improve its representation in Earth system models.

## 2. Background

### 2.1. On the Intensification and Northward Extent of the West African Monsoon During the Mid-Holocene

During the early-to-middle Holocene, spanning from 11,000 to 5,000 years before the present, the arid landscapes of the Sahel and Sahara regions transformed into shrubs, grasslands, and water bodies like rivers and lakes (Armitage et al., 2015; Claussen et al., 1999; deMenocal et al., 2000; Holmes, 2008; Kohfeld & Harrison, 2000). The development of this “Green Sahara” was attributed to changes in the insolation cycle, which intensified the equator-to-pole gradient and land-sea thermal contrasts and ultimately lead to an increase in rainfall across the Sahel-Sahara. The associated pressure gradient facilitated the moisture transport from the equatorial Atlantic into the continent. Overall, the changes in the orbital cycles and expansion of vegetation across the Sahel-Sahara caused the strengthening of the WAM and its northward extent (Gaetani et al., 2017; Hopcroft & Valdes, 2022; Patricola & Cook, 2007). This WAM intensification and northward migration have been reflected in many proxy systems such as paleo-lake levels (Hoelzmann et al., 1998; Prentice et al., 2000), leaf wax, and aeolian deposits in sedimentary cores from the Eastern Atlantic (deMenocal et al., 2000; Tierney et al., 2017) and archeological findings that indicate human habitation (Cremaschi & Di Lernia, 1999; Dunne et al., 2012; Gabriel, 1987; Hoelzmann et al., 2001; Manning & Timpson, 2014; Sereno et al., 2008). However, state-of-art climate models still struggle to replicate the level of intensification and the northward reach as suggested by the different proxies, even when appropriate boundary conditions are prescribed (deMenocal et al., 2000; Harrison et al., 2014; Hopcroft & Valdes, 2019; Kutzbach & Liu, 1997; Pausata et al., 2016; Tierney et al., 2017). For instance, MH simulations in PMIP3-CMIP5 experiments estimate a precipitation increase of ~400 mm/year over West Africa, with a northward shift that is underestimated by 20°N when compared to proxy reconstructions

(Perez-Sanz et al., 2014). Thompson et al. (2021) utilized a water isotope-enabled Earth system model (iCESM1) that exhibited enhanced MH precipitation compared to PI conditions, and a northernmost WAM shift of approximately 24°N, which aligns with reconstructions from pollen and dust records (23–28°N). Most of these models, however, lack vegetation feedback or appropriate prescribed MH vegetation reconstruction, which is crucial for sustaining the WAM's northward extension through vegetation-precipitation feedback (Otto-Bliesner et al., 2017; Pausata et al., 2016; Tierney et al., 2017). Rachmayani et al. (2015) demonstrated that using dynamic vegetation-coupled GCMs enhances the orbitally-induced precipitation increase by 20% over West Africa compared to fixed vegetation GCMs.

Recent studies have also highlighted that accounting for dust feedbacks related to the Green Sahara during the MH can further intensify and expand the WAM, aligning it more with proxy reconstructions (e.g., Egerer et al., 2018; Hopcroft & Valdes, 2019; Pausata et al., 2016; Thompson et al., 2019). These findings indicate that the discrepancies between the model and proxy reconstructions are due to the inadequate representation of certain atmospheric physics, such as inaccurate cloud representation, energy fluxes, subgrid-scale convection, and surface conditions in the GCMs. Moreover, the coarse spatial resolution of GCMs fails to capture meso-to-local-scale processes like mesoscale convective systems (e.g., Baidu et al., 2022; Crook et al., 2019; Marsham et al., 2013), potentially contributing to further biases. Thus, understanding the mechanics and dynamics underlying vegetation feedback and natural variability in insolation cycles driving the WAM's northward migration during the MH is crucial for evaluating GCM performance in future projections. While these forcing mechanisms are not linked to anthropogenic emissions, evaluating and improving the GCMs' representation of climate system dynamics and feedbacks is vital for future climate change projections.

## 2.2. Large-Scale Feature of the Last Glacial Maximum and Its Influence on the West African Monsoon

The LGM (~21,000 years BP) is a time period that is suitable for assessing the capabilities of state-of-the-art models due to its starkly different conditions from the present, such as lower atmospheric CO<sub>2</sub> levels (~185 ppm) and eustatic sea levels (~115–130 m below present) (Lambeck et al., 2014; Peltier & Fairbanks, 2006). The extensive continental ice sheets led to significant perturbations in atmospheric radiative forcing and circulation patterns, contributing to alterations in precipitation and temperature that were generally drier and colder than pre-industrial conditions (Clark et al., 2009; D'Agostino et al., 2019, 2020). Since the LGM, the Earth's global mean temperature has risen by approximately 4–6°C (Annan & Hargreaves, 2013, 2015; Friedrich et al., 2016), which is of the same order of magnitude increase projected under moderate to high emission scenarios for near-future climate change. Due to this similarity in global forcing and temperature response from the LGM to the present, and the present to the near future, the LGM is a relevant period to examine (e.g., Brady et al., 2013; Yoshimori et al., 2009). The LGM represents a test bed to conduct the out-of-sample evaluation of the strength and stability of key climate system feedbacks and large-scale responses to regional hydroclimate changes. Furthermore, the interactions between temperature-driven and circulation-driven regional precipitation patterns in response to LGM conditions would help evaluate the ability of climate models to project precipitation under future scenarios, where both thermodynamic and dynamic phenomena contribute to changes in the magnitude and seasonality of precipitation patterns (e.g., Boos, 2012; Lora, 2018; Scheff & Frierson, 2012).

Prior studies have indicated a high sensitivity of Africa's climate to rapid recurring ice sheet instabilities during the last glacial period (Adegbie et al., 2003; Stager et al., 2002, 2011; Weldeab et al., 2011). For example, the cold air temperatures over Greenland (Dansgaard-Oeschger stadials) and the influx of meltwater into the North Atlantic during Heinrich events correlated with the rapid decline in precipitation across much of Africa (Blunier & Brook, 2001; Dansgaard et al., 1993; McManus et al., 2004). Previous modeling studies of PMIP phases 1 to four indicated weakened atmospheric circulation and associated decreased precipitation over West Africa (Kageyama et al., 2021). However, a good understanding of the dynamics leading to the dryness across the WAM region is still lacking. The comparison of the atmospheric dynamics changes of the LGM to other warmer climates will help reveal the predominant atmospheric processes relevant to the variability of the WAM and help improve their representation in climate models for future climate projections.

Pollen-based reconstructions across the WAM and nearby offshore regions generally depict colder and drier conditions than the present (Bartlein et al., 2011). Although fully coupled atmosphere-ocean models can reasonably reproduce large-scale features of the LGM, several challenges remain with regard to the reconstruction of LGM topography and the assessment of inter-model biases for various climate feedbacks (Kageyama

et al., 2021; Werner et al., 2018). Additionally, the spatial resolution of simulations has been identified as a crucial factor for the inter-model variabilities in LGM simulations, primarily due to the representation of ice sheet topography (Kim et al., 2008; Shi et al., 2020). Overall, the complexity and diverse paleoenvironment of LGM conditions offers the opportunity to decipher the relative contributions of individual climate factors that influence precipitation changes across West Africa. The response of regional  $\delta^{18}\text{O}$  in precipitation distribution in the LGM would contribute to the interpretation of proxy signals to ensure robust model-data comparison that can be used to constrain the sensitivity of climate models.

### 2.3. Changes of the WAM in the Mid-Pliocene

The MP (~3 Ma) is an important warm period for understanding the atmospheric dynamics of near-future climate change, because the Earth's geography was similar to the present and  $p\text{CO}_2$  approached present-day values (~400 ppm) (Badger et al., 2013; Bartoli et al., 2011; Dowsett et al., 2016; Haywood et al., 2020; Salzmann et al., 2013; de la Vega et al., 2020). Additionally, the MP provides useful insights into climate feedbacks through the impact of the carbon cycle on geological times and is often considered an analog for a near-future climate (Burke et al., 2018; Jiang et al., 2005). Climate models that participated in the PlioMIP (Pliocene Modeling Intercomparison Project) phases 1 and 2 indicate an increase of 1.4–4.7°C in global mean near-surface anomalies above the pre-industrial levels, along with an enhanced hydrological cycle and strengthened global monsoons (Haywood et al., 2013, 2020; Zhang et al., 2016).

Proxy reconstructions suggest warm and humid conditions, and fewer deserts during the MP. Boreal forests and grasslands expanded into high northern latitude regions that are currently covered by tundra (Salzmann et al., 2008). Dust records along the coast of West Africa indicate a strengthened WAM and wetter conditions over the Sahara (Kuechler et al., 2018; Salzmann et al., 2008). Palynological records also suggest an expansion of vegetation over the WAM region, with high tree cover density and widespread woodland and savanna over the Sahara (Bonnefille, 2010; Salzmann et al., 2008).

Although previous modeling studies indicated that high-latitude warming could lead to a decreased meridional temperature gradient and a weakened tropical circulation, the warming experienced in the Sahara region, along with the corresponding Sahara heat low, actually caused an increased influx of moisture from the tropical Atlantic Ocean, strengthening WAM (Corvec & Fletcher, 2017; Haywood et al., 2020). More specifically, the PlioMIP2 models estimate an increase in precipitation anomalies in the range of 60–120 mm/month (Berntell et al., 2021), compared to a lesser increase of 30–60 mm/month from the PlioMIP1 (R. Zhang et al., 2016). Even though similar magnitude of changes are predicted for the future, models are still limited in capturing rainfall variability over West Africa, and future projections of it are referenced with less confidence (Biasutti, 2013; Cook, 2008; Roehrig et al., 2013). Further work and model development is needed to understand climate feedback over West Africa under high atmospheric  $\text{CO}_2$  conditions.

### 2.4. Stable Oxygen Isotopic Signal as Proxy for Reconstructing the West African Monsoon

Stable water isotopes serve as integrated tracers for diverse climate processes, and reflect changes in the water cycle (Craig & Gordon, 1965; Dansgaard et al., 1993). Consequently, they have been extensively used to investigate historical climate changes and characterize the current hydrological cycle. Reconstructions of the water cycle from proxy materials typically rely on modern calibrations. The modern spatial correlation between water isotopes and climate variables, such as precipitation amount or surface temperature, is used as a transfer function for reconstructing past climatic variations from proxies. However, these paleoclimate reconstructions from isotopic archives are compromised by changes in the transfer functions due to various non-linear climatic processes influencing the spatiotemporal variability of water isotopes, such as monsoon dynamics, evaporative recycling, moisture transport pathways, source variation, vapor mixing, and precipitation dynamics (Bony et al., 2008; Risi et al., 2008, 2013). For example, the oxygen isotopic composition of precipitation ( $\delta^{18}\text{O}_p$ ) reconstructed from calcite in speleothems from (sub)tropical regions is used to reconstruct past monsoon changes (e.g., Wang et al., 2001). However, the relationship between the cave  $\delta^{18}\text{O}$  record and monsoon dynamics is complex and changes across different timescales (e.g., East Asia summer monsoon intensity controls the past cave  $\delta^{18}\text{O}$  in orbital timescales (Cheng et al., 2016) while summer precipitation amount is suggested to reflect the cave  $\delta^{18}\text{O}$  in centennial-decadal timescales (Tan et al., 2009, 2018; H. Zhang et al., 2019)). Hence, GCMs with explicit diagnostics of stable water isotopes can contribute to understanding their controlling mechanisms under different

climatic conditions to ensure accurate paleoclimate reconstructions. Additionally, modeling the spatial representation of water isotopes in response to distinct past climate states aids in identifying potential non-stationarities in their relationships with climate elements like monsoon characteristics or precipitation amounts. While previous studies have employed water isotopes to understand present precipitation seasonality in West Africa (e.g., Risi et al., 2010) and even during the MH (Shi et al., 2023; Thompson et al., 2021), none have explored  $\delta^{18}\text{O}_p$  changes in response to Late Cenozoic paleoenvironmental conditions or assessed how water isotopes correspond to the spatial variability of precipitation and temperature during the WAM season.

### 3. Data and Methods

#### 3.1. ECHAM5-wiso General Circulation Model

Global climate changes in response to late Cenozoic paleoenvironmental conditions (i.e., PI, MH, LGM, and MP) and present-day (PD) conditions were simulated using the isotope-tracking climate model ECHAM5-wiso. ECHAM5 is the fifth generation of the well-established atmospheric general circulation model developed by the Max Planck Institute for Meteorology (Roeckner et al., 2003). It is based on the spectral forecast model of the European Center of Medium Range Weather Forecast (ECMWF) (Simmons et al., 1989) and represents the climate system with prognostic equations and parameterizations. Compared to its previous version, the fifth version has improved the representation of land surfaces, shortwave radiation, cumulus convection, and other factors relevant to atmospheric dynamics across the monsoon region. Specifically, the model employs an implicit scheme for the coupling of land surfaces and the atmosphere, enabling synchronous calculation of surface fluxes due to unconditional stability (Roeckner et al., 2003). It also employs land surface parameters that effectively portray the global distribution of major ecosystem types (Hagemann, 2002). Furthermore, the model simulates clouds using prognostic equations for all water phases (vapor, liquid, and solid), bulk microphysics, and statistical cloud cover parameterization (Lohmann & Roeckner, 1996; Tompkins, 2002). The version employed in this study has been expanded to include isotope tracking capabilities, enabling the simulation of the water's isotopic composition as part of the hydrological cycle (Werner et al., 2011). The incorporated water isotopologues (i.e.,  $\text{H}_2^{16}\text{O}$ ,  $\text{H}_2^{18}\text{O}$ , and HDO) function as independent tracers that undergo both kinetic and equilibrium fractionation during phase transitions in the atmosphere. Comparing the simulated annual mean  $\delta^{18}\text{O}_p$  values with observed GNIP stations for present-day (1979–2014) indicates very similar patterns globally and a linear fit with coefficient of determination ( $R^2$ ) of 0.88 and mean squared error (MSE) of 1.39‰ (Figure S11 in Supporting Information S1). This model-data agreement of ECHAM5-wiso has also been demonstrated in previous studies (Hagemann et al., 2006; Werner et al., 2011), highlighting that the model adequately represents the global hydrological cycle and stable isotopic composition. We further compare the model's present-day simulations with observed and reanalysis precipitation and near-surface temperature data sets across West Africa to assess its capability in representing WAM patterns and their seasonality.

#### 3.2. Model Experiments and Boundary Conditions

Previous simulations of Late Cenozoic climate were conducted with different models and model setups. Varied parameterization schemes, spatial resolution, and prescribed boundary conditions complicate the comparison of the regional climates across the considered time periods. We therefore conducted (paleo)climate simulations for PD, PI, MH, LGM, and MP boundary conditions using only ECHAM5-wiso, while maintaining the same spatial resolution. All climate simulation experiments were performed using a high T159 spectral resolution ( $\sim 80 \times 80$  km around the equator) and 31 vertical levels up to 10 hPa. The model uses prescribed sea surface temperature (SST) as the interface between the ocean and atmosphere and, therefore, requires less time to reach dynamic equilibrium than fully coupled atmosphere-ocean models. However, the prescribed SSTs disregard oceanic decadal variability, making the simulated response inevitably biased by the specific SST reconstructions used. The paleoclimate experiments were run for 18 years with a 6-hr model output and only considered the last 15 years for the analysis. The first 3 years of the model serve as the spin-up period, which is the time required for the model to reach dynamic equilibrium. Given the study's aim to understand the WAM response to the diverse paleoenvironmental conditions, the different experimental set-ups accounting for variations in orbital parameters, greenhouse gases concentration, SSTs, sea ice concentrations (SICs), and land surface cover (e.g., ice sheet and vegetation) were devised for the different climates. The prescribed boundary conditions for the experiments are similar to the Late Cenozoic simulations presented by Mutz et al. (2018) and Botsyun et al. (2022). We build on those by simulating and analyzing the isotopic compositions for all paleoclimates.

To validate the model's ability to represent WAM dynamics, we compared the present-day (PD) simulation conducted by Boateng et al. (2023) with observed and reanalysis precipitation and near-surface temperature data sets. The PD simulation setup follows the Atmospheric Model Intercomparison Project (AMIP) protocol, using prescribed annual means of SST and SIC from 1979 to 2014. The pre-industrial simulation (the reference year 1850) was also obtained from Boateng et al. (2023). The model was simulated with prescribed SST and SIC from a transient coupled ocean-atmosphere model (Lorenz & Lohmann, 2004). It used an atmospheric CO<sub>2</sub> concentration of 280 ppm in accordance with Dietrich et al. (2013), which was derived from the ice-core record (Etheridge et al., 1996, 1998). Land surface parameters were taken from Hagemann (2002). The initial isotopic composition of the atmosphere was adopted from global gridded data of <sup>18</sup>O composition of seawater provided by LeGrande and Schmidt (2006). In this study, the climate change signals are defined as deviations from the PI estimates. Therefore, all reported anomalies (e.g., MH-PI) throughout the paper, described as either “increases” or “decreases,” use the simulated PI values as a reference. We also represent the H<sub>2</sub><sup>18</sup>O composition using the  $\delta$ -notation and calculate it as precipitation-weighted means using the Vienna Standard Mean Ocean Water (V-SNOW).

The SST and SIC boundary conditions prescribed for the MH experiments were derived from transient MH simulation of a low-resolution ocean-atmosphere coupled model (Etheridge et al., 1996, 1998; Lohmann et al., 2013; Wei & Lohmann, 2012). The GHG concentrations (e.g., CO<sub>2</sub> of 280 ppm) are based on ice-core reconstructions (Etheridge et al., 1996, 1998), and the orbital forcing parameters are taken from Dietrich et al. (2013). On the other hand, the LGM simulation was forced with sea surface variables from reconstructions for the Atlantic, Pacific, and Indian oceans based on the GLAMAP (Sarnthein et al., 2003) and CLIMAP (1981) projects. Moreover, the GHG concentrations (CO<sub>2</sub> of 185 ppm) and orbital parameters follow Otto-Bliesner et al. (2006). The paleogeography and ice sheet extent and thickness are based on the PMIP3 experimental protocol (Abe-Ouchi et al., 2015). The vegetation distribution maps for both the LGM and MH are based on the reconstruction of plant functional types from BIOME 6000 of the paleovegetation mapping project (Bigelow et al., 2003; Harrison et al., 2001; Pickett et al., 2004; Prentice et al., 2000). The MP paleoenvironment conditions prescribed in the ECHAM5 model were based on the Pliocene Research, Interpretation, and Synoptic Mapping (PRISM) project (Dowsett et al., 2010; Haywood et al., 2016). More specifically, GHG concentration (e.g., CO<sub>2</sub> of 405 ppm), orbital parameters, land surface variables (e.g., topography, ice cover, and land-sea mask), and sea surface variables (SST, and SIC) were derived from PRISM3D. The vegetation distribution map was regenerated with JSBACH plant functional types using the PRISM reconstruction (Stepanek & Lohmann, 2012). A summary of the major boundary conditions used in this study is presented in Table 1.

Due to the sparse availability of isotopic composition records for the past climates, all the initial conditions of the ocean and the atmosphere were kept the same. The H<sub>2</sub><sup>18</sup>O and HDO starting conditions for the ocean were taken from the equilibrium 3000-year run with MPI-OM-wiso (Xu et al., 2012), and the atmosphere was initialized with  $\delta^{18}\text{O}$  and  $\delta\text{D}$  of  $-10$  and  $-80\text{‰}$ , respectively, similar to previous studies (e.g., Cauquoin et al., 2019; Werner et al., 2011).

### 3.3. Observed and Simulated Data Comparison

Reanalysis products are used as validation data sets to assess how ECHAM5-wiso simulates the climatologies and seasonality of precipitation and near-surface temperature across the WAM region. More specifically, the ERA5 climate reanalysis, produced and maintained by ECMWF, is compared to the simulated long-term seasonal means of the PD climate. ERA5 consists of globally interpolated observations (e.g., ocean buoys, satellites, aircraft, weather stations, and other platforms) and numerical simulations using a four-dimensional variational (4D-var) data assimilation scheme (Hersbach et al., 2020). It has hourly output, an approximately 31 km spatial resolution, and extends back to 1959 (Bell et al., 2021). We only extract the monthly long-term mean for the period 1979–2014 due to the simulated time range of the PD experiment. Moreover, the CRU (Climate Research Unit gridded Time series) high-resolution data set (i.e.,  $0.5^\circ \times 0.5^\circ$  over land regions except for Antarctica), maintained at the University of East Anglia, UK, was used to compare the PD precipitation simulation. CRU relies on the extensive network of global weather stations, which are interpolated using angular-distance weighting (ADW). This data set extends back to 1901 (more details in Harris et al., 2014, 2020).

**Table 1**

Summary of Boundary Conditions for the ECHAM5-Wiso Experiments (This Study) and the List of PMIP4 Models That Simulated the Coeval Climates

Experiment name	Greenhouse gas concentrations	Orbital forcing parameters	Surface conditions	PMIP4 models considered
Pre-industrial (PI): year 1850	CO <sub>2</sub> : 280 ppm, CH <sub>4</sub> : 760 ppb, N <sub>2</sub> O: 270 ppb.	e: 0.016804, o: 23.4725, lop: 278.734	The SST and SIC data are taken from a low-resolution coupled ocean-atmosphere simulation by Dietrich et al. (2013) and Lorenz and Lohmann (2004). Vegetation distribution data was adopted from Hagemann (2002).	All models
Mid-Holocene (MH): ~6 ka	CO <sub>2</sub> : 280 ppm, CH <sub>4</sub> : 650 ppb, N <sub>2</sub> O: 270 ppb.	e: 0.018682, o: 24.1048, lop: 180.918	SSTs and SICs are obtained from a transient, low-resolution coupled ocean-atmosphere simulation of the Mid-Holocene (Lohmann et al., 2013; Wei & Lohmann, 2012). Vegetation reconstructions from the BIOME 6000 data set (Bigelow et al., 2003; Harrison et al., 2001; Pickett et al., 2004; Prentice et al., 2000) converted into plant functional types.	AWI-ESM-1-1-LR, CESM2, EC-Earth3-LR, GISS-E2-1-G, HadGEM3-GC31-LL, IPSL-CM6A-LR, MIROC-ES2L, NorESM1-F
Last Glacial Maximum (LGM): ~21 ka	CO <sub>2</sub> : 185 ppm, CH <sub>4</sub> : 350 ppb, N <sub>2</sub> O: 200 ppb.	e: 0.018994, o: 22.949, lop: 294.42	SSTs and SICs were derived from GLAMAP reconstructions for the Atlantic Ocean (Sarnthein et al., 2003) and CLIMAP reconstructions for the Pacific and Indian Oceans (CLIMAP, 1981). Land-sea distribution, ice sheet extent, and thickness were based on PMIP3 data (Abe-Ouchi et al., 2015). Vegetation patterns were reconstructed using maps of plant functional types from the BIOME 6000 Paleovegetation Mapping Project (Bigelow et al., 2003; Harrison et al., 2001; Pickett et al., 2004; Prentice et al., 2000) and model predictions provided by Arnold et al. (2009).	AWI-ESM-1-1-LR, CESM2-WACCM-FV2, MIROC-ES2L, MPI-ESM1-2-LR, INM-CM4-8
Mid-Pliocene (MP): ~3 Ma	CO <sub>2</sub> : 405 ppm, CH <sub>4</sub> : 760 ppb, N <sub>2</sub> O: 270 ppb.	e: 0.016804, o: 23.4725, lop: 278.734	SSTs, SICs, land-sea mask, topography, and ice cover data were sourced from PRISM3D (Dowsett et al., 2010; Haywood et al., 2010; Sohl et al., 2009). The vegetation boundary condition was established by converting the PRISM vegetation reconstruction into JSBACH plant functional types, following the method outlined by Stepanek and Lohmann (2012).	CESM2, EC-Earth3-LR, GISS-E2-1-G, HadGEM3-GC31-LL, IPSL-CM6A-LR, NorESM1-F

Note. e stands for eccentricity, o for obliquity, and lop for longitude of perihelion.

### 3.4. Comparison to PMIP4 Simulations

Simulated model outputs from various climate models that participated in the fourth phase of the Paleoclimate Model Intercomparison Project (PMIP4), which is a component of the current Coupled Model Intercomparison Project (CMIP6) (Eyring et al., 2016), were analyzed to further compare our simulated responses to paleo-environmental conditions with the current state-of-the-art models. However, we emphasize that our analysis does not constitute a formal inter-model comparison since different experimental protocols were used for the simulations in this study. For instance, we rely on a high-resolution atmosphere-only model with prescribed forcings, in contrast to the fully coupled atmosphere-ocean GCMs used in the PMIP4 experiments. Furthermore, the ECHAM5-wiso simulation time is shorter than that of the PMIP4 models (>100 years) due to the longer period required for fully coupled ocean-atmosphere models to reach quasi-equilibrium and avoid drifts in climate variables. The boundary conditions and experimental setup protocols for the PMIP4 models simulating the MH, LGM, and MP are described in Kageyama et al. (2018) and Otto-Bliesner et al. (2017). We analyzed the last 100 years of monthly precipitation amounts for each model, with climate anomalies estimated using their respective PI control simulations. Moreover, we highlight that the individual PMIP4 models' spatial resolutions were kept for our analysis to disentangle the impact of the model resolution in representing the WAM dynamics.

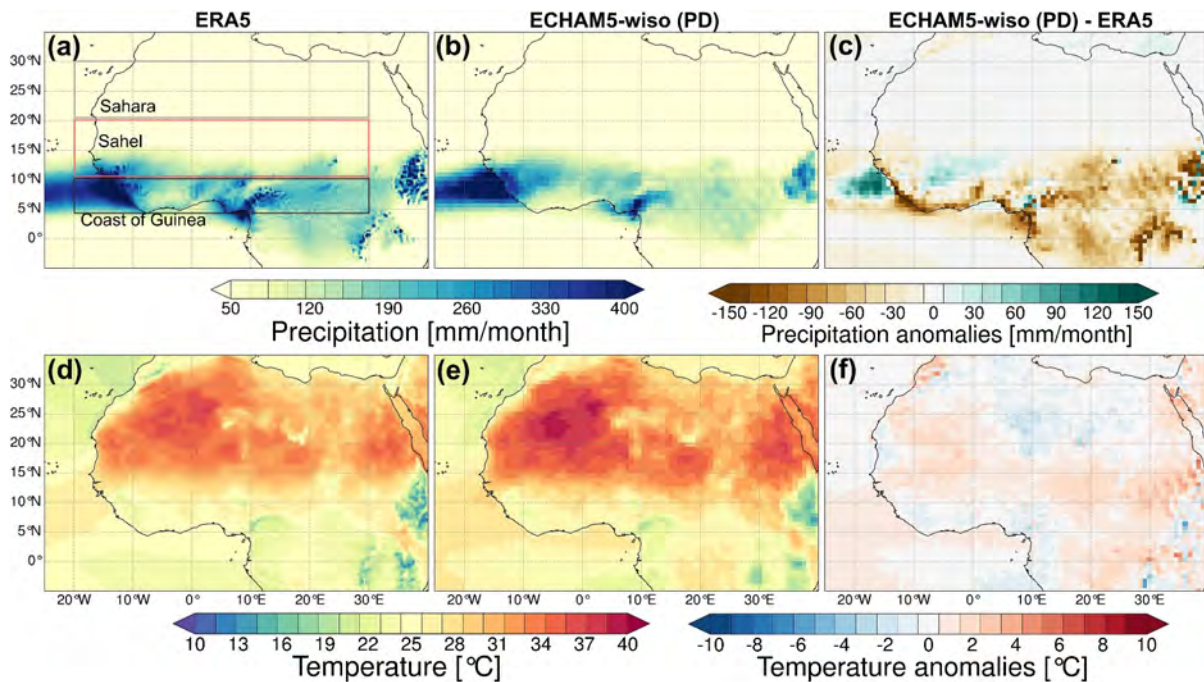


**Figure 1.** Long-term annual means (1979–2014) of ERA5 and ECHAM5-wiso precipitation (a and b) and near-surface temperature (d and e) during the monsoon season (JJAS), and the differences in precipitation and near-surface temperature between the data sets (c and f). The green color range in the precipitation difference indicates a wet bias, while the brown colors indicate a dry bias in the model. The red color range also represents a warm bias, and the blue colors indicate a cold bias in the model. Overall, the simulated patterns of the rain belt and meridional temperature gradient during the monsoon season demonstrate a reasonable model performance. The demarcated regions in (a) are used for estimating the regional means.

### 3.5. West African Monsoon Anomalies and Statistical Test

Long-term seasonal means of the WAM months (JJAS) were estimated using the 6-hr model output from the ECHAM5-wiso experiments and the monthly means from the PMIP4 models. The statistical significance of the long-term anomalies is evaluated using a student *t*-test with a confidence interval threshold of 95%. It is important to note that the analysis is based on uncorrected time, even though orbits were modified in the time slice experiments. However, this does not influence the analysis since climatological means are considered. As the WAM seasonality is zonally distributed (Janicot et al., 2011; S. E. Nicholson & Palao, 1993), three different latitudinal transects were delineated for further analysis. Specifically, zonal averages over the Sahara (30–20°N, 20°W–30°E), Sahel (20–10°N, 20°W–30°E), and Guinea coast (10–5°N, 20°W–30°E) were used to understand the meridional variations of the simulated rain belt across the WAM region.

## 4. Results

### 4.1. Present-Day Simulation and Comparison to Observations

Comparisons of the simulated and the observed spatial patterns and seasonality of precipitation and near-surface temperature revealed that ECHAM5-wiso represents the climate across the WAM region well. More specifically, the simulated and observed precipitation in the monsoon season shows a similar rain belt, that is, a latitudinal band of maximum precipitation of approximately 400 mm/month across Africa. There are only slight deviations in magnitude between ECHAM5-wiso and ERA5 (Figures 1a–1c): ERA5 shows a higher magnitude of precipitation, with ~40 mm/month more than predicted by the simulation. However, comparing the simulated patterns to the CRU data sets reduces these slight differences in precipitation patterns and magnitudes (Figure S1 in Supporting Information S1). Moreover, the simulated near-surface temperature indicates similar spatial patterns with a pronounced meridional gradient, indicating high temperatures of up to 40°C across the Sahara region (Figures 1d–1f).



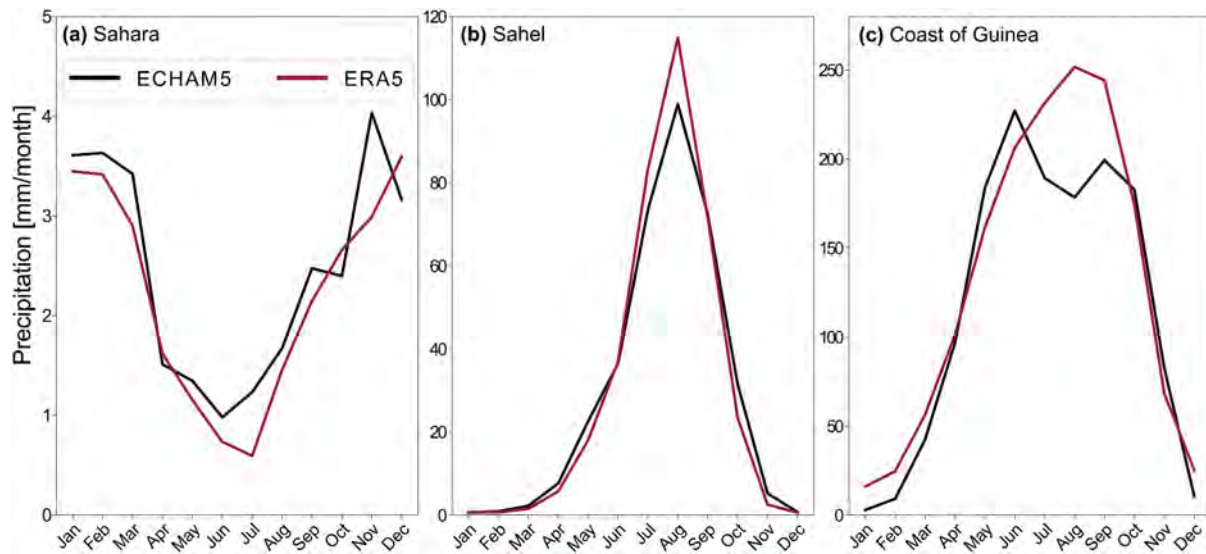


**Figure 2.** Comparison of ERA5 (red) and ECHAM5-wiso (black) monthly precipitation changes across the (a) Sahara (30–20°N, 20°W–30°E), (b) Sahel (20–10°N, 20°W–30°E), and (c) Coast of Guinea (10–5°N, 20°W–30°E) (see Figure 1a). For the Sahara and the Sahel, the modeled evolution of the WAM is consistent with ERA5. However, the model produces the expected bimodal precipitation seasonality across the Guinea coast, while ERA5 only shows a unimodal pattern.

The migration of the WAM drives different seasonal precipitation patterns across West Africa. Consequently, we analyze the seasonal trends using regional monthly means across the Sahara, Sahel, and the coast of Guinea. Overall, the model simulates an accurate seasonal distribution and intensity across most of the transects (Figure 2). Specifically, the observed and the modeled seasonal cycle shows a precipitation increase of >3 mm/month during the winter in the Sahara region (Figure 2a). Moreover, the model also simulates a realistic unimodal monthly distribution across the Sahel, with maximum precipitation of ~100 mm/month in August (Figure 2b). However, ECHAM5-wiso predicts the expected bimodal precipitation seasonality across the Guinea coast, with peak months in June (~225 mm/month) and September (~200 mm/month), while ERA5 indicates wider unimodal patterns of maximum precipitation of ~250 mm/month in June (Figure 2c). Despite the adequate precipitation representation of ERA5 over West Africa, previous studies have indicated their underestimation over the coast of Guinea (e.g., Quagrain et al., 2020). Overall, the present-day simulation results confirm ECHAM5-wiso's ability to represent the hydroclimate of the WAM and its associated teleconnections, validating its use for paleoclimate simulations.

#### 4.2. Simulated Changes of the WAM in the Late Cenozoic

The simulated regional patterns of the WAM in the MH, LGM, and MP deviate significantly from PI conditions. Overall, the model estimates an intensification of the WAM in the MH and MP, with the MH showing a more significant intensification than the MP. On the other hand, the model estimates a pattern of extensive dryness during the WAM season in the LGM (Figure 3). The estimated precipitation anomalies during the WAM season in the MH indicate bidirectional latitudinal patterns. The MH experiment estimates an increase of ~150 mm/month from 7° to 30°N, with statistical significance below 27°N. Conversely, the model indicates a decrease of ~30 mm/month toward the coastal regions (2–6°N) (Figure 3a). Overall, the LGM simulation indicates a precipitation decrease of up to 150 mm/month across the WAM region, with significant anomalies along the coastal regions (Figure 3b). Lastly, MP estimates an increase of ~100 mm/month in precipitation anomalies during the WAM season, with patches of a slight decrease in precipitation along the coast of Guinea, Nigeria, and Cameroon (Figure 3c). The simulated patterns of precipitation anomalies indicate a higher magnitude of the latitudinal extent of the WAM toward the Sahara region in the MH compared to the MP. To assess the relative importance and added value of using ECHAM5-wiso to simulate all the studied periods, we compare our model estimates to those of other models from the CMIP6-PMIP4 experiments (Table 1) that simulate the same periods. We focus our analysis on regional means of precipitation anomalies across the Sahel and also evaluate the latitudinal distribution of the WAM. The simulated WAM seasonal climatologies of the different climates (i.e., MH, LGM, and

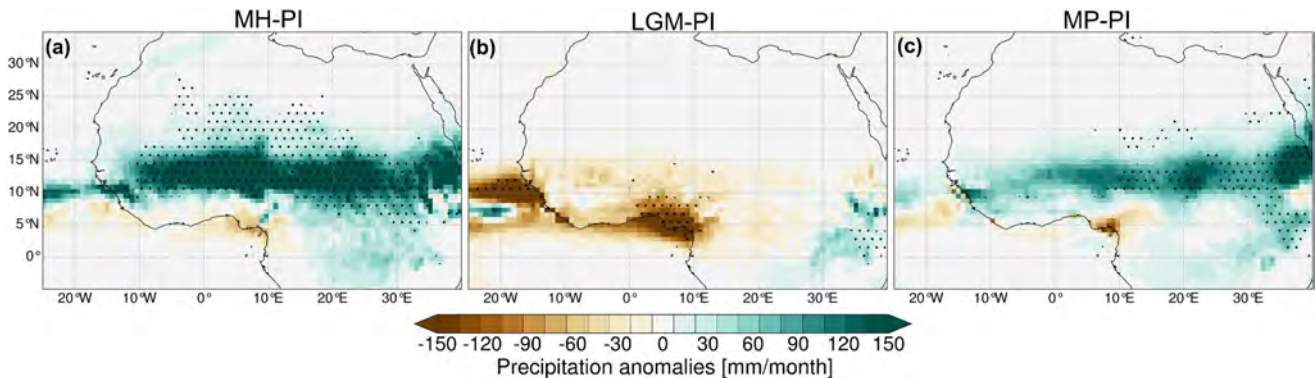


**Figure 3.** Precipitation anomalies during the WAM season (JJAS) for the (a) Mid-Holocene (MH), (b) Last Glacial Maximum (LGM), and (c) Mid-Pliocene (MP), as simulated by ECHAM5-wiso. The green color range represents wetter conditions, while the brown color range represents drier conditions compared to the Pre-Industrial (PI) estimates. The black dot stippling indicates regions with statistically significant differences, assuming a confidence interval of 95% based on a student *t*-test analysis. The precipitation anomalies patterns indicate the highest intensification of the WAM and its northward reach in the MH despite the enhanced hydrological cycle in the MP.

MP) and their respective control means (PI) are presented in the supplementary material (Figures S2, S3, S4, and S5 in Supporting Information S1).

Overall, the inter-model comparison reveals consistent estimates in the direction and magnitude of change in response to different paleoenvironmental conditions, with the exception of CESM2-WCCM-FV2. Surprisingly, this model estimates an increase in precipitation anomalies across the Sahel in the LGM (Figure 4b). However, Zhu et al. (2021) have indicated that this unrealistic sensitivity to colder climates may be attributed to exaggerated shortwave cloud feedback or an unrepresented physical mechanism countering such cloud feedback. Specifically, ECHAM5-wiso estimates the maximum increase in precipitation anomalies of  $\sim 90$  mm/month across the Sahel in the MH for the WAM season, followed by MPI-ESM1-2-LR (with  $\sim 80$  mm/month), while GISS-E2-1-G shows the lowest precipitation anomalies of  $\sim 35$  mm/month (Figure 4a). Alternatively, AWI-ESM-1-1-LR estimates a maximum precipitation decrease of 55 mm/month across the Sahel in the LGM (Figure 4b). The precipitation decreases ( $\sim 20$  mm/month) estimated by ECHAM5-wiso is similar to the estimates by the INN-CM4-8 and MIROC-ES2L models. In the MP, the WAM response across the Sahel exhibits a wider range of precipitation anomalies, with EC-Earth3-LR, indicating the maximum increase of  $\sim 160$  mm/month and GISS-E2-1-G showing the lowest increase of  $\sim 10$  mm/month (Figure 4c). However, ECHAM5-wiso estimates fall within a mid-range of  $\sim 50$  mm/month, which is closer to the estimates by HadGEM3-GC31-LL, IPSL-CM6A-LR, and NorESM1-F models. Even though ECHAM5-wiso indicates a maximum intensification of the WAM across the Sahel in the MH rather than in the MP, other models (e.g., EC-Earth3-LR) suggest the reverse trend. Consequently, the longitudinal regional means of the latitudinal distribution of precipitation anomalies during the WAM season are evaluated to compare the northward migration of the WAM in response to the different paleoenvironments (Figure 4).

In total, most of the PMIP4 models suggest a higher meridional migration of the WAM in the MP than in the MH, while the magnitude of changes in the latitudinal band of maximum precipitation varies among the individual models (Figure 5). Specifically, EC-Earth3-LR estimates maximum latitudinal precipitation of 200 mm/month with a greater northward extent in MP than the  $\sim 100$  mm/month rain belt in the MH (Figures 5a and 5c). However, GISS-E2-1-G suggests a higher intensification of the WAM with an increase in precipitation by 50 mm/month in the MH, and a relatively modest increase of  $\sim 10$  mm/month in the MP (Figures 5a and 5c). The ECHAM5-wiso experiments suggest a slight northward extent of the WAM in the MH and a higher intensification ( $\sim 80$  mm/month more) than in the MP (Figures 5a and 5c). Despite the estimated differences, all the models, including ECHAM5-wiso, indicate a similar meridional distribution in the MH and MP. However, CESM2-WCCM-FV2 and INM-CM4-8 distinctively suggest an increased distribution of meridional precipitation anomalies across the WAM areas and toward the equatorial Atlantic in the LGM (Figure 5b), respectively, despite the general decreasing trend estimated by the other models.

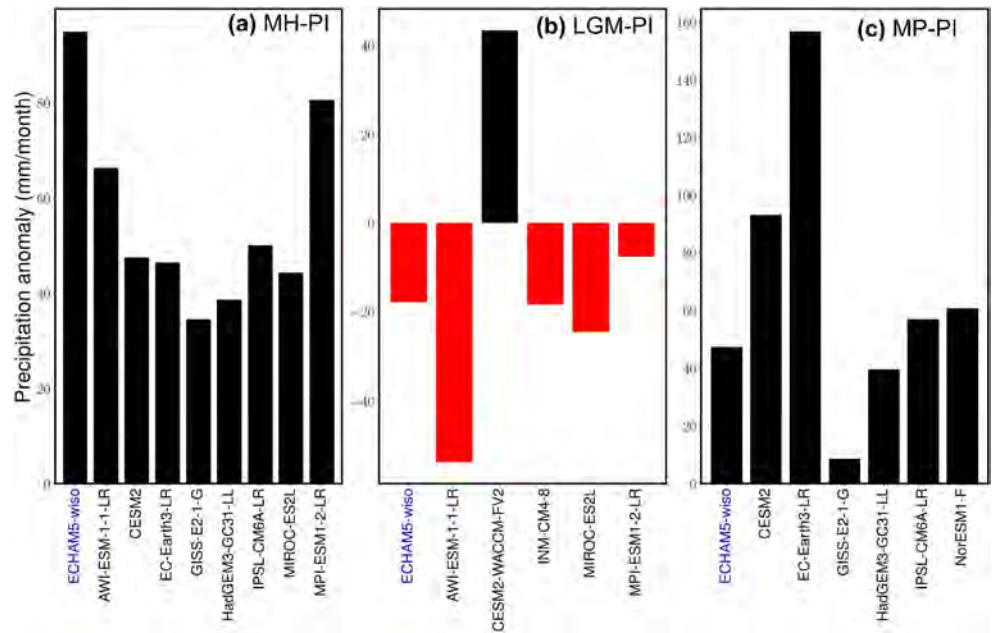


**Figure 4.** Regional means of precipitation anomalies during the WAM season estimated for the Sahel region (see Figure 1a) using ECHAM5-wiso (labeled in blue) and the PMIP4 models considered (Table 1) for the (a) Mid-Holocene (MH), (b) Last Glacial Maximum (LGM), and (c) Mid-Pliocene (MP) paleoenvironmental conditions. The individual precipitation anomalies are estimated based on their respective pre-industrial (PI) runs.

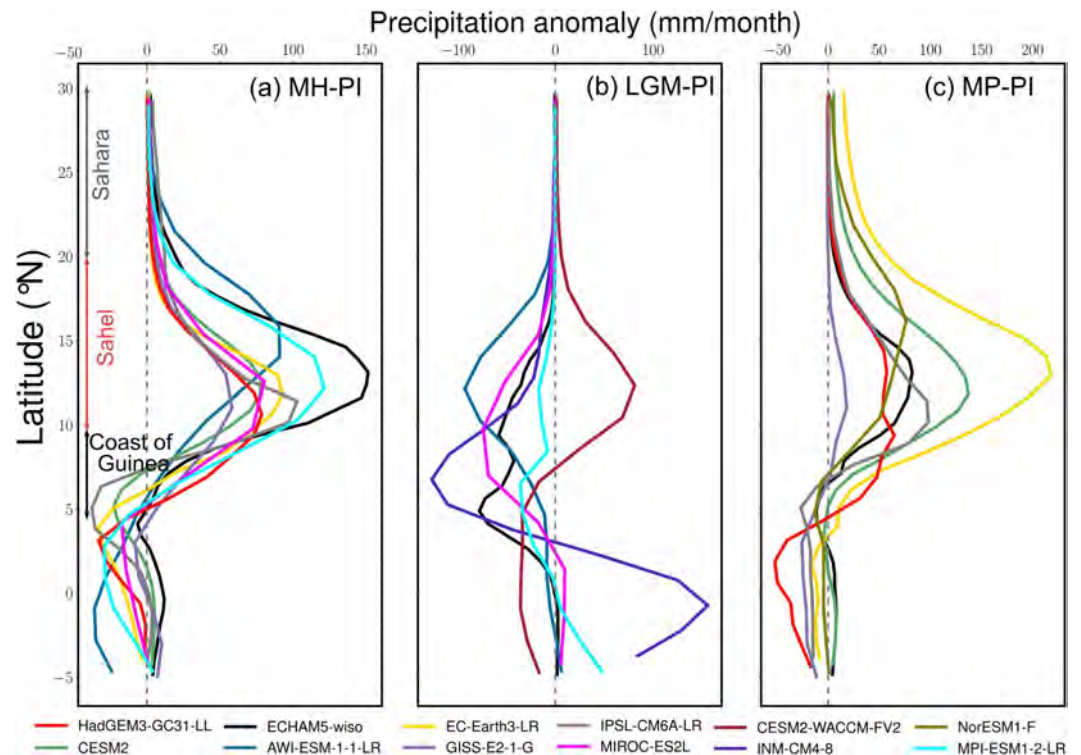


**Figure 5.** Latitudinal regional, seasonal means (JJAS) of precipitation anomalies across the WAM region (averaged between 20°W and 30°E) estimated for the ECHAM5-wiso and PMIP4 models for (a) Mid-Holocene (MH), (b) Last Glacial Maximum (LGM), and (c) Mid-Pliocene (MP) simulations. ECHAM5-wiso estimates show a latitudinal distribution that is consistent with most of the PMIP4 models. ECHAM5-wiso estimates for LGM and MP fall into the PMIP4 model range, while ECHAM5-wiso estimates for the intensification of the WAM in the MH exceed the PMIP4 model range.

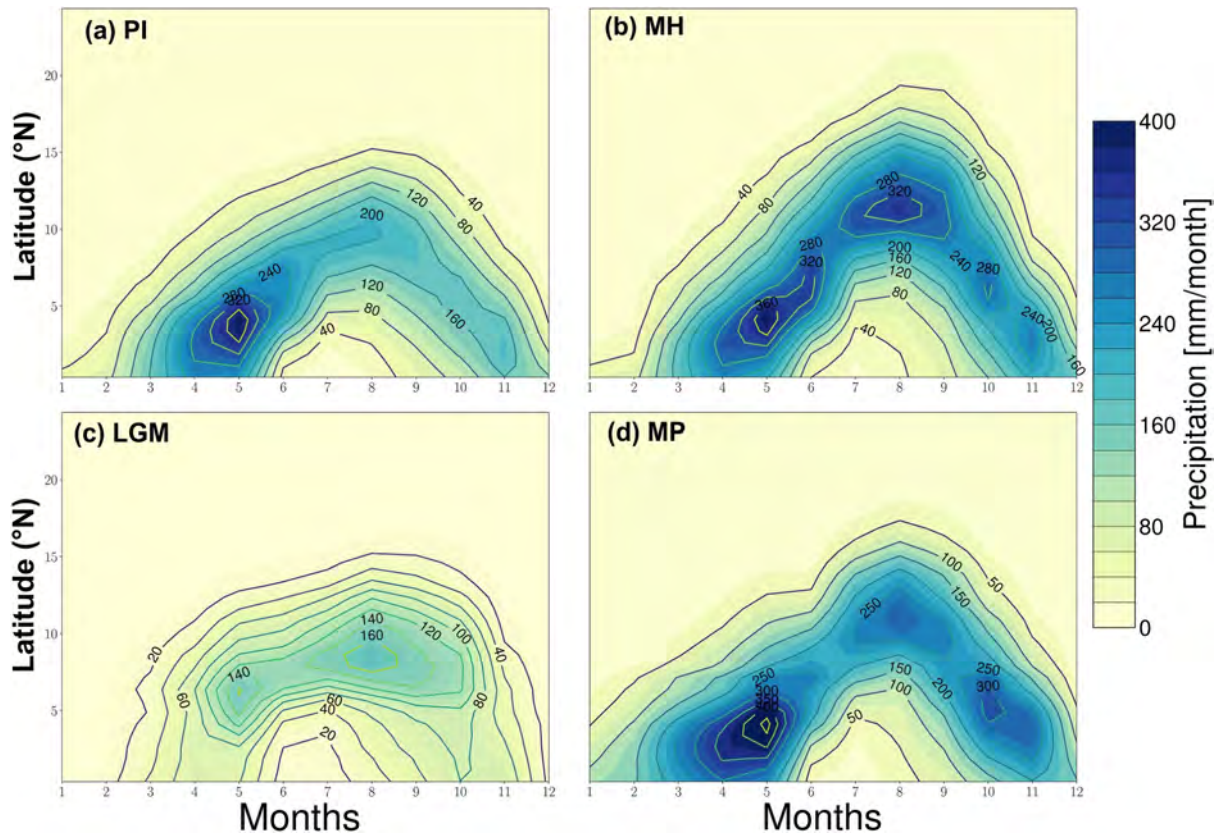


**Figure 6.** Hovmöller diagram (space-time) showing the latitudinal seasonal migration of precipitation across the WAM region (averaged between 20°W and 30°E) for the (a) Pre-industrial (PI), (b) Mid-Holocene (MH), (c) Last Glacial Maximum (LGM), and (d) Mid-Pliocene (MP) experiments using ECHAM5-wiso. The MH seasonal distribution indicates the highest precipitation rate during the high-rainfall period (June–August), while the MP indicates more precipitation in the onset (March–May) and southward retreat (September–October) periods.

### 4.3. Seasonality of the Simulated WAM in the Late Cenozoic

The meridional migration of the WAM is investigated by analyzing the evolution of latitudinal regional means (Hovmöller diagram) (Figure 6) and regional means over the coast of Guinea, Sahel, and Sahara (Figure 7). Generally, the seasonal cycle of the WAM progresses from two rainy season regimes across the coastal areas to a single rainy event across higher latitudes (Figure 2). The progression of the WAM is classically defined in three phases: (a) the onset period (March–May), driven by the low-level south-westerlies moist transport from the South Atlantic toward the coastal regions up to 4°N and the abrupt shift of the ITCZ from the quasi-stationary zone between 5 and 8°N to 8–10°N, (b) the high rain period (June–August), which abruptly shifts the rain belt up to 10°N (also known as monsoon jump), marking the start of the high rainfall events in the Sahel and the end of the first rainy regime across the coast, and (c) the southward retreat (September–October), reflecting the last phase of the WAM annual cycle and the second rainfall region across the coast (Barbé et al., 2002; Sultan et al., 2003; Sultan & Janicot, 2003).

The latitudinal evolution of the WAM in the PI indicates maximum precipitation of up to 320 mm/month during the onset period (from March to May) along the coast, followed by a monsoonal jump up to 15°N in the Sahel with  $\leq 40$  mm/month of precipitation (Figure 6a). Moreover, the southward retreat toward the coast at the end of the annual cycle records half of the precipitation (i.e.,  $\sim 160$  mm/month) during the onset period. The MH evolution exhibits similar phases, but with higher precipitation and a greater northward extent. Specifically, the onset period records precipitation of  $\sim 360$  mm/month and a higher northward shift up to  $\sim 25^\circ\text{N}$  with higher precipitation rates of up to 320 mm/month across the Sahel (Figure 6b). The southward retreat phase in the MH is also characterized by higher precipitation rates of up to 240 mm/month. Overall, the MP seasonal trend shows an inverted V-shape distribution that is similar to the MH pattern, but flatter and with a higher rainfall in the onset and southward

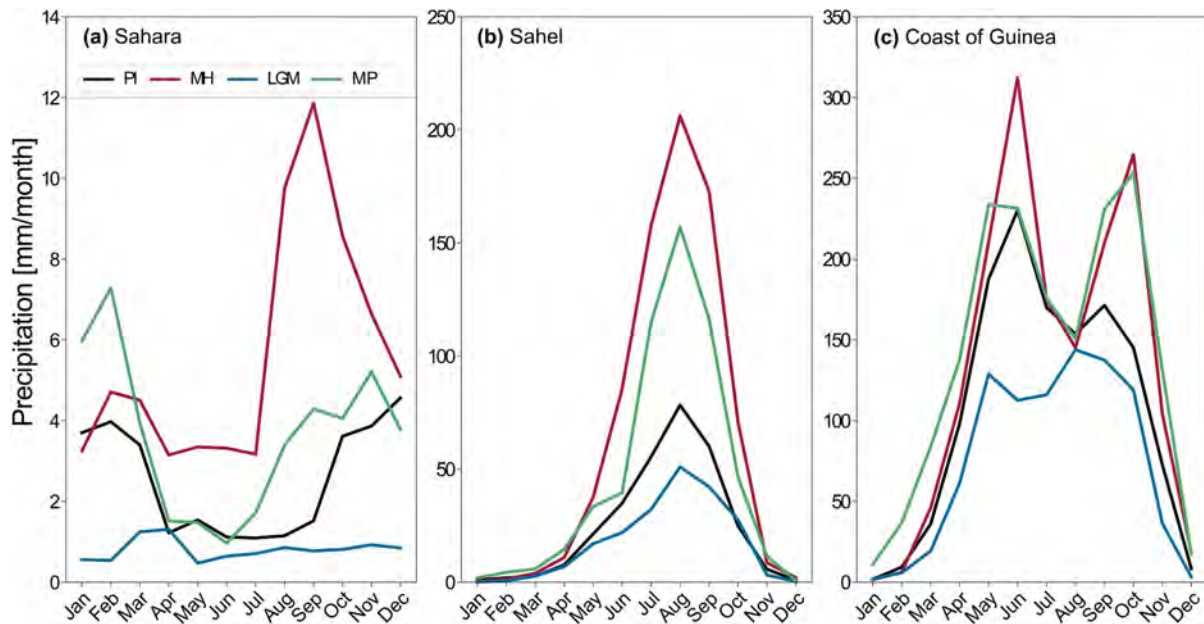


**Figure 7.** Seasonal cycle of precipitation across the (a) Sahara (30–20°N, 20°W–30°E), (b) Sahel (20–10°N, 20°W–30°E), and (c) Guinea coast (10–5°N, 20°W–30°E) (See Figure 1a) estimated for the Pre-industrial (PI; black), Mid-Holocene (MH; red), (c) Last Glacial Maximum (LGM; blue), and (d) Mid-Pliocene (MP; green) simulation using ECHAM5-wiso. The seasonal distribution of precipitation across the Sahara shows different peak months for the different past climates, while the Sahel and Coast of Guinea show a more consistent seasonality.

retreat phases along the coast. The onset and southward retreat phases are characterized by precipitation rates of ~400 mm/month and 300 mm/month across the coast of Guinea and the equatorial Atlantic, respectively (Figure 6d). However, the high-rainfall period is characterized by less rainfall (~250 mm/month) across the Sahel and a lower latitudinal extent ( $\leq 18^\circ\text{N}$ ) when compared to MH. On the other hand, the LGM simulations predict drier conditions in all seasons, with a rainfall increase of only up to 160 mm/month in the Sahel during the high-rain period (Figure 6c).

The seasonal cycle across the different climate zones is assessed through their regional means. The seasonal precipitation cycle exhibits pronounced variations in magnitude, but few changes in precipitation distribution (Figure 7). Among those few changes are variations in peak precipitation months estimated for the Sahara. While the PI estimates indicate higher precipitation (~4 mm/month) in November–February, the MH estimates suggest more precipitation from July to October, with peak precipitation rates of 12 mm/month in September. Overall, the LGM estimates indicate persistently drier conditions across all seasons in the Sahara. The MP also indicates a higher precipitation record in the pre-onset period across the Sahara, with a peak month in February (~7 mm/month). Regarding the bimodal monthly distribution along the coastal regions, all climates show similar patterns. For the MH, the precipitation peaks are highest, that is, a ~300 mm/month peak in June and a ~260 mm/month peak in October. The estimates across the Sahel also exhibit a unimodal distribution and precipitation peak in August. The MH simulation produces the highest peak, with an increase of more than 100% relative to the PI.

#### 4.4. Changes of Stable Oxygen Isotopic Composition in Precipitation Associated With Late Cenozoic Changes in the West African Monsoon

In this section, we explore the simulated seasonal climatological anomalies of the precipitation-weighted stable oxygen isotopic composition of precipitation ( $\delta^{18}\text{O}_p$ ) during the WAM season (Figure 8). Even though  $\delta^{18}\text{O}_p$  values are closely linked to precipitation due to the “amount effect”, the simulated spatial patterns of precipitation and  $\delta^{18}\text{O}_p$  values are different. Overall, the warmer climates (i.e., MH and MP) estimate a decrease in  $\delta^{18}\text{O}_p$  values across the WAM region when compared to the PI patterns during the monsoon season (Figures 8a and 8c). In contrast, the  $\delta^{18}\text{O}_p$  anomalies increase across many parts of the WAM region in response to the colder conditions in the LGM (Figure 8b). The MH is characterized by a significant decrease of  $\delta^{18}\text{O}_p$  values by ~−5‰ between 10 and 20°N, which spatially coincides with the region of the rain belt (Figure 8a). The decrease becomes

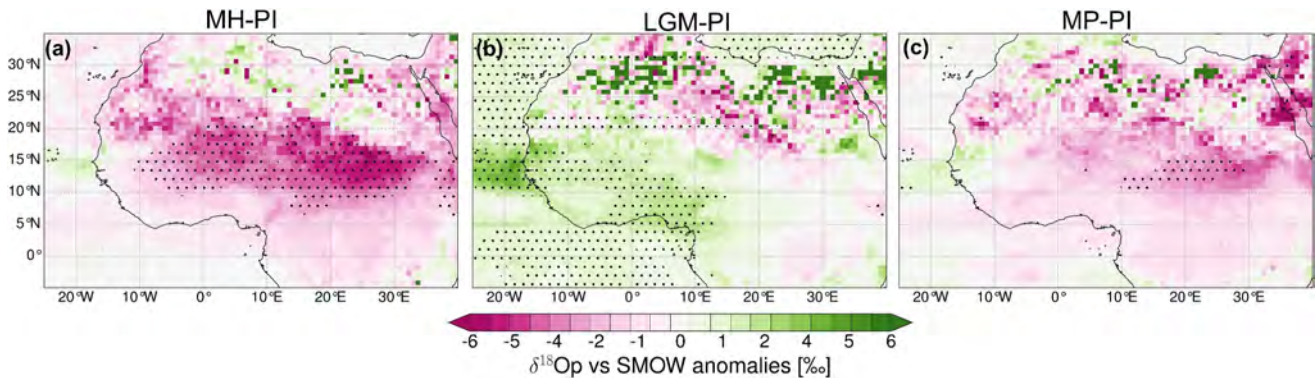


**Figure 8.** Simulated changes in  $\delta^{18}\text{O}_p$  in the WAM season (JJAS) for the (a) Mid-Holocene (MH), (b) Last Glacial Maximum (LGM), and (c) Mid-Pliocene (MP). The pink color range represents heavy isotope depletion, and the green color range represents an enrichment in the heavy isotopes in relation to Pre-industrial (PI) values. The black dot stippling indicates regions with a statistically significant difference, assuming a confidence interval of 95%, using a student  $t$ -test analysis.

less pronounced ( $\sim -1\text{‰}$ ) toward the Sahara region, and shows small areas that experience a slight increase ( $\sim 1\text{‰}$ ) toward the east. Moreover, the equatorial Atlantic region also experiences a slight  $\delta^{18}\text{O}_p$  decrease of about  $1\text{‰}$ . The  $\delta^{18}\text{O}_p$  anomalies during the MP also decrease across the continent, but show an increase of up to  $-6\text{‰}$  across the Sahara (Figure 8c). Furthermore, the decrease of  $\delta^{18}\text{O}_p$  values across the Sahel is less significant than the increase in precipitation anomalies in the MP. On the other hand, the LGM simulation indicates a significant increase in  $\delta^{18}\text{O}_p$  values of  $\sim 3\text{‰}$  across the Atlantic Ocean and the adjacent coastal regions (Figure 8b).

#### 4.5. Changes in the Atmospheric Dynamics Behind the Simulated WAM Changes

Here, we analyze the atmospheric dynamics behind the simulated changes in the WAM. Specifically, we use near-surface temperature, mean sea level pressure, wind patterns at different atmospheric levels, and surface heat fluxes to investigate how these dynamics change in response to different late Cenozoic boundary conditions. Due to our current understanding of WAM dynamics (Section 2.1), we focus on the spatial and intensification changes of the surface temperature and pressure gradients, AEJ, TEJ, and the low-level south-westerly winds as the dynamic feedback contributing to the simulated changes in the WAM. Additionally, we evaluate the changes in the WAM due to land surface conditions (e.g., prescribed vegetation) in the experiments through the responses of surface latent and sensible heat fluxes.

##### 4.5.1. Changes in Near-Surface Temperature

The warmer climate experiments (i.e., MH and MP) produce a north-south near-surface temperature gradient with an increase in the Sahara region, a decrease in the Sahel, and smaller regions of increases (MP) or no (MH) changes at the southern coast (Figure 9). Overall, the MH indicates a pronounced meridional gradient with a significant increase in temperature anomaly of up to  $10^\circ\text{C}$  across the Sahara and a significant decrease of down to  $-8^\circ\text{C}$  toward the Guinea coast (Figure 9a). The MP anomalies indicate similar patterns, but with less pronounced gradients and significant changes only toward Central and East Africa. More specifically, the MP shows an increase of up to  $5^\circ\text{C}$  across the Sahara and a decrease of about  $-3^\circ\text{C}$  across the Sahel, transitioning into a slight increase of up to  $2^\circ\text{C}$  in the equatorial Atlantic (Figure 9c). This spatial variability is consistent with the precipitation patterns. Moreover, the mean sea level pressure patterns also indicate the deepening of the low-pressure area across the Sahara in MH compared to the MP (Figure S6 in Supporting Information S1). However, comparing the cyclonic flow across the Sahara and the strengthened south-westerlies moist transport from the equatorial Atlantic at 850 hPa between the MH and MP reveals no noticeable changes (Figure S6 in Supporting Information S1). Contrarily, the temperature anomalies in the LGM indicate overall colder conditions across the continent with a significant decrease of up to  $-5^\circ\text{C}$ .

##### 4.5.2. Changes in the Vertical Structure of Zonal and Meridional Wind Speeds

We analyzed the latitudinal-altitude cross-sections of zonal and meridional wind speeds across the WAM region to understand the atmospheric circulation associated with the simulated precipitation dynamics. The zonal wind

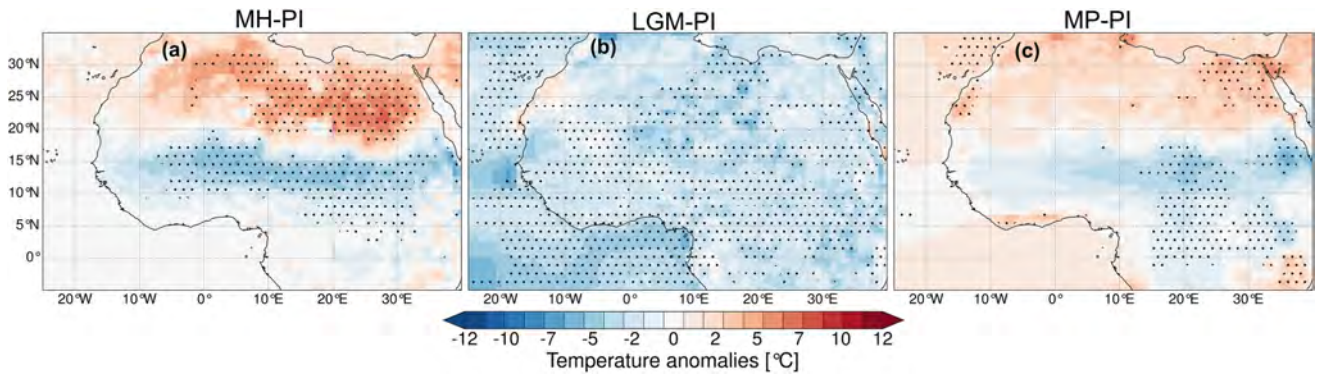


**Figure 9.** Simulated temperature anomalies of the WAM season (JJAS) estimated in response to the (a) Mid-Holocene (MH), (b) Last Glacial Maximum (LGM), and (c) Mid-Pliocene (MP) paleoenvironmental conditions using ECHAM5-wiso. The blue color ranges represent colder conditions, and the red color ranges represent warmer conditions compared to the pre-industrial estimates. The black dot stippling indicates regions with a statistically significant difference, assuming a confidence interval of 95% using a student *t*-test analysis.

patterns reveal a higher altitudinal reach of the low-level southwesterlies and a greater northward propagation in the MH and MP when compared to the PI and LGM (Figure 10). The westerlies reach a latitudinal extent of 17°N and stay below 800 hPa atmospheric level in the PI and LGM, while in the MH and MP, the flows extend over 20°N and up to the 700 hPa level (Figures 10a–10d). The MH and MP simulations estimate a higher northward reach of the winds, but the latter predicts slightly higher wind shear at the core of the low-level flow. Consistently,

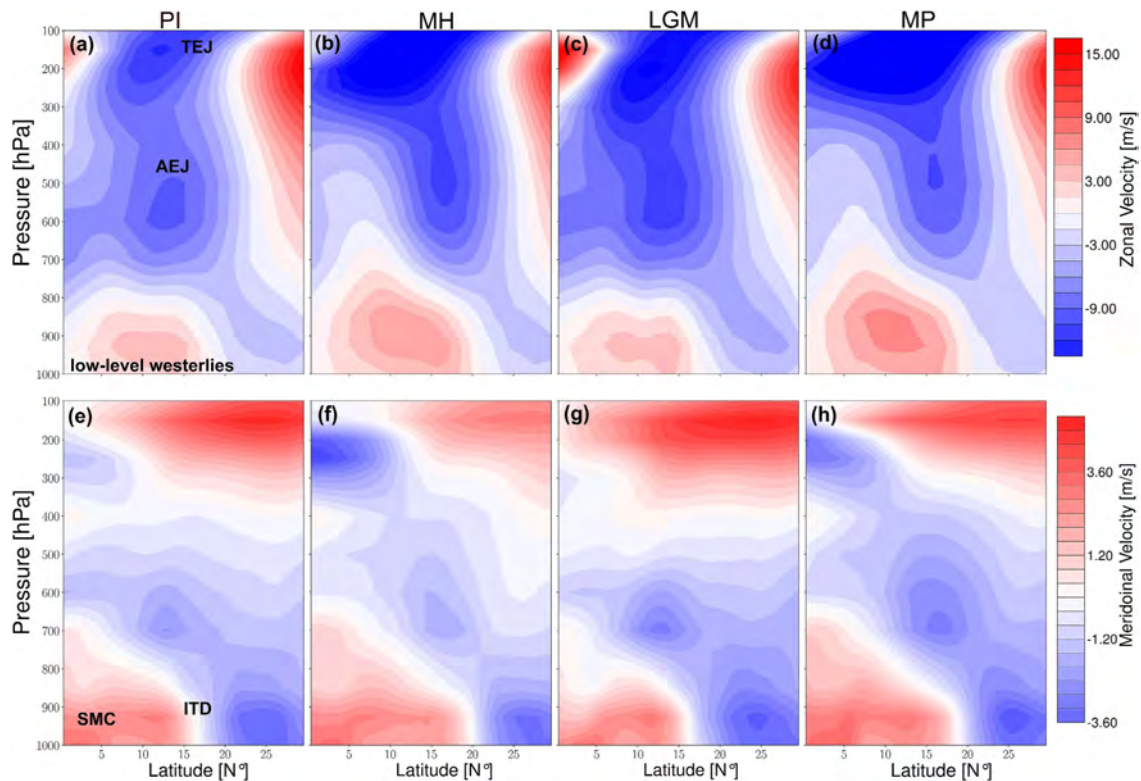


**Figure 10.** Latitudinal vertical cross-sectional for zonal (top panel) patterns, where positive (negative) values indicate westerly (easterly) winds, and for meridional patterns (bottom panel), where positive (negative) values indicate southerly (northerly) wind speeds estimated for the WAM season (JJAS) in response to (a) Pre-industrial (PI), (b) Mid-Holocene (MH), (c) Last Glacial Maximum (LGM), and (d) Mid-Pliocene (MP) paleoenvironmental conditions. The approximate locations of the African Easterly Jet (AEJ), Tropical Easterly Jet (TEJ), Intertropical Discontinuity (ITD), low-level westerlies and Shallow Meridional Cell (SMC) are shown in a and e. The low-level westerlies reach the highest latitude and altitude in the MH. The strengthened WAM conditions are more associated with the northward position of the Africa Easterly Jet (AEJ) than its intensity.

the AEJ is located between 10 and 15°N at approximately 600 hPa in the PI and LGM. However, the LGM indicates a more intense AEJ than the PI despite overall drier conditions. In the MH and MP, the AEJ experiences a greater northward shift between 15 and 20°N, and its core shifts to a higher altitude than in the PI. In contrast to the LGM and PI, the AEJ in the MH indicates higher intensification than the MP.

The latitudinal-altitude cross-section of winds also indicates higher vertical wind shear (inferred from the transition from the low-level westerlies to the mid-level easterlies) in the MH and MP compared to the PI. Stronger southwesterlies (and, therefore, a deeper monsoon depth) are also identified in the MH and MP. The monsoon depth defines the altitudinal reach of moisture transport from the equatorial Atlantic into the continent. In contrast, the LGM experiment estimates a shallow monsoon depth compared to the PI. More specifically, the monsoon depth reaches an altitude of 600 hPa in the MH and MP, and only up to 700 hPa in the PI and LGM (Figures 10e–10h). Moreover, the patterns in the MH and MP indicate a more northward location of the ITD (i.e., the location where the moist southwesterlies deflect the dry northeasterlies from the Sahara) at approximately 20° and 19°N, respectively. For the PI and LGM, the ITD is located further south (<17°N). The intensity of the low-level moisture transport, TEJ, AEJ, and the location of the ITD coincide with the latitudinal band of negative omega values (wind directions away from the ground; updraft) up to 200 hPa and the associated subsidence (positive omega values) across the Sahara (Figure S7 in Supporting Information S1). Overall, the tropospheric structure of the winds reveals stronger southwesterlies moisture transport from the tropical Atlantic, a higher monsoon depth, the northward position of the AEJ, and the intensification of the TEJ, consistent with the increased intensity of the WAM and its northward migration in the MH and MP.

#### 4.5.3. Changes in Sensible and Latent Heat Fluxes

Generally, high vegetation cover yields more water availability through evapotranspiration, which increases latent heat (LH) flux. Moreover, moisture availability due to the increased LH flux leads to a rainfall-induced cooling effect, reducing sensible heat (SH) flux into the atmosphere. Specifically, for the WAM region, the recycling of water vapor through evaporative fluxes also contributes to the northward extent of precipitation. Therefore, the response of the WAM to different surface conditions is described here through the analysis of SH and LH fluxes. However, we highlight that diagnosing the causes of the changes in terrestrial water balance (i.e., precipitation minus evaporation) through moisture budget analysis (Seager & Henderson, 2013) will help better quantify the contribution of the atmospheric circulation and surface moisture fluxes to the precipitation changes (e.g., Feng et al., 2022) and will be addressed in future study.

The paleoclimate experiments indicate varied responses to the surface heat fluxes (Figure 11). In the MH experiment, the results indicate pronounced negative LH anomalies (i.e., upward flux) of up to  $-80 \text{ Wm}^{-2}$  across the Sahel, gradually reducing in magnitude towards the Sahara (Figure 11a). Regions with more upward LH fluxes coincide with regions of a significant increase in precipitation the MH. The LGM reveals overall positive (downward) LH flux anomalies across the Sahel and coastal regions, with no changes towards the Sahara due to colder and drier conditions (Figure 11b). In the MP, the estimated patterns reveal a slight increase in upward fluxes with negative LH anomalies down to  $-30 \text{ Wm}^{-2}$  across the Sahel, and no changes in the Sahara (Figure 11c). Such simulated patterns of releasing LH are consistent with higher enhanced evaporation over vegetated surfaces through radiative forcing (Figure S8 in Supporting Information S1) in the MH. The SH flux anomalies also show consistent results with more downward fluxes and colder surface conditions associated with increased precipitation. The MH experiment estimates negative SH anomalies down to  $-60 \text{ Wm}^{-2}$  across the Sahara, reaching 15°N and positive SH anomalies across the Sahel towards the coastal regions (Figure 11d). The zonal band of the downward SH anomalies is also consistent with the simulated rain belt in both the MH and MP. The MP experiment estimates a similar, albeit less pronounced, north-south gradient of SH. The LGM experiment estimates negative SH anomalies across most regions on the continent, which is consistent with less availability of water to evaporate. The simulated SH flux patterns are consistent with the near-surface temperature anomalies, with a more pronounced meridional gradient in the MH relative to the MP.



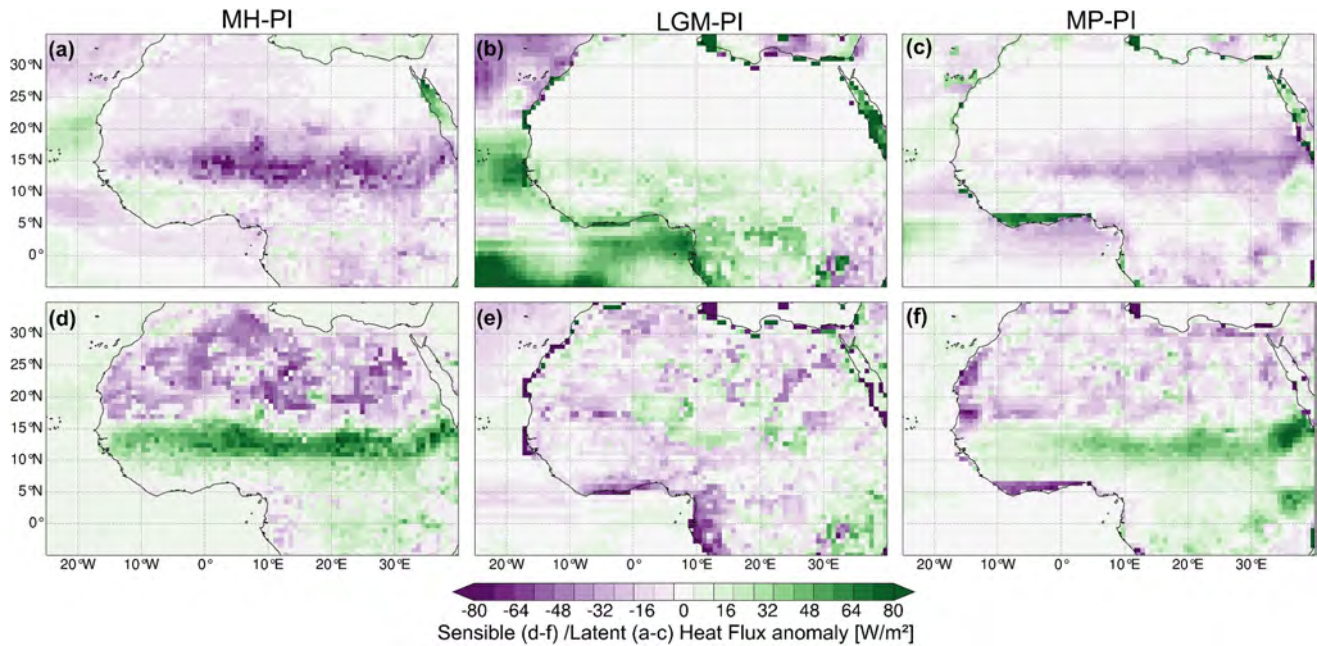


**Figure 11.** Latent (top panel) and Sensible (bottom panel) heat flux anomalies during the WAM months (JJAS) for the (a) Mid-Holocene (MH), (b) Last Glacial Maximum (LGM), and (c) Mid-Pliocene (MP). The purple ranges represent net upward fluxes, and the green color ranges represent downward fluxes.

## 5. Discussion

### 5.1. Simulated Changes of the WAM in Response to the Large-Scale Forcings

#### 5.1.1. Mid-Holocene (~6 ka)

Overall, the analyzed climate model outputs consistently indicate the intensification and expansion of the WAM during the MH, specifically during the boreal summer. These simulated patterns align with findings from previous modeling studies (e.g., Bosmans et al., 2012; Gaetani et al., 2017; Patricola & Cook, 2007; Zhao & Harrison, 2012) and proxy reconstructions (e.g., Bartlein et al., 2011). The increase in precipitation during the WAM season is not surprising, given that the orbital configurations of the MH lead to stronger insolation during the boreal summer and autumn, and to weaker insolation during the winter when compared to PI forcings (Joussaume et al., 1999; Kutzbach & Liu, 1997). These orbital precision variations with stronger seasonal thermal amplitudes also result in more pronounced equator-to-pole and land-sea thermal gradients, contributing to moisture redistribution across the continents (Brierley et al., 2020). Specifically, the stronger thermal gradients and associated continental warming during the WAM season (JJAS) deepen the low-pressure cells over the Sahara. This intensifies the advection of moist air masses from the equatorial Atlantic Ocean, thereby amplifying and expanding the WAM. Moreover, the redistribution of moisture associated with the seasonal insolation distribution can be observed as a weakening of the annual-scale range of precipitation over the ocean and a strengthening over the continent, as suggested in previous studies (e.g., Braconnot et al., 2004). The MH precipitation anomalies in the inter-annual scale are less pronounced than the seasonal changes. These changes reflect that the seasonal variations in insolation primarily drive the MH global climate changes (Kageyama et al., 2013). The ECHAM5-wiso model estimates global warming of approximately  $\sim 0.3^{\circ}\text{C}$  compared to the PI control run (Figure S9 in Supporting Information S1). The bidirectional precipitation anomalies, with drier conditions toward the coastal regions, are also consistent with the rainfall dipole patterns of the African Humid Period (AHP). This phenomenon is explained by the northward shift of the ITCZ during the boreal summer in response to the insolation in the Northern Hemisphere (Braconnot et al., 2007; Coe & Harrison, 2002; deMenocal et al., 2000).

Compared to the model outputs from the PMIP4-CMIP6 experiments, ECHAM5-wiso predicts the highest intensification and greatest northward reach of the WAM. The precipitation anomalies estimated with ECHAM5-wiso indicate a maximum rain belt of approximately 150 mm/month across the Sahel ( $10\text{--}20^{\circ}\text{N}$ ) and less rainfall reaching  $30^{\circ}\text{N}$ . Out of all considered models, ECHAM5-wiso estimates predict the highest regional precipitation

means (~95 mm/month), followed by the MPI-ESM-LR, which has a similar atmospheric model component (i.e., ECHAM6). This also further validates the ability of models in the ECHAM family to reproduce the atmospheric dynamics and hydrological cycle across the African continent. The relatively high precipitation rates predicted by our ECHAM5-wiso simulations might be partly due to the following:

1. The representation of MH vegetation feedbacks. The experimental design for the PMIP4-CMIP6 MH simulation keeps vegetation from the PI, using prescribed surface conditions or dynamic vegetation models. However, previous studies have suggested a “Green Sahara”, characterized by steppe, savanna, and shrub vegetation, and fewer deserts than today (Dallmeyer et al., 2020; Hoelzmann et al., 1998; Jolly et al., 1998). Such vegetation is required to sustain the enhancement and northward extent of the WAM during the MH. The simulation with ECHAM5-wiso used MH vegetation patterns provided by the BIOME6000 vegetation reconstructions (Bigelow et al., 2003; Harrison et al., 2001; Pickett et al., 2004; Prentice et al., 2000), where the Sahara desert was drastically reduced, and the Sahelian vegetation belt, consisting of steppe, tropical dry forest, and xerophytic woods/shrubs, was extended northward (Jolly et al., 1998; Prentice et al., 2000). Through positive feedback, vegetation has been suggested to increase orbitally driven precipitation across North Africa due to the warming effect caused by reduced albedo (Bonfils et al., 2001) and increased evapotranspiration as a result of increased latent heat fluxes (Levis et al., 2004; Texier et al., 2000). Overall, moisture recycling through evapotranspiration and induced surface warming increases convection and inland moisture flux and intensifies the WAM. However, previous studies have also indicated a plausible negative vegetation feedback on precipitation at the annual scale due to a larger contribution of soil evaporation than the albedo feedback under wetter conditions (Notaro et al., 2008; Y. Wang et al., 2008).
2. The lower values of greenhouse gas (GHG) concentrations used for the PMIP4-CMIP6 MH experiments. Lower  $p\text{CO}_2$  would result in a slightly colder climate than that produced by the ECHAM5-wiso simulation. This has been shown for the PMIP3-CMIP5 MH experiments that used GHG concentrations that are similar to those used for our ECHAM5-wiso experiment. The differences between PMIP4-CMIP6 and PMIP3-CMIP5 were due to the simulated difference in effective radiative forcing of  $-0.3 \text{ Wm}^{-2}$  (Otto-Bliesner et al., 2017). Generally, the slightly colder climate would reduce the temperature meridional gradient across the African continent that drives low-level south-westerly moist air masses from the equatorial Atlantic Ocean.
3. The use of the high spatial resolution for the ECHAM5-wiso simulation. Several studies have demonstrated that monsoons are better resolved when resolution is increased, even though the magnitude changes are more susceptible to the model's parameterization (e.g., Gao et al., 2006; Sperber et al., 1994). The higher spatial resolution consequently reproduces the MH patterns through improved representation of important processes, such as large-scale condensation, land-sea interaction, and topographic forcings (Boyle & Klein, 2010). Bosmans et al. (2012) showed that using a high-resolution (T159) for EC-Earth GCM resulted in an increased intensity and a greater northward reach of the WAM in the MH when compared to the low-resolution PMIP2 ocean-atmosphere coupled models. The inter-model variabilities can also be attributed to the differences in complexities and the models' sensitivity to the parameterization of clouds, atmospheric dynamics, and the hydrological cycle in general. We highlight that determining the influence of resolution and model parameterization is beyond the scope of this manuscript. Overall, all the models estimate similar latitudinal precipitation patterns across the WAM region, but the predicted northward reach and regional precipitation amounts are too low to sustain the plant types that existed during the MH (Braconnot et al., 2007; Joussaume et al., 1999).

### 5.1.2. Last Glacial Maximum (~21 ka)

Generally, the global climate during the LGM was characterized by large-scale cooling due to radiative perturbations linked to the extensive continental ice sheets and lower atmospheric greenhouse gas (GHG) concentrations (Clark et al., 2009). These large-scale drivers were further modified by internal feedbacks in the climate system involving factors like sea ice, snow, and water vapor (e.g., Braconnot et al., 2007). ECHAM5-wiso simulates realistic patterns of temperature anomalies, indicating maximum cooling of approximately  $-15^\circ\text{C}$  across regions with ice sheets in the Northern Hemisphere, and moderate cooling ( $-2$  to  $-5^\circ\text{C}$ ) over tropical areas (Figure S9 in Supporting Information S1). These patterns are similar to the results of PMIP4-CMIP6 experiments and align with findings from previous modeling studies (e.g., Cao et al., 2019; Kageyama et al., 2021). The large perturbations in the atmospheric radiative balance due to albedo feedbacks also result in significant changes in atmospheric circulation patterns, contributing to comprehensive changes in precipitation patterns (e.g., Liakka et al., 2016; Liakka & Lofverstrom, 2018). Large ice sheets covering North America and Fennoscandia redirect

low-level winds, which strongly influences moisture transport and regional precipitation. Additionally, the associated thermodynamics, as indicated through specific humidity, can contribute to regional precipitation changes (D'Agostino et al., 2019, 2020). Most of the precipitation on land was substantially decreased due to the large-scale cooling and its associated reduction in evapotranspiration (e.g., Braconnot et al., 2007). The lower SSTs led to reduced evaporation over the oceans, which in turn reduced the surface's moisture flux into the atmosphere. This eventually led to a decreased inland moisture flux, leading to overall large-scale drying. Apart from surface cooling, tropospheric cooling also decreased the amount of atmospheric water vapor by limiting its water-holding capacity through the Clausius-Clapeyron relation. However, in both hemispheres, other regions across the mid-latitudes experienced an increase in precipitation, mainly in areas corresponding to the positions of the North Pacific, North Atlantic, and Southern Ocean storm tracks (Figure S9 in Supporting Information S1). The simulated temperature patterns indicate overall cooling across the African continent, suggesting that the meridional temperature and pressure gradient that drives northward moisture flux from the Atlantic Ocean are suppressed, thereby reducing moisture availability across the WAM areas. Furthermore, the surface cooling over the oceans was more intense than over land, indicating a decrease in the land-sea thermal contrast, which would result in an additional reduction in inland moisture transport.

### 5.1.3. Mid-Pliocene (~3 Ma)

Simulating the MP climate provides the opportunity to evaluate the long-term response of the climate system to currently raised atmospheric GHG concentrations. This period is often considered an analog for future climate change (Burke et al., 2018) due to its similarities to modern paleogeography and high  $p\text{CO}_2$  (400 ppm). As such, the modeling framework of the MP helps assess how important climatic components of the Earth system, such as the El Niño-Southern Oscillation, the global hydrological cycle and monsoon systems, respond to the ongoing rise in  $\text{CO}_2$  concentrations. The simulated temperature patterns predict a global mean near-surface temperature increase of approximately  $3^\circ\text{C}$ , primarily due to direct  $\text{CO}_2$  forcing. The overall warming exhibits polar amplification, with temperature anomalies increasing by more than  $10^\circ\text{C}$  due to associated changes in albedo at higher latitudes (Chandan & Peltier, 2020; de Nooijer et al., 2020; Samakinwa et al., 2020; Tindall et al., 2022). The simulated global mean temperature increase predicted by ECHAM5-wiso falls within the range of model estimates ( $1.4\text{--}4.6^\circ\text{C}$ ) from the PlioMIP Phase 1 and 2 experiments (Haywood et al., 2013, 2020). The significant warming in high latitudes reduces the meridional temperature gradient, weakening the tropical atmospheric circulation, specifically the Hadley circulation (Corvec & Fletcher, 2017; Haywood et al., 2013). Previous studies also indicated a poleward shift of mid-latitude westerly winds (Li et al., 2015), increased intensity of tropical cyclones (Yan et al., 2016), and strengthening and poleward extension of the global land monsoon system (Li et al., 2018). The enhanced hydrological cycle intensifies the East Asian and West African summer monsoons (R. Zhang et al., 2013, 2016). These changes resemble future climate projections (e.g., Erfanian et al., 2016; Seth et al., 2019) and require detailed understanding from a modeling perspective.

Through sensitivity experiments, (Stepanek et al. (2020) determined that MP paleogeography contributes to increased rainfall across the WAM areas. The closure of the Arctic gateway and enhanced topography have also been suggested to strengthen the Atlantic Meridional Overturning Circulation (AMOC), thereby warming the North Atlantic Ocean (Z. Zhang et al., 2021), which impacts the WAM (Mulitza et al., 2008). These findings highlight the importance of other boundary conditions in regulating the WAM. As mentioned earlier, land surface conditions, such as vegetation, contribute to the variability and spatial extent of the WAM through evaporative fluxes. Proxy reconstructions from previous studies suggest more humid conditions across northern Africa, which facilitates an expansion of vegetation. More specifically, palynological records suggest high tree cover density and broadening of woodlands and savannas at the expense of deserts across the Sahara (Bonnefille, 2010; Salzmann et al., 2008). ECHAM5-wiso was set up with converted PRISM3 vegetation reconstructions, which indicate the expansion of grass and forests across North Africa toward the Mediterranean (Figure S10 in Supporting Information S1). Such patterns are also consistent with the COSMOS dynamic vegetation results presented in Stepanek et al. (2020), which estimated an increase in precipitation by 70 mm/month across the WAM region. The PlioMIP2 models with prescribed MP vegetation also indicate a strengthened WAM, with an ensemble mean of precipitation showing an increase by  $\sim 76$  (60–120) mm/month (Berntell et al., 2021). The previous modeling inter-comparison project (i.e., PlioMIP1) estimates a lower magnitude of increase within a range of 30–60 mm/month (R. Zhang et al., 2016). The PlioMIP1 experimental protocol (Haywood et al., 2010) was similar to the model setup used for the ECHAM5-wiso simulation. These findings suggest that ECHAM5-

wiso simulates a higher magnitude of WAM precipitation in the MP than the PlioMIP1 models. This may be due to the higher spatial resolution used for ECHAM5-wiso, which improves representation of land surface conditions (e.g., orography and vegetation) and model parameterization. Overall, PlioMIP1 and PlioMIP2 models suggest that the updated MP boundary conditions from PRISM3 to PRISM4 contribute to the strengthening of the WAM. Samakinwa et al. (2020) confirm this with a sensitivity experiment using COSMOS, which indicated that the updated paleogeography was the main reason for the changes in the large-scale features between PlioMIP1 and PlioMIP2.

The precipitation simulated with ECHAM5-wiso shows an increase of up to 120 mm/month and an intensification toward the east (Figure 3). However, regional means of precipitation across the Sahel increase by only ~50 mm/month, which falls within the broader range of PMIP4-CMIP6 estimates (10–160 mm/month) (Figure 4). The CESM2 and EC-Earth3-LR models estimate significant increases of 90 and 160 mm/month, respectively. The HadGEM3-GC31-LL, IPSL-CM6A-LR, and NorESM1-F estimate a moderate increase of ~50 mm/month, with GISS-E2-G estimating the lowest increase of only ~10 mm/month. The magnitude of the precipitation response simulated by the individual models across the WAM is consistent with the global response. For instance, GISS-E2-1-G indicates a low global response to the MP boundary conditions and consistently estimates the lowest WAM precipitation anomalies. On the contrary, models with large land-sea rainfall anomalies (e.g., EC-Earth3-LR and CESM2) also simulate a strengthened WAM. Even though the updated boundary conditions contributed to the inter-model variabilities, Haywood et al. (2020) suggested model parameterization and initial conditions as the main factors for the varied predictions. Moreover, later model versions tend to have a higher sensitivity than earlier versions when used with the same boundary and initial conditions. These findings suggest that using ECHAM6-wiso (Cauquoin et al., 2019) and even updated PRISM4 reconstructions (Dowsett et al., 2016; Haywood et al., 2016) would increase the strengthening of the WAM in the model.

## 5.2. Control of the Precipitation and Temperature on Stable Oxygen Isotope in the WAM Season in Response to the Different Past Climates

The stable oxygen isotopic composition of tropical precipitation provides information about the hydrological cycle and can be used to reconstruct past tropical climates. Several studies have employed stable isotopes to understand the intraseasonal water cycle variability in western Africa (e.g., Risi et al., 2008, 2010). These studies have revealed that the integrated convective activity in the monsoon season is spatially and temporally reflected in the  $\delta^{18}\text{O}$  values in precipitation and vapor records. On a broader scale, previous studies have used isotopic patterns to identify the strengthening of the Northern Hemisphere monsoon in response to warmer climates, both through modeling (e.g., Cauquoin et al., 2019; Shi et al., 2023; Thompson et al., 2021) and proxy records (Bartlein et al., 2011; Wang et al., 2008). Simulating the isotopic composition allows for a direct comparison of model simulations to isotopic archives and contributes to the understanding of the causal mechanisms behind various proxy archives (Bühler et al., 2022; Phipps et al., 2013; Risi et al., 2012; Werner et al., 2000). Here, we explore the response of simulated  $\delta^{18}\text{O}_p$  to varied paleoenvironmental conditions during the WAM season. The results suggest that meteoric water was more negative in past warmer climates and less negative in colder climates. Similar patterns have been reported in previous isotope-enabled GCM modeling studies (e.g., Cauquoin et al., 2019; Risi et al., 2010). Specifically, the oxygen isotopes are most depleted during the MH, indicating the role of seasonal insolation distribution and associated precipitation dynamics in the isotopic patterns (Thompson et al., 2021). Importantly, the magnitude and spatial patterns, to some extent, are inconsistent with the simulated precipitation anomalies despite the expected dependence of the isotopic composition on convective activity, as suggested in previous studies (e.g., Bony et al., 2008; Lawrence et al., 2004). These changes reveal the plausibility of additional factors controlling  $\delta^{18}\text{O}_p$  in different climates. Therefore, we further explore the relative influence of precipitation and temperature on the simulated  $\delta^{18}\text{O}_p$  patterns to better understand what controls the oxygen isotopes during the monsoon season.

We evaluate the control of precipitation and temperature on  $\delta^{18}\text{O}_p$  values in different time periods by calculating their linear relationship during the WAM season using Spearman correlation analysis. The PI simulation yields north-south bidirectional correlation patterns between precipitation and  $\delta^{18}\text{O}_p$  values, with significant negative correlations ( $\geq -0.8$ ) over the Guinea Coast up to the Sahel (0–15°N) and positive correlations ( $\geq 0.7$ ) across the Sahara (Figure 12). The strong negative relationship along the coastal region toward the Sahel indicates the amount effect, as is expected based on previous studies (Lawrence et al., 2004; Rozanski et al., 1993). Convective activity has been well established as the main factor driving the spatial and temporal patterns of the isotopic

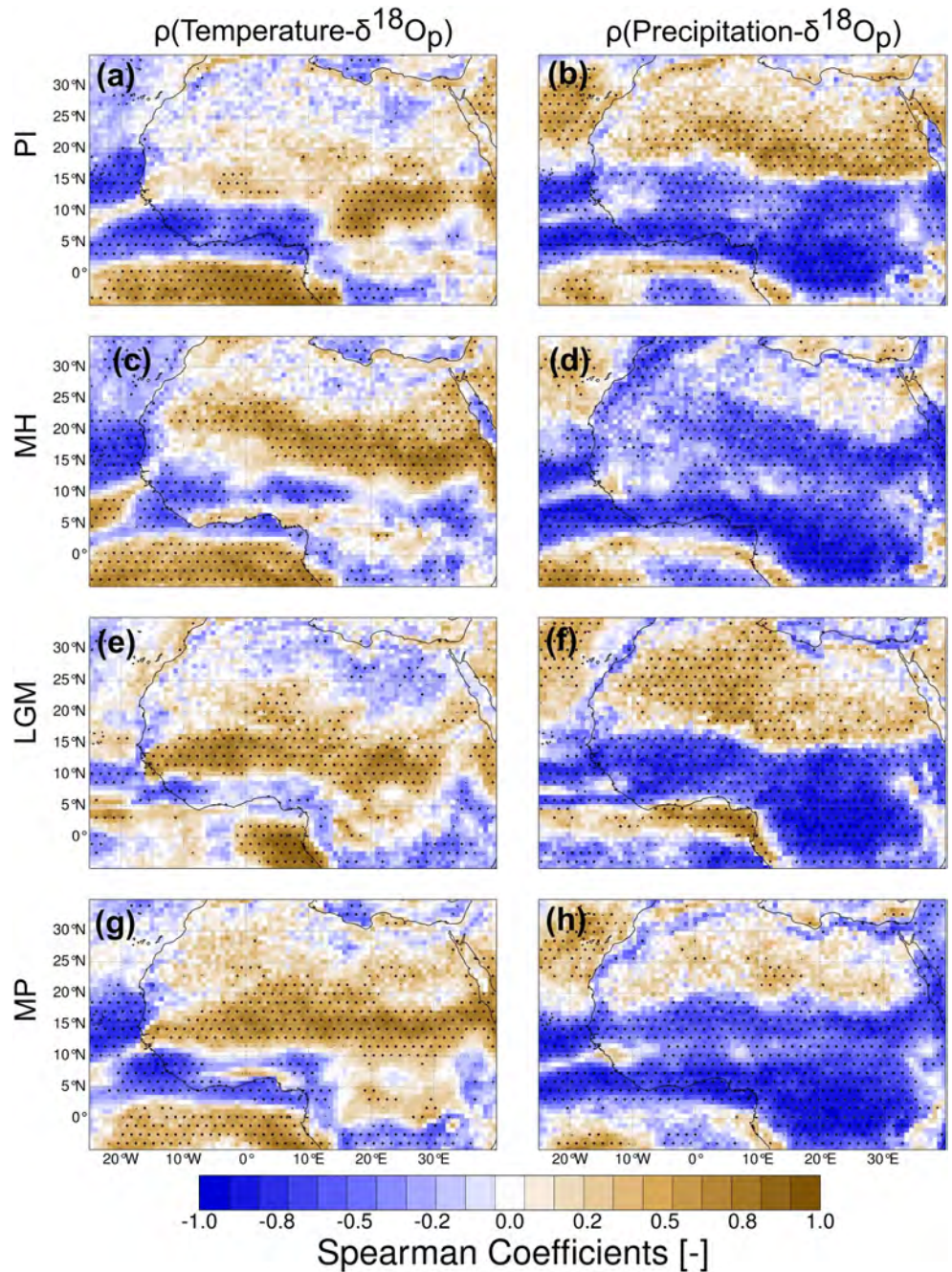


**Figure 12.** Spearman correlation coefficients for the interannual relationship between the simulated monthly means of  $\delta^{18}\text{O}_p$  and precipitation amount (right panel) and temperature (left panel) during the WAM months (JJAS). The dot stippling represents the regions with significant correlation coefficients with a 95% confidence interval. The correlations' magnitude and spatial patterns are not stationary in response to the different climates. For example, the bi-directional north-south  $\delta^{18}\text{O}_p$ -precipitation relation transitions to an overall negative relationship in the Mid-Holocene (MH).

composition of precipitation and vapor (Bony et al., 2008; Lawrence et al., 2004; Risi et al., 2008). The reasons why an increase in precipitation amount results in the depletion of the heavy oxygen isotope across the WAM might be partially due to the fact that (a) the increase in rainfall amount moistens the atmosphere, which reduces rainfall re-evaporation and diffusive fluxes, and ultimately results in lower  $\delta^{18}\text{O}_p$  values in raindrops; (b) intense convective activity increases vertical mixing in the form of unsaturated downdrafts, so that the associated depletion of low-level vapor feeds into subsequent convective systems with lower  $\delta^{18}\text{O}_p$  values (Lawrence

et al., 2004; Risi et al., 2008). The change in correlation direction over the Sahara indicates that the “amount effect” is limited across the Sahel region, where the maximum rain belt is situated during the monsoon season. These changes are unsurprising, as the rainout of the moisture transported from the equatorial Atlantic Ocean would deplete the remaining air masses of heavy oxygen isotopes. However, during the retreat of the WAM, evaporative recycling provides a moist air mass with relatively enriched heavy oxygen isotopes that condense to rainfall. These changes suggest the influence of continental recycling on the isotopic patterns across the Sahel. Surface evaporative fluxes through continental recycling result in air masses that are less negative than oceanic fluxes (Risi et al., 2013). Moreover, the warmer and drier conditions across the Sahara would contribute to more re-evaporation of falling vapor, leading to an enrichment in the heavier isotope in relation to the source (Risi et al., 2008). The LGM and MP simulations indicate similar correlation dipole patterns across the WAM, but the positive relationship across the Sahara in the MP is less significant (Figure 12). Nevertheless, the correlation patterns in the MH indicate an overall negative link across the whole WAM region, suggesting that the amount effect predominantly controls the oxygen isotopic patterns. The changes in the correlation structure across different past climates suggest the non-stationarity of the controlling mechanism across the WAM areas.

The correlation analyses for  $\delta^{18}\text{O}_p$  and temperature yield fewer regions with significant correlation due to the predominant influence of precipitation amount on  $\delta^{18}\text{O}_p$  during the WAM season. The analysis indicates positive correlation patterns over the Sahara, which extends further northward in the MP. The expanded area of positive correlation in the MP highlights the importance of continental recycling during the retreat of the WAM. These patterns also validate the wider spread of precipitation during the retreat months in the MP (Figure 6d), which has also been suggested in previous studies (Berntell et al., 2021). We highlight that the estimated interannual relationships from the simulated paleoclimate time slices only serve as a surrogate to evaluate the non-stationarity of the relationship between the  $\delta^{18}\text{O}_p$  and surface climate variables and do not necessarily reflect the causal mechanisms of the interannual variability of the proxy record. Although this analysis is limited to empirical evidence that does not consider causal mechanisms, the results clearly indicate that proxy reconstructions must efficiently understand the regional climatic influence on various proxy records. This would help resolve the inaccuracies in paleoclimate and paleoenvironment reconstructions that assume the stationarity of the calibrated transfer function (e.g., Kolstad & Screen, 2019; Raible et al., 2014). The comparison of the simulated isotopic values to proxy records and the investigation of the causal mechanisms leading to the available proxy records is beyond the scope of this study.

### 5.3. Atmospheric Dynamics Driving the Simulated WAM Changes

Overall, the response of the WAM to GHG forcing, vegetation changes, and orbital forcing is mostly associated with the changing meridional temperature gradient. A more pronounced gradient drives the increased intensity and higher altitude reach of the low-level southwesterlies and a more northward position of the ITD and AEJ. On the other hand, the weakening of the WAM in response to colder conditions can be attributed to the weak or non-existent meridional temperature and pressure gradient. This less pronounced gradient would lead to moisture transport into the continent and into the troposphere to suppress the wind shear of the AEJ. We discuss these simulated dynamics in the context of what has been suggested in previous studies, while also highlighting the new findings.

The pronounced summer meridional temperature and pressure patterns in the MH and MP climates are consistent with the PMIP4 model results (e.g., Berntell et al., 2021; Brierley et al., 2020; Kageyama et al., 2021). These temperature anomalies reflect the patterns of increased precipitation, namely wetter conditions across the Sahel to coastal regions in the MH and MP. The warming over the high latitudes deepened the Sahara Heat Low, inducing low-level moisture convergence and strengthening the south-westerly flow that transports moisture from the equatorial Atlantic into the continent (Lavaysse et al., 2009). In the MH, the warming across the Sahara and the cooling over the Sahel are more intense than in the MP. The increased insolation across the Northern Hemisphere was the main driver of the intense warming across the Sahara. On the other hand, the cooling over the Sahel is partly due to the cloudiness associated with increased precipitation due to enhanced moisture flux into the Sahel areas. Another factor may be the increased evaporative fraction (Figure S8 in Supporting Information S1) and upward latent heat flux (Figure 11), which moisten the soil and reduce the energy available to heat the near-surface air through sensible heat flux. These mechanisms (a) cool the surface where precipitation increases and (b) further strengthen the north-south gradient to drive moisture advection into the WAM region. This feedback indicates that moisture advection strengthens the WAM more than local recycling does (Marzin &

Braconnot, 2009; Y. Zhao et al., 2005). However, the internal feedback reinforces the pressure gradient and determines the northward migration of the WAM through evaporative recycling. In the MP, the seasonal precipitation distribution indicates a delayed WAM retreat with more precipitation during the southward retreat months than in the MH. Such precipitation seasonality highlights the role of internal feedback since the evaporative recycling supplies more moisture during the retreat months. Furthermore, cooling across the Sahel in the MP is more significant toward the east. These patterns coincide with the relative increase in upward latent heat flux toward the east, suggesting more moisture availability through local feedback to strengthen the cooling (Figure 11). Even though the MP has higher atmospheric CO<sub>2</sub> with an enhanced hydrological cycle, this study reveals that the orbital forcing and expanded vegetation in the MH produces the highest intensity of the WAM. These imply that GCMs must adequately represent these features to ensure accurate projections of the WAM in response to future climate change. In the LGM climate, the overall cooling and drying conditions prevent the initiation of a meridional pressure gradient to drive moisture into the continent. This resulted in continuous wind patterns from the Tropical Atlantic into the North Atlantic Ocean without diverging into the continent, as suggested in previous studies (e.g., Jiang et al., 2015; Kageyama et al., 2021; Otto-Bliesner et al., 2006). Overall, the strengthening of the meridional temperature and pressure gradient determines the intensity of the southwesterlies, northward migration of the WAM, and its altitudinal reach, which affects the location of the ITD and AEJ.

The simulated intensity and location of the AEJ and its relationship to the strengthening of the WAM suggest a complex causal mechanism. More specifically, the simulated core of the AEJ is situated at higher latitudes (15–20°N) and altitudes (600–500 hPa) in summer during the MH and MP than in the PI and LGM. These patterns are not surprising since the strengthened WAM in these climates is associated with a more northward position of the ITD and deeper monsoon depth (Janicot et al., 2011; Nicholson, 2009). Moreover, the surface temperature gradient maintains the AEJ, along with two meridional circulations forced by the dry convection of the Sahara Heat Low to the north and the moist convection driven by the ITCZ to the south (Thorncroft & Blackburn, 1999; Wu et al., 2009). Usually, the monsoonal flow of the low-level southwesterlies reaches far into the mid-troposphere to weaken the shear of the AEJ and shift it to higher latitudes (Patricola & Cook, 2007; Texier et al., 2000). However, the simulated intense monsoonal flow due to the pronounced meridional temperature gradient in the MH induces high AEJ intensity when compared to the MP. On the other hand, the reduced monsoonal flow simulated in the LGM also results in an AEJ intensity that is higher than PI. These causal relationship patterns indicate that the weakening of the AEJ is not entirely associated with the strengthening of the WAM, especially when orbital forcings mainly control large-scale climatic features. Therefore, the atmospheric dynamics response simulated in this study confirms that the position of the AEJ is more important in strengthening the WAM than its intensity, as suggested in previous studies (Jenkins et al., 2005; Nicholson, 2008; Nicholson & Grist, 2001; Nicholson & Webster, 2007). These suggest that the intensity of the AEJ is an effect rather than a cause (Newell & Kidson, 1984). The complexity of the causal relationship between AEJ and Sahel rainfall and its varied feedback, as reported by some studies, might be due to its sensitivity to localised conditions, which is represented differently in GCMs. For instance, Texier et al., 2000; Patricola & Cook, 2007 reveal that the decrease or even disappearance of the AEJ is achieved when the GCM is coupled to a dynamic vegetation model. Contrarily, Texier et al., 2000 produced an increased AEJ located further north without dynamic vegetation feedback in the model.

The simulated TEJ intensity shows consistent patterns of increasing shear due to wetter conditions, as indicated by previous studies (e.g., Nicholson and Klotter 2021). The simulated intensity in the MH and MP revealed no significant changes, but was higher than LGM and PI (Figure 10). The TEJ is mostly driven by large-scale remote features such as convective heating over the North Indian Ocean and the Himalayan-Tibetan plateau (Gill, 1980). However, Redelsperger et al. (2002) indicate that the latent heat release through convection over the WAM can enhance upper-level shear, thereby intensifying the TEJ. The causal mechanisms through which the intensified TEJ increases the Sahel rainfall have been proposed in many studies (Lemburg et al., 2019). These include upper-level divergence (Nicholson & Grist, 2003), vertical and horizontal shear and how it affects dynamic instabilities (Grist, 2002; Nicholson, 2008), and the modulation of the equatorial Rossby wave activity (Yang et al., 2018).

The results reveal both the localised and large-scale impacts of vegetation on precipitation over the WAM areas in response to different climates. Generally, vegetation influences the exchange of mass and energy between the land surface and the atmosphere through the modulation of (a) surface albedo, influencing surface radiation, and (b) evapotranspiration, influencing the partitioning of net radiation into surface heat fluxes. These imply that land cover does not only affect surface climate but also influences atmospheric convection and large-scale circulations

and moisture fluxes, which create further feedback and influence soil moisture and vegetation (Charney et al., 1977; Sylla et al., 2016). In this study, we focus on analyzing the influence of surface conditions through surface heat flux anomalies. Previous modelling studies have highlighted the role of soil moisture and evapotranspiration in the vegetation-precipitation feedback due to their effect on low-level moist static energy, convective instability, and surface latent heat flux anomalies (Patricola & Cook, 2007; Rachmayani et al., 2015). These feedback mechanisms have been shown to strengthen the response of the WAM to external forcing in past warmer climates (e.g., Messori et al., 2019). The expanded vegetation over the Sahara in the MH resulted in a pronounced upward latent heat flux, further strengthening the WAM and the moisture influx through the vegetation-albedo feedback (e.g., Bonfils et al., 2001; Levis et al., 2004). The less expanded vegetation in the MP also strengthened the WAM and contributed to the increased precipitation in the retreat months of the WAM, even though the meridional pressure gradient was weaker than in the MH. Previous studies have indicated wetter conditions and a northward migration of the WAM that is driven by the cyclonic moisture flux anomaly over North Africa due to expanded vegetation into the Sahara region (Chandan & Peltier, 2020; Pausata et al., 2020; Swann et al., 2014). Since the various atmospheric dynamics and surface conditions had a unidirectional influence on the WAM, isolating the impact of vegetation, a local amplifier forced by other large-scale features (e.g., Klein et al., 2017; Messori et al., 2019), would require further sensitivity experiments.

#### 5.4. Comparison of Model Estimates to Proxies

Comparing modeled paleoclimate to proxy reconstructions over Africa is often challenging, because of the varying representation of relevant atmospheric processes in different GCMs, and high spatial variability of proxy signals (e.g., deMenocal et al., 2000; Harrison et al., 2014; Hopcroft & Valdes, 2019; Pausata et al., 2016; Tierney et al., 2017). Moreover, the relatively low availability of paleohydrological records over Africa precludes a robust model-data comparison (e.g., Salzmann et al., 2008, 2013). The sparsity of proxies also prevents the merited direct comparison of simulated isotopic composition with past isotopic archives. Here, we focus on the MH model-data comparison due to the relatively large number of proxy reconstructions available (Figure S12a in Supporting Information S1) and the ongoing debate about the northward migration and intensification of the WAM during the African Humid Period (e.g., Pausata et al., 2020). The sparse tropical African proxy records for the LGM reported in previous studies have shown consistent cooling and drying conditions (Figure S12b in Supporting Information S1; Bartlein et al., 2011). It has been suggested that the dryness induced a downward elevational shift of broadleaved evergreen or warm mixed forest and the enrichment of steppe into regions now occupied by tropical forests (e.g., Elenga et al., 2000). The reconstructed proxy records over North Africa during the MP consistently suggested more humid conditions (Figure S12c in Supporting Information S1; Feng et al., 2022). More specifically, palynological data reveals denser tree cover and expanded woodland and savanna at the expense of deserts over North Africa (Bonnefille, 2010; Salzmann et al., 2008). Such vegetation expansion patterns are consistent with the only dynamic vegetation GCM output participating in PlioMIP2 (Stepanek et al., 2020). Moreover, multi-proxy records, including plant wax and dust from marine sediment cores from offshore West Africa (Figure S12c in Supporting Information S1), suggest consistent wetter conditions in the MP (deMenocal, 2004; Feng et al., 2022; Kuechler et al., 2018). These reconstructed patterns are consistent with the more humid and dryness simulated for the LGM and MP in this study.

In the remainder of this section, we compare the simulated latitudinal variation of Mean Annual Precipitation (MAP) during the MH to pollen-based reconstructions by Bartlein et al. (2011) and leaf wax isotope-based reconstruction by Tierney et al. (2017). Overall, the simulated MAP magnitudes and latitudinal distribution by ECHAM5-wiso are closer to the proxy reconstructions than the PMIP4 models (Figure 13). More specifically, the ECHAM5-wiso inter-annual means of the WAM's northward extent compare well to the lower latitudes of the proxy data over the Sahara with regards to the magnitude of changes and the patterns from the Sahel towards the tropical ocean. However, all models (i.e., PMIP4 models and ECHAM5-wiso) failed to match the magnitudes of the proxy-based MAP increase over the high latitudes of the Sahara. The simulated MAP increase over the Sahara was 100–300 mm/year less than the proxy reconstruction. It is important to note that the calculated MAP anomalies of the pollen-inferred precipitation proxy records used present-day CRU observation data as a reference period, while the GCMs used their PI simulations. Although the different reference periods can contribute slightly to the discrepancies, the magnitude of the difference is large enough to acknowledge significant deviations and thus potential limitations of either the GCMs or the proxy-based reconstructions. The simulated ECHAM5-wiso anomalies during the monsoon season indicated wetter conditions up to 25°N, with increased



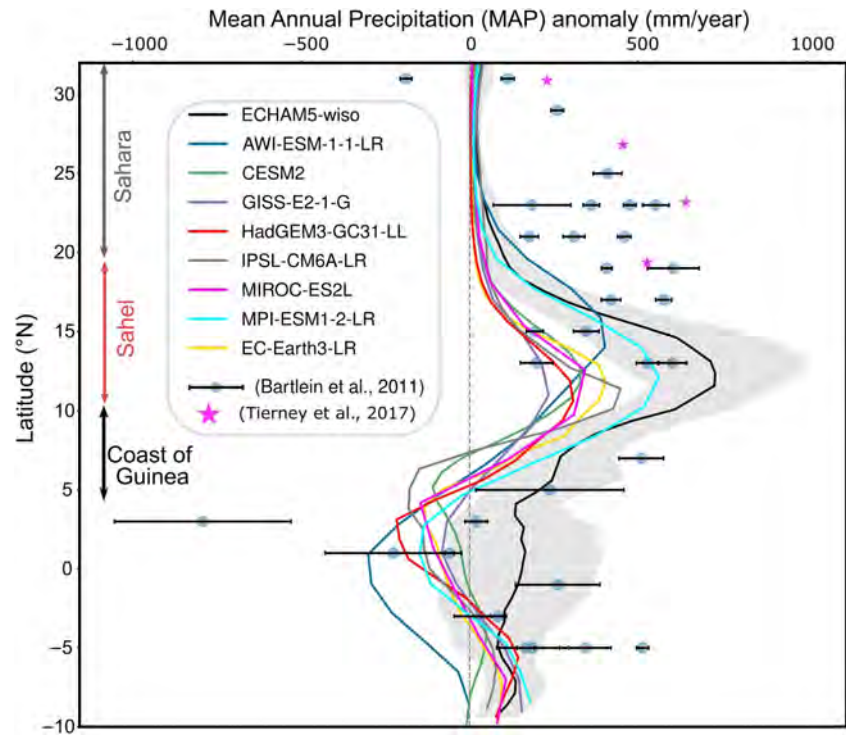


**Figure 13.** Comparison of the mean annual precipitation (MAP) anomalies of the latitudinal extent of WAM in the Mid-Holocene for all models (ECHAM5-wiso (black) and PMIP4 models) to pollen-inferred (Bartlein et al., 2011; blue circles) and leaf wax-inferred (Tierney et al., 2017; magenta stars) precipitation reconstruction. The black shadings denote one standard deviation value from the regional means of the ECHAM5-wiso simulation. The error bars of the proxies represent the standard errors of the precipitation reconstructions.

precipitation anomalies of approximately 700 mm/year (Figure 3). This suggests a potential overestimation of precipitation anomalies from the pollen-based records on the annual scale due to their potentially biased representation of the dry seasons across the Sahara. In addition to the pollen-based reconstructions, other diverse archives over West Africa estimate precipitation differences in the range of 300–500 mm/month, which are within the range of our model estimates (Harrison et al., 2014; Kröpelin et al., 2008; Tierney et al., 2017). On the other hand, recent reconstructions of leaf wax-alkane records off the coast of northern Africa suggest MAP increase of up to 600 mm/year (compared to PI) as far north as 31°N (Figure 13), implying an expansion of the WAM in the MH to 15–20° north of its present-day extent (Sultan & Janicot, 2003; Tierney et al., 2017). Sha et al. (2019) interpreted their Moroccan speleothem at 31°N with high negative  $\delta^{18}\text{O}$  of carbonate records as a high rainfall signal created by the expansion of the WAM during the MH. Paleoenvironment reconstructions also reflect wetter conditions in the MH with higher lake levels and moisture-demanding biomes across North Africa (Kohfeld & Harrison, 2000; Peyron et al., 2006; H. Wu et al., 2007). Vegetation reconstructions suggest a northward shift of montane forest and a major extension of the tropical rainforest over North Africa (Jolly et al., 1998; Prentice et al., 2000).

Overall, the model-proxy comparison reveals that all the adopted GCMs show limited skill in reproducing the northward migration of the WAM and associated rainfall increase over the Sahara. This suggests that the shortcomings leading to these discrepancies are shared by all models and are not GCM-specific. The WAM dynamics are sensitive to the representation of climate physics in the GCMs. Their limitations include inaccuracies in representing clouds, surface conditions (e.g., lakes and wetlands), energy fluxes, and subgrid-scale convection parameterisation. Additionally, the coarse spatial resolution of GCMs weakens their ability to reproduce the mesoscale convection systems that are the main driver for the WAM. Previous studies have also indicated that fully coupled models exhibit biases in reproducing the tropical Atlantic dynamics, leading to elevated sea surface temperatures and a weakened monsoonal circulation (Roehring et al., 2013). In this study, the high spatial resolution of the ECHAM5-wiso experiment contributed to a better representation of surface

conditions, such as orography. Furthermore, the model was prescribed MH vegetation reconstruction. Contrarily, the PMIP4 models are fully coupled (atmosphere-ocean), incorporating ocean variability feedback, and some consider dynamic vegetation feedback. Since all models, that is, both ECHAM5-wiso and the PMIP models, exhibit the above-mentioned deviations from proxy reconstructions, we propose that the limitations are neither related solely to spatial resolution nor the use of fully coupled models. Harrison et al. (2015) suggests the simulated biases of the PI control experiments of the PMIP4-CMIP6, which indicate a more equatorward ensemble mean of the global monsoon when compared to observations. Previous models have also shown that atmosphere-vegetation feedback contributes to the northward extent of the WAM, but still underestimates the higher latitude precipitation amount from the leaf wax n-alkanes (Dallmeyer et al., 2020; Pausata et al., 2016; Thompson et al., 2019). Rachmayani et al. (2015) demonstrated that dynamic vegetation enhances the orbitally driven increase in precipitation anomalies over West Africa by 20% when compared to models using fixed vegetation. However, their models with terrestrial and ocean feedback still did not reach the level of vegetation coverage suggested by proxies.

Recent studies have demonstrated that incorporating dust feedbacks associated with the Green Sahara in the MH orbitally driven climate further enhances the northward reach and intensification of the WAM (e.g., Egerer et al., 2018; Hopcroft & Valdes, 2019; Pausata et al., 2016; Thompson et al., 2019) and better matches the paleoclimate reconstructions. This is because the albedo-related feedback causes a reduction of dust concentration and changes in soil properties over the vegetated Sahara, which induce an increase in incoming shortwave radiation on the land surface, strengthening the warming over the Sahara. This further strengthens the meridional temperature gradient and tropical circulation and then intensifies the WAM (Chandan & Peltier, 2020; Pausata et al., 2016). Pausata et al. (2016) demonstrated the northward extent of the WAM up to 31°N in the MH with a model forced with prescribed vegetation and reduced dust concentrations, while the prescribed vegetation only reached ~26°N. These suggest that simulating vegetation feedback with interactive dust dynamics on a high spatial resolution grid would improve the representation of the MH. However, the state-of-art GCMs would require improvement of their physical representation of dust dynamics, since they fail to reproduce dust emission and transport (Evan et al., 2014; Kok, 2010; Leung et al., 2023; A. Zhao et al., 2022). On the other hand, the plausible non-stationarity of the pollen-precipitation transfer function due to changes in past climate dynamics from present conditions can also contribute to the mismatch between climate simulation and paleoclimate reconstructions. Therefore, using a multi-proxy system with varied causal mechanisms could ensure an accurate representation of the WAM complex dynamics.

## 6. Conclusions

This study presents new and existing climate model simulations of the WAM and associated features in the Late Cenozoic (i.e., the PI, MH, LGM and MP). More specifically, the study presents an overview of the hydroclimate changes over West Africa and highlights the components of the regional climate system that are important for generating accurate projections of future climate. The paleoclimate experiments were conducted using the isotope-tracking model (ECHAM5-wiso). The simulated results are similar to the CMIP6-PMIP4 experiments and proxy reconstructions over West Africa. However, our simulations also show some improvement over previous experiments, and yield new insights. We summarize the key results as follows:

1. A comparison between the present-day ECHAM5-wiso simulation and observation-based data sets (i.e., ERA5 and CRU precipitation and temperature data sets) demonstrates the model's ability to represent the atmospheric dynamics over West Africa reasonably well.
2. The ECHAM5-wiso paleoclimate simulations produce the most intense WAM during the MH, despite the MP's more enhanced hydrological cycle. In comparison, some of the CMIP6-PMIP4 models suggest the highest intensification of the WAM in the MH (e.g., GISS-E2-1-G), while others suggest the MP (e.g., EC-Earth3-LR).
3. The intensification of the WAM is associated with a pronounced meridional gradient, northward position of the ITD, northward reach of the core of the AEJ, higher altitudinal reach of the WAM (deeper monsoon depth), and higher moisture recycling through surface heat fluxes due to vegetation across the Sahel-Sahara region. Most importantly, the AEJ is not entirely responsible for the strengthening of the WAM, especially when large-scale features are predominantly controlled by orbital forcings, as is the case in the MH. This needs to be well-represented in GCMs to ensure realistic and accurate future projections.

4. The simulation of the patterns and magnitude of  $\delta^{18}\text{O}_p$  values and associated regional climate elements (e.g., temperature and precipitation) during the monsoon season reveal a non-stationarity of their relationship throughout the late Cenozoic. Their changing relationships stress the need to understand the causal mechanisms for each proxy system and refine their transfer function to ensure accurate proxy-based reconstructions.
5. ECHAM5-wiso simulates the higher precipitation rates over the WAM region in the MH than the CMIP6-PMIP4 models. Since our model uses a more accurate vegetation reconstruction and a higher resolution, we propose that a greater consideration of vegetation feedbacks, and sub-grid processes will increase other models' representation of West African climate during the MH.
6. All models still underestimate the northward extent of the WAM, as reconstructed with proxies. If proxy reconstructions are taken as accurate, this suggests that the representation of additional climate processes, such as dust loading, interactive vegetation, and surface conditions, such as lakes, will have to be improved to ensure a more realistic prediction of the WAM's northward extent.

### Data Availability Statement

The postprocessed model output variables required to reproduce the figures of this study are available in NetCDF format at <https://doi.org/10.5281/zenodo.10455772> (Boateng, 2024). The CMIP6-PMIP4 (Eyring et al., 2016) models output are available at <https://esgf-node.llnl.gov/projects/esgf-llnl/> (last access: 03 January 2024). The Climate Research Unit (CRUv4.01) (Harris et al., 2020) precipitation data were obtained from [https://crudata.uea.ac.uk/cru/data/hrg/cru\\_ts\\_4.01/](https://crudata.uea.ac.uk/cru/data/hrg/cru_ts_4.01/) (last access: 03 January 2024).

The ERA5 reanalysis products (Hersbach et al., 2020) were obtained from the Copernicus Climate Data Store at <https://cds.climate.copernicus.eu/cdsapp#!home> (last access: 03 January 2024).

*Code availability statement:* The ECHAM model code is available under a version of the MPI-M software license agreement (<https://www.mpimet.mpg.de/en/science/models/license/>, last access: 03 January 2024). The code of the isotopic version ECHAM5-wiso (Werner et al., 2011) is available upon request on the Alfred Wegner Institute's GitLab repository (<https://gitlab.awi.de/mwerner/mppi-esm-wiso>, last access: 03 January 2024). The scripts used for postprocessing, analysis, and visualisation are based on a Python package (pyClimat) available at <https://doi.org/10.5281/zenodo.7143044> (Boateng, 2022) and also on Github: <https://github.com/Dan-Boat/pyClimat> (last access: 03 January 2024).

### Acknowledgments

This research was supported by the German Science Foundation (DFG) Grants EH329/19-1 and EH329/23-1 (awarded to Todd A. Ehlers), MU4188/3-1 and MU4188/1-1 (awarded to Sebastian G. Mutz). We acknowledge the World Climate Research Programme, which, through its Working Group on Coupled Modelling, coordinated and promoted CMIP6. We thank the climate modelling groups for producing and making their model output available, the Earth System Grid Federation (ESGF) for archiving the data and providing access, and the multiple funding agencies supporting CMIP and ESGF. Additionally, we thank the European Centre for Medium-Range Weather Forecasts for providing ERA5 data sets and the University of East Anglia for producing the CRU data sets. Open Access funding enabled and organized by Projekt DEAL through the University of Tübingen. Open Access funding enabled and organized by Projekt DEAL.

### References

- Abe-Ouchi, A., Saito, F., Kageyama, M., Braconnot, P., Harrison, S. P., Lambeck, K., et al. (2015). Ice-sheet configuration in the CMIP5/PMIP3 Last Glacial Maximum experiments. *Geoscientific Model Development*, 8(11), 3621–3637. <https://doi.org/10.5194/gmd-8-3621-2015>
- Adegbe, A. T., Schneider, R. R., Röhl, U., & Wefer, G. (2003). Glacial millennial-scale fluctuations in central African precipitation recorded in terrigenous sediment supply and freshwater signals offshore Cameroon. *Palaeogeography, Palaeoclimatology, Palaeoecology*, 197(3), 323–333. [https://doi.org/10.1016/S0031-0182\(03\)00474-7](https://doi.org/10.1016/S0031-0182(03)00474-7)
- Ait Brahimi, Y., Sha, L., Wassenburg, J. A., Azennoud, K., Cheng, H., Cruz, F. W., & Bouchaou, L. (2023). The spatiotemporal extent of the Green Sahara during the last glacial period. *iScience*, 26(7), 107018. <https://doi.org/10.1016/j.isci.2023.107018>
- Annan, J. D., & Hargreaves, J. C. (2013). A new global reconstruction of temperature changes at the Last Glacial Maximum. *Climate of the Past*, 9(1), 367–376. <https://doi.org/10.5194/cp-9-367-2013>
- Annan, J. D., & Hargreaves, J. C. (2015). A perspective on model-data surface temperature comparison at the Last Glacial Maximum. *Quaternary Science Reviews*, 107, 1–10. <https://doi.org/10.1016/j.quascirev.2014.09.019>
- Armitage, S. J., Bristow, C. S., & Drake, N. A. (2015). West African monsoon dynamics inferred from abrupt fluctuations of Lake Mega-Chad. *Proceedings of the National Academy of Sciences*, 112(28), 8543–8548. <https://doi.org/10.1073/pnas.1417655112>
- Arnold, L., Bréon, F.-M., & Brewer, S. (2009). The Earth as an extrasolar planet: The vegetation spectral signature today and during the last Quaternary climatic extrema. *International Journal of Astrobiology*, 8(2), 81–94. <https://doi.org/10.1017/S1473550409004406>
- Badger, M. P. S., Schmidt, D. N., Mackensen, A., & Pancost, R. D. (2013). High-resolution alkenone palaeobarometry indicates relatively stable pCO<sub>2</sub> during the Pliocene (3.3–2.8 Ma). *Philosophical Transactions of the Royal Society A: Mathematical, Physical & Engineering Sciences*, 371(2001), 20130094. <https://doi.org/10.1098/rsta.2013.0094>
- Baidu, M., Schwendike, J., Marsham, J. H., & Bain, C. (2022). Effects of vertical wind shear on intensities of mesoscale convective systems over West and Central Africa. *Atmospheric Science Letters*, 23(8), e1094. <https://doi.org/10.1002/asl.1094>
- Barbé, L. L., Lebel, T., & Tapsoba, D. (2002). Rainfall variability in West Africa during the years 1950–90. *Journal of Climate*, 15(2), 187–202. [https://doi.org/10.1175/1520-0442\(2002\)015<0187:RVIWAD>2.0.CO;2](https://doi.org/10.1175/1520-0442(2002)015<0187:RVIWAD>2.0.CO;2)
- Bartlein, P. J., Harrison, S. P., Brewer, S., Connor, S., Davis, B. A. S., Gajewski, K., et al. (2011). Pollen-based continental climate reconstructions at 6 and 21 ka: A global synthesis. *Climate Dynamics*, 37(3), 775–802. <https://doi.org/10.1007/s00382-010-0904-1>
- Bartoli, G., Hönisch, B., & Zeebe, R. E. (2011). Atmospheric CO<sub>2</sub> decline during the Pliocene intensification of Northern Hemisphere glaciations. *Paleoceanography*, 26(4). <https://doi.org/10.1029/2010PA002055>
- Bell, B., Hersbach, H., Simmons, A., Berrisford, P., Dahlgren, P., Horányi, A., et al. (2021). The ERA5 global reanalysis: Preliminary extension to 1950. *Quarterly Journal of the Royal Meteorological Society*, 147(741), 4186–4227. <https://doi.org/10.1002/qj.4174>

- Bereiter, B., Eggleston, S., Schmitt, J., Nehrbass-Ahles, C., Stocker, T. F., Fischer, H., et al. (2015). Revision of the EPICA Dome C CO<sub>2</sub> record from 800 to 600 kyr before present. *Geophysical Research Letters*, 42(2), 542–549. <https://doi.org/10.1002/2014GL061957>
- Bertell, E., Zhang, Q., Li, Q., Haywood, A. M., Tindall, J. C., Hunter, S. J., et al. (2021). Mid-Pliocene West African monsoon rainfall as simulated in the PlioMIP2 ensemble. *Climate of the Past*, 17(4), 1777–1794. <https://doi.org/10.5194/cp-17-1777-2021>
- Biasutti, M. (2013). Forced Sahel rainfall trends in the CMIP5 archive. *Journal of Geophysical Research: Atmospheres*, 118(4), 1613–1623. <https://doi.org/10.1002/jgrd.50206>
- Bigelow, N. H., Brubaker, L. B., Edwards, M. E., Harrison, S. P., Prentice, I. C., Anderson, P. M., et al. (2003). Climate change and Arctic ecosystems: 1. Vegetation changes North of 55°N between the last glacial maximum, mid-Holocene, and present. *Journal of Geophysical Research*, 108(D19). <https://doi.org/10.1029/2002JD002558>
- Blunier, T., & Brook, E. J. (2001). Timing of millennial-scale climate change in Antarctica and Greenland during the last glacial period. *Science*, 291(5501), 109–112. <https://doi.org/10.1126/science.291.5501.109>
- Boateng, D. (2022). A functional based python module for processing, analysis and visualization of climate model output (pyClimat) (Version 0.0.1). [Software]. Zenodo. <https://doi.org/10.5281/zenodo.7143044>
- Boateng, D. (2024). West African Monsoon dynamics and its control on the stable oxygen isotopic composition of precipitation in the Late Cenozoic. [Dataset]. Zenodo. <https://doi.org/10.5281/zenodo.10455772>
- Boateng, D., Mutz, S. G., Ballian, A., Meijers, M. J. M., Methner, K., Botsyun, S., et al. (2023). The effects of diachronous surface uplift of the European Alps on regional climate and the oxygen isotopic composition of precipitation. *Earth System Dynamics*, 14(6), 1183–1210. <https://doi.org/10.5194/esd-14-1183-2023>
- Bonfils, C., Noblet-Ducoudré, N., Braconnot, P., & Joussaume, S. (2001). Hot Desert albedo and climate change: Mid-Holocene monsoon in North Africa. *Journal of Climate*, 14(17), 3724–3737. [https://doi.org/10.1175/1520-0442\(2001\)014<3724:HDAACC>2.0.CO;2](https://doi.org/10.1175/1520-0442(2001)014<3724:HDAACC>2.0.CO;2)
- Bonnefille, R. (2010). Cenozoic vegetation, climate changes and hominid evolution in tropical Africa. *Global and Planetary Change*, 72(4), 390–411. <https://doi.org/10.1016/j.gloplacha.2010.01.015>
- Bony, S., Risi, C., & Vimeux, F. (2008). Influence of convective processes on the isotopic composition ( $\delta^{18}O$  and  $\delta D$ ) of precipitation and water vapor in the tropics: 1. Radiative-Convective equilibrium and tropical ocean–global atmosphere–coupled ocean–atmosphere response experiment (TOGA-COARE) simulations. *Journal of Geophysical Research*, 113(D19). <https://doi.org/10.1029/2008JD009942>
- Boos, W. R. (2012). Thermodynamic scaling of the hydrological cycle of the Last Glacial Maximum. *Journal of Climate*, 25(3), 992–1006. <https://doi.org/10.1175/JCLI-D-11-00010.1>
- Bosmans, J. H. C., Drijfhout, S. S., Tuentner, E., Lourens, L. J., Hilgen, F. J., & Weber, S. L. (2012). Monsoonal response to mid-Holocene orbital forcing in a high resolution GCM. *Climate of the Past*, 8(2), 723–740.
- Botsyun, S., Mutz, S. G., Ehlers, T. A., Koptev, A., Wang, X., Schmidt, B., et al. (2022). Influence of large-scale atmospheric dynamics on precipitation seasonality of the Tibetan Plateau and Central Asia in cold and warm climates during the late cenozoic. *Journal of Geophysical Research: Atmospheres*, 127(12), e2021JD035810. <https://doi.org/10.1029/2021JD035810>
- Boyle, J., & Klein, S. A. (2010). Impact of horizontal resolution on climate model forecasts of tropical precipitation and diabatic heating for the TWP-ICE period. *Journal of Geophysical Research*, 115(D23). <https://doi.org/10.1029/2010JD014262>
- Braconnot, P., Harrison, S. P., Joussaume, S., Hewitt, C. D., Kitoh, A., Kutzbach, J. E., et al. (2004). Evaluation of PMIP coupled ocean-atmosphere simulations of the mid-Holocene. In R. W. Battarbee, F. Gasse, & C. E. Stickley (Eds.), *Past climate variability through Europe and Africa* (pp. 515–533). Springer Netherlands. [https://doi.org/10.1007/978-1-4020-2121-3\\_24](https://doi.org/10.1007/978-1-4020-2121-3_24)
- Braconnot, P., Harrison, S. P., Kageyama, M., Bartlein, P. J., Masson-Delmotte, V., Abe-Ouchi, A., et al. (2012). Evaluation of climate models using palaeoclimatic data. *Nature Climate Change*, 2(6), 417–424. <https://doi.org/10.1038/nclimate1456>
- Braconnot, P., Otto-Bliesner, B., Harrison, S., Joussaume, S., Peterchmitt, J.-Y., Abe-Ouchi, A., et al. (2007). Results of PMIP2 coupled simulations of the Mid-Holocene and Last Glacial Maximum – Part 1: Experiments and large-scale features. *Climate of the Past*, 3(2), 261–277. <https://doi.org/10.5194/cp-3-261-2007>
- Brady, E. C., Otto-Bliesner, B. L., Kay, J. E., & Rosenbloom, N. (2013). Sensitivity to glacial forcing in the CCSM4. *Journal of Climate*, 26(6), 1901–1925. <https://doi.org/10.1175/JCLI-D-11-00416.1>
- Brierley, C. M., Zhao, A., Harrison, S. P., Braconnot, P., Williams, C. J. R., Thornalley, D. J. R., et al. (2020). Large-scale features and evaluation of the PMIP4-CMIP6 midHolocene simulations. *Climate of the Past*, 16(5), 1847–1872. <https://doi.org/10.5194/cp-16-1847-2020>
- Bühler, J. C., Axelsson, J., Lechleitner, F. A., Fohlmeister, J., LeGrande, A. N., Midhun, M., et al. (2022). Investigating stable oxygen and carbon isotopic variability in speleothem records over the last millennium using multiple isotope-enabled climate models. *Climate of the Past*, 18(7), 1625–1654. <https://doi.org/10.5194/cp-18-1625-2022>
- Burke, K. D., Williams, J. W., Chandler, M. A., Haywood, A. M., Lunt, D. J., & Otto-Bliesner, B. L. (2018). Pliocene and Eocene provide best analogs for near-future climates. *Proceedings of the National Academy of Sciences*, 115(52), 13288–13293. <https://doi.org/10.1073/pnas.1809600115>
- Cao, J., Wang, B., & Ma, L. (2019). Attribution of global monsoon response to the last glacial maximum forcings. *Journal of Climate*, 32(19), 6589–6605. <https://doi.org/10.1175/JCLI-D-18-0871.1>
- Cauquoin, A., Werner, M., & Lohmann, G. (2019). Water isotopes – Climate relationships for the mid-Holocene and preindustrial period simulated with an isotope-enabled version of MPI-ESM. *Climate of the Past*, 15(6), 1913–1937. <https://doi.org/10.5194/cp-15-1913-2019>
- Chandan, D., & Peltier, W. R. (2020). African Humid Period precipitation sustained by robust vegetation, soil, and lake feedbacks. *Geophysical Research Letters*, 47(21), e2020GL088728. <https://doi.org/10.1029/2020GL088728>
- Charney, J., Quirk, W. J., Chow, S., & Kornfield, J. (1977). A comparative study of the effects of albedo change on drought in semi-arid regions. *Journal of the Atmospheric Sciences*, 34(9), 1366–1385. [https://doi.org/10.1175/1520-0469\(1977\)034<1366:ACSTO>2.0.CO;2](https://doi.org/10.1175/1520-0469(1977)034<1366:ACSTO>2.0.CO;2)
- Cheng, H., Edwards, R. L., Sinha, A., Spötl, C., Yi, L., Chen, S., et al. (2016). The Asian monsoon over the past 640,000 years and ice age terminations. *Nature*, 534(7609), 640–646. <https://doi.org/10.1038/nature18591>
- Clark, P. U., Dyke, A. S., Shakun, J. D., Carlson, A. E., Clark, J., Wohlfarth, B., et al. (2009). The last glacial maximum. *Science*, 325(5941), 710–714. <https://doi.org/10.1126/science.1172873>
- Claussen, M., Kubatzki, C., Brovkin, V., Ganopolski, A., Hoelzmann, P., & Pachur, H.-J. (1999). Simulation of an abrupt change in Saharan vegetation in the Mid-Holocene. *Geophysical Research Letters*, 26(14), 2037–2040. <https://doi.org/10.1029/1999GL900494>
- CLIMAP, P. (1981). Seasonal reconstructions of the Earth's surface at the last glacial maximum. *Geological Society of America*.
- Coe, M., & Harrison, S. (2002). The water balance of northern Africa during the mid-Holocene: An evaluation of the 6 ka BP PMIP simulations. *Climate Dynamics*, 19(2), 155–166. <https://doi.org/10.1007/s00382-001-0219-3>
- Cook, K. H. (2008). The mysteries of Sahel droughts. *Nature Geoscience*, 1(10), 647–648. <https://doi.org/10.1038/ngeo320>
- Corvec, S., & Fletcher, C. G. (2017). Changes to the tropical circulation in the mid-Pliocene and their implications for future climate. *Climate of the Past*, 13(2), 135–147. <https://doi.org/10.5194/cp-13-135-2017>

- Craig, H., & Gordon, L. I. (1965). Deuterium and oxygen 18 variations in the ocean and the marine atmosphere.
- Cremaschi, M., & Di Lernia, S. (1999). Holocene climatic changes and cultural dynamics in the Libyan Sahara. *African Archaeological Review*, 16(4), 211–238. <https://doi.org/10.1023/A:1021609623737>
- Crook, J., Klein, C., Folwell, S., Taylor, C. M., Parker, D. J., Stratton, R., & Stein, T. (2019). Assessment of the representation of West African storm lifecycles in convection-permitting simulations. *Earth and Space Science*, 6(5), 818–835. <https://doi.org/10.1029/2018EA000491>
- D'Agostino, R., Bader, J., Bordoni, S., Ferreira, D., & Jungclaus, J. (2019). Northern hemisphere monsoon response to mid-Holocene orbital forcing and greenhouse gas-induced global warming. *Geophysical Research Letters*, 46(3), 1591–1601. <https://doi.org/10.1029/2018GL081589>
- D'Agostino, R., Brown, J. R., Moise, A., Nguyen, H., Dias, P. L. S., & Jungclaus, J. (2020). Contrasting Southern Hemisphere monsoon response: MidHolocene orbital forcing versus future greenhouse gas-induced global warming. *Journal of Climate*, 33(22), 9595–9613. <https://doi.org/10.1175/JCLI-D-19-0672.1>
- Dallmeyer, A., Claussen, M., Lorenz, S. J., & Shanahan, T. (2020). The end of the African humid period as seen by a transient comprehensive Earth system model simulation of the last 8000 years. *Climate of the Past*, 16(1), 117–140. <https://doi.org/10.5194/cp-16-117-2020>
- Dansgaard, W., Johnsen, S. J., Clausen, H. B., Dahl-Jensen, D., Gundestrup, N. S., Hammer, C. U., et al. (1993). Evidence for general instability of past climate from a 250-kyr ice-core record. *Nature*, 364(6434), 218–220. <https://doi.org/10.1038/364218a0>
- de la Vega, E., Chalk, T. B., Wilson, P. A., Bysani, R. P., & Foster, G. L. (2020). Atmospheric CO<sub>2</sub> during the mid-Piacenzian warm period and the M2 glaciation. *Scientific Reports*, 10(1), 11002. <https://doi.org/10.1038/s41598-020-67154-8>
- deMenocal, P., Ortiz, J., Guilderson, T., Adkins, J., Sarnthein, M., Baker, L., & Yarusinsky, M. (2000). Abrupt onset and termination of the African Humid Period: Rapid climate responses to gradual insolation forcing. *Quaternary Science Reviews*, 19(1), 347–361. [https://doi.org/10.1016/S0277-3791\(99\)00081-5](https://doi.org/10.1016/S0277-3791(99)00081-5)
- deMenocal, P. B. (2004). African climate change and faunal evolution during the Pliocene–Pleistocene. *Earth and Planetary Science Letters*, 220(1), 3–24. [https://doi.org/10.1016/S0012-821X\(04\)00003-2](https://doi.org/10.1016/S0012-821X(04)00003-2)
- de Nooijer, W., Zhang, Q., Li, Q., Zhang, Q., Li, X., Zhang, Z., et al. (2020). Evaluation of Arctic warming in mid-Pliocene climate simulations. *Climate of the Past*, 16(6), 2325–2341. <https://doi.org/10.5194/cp-16-2325-2020>
- Dietrich, S., Werner, M., Spanghel, T., & Lohmann, G. (2013). Influence of orbital forcing and solar activity on water isotopes in precipitation during the mid- and late Holocene. *Climate of the Past*, 9(1), 13–26. <https://doi.org/10.5194/cp-9-13-2013>
- Dowsett, H., Dolan, A., Rowley, D., Moucha, R., Forte, A. M., Mitrovica, J. X., et al. (2016). The PRISM4 (mid-Piacenzian) paleoenvironmental reconstruction. *Climate of the Past*, 12(7), 1519–1538. <https://doi.org/10.5194/cp-12-1519-2016>
- Dowsett, H., Robinson, M., Haywood, A. M., Salzmann, U., Hill, D., Sohl, L. E., et al. (2010). The PRISM3D paleoenvironmental reconstruction. *Stratigraphy*.
- Dunne, J., Evershed, R. P., Salque, M., Cramp, L., Bruni, S., Ryan, K., et al. (2012). First dairying in green Saharan Africa in the fifth millennium BC. *Nature*, 486(7403), 390–394. <https://doi.org/10.1038/nature11186>
- Egerer, S., Claussen, M., & Reick, C. (2018). Rapid increase in simulated North Atlantic dust deposition due to fast change of northwest African landscape during the Holocene. *Climate of the Past*, 14(7), 1051–1066. <https://doi.org/10.5194/cp-14-1051-2018>
- Elenga, H., Peyron, O., Bonnefille, R., Jolly, D., Cheddadi, R., Guiot, J., et al. (2000). Pollen-based biome reconstruction for southern Europe and Africa 18,000 yr bp. *Journal of Biogeography*, 27(3), 621–634. <https://doi.org/10.1046/j.1365-2699.2000.00430.x>
- Erfanian, A., Wang, G., Yu, M., & Anyah, R. (2016). Multimodel ensemble simulations of present and future climates over West Africa: Impacts of vegetation dynamics. *Journal of Advances in Modeling Earth Systems*, 8(3), 1411–1431. <https://doi.org/10.1002/2016MS000660>
- Etheridge, D. M., Steele, L. P., Francey, R. J., & Langenfelds, R. L. (1998). Atmospheric methane between 1000 A.D. and present: Evidence of anthropogenic emissions and climatic variability. *Journal of Geophysical Research*, 103(D13), 15979–15993. <https://doi.org/10.1029/98JD00923>
- Etheridge, D. M., Steele, L. P., Langenfelds, R. L., Francey, R. J., Barnola, J.-M., & Morgan, V. I. (1996). Natural and anthropogenic changes in atmospheric CO<sub>2</sub> over the last 1000 years from air in Antarctic ice and firn. *Journal of Geophysical Research*, 101(D2), 4115–4128. <https://doi.org/10.1029/95JD03410>
- Evan, A. T., Flamant, C., Fiedler, S., & Doherty, O. (2014). An analysis of aeolian dust in climate models. *Geophysical Research Letters*, 41(16), 5996–6001. <https://doi.org/10.1002/2014GL060545>
- Eyring, V., Bony, S., Meehl, G. A., Senior, C. A., Stevens, B., Stouffer, R. J., & Taylor, K. E. (2016). Overview of the coupled model Inter-comparison project phase 6 (CMIP6) experimental design and organization. *Geoscientific Model Development*, 9(5), 1937–1958. <https://doi.org/10.5194/gmd-9-1937-2016>
- Feng, R., Bhattacharya, T., Otto-Bliesner, B. L., Brady, E. C., Haywood, A. M., Tindall, J. C., et al. (2022). Past terrestrial hydroclimate sensitivity controlled by Earth system feedbacks. *Nature Communications*, 13(1), 1306. <https://doi.org/10.1038/s41467-022-28814-7>
- Friedrich, T., Timmermann, A., Tigchelaar, M., Elison Timm, O., & Ganopolski, A. (2016). Nonlinear climate sensitivity and its implications for future greenhouse warming. *Science Advances*, 2(11), e1501923. <https://doi.org/10.1126/sciadv.1501923>
- Gabriel, B. (1987). Palaeoecological evidence from neolithic fireplaces in the Sahara. *African Archaeological Review*, 5(1), 93–103. <https://doi.org/10.1007/BF01117085>
- Gaetani, M., Messori, G., Zhang, Q., Flamant, C., & Pausata, F. S. R. (2017). Understanding the mechanisms behind the northward extension of the West African monsoon during the mid-Holocene. *Journal of Climate*, 30(19), 7621–7642. <https://doi.org/10.1175/JCLI-D-16-0299.1>
- Gao, X., Xu, Y., Zhao, Z., Pal, J. S., & Giorgi, F. (2006). On the role of resolution and topography in the simulation of East Asia precipitation. *Theoretical and Applied Climatology*, 86(1), 173–185. <https://doi.org/10.1007/s00704-005-0214-4>
- Gill, A. E. (1980). Some simple solutions for heat-induced tropical circulation. *Quarterly Journal of the Royal Meteorological Society*, 106(449), 447–462. <https://doi.org/10.1002/qj.49710644905>
- Grist, J. P. (2002). Easterly waves over Africa. Part I: The seasonal cycle and contrasts between wet and dry years. *Monthly Weather Review*, 130(2), 197–211. [https://doi.org/10.1175/1520-0493\(2002\)130<0197:EWOAPI>2.0.CO;2](https://doi.org/10.1175/1520-0493(2002)130<0197:EWOAPI>2.0.CO;2)
- Hagemann, S. (2002). Validierung des Niederschlags in globalen Klimamodellen. 5. Workshop Zur Hydrologischen Modellierung: Möglichkeiten Und Grenzen Für Den Einsatz Hydrologischer Modelle in Politik, Wirtschaft Und Klimafolgenforschung (pp. 115–127).
- Hagemann, S., Arpe, K., & Roeckner, E. (2006). Evaluation of the hydrological cycle in the ECHAM5 model. *Journal of Climate*, 19(16), 3810–3827. <https://doi.org/10.1175/JCLI3831.1>
- Harris, I., Jones, P. d., Osborn, T. j., & Lister, D. h. (2014). Updated high-resolution grids of monthly climatic observations – The CRU TS3.10 dataset. *International Journal of Climatology*, 34(3), 623–642. <https://doi.org/10.1002/joc.3711>
- Harris, I., Osborn, T. J., Jones, P., & Lister, D. (2020). Version 4 of the CRU TS monthly high-resolution gridded multivariate climate dataset. *Scientific Data*, 7(1), 109. <https://doi.org/10.1038/s41597-020-0453-3>

- Harrison, S. P., Bartlein, P. J., Brewer, S., Prentice, I. C., Boyd, M., Hessler, I., et al. (2014). Climate model benchmarking with glacial and mid-Holocene climates. *Climate Dynamics*, 43(3), 671–688. <https://doi.org/10.1007/s00382-013-1922-6>
- Harrison, S. P., Bartlein, P. J., Izumi, K., Li, G., Annan, J., Hargreaves, J., et al. (2015). Evaluation of CMIP5 palaeo-simulations to improve climate projections. *Nature Climate Change*, 5(8), 735–743. <https://doi.org/10.1038/nclimate2649>
- Harrison, S. P., Yu, G., Takahara, H., & Prentice, I. C. (2001). Diversity of temperate plants in east Asia. *Nature*, 413(6852), 129–130. <https://doi.org/10.1038/35093166>
- Haywood, A. M., Dowsett, H. J., Dolan, A. M., Rowley, D., Abe-Ouchi, A., Otto-Bliesner, B., et al. (2016). The Pliocene model Intercomparison project (PlioMIP) phase 2: Scientific objectives and experimental design. *Climate of the Past*, 12(3), 663–675. <https://doi.org/10.5194/cp-12-663-2016>
- Haywood, A. M., Dowsett, H. J., Otto-Bliesner, B., Chandler, M. A., Dolan, A. M., Hill, D. J., et al. (2010). Pliocene model Intercomparison project (PlioMIP): Experimental design and boundary conditions (experiment 1). *Geoscientific Model Development*, 3(1), 227–242. <https://doi.org/10.5194/gmd-3-227-2010>
- Haywood, A. M., Hill, D. J., Dolan, A. M., Otto-Bliesner, B. L., Bragg, F., Chan, W.-L., et al. (2013). Large-scale features of Pliocene climate: Results from the Pliocene model Intercomparison project. *Climate of the Past*, 9(1), 191–209. <https://doi.org/10.5194/cp-9-191-2013>
- Haywood, A. M., Tindall, J. C., Dowsett, H. J., Dolan, A. M., Foley, K. M., Hunter, S. J., et al. (2020). The Pliocene model Intercomparison project phase 2: Large-scale climate features and climate sensitivity. *Climate of the Past*, 16(6), 2095–2123. <https://doi.org/10.5194/cp-16-2095-2020>
- Hersbach, H., Bell, B., Berrisford, P., Hirahara, S., Horányi, A., Muñoz-Sabater, J., et al. (2020). The ERA5 global reanalysis. *Quarterly Journal of the Royal Meteorological Society*, 146(730), 1999–2049. <https://doi.org/10.1002/qj.3803>
- Hoelzmann, P., Jolly, D., Harrison, S. P., Laarif, F., Bonnefille, R., & Pachur, H.-J. (1998). Mid-Holocene land-surface conditions in northern Africa and the Arabian peninsula: A data set for the analysis of biogeophysical feedbacks in the climate system. *Global Biogeochemical Cycles*, 12(1), 35–51. <https://doi.org/10.1029/97GB02733>
- Hoelzmann, P., Keding, B., Berke, H., Kröpelin, S., & Kruse, H.-J. (2001). Environmental change and archaeology: Lake evolution and human occupation in the eastern Sahara during the holocene. *Palaeogeography, Palaeoclimatology, Palaeoecology*, 169(3), 193–217. [https://doi.org/10.1016/S0031-0182\(01\)00211-5](https://doi.org/10.1016/S0031-0182(01)00211-5)
- Holmes, J. A. (2008). How the Sahara became dry. *Science*, 320(5877), 752–753. <https://doi.org/10.1126/science.1158105>
- Hopcroft, P. O., & Valdes, P. J. (2019). On the role of dust-climate feedbacks during the mid-Holocene. *Geophysical Research Letters*, 46(3), 1612–1621. <https://doi.org/10.1029/2018GL080483>
- Hopcroft, P. O., & Valdes, P. J. (2022). Green Sahara tipping points in transient climate model simulations of the Holocene. *Environmental Research Letters*, 17(8), 085001. <https://doi.org/10.1088/1748-9326/ac7c2b>
- Janicot, S., Caniaux, G., Chauvin, F., de Coëtlogon, G., Fontaine, B., Hall, N., et al. (2011). Intraseasonal variability of the West African monsoon. *Atmospheric Science Letters*, 12(1), 58–66. <https://doi.org/10.1002/asl.280>
- Jenkins, G. S., Gaye, A. T., & Sylla, B. (2005). Late 20th century attribution of drying trends in the Sahel from the regional Climate model (RegCM3). *Geophysical Research Letters*, 32(22). <https://doi.org/10.1029/2005GL024225>
- Jiang, D., Tian, Z., Lang, X., Kageyama, M., & Ramstein, G. (2015). The concept of global monsoon applied to the last glacial maximum: A multi-model analysis. *Quaternary Science Reviews*, 126, 126–139. <https://doi.org/10.1016/j.quascirev.2015.08.033>
- Jiang, D., Wang, H., Ding, Z., Lang, X., & Drange, H. (2005). Modeling the middle Pliocene climate with a global atmospheric general circulation model. *Journal of Geophysical Research*, 110(D14). <https://doi.org/10.1029/2004JD005639>
- Jolly, D., Prentice, I. C., Bonnefille, R., Ballouche, A., Bengo, M., Brenac, P., et al. (1998). Biome reconstruction from pollen and plant macrofossil data for Africa and the Arabian peninsula at 0 and 6000 years. *Journal of Biogeography*, 25(6), 1007–1027. <https://doi.org/10.1046/j.1365-2699.1998.00238.x>
- Joussaume, S., Taylor, K. E., Braconnot, P., Mitchell, J. F. B., Kutzbach, J. E., Harrison, S. P., et al. (1999). Monsoon changes for 6000 years ago: Results of 18 simulations from the paleoclimate modeling Intercomparison project (PMIP). *Geophysical Research Letters*, 26(7), 859–862. <https://doi.org/10.1029/1999GL900126>
- Jungandreas, L., Hohenegger, C., & Claussen, M. (2021). Influence of the representation of convection on the mid-Holocene West African monsoon. *Climate of the Past*, 17(4), 1665–1684. <https://doi.org/10.5194/cp-17-1665-2021>
- Kageyama, M., Braconnot, P., Bopp, L., Caubel, A., Foujols, M.-A., Guilyardi, E., et al. (2013). Mid-Holocene and Last Glacial Maximum climate simulations with the IPSL model—Part I: Comparing IPSL\_CM5A to IPSL\_CM4. *Climate Dynamics*, 40(9), 2447–2468. <https://doi.org/10.1007/s00382-012-1488-8>
- Kageyama, M., Braconnot, P., Harrison, S. P., Haywood, A. M., Jungclauss, J. H., Otto-Bliesner, B. L., et al. (2018). The PMIP4 contribution to CMIP6 – Part 1: Overview and over-arching analysis plan. *Geoscientific Model Development*, 11(3), 1033–1057. <https://doi.org/10.5194/gmd-11-1033-2018>
- Kageyama, M., Harrison, S. P., Kapsch, M.-L., Lofverstrom, M., Lora, J. M., Mikolajewicz, U., et al. (2021). The PMIP4 Last Glacial Maximum experiments: Preliminary results and comparison with the PMIP3 simulations. *Climate of the Past*, 17(3), 1065–1089. <https://doi.org/10.5194/cp-17-1065-2021>
- Kim, S.-J., Crowley, T. J., Erickson, D. J., Govindasamy, B., Duffy, P. B., & Lee, B. Y. (2008). High-resolution climate simulation of the last glacial maximum. *Climate Dynamics*, 31(1), 1–16. <https://doi.org/10.1007/s00382-007-0332-z>
- Klein, C., Bliedernicht, J., Heinzeller, D., Gessner, U., Klein, I., & Kunstmann, H. (2017). Feedback of observed interannual vegetation change: A regional climate model analysis for the West African monsoon. *Climate Dynamics*, 48(9), 2837–2858. <https://doi.org/10.1007/s00382-016-3237-x>
- Kohfeld, K. E., & Harrison, S. P. (2000). How well can we simulate past climates? Evaluating the models using global palaeoenvironmental datasets. *Quaternary Science Reviews*, 19(1), 321–346. [https://doi.org/10.1016/S0277-3791\(99\)00068-2](https://doi.org/10.1016/S0277-3791(99)00068-2)
- Kok, J. F. (2010). An improved parameterization of wind-blown sand flux on Mars that includes the effect of hysteresis. *Geophysical Research Letters*, 37(12). <https://doi.org/10.1029/2010GL043646>
- Kolstad, E. W., & Screen, J. A. (2019). Nonstationary relationship between autumn Arctic sea ice and the winter North Atlantic oscillation. *Geophysical Research Letters*, 46(13), 7583–7591. <https://doi.org/10.1029/2019GL083059>
- Kröpelin, S., Verschuren, D., Lézine, A.-M., Eggermont, H., Cocquyt, C., Francus, P., et al. (2008). Climate-driven ecosystem succession in the Sahara: The past 6000 years. *Science*, 320(5877), 765–768. <https://doi.org/10.1126/science.1154913>
- Kuechler, R. R., Dupont, L. M., & Schefuß, E. (2018). Hybrid insolation forcing of Pliocene monsoon dynamics in West Africa. *Climate of the Past*, 14(1), 73–84. <https://doi.org/10.5194/cp-14-73-2018>
- Kutzbach, J. E., & Liu, Z. (1997). Response of the African monsoon to orbital forcing and ocean feedbacks in the middle Holocene. *Science*, 278(5337), 440–443. <https://doi.org/10.1126/science.278.5337.440>

- Lambeck, K., Rouby, H., Purcell, A., Sun, Y., & Sambridge, M. (2014). Sea level and global ice volumes from the Last Glacial Maximum to the Holocene. *Proceedings of the National Academy of Sciences*, 111(43), 15296–15303. <https://doi.org/10.1073/pnas.1411762111>
- Lavaysse, C., Flamant, C., Janicot, S., Parker, D. J., Lafore, J.-P., Sultan, B., & Pelon, J. (2009). Seasonal evolution of the West African heat low: A climatological perspective. *Climate Dynamics*, 33(2), 313–330. <https://doi.org/10.1007/s00382-009-0553-4>
- Lawrence, J. R., Gedzelman, S. D., Dexheimer, D., Cho, H.-K., Carrie, G. D., Gasparini, R., et al. (2004). Stable isotopic composition of water vapor in the tropics. *Journal of Geophysical Research*, 109(D6). <https://doi.org/10.1029/2003JD004046>
- LeGrande, A. N., & Schmidt, G. A. (2006). Global gridded data set of the oxygen isotopic composition in seawater. *Geophysical Research Letters*, 33(12). <https://doi.org/10.1029/2006GL026011>
- Lemburg, A., Bader, J., & Claussen, M. (2019). Sahel rainfall–tropical easterly jet relationship on synoptic to intraseasonal time scales. *Monthly Weather Review*, 147(5), 1733–1752. <https://doi.org/10.1175/MWR-D-18-0254.1>
- Leung, D. M., Kok, J. F., Li, L., Okin, G. S., Prigent, C., Kloose, M., et al. (2023). A new process-based and scale-aware desert dust emission scheme for global climate models – Part I: Description and evaluation against inverse modeling emissions. *Atmospheric Chemistry and Physics*, 23(11), 6487–6523. <https://doi.org/10.5194/acp-23-6487-2023>
- Levis, S., Bonan, G. B., & Bonfils, C. (2004). Soil feedback drives the mid-Holocene North African monsoon northward in fully coupled CCSM2 simulations with a dynamic vegetation model. *Climate Dynamics*, 23(7), 791–802. <https://doi.org/10.1007/s00382-004-0477-y>
- Li, X., Jiang, D., Tian, Z., & Yang, Y. (2018). Mid-Pliocene global land monsoon from PlioMIP1 simulations. *Palaeogeography, Palaeoclimatology, Palaeoecology*, 512, 56–70. <https://doi.org/10.1016/j.palaeo.2018.06.027>
- Li, X., Jiang, D., Zhang, Z., Zhang, R., Tian, Z., & Yan, Q. (2015). Mid-Pliocene westerlies from PlioMIP simulations. *Advances in Atmospheric Sciences*, 32(7), 909–923. <https://doi.org/10.1007/s00376-014-4171-7>
- Liakka, J., & Lofverstrom, M. (2018). Arctic warming induced by the Laurentide ice sheet topography. *Climate of the Past*, 14(6), 887–900. <https://doi.org/10.5194/cp-14-887-2018>
- Liakka, J., Löfverström, M., & Colleoni, F. (2016). The impact of the North American glacial topography on the evolution of the Eurasian ice sheet over the last glacial cycle. *Climate of the Past*, 12(5), 1225–1241. <https://doi.org/10.5194/cp-12-1225-2016>
- Lohmann, G., Pfeiffer, M., Laepple, T., Leduc, G., & Kim, J.-H. (2013). A model–data comparison of the Holocene global sea surface temperature evolution. *Climate of the Past*, 9(4), 1807–1839. <https://doi.org/10.5194/cp-9-1807-2013>
- Lohmann, U., & Roeckner, E. (1996). Design and performance of a new cloud microphysics scheme developed for the ECHAM general circulation model. *Climate Dynamics*, 12(8), 557–572. <https://doi.org/10.1007/BF00207939>
- Lora, J. M. (2018). Components and mechanisms of hydrologic cycle changes over North America at the last glacial maximum. *Journal of Climate*, 31(17), 7035–7051. <https://doi.org/10.1175/JCLI-D-17-0544.1>
- Lorenz, S. J., & Lohmann, G. (2004). Acceleration technique for Milankovitch type forcing in a coupled atmosphere–ocean circulation model: Method and application for the Holocene. *Climate Dynamics*, 23(7–8), 727–743. <https://doi.org/10.1007/s00382-004-0469-y>
- Manning, K., & Timpson, A. (2014). The demographic response to Holocene climate change in the Sahara. *Quaternary Science Reviews*, 101, 28–35. <https://doi.org/10.1016/j.quascirev.2014.07.003>
- Marsham, J. H., Dixon, N. S., Garcia-Carreras, L., Lister, G. M. S., Parker, D. J., Knippertz, P., & Birch, C. E. (2013). The role of moist convection in the West African monsoon system: Insights from continental-scale convection-permitting simulations. *Geophysical Research Letters*, 40(9), 1843–1849. <https://doi.org/10.1002/grl.50347>
- Marzin, C., & Braconnot, P. (2009). Variations of Indian and African monsoons induced by insolation changes at 6 and 9.5 kyr BP. *Climate Dynamics*, 33(2), 215–231. <https://doi.org/10.1007/s00382-009-0538-3>
- McManus, J. F., Francois, R., Gherardi, J.-M., Keigwin, L. D., & Brown-Leger, S. (2004). Collapse and rapid resumption of Atlantic meridional circulation linked to deglacial climate changes. *Nature*, 428(6985), 834–837. <https://doi.org/10.1038/nature02494>
- Messori, G., Gaetani, M., Zhang, Q., Zhang, Q., & Pausata, F. S. R. (2019). The water cycle of the mid-Holocene West African monsoon: The role of vegetation and dust emission changes. *International Journal of Climatology*, 39(4), 1927–1939. <https://doi.org/10.1002/joc.5924>
- Mulitza, S., Prange, M., Stuet, J.-B., Zabel, M., von Döbenek, T., Itambi, A. C., et al. (2008). Sahel megadroughts triggered by glacial slowdowns of Atlantic meridional overturning. *Paleoceanography*, 23(4). <https://doi.org/10.1029/2008PA001637>
- Mutz, S. G., Ehlers, T. A., Werner, M., Lohmann, G., Stepanek, C., & Li, J. (2018). Estimates of late Cenozoic climate change relevant to Earth surface processes in tectonically active orogens. *Earth Surface Dynamics*, 6(2), 271–301. <https://doi.org/10.5194/esurf-6-271-2018>
- Newell, R. E., & Kidson, J. W. (1984). African mean wind changes between sahelian wet and dry periods. *Journal of Climatology*, 4(1), 27–33. <https://doi.org/10.1002/joc.3370040103>
- Nicholson, S. E. (2008). The intensity, location and structure of the tropical rainbelt over west Africa as factors in interannual variability. *International Journal of Climatology*, 28(13), 1775–1785. <https://doi.org/10.1002/joc.1507>
- Nicholson, S. E. (2009). On the factors modulating the intensity of the tropical rainbelt over West Africa. *International Journal of Climatology*, 29(5), 673–689. <https://doi.org/10.1002/joc.1702>
- Nicholson, S. E., & Klotter, D. (2021). The Tropical Easterly Jet over Africa, its representation in six reanalysis products, and its association with Sahel rainfall. *International Journal of Climatology*, 41(1), 328–347. <https://doi.org/10.1002/joc.6623>
- Nicholson, S. E., & Grist, J. P. (2001). A conceptual model for understanding rainfall variability in the West African Sahel on interannual and interdecadal timescales. *International Journal of Climatology*, 21(14), 1733–1757. <https://doi.org/10.1002/joc.648>
- Nicholson, S. E., & Grist, J. P. (2003). The seasonal evolution of the atmospheric circulation over West Africa and equatorial Africa. *Journal of Climate*, 16(7), 1013–1030. [https://doi.org/10.1175/1520-0442\(2003\)016<1013:TSEOTA>2.0.CO;2](https://doi.org/10.1175/1520-0442(2003)016<1013:TSEOTA>2.0.CO;2)
- Nicholson, S. E., & Palao, I. M. (1993). A re-evaluation of rainfall variability in the sahel. Part I. Characteristics of rainfall fluctuations. *International Journal of Climatology*, 13(4), 371–389. <https://doi.org/10.1002/joc.3370130403>
- Nicholson, S. E., & Webster, P. J. (2007). A physical basis for the interannual variability of rainfall in the Sahel. *Quarterly Journal of the Royal Meteorological Society*, 133(629), 2065–2084. <https://doi.org/10.1002/qj.104>
- Notaro, M., Wang, Y., Liu, Z., Gallimore, R., & Levis, S. (2008). Combined statistical and dynamical assessment of simulated vegetation–rainfall interactions in North Africa during the mid-Holocene. *Global Change Biology*, 14(2), 347–368. <https://doi.org/10.1111/j.1365-2486.2007.01495.x>
- Otto-Bliesner, B. L., Braconnot, P., Harrison, S. P., Lunt, D. J., Abe-Ouchi, A., Albani, S., et al. (2017). The PMIP4 contribution to CMIP6 – Part 2: Two interglacials, scientific objective and experimental design for Holocene and Last Interglacial simulations. *Geoscientific Model Development*, 10(11), 3979–4003. <https://doi.org/10.5194/gmd-10-3979-2017>
- Otto-Bliesner, B. L., Brady, E. C., Clauzet, G., Tomas, R., Levis, S., & Kothavala, Z. (2006). Last Glacial Maximum and Holocene climate in CCSM3. *Journal of Climate*, 19(11), 2526–2544. <https://doi.org/10.1175/JCLI3748.1>
- Patricola, C. M., & Cook, K. H. (2007). Dynamics of the West African monsoon under Mid-Holocene precessional forcing: Regional climate model simulations. *Journal of Climate*, 20(4), 694–716. <https://doi.org/10.1175/JCLI4013.1>

- Pausata, F. S. R., Gaetani, M., Messori, G., Berg, A., Maia de Souza, D., Sage, R. F., & deMenocal, P. B. (2020). The greening of the Sahara: Past changes and future implications. *One Earth*, 2(3), 235–250. <https://doi.org/10.1016/j.oneear.2020.03.002>
- Pausata, F. S. R., Messori, G., & Zhang, Q. (2016). Impacts of dust reduction on the northward expansion of the African monsoon during the Green Sahara period. *Earth and Planetary Science Letters*, 434, 298–307. <https://doi.org/10.1016/j.epsl.2015.11.049>
- Peltier, W. R., & Fairbanks, R. G. (2006). Global glacial ice volume and Last Glacial Maximum duration from an extended Barbados sea level record. *Quaternary Science Reviews*, 25(23), 3322–3337. <https://doi.org/10.1016/j.quascirev.2006.04.010>
- Perez-Sanz, A., Li, G., González-Sampériz, P., & Harrison, S. P. (2014). Evaluation of modern and mid-Holocene seasonal precipitation of the Mediterranean and northern Africa in the CMIP5 simulations. *Climate of the Past*, 10(2), 551–568. <https://doi.org/10.5194/cp-10-551-2014>
- Peyron, O., Jolly, D., Braconnot, P., Bonnefille, R., Guiot, J., Wirmann, D., & Chalié, F. (2006). Quantitative reconstructions of annual rainfall in Africa 6000 years ago: Model-data comparison. *Journal of Geophysical Research*, 111(D24). <https://doi.org/10.1029/2006JD007396>
- Phipps, S. J., McGregor, H. V., Gergis, J., Gallant, A. J. E., Neukom, R., Stevenson, S., et al. (2013). Paleoclimate data–model comparison and the role of climate forcings over the past 1500 years. *Journal of Climate*, 26(18), 6915–6936. <https://doi.org/10.1175/JCLI-D-12-00108.1>
- Pickett, E. J., Harrison, S. P., Hope, G., Harle, K., Dodson, J. R., Peter Kershaw, A., et al. (2004). Pollen-based reconstructions of biome distributions for Australia, Southeast Asia and the Pacific (SEAPAC region) at 0, 6000 and 18,000 14C yr BP. *Journal of Biogeography*, 31(9), 1381–1444. <https://doi.org/10.1111/j.1365-2699.2004.01001.x>
- Prentice, I. C., Jolly, D., & Participants, B. (2000). Mid-Holocene and glacial-maximum vegetation geography of the northern continents and Africa. *Journal of Biogeography*, 27(3), 507–519. <https://doi.org/10.1046/j.1365-2699.2000.00425.x>
- Quagraine, K. A., Nkrumah, F., Klein, C., Klutse, N. A. B., & Quagraine, K. T. (2020). West African summer monsoon precipitation variability as represented by reanalysis datasets. *Climate*, 8(10), 111. <https://doi.org/10.3390/cli8100111>
- Rachmayani, R., Prange, M., & Schulz, M. (2015). North African vegetation–precipitation feedback in early and mid-Holocene climate simulations with CCSM3-DGVM. *Climate of the Past*, 11(2), 175–185. <https://doi.org/10.5194/cp-11-175-2015>
- Raible, C. C., Lehner, F., González-Rouco, J. F., & Fernández-Donado, L. (2014). Changing correlation structures of the Northern Hemisphere atmospheric circulation from 1000 to 2100 AD. *Climate of the Past*, 10(2), 537–550. <https://doi.org/10.5194/cp-10-537-2014>
- Redelsperger, J.-L., Parsons, D. B., & Guichard, F. (2002). Recovery processes and factors limiting cloud-top height following the arrival of a dry intrusion observed during TOGA COARE. *Journal of the Atmospheric Sciences*, 59(16), 2438–2457. [https://doi.org/10.1175/1520-0469\(2002\)059<2438:RPAFLC>2.0.CO;2](https://doi.org/10.1175/1520-0469(2002)059<2438:RPAFLC>2.0.CO;2)
- Risi, C., Bony, S., Vimeux, F., Descroix, L., Ibrahim, B., Lebreton, E., et al. (2008). What controls the isotopic composition of the African monsoon precipitation? Insights from event-based precipitation collected during the 2006 AMMA field campaign. *Geophysical Research Letters*, 35(24). <https://doi.org/10.1029/2008GL035920>
- Risi, C., Bony, S., Vimeux, F., Frankenberg, C., Noone, D., & Worden, J. (2010). Understanding the Sahelian water budget through the isotopic composition of water vapor and precipitation. *Journal of Geophysical Research*, 115(D24). <https://doi.org/10.1029/2010JD014690>
- Risi, C., Noone, D., Frankenberg, C., & Worden, J. (2013). Role of continental recycling in intraseasonal variations of continental moisture as deduced from model simulations and water vapor isotopic measurements: Continental Recycling and Water Isotopes. *Water Resources Research*, 49(7), 4136–4156. <https://doi.org/10.1002/wrcr.20312>
- Risi, C., Noone, D., Worden, J., Frankenberg, C., Stiller, G., Kiefer, M., et al. (2012). Process-evaluation of tropospheric humidity simulated by general circulation models using water vapor isotopologues: 1. Comparison between models and observations. *Journal of Geophysical Research*, 117(D5). <https://doi.org/10.1029/2011JD016621>
- Roeckner, E., Bäuml, G., Bonaventura, L., Brokopf, R., Esch, M., Giorgetta, M., et al. (2003). The atmospheric general circulation model ECHAM 5. PART I. *Model description*. <https://doi.org/10.17617/2.995269>
- Roehrig, R., Bouniol, D., Guichard, F., Hourdin, F., & Redelsperger, J.-L. (2013). The present and future of the West African monsoon: A process-oriented assessment of CMIP5 simulations along the AMMA transect. *Journal of Climate*, 26(17), 6471–6505. <https://doi.org/10.1175/JCLI-D-12-00505.1>
- Rozanski, K., Araguás-Araguás, L., & Gonfiantini, R. (1993). Climate change in continental isotopic records. Retrieved from [https://scholar.google.com/scholar\\_lookup?hl=en&publication\\_year=1993&pages=1-36&author=K.+Rozanski&author=L.+Aragu%C3%A1s&author=R.+Gonfiantini&title=Climate+Change+in+Continental+Isotopic+Records](https://scholar.google.com/scholar_lookup?hl=en&publication_year=1993&pages=1-36&author=K.+Rozanski&author=L.+Aragu%C3%A1s&author=R.+Gonfiantini&title=Climate+Change+in+Continental+Isotopic+Records)
- Salzmann, U., Dolan, A. M., Haywood, A. M., Chan, W.-L., Voss, J., Hill, D. J., et al. (2013). Challenges in quantifying Pliocene terrestrial warming revealed by data–model discord. *Nature Climate Change*, 3(11), 969–974. <https://doi.org/10.1038/nclimate2008>
- Salzmann, U., Haywood, A. M., Lunt, D. J., Valdes, P. J., & Hill, D. J. (2008). A new global biome reconstruction and data-model comparison for the Middle Pliocene. *Global Ecology and Biogeography*, 17(3), 432–447. <https://doi.org/10.1111/j.1466-8238.2008.00381.x>
- Samakinwa, E., Stepanek, C., & Lohmann, G. (2020). Sensitivity of mid-Pliocene climate to changes in orbital forcing and PlioMIP’s boundary conditions. *Climate of the Past*, 16(4), 1643–1665. <https://doi.org/10.5194/cp-16-1643-2020>
- Sarnthein, M., Gersonde, R., Niebler, S., Pflaumann, U., Spielhagen, R., Thiede, J., et al. (2003). Overview of glacial Atlantic Ocean mapping (GLAMAP 2000). *Paleoceanography*, 18(2). <https://doi.org/10.1029/2002PA000769>
- Scheff, J., & Frierson, D. M. W. (2012). Robust future precipitation declines in CMIP5 largely reflect the poleward expansion of model subtropical dry zones. *Geophysical Research Letters*, 39(18). <https://doi.org/10.1029/2012GL052910>
- Seager, R., & Henderson, N. (2013). Diagnostic computation of moisture budgets in the ERA-interim reanalysis with reference to analysis of CMIP-archived atmospheric model data. *Journal of Climate*, 26(20), 7876–7901. <https://doi.org/10.1175/JCLI-D-13-00018.1>
- Sereno, P. C., Garcea, E. A. A., Jousse, H., Stojanowski, C. M., Saliège, J.-F., Maga, A., et al. (2008). Lakeside cemeteries in the Sahara: 5000 Years of Holocene population and environmental change. *PLoS One*, 3(8), e2995. <https://doi.org/10.1371/journal.pone.0002995>
- Seth, A., Giannini, A., Rojas, M., Rauscher, S. A., Bordoni, S., Singh, D., & Camargo, S. J. (2019). Monsoon responses to climate changes—Connecting past, present and future. *Current Climate Change Reports*, 5(2), 63–79. <https://doi.org/10.1007/s40641-019-00125-y>
- Sha, L., Ait Brahim, Y., Wassenburg, J. A., Yin, J., Peros, M., Cruz, F. W., et al. (2019). How far north did the African monsoon fringe expand during the African Humid Period? Insights from southwest Moroccan speleothems. *Geophysical Research Letters*, 46(23), 14093–14102. <https://doi.org/10.1029/2019GL084879>
- Shi, X., Cauquoin, A., Lohmann, G., Jonkers, L., Wang, Q., Yang, H., et al. (2023). Simulated stable water isotopes during the mid-Holocene and pre-industrial using AWI-ESM-2.1-wiso. *Geoscientific Model Development Discussions*, 1–39. <https://doi.org/10.5194/gmd-2023-68>
- Shi, X., Lohmann, G., Sidorenko, D., & Yang, H. (2020). Early-Holocene simulations using different forcings and resolutions in AWI-ESM. *The Holocene*, 30(7), 996–1015. <https://doi.org/10.1177/0959683620908634>
- Simmons, A. J., Burridge, D. M., Jarraud, M., Girard, C., & Wergen, W. (1989). The ECMWF medium-range prediction models development of the numerical formulations and the impact of increased resolution. *Meteorology and Atmospheric Physics*, 40(1), 28–60. <https://doi.org/10.1007/BF01027467>



- Sohl, L. E., Chandler, M. A., Schmunk, R. B., Mankoff, K., Jonas, J. A., Foley, K. M., & Dowsett, H. J. (2009). *PRISM3/GISS topographic reconstruction (No. 419). Data series*. U.S. Geological Survey. <https://doi.org/10.3133/ds419>
- Sperber, K. R., Hameed, S., Potter, G. L., & Boyle, J. S. (1994). Simulation of the northern summer monsoon in the ECMWF model: Sensitivity to horizontal resolution. *Monthly Weather Review*, *122*(11), 2461–2481. [https://doi.org/10.1175/1520-0493\(1994\)122<2461:SOTNSM>2.0.CO;2](https://doi.org/10.1175/1520-0493(1994)122<2461:SOTNSM>2.0.CO;2)
- Stager, J. C., Mayewski, P. A., & Meeker, L. D. (2002). Cooling cycles, Heinrich event 1, and the desiccation of Lake Victoria. *Palaeogeography, Palaeoclimatology, Palaeoecology*, *183*(1), 169–178. [https://doi.org/10.1016/S0031-0182\(01\)00468-0](https://doi.org/10.1016/S0031-0182(01)00468-0)
- Stager, J. C., Ryves, D. B., Chase, B. M., & Pausata, F. S. R. (2011). Catastrophic drought in the Afro-Asian monsoon region during Heinrich event 1. *Science*, *331*(6022), 1299–1302. <https://doi.org/10.1126/science.1198322>
- Stepanek, C., & Lohmann, G. (2012). Modelling mid-Pliocene climate with COSMOS. *Geoscientific Model Development*, *5*(5), 1221–1243. <https://doi.org/10.5194/gmd-5-1221-2012>
- Stepanek, C., Samakinwa, E., Knorr, G., & Lohmann, G. (2020). Contribution of the coupled atmosphere–ocean–sea ice–vegetation model COSMOS to the PlioMIP2. *Climate of the Past*, *16*(6), 2275–2323. <https://doi.org/10.5194/cp-16-2275-2020>
- Su, H., & Neelin, J. D. (2005). Dynamical mechanisms for African monsoon changes during the mid-Holocene. *Journal of Geophysical Research*, *110*(D19). <https://doi.org/10.1029/2005JD005806>
- Sultan, B., Baron, C., Dingkuhn, M., Sarr, B., & Janicot, S. (2005). Agricultural impacts of large-scale variability of the West African monsoon. *Agricultural and Forest Meteorology*, *128*(1), 93–110. <https://doi.org/10.1016/j.agrformet.2004.08.005>
- Sultan, B., & Janicot, S. (2003). The West African monsoon dynamics. Part II: The “preonset” and “onset” of the summer monsoon. *Journal of Climate*, *16*(21), 3407–3427.
- Sultan, B., Janicot, S., & Diedhiou, A. (2003). The West African monsoon dynamics. Part I: Documentation of intraseasonal variability. *Journal of Climate*, *16*(21), 3389–3406.
- Swann, A. L. S., Fung, I. Y., Liu, Y., & Chiang, J. C. H. (2014). Remote vegetation feedbacks and the mid-Holocene Green Sahara. *Journal of Climate*, *27*(13), 4857–4870. <https://doi.org/10.1175/JCLI-D-13-00690.1>
- Sylla, M. B., Nikiema, P. M., Gibba, P., Kebe, I., & Klutse, N. A. B. (2016). Climate change over West Africa: Recent trends and future projections. In J. A. Yaro & J. Hesselberg (Eds.), *Adaptation to climate change and variability in rural West Africa* (pp. 25–40). Springer International Publishing. [https://doi.org/10.1007/978-3-319-31499-0\\_3](https://doi.org/10.1007/978-3-319-31499-0_3)
- Tan, L., Cai, Y., Cheng, H., An, Z., & Edwards, R. L. (2009). Summer monsoon precipitation variations in central China over the past 750 years derived from a high-resolution absolute-dated stalagmite. *Palaeogeography, Palaeoclimatology, Palaeoecology*, *280*(3), 432–439. <https://doi.org/10.1016/j.palaeo.2009.06.030>
- Tan, L., Cai, Y., Cheng, H., Edwards, L. R., Lan, J., Zhang, H., et al. (2018). High resolution monsoon precipitation changes on southeastern Tibetan Plateau over the past 2300 years. *Quaternary Science Reviews*, *195*, 122–132. <https://doi.org/10.1016/j.quascirev.2018.07.021>
- Texier, D., Noblet, N., & Braconnot, P. (2000). Sensitivity of the African and Asian monsoons to mid-Holocene insolation and data-inferred surface changes. *Journal of Climate*, *13*(1), 164–181. [https://doi.org/10.1175/1520-0442\(2000\)013<0164:SOTAAA>2.0.CO;2](https://doi.org/10.1175/1520-0442(2000)013<0164:SOTAAA>2.0.CO;2)
- Thompson, A. J., Skinner, C. B., Poulsen, C. J., & Zhu, J. (2019). Modulation of mid-Holocene African rainfall by dust aerosol direct and indirect effects. *Geophysical Research Letters*, *46*(7), 3917–3926. <https://doi.org/10.1029/2018GL081225>
- Thompson, A. J., Tabor, C. R., Poulsen, C. J., & Skinner, C. B. (2021). Water isotopic constraints on the enhancement of the mid-Holocene West African monsoon. *Earth and Planetary Science Letters*, *554*, 116677. <https://doi.org/10.1016/j.epsl.2020.116677>
- Thorncroft, C. D., & Blackburn, M. (1999). Maintenance of the African easterly jet. *Quarterly Journal of the Royal Meteorological Society*, *125*(555), 763–786. <https://doi.org/10.1002/qj.4971255502>
- Tierney, J. E., Pausata, F. S. R., & deMenocal, P. B. (2017). Rainfall regimes of the Green Sahara. *Science Advances*, *3*(1), e1601503. <https://doi.org/10.1126/sciadv.1601503>
- Tindall, J. C., Haywood, A. M., Salzmann, U., Dolan, A. M., & Fletcher, T. (2022). The warm winter paradox in the Pliocene northern high latitudes. *Climate of the Past*, *18*(6), 1385–1405. <https://doi.org/10.5194/cp-18-1385-2022>
- Tompkins, A. M. (2002). A prognostic parameterization for the subgrid-scale variability of water vapor and clouds in large-scale models and its use to diagnose cloud cover. *Journal of the Atmospheric Sciences*, *59*(12), 1917–1942. [https://doi.org/10.1175/1520-0469\(2002\)059<1917:APPFTS>2.0.CO;2](https://doi.org/10.1175/1520-0469(2002)059<1917:APPFTS>2.0.CO;2)
- Wang, Y., Notaro, M., Liu, Z., Gallimore, R., Levis, S., & Kutzbach, J. E. (2008). Detecting vegetation-precipitation feedbacks in mid-Holocene North Africa from two climate models. *Climate of the Past*, *4*(1), 59–67. <https://doi.org/10.5194/cp-4-59-2008>
- Wang, Y. J., Cheng, H., Edwards, R. L., An, Z. S., Wu, J. Y., Shen, C.-C., & Dorale, J. A. (2001). A high-resolution absolute-dated late pleistocene monsoon record from Hulu Cave, China. *Science*, *294*(5550), 2345–2348. <https://doi.org/10.1126/science.1064618>
- Wei, W., & Lohmann, G. (2012). Simulated Atlantic multidecadal oscillation during the Holocene. *Journal of Climate*, *25*(20), 6989–7002. <https://doi.org/10.1175/JCLI-D-11-00667.1>
- Weldeab, S., Frank, M., Stichel, T., Haley, B., & Sangen, M. (2011). Spatio-temporal evolution of the West African monsoon during the last deglaciation. *Geophysical Research Letters*, *38*(13). <https://doi.org/10.1029/2011GL047805>
- Werner, M., Jouzel, J., Masson-Delmotte, V., & Lohmann, G. (2018). Reconciling glacial Antarctic water stable isotopes with ice sheet topography and the isotopic paleothermometer. *Nature Communications*, *9*(1), 3537. <https://doi.org/10.1038/s41467-018-05430-y>
- Werner, M., Langebroek, P. M., Carlsen, T., Herold, M., & Lohmann, G. (2011). Stable water isotopes in the ECHAM5 general circulation model: Toward high-resolution isotope modeling on a global scale. *Journal of Geophysical Research*, *116*(D15), D15109. <https://doi.org/10.1029/2011JD015681>
- Werner, M., Mikolajewicz, U., Heimann, M., & Hoffmann, G. (2000). Borehole versus isotope temperatures on Greenland: Seasonality does matter. *Geophysical Research Letters*, *27*(5), 723–726. <https://doi.org/10.1029/1999GL006075>
- Wu, H., Guiot, J., Brewer, S., & Guo, Z. (2007). Climatic changes in Eurasia and Africa at the last glacial maximum and mid-Holocene: Reconstruction from pollen data using inverse vegetation modelling. *Climate Dynamics*, *29*(2), 211–229. <https://doi.org/10.1007/s00382-007-0231-3>
- Wu, M.-L. C., Reale, O., Schubert, S. D., Suarez, M. J., Koster, R. D., & Pegion, P. J. (2009). African easterly jet: Structure and maintenance. *Journal of Climate*, *22*(17), 4459–4480. <https://doi.org/10.1175/2009JCLI2584.1>
- Xu, X., Werner, M., Butzin, M., & Lohmann, G. (2012). Water isotope variations in the global ocean model MPI-OM. *Geoscientific Model Development*, *5*(3), 809–818. <https://doi.org/10.5194/gmd-5-809-2012>
- Yan, Q., Wei, T., Korty, R. L., Kossin, J. P., Zhang, Z., & Wang, H. (2016). Enhanced intensity of global tropical cyclones during the mid-Pliocene warm period. *Proceedings of the National Academy of Sciences*, *113*(46), 12963–12967. <https://doi.org/10.1073/pnas.1608950113>

- Yang, G.-Y., Methven, J., Woolnough, S., Hodges, K., & Hoskins, B. (2018). Linking African easterly wave activity with equatorial waves and the influence of Rossby waves from the southern hemisphere. *Journal of the Atmospheric Sciences*, 75(6), 1783–1809. <https://doi.org/10.1175/JAS-D-17-0184.1>
- Yoshimori, M., Yokohata, T., & Abe-Ouchi, A. (2009). A comparison of climate feedback strength between CO<sub>2</sub> doubling and LGM experiments. *Journal of Climate*, 22(12), 3374–3395. <https://doi.org/10.1175/2009JCLI2801.1>
- Zhang, H., Ait Brahim, Y., Li, H., Zhao, J., Kathayat, G., Tian, Y., et al. (2019). The Asian summer monsoon: Teleconnections and forcing mechanisms—A review from Chinese speleothem δ<sup>18</sup>O records. *Quaternary*, 2(3), 26. <https://doi.org/10.3390/quat2030026>
- Zhang, R., Yan, Q., Zhang, Z. S., Jiang, D., Otto-Bliesner, B. L., Haywood, A. M., et al. (2013). Mid-pliocene East Asian monsoon climate simulated in the PlioMIP. *Climate of the Past*, 9(5), 2085–2099. <https://doi.org/10.5194/cp-9-2085-2013>
- Zhang, R., Zhang, Z., Jiang, D., Yan, Q., Zhou, X., & Cheng, Z. (2016). Strengthened African summer monsoon in the mid-Piacenzian. *Advances in Atmospheric Sciences*, 33(9), 1061–1070. <https://doi.org/10.1007/s00376-016-5215-y>
- Zhang, Z., Li, X., Guo, C., Otterå, O. H., Nisancioglu, K. H., Tan, N., et al. (2021). Mid-Pliocene Atlantic meridional overturning circulation simulated in PlioMIP2. *Climate of the Past*, 17(1), 529–543. <https://doi.org/10.5194/cp-17-529-2021>
- Zhao, A., Ryder, C. L., & Wilcox, L. J. (2022). How well do the CMIP6 models simulate dust aerosols? *Atmospheric Chemistry and Physics*, 22(3), 2095–2119. <https://doi.org/10.5194/acp-22-2095-2022>
- Zhao, Y., Braconnot, P., Marti, O., Harrison, S. P., Hewitt, C., Kitoh, A., et al. (2005). A multi-model analysis of the role of the ocean on the African and Indian monsoon during the mid-Holocene. *Climate Dynamics*, 25(7), 777–800. <https://doi.org/10.1007/s00382-005-0075-7>
- Zhao, Y., & Harrison, S. P. (2012). Mid-Holocene monsoons: A multi-model analysis of the inter-hemispheric differences in the responses to orbital forcing and ocean feedbacks. *Climate Dynamics*, 39(6), 1457–1487. <https://doi.org/10.1007/s00382-011-1193-z>
- Zheng, W., & Braconnot, P. (2013). Characterization of model spread in PMIP2 mid-Holocene simulations of the African monsoon. *Journal of Climate*, 26(4), 1192–1210. <https://doi.org/10.1175/JCLI-D-12-00071.1>
- Zhu, J., Otto-Bliesner, B. L., Brady, E. C., Poulsen, C. J., Tierney, J. E., Lofverstrom, M., & DiNezio, P. (2021). Assessment of equilibrium climate sensitivity of the Community Earth System Model version 2 through simulation of the Last Glacial Maximum. *Geophysical Research Letters*, 48(3), e2020GL091220. <https://doi.org/10.1029/2020GL091220>

## 2 S1: supporting results for NAO- $\delta^{18}O_p$ non-stationarity

Supplementary results for NAO- $\delta^{18}O_p$  non-stationarity analysis (S1)

### Contents of this file

#### 1. Figure S1 to S8

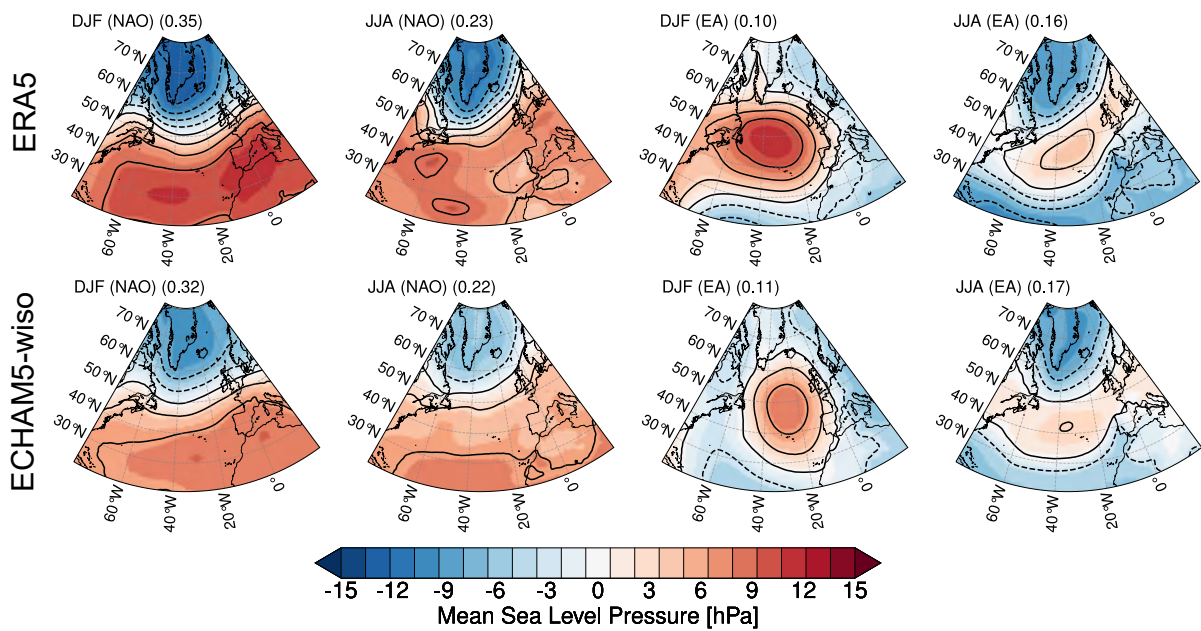


**Figure 1:** The spatial maps and explained variance of the first (NAO) and second (EA) leading modes of variability of the EOFs (eigenvectors or covariance matrix of the Principal component time series and the EOFs) of the winter and summer monthly sea-level pressure (SLP) anomalies for the North Atlantic region. These are calculated with SLP anomalies data from (top panel) ERA5 and (bottom panel) ECHAM5-wiso model outputs.

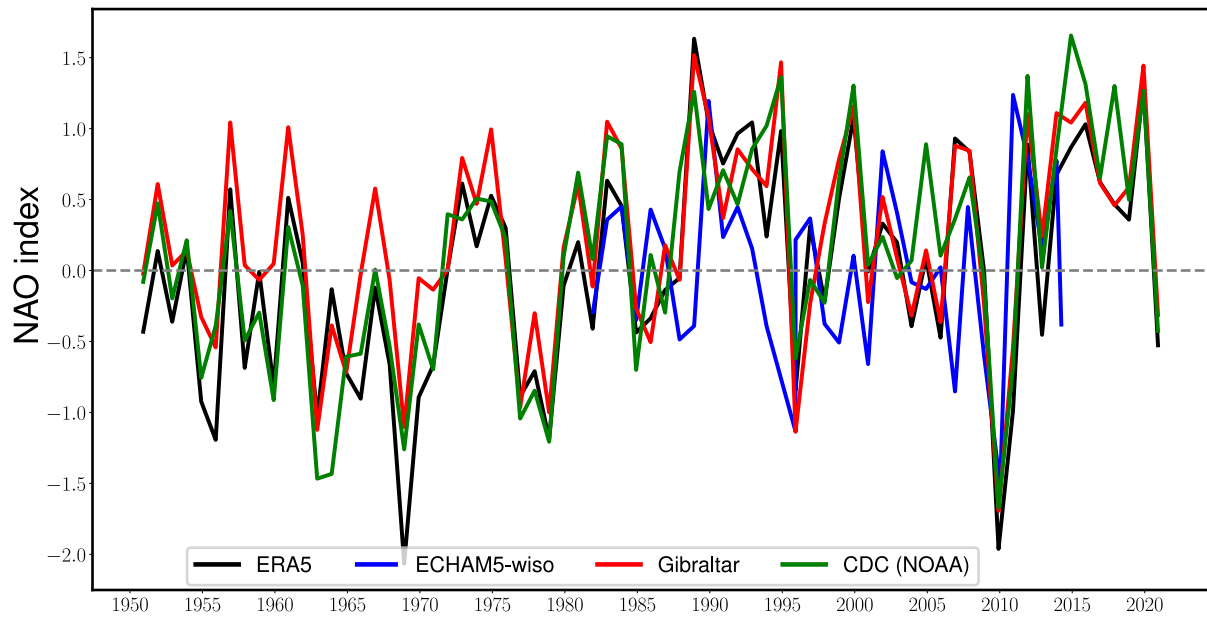


**Figure 2:** Comparison of the time series of the NAO index calculated using the SLP from ECHAM5-wiso model output (blue), reanalysis datasets (black; ERA5; Hersbach et al. [196] and green; CDC (NOAA); Kistler et al. [263]) and instrumental NAO index (red; Gibraltar) are based on standardized SLP data from Gibraltar and Iceland stations (Jones et al. [264]) in winter

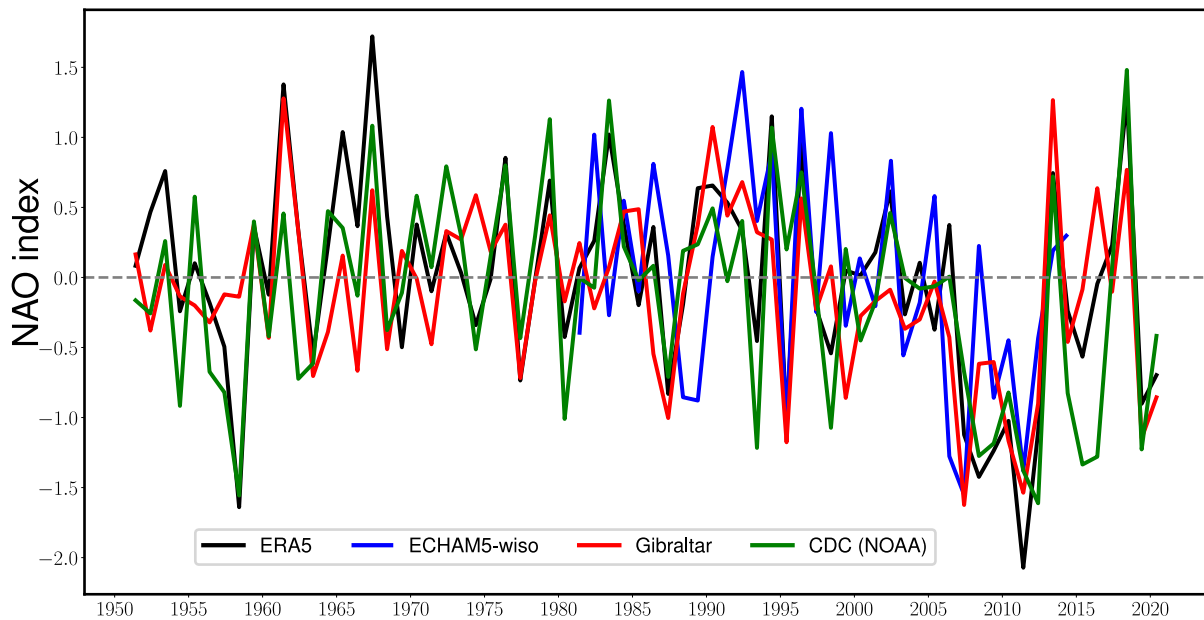


**Figure 3:** Comparison of the time series of the NAO index calculated using the SLP from ECHAM5-wiso model output (blue), reanalysis datasets (black; ERA5; Hersbach et al. [196] and green; CDC (NOAA); Kistler et al. [263]) and instrumental NAO index (red; Gibraltar) are based on standardized SLP data from Gibraltar and Iceland stations (Jones et al. [264]) in summer

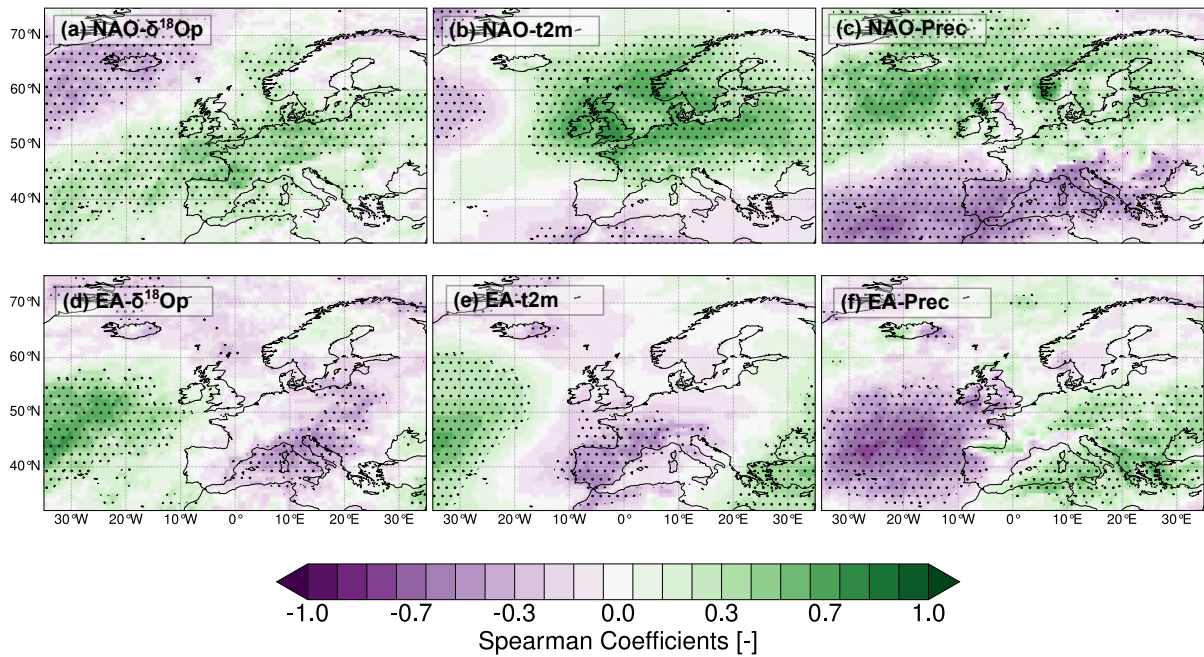


**Figure 4:** Correlation coefficients between winter  $\delta^{18}O_p$ , temperature and precipitation and (top) NAO and (bottom) EA using the ECHAM5-wiso model output (1979-2014). Dot stipplings indicate areas with a significance level of 95%.

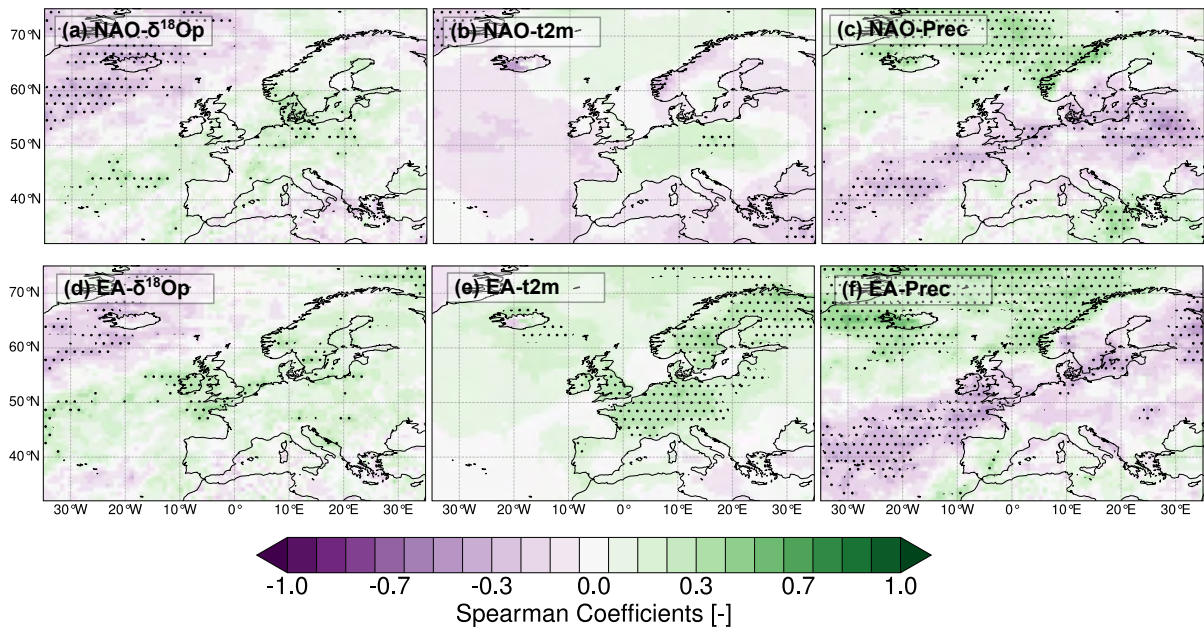


**Figure 5:** Correlation coefficients between summer  $\delta^{18}O_p$ , temperature and precipitation and (top) NAO and (bottom) EA using the ECHAM5-wiso model output (1979-2014). Dot stipplings indicate areas with a significance level of 95%.

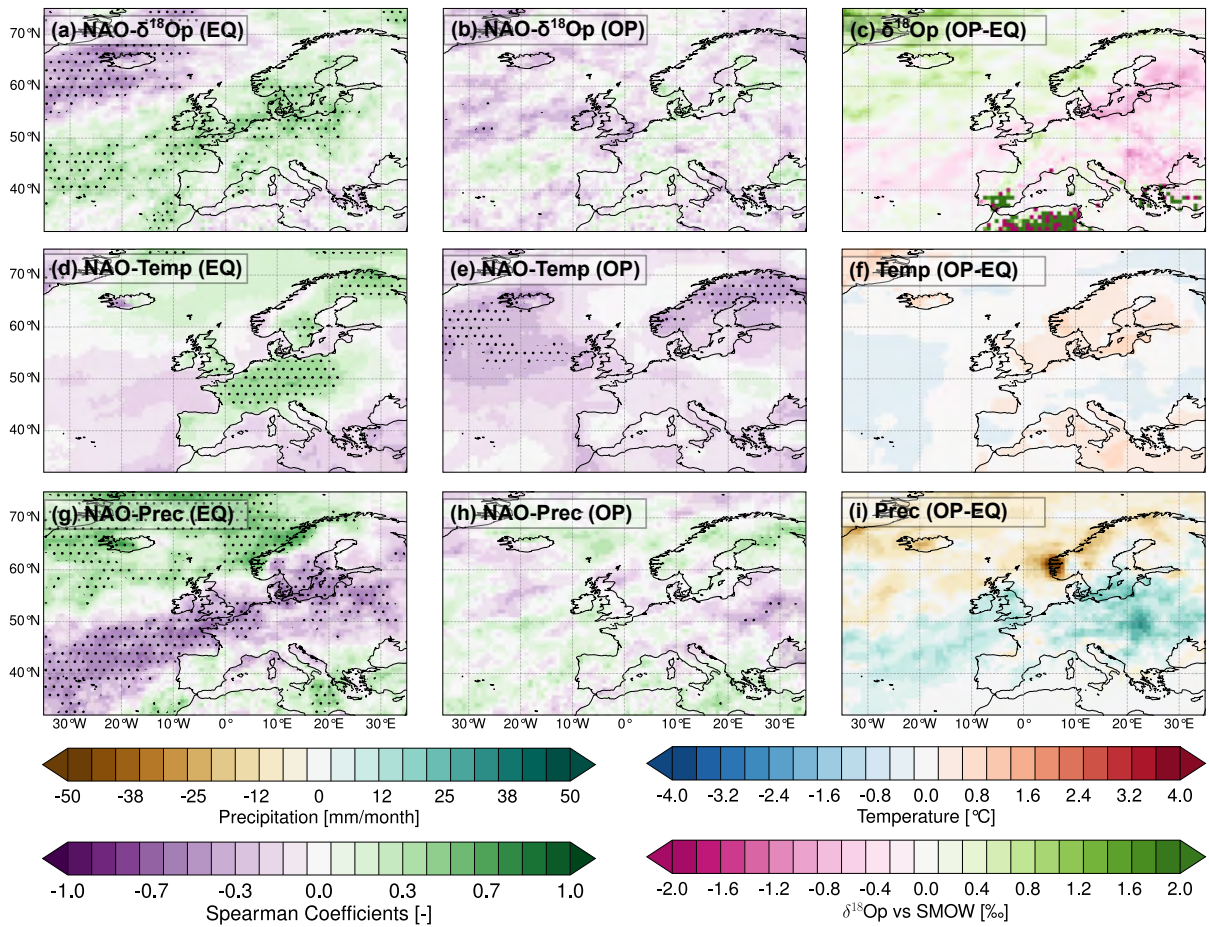


**Figure 6:** Spearman correlation between winter  $\delta^{18}O_p$ -NAO index (a-b),  $\delta^{18}O_p$ -temperature (d-e), and  $\delta^{18}O_p$ -precipitation (g-h) for yearly winters (1979-2014) with the same (EQ) and opposite (OP) phases of NAO and EA indices, including OP, EQ, and the difference between OP and EQ. Dot stippling represents regions with significant correlation coefficients within a 95 % confidence interval. Composite differences between OP and EQ regional climate variables are depicted for (c)  $\delta^{18}O_p$  values, (f) temperature, and (i) precipitation.

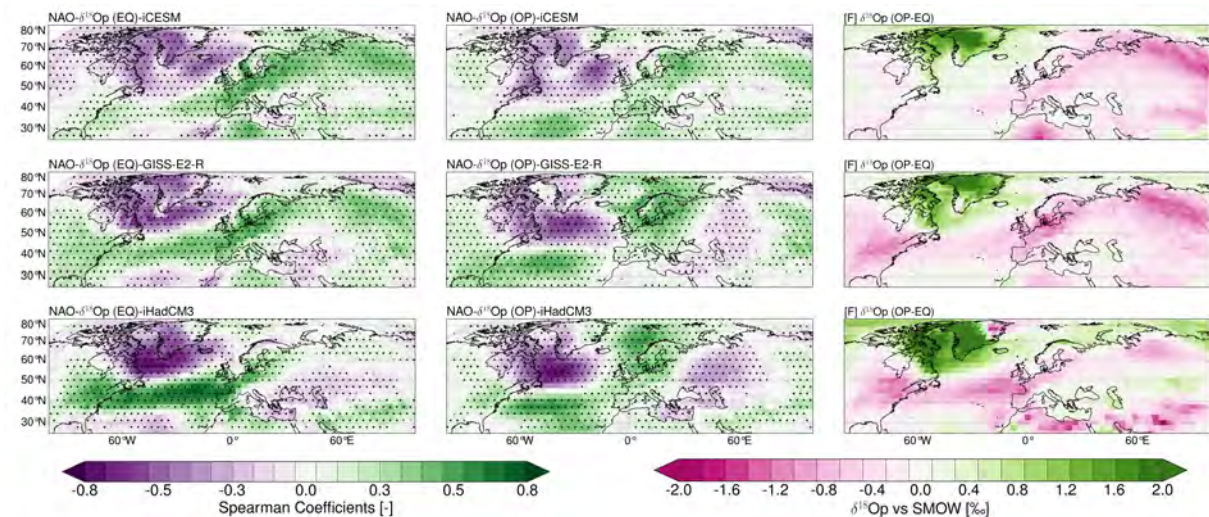


**Figure 7:** Spearman correlation between winter  $\delta^{18}O_p$ -NAO index (a-b),  $\delta^{18}O_p$ -temperature (d-e), and  $\delta^{18}O_p$ -precipitation (g-h) for yearly winters (Last millennium; simulations from Bühler et al. [132]) with the same (EQ) and opposite (OP) phases of NAO and EA indices, including OP, EQ, and the difference between OP and EQ. Dot stippling represents regions with significant correlation coefficients within a 95 % confidence interval. Composite differences between OP and EQ regional climate variables are depicted for (c)  $\delta^{18}O_p$  values, (f) temperature, and (i) precipitation.

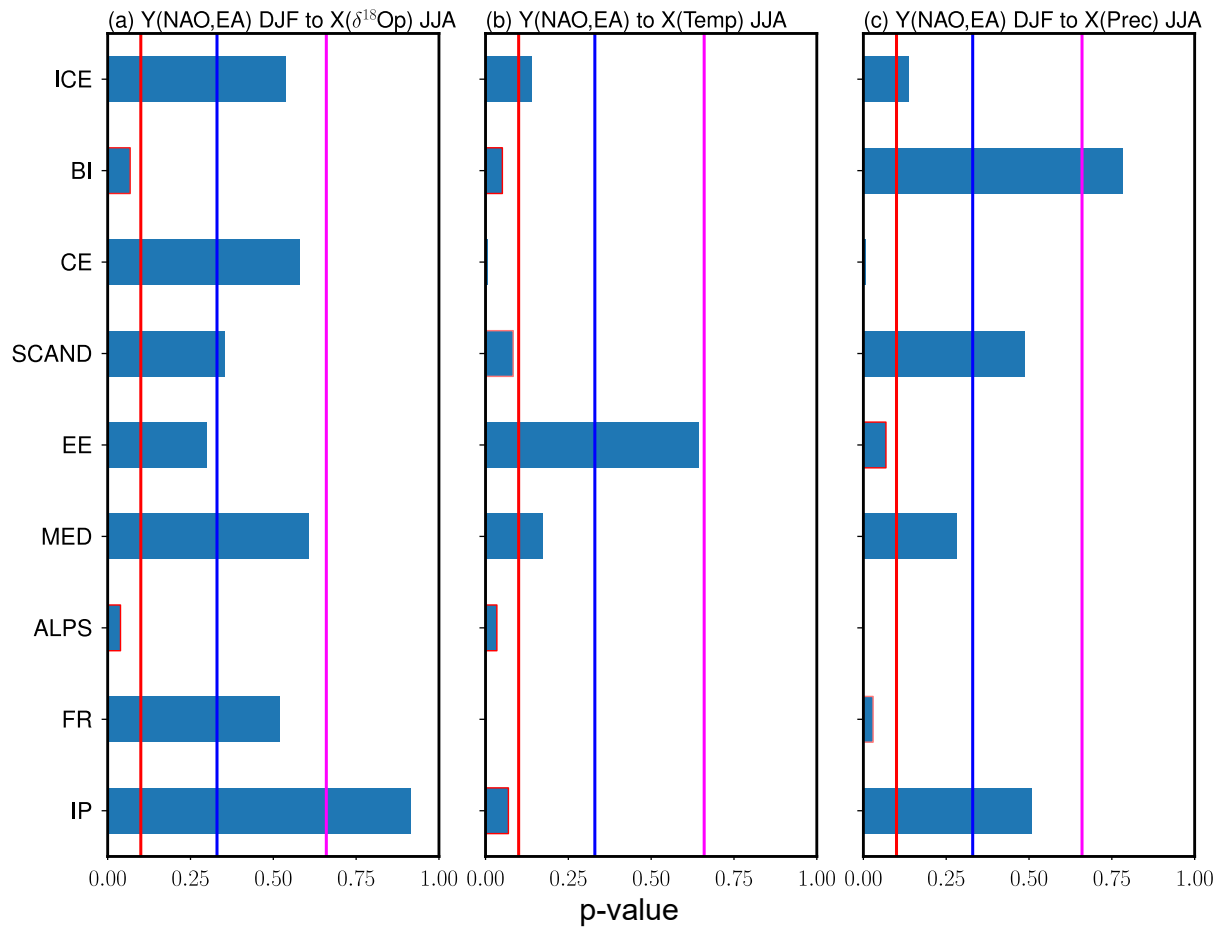


**Figure 8:** Probability of no Granger from winter (NAO, EA) to summer (a)  $\delta^{18}O_p$ , temperature, and precipitation of the regional means over Iceland, British Isles, Central Europe, Scandinavian, Eastern Europe, Mediterranean, Alps, France, and Iberian Peninsula. The red, blue and magenta lines represent the probability of 0.1, 0.33, and 0.66. Details of the multivariate predictive model used to estimate the causal links are based on Mosedale et al. [240]. The p-values from 0-10% indicate a very likely causal mechanism from Y to X.





**Part VII.**

Appendix



# Manuscripts for Part 3 (P5, S2)

## 1 P5: Boateng and Mutz [4]

(P5) Boateng, D. and Mutz, S. G.: pyESDv1.0.1: An open-source Python framework for empirical-statistical downscaling of climate information, Geoscientific Model Development Discussions, 1–58, <https://doi.org/10.5194/gmd-2023-67>, 2023.

1 P5: Boateng and Mutz [4] 251

2 S2: supporting results for predicting  $\delta^{18}\text{O}_p$  variability across Europe . . . . . 288



# pyESDv1.0.1: an open-source Python framework for empirical-statistical downscaling of climate information

Daniel Boateng<sup>1</sup> and Sebastian G. Mutz<sup>1,2</sup>

<sup>1</sup>Department of Geosciences, University of Tübingen, Tübingen, Germany

<sup>2</sup>School of Geographical and Earth Sciences, University of Glasgow, Scotland, UK

**Correspondence:** Daniel Boateng (daniel.boateng@uni-tuebingen.de)

Received: 26 March 2023 – Discussion started: 5 April 2023

Revised: 20 September 2023 – Accepted: 21 September 2023 – Published: 14 November 2023

**Abstract.** The nature and severity of climate change impacts vary significantly from region to region. Consequently, high-resolution climate information is needed for meaningful impact assessments and the design of mitigation strategies. This demand has led to an increase in the application of empirical-statistical downscaling (ESD) models to general circulation model (GCM) simulations of future climate. In contrast to dynamical downscaling, the perfect prognosis ESD (PP-ESD) approach has several benefits, including low computation costs, the prevention of the propagation of GCM-specific errors, and high compatibility with different GCMs. Despite their advantages, the use of ESD models and the resulting data products is hampered by (1) the lack of accessible and user-friendly downscaling software packages that implement the entire downscaling cycle, (2) difficulties reproducing existing data products and assessing their credibility, and (3) difficulties reconciling different ESD-based predictions for the same region. We address these issues with a new open-source Python PP-ESD modeling framework called pyESD. pyESD implements the entire downscaling cycle, i.e., routines for data preparation, predictor selection and construction, model selection and training, evaluation, utility tools for relevant statistical tests, visualization, and more. The package includes a collection of well-established machine learning algorithms and allows the user to choose a variety of estimators, cross-validation schemes, objective function measures, and hyperparameter optimization in relatively few lines of code. The package is well-documented, highly modular, and flexible. It allows quick and reproducible downscaling of any climate information, such as precipitation, temperature, wind speed, or even short-term glacier length and mass changes. We demonstrate the

use and effectiveness of the new PP-ESD framework by generating weather-station-based downscaling products for precipitation and temperature in complex mountainous terrain in southwestern Germany. The application example covers all important steps of the downscaling cycle and different levels of experimental complexity. All scripts and datasets used in the case study are publicly available to (1) ensure the reproducibility and replicability of the modeled results and (2) simplify learning to use the software package.

## 1 Introduction

The impacts of anthropogenic climate change are far-reaching and spatially heterogeneous. Consequently, regional- and local-scale predictions of 21st century climate evolution are needed to help guide the design of adaptation measures, vulnerability assessments, and resilience strategies (Field and Barros, 2014; Weaver et al., 2013). General circulation models (GCMs) are well-established tools for simulating climate trends in response to different anthropogenic and natural forcings, such as atmospheric CO<sub>2</sub> concentrations, land cover, and orbital changes. They are process-driven models based on our understanding of atmospheric physics. They are commonly used to predict future trends of climate change by prescribing predicted future forcings described by the Representative Concentration Pathways (RCPs). RCPs are greenhouse gas concentration scenarios that quantify the radiative forcing of plausible demographic and technological developments, as well as anthropogenic activities (Meinshausen et al., 2011; Pachauri et al., 2014). While GCMs can produce useful estimates of

many climate system elements on the global and synoptic scale (such as circulation patterns), mesoscale atmospheric processes, clouds, and specific climate variables like precipitation are still relatively poorly represented (e.g., Steppeler et al., 2003). Moreover, GCM simulations are affected by systematic biases on the local and regional scale due to their coarse resolutions and model parameterization (e.g., Errico et al., 2001). These can lead to inaccurate predictions on the spatial scales that are relevant for regional climate change impact assessments, such as studies investigating the impacts on the hydrological cycle (Boé et al., 2009), mountain glaciers (Mutz et al., 2016; Mutz and Aschauer, 2022), air quality (e.g., Colette et al., 2012), and agriculture (e.g., Shahhosseini et al., 2020). Therefore, GCM-based predictions are downscaled by performing dynamical downscaling or statistical downscaling, with empirical-statistical downscaling (ESD) being one type of statistical downscaling (Murphy, 2000; Schmidli et al., 2007; Wilby and Dawson, 2013).

Dynamical downscaling involves the nesting of regional climate models (RCMs) into coarse-resolution GCM simulations to produce higher-resolution regional estimates. While RCMs allow an easy exploration of physical processes leading to the predicted climate, they are computationally costly. Furthermore, slight changes in the model domain and boundary conditions require the repetition of the whole process, thereby limiting their application in many climate impact studies (e.g., Giorgi and Mearns, 1991; Xu et al., 2019). ESD is computationally less costly and implicitly considers local conditions, such as topography and vegetation, without the need to parameterize them explicitly. It is widely used for climate change impact studies and relies on establishing empirical transfer functions to relate large-scale atmospheric variables (predictors) to a local-scale observation (predictand). ESD models can be directly coupled to GCMs (e.g., Mutz et al., 2021) or RCMs (e.g., Sunyer et al., 2015; Laflamme et al., 2016; Jakob Themeßl et al., 2011) in a one-way coupling or pipeline with no feedback into the climate models. ESD can be broadly categorized into perfect prognosis (PP) and model output statistics (MOS) approaches (Maraun and Widmann, 2018; Marzban et al., 2006). MOS uses simulated predictors from the GCM or RCM to find the transfer function and generate a predictand time series with bias corrections (e.g., Sachindra et al., 2014; Wilby et al., 1998). Therefore, the MOS-ESD transfer functions are specific to a particular GCM or RCM and not easily transferable to other models. In contrast, the PP-ESD approach is GCM- and RCM-agnostic: ESD models are obtained from observational data for both the predictand and predictors and can therefore be coupled to any GCM or RCM (e.g., Hertig et al., 2019; Mutz et al., 2021; Ramon et al., 2021; Tatli et al., 2004). Therefore, this paper, and the software package presented in it, focuses primarily on the PP-ESD approach.

The PP-ESD modeling framework consists of four critical steps to establish and evaluate the empirical transfer func-

tions that constitute an ESD model (e.g., Maraun et al., 2010; Maraun and Widmann, 2018): (1) the first step involves the selection and construction of predictors. The selection of the most informative and relevant predictors generally increases the performance and robustness of PP-ESD models. Preliminary predictor selection should be guided by knowledge of the atmospheric dynamics that govern a specific regional climate. This selection may be refined using statistical dependency measures such as correlation analysis (e.g., Wilby et al., 2002; Wilby and Wigley, 2002), regularization regression (e.g., Hammami et al., 2012), stepwise multi-linear regression (e.g., Mutz et al., 2021), and decision tree selection (e.g., Nourani et al., 2019). The selected predictors should be able to explain most of the predictand's variability and must be represented well by the GCMs (Maraun and Widmann, 2018; Wilby et al., 2004). (2) The second step involves the selection of the learning algorithms (i.e., the learning model used for training the ESD model). These range from classical regressions and analog models, including parametric and nonparametric models (Gutiérrez et al., 2013; Zorita and Storch, 1999; Lorenz, 1969), to advanced machine learning (ML) algorithms (e.g., Sachindra et al., 2018; Xu et al., 2020). The various techniques vary in complexity, scalability, interpretability, and underlying assumptions. For example, classical regressions and analog models allow better interpretations of the simulated results and are usually simpler to implement. On the other hand, several ML algorithms have the ability to capture more complex links between predictors and predictands and do not require an explicit assumption of the distribution of observational data during the optimization process (Jordan and Mitchell, 2015; Raissi and Karniadakis, 2018). The choice of the optimal PP-ESD training technique depends on the predictand variable (e.g., precipitation and temperature), length of the observational records, spatiotemporal variability, spatial coherence, regional setting, and temporal stationarity of the transfer functions. (3) The third step involves the actual training and validation of the PP-ESD models, and (4) the final step is the PP-ESD model evaluation.

The high demand for climate change information on the regional and local scale has led to the widespread use of ESD methods and an overwhelming body of research to sort through in order to select the most suitable technique for a specific problem. In the past, generalized linear models (GLMs) (e.g., Fealy and Sweeney, 2007), regularization models (e.g., Li et al., 2020), Bayesian regression models (Das et al., 2014; e.g., Zhang and Yan, 2015), support vector machines (SVMs) (e.g., Chen et al., 2010; Ghosh and Mujumdar, 2008), artificial neural networks (ANNs) (e.g., Sachindra et al., 2018; Vu et al., 2016; Xu et al., 2020), homogeneous (e.g., random forest) and heterogeneous (e.g., stacking) ensemble learning models (e.g., Massaoudi et al., 2021; Pang et al., 2017; Zhang et al., 2021), and others have been used to construct PP-ESD models and downscale climate information. However, there is no universal protocol to

help choose a robust model for a specific region and climate variable (Gutiérrez et al., 2019), thus making the selection of the most suitable learning algorithm challenging. Moreover, the recent increase in ML algorithms and platforms (e.g., programming languages and software) exacerbates the problem by creating an even wider range of PP-ESD techniques without well-defined protocols. These have shifted the focus toward the establishment of standardized user-friendly tools that would resolve most of the issues related to the development of PP-ESD models. Such tools exist in various forms and tackle a certain aspect of the inherent ESD modeling complexities to ensure fast and efficient climate-impact-related studies. For example, the R-package *esd*, developed and maintained by the Norwegian Meteorological Institute (MET Norway), comprises many utility functions for data retrieval, manipulation and visualization, commonly used statistical tools, and implementations of GLM and regression techniques for generating ESD models (Benestad et al., 2015b). Moreover, an interactive web-based downscaling tool developed as part of the EU-funded ENSEMBLES project (van der Linden and Mitchell, 2009) provides an end-to-end framework through data access, computing resources, and ESD model alternatives (Gutiérrez et al., 2012). The decision support tool *sds*m (Wilby et al., 2002) provides auxiliary downscaling routines like predictor screening, regression, model evaluation, and visualization for near-surface weather variables on a daily scale. Most recently, the climate analysis tool Climate4R has been extended with statistical downscaling functionalities (*downscaleR*) that provide a wide range of MOS and PP techniques (Bedia et al., 2020). While these tools provide specialist solutions, there is no single tool or modeling framework that provides a wide range of contemporary (and commonly used) algorithms and implements all downscaling steps (i.e., predictor selection and construction, learning algorithm selection, training and validation of ESD models, GCM–ESD model coupling, model evaluation, visualization, and relevant statistical tools). Moreover, there is no user-friendly ESD tool written in a widely used programming language like Python, which would remove barriers for the use of ESD techniques in research and teaching. Many of the Python-based tools currently available are primarily designed for bias correction in MOS downscaling, and extending these tools to the PP-ESD framework would diversify the publicly available downscaling tools (e.g., *xclim*, Bourgault et al., 2023; *ibicus*, Spuler et al., 2023; *CCdownscaling*, Polasky et al., 2023). A complete, user-friendly, robust, and efficient open-source downscaling framework would contribute significantly to climate change impact assessment studies by (a) empowering researchers through accessible software and easy switches between alternative methods, (b) allowing for efficient updating of predictions in a consistent modeling framework, (c) increasing the transparency and reproducibility of results, and (d) removing barriers in teaching in order to familiarize future generations of researchers with the ESD approach.

Here, we introduce a new PP-ESD framework that addresses the gaps highlighted above. It is the thoroughly tested, heavily documented, efficient, and user-friendly open-source Python Empirical-Statistical Downscaling (*pyESD*) package. *pyESD* adopts an object-oriented programming (OOP) style and treats the predictand data archives (e.g., the weather station) as objects with many functionalities and attributes relevant to ESD modeling. It is flexible with regards to the training dataset and predictand variable. For example, *pyESD*'s predecessors were successfully applied for the prediction of local temperatures (Mutz et al., 2021) and glacier mass balance (Mutz and Aschauer, 2022) in South America. Here, we additionally demonstrate its capabilities in downscaling precipitation in complex terrain in southwestern Germany. *pyESD* comprises a collection of utilities and methods for data preparation, predictor selection, data transformation, predictor construction, model selection and training, evaluation, statistical testing, and visualization. Unlike existing packages, *pyESD* also includes common machine learning algorithms (i.e., different estimators, cross-validation schemes, objective function measures, hyperparameter optimizers, etc.) that can be experimented with in a few lines of code.

In the first part of this paper (Sect. 2), we provide detailed descriptions of the model structure and the theoretical background for the implemented methods. In the second part (Sect. 3), we demonstrate the package's functionalities with an illustrative case study for a hydrological subcatchment in mountainous terrain in southwestern Germany. Here, we walk the reader through a typical downscaling process with *pyESD*. More specifically, we generate station-based downscaling products for precipitation and temperature changes in response to different RCPs. When discussing downscaling-related tasks, we list the corresponding *pyESD* routines as italicized function names. We only use publicly available data for a set of weather stations to ensure the reproducibility and replicability of the results (see Sect. 3). Moreover, all the scripts used for the case study are provided and can be easily adapted to suit the researcher's focus. We discuss the application example in Sect. 4 and conclude with a summary and important remarks in Sect. 5.

## 2 Model structure

The PP-ESD downscaling cycle involves technical and laborious steps that must be carefully addressed to ensure the robustness and accuracy of local-scale climate predictions. The *pyESD* package implements all these steps in an efficient modeling pipeline for an easier workflow. In this section, we describe this workflow (Fig. 1) along with the main features of the package.

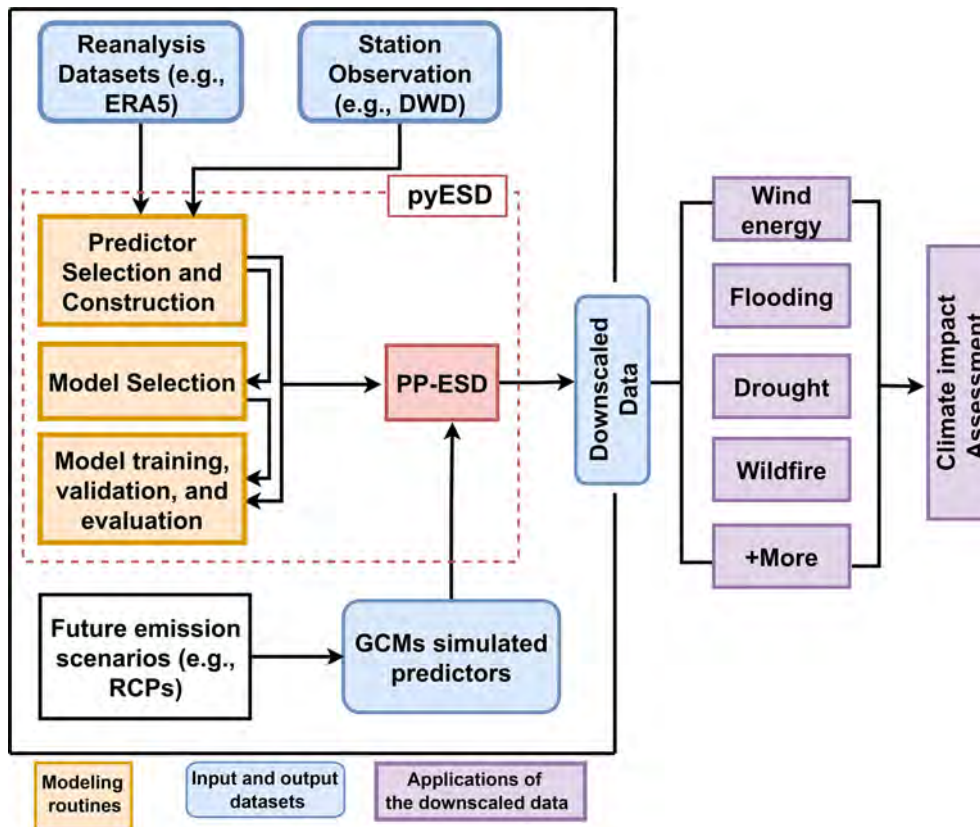


**Figure 1.** The main features and workflow of PP-ESD implemented in the pyESD package (highlighted by the dashed red box). The weather station and reanalysis datasets are used to select the robust predictors for model training and validation. The trained PP-ESD model is then coupled to GCM simulations forced with different scenarios to predict the local-scale future estimates that can be used for climate change impact assessment (not included in the pyESD package).

## 2.1 Data structure and preprocessing

PP-ESD modeling requires (1) predictand data from weather stations or other observational systems, (2) reanalysis datasets for the construction of predictors, and (3) GCM or RCM output for the construction of simulated predictors if the PP-ESD models are used for downscaling simulated climates. To understand the workflow demonstrated in later sections, the reader needs to be aware of few important package design choices related to data structure and preprocessing.

- The package adopts the OOP paradigm and treats every predictand data archive (e.g., weather station or glacier) as an object. Since the current version of the package focuses only on station-based downscaling, we will henceforth describe it only as the weather station object. The package accepts the (typical for weather stations) comma-separated value (CSV) file format. These files contain the predictand time series, such as a temperature record, as well as weather station attributes like the weather station's name, ID, and location. The `read_station_csv` from the `pyESD.weatherstation` module initiates each weather station as a separate object us-

ing the `StationOperator` that features all the other functionalities. The weather station object is associated with at least one predictand dataset (i.e., the values of at least one climate variable recorded at that particular station). Furthermore, the initialized object includes all attributes and methods required for the complete downscaling cycle. For instance, the package adopts the `fit` and `predict` framework of the scikit-learn Python package (Pedregosa et al., 2011) that can be directly applied to the weather station object.

- The data needed for predictor construction are read from files in the network Common Data Form (netCDF) format with the Xarray toolkit (Hoyer and Hamman, 2017). Due to the size of these datasets and the computations required to construct the predictors, the memory demand can be very high, and repeating this step every time a new model is trained or applied becomes computationally very costly. This problem is circumvented by storing the constructed predictors for each weather station in pickle files. At the next runtime, these can quickly be read (or unpacked) to reduce the computa-

tional costs and facilitate faster experimentation with the package.

- Since reanalysis datasets, climate model output, and weather station data are provided by different data centers and have varied structures and attributes, it is well outside the scope of our project to write and include a unified data processing function for all. Instead, the preprocessing functions of the current version of pyESD are written for state-of-the-art, representative, and publicly available datasets. More specifically, they work with weather station data from the German Weather Service (Deutscher Wetterdienst, DWD) and the ERA5 reanalysis product (Hersbach et al., 2020). These preprocessing functions are provided as part of the package utilities (*pyESD.data\_preprocess\_utils*) and can easily be adapted to work for researchers' preferred datasets. The functions will be expanded in the future to allow experimentation with other popular datasets and assess the sensitivity of ESD model performance to the choice of reanalysis datasets (e.g., Brands et al., 2012).

## 2.2 Predictor selection and construction

The PP-ESD approach is highly sensitive to the choice of predictors and learning models (Maraun et al., 2019a; Gutiérrez et al., 2019). Moreover, since PP-ESD models are empirical in nature, the predictors serve as proxies for all the relevant physical processes and must be informative enough to account for the local predictand variability (Huth, 1999, 2004; Maraun and Widmann, 2018). Therefore, the selection of potential predictors should be informed by our knowledge of the atmospheric dynamics that control the climate variability of the study area. For example, synoptic-scale climate features, such as atmospheric teleconnection patterns, control much of the regional-scale climate variability. It is therefore recommended to consider these as potential predictors. Statistical techniques, such as methods for feature selection or dimension reduction, may then be applied to reduce the list of physically relevant potential predictors to a smaller selection of predictors that have a robust statistical relationship with the predictand. These steps contribute to the performance of the models and also resolve some of the issues related to multicollinearity and overfitting (e.g., Mutz et al., 2016). The pyESD package adopts three different wrapper feature selection techniques that can be explored for different models: (1) recursive feature elimination (Chen and Jeong, 2007), (2) tree-based feature selection (Zhou et al., 2021), and (3) sequential feature selection (Ferri et al., 1994). The methods are included in *pyESD.feature\_selection* as *RecursiveFeatureElimination*, *TreeBasedSelection*, and *SequentialFeatureSelection*, respectively. Furthermore, classical filter feature selection techniques, such as correlation analyses, are also included as a method of the weather station object.

Predictors are typically constructed by (1) computing the regional means of a physically relevant climate variable or (2) constructing index time series for relevant synoptic-scale climate phenomena. The package allows the user to consider a few important aspects for each type of predictor.

1. The area over which the climate variable is averaged can significantly affect model performance. In complex terrain with high-frequency topography, for example, choosing a smaller spatial extent may result in the predictor having a higher explanatory power. Therefore, a radius (with a default value of 200 km) around the weather station may be defined by the user to determine the size of the area used for the computation of the regional means.
2. Empirical orthogonal function (EOF) analysis is a well-established tool for capturing atmospheric teleconnection patterns and reducing high-dimensional climate datasets to index time series that represent the variability of prominent modes of synoptic-scale climate phenomena (Storch and von Zwiers, 2002). The current version of pyESD includes functions for the extraction of EOF-based index time series for dominant extratropical teleconnection patterns in the Northern Hemisphere (*pyESD.teleconnections*). More specifically, it allows the computation of index values for the North Atlantic Oscillation (NAO) as well as the East Atlantic (EA), Scandinavian (SCAN), and East Atlantic–Western Russian (EAWR) oscillation patterns (e.g., Boateng et al., 2022). It will be expanded to consider Southern Hemisphere patterns in future versions.

After the selection and construction of predictors, their raw values can be transformed before model training. For instance, *MonthlyStandardizer* implemented in *pyESD.standardizer* can be used to remove the seasonal trends in each predictor by centering and scaling the data. Such transformation can reduce biases toward high-variance predictors, ensure generalization, and improve the representation of predictors constructed from GCM output (e.g., Bedia et al., 2020; Benestad et al., 2015a). Principal component analysis (PCA) is another transformation tool included in the package (*pyESD.standardizer.PCAScaling*). It can be applied to (a) reduce the raw predictor values to information that is relevant to the predictand and (b) prevent multicollinearity-related problems during model training (e.g., Mutz et al., 2016).

## 2.3 Learning models

The empirical relationship between local predictand and large-scale predictors is often complicated due to the complex dynamics in the climate system. However, ML algorithms have been demonstrated to perform well in extracting hidden patterns in climate data that are relevant for build-



ing more complex transfer functions (e.g., Raissi and Karniadakis, 2018). Specifically, neural networks have been explored for downscaling climate information due to their ability to establish a complex and nonlinear relationship between predictands and predictors (e.g., Nourani et al., 2019; Gardner and Dorling, 1998; Vu et al., 2016). Moreover, support vector machine (SVM) models have been used to capture the links between predictors and predictands by mapping the low-dimensional data into a high-dimensional feature space with the use of kernel functions (e.g., Anandhi et al., 2008; Tripathi et al., 2006). Previous studies have also applied multi-model ensembles due to their ability to reduce model variance and capture the distribution of the training data (e.g., Xu et al., 2020; Massaoudi et al., 2021; Gu et al., 2022).

Selecting the most appropriate model or algorithm for a specific location or predictand can be challenging because one needs to consider many case-specific factors like data dimensionality, distribution, temporal resolution, and explainability. This problem is exacerbated by the lack of well-established frameworks for climate information downscaling (Gutiérrez et al., 2019). The pyESD package addresses this challenge with the implementation of many ML models that are different with regard to their theoretical paradigms, assumptions, and model structure. The implementation of commonly used models in the same package allows researchers to experiment with different learning models and to replicate and update their research based on emerging recommendations for specific predictands and geographical locations. The implementation of statistical and ML models in pyESD mainly relies on the open-source scientific framework scikit-learn tool (Pedregosa et al., 2011). In the following subsections, we briefly explain the principles behind the ML methods that are included in the pyESD package.

### 2.3.1 Regularization regressors

Regularization models are penalized regression techniques that shrink the coefficients of uninformative predictors to improve model accuracy and prediction interpretability (Hastie et al., 2001; Tibshirani, 1996; Gareth et al., 2013). The coefficients of non-robust predictors are set to zero by minimizing the absolute values of regression coefficients or minimizing the sum of squares of the coefficients. The former is referred to as L1 regularization and adopted by the least absolute shrinkage and selection operator (LASSO) method. The latter is referred to as L2 regularization and adopted by the ridge regression method. The regularization term ( $R$ ) and the updated cost function for a linear equation of  $p$  independent variables or predictors,  $X_i$ , are defined as

$$R(\beta) = \sum_{i=1}^p |\beta_i| \quad (1)$$

for L1 regularization and

$$R(\beta) = \sum_{i=1}^p \beta_i^2 \quad (2)$$

for L2 regularization. Therefore, the updated cost function is defined as

$$\text{cost} = \sum_{j=1}^n \left( y_j - \sum_{i=1}^p X_{ij} \beta_i \right)^2 + \lambda R(\beta), \quad (3)$$

where  $\lambda$  is the tuning parameter that controls the severity of the penalty defined in Eqs. (1) and (2), and  $\beta_i$  represents the coefficients. The package features implementations of the LASSO and ridge regression using a cross-validation (CV) scheme with random bootstrapping to iteratively optimize  $\lambda$ . These are included as LassoCV and RidgeCV, respectively. The optimization of the cost function in Eq. (3) is usually based on the coordinate descent algorithm to fit the coefficients (Wu and Lange, 2008). The pyESD package also includes an implementation of LassoCV that uses a less greedy version of the optimizer (LassoLarsCV). It is computationally more efficient by using the least angle regression (Efron et al., 2004) for fitting the coefficients.

### 2.3.2 Bayesian regression

Bayesian regression employs a type of conditional modeling to obtain the posterior probability ( $p$ ) of the target variable ( $y$ ), given a combination of predictor variables ( $X$ ), regression coefficients ( $w$ ), and random variables ( $\alpha$ ) estimated from the data (Bishop and Nasrabadi, 2006; Neal, 2012). In its simplest form, the normal linear model, the predictand  $y_i$  (given the predictors  $X_j$ ), follows a Gaussian distribution  $N(\mu, \sigma)$ . Therefore, to estimate the full probabilistic model,  $y_i$  is assumed to be normally distributed around  $X_{ij} w$ :

$$p(y_i | X, w, \alpha) = N(y_i | X_{ij} w, \alpha). \quad (4)$$

This approach also permits the use of regularizers in the optimization process. The Bayesian ridge regression procedure (BayesianRidge) estimates the regression coefficients from a spherical Gaussian and L2 regularization (Eq. 2). The regularizer parameters ( $\alpha, \lambda$ ) are estimated by maximizing the log marginal likelihood under a Gaussian prior over  $w$  with a precision of  $\lambda^{-1}$  (Tipping, 2001; MacKay, 1992):

$$p(w | \alpha) = N(w | 0, \lambda^{-1} |_p). \quad (5)$$

This means that the parameters ( $\alpha, \lambda$ , and  $w$  in Eqs. 4 and 5) are estimated jointly in the calibration process. Automatic relevance determination regression (ARD) is an alternative model included in the package. It differs from BayesianRidge in estimating sparse regression coefficients and using centered elliptic Gaussian priors over the coefficients  $w$  (Wipf and Nagarajan, 2007; Tipping, 2001). Previous studies have

used sparse Bayesian learning (relevance vector machine – RVM) for downscaling climate information (e.g., Das et al., 2014; Ghosh and Mujumdar, 2008).

### 2.3.3 Artificial neural network

The multilayer perceptron (MLP) is a classical example of a feed-forward ANN, meaning that the flow of data through the neural network is unidirectional without recurrent connections between the layers (Gardner and Dorling, 1998; Pal and Mitra, 1992). MLP is a supervised learning algorithm that consists of three layers (i.e., an input, hidden, and output layer) connected by transformation coefficients (weights) using nonlinear activation such as the hyperbolic function. More specifically, the learning algorithm with one hidden layer for the training sets  $(X_1, y_1), (X_2, y_2), \dots, (X_n, y_n)$ , where  $X_i \in R^n$  and  $y_i \in \{0, 1\}$ , can be defined as

$$f(X) = W_2 \theta \left( W_1^T X + b_1 \right) + b_2, \quad (6)$$

where  $\theta$  is the activation function, and  $b_1$  and  $b_2$  are the model biases added to the hidden and output layer. The weights connecting the layers are optimized with the back-propagation algorithm (Hecht-Nielsen, 1992; Rumelhart et al., 1986) with a mean squared error loss function. Moreover, the L2 regularization (Eq. 2) method is applied to avoid overfitting by shrinking the weights with higher magnitudes. Therefore, the optimized squared error loss function is defined as

$$\text{Loss}(\hat{y}, y, W) = \frac{1}{2} \|\hat{y} - y\|_2^2 + \frac{\alpha}{2} \|W\|_2^2, \quad (7)$$

where  $\frac{\alpha}{2} \|W\|_2^2$  is the L2 penalty that shrinks the model complexity. Often, the derivative of the loss function with respect to the weights is determined until the residual error of the model is satisfactory. The stochastic gradient descent algorithm (Bottou, 1991; Kingma and Ba, 2014) is used as a solver for updating the weights (defined in Eq. 6) in a maximum number of iterations until a satisfactory loss (Eq. 7) is achieved. Moreover, the choice of the parameters, such as the size of hidden layers, activation function, and learning algorithm, is relevant to the performance of the model (Diaz et al., 2017). The exhaustive search algorithm with CV bootstrapping is a simple and efficient method for parameter optimization (Pontes et al., 2016) and therefore included in the pyESD package (GridSearchCV).

### 2.3.4 Support vector machine

Support vector regression (SVR) uses the principles of SVM as a regression technique. The learning algorithms are based on Vapnik–Chervonenkis (VC) theory and empirical risk minimization that is designed to solve linear and nonlinear problems. This is achieved by applying kernel functions to map low-dimensional data to higher- or even infinite-dimensional feature space (Vapnik, 2000; Cristianini and

Shawe-Taylor, 2000). In principle, the model creates a hyperplane in a vector space containing groups of data points. This hyperplane is a linear classifier that maximizes the group margins. Given finite predictor and predictand data points  $(X_1, y_1), (X_2, y_2), \dots, (X_n, y_n)$ , where  $X_i \in R^n$  and  $y_i \in R$ , the regressor can be defined as

$$f(X, w) = w^T \phi(X) + b, \quad (8)$$

where the support vectors  $w$  and model bias  $b$  are the optimal parameters that minimize the cost function in Eqs. (9):

$$\text{cost} = \frac{1}{2} w^T w + C \sum_{i=1}^n (\xi_i + \hat{\xi}_i), \quad (9)$$

subject to

$$\left\{ y_i - f(X_i, w) \leq \varepsilon + \hat{\xi}_i, f(X_i, w) - y_i \leq \varepsilon + \xi_i, \right\}$$

where  $\xi_i, \hat{\xi}_i \geq 0$ , and  $i = 1..n$  are the slack variables (the upper and lower training errors) subject to the error tolerance of  $\varepsilon$  that prevents overfitting.  $C$  represents a regularization term that determines the balance between minimal loss and maximal margins. The cost function in Eq. (9) is solved using Lagrange's formula (Balasundaram and Tanveer, 2013) to obtain the optimized function:

$$f(X) = \sum_{i=1}^n (\alpha_i - \hat{\alpha}_i) \phi(X_i, X_j) + b, \quad (10)$$

where  $\alpha_i$  and  $\hat{\alpha}_i$  are Lagrange multipliers, and  $\phi(X_i, X_j)$  is the kernel function which implicitly maps the training vectors in Eq. (8) into a higher-dimensional space. The SVR method of the pyESD package includes linear, polynomial, sigmoid, and Gaussian radial basis function (RBF) kernels (Hofmann et al., 2008). Moreover, the degree of regularization ( $C$ ) and the coefficient of the kernels ( $\gamma$ ) is given a range of values so that the hyperparameter optimization algorithm can determine the best model. Due to the expensive nature of SVR, the package uses a randomized search algorithm in a CV setting for the hyperparameter optimization (Bergstra and Bengio, 2012). However, hyperparameters optimization algorithms, such as Bayesian and grid search (Snoek et al., 2012; Pontes et al., 2016; Bergstra et al., 2011) methods, are also provided as alternatives. Previous downscaling projects have taken advantage of the SVR method due to its ability to map data into higher-dimensional space and exclude outliers from the training process (Ghosh and Mujumdar, 2008; Chen et al., 2010; Sachindra et al., 2018; Anandhi et al., 2008; Tripathi et al., 2006).

### 2.3.5 Ensemble machine learning

Each ML technique is associated with challenges that arise from the method's limitations and underlying assumptions.

These have to be considered carefully in the evaluation of the resulting downscaling product. Some of these challenges can be overcome by an integration of different ML models for a specific task (Dietterich, 2000; Zhang and Ma, 2012). Integrated ML models have been suggested to outperform single ML models in downscaling climate information (e.g., Liu et al., 2015). Ensemble models typically use different ML algorithms (base learners) to extract information from the training data, then use a second set of ML algorithms (meta-learners) that learn from the first and combine the individual predictions into an ensemble. Ensemble models can be categorized by (a) the selection of base learners and (b) the method of combining the individual predictions from the base learners. Here, we summarize the more prominent ensemble models that are included in the pyESD package.

### Bagging

Bagging ensemble models consist of ML algorithms that generate several instances of base learners using random subsets of the training data and then aggregate the information for the final estimates (Breiman, 1996a; Quinlan, 1996). Such algorithms integrate randomization into the learning process and thereby often ensure the reduction of the variance of the individual base learners (e.g., decision trees). Moreover, bagging techniques constitute a simple way to improve model performance without the need to adapt the underlying base algorithm. Since bagging works well with complex algorithms like decision trees, we also consider tree-based ensembles for the pyESD package. More specifically, we include implementations of the random forest (RandomForest) and extremely randomized tree (ExtraTree) methods in addition to classical bagging.

The RandomForest algorithm builds multiple independent tree-based learners. The trees can be constructed with the full set of predictors or a random subset. Each tree is constructed from a random sample of the training data in a bootstrapping process (Breiman, 2001). The algorithm uses the remaining training data (i.e., out-of-bag data) to estimate the error rate and evaluate the model's robustness. In contrast, the Extra-Tree algorithm considers the discriminative thresholds from each predictor rather than the subset of predictors (Geurts et al., 2006). This usually adds more weight to the variance reduction and slightly improves the model bias. Tree-based ensembles are particularly suitable for establishing a nonlinear relationship between predictors and predictands (e.g., Pang et al., 2017; He et al., 2016).

### Boosting

In recent years, boosting models have also been applied for the downscaling of climate information (e.g., Fan et al., 2021; Zhang et al., 2021). Boosting models are meta-estimators that are built sequentially from multiple base learners with the primary objective of reducing the model

bias and variance. In principle, the method “boosts” weaker base learners (i.e., estimators that perform only slightly better than random guessing) by converting them into strong ones in an iterative process. The technique assumes that the base learning model is distribution-free (Schapire, 1999) and iteratively improves the weaker base learners by applying weights to the training data through the adjustment of the input points with prediction errors from the previous prediction (Schapire, 2003; Schapire and Freund, 2013). There are many boosting algorithms due to the many possible methods of weighting the training data and tuning the weaker base learners. In the pyESD package, we include (1) adaptive boosting (Adaboost), (2) gradient tree boosting (GradientBoost) with a gradient boosting algorithm by Friedman (2001), and (3) extreme gradient boosting (XGBoost). A brief summary of each is provided below.

1. The Adaboost algorithm is a well-established model for improving the accuracy of weak base learners (Freund and Schapire, 1997). The model is adaptive in the sense that the training data are sequentially adjusted based on the previous performance of the weaker model. The model uses a weighted majority vote (or sum) to combine the individual prediction from the weaker learners and produce a robust final prediction. The implemented version uses a decision tree algorithm as the base estimator to develop the boosted ensemble predictions.
2. The GradientBoost algorithm considers the boosting process to be a numerical optimization problem that minimizes a loss function in a stage-wise additive model by adding weaker learners using a gradient descent procedure. This generalization allows the tuning of an arbitrary differentiable loss function which can be selected based on a specific problem. Specifically, in pyESD, squared errors are used in the minimization of the loss function.
3. XGBoost, a recent extension of the GradientBoost algorithm, is designed to reduce computational time and improve model performance (Chen and Guestrin, 2016). The model uses regularization terms to penalize the final weights and prevent overfitting. The algorithm also uses shrinkage and column subsampling techniques to avoid overfitting. Moreover, the model can handle sparse data by using a sparsity-aware split function.

### Stacked generalization

The stacked generalization method (or “stacking”) has previously been used for the downscaling climate information and has shown improved prediction robustness over singular models (e.g., Massaoudi et al., 2021; Gu et al., 2022). It is designed to enhance prediction accuracy and generality by taking advantage of the mutual complementarity of the base-model predictions. The approach was introduced by

Wolpert (1992) and demonstrated for regression tasks and unsupervised learning by Breiman (1996b) and Leblanc and Tibshirani (1996), respectively. In principle, the following process is implemented: in the first step, the training data and base models, referred to as level-0 data and level-0 models by Wolpert (1992), are used to generate the first set of predictions. Then a meta-learning model (level-1 generalizer) is used to optimally combine the previous predictions (level-1 data) into final estimates. Lastly, the method applies a cross-validation technique and generates new “stacked” datasets for a final learning step. Generally, the performance of stacked generalization is constrained by the attributes used to generate the level-1 data and the type of algorithm used for higher-level learning (Ting and Witten, 1999). We consider these limitations by providing a wide range of models that can be used as the level-0 models and the level-1 generalizer. The base learners can be selected from the different ML models presented in the previous sections. The reader is advised that previous studies (e.g., Reid and Grudic, 2009) suggest the use of a more restrictive model like LassoCV and ExtraTree as the meta-learner to prevent overfitting.

## 2.4 Model training

The process of training and testing the PP-ESD models is the most critical stage in the downscaling procedure, since it determines much of the robustness of the final models, as well as the accuracy of the predictions they generate. The process typically involves the following steps: (1) the observational records are separated into training and testing datasets. (2) The training datasets are used to establish the transfer functions that make up the PP-ESD models. (3) The trained models are then evaluated on the independent testing datasets (Sect. 2.5). In the model training process, hyperparameter optimization techniques (e.g., GridSearchCV) are used to fine-tune the transfer function parameters, such as regression coefficients, to optimize model performance. Cross-validation (CV) techniques are applied to split the whole training dataset into smaller training and validation data sections and allow the assessment and iterative improvement of the model parameters during training while also preventing overfitting (Moore, 2001; Santos et al., 2018). In this category of techniques, the  $k$ -fold framework is the most used for climate information downscaling models. It partitions the training data into  $k$  equally sized and mutually exclusive subsamples, which are also referred to as folds (Stone, 1976; Markatou et al., 2005). More specifically, for each iteration step, one fold is used for model validation, and the remaining  $k - 1$  folds are used for model training. The leave-one-out CV technique (Lachenbruch and Mickey, 1968) is an alternative and has been used for the development of ESD models (e.g., Gutiérrez et al., 2013). Cross-validation techniques rely on the fundamental assumption of independent and identically distributed (i.i.d) data. They, therefore, treat the data as a result of a generative process that has no memory of

previously generated samples (Arlot and Celisse, 2010). The assumption of i.i.d might not be valid for time series data (e.g., Bergmeir and Benítez, 2012) due to seasonal effects, for example. To circumvent this problem, monthly bootstrapped resampling and time series splitters are included in the pyESD package. The *pyESD.splitter* module contains all CV frameworks available for model training, including the  $k$ -fold, leave-one-out, and other CV schemes. The validation metrics used for optimizing the model parameters include the coefficient of determination ( $R^2$ ) (Eq. 11), root mean squared error (RMSE) (Eq. 13), mean absolute error (MAE) (Eq. 14), and others that are summarized in Sect. 2.5. The final values for the validation metrics, which reflect the model performance during training, are arithmetic means of the individual values for each iteration. In this paper, we refer to them as CV performance metrics (i.e., CV  $R^2$ , CV RMSE, and CV MAE).

## 2.5 Model evaluation

In the process of downscaling climate information, best practice involves the use of stringent model evaluation schemes with independent data outside the training data range (Wilby et al., 2004). Retaining a section of the data as a testing dataset (Sect. 2.4) is recommended if longer records (e.g.,  $\geq 30$  years) are available. It allows (a) a completely independent evaluation of the trained model’s performance and (b) an assessment of the sensitivity of the model to the chosen training dataset. In the case of time series, the latter can provide insights into the model’s sensitivity to the calibration period and the temporal stationarity of the model’s transfer functions. If the records are short (e.g.,  $< 30$  years), the CV metrics (Sect. 2.4) can be used, albeit with caveats, as non-ideal estimates for the model’s performance (e.g., Mutz et al., 2021). For the remainder of this section, however, we will assume that longer records and completely independent testing datasets are available.

The PP-ESD model is evaluated on the basis of the model’s predictions  $\hat{y}$  and the observed values  $y$ . In pyESD, the following performance metrics are implemented.

1. The coefficient of determination ( $R^2$ ) represents the fraction of the predictand’s observed variance that can be explained by the predictors. It can be seen as a measure of how well the model predicts the unseen data (Wilks, 2011). The  $R^2$  for the predicted values  $\hat{y}_i$  in relation to the observed data  $y_i$  for  $i = 1, \dots, n$  samples is defined as

$$R^2(y, \hat{y}) = 1 - \frac{\sum_{i=1}^n (y_i - \hat{y}_i)^2}{\sum_{i=1}^n (y_i - \bar{y})^2}, \quad (11)$$

where  $\bar{y}$  is the mean of the observed data,  $\sum_{i=1}^n (y_i - \hat{y}_i)^2$  is the sum of squared residuals (SSR),

and  $\sum_{i=1}^n (y_i - \bar{y})^2$  is the total sum of squares (SST).  $R^2$  can range from  $-\infty$  to 1, where 1 is the best possible score and negative values are indicative of an arbitrary, worse model. An  $R^2$  value of 0 is indicative of a model that would always predict the  $\bar{y}$ . In this case, the model represents no improvement over simply using the mean  $\bar{y}$  as a model.

Pearson's correlation coefficient (PCC) evaluates the linear correlation between the model predictions  $y_i$  and observed data  $x_i$ . The PCC of 1 indicates a perfect positive correlation,  $-1$  indicates a perfect anticorrelation, and 0 indicates no correlation between the predicted and observed values. The PCC for  $n$  samples is defined as

$$\text{PCC}_{xy} = \frac{\sum_{i=1}^n (x_i - \bar{x})(y_i - \bar{y})}{\sqrt{\sum_{i=1}^n (x_i - \bar{x})^2} \sqrt{\sum_{i=1}^n (y_i - \bar{y})^2}}, \quad (12)$$

where the  $\bar{x}$  and  $\bar{y}$  are the means of the  $x_i$  and  $y_i$  values, respectively.

The root mean squared error (RMSE) estimates the mean magnitude of error between the predictions and observations. The RMSE is given in the physical units of the observed data and not standardized. Smaller values indicate better model performance. The RMSE for predictions  $\hat{y}_i$  and observations  $y_i$  of  $n$  samples is calculated as

$$\text{RMSE}(y, \hat{y}) = \sqrt{\frac{1}{n} \sum_{i=1}^n (\hat{y}_i - y_i)^2}. \quad (13)$$

The mean absolute error (MAE) is a scale-dependent accuracy measure that also provides information on the errors between the predictions and observations. The MAE is estimated as the sum of absolute errors normalized by the sample size ( $n$ ). The MAE is calculated as

$$\text{MAE}(y, \hat{y}) = \frac{1}{n} \sum_{i=1}^n |\hat{y}_i - y_i|. \quad (14)$$

Additional metrics such as the mean squared error (MSE), mean absolute percentage error (MAPE), maximum error, adjusted  $R^2$  (Miles, 2014), and Nash–Sutcliffe efficiency (NSE) (Nash and Sutcliffe, 1970) are included in pyESD. However, the predicted values from the trained model and their corresponding observed values can be evaluated using other metrics not included in pyESD. For example, additional metrics like the model skill score  $E$  and the revised  $R^2$  (RRS), which combines correlation, bias measure, and the capacity to capture variability, can be used (Onyutha, 2021).

We highlight that the limitations and assumptions underpinning these metrics should be considered when interpreting performance metrics. For example, the RMSE is sensitive to outliers because the squaring of errors assigns more weight to large errors. This implies that a single outlier can bias its estimate and lead to a misinterpretation of extreme data points in the predictand. Although MAE is less sensitive to outliers compared to RMSE, its treatment of all errors with equal weight may not adequately account for the impact of extreme errors on model performance. Consequently, both metrics should be interpreted with respect to the mean of the observed values. On the other hand, the Pearson correlation coefficient (PCC) assumes a linear relationship between the predicted and observed values and a bivariate normal distribution. However, distance correlation (Székely et al., 2007), which is more computationally demanding and makes no assumptions about the relationship or distribution, can be considered. Chaudhuri and Hu (2019) demonstrated a fast algorithm that can be used to compute the distance correlation.

## 2.6 GCM–ESD coupling and local-scale predictions

The developed and tested PP-ESD model can finally be coupled to coarse-scale climate information. If the PP-ESD model was developed with the intention to downscale predictions of future climate change, the next logical step is to couple it to GCM simulations forced with different greenhouse gas concentration scenarios. Since PP-ESD is the bias-free downscaling alternative to MOS-ESD, PP-ESD models may be coupled to all GCMs, provided that the predictors are adequately represented by the GCMs. This condition may be alleviated to an extent by standardizing the simulated predictor (Bedia et al., 2020). An analysis of the distribution similarity between the observed and simulated predictors can be conducted to test the assumption of representation. For example, the Kolmogorov–Smirnov (KS) test, which is implemented as part of the pyESD package utilities, is a nonparametric statistical hypothesis test that can be used to evaluate the null hypothesis ( $H_0$ ) that the observation-based predictors and simulated predictors are of the same theoretical distribution.

The first step in ESD–GCM coupling is to utilize the GCM output to recreate the predictors used in the training of the ESD model. This may involve anything from constructing simple temperature regional means to reconstructing multivariate indices for more complex climate phenomena. In the case of index-based predictors such as NAO, EA, SCAN, and others, the simulated indices are reconstructed by projecting the pressure anomalies of the GCM onto the EOF loading patterns of the predictors (e.g., Mutz et al., 2016). This ensures that the physical meaning of the index values is maintained. The ESD model then takes these simulated predictors as input and generates local-scale predictions according to the model's transfer functions. The added value of the resulting downscaling product can be evaluated by comparing

the downscaled values to the raw outputs of different GCMs and RCMs. Finally, the high-resolution local-scale predictions can be used to drive climate change impact assessment models to predict flood frequency (e.g., Padulano et al., 2021; Hodgkins et al., 2017), agricultural changes (e.g., Mearns et al., 1996), changes in water resources (e.g., Dau et al., 2021), and more.

### 3 Illustrative case study: Neckar catchment

We demonstrate the complete downscaling workflow and highlight most of the functionalities of the pyESD package in an illustrative case study. The study uses the PP-ESD approach and is set in the Neckar catchment, a hydrological catchment in southwestern Germany that consists of complex mountainous terrain with topographic elevations between 200 and 1000 m above sea level (Fig. 2). The region is climatically complex, since local climates are influenced by atmospheric teleconnection patterns (e.g., NAO, EA, and SCAND), orographic effects (e.g., Kunstmann et al., 2004), and the Mediterranean climate (Bárdossy, 2010; Ludwig et al., 2003). The catchment experiences maximum precipitation (80–120 mm per month) and temperature (15–18 °C) in the summer months (Fig. 3). The catchment serves as a water supply for drinking and agricultural activities (Selle et al., 2013). We use this catchment for our case study because (a) it is a suitable region to test the strengths and limitations of the pyESD downscaling package, and (b) generating 21st century climate change estimates can contribute to regional climate impact assessments and adaptation.

In this case study, we apply pyESD to predict local temperature and precipitation changes for 22 weather stations located in the catchment (Table 1) and demonstrate the package's flexibility by performing experiments with the different modeling alternatives. We show most of the PP-ESD steps required for generating robust downscaling products. These steps include (1) predictor selection and construction; (2) model selection, training, and cross-validation; (3) model evaluation; and (4) generating future predictions through ESD–GCM coupling (see Sect. 3.2 for details). We note that the focus of the case study is more on demonstrating the pyESD workflow and functionality and less on detailed discussions of the downscaled results and their implications. In order to allow readers to reproduce and learn from this application example, we only use public and freely available datasets (see Sect. 3.1 for more details about the data). Moreover, all scripts used in this study (i.e., data preprocessing, modeling, and visualization scripts) are provided in the code and data availability section.

## 3.1 Datasets

### 3.1.1 Weather station data

Monthly precipitation and temperature station data from the German Weather Service (Deutscher Wetterdienst, DWD accessible from <https://cdc.dwd.de/portal/>, last access: 30 October 2023) served as the predictand time series in this study. We considered all weather station records that (a) originated from measurements in the Quelle–Enz subcatchment, (b) covered the time period of 1958 to 2020, and (c) were at least 30 years in length. Even though there is no well-established and universally valid recommendation for the minimum record length in a PP-ESD approach (e.g., Hewitson et al., 2014), we chose a conservative 30-year threshold to ensure the models can be evaluated with truly independent, retained data (see Sect. 2.5). The remaining weather stations are summarized in Table 1. These were loaded into predictand station objects (SOs) as follows.

```
1 from pyESD.Weatherstation import
  read_station_csv
2 variable = "Temperature" #or
  'Precipitation'
3 SO = read_station_csv(filename,
  variable)
```

### 3.1.2 Reanalysis datasets

The ERA5 reanalysis products, produced and managed by the European Centre for Medium-Range Weather Forecasting (ECMWF), were used to construct the predictors in this study. ERA5 is based on historical records from various observational systems (e.g., oceans buoys, aircraft, weather stations) that are dynamically interpolated with numerical forecasting models in a four-dimensional variational (4D-Var) data assimilation scheme to generate global, homogeneous, spatially gridded datasets (Bell et al., 2021). It has a spatial resolution of approximately 31 km (or TL639) and is available as hourly data, covering 1950 to the present day with a 5 d lag of data availability (Hersbach et al., 2020). For this study, however, mean monthly values were used in the construction of potential predictors (Table 2). These are publicly available from the Copernicus Climate Data Store (CDS) (accessible at <https://cds.climate.copernicus.eu>, last access: 30 October 2023).

### 3.1.3 GCM simulation datasets

For the ESD–GCM coupling, the predictors were reconstructed from an MPI-ESM (Max Planck Institute Earth System Model) GCM simulation that follows the protocols of the World Climate Research Programme's (WCRP) Coupled Model Intercomparison Project phase 5 (CMIP5) (Taylor et al., 2012). We highlight that CMIP5 model output was chosen in this illustrative study to enable consistent comparison with previous regional climate models over the re-

**Table 1.** IDs (specific to this study), names, coordinates, and elevation (m) for weather stations recording (a) precipitation and (b) temperature.

(a) ID	Name	Longitude	Latitude	Elevation
1	Baltmannsweiler–Hohengehren	9.45	48.76	457
2	Boll Bad	9.62	48.64	423
3	Eschbronn–Mariazell	8.47	48.19	716
4	Fellbach	9.27	48.81	280
5	Goeppingen–Jebenhausen	9.63	48.69	368
6	Haigerloch–Weildorf	8.77	48.37	524
7	Hechingen	8.98	48.38	518
8	Heubach Ostalb	9.94	48.80	450
9	Horb–Betra	8.66	48.41	544
10	Klippeneck	8.75	48.11	973
11	Lorch Kreis Ostalb–Waldhausen	9.64	48.78	296
12	Metzingen	9.27	48.54	354
13	Oberndorf Neckar	8.58	48.29	516
14	Rosenfeld–Bickelsberg	8.69	48.29	676
15	Stoetten	9.86	48.67	734
16	Stuttgart–Echterdingen	9.22	48.69	371
17	Stuttgart (Schnarrenberg)	9.20	48.83	314
18	Winterbach Rems–Murr–Kreis	9.47	48.80	240
(b) ID	Name	Longitude	Latitude	Elevation
1	Hechingen	8.98	48.38	518
2	Klippeneck	8.75	48.11	973
3	Lenningen–Schopfloch	9.53	48.54	758
4	Murrhardt	9.57	48.97	344
5	Rottweil	8.64	48.18	588
6	Schwaebisch Gmuend–Strassdorf	9.80	48.78	415
7	Stoetten	9.86	48.67	734
8	Stuttgart–Echterdingen	9.22	48.69	371
9	Stuttgart (Schnarrenberg)	9.20	48.83	314

**Table 2.** Potential predictors considered for PP-ESD models and the frequency of their selection for (a) precipitation and (b) temperature stations (based on the final predictor selection method).

Name	Description	(a)	(b)	
1	t2m	Near-surface temperature	8	8
2	tp	Total precipitation	18	9
3	msl	Mean sea level pressure	4	6
4	v10	Near-surface meridional wind	7	7
5	u10	Near-surface zonal wind	10	7
6	NAO	North Atlantic Oscillation index	9	5
7	EAWR	East Atlantic–Western Russian oscillation index	11	3
8	SCAN	Scandinavian oscillation patterns	11	5
9	EA	East Atlantic patterns	10	4
10	v_plev	Meridional wind at pressure levels 250, 500, 700, 850, and 1000 hPa	9, 7, 7, 10, 8	7, 3, 8, 5, 7
11	u_plev	Zonal wind at pressure levels 250, 500, 700, 850, and 1000 hPa	4, 9, 7, 6, 11	7, 5, 5, 5, 8
12	r_plev	Relative humidity at pressure levels 250, 500, 700, 850, and 1000 hPa	7, 8, 15, 7, 11	7, 4, 5, 5, 6
13	z_plev	Geopotential height at pressure levels 250, 500, 700, 850, and 1000 hPa	3, 6, 4, 6, 5	4, 6, 5, 7, 5
14	t_plev	Temperature at pressure levels 250, 500, 700, 850, and 1000 hPa	10, 9, 7, 7, 6	5, 5, 6, 8, 9
15	d2m	Near-surface dew-point temperature	6	5
16	dtd	Dew-point temperature depression at pressure levels 250, 500, 700, 850, and 1000 hPa	7, 6, 13, 7, 11	4, 2, 2, 3, 1

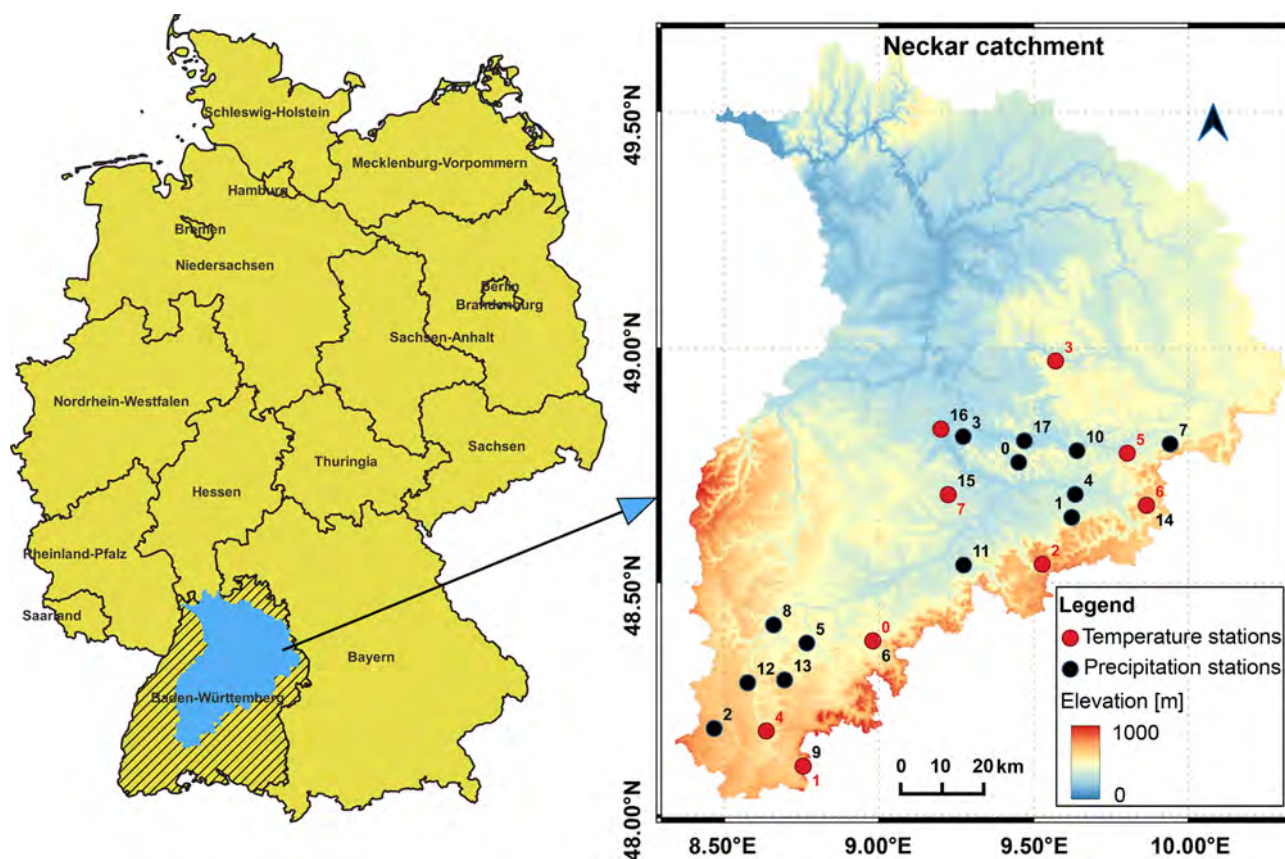


**Figure 2.** Weather station locations and elevations in the Neckar catchment. The red circles represent temperature stations (ID corresponds to Table 1b), and the black circles represent precipitation stations (ID corresponds to Table 1a). The color map shows the elevation and delineates the extent of the catchment.

gion and any GCM outputs (e.g., CMIP6) can be combined with pyESD. For the case study, we consider several simulations (accessible at <https://cds.climate.copernicus.eu>, last access: 30 October 2023) forced with different RCP scenarios (Moss et al., 2010) to predict the local-scale response to the plausible range of forcings. In order to highlight the added value of the downscaled product, the local-scale future estimates are compared to the coarser predictions of several GCMs (i.e., MPI-ESM, CESM1-CAM5 of the National Center for Atmospheric Research – NCAR, Kay et al., 2015, and HadGE2-ES of the Hadley Centre of the UK Met Office, Collins et al., 2008) and RCMs (CORDEX-Europe simulation with MPI-CSC-REMO2009 driven with boundary conditions from MPI-ESM).

## 3.2 Methods

### 3.2.1 Predictor selection and construction

The considered predictors must be large-scale climate elements that are both physically and empirically relevant to predicting the local-scale climate variability in the vicinity of the weather station. The physical relevance of considered

predictors (Table 2) is established through previous studies and general climatological merit. We then apply a monthly standardizer transformer to remove the seasonality trends and scale the individual predictors. The empirical relationship with the predictand is then evaluated with PCCs defined in Eq. (12). Finally, first estimates of their predictive skills are obtained through the application of the package’s recursive, sequential, and tree-based algorithms in a CV setting. These preliminary experiments are conducted to refine the selection of predictors further. After the predictor selection process, each weather station and predictand is associated with a particular subset of predictors (Table 2) that are later used to train the final ESD model for the station (Sect. 3.2.2).

The steps above are implemented with pyESD as follows.

1. We create a list (predictors) of all considered predictors with physical relevance to the predictand. We then use the `set_predictors` method of the station object (SO) to read the data in the local directory (`predictordir`) and construct regional means with a defined radius of 200 km around the station location. These are regional means of relevant climate variables and serve as the simplest type of predictor. For the



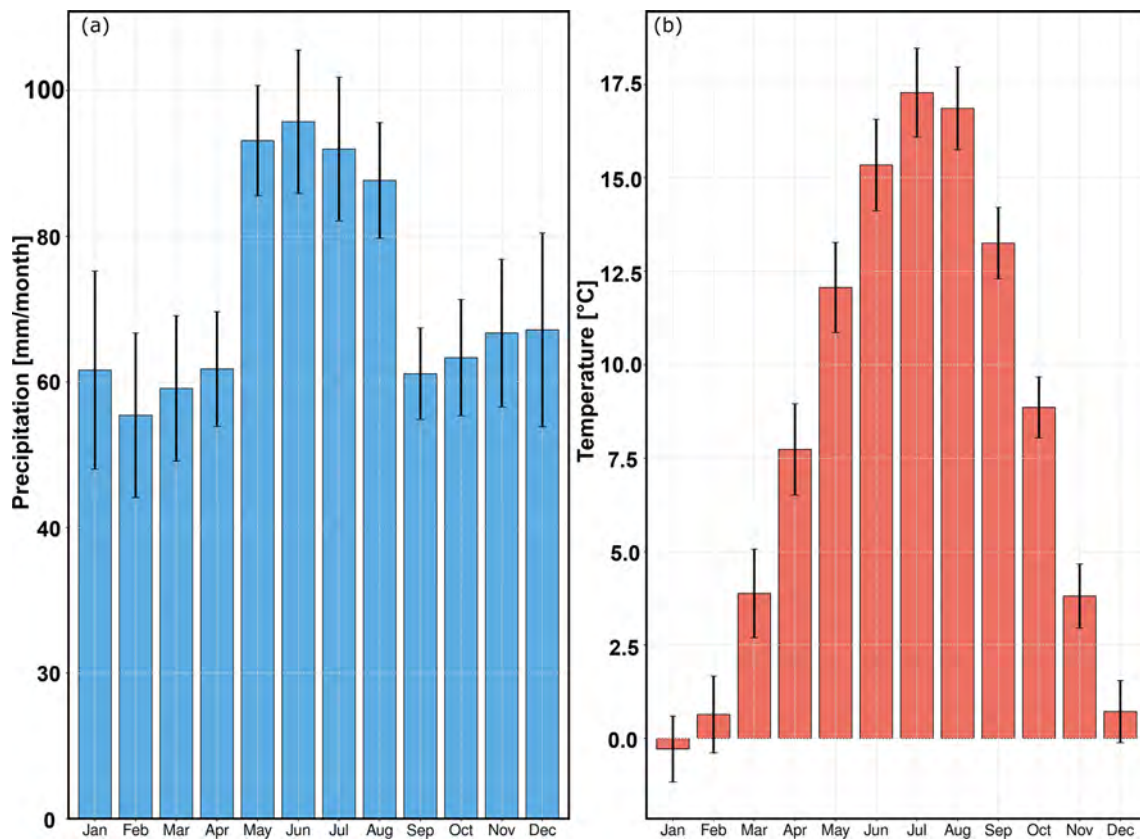


**Figure 3.** Long-term (1958–2020) monthly means of (a) precipitation and (b) temperature, averaged over all stations in the catchment. The error bars are the standard deviations that represent inter-station variability. The maximum precipitation and temperature in the catchment are recorded in the summer season (JJA).

construction of indices for atmospheric teleconnection patterns (i.e., NAO, EA, SCAN, and EAWR), which serve as further predictors, the package automatically calls the *pyESD.teleconnections* module if the pattern's acronym is included in the list of predictors.

```
1 predictors = ["t2m", "tp", "NAO",
..., "nth predictor"]
2 SO.set_predictors(variable,
predictors, predictor_dir,
radius=200) # radius in km
```

2. We apply the monthly standardizer and then use the *predictor\_correlation* method to estimate the PCC between the predictand and predictors.

```
1 SO.set_standardizer(variable,
standardizer = MonthlyStandardizer
(detrening=True, scaling=True))
2 df_corr = SO.predictor_correlation
(variable, predictor_range,
ERA5Data, fit_predictors=True,
fit_predictand=True,
method="pearson")
```

3. The final refinement of the predictor list is implemented as part of the *fit* method. We use the *set\_model* method to define the ARD regressor, *TimeSeriesSplitter* CV setting, and call the *fit* method in a loop through the three types of selector methods.

```
1 SO.set_model(variable,
method="ARD",
cv=TimeSeriesSplit(n_splits=10))
2 selector_methods = ["Recursive",
"TreeBased", "Sequential"]
3 for selector_method in
selector_methods:
4 SO.fit(variable, predictor_range,
ERA5Data, fit_predictors=True,
predictor_selector=True,
selector_method =
selector_method, select_regressor)
```

### 3.2.2 Model training and validation

Model training and validation are performed separately for each predictand and weather station. The models are trained in a CV setting for the period 1958–2010 and then assessed

on independent retained data for the period 2011–2020. In the training process, we use seven different methods before deciding on an estimator for the final model. These methods include at least one representative for each of the families of ML algorithms (see Sect. 2.3) except SVR. We exclude SVR due to its high computational demands for optimization and to ensure the easy reproducibility of the illustrative example on less powerful computers. We perform the initial model training and validation with the LassoLarsCV, ARD, MLP, RandomForest, XGBoost, bagging, and stacking regressors using a  $KFold(n\_splits=10)$  validation scheme for hyperparameter optimization. For the stacking regressor, we use all the other regressors as base estimators (i.e., level-0 learners) and ExtraTree as the meta-learner. The final ESD model is then selected based on the CV metrics (i.e., CV  $R^2$  and CV RMSE) of the individual models.

The steps above are implemented with pyESD as follows: the models are trained with the `fit` method as described within Sect. 3.2.2. The `cross_validate_and_predict` method is applied to calculate the CV metrics and generate the predictions for the training period 1958–2010. The `predict` method is then used to generate predictions for the 2011–2020 period from the models trained in the 1958–2010 period. Finally, the `evaluate` method is used to obtain the model performance metrics based on the 2011–2020 predictions and retained data. The  $R^2$ , RMSE, and MAE (see Sect. 2.5) are used as both CV and evaluation metrics in this study. The ERA5 reanalysis product is specified as the predictor dataset for all these methods.

```
1 cv_score_1958to2010,
predict_1958to2010 =
SO.cross_validate_and_predict(variable,
from1958to2010, ERA5Data)
2 predict_2011to2020 =
SO.predict(variable, from2011to2020,
ERA5Data)
3 scores_2011to2020 =
SO.evaluate(variable, from2011to2020,
ERA5Data)
```

### 3.2.3 Future prediction

Future predictions are generated by coupling the final ESD models to GCM simulations for the 21st century. In the illustrative example, we use MPI-ESM simulations that were forced with greenhouse gas concentration scenarios RCP2.6, RCP4.5, and RCP8.5. This coupling is achieved as follows: the predictors selected during model training are reconstructed from the GCM output. These simulated predictors are standardized with the `MonthlyStandardizer` parameters obtained from the reanalysis predictors to ensure data homogenization. Prediction anomalies are calculated using the training period 1958–2010 as a reference. The resulting RCP-specific 21st century prediction anomaly time series are then used to calculate the annual means (2020–2100),

as well as the seasonal (DJF, MAM, JJA, SON) and annual 30-year climatologies for the mid-century (2040–2070) and the end of the century (2070–2100). The predicted anomalies are then back-transformed to their respective absolute values for all stations and compared to the raw outputs of GCMs (i.e., CESM1-CAM5, HadGE2-ES, EURO-CORDEX, and MPI-ESM; see Sect. 3.1.3) using the nearest grid point. In pyESD, a future prediction can be generated by using the `predict` method (Sect. 3.2.2) and specifying the GCM output as the predictor data source.

The PP-ESD approach relies on the assumption that the predictors are well-represented by the GCM. We therefore perform KS tests to evaluate the distribution similarity between GCM and ERA5 predictors for the datasets' temporal overlap. The KS statistic lies within the 0–1 range, with lower values indicating greater distribution similarity. For our two-sided tests, we reject the null hypothesis ( $H_0$  means the datasets have identical underlying distributions) in the case of  $p$  values being smaller than 0.05. We perform the test on the raw monthly time series, monthly anomalies, and standardized anomalies in order to isolate the distributional differences of the first and second moments error propagation (Bedia et al., 2020). The `KS_stat` function implemented in the `pyESD.utils` module is used to test several of the informative predictors (such as tp, t2m, r850, u850, and v850).

## 4 Results and discussion

In this section, we present and discuss the results of the illustrative case study. The discussion places more emphasis on the functionalities of the package than the climatological implications. Specifically, we discuss the results of the predictor selection step (Sect. 4.1), the training and validation of the model (Sect. 4.2), the final model performance (Sect. 4.3), and the future predictions generated through the ESD–GCM coupling (Sect. 4.4).

### 4.1 Predictor selection

All implemented predictor selection methods demonstrated merit, and the correlation analyses revealed strong linear dependencies between the predictand variables and potential predictors (Figs. A1 and A2). For example, precipitation records are highly correlated ( $PCC \geq 0.5$ ) with large-scale total precipitation (tp), atmospheric relative humidity ( $r$ ), and zonal wind velocity ( $u$ ) up to the mid-tropospheric level (i.e., 500–1000 hPa) (Fig. A1). The temperature records are highly correlated ( $PPC \geq 0.7$ ) with near-surface temperature (t2m), atmospheric temperature ( $t$  on all levels), and dew-point temperature depression (dtd) up to the mid-troposphere (Fig. A2). Both predictands also show a good correlation ( $PCC \geq 0.25$ ) with the indices of the atmospheric teleconnection patterns (i.e., NAO, EA, EAWR, and SCAN). The predictor selection methods (i.e., recursive, tree-based,

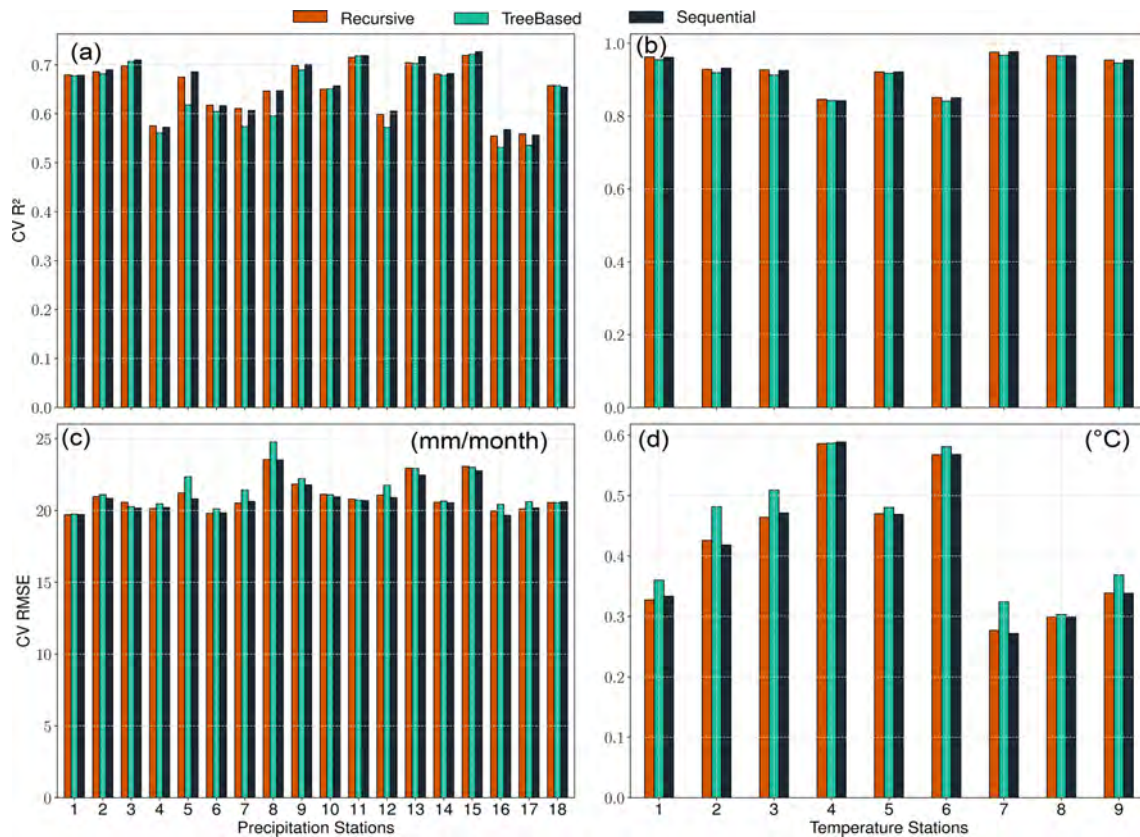


**Figure 4.** Cross-validation  $R^2$  and RMSE for the predictor selection methods (recursive in red, tree-based in green, and sequential in black) for precipitation (a, c) and temperature (b, d) station records. The individual methods performed similarly well, suggesting that each of the implemented methods may be used to refine the list of potential predictors.

and sequential) perform similarly for all the precipitation and temperature stations (Fig. 4). More specifically, the three methods yield CV  $R^2$  values of 0.5 to 0.75 (Fig. 4a), CV RMSE values of  $\leq 25$  mm per month (Fig. 4c) for precipitation, CV  $R^2$  values of  $\geq 0.95$  (Fig. 4b), and CV RMSE values of 0.3 to 0.6 °C (Fig. 4d) for temperature stations. Since the methods did not show a significant difference in performance, the recursive method was applied for the refinement of the set of predictors, since it allows more flexibility and a stepwise iteration of several combinations of potential predictors (e.g., Mutz et al., 2021; Hammami et al., 2012; Li et al., 2020). The frequencies with which specific predictors were selected using the recursive method are listed in Table 2.

The predictors tp and t2m were included for most of the precipitation and temperature station records, respectively. This indicates that variations in the larger-scale precipitation and temperature fields already explain much of the local-scale predictand variability in the vicinity of the weather stations. Many of the refined predictor sets also included indices of the NAO (9 of 18 precipitation stations, 5 of 9 temperature stations), SCAN (11 of 18 precipitation stations, 5 of 9 temperature stations), EA (10 of 18 precipitation stations, 4 of 9

temperature stations), and EAWR (11 of 18 precipitation stations, 3 of 9 temperature stations). This confirms the strong manifestation of Northern Hemisphere atmospheric teleconnection patterns in the local-scale precipitation and temperature in the catchment (e.g., Bárdossy, 2010; Ludwig et al., 2003). Their exclusion from the other stations is likely due to the fact that their variability might already be captured by zonal and meridional wind speeds and synoptic pressure variables like geopotential height ( $z$ ) and mean sea level pressure (slp) (Hurrell and Van Loon, 1997; Hurrell, 1995; Barnston and Livezey, 1987; Maraun and Widmann, 2018). Relative humidity was selected as a predictor for most of the precipitation stations. This is consistent with the results of many other studies (e.g., Gutiérrez et al., 2019; Hammami et al., 2012) and our physical understanding of it as a measure of humidity that takes saturation vapor pressure into consideration.

#### 4.2 Performance of individual estimators

We experimented with seven different regressors before deciding on the regressor that would be used to establish the final ESD models (see Sect.3.2.2). A total of 126 precipita-

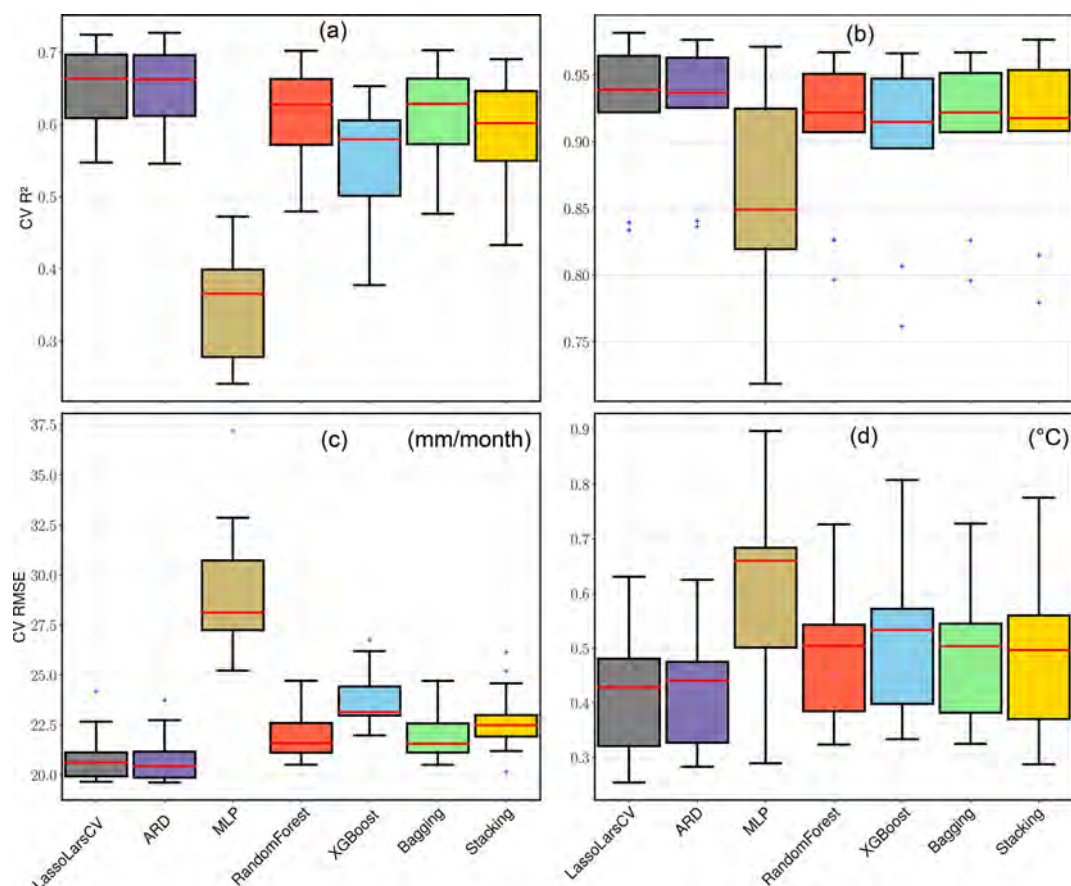


**Figure 5.** Cross-validation  $R^2$  and RMSE box plots comparing the experimental regressors' performance for all the precipitation (a, c) and temperature (b, d) stations. The red lines inside the box represent the median, the lower and upper box boundaries indicate the 25th and 75th percentiles, and the lower and upper error lines show the 10th and 90th percentiles, respectively. The black plus marks show the outliers outside the range of the 10th and 90th percentile.

tion and 63 temperature experimental models were generated with the seven regressors. Overall, most of the experimental models performed reasonably well with a mean  $CV R^2$  of  $\geq 0.5$  for precipitation and  $\geq 0.9$  for temperature stations (Fig. 5). The MLP models, on the other hand, performed relatively poorly with  $CV R^2$  values of  $\leq 0.4$  for precipitation and  $\leq 0.9$  for temperature. This is due to the fact that MLP model calibration requires longer records and a more complex architecture to capture most of the informative patterns in the training data. This study, however, uses a simplified architecture to make the results reproducible without higher computational requirements. The result can likely be improved with more data (e.g., by using daily values) and an increase in hidden layers (Sect. 2.2.3). The overall performance of the experimental models underlines the methods' suitability for downscaling.

Among the better-performing precipitation models, the LassoLarsCV and ARD methods yielded the best results ( $CV R^2 = 0.55\text{--}0.75$ ,  $CV RMSE = 20\text{--}23$  mm per month), followed by the RandomForest and bagging ensembles ( $CV R^2 = 0.48\text{--}0.70$ ,  $CV RMSE = 21$  to  $25$  mm per month), as

well as the XGBoost ensemble regressor ( $CV R^2 = 0.39\text{--}0.65$ ,  $CV RMSE = 22\text{--}27$  mm per month). Stacking all experimental models into a meta-regressor also yields good results ( $CV R^2 = 0.45\text{--}0.7$ ,  $CV RMSE = 20\text{--}26$  mm per month) despite the poor performance of the MLP regressors. Based on these results, the LassoLarsCV, ARD, RandomForest, and bagging regressors were selected as the final base learner for the stacking model. ExtraTree was chosen as the final meta-learner to prevent overfitting issues by placing an additional discriminative threshold on all the base regressor's predictions (Geurts et al., 2006).

The experimental temperature models showed similar patterns in performance but performed better overall. LassoLarsCV and ARD emerge as the best-performing models ( $CV R^2 = 0.85\text{--}0.98$ ,  $CV RMSE = 0.2\text{--}0.6$  °C), followed by the RandomForest and bagging regressors ( $CV R^2 = 0.8\text{--}0.96$ ,  $CV RMSE = 0.3\text{--}0.7$  °C), as well as the XGBoost and stacking ensemble regressors ( $CV R^2 = 0.75\text{--}0.96$ ,  $CV RMSE = 0.3\text{--}0.8$  °C). Therefore, we also selected stacking (with LassoLarsCV, ARD, RandomForest, bagging) for the final temperature models, too.

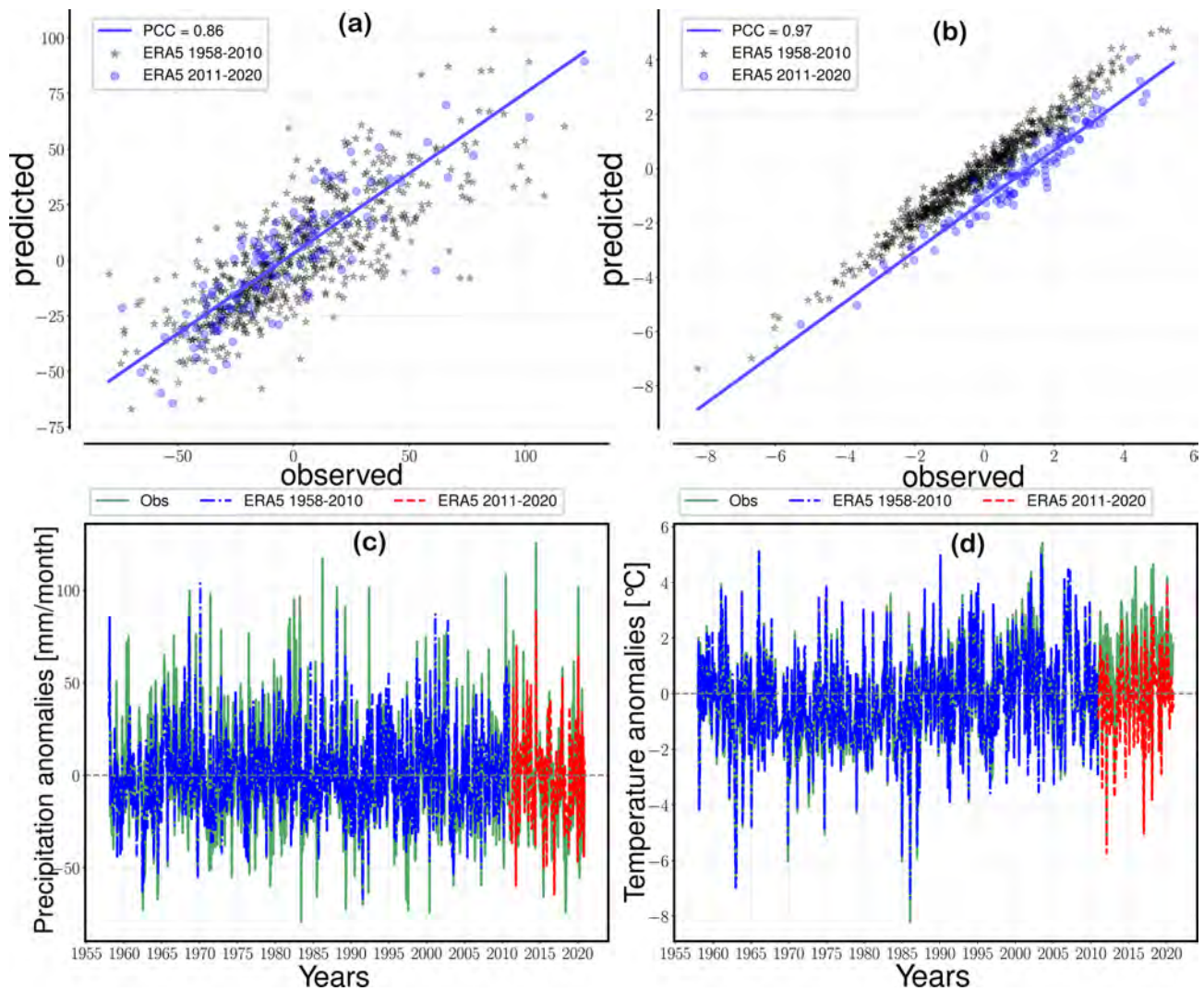


**Figure 6.** Prediction example for the Hechingen station using the final regressor for precipitation (a, c) and temperature (b, d). The top panels (a, b) show the linear relationship between the predictions and observed values, as well as the PCC ( $R$  value) for the testing data (blue-colored circles). The bottom panels (c, d) show the 1-year moving average of the observed (green, solid) and ERA5-driven predictions for the training period (blue, dash-dotted) and the testing period (red, dashed).

### 4.3 Performance of the final estimator

Following the analysis of the seven experimental models (Sect. 4.2), the recursive predictor selection method and stacking learning model (with LassoLarsCV, ARD, Random-Forest, and bagging) were selected for the generation of the final ESD models. The models were trained on the 1958–2010 data in a CV setting and evaluated on the retained data in the 2011–2020 period.  $R^2$ , RMSE, and MAE were used as performance metrics for the CV setting and the final evaluation (Tables 3 and 4). The models' performance was good overall but varied notably between different stations. The prediction skill estimates were higher for temperature than for precipitation. For temperature (Table 4), the explained variance estimates (“Fit  $R^2$ ”) are in the range of

0.81–0.98 ( $\mu = 0.94$ ), and CV  $R^2$  values are in the range of 0.84 to 0.98 ( $\mu = 0.93$ ), whereas for precipitation (Table 3), the explained variance estimates are in the range of 0.58–0.84 ( $\mu = 0.71$ ), and CV  $R^2$  values are in the range of 0.54–0.72 (0.65). The accuracy measures display a similar discrepancy with CV RMSE of 0.3–0.6 °C ( $\mu = 0.42$  °C) and CV MAE of 0.2–0.50 °C ( $\mu = 0.34$  °C) for temperature, as well as CV RMSE of 20–24 mm per month ( $\mu = 21$  mm per month) and CV MAE of 14–18 mm per month ( $\mu = 16$  mm per month) for precipitation.

The final model evaluation using independent, retained data from 2011–2020 yielded  $R^2$  values of up to 0.95 as well as average RMSE and MAE of  $\sim 1.0$  °C for temperature and  $R^2$  values of up to 0.74, average RMSE of 22 mm per month, and MAE of 17 mm per month for precipitation. The discrep-

**Table 3.** Model performance metrics (i.e.,  $R^2$ , RMSE, and MAE) for all the precipitation stations. The final ESD models were trained in a CV setting on datasets from 1958–2010 and evaluated on independent, retained data from 2011–2020.

ID	Name	(Fit) $R^2$	CV $R^2$	CV RMSE	CV MAE	$R^2$	RMSE	MAE
1	Baltmannsweiler–Hohengehren	0.71	0.67	20	15	0.63	22	18
2	Boll Bad	0.70	0.69	21	15	0.60	24	19
3	Eschbronn–Mariazell	0.74	0.69	20	16	0.59	23	18
4	Fellbach	0.61	0.57	20	15	0.59	20	15
5	Goeppingen–Jebenhausen	0.71	0.68	21	16	0.62	23	18
6	Haigerloch–Weildorf	0.64	0.62	20	15	0.74	17	13
7	Hechingen	0.63	0.61	20	15	0.74	17	13
8	Heubach Ostalb	0.78	0.65	24	18	0.65	25	21
9	Horb–Betra	0.84	0.72	21	16	0.74	21	16
10	Klippeneck	0.67	0.63	21	16	0.70	21	17
11	Lorch Kreis Ostalb–Waldhausen	0.79	0.72	21	15	0.64	24	20
12	Metzingen	0.79	0.61	20	16	0.64	20	16
13	Oberndorf Neckar	0.75	0.71	23	17	0.66	28	22
14	Rosenfeld–Bickelsberg	0.70	0.69	20	15	0.70	21	16
15	Stoetten	0.75	0.72	23	17	0.68	25	20
16	Stuttgart–Echterdingen	0.61	0.56	20	14	0.68	16	13
17	Stuttgart (Schnarrenberg)	0.58	0.54	20	14	0.50	21	15
18	Winterbach Rems–Murr–Kreis	0.72	0.66	20	15	0.61	23	18

**Table 4.** Model performance metrics (i.e.,  $R^2$ , RMSE, and MAE) for all the temperature stations. The final ESD models were trained in a CV setting on datasets from 1958–2010 and evaluated on independent, retained data from 2011–2020.

ID	Name	Train $R^2$	CV $R^2$	CV RMSE	CV MAE	$R^2$	RMSE	MAE
1	Hechingen	0.96	0.96	0.30	0.30	0.93	1.3	1.2
2	Klippeneck	0.94	0.94	0.40	0.30	0.94	1.3	1.2
3	Lenningen–Schopfloch	0.95	0.93	0.50	0.40	0.91	0.9	0.7
4	Murrhardt	0.81	0.84	0.60	0.50	0.77	1	0.8
5	Rottweil	0.94	0.92	0.50	0.40	0.92	1.1	1
6	Schwaebisch Gmuend–Strassdorf	0.89	0.85	0.60	0.50	0.91	0.5	0.4
7	Stoetten	0.98	0.98	0.30	0.20	0.94	1.4	1.4
8	Stuttgart–Echterdingen	0.98	0.97	0.30	0.20	0.94	1.5	1.4
9	Stuttgart (Schnarrenberg)	0.98	0.96	0.30	0.30	0.95	1.6	1.5

ancy in temperature and precipitation model performance is unsurprising, since the thermodynamics and atmospheric dynamics controlling precipitation variability are more difficult to represent (e.g., Shepherd, 2014). Regardless, the overall performance speaks in favor of applying the study's approach to downscale midlatitude climate in complex terrain. Moreover, the models' similar performance during CV and the final evaluation indicates that the models were not overfitted and that the predictand–predictor relationships hold outside the observed period. Finally, it is worth noting that the stacking regressor performed better than the individual base models, even when all the potential regressors of the initial experiments (Sect. 4.2) were stacked into a meta-regressor. Such improvements demonstrate the advantage of the ease of experimentation through a package like pyESD.

We visualize a prediction example (Fig. 6) to (a) provide a less abstract presentation of these results and (b) demonstrate

the type of figure generated by the plotting utility functions in the *pyESD.plot* module. The figure depicts the predictions generated by the final ESD model for the Hechingen station, a station that records precipitation and temperature (station ID 7 and 1, respectively). The observed and predicted values for 2011–2020 are highly correlated, with PCCs of 0.85 (Fig. 6a) for precipitation and 0.97 (Fig. 6b) for temperature. The time series comparisons also demonstrate the models' abilities to predict the variability of the observed values in both the training and testing period (Fig. 6a and b). Prior to this study, PP-ESD models had not been directly applied to the weather stations in the catchment. However, our models are among the best performing for temperature and precipitation when we compare them to models from other studies across Europe (e.g., Gutiérrez et al., 2019; Hertig et al., 2019; Schmidli et al., 2007). For instance, Gutiérrez et al. (2019) performed an intercomparison of statistical down-

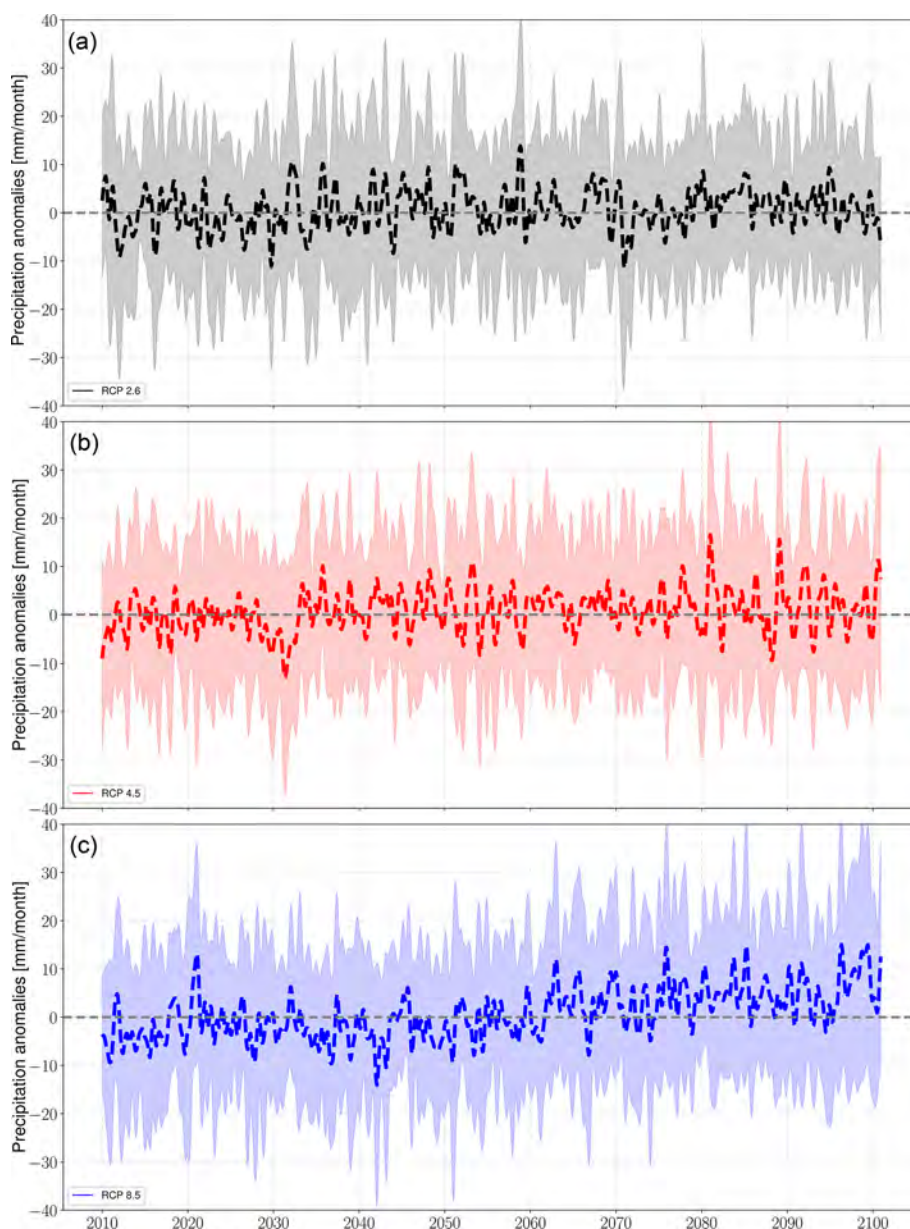


**Figure 7.** Predicted regional annual means of precipitation in response to (a) RCP2.6 (black), (b) RCP4.5 (red), and (c) RCP8.5 (blue). The solid lines represent the values averaged over all stations, and the shaded boundaries indicate the corresponding variability range (1 standard deviation). The time series are smoothed with a 1-year moving average with a centered mean.

scaling model performance for 86 stations across Europe using the MOS, PP, and WG methods. The Spearman correlation of the downscaled and observed values yielded  $R$  values in the range of  $\sim 0.0$ – $0.7$  (with many stations  $\leq 0.5$ ) for precipitation and  $0.3$ – $0.95$  for temperature. These comparisons also underline the suitability of the pyESD methods for downscaling climate information even in complex mountainous regions.

#### 4.4 Prediction of local responses to 21st century climate change

The predictions of local precipitation and temperature responses to 21st century climate change were generated by coupling the final ESD models to MPI-ESM simulations forced with greenhouse gas concentration scenarios RCP2.6, RCP4.5, and RCP8.5 (Sect. 3.2.3). The results are presented as deviations from the monthly long-term means of the training period (1958–2010) and referred to as “anomalies” hereafter. The annual mean anomaly time series were computed

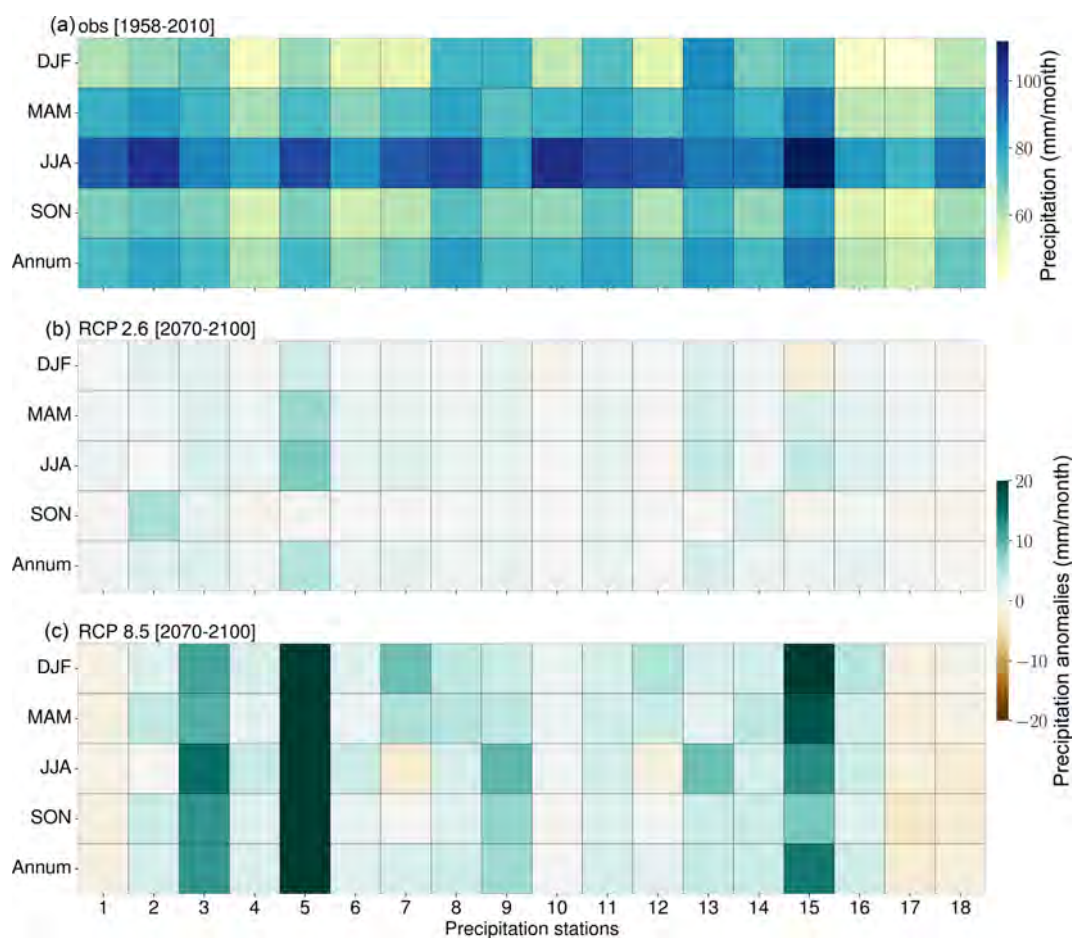


**Figure 8.** (a) Observed precipitation (1958–2100) as well as seasonal (i.e., spring – MAM, summer – JJA, autumn – SON, and winter – DJF) and annual end-of-century (30-year) precipitation climatologies as a result of RCP2.6 (b) and RCP8.5 (c) forcing. Brown (green) indicates a decrease (increase) in precipitation relative to the observed means (1958–2010).

with a 1-year moving average with a centered mean (Figs. 7 and 9).

The precipitation predictions (Fig. 7) for RCP8.5 (RCP4.5) show a strong (weak) positive trend towards the end of the century. This trend is even more pronounced for the predicted temperatures (Fig. 9) in the catchment. The predicted precipitation changes vary greatly between weather stations. Furthermore, the RCPs change the magnitude but not the pattern of the predictions for each station. For instance, stations that show an increase (decrease) in precipitation for the RCP2.6 predict a greater increase (decrease) in response to RCP4.5 and RCP8.5. The annual and seasonal 30-year end-of-century climatologies show an overall increase in precipitation in response to both RCP2.6 and RCP4.5 (Fig. 8) for most of the stations. The annual end-of-century climatologies deviate from the present day (1958–2010) by ca.  $-5$  to  $20$  mm per month for RCP8.5 and ca.  $\leq 5$  mm per month for RCP2.6. Overall, the ESD models predict a precipitation increase of ca.  $10\%$ – $20\%$  until the end of the century. Furthermore, the seasonal climatologies reveal a

shift of maximum precipitation away from the summer season for some stations. Such shifts in seasonality and an overall decrease in summer precipitation have previously been predicted (e.g., Gobiet et al., 2014; Paparrizos et al., 2017; Feldmann et al., 2013). Prior to this study, no ESD–GCM-based predictions of the 21st century precipitation changes had been developed for the weather stations of the catchment. However, the models' predictions of the precipitation response to higher greenhouse gas concentration scenarios are comparable to coarser predictions by other studies using RCMs or ESD models (Feldmann et al., 2013; Kunstmann et al., 2004; Paparrizos et al., 2017; Lau et al., 2013). The precipitation predictions generated in this case study can be used further for climate impact assessments, such as assessments of the probability of flooding and drought across the hydrological catchment. The projected shifts in seasonality across the catchment represents potentially valuable information for agricultural planning.

The predicted temperature anomalies (Fig. 9) reveal a strong (weak) positive trend for RCP8.5 (RCP4.5). The end-



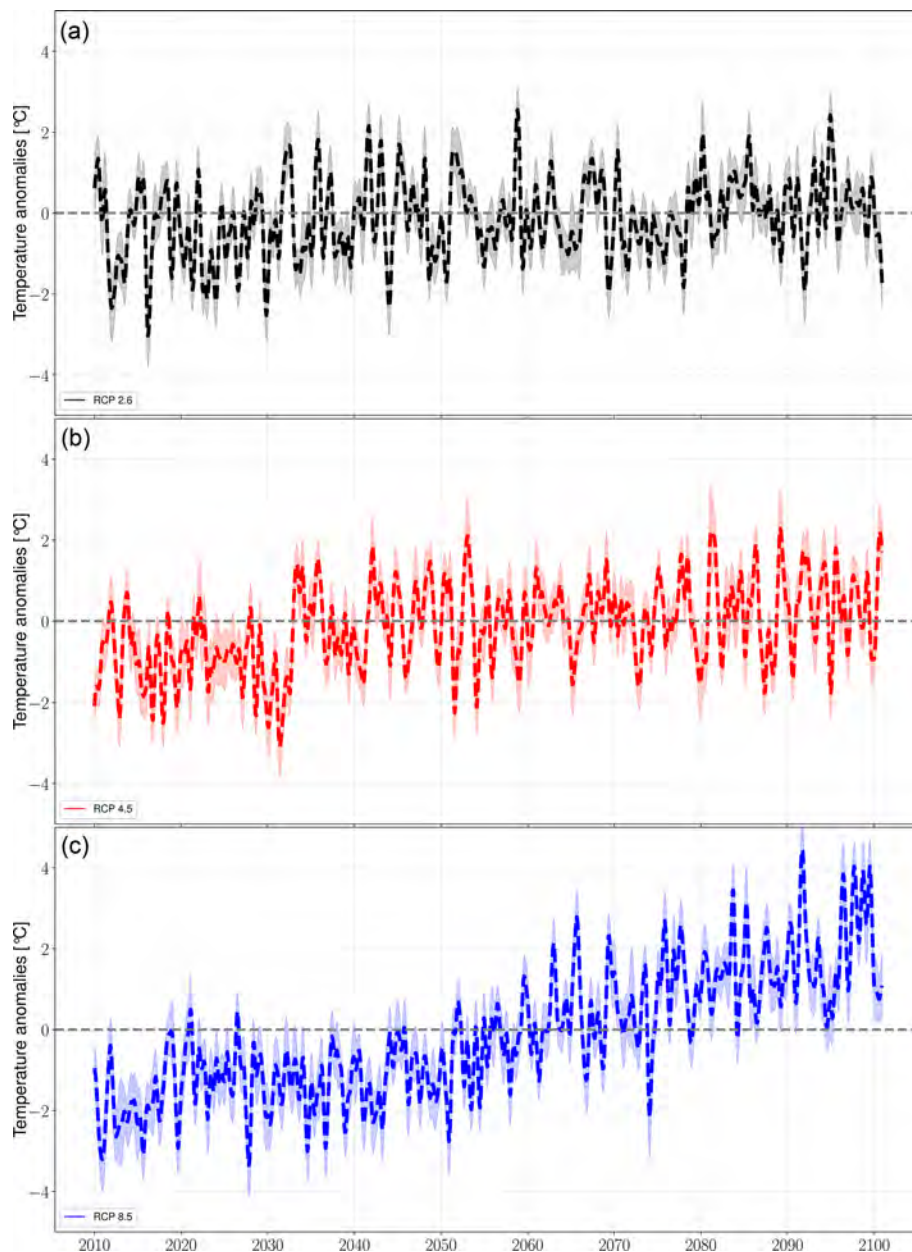


**Figure 9.** Predicted regional annual means of the temperature in response to (a) RCP2.6 (black), (b) RCP4.5 (red), and (c) RCP8.5 (blue). The solid lines represent the values averaged over all stations, and the shaded boundaries indicate the corresponding variability range (1 standard deviation). The time series are smoothed with a 1-year moving average with a centered mean.

of-century climatologies reveal only moderate warming of ca.  $-0.5$  to  $1$  °C for RCP2.6 and significant warming (ca.  $2$ – $4$  °C) for all seasons in response to RCP8.5 (Fig. 10). More specifically, the investigated region is predicted to experience the most warming ( $\geq 3$  °C) in the summer season. There are few differences in predicted warming between the stations of the catchment. Generally, the estimated magnitude of warming towards the end of the century is in agreement with the IPCC report (IPCC, 2021) and other downscaled estimates (e.g., Kunstmann et al., 2004; Gutiérrez et al., 2019). The

predicted warming would likely implicate societal and ecological systems and stresses the need for efficient adaptation and mitigation strategies.

The case study highlights the efficiency and robustness of the downscaling steps implemented in the pyESD package. However, as noted in previous sections, the accuracy of the predictions generated by a GCM–ESD model coupling relies on the predictors being adequately represented by the GCMs. KS tests were performed to evaluate this for the temporal overlap (1979–2000) between the ERA5 reanalysis

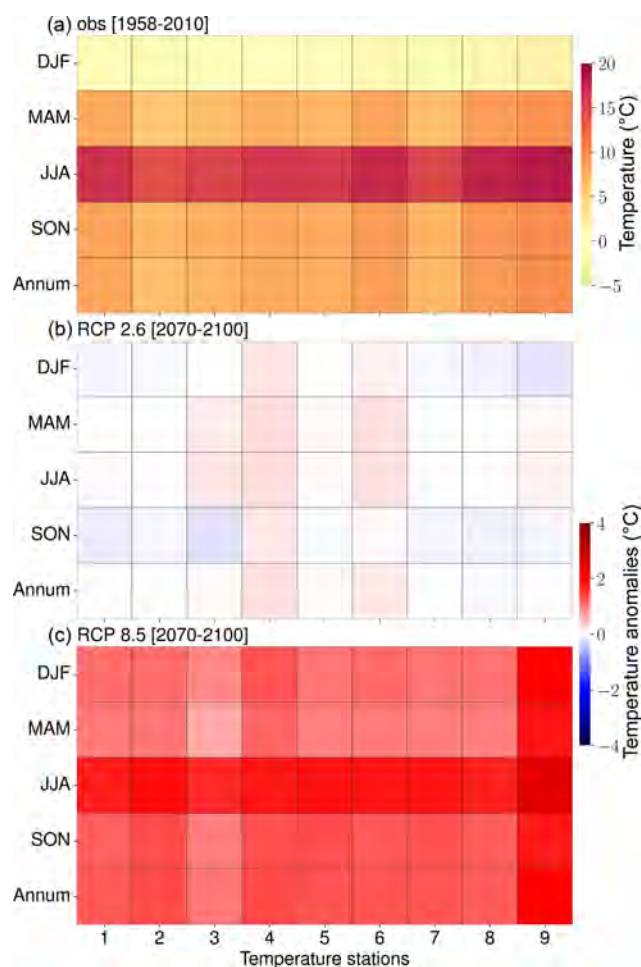


**Figure 10.** (a) Observed temperature (1958–2100) as well as seasonal (i.e., spring – MAM, summer – JJA, autumn – SON, and winter – DJF) and annual end-of-century (30-year) temperature climatologies as a result of RCP2.6 (b) and RCP8.5 (c) forcing. Blue (red) indicates a decrease (increase) in temperature relative to the observed means (1958–2010).

product and the MPI-ESM GCM output (Sect. 3.2.3). Results from these tests show significant differences in the distribution of ERA5 and MPI-ESM when the raw monthly time series are considered, thus violating the assumptions of the PP-ESD approach. However, this issue does not persist for monthly standardized anomalies of precipitation and temperature (Fig. 11). Previous studies yielded similar results when using seasonal standardizers (Bedia et al., 2020) and principal component transformations (Benestad et al., 2015a), both of which are included in the pyESD package.

#### 4.5 Comparison of GCM and ESD-based predictions

A comparison of the ESD-generated annual 20-year climatologies for the mid-century (2040–2060) and the end of the century (2080–2100) to the model output of GCMs and RCMs (i.e., EURO-CORDEX) reveals several differences.

The GCMs (MPI-ESM and HadGEM2) predict  $\sim 20$  mm per month ( $\sim 30\%$ ) higher precipitation rates than the ESD models and RCMs. The ESD-based precipitation predictions of this study are closest to the RCM estimates but  $\sim \geq 5$  mm per month higher in magnitude for most of the stations (Fig. 12). The closeness of the ESD-based and RCM-based estimates underlines the added value of our ESD approach for downscaling precipitation. However, there are significant ( $\sim 4^\circ\text{C}$ ) differences between the ESD-based and RCM-based temperature estimates (Fig. 13). The ESD-based temperature predictions were higher than those of the RCM but lower than those of the GCM. Both the RCM and ESD models used boundary conditions from the same GCM (MPI-ESM). The RCM reduced the GCM temperatures by more ( $\sim 8^\circ\text{C}$ ) than the ESD models ( $\sim 4^\circ\text{C}$  or less). This may be a reflection of both (a) the selection of GCM near-surface temperatures as predictors in the ESD models and (b) the shrinking of regression coefficients when the ESD transfer functions are determined.

## 5 Summary and conclusion

Contemporary climate change and its impacts increase the demand for high-resolution, regional- and local-scale predictions. These can be generated in a most cost-effective way through the application of the PP-ESD (perfect prognosis empirical-statistical downscaling) approach. The pyESD Python package we introduce here is a well-developed tool and modeling framework for applying and experimenting with PP-ESD for any climate variable (e.g., precipitation, wind speed, and temperature). The package complements existing tools through the following key specialties and strengths.

1. The package is well-structured and designed in OOP style that treats the weather stations as objects with many functionality attributes that cover all the PP-ESD modeling routines. As a result, all modeling steps can be executed on the initialized station objects with a few lines of code.
2. The package is designed in a way that knowing its API (Application Programming Interface), which is introduced in the package's extensive documentation, is sufficient to implement all downscaling steps. In other words, no advanced knowledge of Python (or programming) is required to use the package for research purposes. On the other hand, the package's design is modular and flexible enough to allow advanced users to build on it or adjust it to their needs.
3. The package implements different predictor selection techniques (i.e., recursive, tree-based, and sequential) that can be manually selected and experimented with. The package allows the user to include a variety of

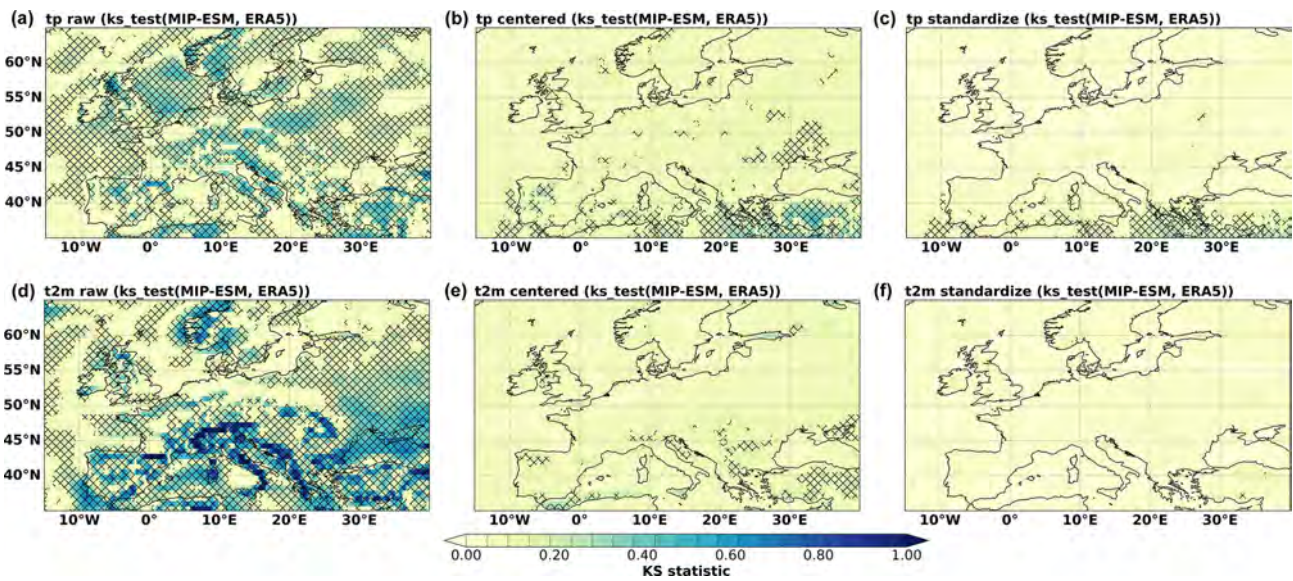


**Figure 11.** The KS two-sided statistical testing score maps the ERA5 reanalysis product and MPI-ESM GCM output for precipitation (a–c) and temperature (d–f). The KS test was applied to raw values, anomalies (centered with zero means), and standardized anomalies with unit variance values (columns from left to right, respectively). The grid boxes with black cross stippling represent low  $p$  values ( $p < 0.05$ ), suggesting statistically significant differences in distribution between the ERA5 and MPI-ESM time series.

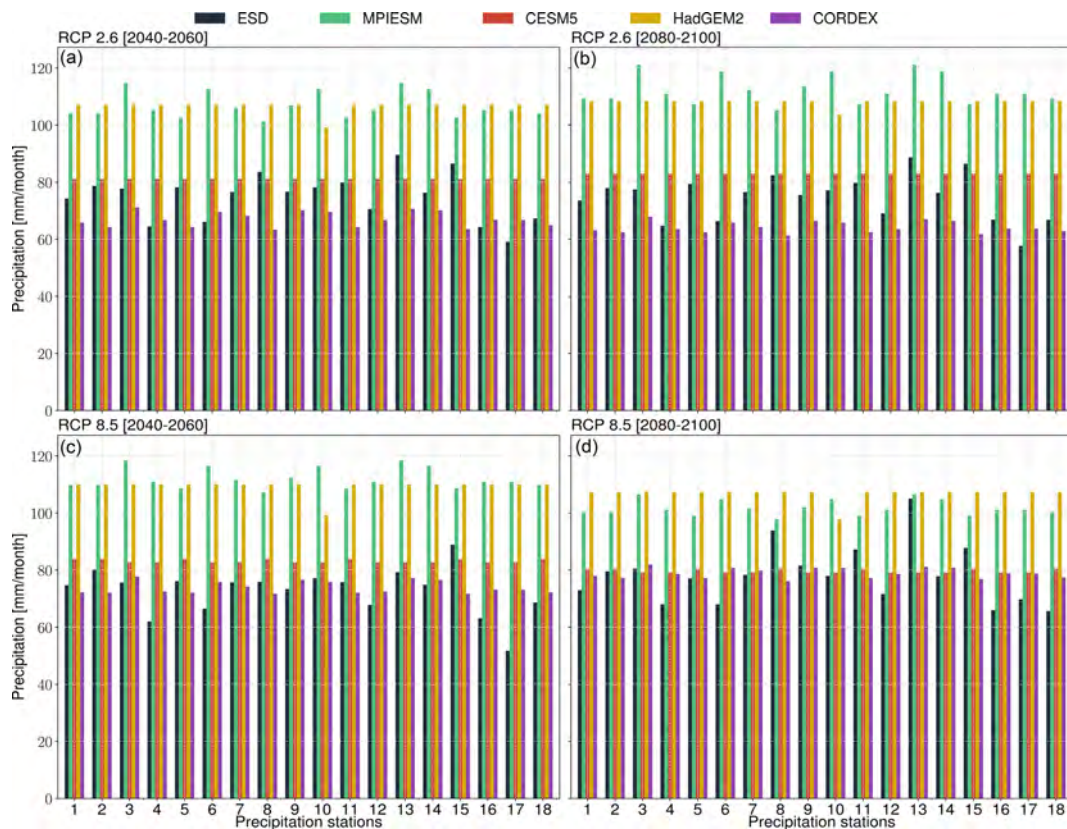


**Figure 12.** Comparison of 20-year annual precipitation climatologies predicted by the ESD models of this study (black), GCMs (i.e., MPI-ESM in green, CESM5 in red, HadGEM2 in gold), and RCMs (i.e., and CORDEX in purple) for RCP2.6 (a, b) and RCP8.5 (c, d).

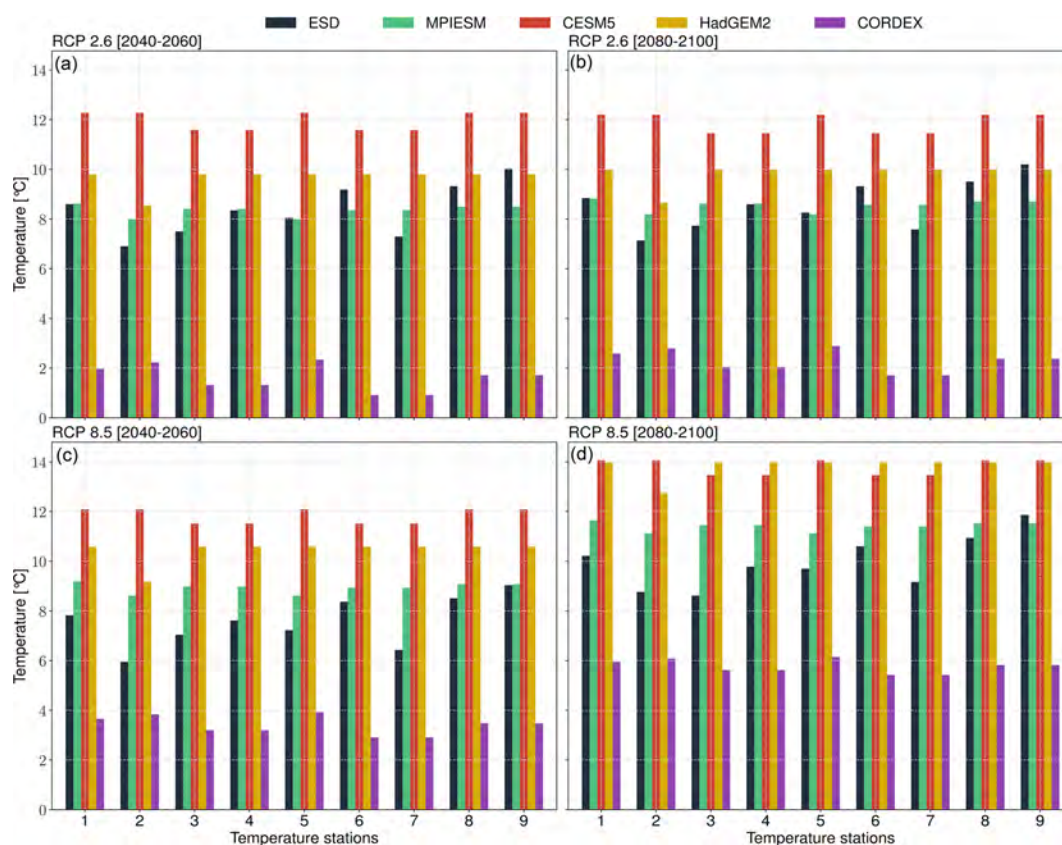


**Figure 13.** Comparison of 20-year annual temperature climatologies predicted by the ESD models of this study (black), GCMs (i.e., MPI-ESM in green, CESM5 in red, HadGEM2 in gold), and RCMs (i.e., and CORDEX in purple) for RCP2.6 (a, b) and RCP8.5 (c, d).

predictors, ranging from regional near-surface temperatures to synoptic-scale teleconnection patterns. The package features many transformation techniques such as *MonthlyStandardizer* and *PCAScaling* that can be used to reduce biases towards specific predictors.

4. The package includes a variety of machine learning techniques with different underlying principles and theorems. The package also features many ensemble models (Sect. 2.3), cross-validation schemes, and hyperparameter optimization techniques that can easily be experimented with in a few lines of code.
5. The package's core modules are accompanied by utility functions for data preprocessing, post-processing, and serialization to save computational resources, as well as visualization tools and ESD-relevant statistical methods like EOF analysis, correlation, and distribution similarity tests.

We demonstrated some of the package's functionalities by developing and applying ESD models to generate precipitation and temperature predictions for a sub-hydrological catchment in complex mountainous terrain in southwestern Germany. The models were evaluated with different metrics

and were found to perform well (e.g.,  $R^2 \geq 0.7$  for precipitation and  $R^2 \geq 0.9$  for temperature). In order to ensure the reproducibility of the results and allow easy practical entry for potential users, the application example uses publicly available datasets, and all the scripts used for this study are made available.

Despite the promising results of the illustrative case study, the reader is informed of the following important limitations: generally, the PP-ESD approach to predictions relies on the assumption that the empirical relationships between predictor and predictand remain valid through time. While statistical downscaling models have successfully been used for the past climate of the pre-industrial era (Reichert et al., 1999) and Last Glacial Maximum (Vrac et al., 2007), the merit of this assumption must be evaluated on a case-by-case basis. For example, geographical boundary conditions that affect the local climate, such as topography or vegetation cover, are only implicitly considered in the empirical transfer functions. The empirical relationship between predictors and predictands may break down if these boundary conditions change significantly (e.g., Mutz and Aschauer, 2022). Furthermore, the performance of PP-ESD models also depends on the accuracy of the GCMs they are coupled to. In our case study, the developed ESD models were coupled to a single, albeit

well-established, GCM (MPI-ESM). However, we generally recommend the use of GCM ensembles to prevent biases towards a specific GCM.

The current version of the package includes all functions needed to develop, evaluate, and apply station-based ESD models and generate predictions of local-scale climate change. Nevertheless, the package remains under active development to expand upon its functionality. Planned improvements include an extension of functions to make pyESD suitable for downscaling gridded datasets or satellite observations. The grid-based analysis would contribute to the design of spatial downscaling models (e.g., Chen et al., 2012; Jia et al., 2011). Moreover, we intend to expand the selection of machine learning techniques by including deep learning models that have been proven useful in downscaling (e.g., Baño-Medina et al., 2020; Quesada-Chacón et al., 2022). Finally, we intend to build a graphical, web-based interface to make the package more accessible and easy to use for researchers, students, and people outside the scientific community.

Appendix A: Supplementary results of the illustrative case study

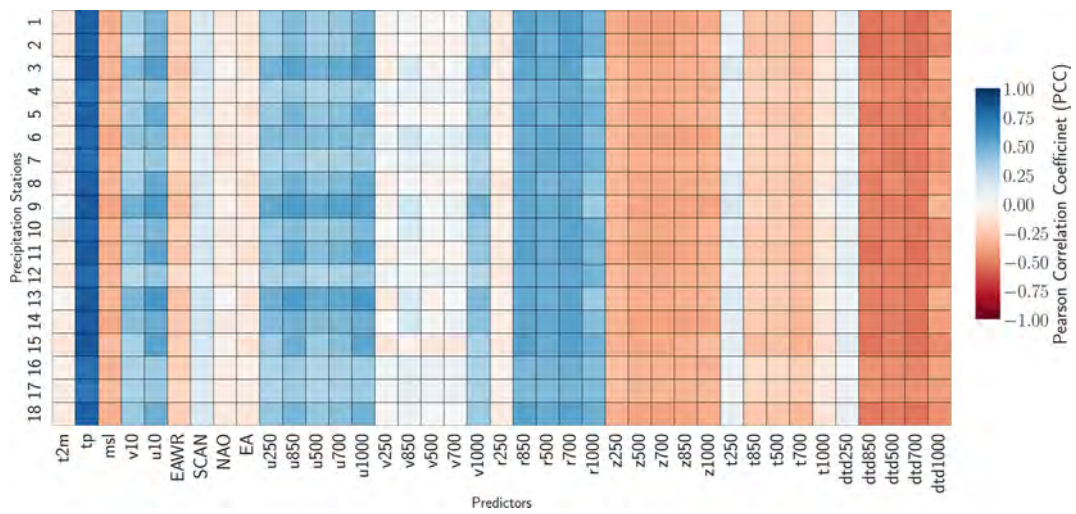


Figure A1. Correlation between the precipitation predictand and the potential predictors listed in Table 2, expressed as PCCs.

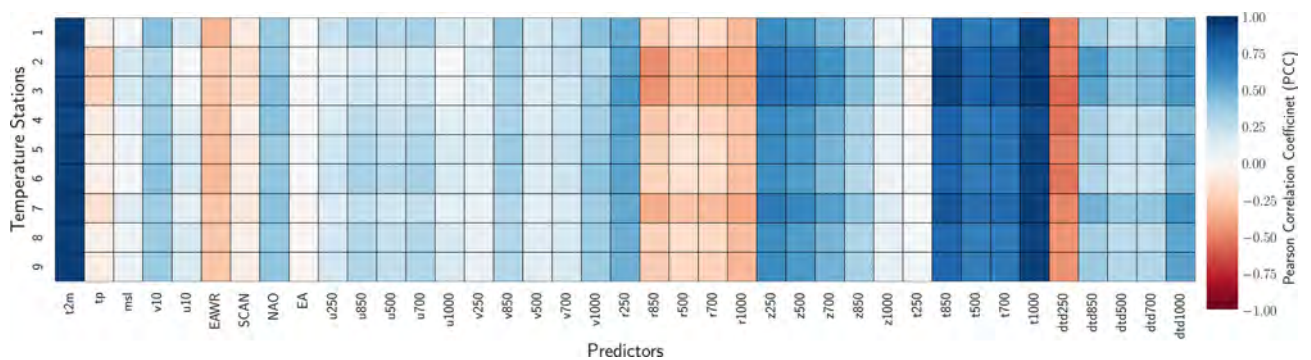
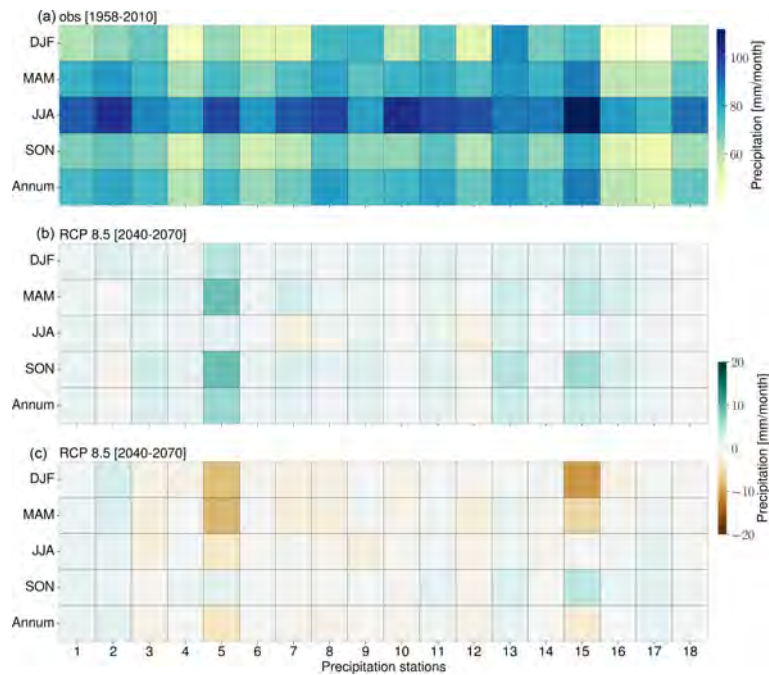
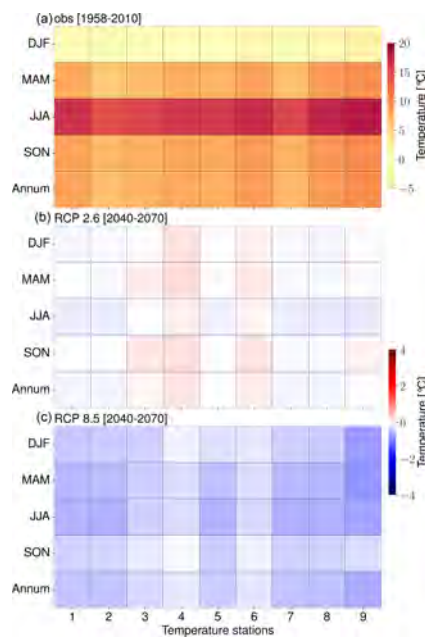


Figure A2. Correlation between the temperature predictand and the potential predictors listed in Table 2, expressed as PCCs.



**Figure A3.** (a) Observed precipitation (1958–2010) as well as seasonal (i.e., spring – MAM, summer – JJA, autumn – SON, and winter – DJF) and annual mid-century (30-year) precipitation climatologies as a result of RCP2.6 (b) and RCP8.5 (c) forcing. Brown (green) indicates a decrease (increase) in precipitation relative to the observed means (1958–2010).



**Figure A4.** Observed temperature (1958–2010) as well as seasonal (i.e., spring – MAM, summer – JJA, autumn – SON, and winter – DJF) and annual mid-century (30-year) temperature climatologies as a result of RCP2.6 (b) and RCP8.5 (c) forcing. Blue (red) indicates a decrease (increase) in temperature relative to the observed means (1958–2010).

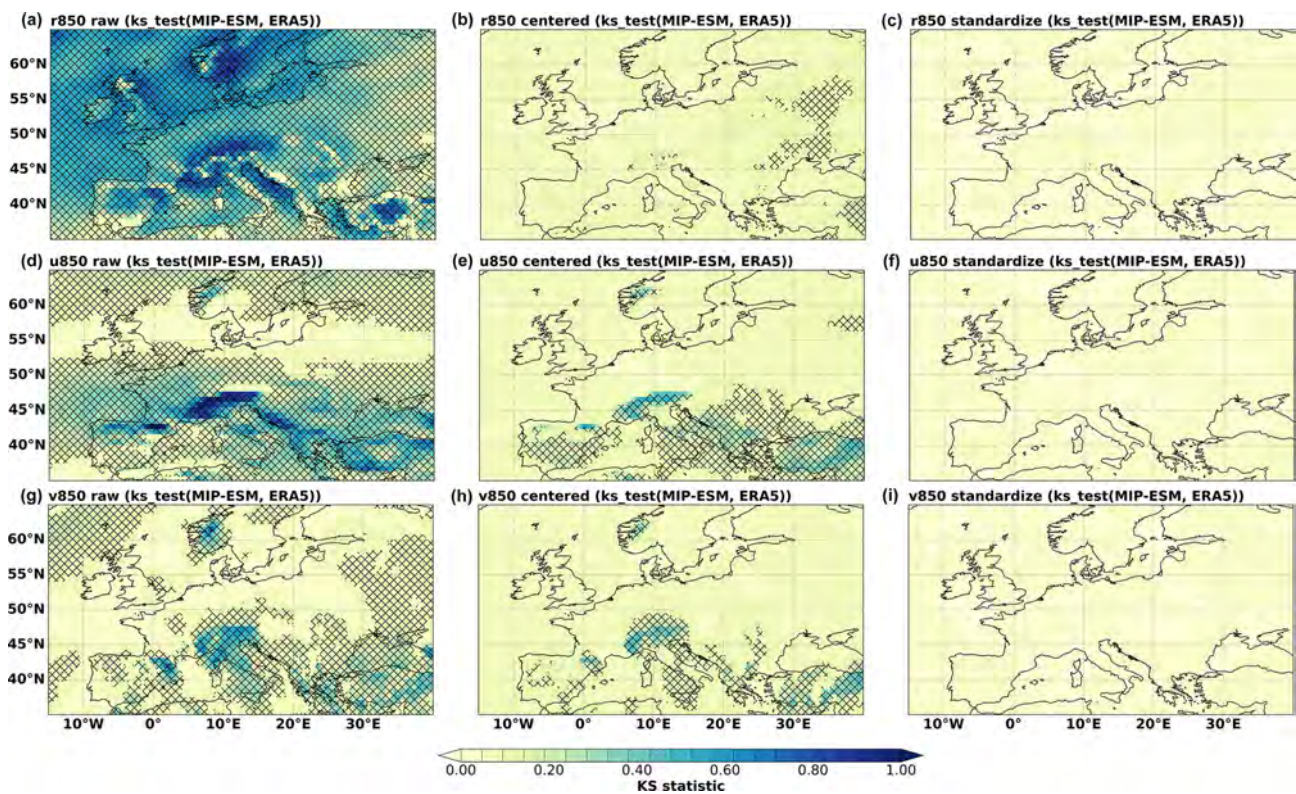


**Figure A5.** The KS two-sided statistical testing score maps the ERA5 reanalysis product and MPI-ESM GCM output for relative humidity (a–c), zonal wind velocity (d–f), and meridional wind velocity (g–i) at 850 hPa. The KS test was applied to raw values, anomalies (centered with zero means), and standardized anomalies with unit variance values (columns from left to right, respectively). The grid boxes with black cross stippling represent low  $p$  values ( $p < 0.05$ ), suggesting statistically significant differences in distribution between the ERA5 and MPI-ESM time series.



*Code and data availability.* The study's illustrative case study relies on publicly available datasets. More specifically, the precipitation and temperature datasets are accessible through the Climate Data Centre of the DWD (Deutscher Wetterdienst, version V21.3). The subcatchment datasets used in this study are interactively available through <https://cdc.dwd.de/portal/shortlink/425267fe-e4fd-4fff-9969-14c7d3aa25de> (Deutscher Wetterdienst, 2023) and <https://cdc.dwd.de/portal/shortlink/da6f555d-d6f6-426a-a8ba-b96683c76ea9> (last access: 30 October 2023) for precipitation and temperature stations, respectively. The ERA5 reanalysis datasets can also be downloaded through the Copernicus Climate Data Store (CDS) at <https://doi.org/10.24381/cds.6860a573> (Hersbach et al., 2023) for pressure level and <https://doi.org/10.24381/cds.68d2bb30> (Muñoz Sabater, 2019) for surface-level variables. However, the processed weather stations and the serialized pickle files of the regional means of the predictors for all the stations are provided as part of the supporting material (<https://doi.org/10.5281/zenodo.7767681>, Boateng and Mutz, 2023). The MPI-ESM GCM datasets used as simulated predictors can also be downloaded from the CDS by selecting MPI-ESM-LR as the model for the AMIP as well as the RCP2.6, 4.5, and 8.5 experiments: see <https://doi.org/10.24381/cds.3b4b5bc9> (Copernicus Climate Change Service, Climate Data Store, 2018a) for pressure-level variables and <https://doi.org/10.24381/cds.9d44a987> (Copernicus Climate Change Service, Climate Data Store, 2018b) for surface variables. Moreover, the station-based downscaling estimates of future climate scenarios for all the stations are also included in the supporting material (<https://doi.org/10.5281/zenodo.7767681>, Boateng and Mutz, 2023).

The pyESD (version 1.0.1) software, including the documentation website source files, is available through many platforms, including the following.

- GitHub: <https://github.com/Dan-Boat/PyESD> (last access: 30 October 2023)
- Python package index (PyPI): <https://pypi.org/project/PyESD/> (last access: 30 October 2023)
- Zenodo (v1.0.1 release): <https://doi.org/10.5281/zenodo.7767629> (Boateng, 2023)

Developer: Daniel Boateng, University of Tübingen

Hardware requirements: general-purpose computer

Programming language: Python (version 3.7 or later)

The installation of the package and its required dependencies are highlighted on the documentation website: <https://dan-boat.github.io/PyESD/> (last access: 30 October 2023). The usage of the package and its functionalities are also presented in the documentation. The control scripts of the study's illustrative case study are also provided as part of the supporting material (<https://doi.org/10.5281/zenodo.7767681>, Boateng and Mutz, 2023) and also presented in the example section of the documentation.

*Author contributions.* DB: pyESD software and documentation website development, conceptualization, modeling, data analysis, visualization, and writing of the original paper. SGM: supervision, paper editing, and funding acquisition.

*Competing interests.* The contact author has declared that neither of the authors has any competing interests.

*Disclaimer.* Publisher's note: Copernicus Publications remains neutral with regard to jurisdictional claims made in the text, published maps, institutional affiliations, or any other geographical representation in this paper. While Copernicus Publications makes every effort to include appropriate place names, the final responsibility lies with the authors.

*Acknowledgements.* This study was partially supported by the German Science Foundation (DFG) under grant nos. MU4188/3-1 and MU4188/1-1, awarded to Sebastian G. Mutz. We acknowledge the World Climate Research Programme, which, through its Working Group on Coupled Modelling, coordinated and promoted CMIP5. We thank the climate modeling groups for producing and making available their model output, the Earth System Grid Federation (ESGF) for archiving the data and providing access, and the multiple funding agencies who support CMIP5 and ESGF. We also thank the European Centre for Medium-Range Weather Forecasts for providing the ERA5 data product and the Deutsche Wetterdienst (DWD) for providing the weather station records. We thank Charles Onyutha and the three anonymous reviewers for their constructive reviews.

*Financial support.* This research has been supported by the Deutsche Forschungsgemeinschaft (grant nos. MU4188/3-1 and MU4188/1-1).

This open-access publication was funded by the University of Tübingen.

*Review statement.* This paper was edited by Charles Onyutha and reviewed by three anonymous referees.

## References

- Anandhi, A., Srinivas, V. V., Nanjundiah, R. S., and Nagesh Kumar, D.: Downscaling precipitation to river basin in India for IPCC SRES scenarios using support vector machine, *Int. J. Climatol.*, 28, 401–420, <https://doi.org/10.1002/joc.1529>, 2008.
- Arlot, S. and Celisse, A.: A survey of cross-validation procedures for model selection, *Stat. Surv.*, 4, 40–79, <https://doi.org/10.1214/09-SS054>, 2010.
- Balasundaram, S. and Tanveer, M.: On Lagrangian twin support vector regression, *Neural Comput. Appl.*, 22, 257–267, 2013.
- Baño-Medina, J., Manzanar, R., and Gutiérrez, J. M.: Configuration and intercomparison of deep learning neural models for statistical downscaling, *Geosci. Model Dev.*, 13, 2109–2124, <https://doi.org/10.5194/gmd-13-2109-2020>, 2020.
- Bárdossy, A.: Atmospheric circulation pattern classification for South-West Germany using hydrological vari-

- ables, *Phys. Chem. Earth Parts A/B/C*, 35, 498–506, <https://doi.org/10.1016/j.pce.2010.02.007>, 2010.
- Barnston, A. G. and Livezey, R. E.: Classification, Seasonality and Persistence of Low-Frequency Atmospheric Circulation Patterns, *Mon. Weather Rev.*, 115, 1083–1126, [https://doi.org/10.1175/1520-0493\(1987\)115<1083:CSAPOL>2.0.CO;2](https://doi.org/10.1175/1520-0493(1987)115<1083:CSAPOL>2.0.CO;2), 1987.
- Bedia, J., Baño-Medina, J., Legasa, M. N., Iturbide, M., Manzanas, R., Herrera, S., Casanueva, A., San-Martín, D., Cofiño, A. S., and Gutiérrez, J. M.: Statistical downscaling with the downscaleR package (v3.1.0): contribution to the VALUE intercomparison experiment, *Geosci. Model Dev.*, 13, 1711–1735, <https://doi.org/10.5194/gmd-13-1711-2020>, 2020.
- Bell, B., Hersbach, H., Simmons, A., Berrisford, P., Dahlgren, P., Horányi, A., Muñoz-Sabater, J., Nicolas, J., Radu, R., Schepers, D., Soci, C., Villaume, S., Bidlot, J.-R., Haimberger, L., Woollen, J., Buontempo, C., and Thépaut, J.-N.: The ERA5 global reanalysis: Preliminary extension to 1950, *Q. J. Roy. Meteor. Soc.*, 147, 4186–4227, <https://doi.org/10.1002/qj.4174>, 2021.
- Benestad, R. E., Chen, D., Mezghani, A., Fan, L., and Parding, K.: On using principal components to represent stations in empirical–statistical downscaling, *Tellus A*, 67, 28326, <https://doi.org/10.3402/tellusa.v67.28326>, 2015a.
- Benestad, R. E., Mezghani, A., and Parding M. K.: “esd” – The Empirical-Statistical Downscaling tool & its visualisation capabilities, *Figshare*, <https://doi.org/10.6084/m9.figshare.1454425.v1>, 2015b.
- Bergmeir, C. and Benítez, J. M.: On the use of cross-validation for time series predictor evaluation, *Inform. Sciences*, 191, 192–213, <https://doi.org/10.1016/j.ins.2011.12.028>, 2012.
- Bergstra, J. and Bengio, Y.: Random search for hyper-parameter optimization, *J. Mach. Learn. Res.*, 13, 281–305, 2012.
- Bergstra, J., Bardenet, R., Bengio, Y., and Kégl, B.: Igorithms for hyper-parameter optimization, in: *Proceedings of the 24th International Conference on Neural Information Processing Systems*, 2546–2554, 2011.
- Bishop, C. M. and Nasrabadi, N. M.: *Pattern recognition and machine learning*, Springer, ISBN 978-1-4939-3843-8, 2006.
- Boateng, D.: Dan-Boat/PyESD: PyESDv1.0.1 (v1.0.1), Zenodo [code], <https://doi.org/10.5281/zenodo.7767629>, 2023.
- Boateng, D. and Mutz, S. G.: Supporting material for PyESDv1.0.1 An open-source Python framework for empirical-statistical downscaling of climate information, Zenodo [data set], <https://doi.org/10.5281/zenodo.7767681>, 2023.
- Boateng, D., Mutz, S. G., Ballian, A., Meijers, M. J. M., Methner, K., Botsyun, S., Mulch, A., and Ehlers, T. A.: The effects of diachronous surface uplift of the European Alps on regional climate and the oxygen isotopic composition of precipitation, *Earth Syst. Dynam. Discuss.* [preprint], <https://doi.org/10.5194/esd-2022-48>, in review, 2022.
- Boé, J., Terray, L., Martin, E., and Habets, F.: Projected changes in components of the hydrological cycle in French river basins during the 21st century, *Water Resour. Res.*, 45, W08426, <https://doi.org/10.1029/2008WR007437>, 2009.
- Bottou, L.: Stochastic gradient learning in neural networks, *Proc. Neuro-Nimes*, 91, <https://leon.bottou.org/publications/pdf/nimes-1991.pdf> (last access 30 October 2023), 1991.
- Bourgault, P., Huard, D., Smith, T. J., Logan, T., Aoun, A., Lavoie, J., Dupuis, É., Rondeau-Genesse, G., Alegre, R., Barnes, C., Laperrière, A. B., Biner, S., Caron, D., Ehbrecht, C., Fyke, J., Keel, T., Labonté, M.-P., Lierhammer, L., Low, J.-F., Quinn, J., Roy, P., Squire, D., Stephens, A., Tanguy, M., and Whelan, C.: xclim: xarray-based climate data analytics, *J. Open Source Softw.*, 8, 5415, <https://doi.org/10.21105/joss.05415>, 2023.
- Brands, S., Gutiérrez, J. M., Herrera, S., and Cofiño, A. S.: On the Use of Reanalysis Data for Downscaling, *J. Climate*, 25, 2517–2526, <https://doi.org/10.1175/JCLI-D-11-00251.1>, 2012.
- Breiman, L.: Bagging predictors, *Mach. Learn.*, 24, 123–140, 1996a.
- Breiman, L.: Stacked regressions, *Mach. Learn.*, 24, 49–64, <https://doi.org/10.1007/BF00117832>, 1996b.
- Breiman, L.: Random forests, *Mach. Learn.*, 45, 5–32, 2001.
- Chaudhuri, A. and Hu, W.: A fast algorithm for computing distance correlation, *Comput. Stat. Data Anal.*, 135, 15–24, <https://doi.org/10.1016/j.csda.2019.01.016>, 2019.
- Chen, J., Brissette, F. P., and Leconte, R.: Coupling statistical and dynamical methods for spatial downscaling of precipitation, *Clim. Change*, 114, 509–526, <https://doi.org/10.1007/s10584-012-0452-2>, 2012.
- Chen, S.-T., Yu, P.-S., and Tang, Y.-H.: Statistical downscaling of daily precipitation using support vector machines and multivariate analysis, *J. Hydrol.*, 385, 13–22, <https://doi.org/10.1016/j.jhydrol.2010.01.021>, 2010.
- Chen, T. and Guestrin, C.: XGBoost: A Scalable Tree Boosting System, in: *Proceedings of the 22nd ACM SIGKDD International Conference on Knowledge Discovery and Data Mining, KDD '16: The 22nd ACM SIGKDD International Conference on Knowledge Discovery and Data Mining, San Francisco California USA*, 785–794, <https://doi.org/10.1145/2939672.2939785>, 2016.
- Chen, X. and Jeong, J. C.: Enhanced recursive feature elimination, in: *Sixth International Conference on Machine Learning and Applications (ICMLA 2007), Sixth International Conference on Machine Learning and Applications (ICMLA 2007)*, 429–435, <https://doi.org/10.1109/ICMLA.2007.35>, 2007.
- Colette, A., Granier, C., Hodnebrog, Ø., Jakobs, H., Maurizi, A., Nyiri, A., Rao, S., Amann, M., Bessagnet, B., D’Angiola, A., Gauss, M., Heyes, C., Klimont, Z., Meleux, F., Memmesheimer, M., Mieville, A., Rouil, L., Russo, F., Schucht, S., Simpson, D., Stordal, F., Tampieri, F., and Vrac, M.: Future air quality in Europe: a multi-model assessment of projected exposure to ozone, *Atmos. Chem. Phys.*, 12, 10613–10630, <https://doi.org/10.5194/acp-12-10613-2012>, 2012.
- Collins, W. J., Bellouin, N., Doutriaux-Boucher, M., Gedney, N., Hinton, T., Jones, C. D., Liddicoat, S., Martin, G., O’Connor, F., and Rae, J.: Evaluation of the HadGEM2 model, *Met Office Exeter, UK*, 2008.
- Copernicus Climate Change Service, Climate Data Store: CMIP5 monthly data on pressure levels, Copernicus Climate Change Service (C3S) Climate Data Store (CDS) [data set], <https://doi.org/10.24381/cds.3b4b5bc9>, 2018a.
- Copernicus Climate Change Service, Climate Data Store: CMIP5 monthly data on single levels, Copernicus Climate Change Service (C3S) Climate Data Store (CDS) [data set], <https://doi.org/10.24381/cds.9d44a987>, 2018b.
- Cristianini, N. and Shawe-Taylor, J.: An introduction to support vector machines and other kernel-

- based learning methods, Cambridge University Press, <https://doi.org/10.1017/CBO9780511801389>, 2000.
- Das, D., Dy, J., Ross, J., Obradovic, Z., and Ganguly, A. R.: Non-parametric Bayesian mixture of sparse regressions with application towards feature selection for statistical downscaling, *Nonlin. Processes Geophys.*, 21, 1145–1157, <https://doi.org/10.5194/npg-21-1145-2014>, 2014.
- Dau, Q. V., Kuntiyawichai, K., and Adeyoye, A. J.: Future Changes in Water Availability Due to Climate Change Projections for Huong Basin, Vietnam, *Environ. Process.*, 8, 77–98, <https://doi.org/10.1007/s40710-020-00475-y>, 2021.
- Deutscher Wetterdienst: Sub-catchment datasets, Deutscher Wetterdienst [data set], <https://cdc.dwd.de/portal/shortlink/da6f555d-d6f6-426a-a8ba-b96683c76ea9>, (last access: 30 October 2023), 2023.
- Diaz, G. I., Fokoue-Nkoutche, A., Nannicini, G., and Samulowitz, H.: An effective algorithm for hyperparameter optimization of neural networks, *IBM J. Res. Develop.*, 61, 9:1–9:11, <https://doi.org/10.1147/JRD.2017.2709578>, 2017.
- Dietterich, T. G.: Ensemble Methods in Machine Learning, in: *Multiple Classifier Systems*, Berlin, Heidelberg, 1–15, [https://doi.org/10.1007/3-540-45014-9\\_1](https://doi.org/10.1007/3-540-45014-9_1), 2000.
- Efron, B., Hastie, T., Johnstone, I., and Tibshirani, R.: Least angle regression, *Ann. Stat.*, 32, 407–499, <https://doi.org/10.1214/009053604000000067>, 2004.
- Errico, R. M., Stensrud, D. J., and Raeder, K. D.: Estimation of the error distributions of precipitation produced by convective parametrization schemes, *Q. J. Roy. Meteor. Soc.*, 127, 2495–2512, 2001.
- Fan, J., Wu, L., Zheng, J., and Zhang, F.: Medium-range forecasting of daily reference evapotranspiration across China using numerical weather prediction outputs downscaled by extreme gradient boosting, *J. Hydrol.*, 601, 126664, <https://doi.org/10.1016/j.jhydrol.2021.126664>, 2021.
- Fealy, R. and Sweeney, J.: Statistical downscaling of precipitation for a selection of sites in Ireland employing a generalised linear modelling approach, *Int. J. Climatol.*, 27, 2083–2094, <https://doi.org/10.1002/joc.1506>, 2007.
- Feldmann, H., Schädler, G., Panitz, H.-J., and Kottmeier, C.: Near future changes of extreme precipitation over complex terrain in Central Europe derived from high resolution RCM ensemble simulations, *Int. J. Climatol.*, 33, 1964–1977, <https://doi.org/10.1002/joc.3564>, 2013.
- Ferri, F. J., Pudil, P., Hatef, M., and Kittler, J.: Comparative study of techniques for large-scale feature selection, in: *Machine Intelligence and Pattern Recognition*, vol. 16, edited by: Gelsema, E. S. and Kanal, L. S., North-Holland, 403–413, <https://doi.org/10.1016/B978-0-444-81892-8.50040-7>, 1994.
- Field, C. B. and Barros, V. R.: *Climate Change 2014 – Impacts, Adaptation and Vulnerability: Regional Aspects*, Cambridge University Press, 695 pp., 2014.
- Freund, Y. and Schapire, R. E.: A Decision-Theoretic Generalization of On-Line Learning and an Application to Boosting, *J. Comput. Syst. Sci.*, 55, 119–139, <https://doi.org/10.1006/jcss.1997.1504>, 1997.
- Friedman, J. H.: Greedy function approximation: a gradient boosting machine, *Ann. Stat.*, 29, 1189–1232, 2001.
- Gardner, M. W. and Dorling, S. R.: Artificial neural networks (the multilayer perceptron) – a review of applications in the atmospheric sciences, *Atmos. Environ.*, 32, 2627–2636, 1998.
- Gareth, J., Daniela, W., Trevor, H., and Robert, T.: An introduction to statistical learning: with applications in R, Springer, <https://doi.org/10.1007/978-1-4614-7138-7>, 2013.
- Geurts, P., Ernst, D., and Wehenkel, L.: Extremely randomized trees, *Mach. Learn.*, 63, 3–42, 2006.
- Ghosh, S. and Mujumdar, P. P.: Statistical downscaling of GCM simulations to streamflow using relevance vector machine, *Adv. Water Resour.*, 31, 132–146, <https://doi.org/10.1016/j.advwatres.2007.07.005>, 2008.
- Giorgi, F. and Mearns, L. O.: Approaches to the simulation of regional climate change: A review, *Rev. Geophys.*, 29, 191–216, <https://doi.org/10.1029/90RG02636>, 1991.
- Gobiet, A., Kotlarski, S., Beniston, M., Heinrich, G., Rajczak, J., and Stoffel, M.: 21st century climate change in the European Alps – A review, *Sci. Total Environ.*, 493, 1138–1151, <https://doi.org/10.1016/j.scitotenv.2013.07.050>, 2014.
- Gu, J., Liu, S., Zhou, Z., Chalov, S. R., and Zhuang, Q.: A Stacking Ensemble Learning Model for Monthly Rainfall Prediction in the Taihu Basin, China, *Water*, 14, 492, <https://doi.org/10.3390/w14030492>, 2022.
- Gutiérrez, J. M., San Martín, D., Cofiño, A. S., Herrera, S., Manzananas, R., and Frías, M. D.: User Guide of the ENSEMBLES Downscaling Portal (version 2), Tech. Rep. 2.2011, Santander Meteorology Group, CSIC-UC, <https://core.ac.uk/download/pdf/36151579.pdf> (last access: 30 October 2023), 2012.
- Gutiérrez, J. M., San-Martín, D., Brands, S., Manzananas, R., and Herrera, S.: Reassessing Statistical Downscaling Techniques for Their Robust Application under Climate Change Conditions, *J. Climate*, 26, 171–188, <https://doi.org/10.1175/JCLI-D-11-00687.1>, 2013.
- Gutiérrez, J. M., Maraun, D., Widmann, M., Huth, R., Hertig, E., Benestad, R., Roessler, O., Wibig, J., Wilcke, R., Kotlarski, S., San Martín, D., Herrera, S., Bedia, J., Casanueva, A., Manzananas, R., Iturbide, M., Vrac, M., Dubrovsky, M., Ribalaygua, J., Pórtoles, J., Rätty, O., Räisänen, J., Hingray, B., Raynaud, D., Casado, M. J., Ramos, P., Zerenner, T., Turco, M., Bosshard, T., Štěpánek, P., Bartholy, J., Pongracz, R., Keller, D. E., Fischer, A. M., Cardoso, R. M., Soares, P. M. M., Czernecki, B., and Pagé, C.: An intercomparison of a large ensemble of statistical downscaling methods over Europe: Results from the VALUE perfect predictor cross-validation experiment, *Int. J. Climatol.*, 39, 3750–3785, <https://doi.org/10.1002/joc.5462>, 2019.
- Hammami, D., Lee, T. S., Ouarda, T. B. M. J., and Lee, J.: Predictor selection for downscaling GCM data with LASSO, *J. Geophys. Res.-Atmos.*, 117, D17116, <https://doi.org/10.1029/2012JD017864>, 2012.
- Hastie, T., Friedman, J., and Tibshirani, R.: *The Elements of Statistical Learning*, Springer New York, New York, NY, <https://doi.org/10.1007/978-0-387-21606-5>, 2001.
- He, X., Chaney, N. W., Schleiss, M., and Sheffield, J.: Spatial downscaling of precipitation using adaptable random forests, *Water Resour. Res.*, 52, 8217–8237, <https://doi.org/10.1002/2016WR019034>, 2016.
- Hecht-Nielsen, R.: Theory of the backpropagation neural network, in: *Neural networks for perception*, Elsevier, 65–93, 1992.

- Hersbach, H., Bell, B., Berrisford, P., Hirahara, S., Horányi, A., Muñoz-Sabater, J., Nicolas, J., Peubey, C., Radu, R., Schepers, D., Simmons, A., Soci, C., Abdalla, S., Abellan, X., Balsamo, G., Bechtold, P., Biavati, G., Bidlot, J., Bonavita, M., De Chiara, G., Dahlgren, P., Dee, D., Diamantakis, M., Dragani, R., Fleming, J., Forbes, R., Fuentes, M., Geer, A., Haimberger, L., Healy, S., Hogan, R. J., Hólm, E., Janisková, M., Keeley, S., Laloyaux, P., Lopez, P., Lupu, C., Radnoti, G., de Rosnay, P., Rozum, I., Vamborg, F., Villaume, S., and Thépaut, J.-N.: The ERA5 global reanalysis, *Q. J. Roy. Meteor. Soc.*, 146, 1999–2049, <https://doi.org/10.1002/qj.3803>, 2020.
- Hersbach, H., Bell, B., Berrisford, P., Biavati, G., Horányi, A., Muñoz Sabater, J., Nicolas, J., Peubey, C., Radu, R., Rozum, I., Schepers, D., Simmons, A., Soci, C., Dee, D., and Thépaut, J.-N.: ERA5 monthly averaged data on pressure levels from 1940 to present, Copernicus Climate Change Service (C3S) Climate Data Store (CDS) [data set], <https://doi.org/10.24381/cds.6860a573>, 2023.
- Hertig, E., Maraun, D., Bartholy, J., Pongracz, R., Vrac, M., Mares, I., Gutiérrez, J. M., Wibig, J., Casanueva, A., and Soares, P. M. M.: Comparison of statistical downscaling methods with respect to extreme events over Europe: Validation results from the perfect predictor experiment of the COST Action VALUE, *Int. J. Climatol.*, 39, 3846–3867, <https://doi.org/10.1002/joc.5469>, 2019.
- Hewitson, B. C., Daron, J., Crane, R. G., Zermoglio, M. F., and Jack, C.: Interrogating empirical-statistical downscaling, *Clim. Change*, 122, 539–554, <https://doi.org/10.1007/s10584-013-1021-z>, 2014.
- Hodgkins, G. A., Whitfield, P. H., Burn, D. H., Hannaford, J., Renard, B., Stahl, K., Fleig, A. K., Madsen, H., Mediero, L., Korhonen, J., Murphy, C., and Wilson, D.: Climate-driven variability in the occurrence of major floods across North America and Europe, *J. Hydrol.*, 552, 704–717, <https://doi.org/10.1016/j.jhydrol.2017.07.027>, 2017.
- Hofmann, T., Schölkopf, B., and Smola, A. J.: Kernel methods in machine learning, *Ann. Stat.*, 36, 1171–1220, <https://doi.org/10.1214/009053607000000677>, 2008.
- Hoyer, S. and Hamman, J.: xarray: N-D labeled Arrays and Datasets in Python, *J. Open Res. Softw.*, 5, 10, <https://doi.org/10.5334/jors.148>, 2017.
- Hurrell, J. W.: Decadal Trends in the North Atlantic Oscillation: Regional Temperatures and Precipitation, *Science*, 269, 676–679, <https://doi.org/10.1126/science.269.5224.676>, 1995.
- Hurrell, J. W. and Van Loon, H.: Decadal Variations in Climate Associated with the North Atlantic Oscillation, in: *Climatic Change at High Elevation Sites*, edited by: Diaz, H. F., Beniston, M., and Bradley, R. S., Springer Netherlands, Dordrecht, 69–94, [https://doi.org/10.1007/978-94-015-8905-5\\_4](https://doi.org/10.1007/978-94-015-8905-5_4), 1997.
- Huth, R.: Statistical downscaling in central Europe: evaluation of methods and potential predictors, *Clim. Res.*, 13, 91–101, <https://doi.org/10.3354/cr013091>, 1999.
- Huth, R.: Sensitivity of Local Daily Temperature Change Estimates to the Selection of Downscaling Models and Predictors, *J. Climate*, 17, 640–652, [https://doi.org/10.1175/1520-0442\(2004\)017<0640:SOLDTC>2.0.CO;2](https://doi.org/10.1175/1520-0442(2004)017<0640:SOLDTC>2.0.CO;2), 2004.
- IPCC: Climate Change 2021: The Physical Science Basis. Contribution of Working Group I to the Sixth Assessment Report of the Intergovernmental Panel on Climate Change, edited by: Masson-Delmotte, V., Zhai, P., Pirani, A., Connors, S. L., Péan, C., Berger, S., Caud, N., Chen, Y., Goldfarb, L., Gomis, M. I., Huang, M., Leitzell, K., Lonnoy, E., Matthews, J. B. R., Maycock, T. K., Waterfield, T., Yelekçi, O., Yu, R., and Zhou, B., Cambridge University Press, Cambridge, United Kingdom and New York, NY, USA, 2391 pp., <https://doi.org/10.1017/9781009157896>, 2021.
- Jakob Themeßl, M., Gobiet, A., and Leuprecht, A.: Empirical-statistical downscaling and error correction of daily precipitation from regional climate models, *Int. J. Climatol.*, 31, 1530–1544, <https://doi.org/10.1002/joc.2168>, 2011.
- Jia, S., Zhu, W., Lú, A., and Yan, T.: A statistical spatial downscaling algorithm of TRMM precipitation based on NDVI and DEM in the Qaidam Basin of China, *Remote Sens. Environ.*, 115, 3069–3079, <https://doi.org/10.1016/j.rse.2011.06.009>, 2011.
- Jordan, M. I. and Mitchell, T. M.: Machine learning: Trends, perspectives, and prospects, *Science*, 349, 255–260, <https://doi.org/10.1126/science.aaa8415>, 2015.
- Kay, J. E., Deser, C., Phillips, A., Mai, A., Hannay, C., Strand, G., Arblaster, J. M., Bates, S. C., Danabasoglu, G., Edwards, J., Holland, M., Kushner, P., Lamarque, J.-F., Lawrence, D., Lindsay, K., Middleton, A., Munoz, E., Neale, R., Oleson, K., Polvani, L., and Vertenstein, M.: The Community Earth System Model (CESM) Large Ensemble Project: A Community Resource for Studying Climate Change in the Presence of Internal Climate Variability, *B. Am. Meteorol. Soc.*, 96, 1333–1349, <https://doi.org/10.1175/BAMS-D-13-00255.1>, 2015.
- Kingma, D. P. and Ba, J.: Adam: A method for stochastic optimization, *arXiv [preprint]*, arXiv:1412.6980, 2014.
- Kunstmann, H., Schneider, K., Forkel, R., and Knoche, R.: Impact analysis of climate change for an Alpine catchment using high resolution dynamic downscaling of ECHAM4 time slices, *Hydrol. Earth Syst. Sci.*, 8, 1031–1045, <https://doi.org/10.5194/hess-8-1031-2004>, 2004.
- Lachenbruch, P. A. and Mickey, M. R.: Estimation of Error Rates in Discriminant Analysis, *Technometrics*, 10, 1–11, <https://doi.org/10.1080/00401706.1968.10490530>, 1968.
- Laflamme, E. M., Linder, E., and Pan, Y.: Statistical downscaling of regional climate model output to achieve projections of precipitation extremes, *Weather Climate Extremes*, 12, 15–23, <https://doi.org/10.1016/j.wace.2015.12.001>, 2016.
- Lau, W. K.-M., Wu, H.-T., and Kim, K.-M.: A canonical response of precipitation characteristics to global warming from CMIP5 models, *Geophys. Res. Lett.*, 40, 3163–3169, <https://doi.org/10.1002/grl.50420>, 2013.
- Leblanc, M. and Tibshirani, R.: Combining Estimates in Regression and Classification, *J. Am. Stat. A.*, 91, 1641–1650, <https://doi.org/10.1080/01621459.1996.10476733>, 1996.
- Li, J., Pollinger, F., and Paeth, H.: Comparing the Lasso Predictor-Selection and Regression Method with Classical Approaches of Precipitation Bias Adjustment in Decadal Climate Predictions, *Mon. Weather Rev.*, 148, 4339–4351, <https://doi.org/10.1175/MWR-D-19-0302.1>, 2020.
- Liu, J., Yuan, D., Zhang, L., Zou, X., and Song, X.: Comparison of Three Statistical Downscaling Methods and Ensemble Downscaling Method Based on Bayesian Model Averaging in Upper Hanjiang River Basin, China, *Adv. Meteorol.*, 2016, e7463963, <https://doi.org/10.1155/2016/7463963>, 2015.

- Lorenz, E. N.: Atmospheric Predictability as Revealed by Naturally Occurring Analogues, *J. Atmos. Sci.*, 26, 636–646, [https://doi.org/10.1175/1520-0469\(1969\)26<636:APARBN>2.0.CO;2](https://doi.org/10.1175/1520-0469(1969)26<636:APARBN>2.0.CO;2), 1969.
- Ludwig, R., Taschner, S., and Mauser, W.: Modelling floods in the Ammer catchment: limitations and challenges with a coupled meteo-hydrological model approach, *Hydrol. Earth Syst. Sci.*, 7, 833–847, <https://doi.org/10.5194/hess-7-833-2003>, 2003.
- MacKay, D. J.: Bayesian interpolation, *Neural Comput.*, 4, 415–447, 1992.
- Maraun, D. and Widmann, M. (Eds.): Structure of Statistical Downscaling Methods, in: *Statistical Downscaling and Bias Correction for Climate Research*, Cambridge University Press, Cambridge, 135–140, <https://doi.org/10.1017/9781107588783.011>, 2018.
- Maraun, D., Wetterhall, F., Ireson, A. M., Chandler, R. E., Kendon, E. J., Widmann, M., Brienen, S., Rust, H. W., Sauter, T., Themeßl, M., Venema, V. K. C., Chun, K. P., Goodess, C. M., Jones, R. G., Onof, C., Vrac, M., and Thiele-Eich, I.: Precipitation downscaling under climate change: Recent developments to bridge the gap between dynamical models and the end user, *Rev. Geophys.*, 48, RG3003, <https://doi.org/10.1029/2009RG000314>, 2010.
- Maraun, D., Huth, R., Gutiérrez, J. M., Martín, D. S., Dubrovsky, M., Fischer, A., Hertig, E., Soares, P. M. M., Bartholy, J., Pongrácz, R., Widmann, M., Casado, M. J., Ramos, P., and Bedia, J.: The VALUE perfect predictor experiment: Evaluation of temporal variability, *Int. J. Climatol.*, 39, 3786–3818, <https://doi.org/10.1002/joc.5222>, 2019a.
- Maraun, D., Widmann, M., and Gutiérrez, J. M.: Statistical downscaling skill under present climate conditions: A synthesis of the VALUE perfect predictor experiment, *Int. J. Climatol.*, 39, 3692–3703, <https://doi.org/10.1002/joc.5877>, 2019b.
- Markatou, M., Tian, H., Biswas, S., and Hripcsak, G. M.: Analysis of variance of cross-validation estimators of the generalization error, *J. Mach. Learn. Res.*, 6, 1127–1168, 2005.
- Marzban, C., Sandgathe, S., and Kalnay, E.: MOS, Perfect Prog, and Reanalysis, *Mon. Weather Rev.*, 134, 657–663, <https://doi.org/10.1175/MWR3088.1>, 2006.
- Massaoudi, M., Refaat, S. S., Chihi, I., Trabelsi, M., Oueslati, F. S., and Abu-Rub, H.: A novel stacked generalization ensemble-based hybrid LGBM-XGB-MLP model for Short-Term Load Forecasting, *Energy*, 214, 118874, <https://doi.org/10.1016/j.energy.2020.118874>, 2021.
- Mearns, L. O., Rosenzweig, C., and Goldberg, R.: The effect of changes in daily and interannual climatic variability on CERES-Wheat: A sensitivity study, *Clim. Change*, 32, 257–292, <https://doi.org/10.1007/BF00142465>, 1996.
- Meinshausen, M., Smith, S. J., Calvin, K., Daniel, J. S., Kainuma, M. L. T., Lamarque, J.-F., Matsumoto, K., Montzka, S. A., Raper, S. C. B., Riahi, K., Thomson, A., Velders, G. J. M., and van Vuuren, D. P. P.: The RCP greenhouse gas concentrations and their extensions from 1765 to 2300, *Clim. Change*, 109, 213, <https://doi.org/10.1007/s10584-011-0156-z>, 2011.
- Miles, J.: R Squared, Adjusted R Squared, in: *Wiley StatsRef: Statistics Reference Online*, John Wiley & Sons, Ltd, <https://doi.org/10.1002/9781118445112.stat06627>, 2014.
- Moore, A. W.: Cross-validation for detecting and preventing overfitting, School of Computer Science Carnegie Mellon University, 133, 2001.
- Moss, R. H., Edmonds, J. A., Hibbard, K. A., Manning, M. R., Rose, S. K., van Vuuren, D. P., Carter, T. R., Emori, S., Kainuma, M., Kram, T., Meehl, G. A., Mitchell, J. F. B., Nakicenovic, N., Riahi, K., Smith, S. J., Stouffer, R. J., Thomson, A. M., Weyant, J. P., and Wilbanks, T. J.: The next generation of scenarios for climate change research and assessment, *Nature*, 463, 747–756, <https://doi.org/10.1038/nature08823>, 2010.
- Muñoz Sabater, J.: ERA5-Land monthly averaged data from 1950 to present, Copernicus Climate Change Service (C3S) Climate Data Store (CDS), <https://doi.org/10.24381/cds.68d2bb30>, 2019.
- Murphy, J.: Predictions of climate change over Europe using statistical and dynamical downscaling techniques, *Int. J. Climatol.*, 20, 489–501, [https://doi.org/10.1002/\(SICI\)1097-0088\(200004\)20:5<489::AID-JOC484>3.0.CO;2-6](https://doi.org/10.1002/(SICI)1097-0088(200004)20:5<489::AID-JOC484>3.0.CO;2-6), 2000.
- Mutz, S., Paeth, H., and Winkler, S.: Modelling of future mass balance changes of Norwegian glaciers by application of a dynamical–statistical model, *Clim. Dynam.*, 46, 1581–1597, <https://doi.org/10.1007/s00382-015-2663-5>, 2016.
- Mutz, S. G. and Aschauer, J.: Empirical glacier mass-balance models for South America, *J. Glaciol.*, 68, 912–926, <https://doi.org/10.1017/jog.2022.6>, 2022.
- Mutz, S. G., Scherrer, S., Muceniece, I., and Ehlers, T. A.: Twenty-first century regional temperature response in Chile based on empirical-statistical downscaling, *Clim. Dynam.*, 56, 2881–2894, <https://doi.org/10.1007/s00382-020-05620-9>, 2021.
- Nash, J. E. and Sutcliffe, J. V.: River flow forecasting through conceptual models part I – A discussion of principles, *J. Hydrol.*, 10, 282–290, [https://doi.org/10.1016/0022-1694\(70\)90255-6](https://doi.org/10.1016/0022-1694(70)90255-6), 1970.
- Neal, R. M.: Bayesian learning for neural networks, Springer Science & Business Media, <https://doi.org/10.1007/978-1-4612-0745-0>, 2012.
- Nourani, V., Razzaghzadeh, Z., Baghanam, A. H., and Molajou, A.: ANN-based statistical downscaling of climatic parameters using decision tree predictor screening method, *Theor. Appl. Climatol.*, 137, 1729–1746, <https://doi.org/10.1007/s00704-018-2686-z>, 2019.
- Onyutha, C.: A hydrological model skill score and revised R-squared, *Hydrol. Res.*, 53, 51–64, <https://doi.org/10.2166/nh.2021.071>, 2021.
- Pachauri, R. K., Allen, M. R., Barros, V. R., Broome, J., Cramer, W., Christ, R., Church, J. A., Clarke, L., Dahe, Q., Dasgupta, P., Dubash, N. K., Edenhofer, O., Elgizouli, I., Field, C. B., Forster, P., Friedlingstein, P., Fuglestad, J., Gomez-Echeverri, L., Hallegatte, S., Hegerl, G., Howden, M., Jiang, K., Jimenez Cisneros, B., Kattsov, V., Lee, H., Mach, K. J., Marotzke, J., Mastrandrea, M. D., Meyer, L., Minx, J., Mulugetta, Y., O'Brien, K., Oppenheimer, M., Pereira, J. J., Pichs-Madruga, R., Plattner, G.-K., Pörtner, H.-O., Power, S. B., Preston, B., Ravindranath, N. H., Reisinger, A., Riahi, K., Rusticucci, M., Scholes, R., Seyboth, K., Sokona, Y., Stavins, R., Stocker, T. F., Tschakert, P., van Vuuren, D., and van Ypersele, J.-P.: Climate Change 2014: Synthesis Report. Contribution of Working Groups I, II and III to the Fifth Assessment Report of the Intergovernmental Panel on Climate Change, edited by: Pachauri, R. K. and Meyer, L., IPCC, Geneva, Switzerland, 151 pp., 2014.
- Padulano, R., Rianna, G., Costabile, P., Costanzo, C., Del Giudice, G., and Mercogliano, P.: Propagation of variability in climate projections within urban flood modelling:

- A multi-purpose impact analysis, *J. Hydrol.*, 602, 126756, <https://doi.org/10.1016/j.jhydrol.2021.126756>, 2021.
- Pal, S. K. and Mitra, S.: Multilayer perceptron, fuzzy sets, classification, *IEEE Trans Neural Netw.*, 3, 683–397, <https://doi.org/10.1109/72.159058>, 1992.
- Pang, B., Yue, J., Zhao, G., and Xu, Z.: Statistical Downscaling of Temperature with the Random Forest Model, *Adv. Meteorol.*, 2017, e7265178, <https://doi.org/10.1155/2017/7265178>, 2017.
- Paparrizos, S., Schindler, D., Potouridis, S., and Matzarakis, A.: Spatio-temporal analysis of present and future precipitation responses over South Germany, *J. Water Clim. Change*, 9, 490–499, <https://doi.org/10.2166/wcc.2017.009>, 2017.
- Pedregosa, F., Varoquaux, G., Gramfort, A., Michel, V., Thirion, B., Grisel, O., Blondel, M., Prettenhofer, P., Weiss, R., Dubourg, V., Vanderplas, J., Passos, A., Cournapeau, D., Brucher, M., Perrot, M., and Duchesnay, É.: Scikit-learn: Machine Learning in Python, *J. Mach. Learn. Res.*, 12, 2825–2830, 2011.
- Polasky, A. D., Evans, J. L., and Fuentes, J. D.: CCdownscaling: A Python package for multivariable statistical climate model downscaling, *Environ. Model. Softw.*, 165, 105712, <https://doi.org/10.1016/j.envsoft.2023.105712>, 2023.
- Pontes, F. J., Amorim, G. F., Balestrassi, P. P., Paiva, A. P., and Ferreira, J. R.: Design of experiments and focused grid search for neural network parameter optimization, *Neurocomputing*, 186, 22–34, <https://doi.org/10.1016/j.neucom.2015.12.061>, 2016.
- Quesada-Chacón, D., Barfus, K., and Bernhofer, C.: Repeatable high-resolution statistical downscaling through deep learning, *Geosci. Model Dev.*, 15, 7353–7370, <https://doi.org/10.5194/gmd-15-7353-2022>, 2022.
- Quinlan, J. R.: Bagging, boosting, and C4.5, in: Proceedings of the thirteenth national conference on Artificial intelligence – Volume 1, Portland, Oregon, 725–730, 1996.
- Raissi, M. and Karniadakis, G. E.: Hidden physics models: Machine learning of nonlinear partial differential equations, *J. Comput. Phys.*, 357, 125–141, <https://doi.org/10.1016/j.jcp.2017.11.039>, 2018.
- Ramon, J., Lledó, L., Bretonnière, P.-A., Samsó, M., and Doblado-Reyes, F. J.: A perfect prognosis downscaling methodology for seasonal prediction of local-scale wind speeds, *Environ. Res. Lett.*, 16, 054010, <https://doi.org/10.1088/1748-9326/abe491>, 2021.
- Reichert, B. K., Bengtsson, L., and Åkesson, O.: A statistical modeling approach for the simulation of local paleoclimatic proxy records using general circulation model output, *J. Geophys. Res.-Atmos.*, 104, 19071–19083, <https://doi.org/10.1029/1999JD900264>, 1999.
- Reid, S. and Grudic, G.: Regularized Linear Models in Stacked Generalization, in: Multiple Classifier Systems, Berlin, Heidelberg, 112–121, [https://doi.org/10.1007/978-3-642-02326-2\\_12](https://doi.org/10.1007/978-3-642-02326-2_12), 2009.
- Rumelhart, D. E., Hinton, G. E., and Williams, R. J.: Learning representations by back-propagating errors, *Nature*, 323, 533–536, 1986.
- Sachindra, D. A., Huang, F., Barton, A., and Perera, B. J. C.: Statistical downscaling of general circulation model outputs to precipitation – part 2: bias-correction and future projections, *Int. J. Climatol.*, 34, 3282–3303, <https://doi.org/10.1002/joc.3915>, 2014.
- Sachindra, D. A., Ahmed, K., Rashid, Md. M., Shahid, S., and Perera, B. J. C.: Statistical downscaling of precipitation using machine learning techniques, *Atmos. Res.*, 212, 240–258, <https://doi.org/10.1016/j.atmosres.2018.05.022>, 2018.
- Santos, M. S., Soares, J. P., Abreu, P. H., Araujo, H., and Santos, J.: Cross-Validation for Imbalanced Datasets: Avoiding Overoptimistic and Overfitting Approaches [Research Frontier], *IEEE Comput. Intell. M.*, 13, 59–76, <https://doi.org/10.1109/MCI.2018.2866730>, 2018.
- Schapire, R. E.: A brief introduction to boosting, in: *Ijcai*, 1401–1406, 1999.
- Schapire, R. E.: The Boosting Approach to Machine Learning: An Overview, in: Nonlinear Estimation and Classification. Lecture Notes in Statistics, edited by: Denison, D. D., Hansen, M. H., Holmes, C. C., Mallick, B., and Yu, B., Springer, New York, NY, vol. 171, [https://doi.org/10.1007/978-0-387-21579-2\\_9](https://doi.org/10.1007/978-0-387-21579-2_9), 2003.
- Schapire, R. E. and Freund, Y.: Boosting: Foundations and algorithms, *Kybernetes*, 42, 164–166, <https://doi.org/10.1108/0368492131129554>, 2013.
- Schmidli, J., Goodess, C. M., Frei, C., Haylock, M. R., Hundscha, Y., Ribalaygua, J., and Schmuth, T.: Statistical and dynamical downscaling of precipitation: An evaluation and comparison of scenarios for the European Alps, *J. Geophys. Res.*, 112, D04105, <https://doi.org/10.1029/2005JD007026>, 2007.
- Selle, B., Rink, K., and Kolditz, O.: Recharge and discharge controls on groundwater travel times and flow paths to production wells for the Ammer catchment in southwestern Germany, *Environ. Earth Sci.*, 69, 443–452, <https://doi.org/10.1007/s12665-013-2333-z>, 2013.
- Shahhosseini, M., Hu, G., and Archontoulis, S. V.: Forecasting Corn Yield With Machine Learning Ensembles, *Front. Plant Sci.*, 11, 1120, <https://doi.org/10.3389/fpls.2020.01120>, 2020.
- Shepherd, T. G.: Atmospheric circulation as a source of uncertainty in climate change projections, *Nat. Geosci.*, 7, 703–708, <https://doi.org/10.1038/ngeo2253>, 2014.
- Snoek, J., Larochelle, H., and Adams, R. P.: Practical bayesian optimization of machine learning algorithms, *Adv. Neur. In.*, 25, 2951–2959, 2012.
- Spuler, F. R., Wessel, J. B., Comyn-Platt, E., Varndell, J., and Cagnazzo, C.: ibicus: a new open-source Python package and comprehensive interface for statistical bias adjustment and evaluation in climate modelling (v1.0.1), *EGU sphere* [preprint], <https://doi.org/10.5194/egusphere-2023-1481>, 2023.
- Stappeler, J., Doms, G., Schättler, U., Bitzer, H. W., Gassmann, A., Damrath, U., and Gregoric, G.: Meso-gamma scale forecasts using the nonhydrostatic model LM, *Meteorol. Atmos. Phys.*, 82, 75–96, <https://doi.org/10.1007/s00703-001-0592-9>, 2003.
- Stone, M.: Cross-Validatory Choice and Assessment of Statistical Predictions (With Discussion), *J. Roy. Stat. Soc. B*, 38, 102–102, <https://doi.org/10.1111/j.2517-6161.1976.tb01573.x>, 1976.
- Storch, H. von and Zwiers, F. W.: *Statistical Analysis in Climate Research*, Cambridge University Press, 995 pp., 2002.
- Sunyer, M. A., Gregersen, I. B., Rosbjerg, D., Madsen, H., Luchner, J., and Arnbjerg-Nielsen, K.: Comparison of different statistical downscaling methods to estimate changes in hourly extreme precipitation using RCM projections from ENSEMBLES, *Int. J. Climatol.*, 35, 2528–2539, <https://doi.org/10.1002/joc.4138>, 2015.
- Székely, G. J., Rizzo, M. L., and Bakirov, N. K.: Measuring and testing dependence by correlation of distances, *Ann. Stat.*, 35, 2769–2794, <https://doi.org/10.1214/009053607000000505>, 2007.

- Tatli, H., Nüzhet Dalfes, H., and Sibel Menteş, Ş.: A statistical downscaling method for monthly total precipitation over Turkey, *Int. J. Climatol.*, 24, 161–180, <https://doi.org/10.1002/joc.997>, 2004.
- Taylor, K. E., Stouffer, R. J., and Meehl, G. A.: An Overview of CMIP5 and the Experiment Design, *B. Am. Meteorol. Soc.*, 93, 485–498, <https://doi.org/10.1175/BAMS-D-11-00094.1>, 2012.
- Tibshirani, R.: Regression Shrinkage and Selection Via the Lasso, *J. Roy. Stat. Soc. B*, 58, 267–288, <https://doi.org/10.1111/j.2517-6161.1996.tb02080.x>, 1996.
- Ting, K. M. and Witten, I. H.: Issues in Stacked Generalization, *J. Artif. Intell. Res.*, 10, 271–289, <https://doi.org/10.1613/jair.594>, 1999.
- Tipping, M. E.: Sparse Bayesian learning and the relevance vector machine, *J. Mach. Learn. Res.*, 1, 211–244, 2001.
- Tripathi, S., Srinivas, V. V., and Nanjundiah, R. S.: Downscaling of precipitation for climate change scenarios: A support vector machine approach, *J. Hydrol.*, 330, 621–640, <https://doi.org/10.1016/j.jhydrol.2006.04.030>, 2006.
- van der Linden, P. and Mitchell, J.: ENSEMBLES: Climate Change and its Impacts: Summary of research and results from the ENSEMBLES project – European Environment Agency (EEA), Tech. rep., Met Office Hadley Centre, FitzRoy Road, Exeter EX1 3PB, UK, <http://www.eea.europa.eu/data-and-maps/indicators/global-and-european-temperature/ensembles-climate-change-and-its> (last access: 30 October 2023), 2009.
- Vapnik, V.: The nature of statistical learning theory, Springer, New York, NY, <https://doi.org/10.1007/978-1-4757-3264-1>, 1999.
- Vrac, M., Marbaix, P., Paillard, D., and Naveau, P.: Non-linear statistical downscaling of present and LGM precipitation and temperatures over Europe, *Clim. Past*, 3, 669–682, <https://doi.org/10.5194/cp-3-669-2007>, 2007.
- Vu, M. T., Aribarg, T., Supratid, S., Raghavan, S. V., and Li-ong, S.-Y.: Statistical downscaling rainfall using artificial neural network: significantly wetter Bangkok?, *Theor. Appl. Climatol.*, 126, 453–467, <https://doi.org/10.1007/s00704-015-1580-1>, 2016.
- Weaver, C. P., Lempert, R. J., Brown, C., Hall, J. A., Revell, D., and Sarewitz, D.: Improving the contribution of climate model information to decision making: the value and demands of robust decision frameworks, *WIREs Clim. Change*, 4, 39–60, <https://doi.org/10.1002/wcc.202>, 2013.
- Wilby, R. L. and Dawson, C. W.: The Statistical DownScaling Model: insights from one decade of application, *Int. J. Climatol.*, 33, 1707–1719, <https://doi.org/10.1002/joc.3544>, 2013.
- Wilby, R. L. and Wigley, T. M. L.: Future changes in the distribution of daily precipitation totals across North America, *Geophys. Res. Lett.*, 29, 39-1–39-4, <https://doi.org/10.1029/2001GL013048>, 2002.
- Wilby, R. L., Wigley, T. M. L., Conway, D., Jones, P. D., Hewitson, B. C., Main, J., and Wilks, D. S.: Statistical downscaling of general circulation model output: A comparison of methods, *Water Resour. Res.*, 34, 2995–3008, <https://doi.org/10.1029/98WR02577>, 1998.
- Wilby, R. L., Dawson, C. W., and Barrow, E. M.: sdsms – a decision support tool for the assessment of regional climate change impacts, *Environ. Model. Softw.*, 17, 145–157, [https://doi.org/10.1016/S1364-8152\(01\)00060-3](https://doi.org/10.1016/S1364-8152(01)00060-3), 2002.
- Wilby, R. L., Charles, S. P., Zorita, E., Timbal, B., Whetton, P., and Mearns, L. O.: Guidelines for use of climate scenarios developed from statistical downscaling methods, Supporting material of the Intergovernmental Panel on Climate Change, available from the DDC of IPCC TG CIA, 27, 2004.
- Wilks, D. S.: Statistical methods in the atmospheric sciences, Academic press, 698 pp., 2011.
- Wipf, D. and Nagarajan, S.: A new view of automatic relevance determination, *Adv. Neur. In.*, 20, 2007.
- Wolpert, D. H.: Stacked generalization, *Neural Networks*, 5, 241–259, [https://doi.org/10.1016/S0893-6080\(05\)80023-1](https://doi.org/10.1016/S0893-6080(05)80023-1), 1992.
- Wu, T. T. and Lange, K.: Coordinate descent algorithms for lasso penalized regression, *Ann. Appl. Stat.*, 2, 224–244, <https://doi.org/10.1214/07-AOAS147>, 2008.
- Xu, R., Chen, N., Chen, Y., and Chen, Z.: Downscaling and Projection of Multi-CMIP5 Precipitation Using Machine Learning Methods in the Upper Han River Basin, *Adv. Meteorol.*, 2020, e8680436, <https://doi.org/10.1155/2020/8680436>, 2020.
- Xu, Z., Han, Y., and Yang, Z.: Dynamical downscaling of regional climate: A review of methods and limitations, *Sci. China Earth Sci.*, 62, 365–375, <https://doi.org/10.1007/s11430-018-9261-5>, 2019.
- Zhang, C. and Ma, Y. (Eds.): Ensemble Machine Learning: Methods and Applications, Springer, New York, NY, <https://doi.org/10.1007/978-1-4419-9326-7>, 2012.
- Zhang, J., Liu, K., and Wang, M.: Downscaling Groundwater Storage Data in China to a 1-km Resolution Using Machine Learning Methods, *Remote Sens.*, 13, 523, <https://doi.org/10.3390/rs13030523>, 2021.
- Zhang, X. and Yan, X.: A new statistical precipitation downscaling method with Bayesian model averaging: a case study in China, *Clim. Dynam.*, 45, 2541–2555, <https://doi.org/10.1007/s00382-015-2491-7>, 2015.
- Zhou, H., Zhang, J., Zhou, Y., Guo, X., and Ma, Y.: A feature selection algorithm of decision tree based on feature weight, *Expert Syst. Appl.*, 164, 113842, <https://doi.org/10.1016/j.eswa.2020.113842>, 2021.
- Zorita, E. and von Storch, H.: The Analog Method as a Simple Statistical Downscaling Technique: Comparison with More Complicated Methods, *J. Climate*, 12, 2474–2489, [https://doi.org/10.1175/1520-0442\(1999\)012<2474:TAMAAS>2.0.CO;2](https://doi.org/10.1175/1520-0442(1999)012<2474:TAMAAS>2.0.CO;2), 1999.





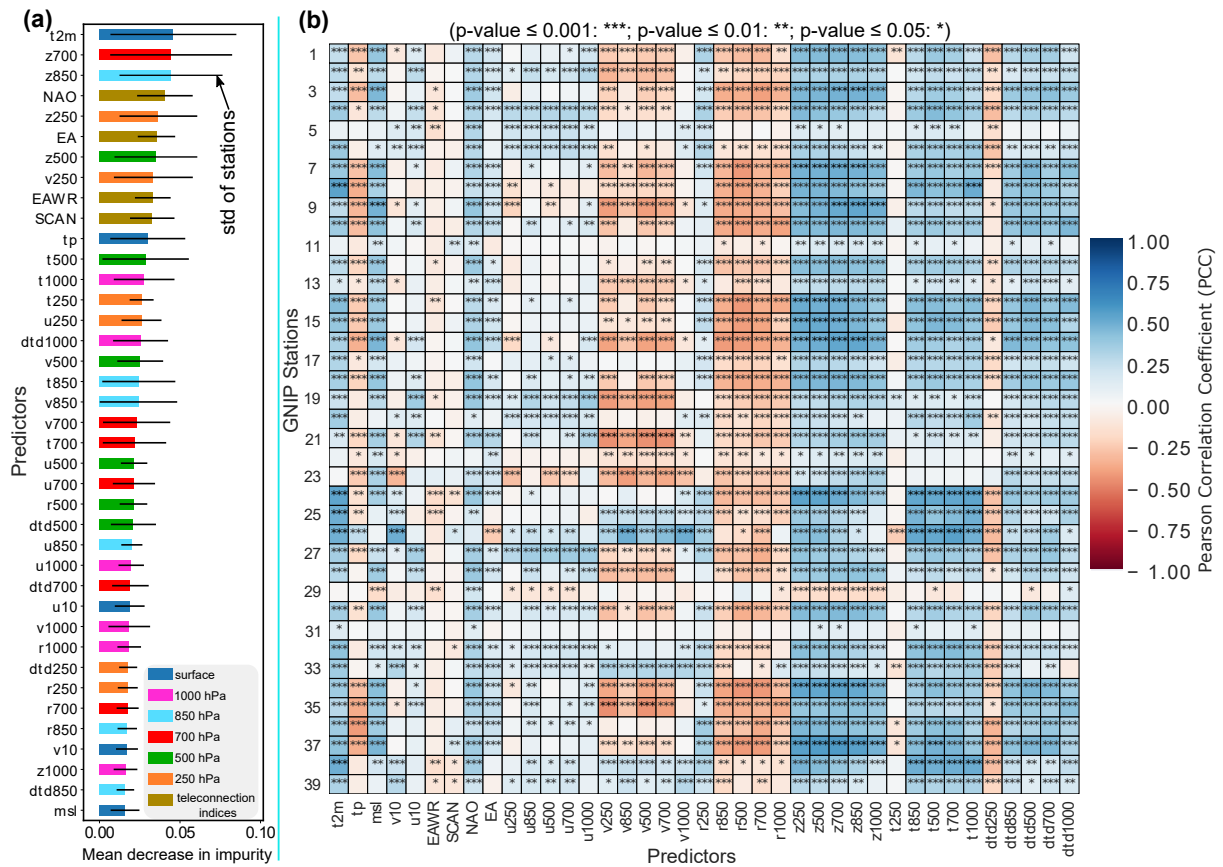


**Figure 2:** Predictor importance distribution for all stations using mean decrease impurity from the Tree-based selection method. From top to bottom, the rank of the predictive skill of the predictors for learning the relationship between the  $\delta^{18}O_p$  values and large-scale predictors is indicated. (b) Correlation between the  $\delta^{18}O_p$  values and the potential predictors selected. See Boateng and Mutz [4] for the details about the predictors' construction

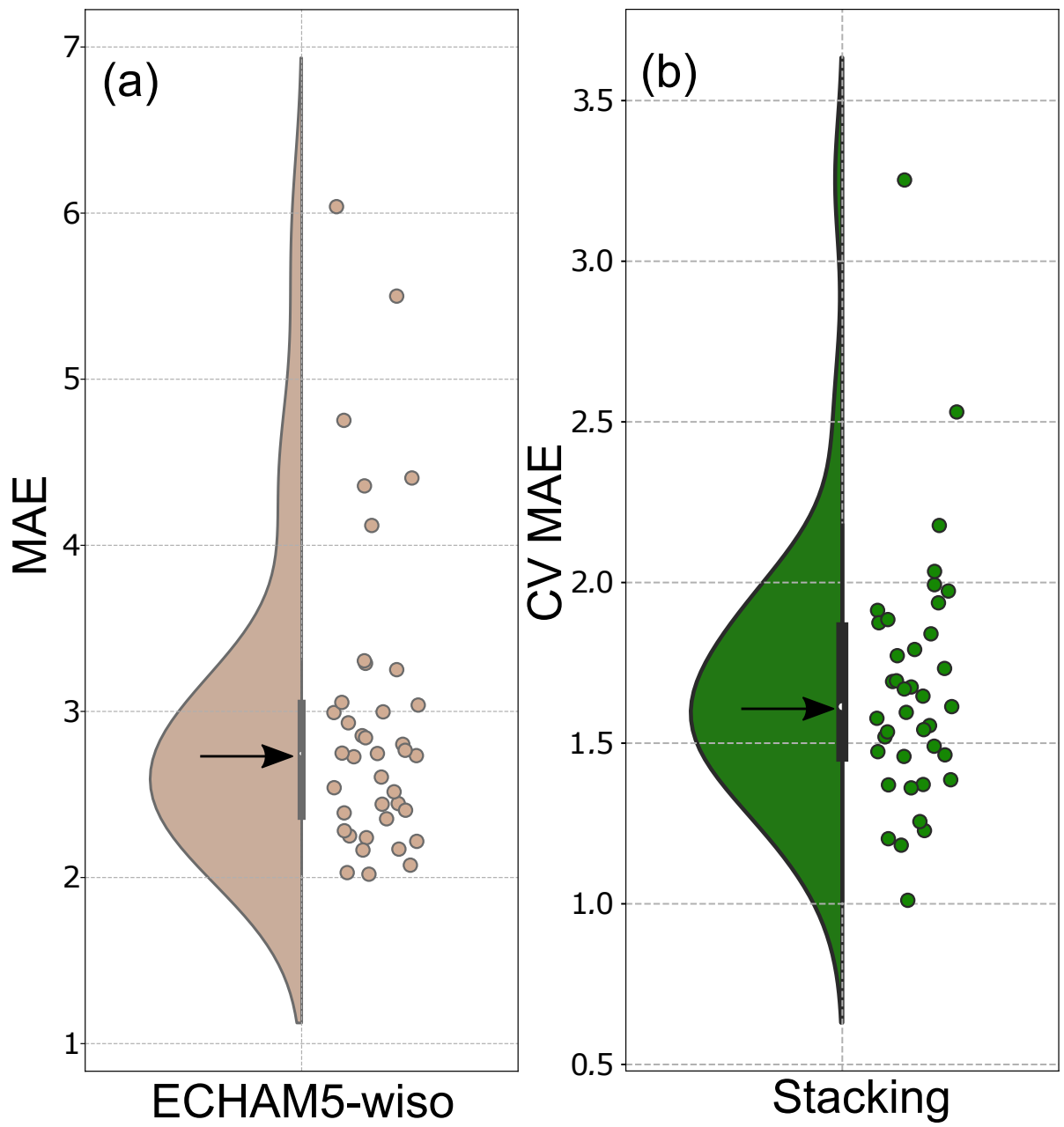


Figure 3: Comparison between the distribution of MAE calculated between the GNIP  $\delta^{18}O_p$  values and predicted values from (a) ECHAM5-wiso and (b) final Stacking regressor model.